Alessandro De Angelis and Mário Pimenta

Introduction to Astroparticle Physics

Multimessenger Astrophysics with a Particle Physics Toolbox

February 25, 2018

Springer

Foreword by Francis Halzen

My generation of particle physicists has been incredibly fortunate. The first paper I ever read was George Zweig's highly speculative CERN preprint on "aces," now called quarks. After an exhilarating ride, from the chaos of particles and resonances of the sixties to the discovery of the Higgs boson that gives them mass, quarks are now routinely featured in standard physics texts along with the levers and pulleys of the first chapter.

My office was one floor below that of Monseigneur Lemaitre; strangely, I only knew of his existence because I used the computer that he had built. That was just before the discovery of the microwave background brought him fame and the juggernaut that is now precision cosmology changed cosmology from boutique science to a discipline pushing the intellectual frontier of physics today.

Over the same decades, the focus of particle physics shifted from cosmic rays to accelerators, returning in the disguise of particle astrophysics with the discovery of neutrino mass in the oscillating atmospheric neutrino beam, the first chink in the armor of the Standard Model.

This triptych of discoveries represents a masterpiece that is also strikingly incomplete – like a Titian painting, only the details are missing, to borrow Pauli's description of Heisenberg's early theory of strong interactions. The mechanism by which the Higgs endows the heaviest quark, the top, with its mass is unstable in the Standard Model. In fact, the nonvanishing neutrino mass directly and unequivocally exposes the incompleteness of the symmetries of the Standard Model of quarks and leptons. Precision cosmology has given birth to a strange Universe of some hydrogen and helium (with traces of the other chemical elements) but mostly dark energy and dark matter. The stars, neutrinos, microwave photons, and supermassive black holes that constitute the rest do not add up to very much. But this is business as usual – deeper insights reveal more fundamental questions whose resolution is more challenging. Their resolution has inspired a plethora of novel and ambitious instrumentation on all fronts.

After decades of development on the detectors, we recently inaugurated the era of multimessenger astronomy for both gravitational waves and high-energy neutrinos. On August 17, 2017, a gravitational wave detected by the LIGO-Virgo interferometers pointed at the merger of a pair of neutron stars that was subsequently scrutinized by astronomical telescopes in all wavelengths of astronomy, from radio waves to gamma rays. Barely a month later, some of the same instruments traced the origin of a IceCube cosmic neutrino of 300 TeV energy to a distant flaring active galaxy.

At the close of the nineteenth century, many physicists believed that physics had been essentially settled – we do not live with that illusion today. Yet, the key is still to focus on the unresolved issues, as was the case then. Based on the size of the Sun and given the rate that it must be contracting to transform gravitational energy into its radiation, Lord Kelvin concluded that the Sun cannot be more than 20-40 million years old. His estimate was correct and directly in conflict with known geology. Moreover, it did not leave sufficient time for Darwin's evolution to run its course. The puzzle was resolved after Becquerel accidentally discovered radioactivity, and Rutherford eventually identified nuclear fusion as the source of the Sun's energy in 1907. The puzzling gap between some ten million and 4.5 billion for the age of the solar system provided the hint of new physics to be discovered at a time when many thought "only the details were missing." Today we are blessed by an abundance of puzzles covering all aspects of particle physics, including the incompleteness of the Standard Model, the origin of neutrino mass, and the perplexing nature of dark matter and dark energy.

This book will inspire and prepare students for the next adventures. As always, the science will proceed with detours, dead ends, false alarms, missed opportunities, and unexpected surprises, but the journey will be exhilarating and progress is guaranteed, as before.

Francis Halzen is the principal investigator of the IceCube project, and Hilldale and Gregory Breit Professor in the department of physics at the University of Wisconsin–Madison.

Preface

This book introduces particle physics, astrophysics and cosmology starting from experiment. It provides a unified view of these fields, which is needed to answer our questions to the Universe–a unified view that has been lost somehow in recent years due to increasing specialization.

This is the second edition of a book we published only three years ago, a book which had a success beyond our expectations. We felt that the recent progress on gravitational waves, gamma-ray and neutrino astrophysics deserved a new edition including all these new developments: multimessenger astronomy is now a reality. In addition, the properties of the Higgs particle are much better known now than three years ago. Thanks to this second edition we had the opportunity to fix some bugs, to extend the material related to exercises, and to change in a more logical form the order of some items. Last but not least, our editor encouraged us a lot to write a second edition.

Particle physics has recently seen the incredible success of the so-called "standard model". A 50-years long search for the missing ingredient of the model, the Higgs particle, has been concluded successfully, and some scientists claim that we are close to the limit of the physics humans may know.

Also astrophysics and cosmology have shown an impressive evolution, driven by experiments and complemented by theories and models. We have nowadays a "standard model of cosmology" which successfully describes the evolution of the Universe from a tiny time after its birth to any foreseeable future. The experimental field of astroparticle physics is rapidly evolving, and its discovery potential appears still enormous: during the three years between the first and the second edition of this book gravitational waves have been detected, an event in which gravitational waves were associated to electromagnetic waves has been detected, and an extragalactic source of astrophysical neutrinos has been located and associated to a gamma-ray emitter.

The situation is similar to the one that physics lived at the end of the nineteenth century, after the formulation of Maxwell's equations – and we know how the story went. As then, there are today some clouds which might hide a new revolution in physics. The main cloud is that experiments indicate that we are still missing the description of the main ingredients of the Universe from the point of view of its energy budget. We believe one of these ingredients to be a new particle, of which we know very little; and the other to be a new form of energy. The same experiments indicating the need for these new ingredients are probably not powerful enough to unveil them, and we must invent new experiments to do it.

The scientists who solve this puzzle will base their project on a unified vision of physics, and this book helps to provide such a vision.

This book is addressed primarily to advanced undergraduate or beginning graduate students, since the reader is only assumed to know quantum physics and "classical" physics, in particular electromagnetism and analytical mechanics, at an introductory level; but it can also be useful for graduates and postgraduates, and postdoc researchers involved in high-energy physics or astrophysics research. It is also aimed at senior particle and astroparticle physicists as a consultation book. Exercises at the end of each chapter help the reader to review material from the chapter itself and synthesize concepts from several chapters. A "further reading" list is also provided for readers who want to explore in more detail particular topics.

Our experience is based on research both at artificial particle accelerators (in our younger years) and in astroparticle physics after the late 1990s. We have worked as professors since more than twenty years, teaching courses on particle and/or astroparticle physics at undergraduate and graduate levels. We spent a long time in several research institutions outside our countries, also teaching there and gaining experience with students with different backgrounds.

This book contains a broad and interdisciplinary material, which is appropriate for a consultation book, but it can be too much for a textbook. In order to give coherence to the material for a course, one can think of at least three paths through the manuscript:

- For an "old-style" one-semester course on particle physics for students with a good mathematical background, one could select chapters 1, 2, 3, 4, 5, 6, part of 7, and possibly (part of) 9.
- For a basic particle physics course centered in astroparticle physics one could instead use chapters 1, 2, 3, 4 (excluding 4.4), 5.1, 5.2, part of 5.4, part of 5.5, 5.6, 5.7, possibly 6.1, 8.1, 8.4, 8.5, part of 10, and if possible 11.
- A one-semester course in high-energy astroparticle physics for students who already know the foundations of particle physics could be based on chapters 1, 3, 4.3.2, 4.5, 4.6, 8, 10, 11; if needed, an introduction to experimental techniques could be given based on 4.1 and 4.2.
- A specialized half-semester course in high-energy astroparticle physics could be based on chapters 4.3.2, 4.5, 4.6, 8.1, 8.4, 8.5, 10; an introduction to experimental techniques could be given based on 4.1 and 4.2 if needed.

Unfortunately we know that several mistakes will affect also this second edition. Readers can find at the web site

http://ipap.uniud.it

a "living" errata corrige, plus some extra material related in particular to the exercises. Please help us to improve the book by making suggestions and corrections: we shall answer all criticisms with gratitude.

Most of all, we thank all our students who patiently listened and discussed with us during all the past years.

Alessandro De Angelis and Mário Pimenta

Lisbon and Padua, 24 February 2018

Contents

About the Authors

Alessandro De Angelis is a high energy physicist and astrophysicist. Professor at the Universities of Udine, Padua and Lisbon, he is currently the Principal Investigator of the proposed space mission e-ASTROGAM and for many years has been director of research at INFN Padua, and scientific coordinator and chairman of the board managing the MAGIC gamma-ray telescopes in the Canary Island of La Palma. His main research interest is on fundamental physics, especially astrophysics and elementary particle physics at accelerators. He graduated from Padua, was employed at CERN for seven years in the 1990s ending as a staff member, and later was among the founding member of NASA's *Fermi* gamma-ray telescope. His original scientific contributions have been mostly related to electromagnetic calorimeters, advanced trigger systems, QCD, artificial neural networks, and to the study of the cosmological propagation of photons. He has taught electromagnetism and astroparticle physics in Italy and Portugal and has been a visiting professor in the ICRR of Tokyo, at the Max-Planck Institute in Munich, and at the University of Paris VI.

Mário Pimenta is a high energy physicist and astrophysicist. Professor at the Instituto Superior Técnico of the University of Lisbon, he is currently the president of the Portuguese national organization for Particle and Astroparticle Physics, coordinator of the international PhD doctoral network IDPASC, and the representative for Portugal at the Pierre Auger Observatory in Argentina. Formerly member of the WA72, WA74, NA38 and DELPHI experiments at CERN and of the EUSO collaboration at ESA, his main interest of research is on high-energy physics, especially cosmic rays of extremely high energy and development of detectors for astroparticle physics. He graduated from Lisbon and Paris VI, and was employed at CERN in the late 1980s. His original contributions have been mostly related to advanced trigger systems, search for new particles, hadronic interactions at extremely high energies, and recently to innovative particle detectors. He has taught general physics and particle physics in Portugal, has lectured at the University of Udine and has been visiting professor at SISSA/ISAS in Trieste.

Chapter 1
Understanding the Universe: Cosmology, Astrophysics, Particles, and their Interactions

Alessandro De Angelis and Mário Pimenta

Cosmology, astrophysics, and the physics of elementary particles and interactions are intimately connected. After reading this chapter, it will be clear that these subjects are part of the same field of investigation: this book will show you some of the connections, and maybe many more you will discover yourself in the future.

1.1 Particle and Astroparticle Physics

The Universe around us, the objects surrounding us, display an enormous diversity. Is this diversity built over small hidden structures? This interrogation started out, as it often happens, as a philosophical question, only to become, several thousand years later, a scientific one. In the sixth and fifth century BC in India and Greece the atomic concept was proposed: matter was formed by small, invisible, indivisible, and eternal particles: the atoms—a word invented by Leucippus (460 BC) and made popular by his disciple Democritos. In the late eighteenth and early nineteenth century, chemistry gave finally to atomism the status of a scientific theory (mass conservation law, Lavoisier 1789; ideal gas laws, Gay-Lussac 1802; multiple proportional law, Dalton 1805), which was strongly reinforced with the establishment of the periodic table of elements by Mendeleev in 1869—the chemical properties of an element depend on a "magic" number, its atomic number.

If atoms did exist, their shape and structure were to be discovered. For Dalton, who lived before the formalization of electromagnetism, atoms had to be able to establish mechanical links with each other. After Maxwell (who formulated the electromagnetic field equations) and J.J. Thomson (who discovered the electron) the binding force was supposed to be the electric one and in atoms an equal number of positive and negative electric charges had to be accommodated in stable configurations. Several solutions were proposed (Fig. 1.1), from the association of small electric dipoles by Philip Lenard (1903) to the Saturnian model of Hantora Nagaoka (1904), where the positive charges were surrounded by the negative ones like the planet Saturn and its rings. In the Anglo-Saxon world the most popular model was, however, the so-called plum pudding model of Thomson (1904), where the negative charges, the electrons, were immersed in a "soup" of positive charges. This model was clearly dismissed by Rutherford, who demonstrated in the beginning of the twentieth century that the positive charges had to be concentrated in a very small nucleus.

Natural radioactivity was the first way to investigate the intimate structure of matter; then people needed higher energy particles to access smaller distance scales. These particles came again from natural sources: it was discovered in the beginning of the twentieth century that the Earth is bombarded by very high energy particles coming from extraterrestrial sources. These particles were named "cosmic rays." A rich and not predicted spectrum of new particles was discovered. Particle physics, the study of the elementary structure of matter, also called "high energy physics," was born.

High energy physics is somehow synonymous with fundamental physics. The reason is that, due to Heisenberg's[1] principle, the minimum scale of distance Δx we can sample is inversely proportional to the momentum (which approximately equals the ratio of the energy E by the speed of light c for large energies) of the probe we are using for the investigation itself:

$$\Delta x \simeq \frac{\hbar}{\Delta p} \simeq \frac{\hbar}{p}\,.$$

---

[1] Werner Heisenberg (1901–1976) was a German theoretical physicist and was awarded the Nobel Prize in Physics for 1932 "for the creation of quantum mechanics." He also contributed to the theories of hydrodynamics, ferromagnetism, cosmic rays, and subatomic physics. During World War II he worked on atomic research, and after the end of the war he was arrested, then rehabilitated. Finally he organized the Max Planck Institute for Physics, which presently in Munich is named after him.
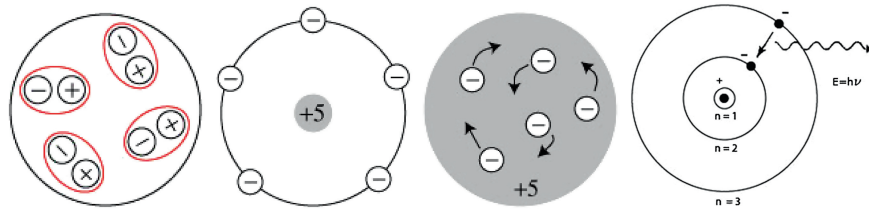
Fig. 1.1 Sketch of the atom according to atomic models by several scientists in the early twentieth century: from left to right, the Lenard model, the Nagaoka model, the Thomson model, and the Bohr model with the constraints from the Rutherford experiment. Source: http://skullsinthestars.com/2008/05/27/the-gallery-of-failed-atomic-models-1903-1913.

In the above equation, $\hbar = h/2\pi \simeq 10^{-34}$ J s is the so-called Planck[2] constant (sometimes the name of Planck constant is given to h). Accelerating machines, developed in the mid-twentieth century, provided higher and higher energy beams in optimal experimental conditions. The collision point was well-defined and multi-layer detectors could be built around it. Subnuclear particles (quarks) were discovered, and a "Standard Model of Particle Physics" was built, piece by piece, until its final consecration with the recent discovery of the Higgs boson. The TeV energy scale (that corresponds to distances down to 10^{-19}–10^{-20} m) is, for the time being, understood.

However, at the end of the twentieth century, the "end of fundamental physics research" announced once again by some, was dramatically dismissed by new and striking experimental evidence which led to the discovery of neutrino oscillations, which meant nonzero neutrino mass, and by the proof that the Universe is in a state of accelerated expansion and that we are immersed in a dark Universe composed mainly of Dark Matter and Dark Energy—whatever those entities, presently unknown to us, are. While the discovery that neutrinos have nonzero mass could be incorporated in the Standard Model by a simple extension, the problem of Dark Matter is still wide open.

The way to our final understanding of the fundamental constituents of the Universe, which we think will occur at energies of 10^{19} GeV (the so-called Planck scale), is hopelessly long. What is worse, despite the enormous progress made by particle acceleration technology, the energies we shall be able to reach at Earth will always be lower than those of the most energetic cosmic rays—particles reaching the Earth from not yet understood extraterrestrial accelerators. These high-energy beams from space may advance our knowledge of fundamental physics and interactions, and of astrophysical phenomena; last but not least, the messengers from space may advance our knowledge of the Universe on a large scale, from cosmology to the ultimate quest on the origins of life, astrobiology. That is the domain and the ambition of the new field of fundamental physics, called astroparticle physics. This book is addressed to this field.

Let us start from the fundamental entities: particles and their interactions.

1.2 Particles and Fields

The paradigm which is currently accepted by most researchers, and which is at the basis of the standard model, is that there is a set of elementary particles constituting matter. From a philosophical point of view, even the very issue of the existence of elementary particles is far from being established: the concept of elementarity may just depend on the energy scale at which matter is investigated—i.e., ultimately, on the experiment itself. And since we use finite energies, a limit exists to the scale one can probe. The mathematical description of particles, in the modern quantum mechanical view, is that of fields, i.e., of complex amplitudes associated to points in spacetime, to which a local probability can be associated.

Interactions between elementary particles are described by fields representing the forces; in the quantum theory of fields, these fields can be also seen as particles by themselves. In classical mechanics fields were just a mathematical abstraction; the real thing were the forces. The paradigmatic example was Newton's[3]

---

[2] Max Planck (1858–1934) was the originator of quantum theory, and deeply influenced the human understanding of atomic and subatomic processes. A professor in Berlin, he was awarded the Nobel Prize in 1918 "in recognition of the services he rendered to the advancement of Physics by his discovery of energy quanta." Politically aligned with the German nationalistic positions during World War I, Planck was later opposed to Nazism. Planck's son, Erwin, was arrested after an assassination attempt of Hitler, and died at the hands of the Gestapo.

[3] Sir Isaac Newton (1642–1727) was an English physicist, mathematician, astronomer, alchemist, and theologian, who deeply influenced science and culture down to the present days. His monograph Philosophiae Naturalis Principia Mathematica (1687)

instantaneous and universal gravitation law. Later, Maxwell gave to the electromagnetic field the status of a physical entity: it transports energy and momentum in the form of electromagnetic waves and propagates at a finite velocity—the speed of light. Then, Einstein[4] explained the photoelectric effect postulating the existence of photons—the interaction of the electromagnetic waves with free electrons, as discovered by Compton,[5] was equivalent to elastic collisions between two particles: the photon and the electron. Finally with quantum mechanics the wave-particle duality was extended to all "field" and "matter" particles.

Field particles and matter particles have different behaviors. Whereas matter particles comply with the Pauli[6] exclusion principle—only one single particle can occupy a given quantum state (matter particles obey Fermi-Dirac statistics, and are called "fermions")—there is no limit to the number of identical and indistinguishable field particles that can occupy the same quantum state (field particles obey Bose–Einstein statistics, and are called "bosons"). Lasers (coherent streams of photons) and the electronic structure of atoms are thus justified. The spin of a particle and the statistics it obeys are connected by the spin-statistics theorem: according to this highly nontrivial theorem, demonstrated by Fierz (1939) and Pauli (1940), fermions have half-integer spins, whereas bosons have integer spins.

At the present energy scales and to our current knowledge, there are 12 elementary "matter" particles; they all have spin 1/2, hence they are fermions. The 12 "matter particles" currently known can be divided into two big families: 6 leptons (e.g., the electron, of charge $-e$, and the neutrino, neutral), and 6 quarks (a state of 3 bound quarks constitutes a nucleon, like the proton or the neutron). Each big family can be divided into three families of two particles each; generations have similar properties—but different masses. This is summarized in Fig. 1.2. A good scale for masses is one GeV/c^2, approximately equal to 1.79×10^{-27} kg – we are implicitly using the relation $E = mc^2$; the proton mass is about $0.938 \text{ GeV}/c^2$. Notice, however, that masses of the elementary "matter" particles vary by many orders of magnitude, from the neutrino masses which are of the order of a fraction of eV/c^2, to the electron mass (about half a MeV/c^2), to the top quark mass (about $173 \text{ GeV}/c^2$). Quarks have fractional charges with respect to the absolute value of the electron charge, e: $\frac{2}{3}e$ for the up, charm, top quark, and $-\frac{1}{3}e$ for the down, strange, bottom. Quark names are just fantasy names.

The material constituting Earth can be basically explained by only three particles: the electron, the up quark, and the down quark (the proton being made of two up quarks and one down, uud, and the neutron by one up and two down, udd).

To each known particle there is an antiparticle (antimatter) counterpart, with the same mass and opposite charge quantum numbers. To indicate antiparticles, the following convention holds: if a particle is indicated by P, its antiparticle is in general written with a bar over it, i.e., $\bar{P}$. For example, to every quark, q, an antiquark, $\bar{q}$, is associated; the antiparticle of the proton p (uud) is the antiproton $\bar{p}$ ($\bar{u}\bar{u}\bar{d}$), with negative electric charge. The antineutron $\bar{n}$ is the antiparticle of the neutron (note the different quark composition of the two). To the electron neutrino ν_e an anti-electron neutrino $\bar{\nu}_e$ corresponds (we shall see later in the book that neutrinos, although electrically neutral, have quantum numbers allowing them to be distinguished from their antiparticles). A different naming convention is used in the case of the anti-electron or positron

provided the foundations for classical mechanics. Newton built the first reflecting telescope and developed theories of color and sound. In mathematics, Newton developed differential and integral calculus (independently from Leibnitz). Newton was also deeply involved in occult studies and interpretations of religion.

[4] Albert Einstein (1879–1955) was a German-born physicist who deeply changed the human representation of the Universe, and our concepts of space and time. Although he is best known by the general public for his theories of relativity and for his mass-energy equivalence formula $E = mc^2$ (the main articles on the special theory of relativity and the $E = mc^2$ articles were published in 1905), he received the 1921 Nobel Prize in Physics "especially for his discovery of the law of the photoelectric effect" (also published in 1905), which was fundamental for establishing quantum theory. The young Einstein noticed that Newtonian mechanics could not reconcile the laws of dynamics with the laws of electromagnetism; this led to the development of his special theory of relativity. He realized, however, that the principle of relativity could also be extended to accelerated frames of reference when one was including gravitational fields, which led to his general theory of relativity (1916). A professor in Berlin, he moved to the United States when Adolf Hitler came to power in 1933, becoming a US citizen in 1940. During World War II, he cooperated with the Manhattan Project, which led to the atomic bomb. Later, however, he took a position against nuclear weapons. In the US, Einstein was affiliated with the Institute for Advanced Study in Princeton.

[5] Arthur H. Compton (1892 - 1962) was awarded the Nobel Prize in Physics in 1927 for his 1923 discovery of the now-called Compton effect, which demonstrated the particle nature of electromagnetic radiation. During World War II, he was a key figure in the Manhattan Project. He championed the idea of human freedom based on quantum indeterminacy,

[6] Wolfgang Ernst (the famous physicist Ernst Mach was his godfather) Pauli (Vienna, Austria, 1900—Zurich, Switzerland, 1958) was awarded the 1945 Nobel prize in physics "for the discovery of the exclusion principle, also called the Pauli principle." He also predicted the existence of neutrinos. Professor in ETH Zurich and in Princeton, he had a rich exchange of letters with psychologist Carl Gustav Jung. According to anecdotes, Pauli was a very bad experimentalist, and the ability to break experimental equipment simply by being in the vicinity was called the "Pauli effect".
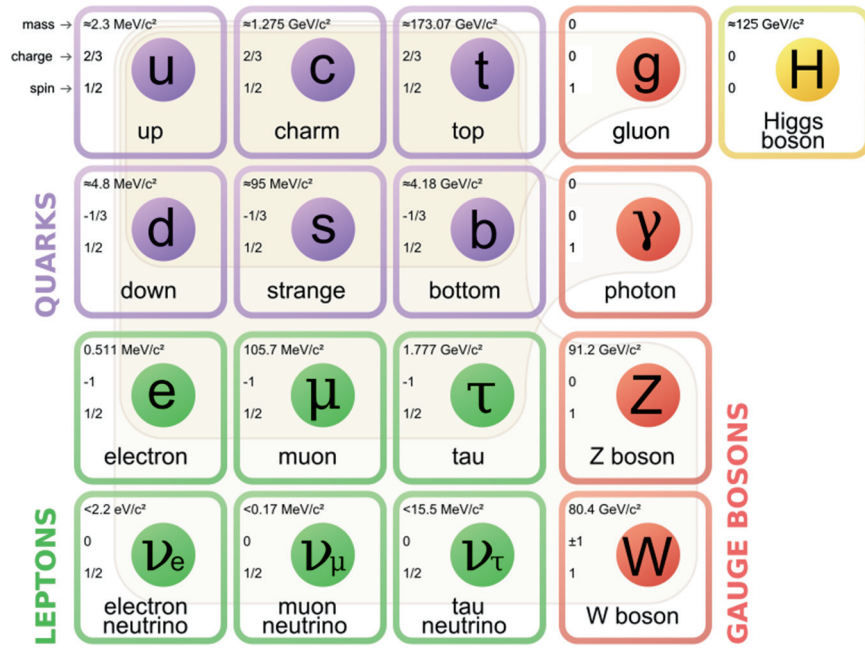
Fig. 1.2 Presently observed elementary particles. Fermions are listed in the first three columns; gauge bosons are listed in the fourth column. Adapted from MissMJ [CC BY 3.0 (http://creativecommons.org/licenses/by/3.0)], via Wikimedia Commons.

e^+: the superscript denoting the charge makes explicit the fact that the antiparticle has the opposite electric charge to that of its associated particle. The same applies to the heavier leptons ($\mu^\pm$, $\tau^\pm$) and to the "field particles" $W^\pm$.

At the current energy scales of the Universe, particles interact via four fundamental interactions. There are indications that this view is related to the present-day energy of the Universe: at higher energies—i.e., earlier epochs—some interactions would "unify" and the picture would become simpler. In fact, theorists think that these interactions might be the remnant of one single interaction that would occur at extreme energies—e.g., the energies typical of the beginning of the Universe. By increasing order of strength:

1. The gravitational interaction, acting between whatever pair of bodies and dominant at macroscopic scales.
2. The electromagnetic interaction, acting between pairs of electrically charged particles (i.e., all matter particles, excluding neutrinos).
3. The weak interaction, also affecting all matter particles (with certain selection rules) and responsible, for instance, for the beta decay and thus for the energy production in the Sun.
4. The color force, acting among quarks. The strong interaction,[7] responsible for binding the atomic nuclei (it ensures electromagnetic repulsion among protons in nuclei does not break them up) and for the interaction of cosmic protons with the atmosphere, is just a residual shadow (à la van der Waals) shadow of the very strong interaction between quarks.

The relative intensity of such interactions spans many orders of magnitude. In a ^{2}H atom, in a scale where the intensity of strong interactions between the nucleons is 1, the intensity of electromagnetic interactions between electrons and the nucleus is 10^{-5}, the intensity of weak interactions is 10^{-13}, and the intensity of gravitational interactions between the electron and the nucleus is 10^{-45}. However, intensity is not the only relevant characteristics in this context: one should consider also the range and the interactions and the characteristics of the charges. The weak and strong interactions act at subatomic distances, smaller than ~ 1 fm, and they are not very important at astronomical scales. The electromagnetic and gravitational forces have instead a $1/r^2$ dependence. On small (molecular) scales, gravity is negligible compared to electromagnetic forces; but on large scales, the universe is electrically neutral, so that electrostatic forces become negligible.

---

[7] This kind of interaction was first conjectured and named by Isaac Newton at the end of the seventeenth century: "There are therefore agents in Nature able to make the particles of bodies stick together by very strong attractions. And it is the business of experimental philosophy to find them out. Now the smallest particles of matter may cohere by the strongest attractions, and compose bigger particles of weaker virtue; and many of these may cohere and compose bigger particles whose virtue is still weaker, and so on for divers successions, until the progression ends in the biggest particles on which the operations in chemistry, and the colors of natural bodies depend." (I. Newton, Opticks)

Gravity, the weakest of all forces from a particle physics point of view, is the force determining the evolution of the Universe at large scales.

In the quantum mechanical view of interaction, interaction itself is mediated by quanta of the force field.

Quanta of the interaction fields	
Strong interaction	Eight gluons
Electromagnetic interaction	Photon (γ)
Weak interaction	Bosons W^+, W^-, Z
Gravitational interaction	Graviton (?)

According to most scientists, the gravitational interaction is mediated by the graviton, an electrically neutral boson of mass 0 and spin 2, yet undiscovered. The weak interaction is mediated by three vectors: two are charged, the W^+ (of mass $\sim 80.4\,\mathrm{GeV}/c^2$) and its antiparticle, the W^-; one is neutral, the Z (with mass $\sim 91.2\,\mathrm{GeV}/c^2$). The electromagnetic interaction is mediated by the well-known photon. The color interaction is exchanged by eight massless neutral particles called gluons. The couplings of each particle to the boson(s) associated to a given interaction are determined by the strength of the interaction and by "magic" numbers, called charges. The gravitational charge of a particle is proportional to its mass (energy); the weak charge is the weak isospin charge ($\pm 1/2$ for the fermions sensitive to the weak interaction, 0, ± 1 for bosons); the electrical charge is the well-known (positive and negative) charge; the strong charge comes in three types designated by color names (red, green, blue). Particles or combinations of particles can be neutral to the electromagnetic, weak or strong interaction, but not to the gravitational interaction. For instance, electrons have electric and weak charges but no color charge, and atoms are electrically neutral. At astrophysical scales, the dominant interaction is gravitation; at atomic scales, $\mathcal{O}(1\,\mathrm{nm})$, it is the electromagnetic interaction; and at the scale of nuclei, $\mathcal{O}(1\mathrm{fm})$, it is the strong interaction.

In quantum physics the vacuum is not empty at all. Heisenberg's uncertainty relations allow energy conservation violations by a quantity ΔE within small time intervals Δt such that $\Delta t \simeq \hbar/\Delta E$. Massive particles that live in such tiny time intervals are called "virtual." But, besides such particles which are at the origin of measurable effects (like the Casimir effect, see Chap. 6), we have just discovered that space is filled by an extra field to which is associated the Higgs boson, a neutral spinless particle with mass about 125 GeV/c^2. Particles in the present theory are intrinsically massless, and it is their interaction with the Higgs field that originates their mass: the physical properties of particles are related to the properties of the quantum vacuum.

1.3 The Particles of Everyday Life

As we have seen, matter around us is essentially made of atoms; these atoms can be explained by just three particles: protons and neutrons (making up the atomic nuclei) and electrons. Electrons are believed to be elementary particles, while protons and neutrons are believed to be triplets of quarks - *uud* and *udd* respectively. Particles made of triplets of quarks are called baryons. Electrons and protons are stable particles to the best of our present knowledge, while neutrons have an average lifetime (τ) of about 15 minutes if free, and then they decay, mostly into a proton, an electron and an antineutrino - the so-called β-decay. Neutrons in atoms, however, can be stable: the binding energy constraining them in the atomic nucleus can be such that the decay becomes energetically forbidden.

Baryons are not the only allowed combination of quarks: notably, mesons are allowed combinations of a quark and of an antiquark. All mesons are unstable. The lightest mesons, called pions, are combinations of u and d quarks and of their antiparticles; they come in a triplet of charge (π^+, π^-, π^0), and have masses of about 0.14 GeV/c^2. Although unstable ($\tau_{\pi^\pm} \simeq 26$ ns, mostly decaying through $\pi^+ \to \mu^+ \nu_\mu$ and similarly for π^-; $\tau_{\pi^0} \simeq 10^{-16}$ s, mostly decaying through $\pi^0 \to \gamma\gamma$), pions are also quite common, since they are one of the final products of the chain of interactions of particles coming from the cosmos (cosmic rays, see later) with the Earth's atmosphere.

All baryons and mesons (i.e., hadrons) considered up to now are combinations of u and d quarks and of their antiparticles. *Strange* hadrons (this is the term we use for baryons and mesons involving the s, or *strange*, quark) are less common, since the mass of the s is larger and the lifetimes of strange particles are

of the order of 1 ns. The lightest strange mesons are called the K mesons, which can be charged (K^+, K^-) or neutral; the lightest strange baryon (uds) is called the Λ.

The heavier brothers of the electrons, the muons (with masses of about $0.11 \text{ GeV}/c^2$), are also common, since they have a relatively long lifetime ($\tau_{\mu^\pm} \simeq 2.2\,\mu\text{s}$) and they can propagate for long distances in the atmosphere. They also appear in the chain of interactions/decays of the products of cosmic rays.

Last but not least, a "field particle" is fundamental for our everyday life: the quantum of electromagnetic radiation, the photon (γ). The photon is massless to the best of our knowledge, electrically neutral. Photon energies are related to their wavelength λ through $E = hc/\lambda$, and the photons of wavelengths between about $0.4\,\mu\text{m}$ and $0.7\,\mu\text{m}$ can be perceived by our eyes as light.

1.4 The Modern View of Interactions: Quantum Fields and Feynman Diagrams

The purpose of physics is to describe (and possibly predict) change with time. A general concept related to change is the concept of interaction, i.e., the action that occurs as two or more objects have an effect upon one another. Scattering and decay are examples of interactions, leading from an initial state to a final state. The concept of interaction is thus a generalization of the concept of force exchange in classical physics.

Quantum field theories (QFT), which provide in modern physics the description of interactions, describe nature in terms of fields, i.e., of wavefunctions defined in spacetime. A force between two particles (described by "particle fields") is described in terms of the exchange of virtual force carrier particles (again described by appropriate fields) between them. For example, the electromagnetic force is mediated by the photon field, weak interactions are mediated by the Z and $W^\pm$ fields, while the mediators of the strong interaction are called gluons. "Virtual" means that these particles can be off-shell, i.e., they do not need to have the "right" relationship between mass, momentum and energy - this is related to the virtual particles that we discussed when introducing the uncertainty relations, which can violate energy-momentum conservation for short times.

Feynman diagrams are pictorial representations of interactions, used in particular for interactions involving subatomic particles, introduced by Richard Feynman[8] in the late 1940s.

The orientation from left to right in a Feynman diagram normally represents time: an interaction process begins on the left and ends on the right. Basic fermions are represented by straight lines with possibly an arrow to the right for particles, and to the left for antiparticles. Force carriers are represented typically by wavy lines (photons), springs (gluons), dashed lines ($W^\pm$ and Z). Two important rules that the Feynman diagrams must satisfy clarify the meaning of such representation:

- conservation of energy and momentum is required at every vertex;
- lines entering or leaving the diagram represent real particles and must have $E^2 = p^2 c^2 + m^2 c^4$ (see in the next Chapter the discussion on Einstein's special relativity).

Associated with Feynman diagrams are mathematical rules (called the "Feynman rules") that enable the calculation of the probability (quantum mechanically, the square of the absolute value of the amplitude) for a given reaction to occur; we shall describe the quantitative aspect in larger detail in Chapter 6 and Chapter 7. Fig. 1.3, left, represents a simple Feynman diagram, in which an electron and a proton are mutually scattered as the result of an electromagnetic interaction (virtual photon exchange) between them. This process requires two vertices in which the photon interacts with the charged particle (one for each particle), and for this kind of scattering this is the minimum number of vertices – we say that this is the representation of the process at *leading order*.

The Feynman rules allow associating to each vertex a multiplication factor contributing to the total "amplitude"; the probability of a process is proportional to the square of the amplitude. For example in the case of a photon coupling (two photon vertices) this factor is the "coupling parameter"

---

[8] Richard Feynman (New York 1918 - Los Angeles 1988), longtime professor at Caltech, is known for his work in quantum mechanics, in the theory of quantum electrodynamics, as well as in particle physics; he participated in the Manhattan project. In addition, he proposed quantum computing. He received the Nobel Prize in Physics in 1965 for his "fundamental work in quantum electrodynamics, with deep-ploughing consequences for the physics of elementary particles". His life was quite adventurous, and full of anecdotes. In the divorce file related to this second marriage, his wife complained that "He begins working calculus problems in his head as soon as he awakens. He did calculus while driving in his car, while sitting in the living room, and while lying in bed at night.". He wrote several popular physics books, and an excellent general physics textbook now freely available at http://www.feynmanlectures.caltech.edu/.

$$\frac{1}{4\pi\epsilon_0}\frac{e^2}{\hbar c} \simeq \frac{1}{137}$$

for each photon, so the amplitudes for diagrams with many photons (see for example Fig. 1.3, right) are small, compared to those with only one.

Technically, the Feynman rules allow expressing the probability of a process as a power series expansion in the coupling parameter. One can draw all possible diagrams up to some number of mediators of the exchange, depending on the accuracy desired; then compute the amplitude for each diagram following the Feynman rules, sum all the amplitudes (note that the diagrams could display negative interference) and calculate the square of the modulus of the amplitude, which will give the probability. This perturbative technique is only of practical use when the coupling parameter is small, that is, as we shall see, for electromagnetic or weak interactions, but not for strong interactions, except at very high energies (the coupling parameter of strong interactions decreases with energy).
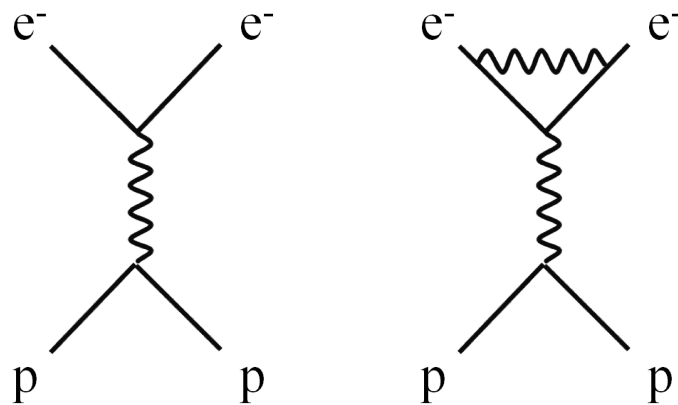
Fig. 1.3 Electromagnetic scattering: interaction between en electron and a proton. Left: via the exchange of one virtual photon. Right: the same process with one more virtual photon – the amplitude decreases by a factor of approximately 1/137.

1.5 A Quick Look at the Universe

The origin and destiny of the Universe is, for most researchers, the fundamental question. Many answers were provided over the ages, a few of them built over scientific observations and reasoning. Over the last century enormous scientific theoretical and experimental breakthroughs have occurred: less than a century ago, people believed that the Milky Way, our own Galaxy, was the only galaxy in the Universe; now we know that there are 10^{11} galaxies within the observable universe, each containing some 10^{11} stars. Most of them are so far, that we cannot even hope to explore them.

Let us start an imaginary trip across the Universe from the Earth. The Earth, which has a radius of about 6400 km, is one of the planets orbiting around the Sun (we shall often identify the Sun with the symbol $\odot$, which comes from its hieroglyphic representation). The latter is a star with a mass of about 2×10^{30} kg located at a distance from us of about 150 million km (i.e., 500 light seconds). We call the average Earth-Sun distance the astronomical unit, in short AU or au. The ensemble of planets orbiting the Sun is called the Solar System. Looking to the aphelion of the orbit of the farthest acknowledged planet, Neptune, the Solar System has a diameter of 9 billion km (about 10 light hours, or 60 AU).

The Milky Way (Fig. 1.4) is the galaxy that contains our Solar System. Its name "milky" is derived from its appearance as a dim glowing band arching across the night sky in which the naked eye cannot distinguish individual stars. The ancient Romans named it "via lactea," which literally corresponds to the present name (being *lac* the latin word for milk)—the term "galaxy," too, descends from a Greek word indicating milk. Seen from Earth with the unaided eye, the Milky Way appears as a band because its disk-shaped structure
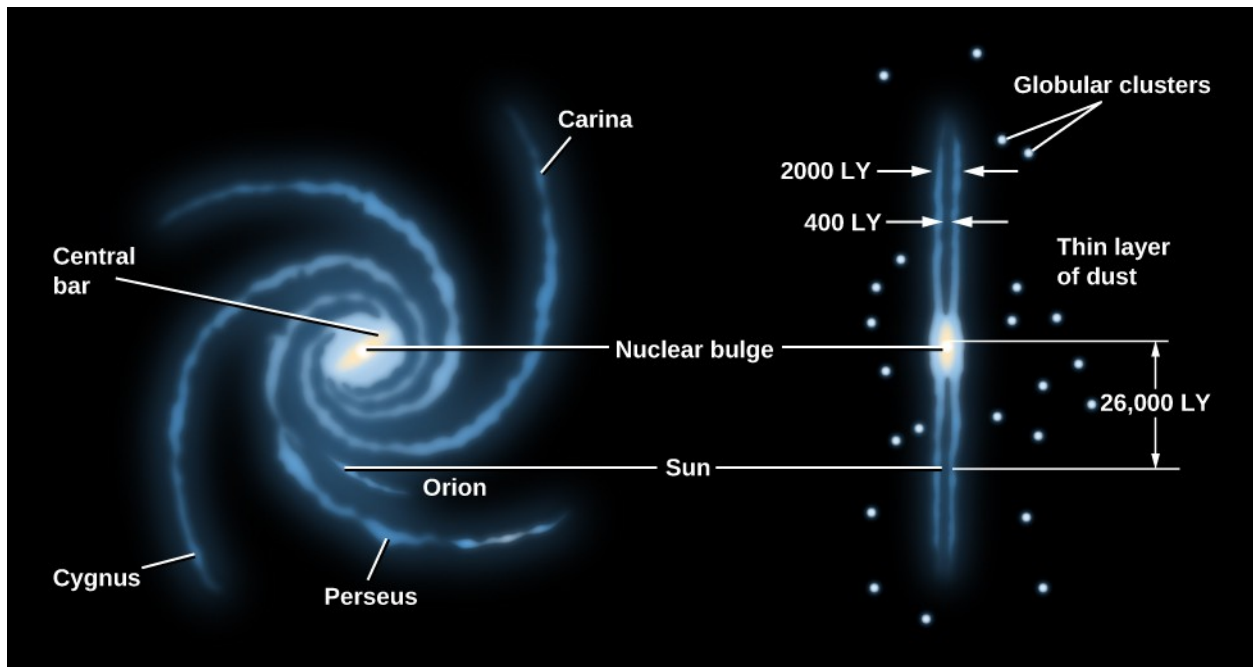
Fig. 1.4 The Milky Way seen from top and from side. From https://courses.lumenlearning.com/astronomy.

is viewed edge-on from the periphery of the Galaxy itself. Galilei[9] first resolved such band of light into individual stars with his telescope, in 1610.

The Milky Way is a spiral galaxy some 100 000 light-years (ly) across, 1000 ly to 2000 ly thick, with the Solar System located within the disk, about 30 000 ly away from the Galactic Center, in the so-called Orion arm. The stars in the inner 10 000 ly form a bulge and a few bars that radiate from the bulge. The very center of the Galaxy, in the constellation of Sagittarius, hosts a supermassive black hole of some 4 million solar masses, as determined by studying the orbits of nearby stars. The interstellar medium (ISM) is filled by partly ionized gas, dust and cosmic rays and it accounts for some 15% of the total mass of the disk. The gas is inhomogeneously distributed and it is mostly confined to discrete clouds occupying a few per cent of the volume. A magnetic field of a few μG interacts with the ISM.

With its $\sim 10^{11}$ stars, the Milky Way is a relatively large galaxy. Teaming up with a similar-sized partner (called the Andromeda galaxy), it has gravitationally trapped many smaller galaxies: together, they all constitute the so-called Local Group. The Local Group comprises more than 50 galaxies, including numerous dwarf galaxies—some are just spherical collections of hundreds of stars that are called globular clusters. Its gravitational center is located somewhere between the Milky Way and the Andromeda galaxies. The Local Group covers a diameter of 10 million light-years, or 10 Mly (i.e., 3.1 megaparsec,[10] Mpc); it has a total mass of about 10^{12} solar masses.

---

[9] Galileo Galilei (1564–1642) was an Italian physicist, mathematician, astronomer, and philosopher who deeply influenced scientific thoughts down to the present days. He first formulated some of the fundamental laws of mechanics, like the principle of inertia and the law of accelerated motion; he formally proposed, with some influence from previous works by Giordano Bruno, the principle of relativity. Galilei was professor in Padua, nominated by the Republic of Venezia, and astronomer in Firenze. He built the first practical telescope (using lenses) and using this instrument he could perform astronomical observations which supported Copernicanism; in particular he discovered the phases of Venus, the four largest satellites of Jupiter (named the Galilean moons in his honor), and he observed and analyzed sunspots. Galilei also made major discoveries in military science and technology. He came into conflict with the Catholic Church, for his support of Copernican theories. In 1616 the Inquisition declared heliocentrism to be heretical, and Galilei was ordered to refrain from teaching heliocentric ideas. In 1616 Galilei argued that tides were an additional evidence for the motion of the Earth. In 1633 the Roman Inquisition found Galilei suspect of heresy, sentencing him to indefinite imprisonment; he was kept under house arrest in Arcetri near Firenze until his death.

[10] The parsec (symbol: pc, and meaning "parallax of one arcsecond") is often used in astronomy to measure distances to objects outside the Solar System. It is defined as the length of the longer leg of a right triangle, whose shorter leg corresponds to one astronomical unit, and the subtended angle of the vertex opposite to that leg is one arcsecond. It corresponds to approximately 3×10^{16} m, or about 3.26 light-years. Proxima Centauri, the nearest star, is about 1.3 pc from the Sun.
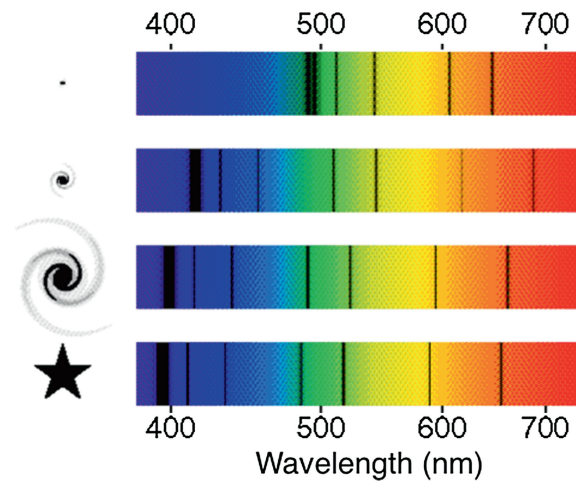
Fig. 1.5 Redshift of emission spectrum of stars and galaxies at different distances. A star in our Galaxy is shown at the bottom left with its spectrum on the bottom right. The spectrum shows the dark absorption lines, which can be used to identify the chemical elements involved. The other three spectra and pictures from bottom to top show a nearby galaxy, a medium distance galaxy, and a distant galaxy. Using the redshift we can calculate the relative radial velocity between these objects and the Earth. From http://www.indiana.edu.

Galaxies are not uniformly distributed; most of them are arranged into groups (containing some dozens of galaxies) and clusters (up to several thousand galaxies); groups and clusters and additional isolated galaxies form even larger structures called superclusters that may span up to 100 Mly.

This is how far our observations can go.

In 1929 the American astronomer Edwin Hubble, studying the emission of radiation from galaxies compared their speed (calculated from the Doppler shift of their emission lines) with the distance (Fig. 1.5), and discovered that objects in the Universe move away from us with velocity

$$v = H_0 d \, , \tag{1.1}$$

where d is the distance between the objects, and H_0 is a parameter called the Hubble constant (whose value is known today to be about $68 \, \text{km s}^{-1}\text{Mpc}^{-1}$, i.e., $21 \, \text{km s}^{-1}\text{Mly}^{-1}$). The above relation is called Hubble's law (Fig. 1.6). Note that at that time galaxies beyond the Milky Way had just been discovered.

The Hubble law means that sources at cosmological distances (where local motions, often resulting from galaxies being in gravitationally bound states, are negligible) are observed to move away at speeds that are proportionally higher for larger distances. The Hubble constant describes the rate of increase of recession velocities for increasing distance. The Doppler redshift

$$z = \frac{\lambda'}{\lambda} - 1$$

can thus also be used as a metric of the distance of objects. To give an idea of what H_0 means, the speed of revolution of the Earth around the Sun is about $30 \, \text{km/s}$. Andromeda, the large galaxy closest to the Milky Way, is at a distance of about 2.5 Mly from us—however we and Andromeda are indeed approaching: this is an example of the effect of local motions.

Dimensionally, we note that H_0 is the inverse of a time: $H_0 \simeq (14 \times 10^9 \, \text{years})^{-1}$. A simple interpretation of the Hubble law is that, if the Universe had always been expanding at a constant rate, about 14 billion years ago its volume was zero—naively, we can think that it exploded through a quantum singularity, such an explosion being usually called the "Big Bang." This age is consistent with present estimates of the age of the Universe within gravitational theories, which we shall discuss later in this book, and slightly larger than the age of the oldest stars, which can be measured from the presence of heavy nuclei. The picture looks consistent.

The adiabatic expansion of the Universe entails a freezing with expansion, which in the nowadays quiet Universe can be summarized as a law for the evolution of the temperature T on the size R,

$$T \propto \frac{1}{R(t)} \, .$$
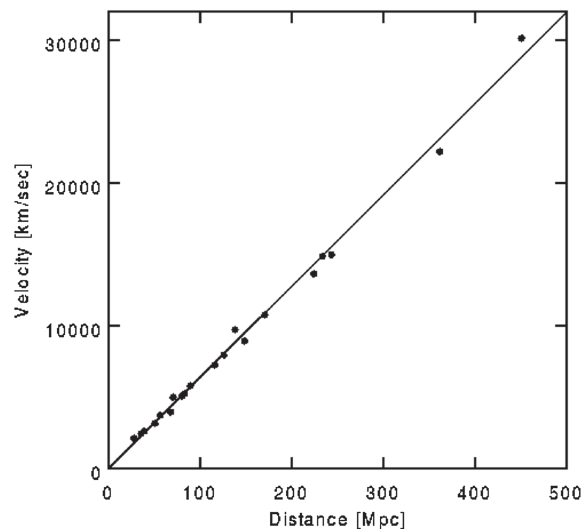
Fig. 1.6 Experimental plot of the relative velocity (in km/s) of known astrophysical objects as a function of distance from Earth (in Mpc). Several methods are used to determine the distances. Distances up to hundreds of parsecs are measured using stellar parallax (i.e., the difference between the angular positions from the Earth with a time delay of 6 months). Distances up to 50 Mpc are measured using Cepheids, i.e., periodically pulsating stars for which the luminosity is related to the pulsation period (the distance can thus be inferred by comparing the intrinsic luminosity with the apparent luminosity). Finally, distances from 1 to 1000 Mpc can be measured with another type of standard candle, Type Ia supernova, a class of remnants of imploded stars. In between (from 15 to 200 Mpc), the Tully-Fisher relation, an empirical relationship between the intrinsic luminosity of a spiral galaxy and the width of its emission lines (a measure of its rotation velocity), can be used. The methods, having large superposition regions, can be cross-calibrated. The line is a Hubble-law fit to the data. From A. G. Riess, W. H. Press and R. P. Kirshner, Astrophys. J. 473 (1996) 88.

The present temperature is slightly less than 3 K, and can be measured from the spectrum of the blackbody (microwave) radiation (the so-called cosmic microwave background, or CMB, permeating the Universe). The formula implies also that studying the ancient Universe in some sense means exploring the high energy world: subatomic physics and astrophysics are naturally connected.

At epochs corresponding to fractions of a second after the Big Bang, tiny quantum fluctuations in the distribution of cosmic matter led to galaxy formation. Density fluctuations grew with time into proto-structures which, after accreting enough mass from their surroundings, overcame the pull of the expanding universe and after the end of an initial era dominated by radiation collapsed into bound, stable structures. The average density of such structures was reminiscent of the average density of the Universe when they broke away from the Hubble expansion: so, earlier-forming structures have a higher mean density than later-forming structures. Proto-galaxies were initially dark. Only later, when enough gas had fallen into their potential well, stars started to form—again, by gravitational instability in the gas—and shine due to the nuclear fusion processes activated by the high temperatures caused by gravitational forces. The big picture of the process of galaxy formation is probably understood by now, but the details are not. The morphological difference between disk (i.e., spiral) galaxies and spheroidal (i.e., elliptical) galaxies are interpreted as due to the competition between the characteristic timescale of the infall of gas into the protogalaxy's gravitational well and the timescale of star formation: if the latter is shorter than the former, a spheroidal (i.e., three-dimensional) galaxy likely forms; if it is longer, a disk (i.e., two-dimensional) galaxy forms. A disk galaxy is rotation supported, whereas a spheroidal galaxy is pressure supported—stars behaving in this case like gas molecules. It is conjectured that the velocity dispersion ($\sim$200 km/s) among proto-galaxies in the earlier universe may have triggered rotation motions in disk galaxies, randomly among galaxies but orderly within individual galaxies.

Stars also formed by gravitational instabilities of the gas. For given conditions of density and temperature, gas (mostly hydrogen and helium) clouds collapse and, if their mass is suitable, eventually form stars. Stellar masses are limited by the conditions that (i) nuclear reactions can switch on in the stellar core ($>$0.1 solar masses), and (ii) the radiation drag of the produced luminosity on the plasma does not disrupt the star's structure ($<$100 solar masses). For a star of the mass of the Sun, formation takes 50 million years—the total lifetime is about 11 billion years before collapsing to a "white dwarf," and in the case of our Sun some 4.5 billion years are already gone.

Stars span a wide range of luminosities and colors, and can be classified according to these characteristics. The smallest stars, known as red dwarfs, may contain as little as 10 % the mass of the Sun and emit only 0.01 % as much energy, having typical surface temperatures of 3000 K, i.e., roughly half the surface temperature of the Sun. Red dwarfs are by far the most numerous stars in the Universe and have lifetimes of tens of billions of years, much larger than the age of the Universe. On the other hand, the most massive stars, known as hypergiants, may be 100 or more times more massive than the Sun, and have surface temperatures of more than 40 000 K. Hypergiants emit hundreds of thousands of times more energy than the Sun, but have lifetimes of only a few million years. They are thus extremely rare today and the Milky Way Galaxy contains only a handful of them.

Luminosity,[11] radius and temperature of a star are in general linked. In a temperature-luminosity plane, most stars populate a locus that can be described (in log scale) as a straight line (Fig. 1.7): this is called the *main sequence*. Our Sun is also found there—corresponding to very average temperature and luminosity.
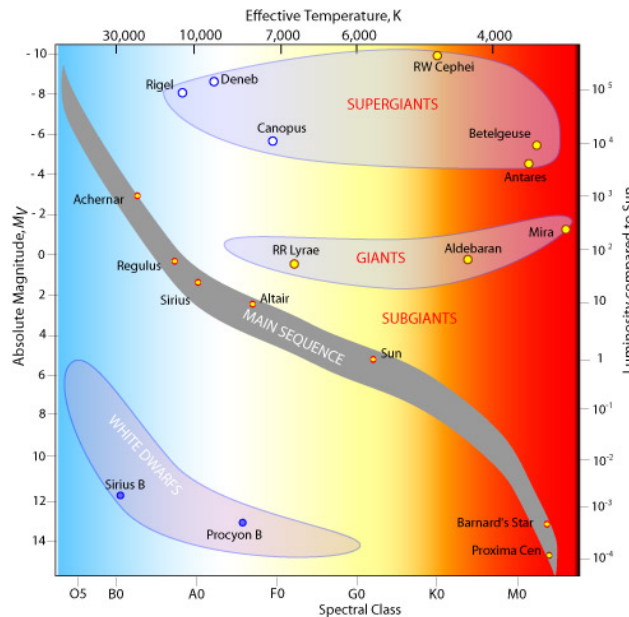
Fig. 1.7 The Hertzsprung-Russell diagram plots the luminosities of stars versus their stellar classification or effective temperature (color). From http://www.atnf.csiro.au/outreach/education.

The fate of a star depends on its mass. The heavier the star, the larger its gravitational energy, and the more effective are the nuclear processes powering it. In average stars like the Sun, the outer layers are supported against gravity until the stellar core stops producing fusion energy; then the star collapses as a "white dwarf"—an Earth-sized object. Main-sequence stars over 8 solar masses can die in a very energetic explosion called a (core-collapse, or Type II) supernova. In a supernova, the star's core, made of iron (which being the most stable atom, i.e., one whose mass defect per nucleon is maximum, is the endpoint of nuclear fusion processes, Fig. 1.8) collapses and the released gravitational energy goes as heating the overlying mass

---

[11] The brightness of a star at an effective wavelength λ as seen by an observer on Earth is given by its apparent *magnitude*. This scale originates in the Hellenistic practice of dividing stars into six magnitudes: the brightest stars were said to be of first magnitude (m = 1), while the faintest were of sixth magnitude (m = 6), the limit of naked eye human visibility. The system is today formalized by defining a first magnitude star as a star that is 100 times as bright as a sixth magnitude star; thus, a first magnitude star is $\sqrt[5]{100}$ (about 2.512) times as bright as a second magnitude star (obviously the brighter an object appears, the lower the value of its magnitude). The stars Arcturus and Vega have an apparent magnitude approximately equal to 0. The absolute magnitude M_V is defined to be the visual ($\lambda \sim 550$ nm) apparent magnitude that the object would have if it were viewed from a distance of 10 parsec, in the absence of light extinction; it is thus a measure of the luminosity of an object. The problem of the relation between apparent magnitude, absolute magnitude, and distance, is related also to cosmology, as discussed in Chap. 8. The absolute magnitude is nontrivially related to the bolometric luminosity, i.e., to the total electromagnetic power emitted by a source; the relation is complicated by the fact that only part of the emission spectrum is observed in a photometric band. The absolute magnitude of the Sun is $M_{V,\odot} \simeq 4.86$, and its absolute bolometric magnitude is $M_{bol,\odot} \simeq 4.76$; the difference M_V-M_{bol} (for the Sun, $M_{V,\odot}$- $M_{bol,\odot} \simeq 0.1$) is called the bolometric correction BC, which is a function of the temperature. It can be approximated as $BC(T) \simeq 29500/T + 10\log_{10} T - 42.62$.
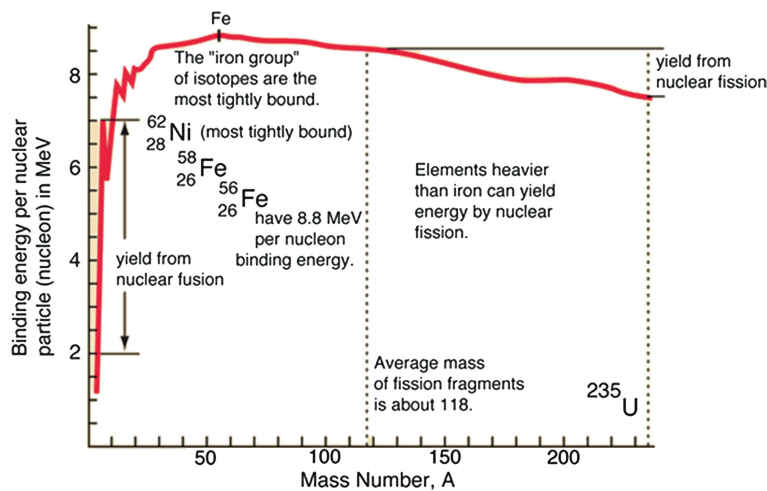
Fig. 1.8 Binding energy per nucleon for stable atoms. Iron (^{56}Fe) is the stable element for which the binding energy per nucleon is the largest (about 8.8 MeV); it is thus the natural endpoint of processes of fusion of lighter elements, and of fission of heavier elements (although ^{58}Fe and ^{56}Ni have a slightly higher binding energy, by less than 0.05 %, they are subject to nuclear photodisintegration). From http://hyperphysics.phy-astr.gsu.edu.

layers which, in an attempt to dissipate the sudden excess heat by increasing the star's radiating surface, expand at high speed (10 000 km/s and more) to the point that the star gets quickly disrupted—i.e., explodes. Supernovae release an enormous amount of energy, about 10^{46} J—mostly in neutrinos from the nuclear processes occurring in the core, and just 1 % in kinetic energies of the ejecta—in a few tens of seconds.[12] For a period of days to weeks, a supernova may outshine its entire host galaxy. Being the energy of the explosion large enough to generate hadronic interactions, basically any element and many subatomic particles are produced in these explosions. On average, in a typical galaxy (e.g., the Milky Way) supernova explosions occur just once or twice per century. Supernovae leave behind neutron stars or black holes[13].

The heavier the star, the more effective the fusion process, and the shorter the lifetime. We need a star like our Sun, having a lifetime of a few tens of billion of years, to both give enough time to life to develop and to guarantee high enough temperatures for humans. The Solar System is estimated to be some 4.6 billion years old and to have started from a molecular cloud. Most of the collapsing mass collected in the center, forming the Sun, while the rest flattened into a disk out of which the planets formed. The Sun is too young to have created heavy elements in such an abundance to justify carbon-based life on Earth. The carbon, nitrogen, and oxygen atoms in our bodies, as well as atoms of all other heavy elements, were created in previous generations of stars somewhere in the Universe.

The study of stellar motions in galaxies indicates the presence of a large amount of unseen mass in the Universe. This mass seems to be of a kind presently unknown to us; it neither emits nor absorbs electromagnetic radiation (including visible light) at any significant level. We call it *dark matter*: its abundance in the Universe amounts to an order of magnitude more than the conventional matter we are made of. Dark matter represents one of the greatest current mysteries of astroparticle physics. Indications exist also of a further form of energy, which we call *dark energy*. Dark energy contributes to the total energy budget of the Universe three times more than dark matter.

The fate of the Universe depends on its energy content. In the crude approximation of a homogeneous and isotropic Universe with a flat geometry, the escape velocity v_{esc} of an astrophysical object of mass m at a distance r from a given point can be computed from the relation

$$\frac{mv_{esc}^2}{2} - GM\frac{m}{r} = \frac{mv_{esc}^2}{2} - G\left[\left(\frac{4}{3}\pi r^3\right)\rho\right]\frac{m}{r} = 0 \implies v_{esc} = \sqrt{\frac{8}{3}\pi G r^2 \frac{\rho}{c^2}},$$

---

[12] Note that frequently astrophysicist use as a unit of energy the old "cgs" (centimeter-gram-second) unit called *erg*; 1 erg = 10^{-7} J.

[13] The Chandrasekhar limit is the maximum mass theoretically possible for a star to end its lifecycle into a dwarf star: Chandrasekhar in 1930 demonstrated that it is impossible for a collapsed star to be stable if its mass is greater than $\sim$1.44 times the mass of the Sun. Above 1.5 to 3 solar masses (the limit is not known, depending on the initial conditions) a star ends its nuclear-burning lifetime into a black hole. In the intermediate range it will become a neutron star.
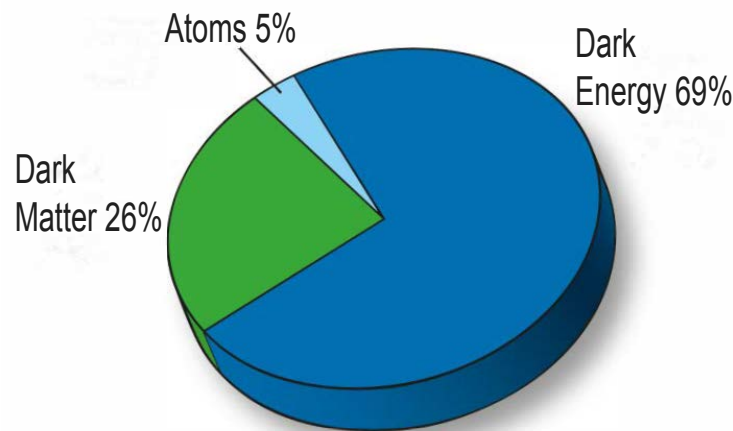
Fig. 1.9 Present energy budget of the Universe.

where $M = \left(\frac{4}{3}\pi r^3\right)\rho/c^2$ is the amount of mass in the sphere of radius r, ρ being the average energy density, and G is the gravitational constant. Given the Hubble law, if

$$v = H_0 r < v_{esc} = \sqrt{\frac{8}{3}\pi G r^2 \frac{\rho}{c^2}} \implies \rho > \rho_{crit} = \frac{3H_0^2 c^2}{8\pi G}$$

the Universe will eventually recollapse, otherwise it will expand forever. ρ_{crit}, about 5 GeV/m^3, is called the critical energy density of the Universe.

In summary, we live in a world that is mostly unknown even from the point of view of the nature of its main constituents (Fig. 1.9). The evolution of the Universe and our everyday life depend on this unknown external world. First of all, the ultimate destiny of the Universe—a perpetual expansion or a recollapse—depends on the amount of all the matter in the Universe. Moreover, every second, high-energy particles (i.e., above 1 GeV) of extraterrestrial origin pass through each square centimeter on the Earth, and they are messengers from regions where highly energetic phenomena take place that we cannot directly explore. These are the so-called *cosmic rays*, discovered in the beginning of the nineteenth century (see Chap. 3). It is natural to try to use these messengers in order to obtain information on the highest energy events occurring in the Universe.

1.6 Cosmic Rays

The distribution in energy (the so-called spectrum) of cosmic rays[14] is quite well described by a power law E^{-p} with p a positive number (Fig. 1.10). The spectral index p is around 3 on average. After the low energy region dominated by cosmic rays from the Sun (the solar wind), the spectrum becomes steeper for energy values of less than ∼1000 TeV (150 times the maximum energy foreseen for the beams of the LHC collider at CERN): this is the energy region that we know to be dominated by cosmic rays produced by astrophysical sources in our galaxy, the Milky Way. For higher energies a further steepening occurs, the point at which this change of slope takes place being called the "knee". Some believe that the region above this energy is dominated by cosmic rays produced by extragalactic sources, mostly supermassive black holes growing at the centers of other galaxies. For even higher energies (more than one million TeV) the cosmic-ray spectrum becomes less steep, resulting in another change of slope, called the "ankle" - some others believe that the knee is caused by a propagation effect, and the threshold for the dominance of extragalactic sources is indeed close to the ankle. Finally, at the highest energies in the figure a drastic suppression is present—as expected

---

[14] In this textbook we define as *cosmic rays* all particles of extraterrestrial origin. It should be noted that other textbooks instead define as cosmic rays only nuclei, or only protons and ions – i.e., they separate gamma rays and neutrinos from cosmic rays.

from the interaction of long-traveling particles with the cosmic microwave background, remnant of the origin of the Universe.[15]

The majority of high-energy particles in cosmic rays are protons (hydrogen nuclei); about 10 % are helium nuclei (nuclear physicists usually call them alpha particles), and 1 % are neutrons or nuclei of heavier elements. Together, these account for 99% of cosmic rays, and electrons and photons make up the remaining 1 %. Note that the composition is expected to vary with energy; given the energy dependence of the flux, however, only the energies below the knee are responsible for this proportion. The number of neutrinos is estimated to be comparable to that of high-energy photons, but it is very high at low energies because of the nuclear processes that occur in the Sun: such processes involve a large production of neutrinos.

Neutral and stable cosmic messengers (gamma rays, high energy neutrinos, gravitational waves) are very precious since they are not deflected by extragalactic (order of 1 nG - 1 fG) or by Galactic (order of 1 μG) magnetic fields, and allow pointing directly to the source. While we detect a large flux of gamma rays and we know several cosmic production sites, evidence for astrophysical neutrinos and gravitational waves was only recently published, respectively in 2014 and in 2016.

---

[15] A theoretical upper limit on the energy of cosmic rays from distant sources was computed in 1966 by Greisen, Kuzmin, and Zatsepin, and it is called today the GZK cutoff. Protons with energies above a threshold of about 10^{20} eV suffer a resonant interaction with the cosmic microwave background photons to produce pions through the formation of a short-lived particle (resonance) called Δ: $p + \gamma \to \Delta \to N + \pi$. This continues until their energy falls below the production threshold. Because of the mean path associated with the interaction, extragalactic cosmic rays from distances larger than 50 Mpc from the Earth and with energies greater than this threshold energy should be strongly suppressed on Earth, and there are no known sources within this distance that could produce them. A similar effect (nuclear photodisintegration) limits the mean free path for the propagation of nuclei heavier than the proton.
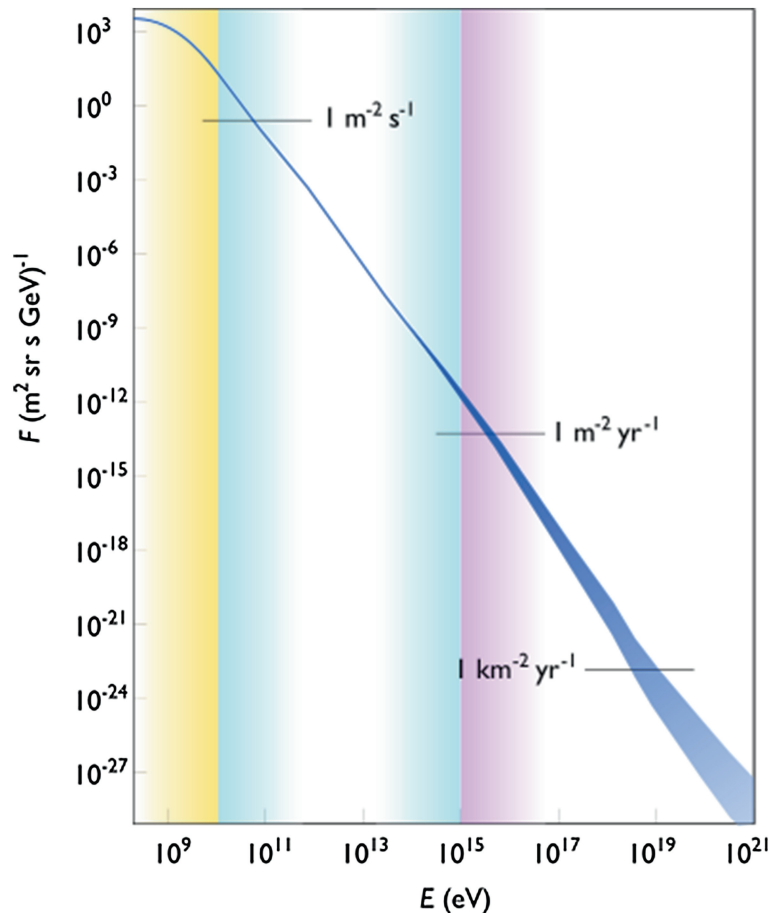
Fig. 1.10 The energy spectrum (number of incident particles per unit of energy, per second, per unit area, and per unit of solid angle) of the primary cosmic rays. The vertical band on the left indicates the energy region in which the emission from the Sun is supposed to be dominant; the central band the region in which most of the emission is presumably of Galactic origin; the band on the right the region of extragalactic origin. By Sven Lafebre (own work) [GFDL http://www.gnu.org/copyleft/fdl.html], via Wikimedia Commons.
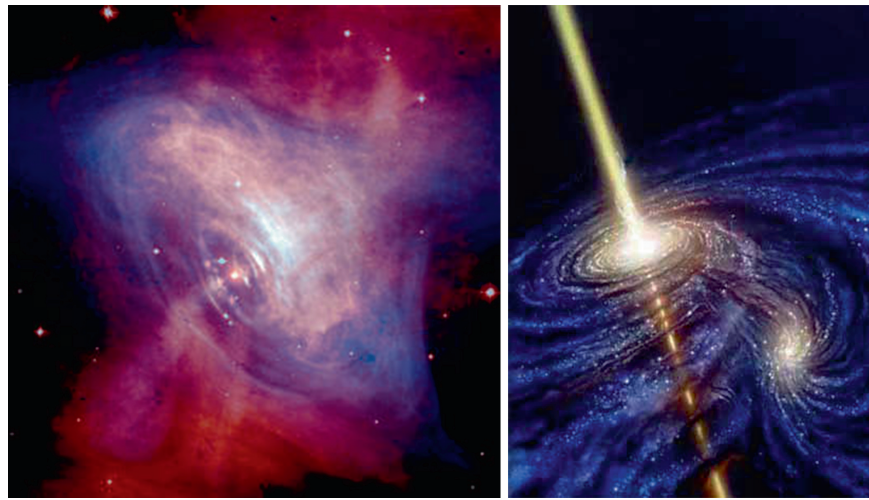
Fig. 1.11 Left: The remnant of the supernova in the Crab region (Crab nebula), a powerful gamma emitter in our galaxy. The supernova exploded in 1054 and the phenomenon was recorded by Chinese astronomers. For 40 years, until 2010, most astronomers regarded the Crab as a standard candle for high energy photon emission, but recently it was discovered that the Crab Nebula from time to time flickers. Anyway, most plots of sensitivity of detectors refer to a "standard Crab" as a reference unit. The vortex around the center is visible; a neutron star rapidly rotating (with a period of around 30 ms) and emitting pulsed gamma-ray streams (pulsar) powers the system. Some supernova remnants, seen from Earth, have an apparent dimension of a few tenths of a degree—about the dimension of the Moon. Right: A supermassive black hole accretes, swallowing neighboring stellar bodies and molecular clouds, and emits jets of charged particles and gamma rays. Credits: NASA.

Cosmic rays hitting the atmosphere (called primary cosmic rays) generally produce secondary particles that can reach the Earth's surface, through multiplicative showers.

About once per minute, a single subatomic particle enters the Earth's atmosphere with an energy larger than 10 J. Somewhere in the Universe there are accelerators that can impart energies 100 million times larger than the energy reached by the most powerful accelerators on Earth to single protons. It is thought that the ultimate engine of the acceleration of cosmic rays is gravity. In gigantic gravitational collapses, such as those occurring in supernovae (stars imploding at the end of their lives, see Fig. 1.11, left) and in the accretion of supermassive black holes (equivalent to millions to billions of solar masses) at the expense of the surrounding matter (Fig. 1.11, right), part of the potential gravitational energy is transformed, through not fully understood mechanisms, into kinetic energy of the particles.

The reason why the maximum energy attained by human-made accelerators cannot compete with the still mysterious cosmic accelerators with the presently known acceleration technologies is simple. The most efficient way to accelerate particles requires their confinement within a radius R by a magnetic field B, and the final energy is proportional to the product $R \times B$. On Earth, it is difficult to imagine reasonable confinement radii greater than one hundred kilometers, and magnetic fields stronger than 10 tesla (i.e., one hundred thousand times the Earth's magnetic field). This combination can provide energies of a few tens of TeV, such as those of the LHC accelerator at CERN. In nature, accelerators with much larger radii exist, such as supernova remnants (light-years) and active galactic nuclei (tens of thousands of light-years). Of course human-made accelerators have important advantages, such as being able to control the flux and the possibility of knowing the initial conditions (cosmic ray researchers do not know a-priori the initial conditions of the phenomena they study).

Among cosmic rays, photons are particularly important. The gamma photons (called gamma rays for historical reasons) are photons of very high energy, and occupy the most energetic part of the electromagnetic spectrum; being neutral they can travel long distances without being deflected by Galactic and extragalactic magnetic fields, hence they allow us to directly study their emission sources. These facts are now pushing us to study in particular the high-energy gamma rays and cosmic rays of hundreds of millions of TeV. However, gamma rays are less numerous than charged cosmic rays of the same energy, and the energy spectrum of charged cosmic rays is such that particles of hundreds of millions of TeV are very rare. The task of experimental physics is, as usual, challenging, and often discoveries correspond to breakthroughs in detector techniques.
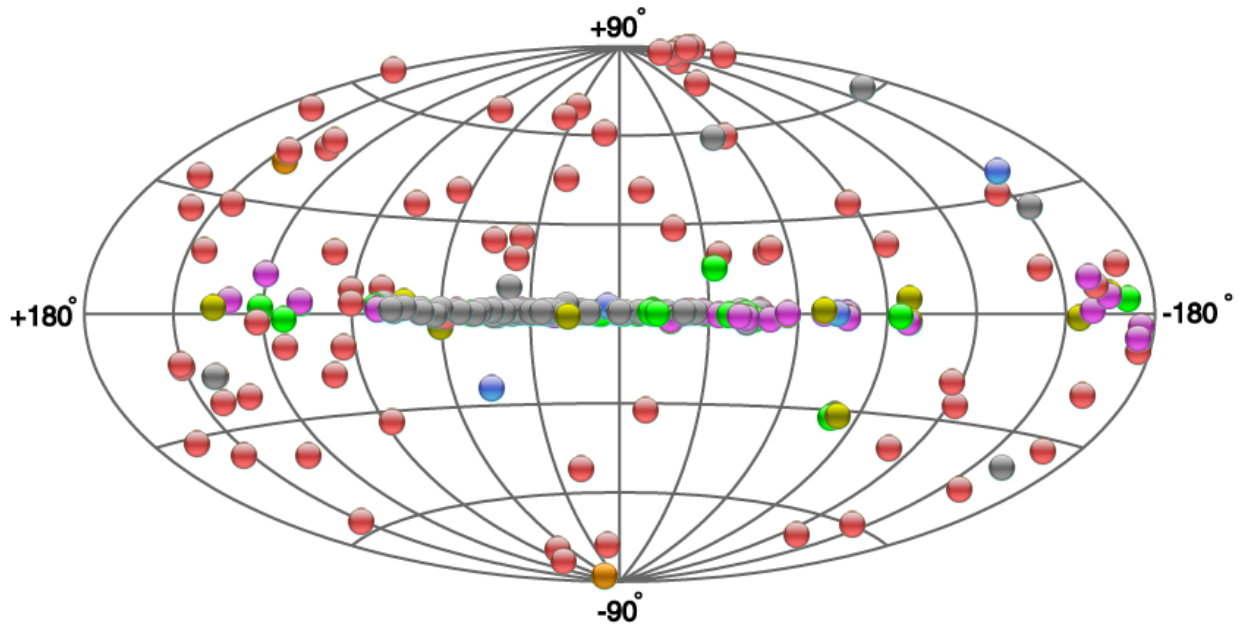
Fig. 1.12 Map of the emitters of photons above 100 GeV in the Universe, in Galactic coordinates (from the TeVCAT catalog). The sources are indicated as circles—the colors represent different kinds of emitters which will be explained in Chap. 10. From http://tevcat.uchicago.edu/ (February 2018).

A sky map of the emitters of very-high energy photons in Galactic coordinates[16] is shown in Fig. 1.12. One can identify both Galactic emitters (in the equatorial plane) and extragalactic emitters. The vast majority of the Galactic emitters is associated to remnants of supernovae, while extragalactic emitters are positionally consistent with active galaxies – instruments do not have the resolution needed to study the morphology of galaxies outside the local group.

---

[16] Usually the planar representations of maps of the Universe are done in Galactic coordinates. To understand what this means, let us start from a celestial coordinate system in spherical coordinates, in which the Sun is at the center, the primary direction is the one joining the Sun with the center of the Milky Way, and the Galactic plane is the fundamental plane. Coordinates are positive toward North and East in the fundamental plane.

We define as Galactic longitude (l or λ) the angle between the projection of the object in the Galactic plane and the primary direction. Latitude (symbol b or ϕ) is the angular distance between the object and the Galactic plane. For example, the North Galactic pole has a latitude of $+90°$.

Plots in Galactic coordinates are then projected onto a plane, typically using an elliptical (Mollweide or Hammer; we shall describe the Mollweide projection here) projection preserving areas. The Mollweide projection transforms latitude and longitude to plane coordinates x and y via the equations (angles are expressed in radians):

$$x = R\frac{2\sqrt{2}}{\pi}\cos\theta$$
$$y = R\sqrt{2}\sin\theta\,,$$

where θ is defined by the equation

$$2\theta + \sin(2\theta) = \pi\sin\phi$$

and R is the radius of the sphere to be projected. The map has area $4\pi R^2$, obviously equal to the surface area of the generating globe. The x-coordinate has a range $[-2R\sqrt{2}, 2R\sqrt{2}]$, and the y-coordinate has a range $[-R\sqrt{2}, R\sqrt{2}]$. The Galactic center is located at (0,0).

Less frequently, a projection using equatorial coordinates is used. In this case, the origin is at the center of Earth, the fundamental plane is the projection of Earth's equator onto the celestial sphere, and the primary direction is towards the March equinox; the projection of the Galactic plane is a curve in the ellipse.

1.7 Multimessenger Astrophysics

Physicists and astronomers have studied during millennia the visible light coming from astrophysical objects. The 20th century has been the century of multiwavelength astronomy: information from light at different wavelengths (radio, microwave, infrared, UV, X-ray and gamma ray) became available and is allowing us, in a joint effort with optical astronomy, to learn more about the various physical processes that occur throughout the Universe.

In the last decade, the detections of astrophysical neutrinos, and especially the detection of gravitational waves, allowed us to learn about objects that were invisible to other astronomical methods, for example merging black hole systems. The new observations paved the way for a new field of research called multimessenger astrophysics: combining the information obtained from the detection of photons, neutrinos, charged particles, and gravitational waves, can shed light on completely new phenomena and objects.

Further Reading

[F1.1] A. Einstein and L. Infeld, "The Evolution of Physics," Touchstone. This inspiring book is about the main ideas in physics. With simplicity and a limited amount of formulas it gives an exciting account for the advancement of science down to the early quantum theory.
[F1.2] L. Lederman and D. Teresi, "The God Particle: If the Universe Is the Answer, What Is the Question?", Dell. This book provides a history of particle physics starting from Greek philosophers down to modern quantum physics.
[F1.3] G. Smoot and K. Davidson, "Wrinkles in Time," Harper. This book discusses modern cosmology in a simple way.
[F1.4] S. Weinberg, "To Explain the World," Harper. This book discusses the evolution of modern science.

Exercises

1. *Size of a molecule.* Explain how you will be able to find the order of magnitude of the size of a molecule using a drop of oil. Make the experiment and check the result.
2. *Thomson atom.* Consider the Thomson model of the atom applied to a helium atom (the two electrons are in equilibrium inside a homogeneous positive charged sphere of radius $r \sim 10^{-10}$ m).

   (a) Determine the distance of the electrons to the center of the sphere.
   (b) Determine the vibration frequency of the electrons in this model and compare it to the first line of the spectrum of hydrogen, at $E \simeq 10.2$ eV.

3. *Atom as a box.* Consider a simplified model where the hydrogen atom is described by a one-dimensional box of length r with the proton at its center and where the electron is free to move around. Compute, considering the Heisenberg uncertainty principle, the total energy of the electron as a function of r and determine the value of r for which this energy is minimized.
4. *Naming conventions for particles.* Write down the symbol, charge and approximate mass for the following particles:

   (a) tau lepton;
   (b) anti muon-neutrino;
   (c) charm quark;
   (d) anti-electron;
   (e) anti-bottom quark.

5. *Strange mesons.* How many quark combinations can you make to build a strange neutral meson, using u, d and s quarks?
6. *The Universe.* Find a dark place close to where you live, and go there in the night. Try to locate the Milky Way and the Galactic Center. Comment on your success (or failure).
7. *Telescopes.* Research the differences between Newtonian and Galileian telescopes; discuss such differences.

8. *Number of stars in the Milky Way.* Our galaxy consists of a disk of a radius $r_d \simeq 15$ kpc about $h_d \simeq 300$ pc thick, and a spherical bulge at its center roughly 3 kpc in diameter. The distance between our Sun and our nearest neighboring stars, the Alpha Centauri system, is about 1.3 pc. Estimate the number of stars in the our Galaxy.

9. *Number of nucleons in the Universe.* Estimate the number of nucleons in the Universe.

10. *Hubble's law.* The velocity of a galaxy can be measured using the Doppler effect. The radiation coming from a moving object is shifted in wavelength, the relation being, for $\Delta\lambda/\lambda \ll 1$,

$$z = \frac{\Delta\lambda}{\lambda} \simeq \frac{v}{c} \,,$$

where λ is the rest wavelength of the radiation, $\Delta\lambda$ is the observed wavelength minus the rest wavelength, and v is defined as positive when the object parts away from the observer. Notice that in this case (for v small compared to the speed of light the formula is the same as for the classical Doppler effect).
An absorption line from a galaxy that is found at 500 nm in the laboratory is found at 505 nm when analyzing the spectrum of a particular galaxy. Estimate the distance of the galaxy.

11. *Luminosity and magnitude.* Suppose that you burn a car on the Moon, heating it at a temperature of 3000 K. What is the absolute magnitude of the car? What is the apparent magnitude m seen at Earth?

12. *Cosmic ray fluxes and wavelength.* The most energetic particles ever observed at Earth are cosmic rays. Make an estimation of the number of such events with an energy between 3×10^{18} and 10^{19} eV that may be detected in one year by an experiment with a footprint of $1000 \, \text{km}^2$. Evaluate the structure scale that can be probed by such particles.

13. *Energy from cosmic rays: Nikola Tesla's "free" energy generator.* "This new power for the driving of the world's machinery will be derived from the energy which operates the universe, the cosmic energy, whose central source for the Earth is the Sun and which is everywhere present in unlimited quantities." Immediately after the discovery of natural radioactivity, in 1901, Nikola Tesla patented an engine using the energy involved (and expressed a conjecture about the origin of such radioactivity). As below, we show a drawing (made by Tesla himself) of Tesla's first radiant energy receiver. If an antenna (the higher the better: why?) is wired to one side of a capacitor (the other going to ground,) the potential difference will charge the capacitor. Suppose you can intercept all high-energy cosmic radiation (assume 1 particle per square centimeter per second with an average energy of 3 GeV); what is the power you could collect with a 1 m^2 antenna, and how does it compare with solar energy?
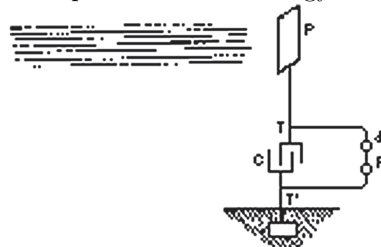
14. *Galactic and extragalactic emitters of gamma rays.* In Fig. 1.12, more than half of the emitters of high-energy photons lie in the Galactic plane (the equatorial line). Guess why.

Chapter 2
Basics of Particle Physics

Alessandro De Angelis and Mário Pimenta

This chapter introduces the basic techniques for the study of the intimate structure of matter, described in a historical context. After reading this chapter, you should understand the fundamental tools which led to the investigation and the description of the subatomic structure, and you should be able to compute the probability of occurrence of simple interaction and decay processes. A short reminder of the concepts of quantum mechanics and of special relativity needed to understand astroparticle physics is also provided.

2.1 The Atom

In the second half of the nineteenth century, the work by Mendeleev[1] on the periodic table of the elements provided the paradigm that paved the way for the experimental demonstration of the atomic structure. The periodic table is an arrangement of the chemical elements. Mendeleev realized that the physical and chemical properties of elements are related to their atomic mass in a quasi-periodic way. He ordered the 63 elements known at his time according to their atomic mass and arranged them in a table so that elements with similar properties would be in the same column. Figure 2.1 shows this arrangement. Hydrogen, the lightest element, is isolated in the first row of the table. The following light elements are then disposed in octets. Mendeleev found some gaps in his table, and predicted that elements then unknown would be discovered which would fill these gaps. His predictions were successful.

Mendeleev's periodic table has been expanded and refined with the discovery of new elements and a better theoretical understanding of chemistry. The most important modification was the use of atomic number (the number of electrons, which indeed characterizes an element) instead of atomic mass to order the elements. Since atoms are neutral, the same number of positive charges (protons) should be present. Starting from the element with atomic number 3, Mendeleev conjectured that electrons are disposed in shells. The n–th shell is complete with $2n^2$ electrons and the external shell alone dictates the chemical properties of an element. As we know, the quantum mechanical view is more complete but not as simple.

The present form of the periodic table (Appendix A) is a grid of elements with 18 columns and 7 rows, with an additional double row of elements. The rows are called periods; the columns, which define the chemical properties, are called groups; examples of groups are "halogens" and "noble gases".

Thanks to Mendeleev's table, a solid conjecture was formulated that atoms are composite states including protons and loosely bound electrons. But how to understand experimentally the inner structure of the atom, i.e., how were protons and electrons arranged inside the atom? Were electrons "orbiting" around a positive nucleus, or were both protons and electrons embedded in a "plum pudding", with electrons (the "plums") more loosely bound? A technique invented around 1900 to answer this question as been influential throughout the history of particle physics.

---

[1] Dimitri Mendeleev (1834–1907) was a Russian chemist born in Tobolsk, Siberia. He studied science in St. Petersburg, where he graduated in 1856 and became full professor in 1863. Mendeleev is best known for his work on the periodic table, published in Principles of Chemistry in 1869, but also, according to a myth popular in Russia, for establishing that the minimum alcoholic fraction of vodka should be 40 % – this requirement was easy to verify, as this is the minimum content at which an alcoholic solution can be ignited at room temperature.

Reihen	Gruppe I. — R²O	Gruppe II. — RO	Gruppe III. — R²O³	Gruppe IV. RH⁴ RO²	Gruppe V. RH³ R²O⁵	Gruppe VI. RH² RO³	Gruppe VII. RH R²O⁷	Gruppe VIII. — RO⁴]
1	H=1							
2	Li=7	Be=9,4	B=11	C=12	N=14	O=16	F=19	
3	Na=23	Mg=24	Al=27,3	Si=28	P=31	S=32	Cl=35,5	
4	K=39	Ca=40	— =44	Ti =48	V=51	Cr=52	Mn=55	Fe=56, Co=59, Ni=59, Cu=63
5	(Cu=63)	Zn=65	— =68	— =72	As=75	Se=78	Br=80	
6	Rb=85	Sr=87	?Yt=88	Zr=90	Nb=94	Mo=96	— =100	Ru=104, Rh=104, Pd=106, Ag=108
7	(Ag=108)	Cd=112	In=113	Sn=118	Sb=122	Te=125	J = 127	
8	Cs=133	Ba=137	?Di=138	?Ce=140	—	—	—	— — — —
9	(—)	—	—	—	—			
10	—	—	?Er=178	?La=180	Ta=182	W=184	—	Os=195, Ir=197, Pt=198, Au=199
11	(Au=199)	Hg=200	Tl=204	Pb=207	Bi=208	—	—	— — — —
12	—	—	—	Th=231	—	U=240	—	

Fig. 2.1 Mendeleev's periodic table as published in Annalen der Chemie 1872 [public domain]. The noble gases had not yet been discovered, and are thus not displayed.
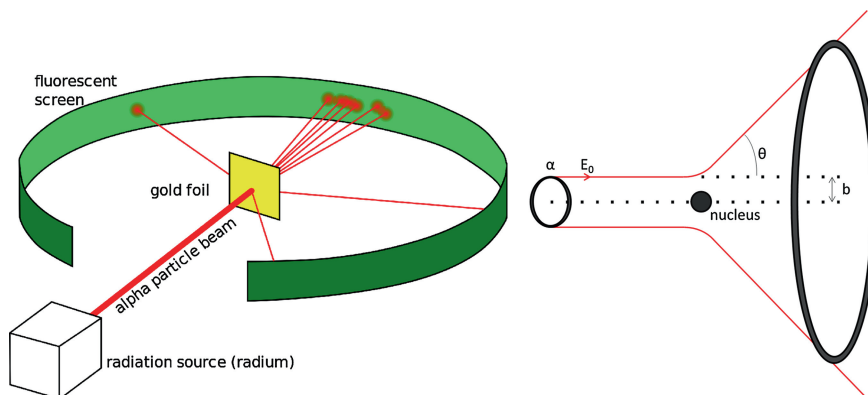
Fig. 2.2 Left: Sketch of the Rutherford experiment (by Kurzon [own work, CC BY-SA 3.0], via Wikimedia Commons). Right: Trajectories of the α particles.

2.2 The Rutherford Experiment

Collide a beam of particles with a target, observe what comes out, and try to infer the properties of the interacting objects and/or of the relevant interaction force. This is the paradigm of particle physics experiments. The first experiment was conducted by Marsden and Geiger starting in 1908 and is known as the Rutherford[2] experiment. The beam consisted of α particles (known today as helium nuclei); the target was a thin (some 400 nm) gold foil; the detector, a scintillating screen which could be read by a microscope. The result of the observation was that around 1 in 8000 α particles were deflected at very large angles (greater than 90°). A sketch of the experiment is shown in Fig. 2.2, left.

The interpretation of this result was given by Rutherford in 1911. It was based on a model in which the positive nucleus of the atom was a point fixed in space and the scattering of the α particles was due to the Coulomb force and obeyed classical mechanics (quantum mechanics was yet to be born). The α particles were thus supposed to follow Keplerian trajectories. As energy and angular momentum are conserved, for a given impact parameter b (the perpendicular distance between the beam particle and the nucleus, see Fig. 2.2, right) there will be a well-defined scattering angle θ, and:

---

[2] Ernest Rutherford (1871–1937) was a New Zealand-born physicist. In early works at McGill University in Canada, he proved that radioactivity involved the transmutation of one chemical element into another; he differentiated and named the α (helium nuclei) and β (electrons) radiations. In 1907, Rutherford moved to Manchester, UK, where he discovered (and named) the proton. In 1908 he was awarded the Nobel Prize in Chemistry "for his investigations into the disintegration of the elements, and the chemistry of radioactive substances". He became director of the Cavendish Laboratory at Cambridge University in 1919. Under his leadership, the neutron was discovered by James Chadwick in 1932. Also in 1932, his students John Cockcroft and Ernest Walton split for the first time the atom with a beam of particles. Rutherford was buried near Newton in Westminster Abbey, London. The chemical element rutherfordium – atomic number 104 – was named after him in 1997.

$$b = \left(\frac{1}{4\pi\epsilon_0} \right) \frac{Q_1 Q_2}{2E_0} \cot \frac{\theta}{2} \tag{2.1}$$

where ϵ_0 is the vacuum dielectric constant, Q_1 and Q_2 are respectively the charges of the beam particle and of the target particle, and E_0 is the kinetic energy of the beam particle.

If the number of beam particles per unit of transverse area n_{beam} does not depend on the transverse coordinates b and ϕ (the beam is uniform and wide with respect to the target size), the differential number of particles as a function of b is:

$$\frac{dN}{db} = 2\pi b\, n_{beam}\,. \tag{2.2}$$

Expressing the differential number of particles as a function of the scattering angle θ:

$$\frac{dN}{d\theta} = \frac{dN}{db} \frac{db}{d\theta} \tag{2.3}$$

we obtain using Eq. 2.1:

$$\frac{dN}{d\theta} = \pi \left(\frac{1}{4\pi\epsilon_0} \frac{Q_1 Q_2}{2E_0} \right)^2 \frac{\cos \frac{\theta}{2}}{\sin^3 \frac{\theta}{2}} n_{beam} \tag{2.4}$$

or, in terms of the solid angle Ω, $(d\Omega = 2\pi \sin \theta d\theta)$:

$$\frac{dN}{d\Omega} = \left(\frac{1}{4\pi\epsilon_0} \frac{Q_1 Q_2}{4E_0} \right)^2 \frac{1}{\sin^4 \frac{\theta}{2}} n_{beam}\,, \tag{2.5}$$

the well-known "Rutherford formula." This equation explained the observation of scattering at large angles and became the paradigm for particle diffusion of nuclei. According to gossip, like some experimentalists Rutherford disliked mathematics, and this formula was derived for him by the mathematician Ralph Fowler, who later married Rutherford's daughter, and finally became a professor of Theoretical Physics in Cambridge.

2.3 Inside the Nuclei: β Decay and the Neutrino

Beta (β) radioactivity, the spontaneous emission of electrons by some atoms, was discovered by Ernest Rutherford just a few years after the discovery by Henri Becquerel that uranium was able to impress photographic plates wrapped in black paper. It took then some years before James Chadwick in 1914 realized that the energy spectrum of the electrons originated in β decays was continuous and not discrete (Fig. 2.3). This was a unique feature in the new quantum world, in which decays were explained as transitions between well-defined energy levels. There was a missing energy problem, and many explanations were tried along the years, but none was proved. In 1930, Niels Bohr went so far as to suggest that the energy conservation law could be violated.

In December 1930, in a famous letter, Wolfgang Pauli proposed as "desperate remedy" the existence of a new neutral particle with spin one-half and low mass named *neutron*: "The continuous β spectrum would then become understandable from the assumption that in the β decay a neutron is emitted along with the electron, in such way that the sum of the energies of the neutron and the electron is constant." This tiny new particle was later renamed *neutrino* by Enrico Fermi. The particle today known as neutron, constituent of the atomic nuclei, was discovered by James Chadwick in 1932, Nobel prize in Physics 1935. Then at the University of Cambridge, Chadwick found a radiation consisting of uncharged particles of approximately the mass of the proton. His group leader Rutherford had conjectured the existence of the neutron already in 1920, in order to explain the difference between the atomic number of an atom and its atomic mass, and he modeled it as an electron orbiting a proton.

Atomic nuclei were thus composed (in the modern language) by protons and neutrons and the β radioactive decay were explained by the decay of one of the neutrons in the nucleus into one proton, one electron, and one neutrino (in fact, as it will be discussed later, an antineutrino):

$$n \to p e^- \bar{\nu}. \tag{2.6}$$

The β^+ decay, i.e., the decay of one proton in the nucleus into one neutron, one positron (the antiparticle of the electron), and one neutrino
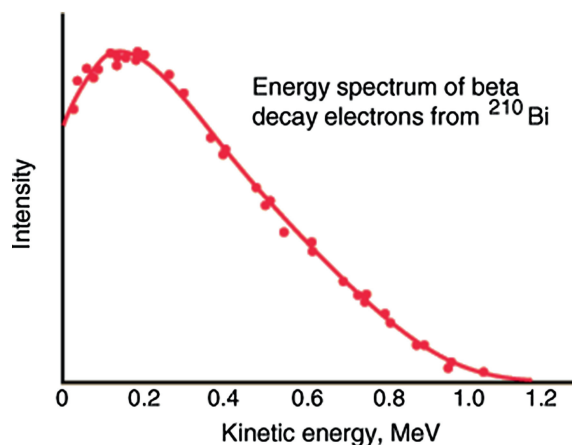
Fig. 2.3 Energy spectrum of electrons coming from the β decay of ^{210}Bi (called historically "Radium E") to ^{210}Po (called historically "Radium F"). From http://hyperphysics.phy-astr.gsu.edu/; the measurements are from G. J. Neary, Roy. Phys. Soc. (London) A175 (1940) 71.

$$p \to n e^+ \nu \tag{2.7}$$

is also possible, although the neutron mass is larger than the proton mass – take into account that nuclei are bound in the nucleus and not free particles.

Neutrinos have almost no interaction with matter, and therefore their experimental discovery was not an easy enterprise: intense sources and massive and performing detectors had to be built. Only in 1956 Reines and Cowan proved the existence of the neutrino, placing a water tank near a nuclear reactor. Some of the antineutrinos produced in the reactor interacted with a proton in the water, giving rise to a neutron and a positron, the so-called inverse beta process:

$$\bar{\nu} p \to n e^+. \tag{2.8}$$

The positron then annihilates with an ordinary electron and the neutron is captured by cadmium chloride atoms dissolved in the water. Three photons were then detected (two from the annihilation and, 5 μs later, one from the de-excitement of the cadmium nucleus).

The mass of the neutrino is indeed very low (but not zero, as discovered by the end of the twentieth century with the observation of the oscillations between neutrinos of different families, a phenomenon that is possible only if neutrinos have nonzero mass) and determines the maximum energy that the electron may have in the beta decay (the energy spectrum end-point). The present measurements are compatible with neutrino masses below a few eV.

A classical description of the neutron decay would be possible only if neutrons were a bound state of a proton, an electron and a neutrino – which experiments demonstrated not to be the case. In order to describe decays in a consistent way, we need to treat initial and final states as wavefunctions, and thus, to use the quantum mechanical formalism.

2.4 A Look Into the Quantum World: Schrödinger's Equation

Schrödinger's[3] wave equation

$$i\hbar \frac{\partial \Psi}{\partial t} = -\frac{\hbar^2}{2m} \boldsymbol{\nabla}^2 \Psi + U \Psi$$

can be seen as the translation into the wave language of the Hamiltonian equation of classical mechanics

---

[3] Erwin Schrödinger was an Austrian physicist who obtained fundamental results in the fields of quantum theory, statistical mechanics and thermodynamics, physics of dielectrics, color theory, electrodynamics, cosmology, and cosmic-ray physics. He also paid great attention to the philosophical aspects of science, re-evaluating ancient and oriental philosophical concepts, and to biology and to the meaning of life. He formulated the famous paradox of the Schrödinger cat. He shared with P.A.M. Dirac the 1933 Nobel Prize in Physics "for the discovery of new productive forms of atomic theory".

$$H = \frac{p^2}{2m} + U,$$

where the Hamiltonian (essentially the total energy of the system, i.e., the kinetic energy plus the potential energy U) is represented by the operator

$$\hat{H} = i\hbar \frac{\partial}{\partial t}$$

and momentum by

$$\hat{\mathbf{p}} = -i\hbar \boldsymbol{\nabla}.$$

The solutions of the equation are in general complex wavefunctions, which can be seen as probability density amplitudes (probability being the square of the modulus of the amplitude).

2.4.1 Properties of Schrödinger's Equation and of its Solutions

In "classical" quantum mechanics, physical states are represented by complex wavefunctions $\Psi(\mathbf{r}, t)$ which are solutions of Schrödinger's equation. Here we recall briefly some of the main characteristics of these solutions; they can be extended in general to any "good" Hamiltonian equation. This is not meant to be a formal description, but will just focus on the concepts.

2.4.1.1 The meaning of wavefunctions

What is a wavefunction, and what can it tell us? In classical physics an elementary particle, by its nature, is localized at a point, whereas its wavefunction is spread out in space. How can such an object be said to describe the state of a particle? The answer is given by the so-called Born's statistical interpretation. If Ψ is normalized such that

$$\int dV\, \Psi^* \Psi = 1 \tag{2.9}$$

(the integral is extended over all the volume), the probability to find the particle in an infinitesimal volume dV around a point $\mathbf{r}$ at a time t is

$$dP = \Psi^*(\mathbf{r}, t)\Psi(\mathbf{r}, t)\, dV = |\Psi(\mathbf{r}, t)|^2\, dV\,.$$

The left term in Eq. 2.9 is defined as the scalar product of the Ψ function by itself.

The statistical interpretation introduces an uncertainty into quantum mechanics: even if you know everything the theory can tell you about the particle (its wavefunction), you cannot predict with certainty the outcome of a simple experiment to measure its position: all the theory gives is statistical information about the possible results.

2.4.1.2 Measurement and operators

The expectation value of the measurement of, say, position along the x coordinate is given by

$$\langle x \rangle = \int dV\, \Psi^*\, x\, \Psi \tag{2.10}$$

and one can easily demonstrate (see for example [F2.1]) that the expectation value of the momentum along x is

$$\langle p_x \rangle = \int dV\, \Psi^* \left(-i\hbar \frac{\partial}{\partial x} \right) \Psi\,. \tag{2.11}$$

In these two examples we saw that measurements are represented by operators acting on wavefunctions. The operator x represents position along x, and the operator $(-i\hbar\partial/\partial x)$ represents the x component of momentum, p_x. When ambiguity is possible, we put a "hat" on top of the operator to distinguish it from the corresponding physical quantity.

When we measure some quantity, we obtain a well-defined value: the wavefunction "collapses" to an eigenfunction, and the measured value is one of the eigenvalues of the measurement operator.

To calculate the expectation value of a measurement, we put the appropriate operator "in sandwich" between Ψ^* and Ψ, and integrate. If A is a quantity and $\hat{A}$ the corresponding operator,

$$\langle A \rangle = \int dV \, \Psi^* \left(\hat{A} \right) \Psi \,. \tag{2.12}$$

2.4.1.3 Dirac notation

In the Dirac notation, the wavefunction is replaced by a state vector identified by the symbol $\mid \Phi \rangle$, and is called *ket*; the symbol $\langle \Psi \mid$ is called *bra*.

The *bracket* $\langle \Psi \mid \Phi \rangle$ is the scalar product of the two vectors:

$$\langle \Psi \mid \Phi \rangle = \int dV \Psi^* \Phi \,.$$

In this notation, an operator $\hat{A}$ acts on a ket $\mid \Phi >$, transforming it into a ket $\mid \hat{A} \, \Phi >$, and thus

$$< \Psi \mid \hat{A} \mid \Phi > = \int dV \, \Psi^* (\hat{A} \Phi) \,.$$

2.4.1.4 Good operators must be Hermitian

We define as Hermitian conjugate or adjoint of $\hat{A}$ an operator $\hat{A}^\dagger$ such that for any $\mid \Psi >$

$$\langle \hat{A}^\dagger \Psi \mid \Psi \rangle = \langle \Psi \mid \hat{A} \Psi \rangle \,.$$

Let $\hat{A}$ represent an observable. One has for the expectation value

$$\langle \Psi \mid \hat{A} \mid \Psi \rangle = \langle \Psi \mid \hat{A} \Psi \rangle = \langle \hat{A} \Psi \mid \Psi \rangle^* = \langle \Psi \mid \hat{A}^\dagger \Psi \rangle^* = \langle \Psi \mid \hat{A}^\dagger \mid \Psi \rangle^*$$

and thus if we want all expectation values (and the results of any measurement) to be real, $\hat{A}$ must be a Hermitian operator (i.e., such that $\hat{A}^\dagger = \hat{A}$).

Now let us call Ψ_i the eigenvectors of $\hat{A}$ (which form a basis) and a_i the corresponding eigenvalues; for Ψ_m, Ψ_n such that $n \neq m$

$$\hat{A} \mid \Psi_m \rangle = a_m \mid \Psi_m \rangle \,; \quad \hat{A} \mid \Psi_n \rangle = a_n \mid \Psi_n \rangle$$

and thus

$$\begin{aligned} a_n \langle \Psi_n \mid \Psi_m \rangle \; &= \langle \Psi_n \mid \hat{A} \mid \Psi_m \rangle = a_m \langle \Psi_n \mid \Psi_m \rangle \\ &\Rightarrow 0 = (a_n - a_m) \langle \Psi_n \mid \Psi_m \rangle \\ &\Rightarrow \langle \Psi_n \mid \Psi_m \rangle = 0 \quad \forall \; m \neq n \,. \end{aligned}$$

If the Ψ_i are properly normalized

$$\langle \Psi_n \mid \Psi_m \rangle = \delta_{mn}.$$

Hermitian operators are thus good operators for representing the measurement of physical quantities: their eigenvalues are real (and thus can be the measurement of a quantity) and the solutions form an orthonormal basis.

2.4.1.5 Time-independent Schrödinger's equation

Schrödinger's equation is an equation for which the eigenvectors are eigenstates of defined energy. For a potential U not explicitly dependent on time, it can be split into two equations. One is a time-independent eigenvalue equation

$$\left(-\frac{\hbar^2}{2m}\boldsymbol{\nabla}^2 + U\right)\psi(\mathbf{r}) = E\psi(\mathbf{r})$$

and the other is an equation involving only time

$$\phi(t) = \exp(-iEt/\hbar)\,.$$

The complete solution is

$$\Psi(\mathbf{r},t) = \psi(\mathbf{r})\phi(t)\,.$$

2.4.1.6 Time evolution of expectation values

We define *commutator* $[\hat{A}, \hat{B}]$ of two operators $\hat{A}$ e $\hat{B}$ the operator

$$[\hat{A}, \hat{B}] = \hat{A}\hat{B} - \hat{B}\hat{A}\,,$$

and we say that the two operators commute when their commutator is zero. We can simultaneously measure observables whose operators commute, since such operators have a complete set of simultaneous eigenfunctions – thus one can have two definite measurements at the same time.

The time evolution of the expectation value of a measurement described by a Hermitian operator $\hat{A}$ is given by the equation

$$\frac{d}{dt}\langle\psi|\hat{A}|\psi\rangle = -\frac{i}{\hbar}\langle\psi|[\hat{H}, \hat{A}]|\psi\rangle\,. \qquad (2.13)$$

2.4.1.7 Probability density and probability current; continuity equation

The probability current $\mathbf{j}$ associated to a wavefunction can be defined as

$$\mathbf{j} = \frac{\hbar}{2mi}\left(\Psi^*\nabla\Psi - \Psi\nabla\Psi^*\right)\,. \qquad (2.14)$$

A continuity equation holds related to the probability density P to find a particle at a given time in a given position:

$$\frac{\partial P}{\partial t} + \boldsymbol{\nabla}\cdot\mathbf{j} = 0\,.$$

2.4.1.8 Spectral decomposition of an operator

Since the eigenfunctions $\{|\Psi_i\rangle\}$ of a Hermitian operator $\hat{A}$ form a basis, we can write

$$\sum_j |\Psi_j\rangle\langle\Psi_j| = I$$

where I is the unity operator.

This means that any wavefunction can be represented in this orthonormal basis by a unique combination:

$$|\Psi\rangle = \sum_m |\Psi_m\rangle\langle\Psi_m|\Psi\rangle = \sum_m c_m |\Psi_m\rangle$$

where $c_m = \langle\Psi_m|\Psi\rangle$ are complex numbers.

The normalization of $|\Psi\rangle$ to 1 implies a relation on the c_m:

$$1 = \langle\Psi|\Psi\rangle = \sum_m \langle\Psi|\Psi_m\rangle\langle\Psi_m|\Psi\rangle = \sum_m |c_m|^2\,,$$

and the probability to obtain from a measurement the eigenvalue a_m is

$$P_m = |\langle\Psi_m|\Psi\rangle|^2 = |c_m|^2\,.$$

In addition, we can determine coefficients $a_{mn} = \langle \Psi_m \mid \hat{A} \mid \Psi_n \rangle$ such that:

$$\hat{A} \mid \Psi \rangle = \sum_{mn} \mid \Psi_m \rangle \langle \Psi_m \mid \hat{A} \mid \Psi_n \rangle \langle \Psi_n \mid \Psi \rangle = \sum_{m,n} a_{mn} c_n \mid \Psi_m \rangle .$$

$[a_{mn}]$ is a square matrix representing $\hat{A}$ in the vector space defined by eigenvectors; the c_n are an n-tuple of components representing $|\Psi\rangle$.

2.4.1.9 Uncertainty relations

Pairs of noncommuting operators cannot give rise to simultaneous measurements arbitrarily precise for the associated quantities (this is usually called Heisenberg's uncertainty principle, but in fact it is a theorem).

Let us define as spread of an operator the operator:

$$\Delta \hat{A} = \hat{A} - \langle A \rangle .$$

Let $\hat{A}$ and $\hat{B}$ be two Hermitian operators; we define $\hat{C}$ such that

$$[\hat{A}, \hat{B}] = i\hat{C}$$

($\hat{C}$ is Hermitian; you can demonstrate it). One has

$$\langle (\Delta A)^2 \rangle \langle (\Delta B)^2 \rangle \geq \frac{\langle C^2 \rangle}{4} . \tag{2.15}$$

In particular, when a simultaneous measurement of position and momentum along an axis, say x, is performed, one has

$$\Delta x \Delta p_x \geq \frac{\hbar}{2} \sim \hbar .$$

Somehow linked to this is the fact that energy is not defined with absolute precision, but, if measured in a time Δt, has an uncertainty ΔE such that

$$\Delta E \Delta t \sim \hbar$$

(energy conservation can be violated for short times). The value of Planck's constant $\hbar \simeq 6.58 \times 10^{-22}$ MeV s is small with respect to the value corresponding to the energies needed to create particles living for a reasonable (detectable) time.

2.4.2 Uncertainty and the Scale of Measurements

If we want to investigate a structure below a length scale Δx, we are limited by the uncertainty theorem. Since a wavelength

$$\lambda \simeq \frac{\hbar}{p} \tag{2.16}$$

can be associated with a particle of momentum p, this means that particles of energy (energy is close to momentum times c for high energy particles):

$$E > \frac{\hbar c}{\Delta x} \tag{2.17}$$

must be used. For example, X-rays with an energy of ~ 1 keV can investigate the structure of a target at a scale

$$\Delta x > \frac{\hbar c}{E} \simeq 2 \times 10^{-11} \, \text{m}, \tag{2.18}$$

an order of magnitude smaller than the atomic radius. A particle with an energy of 7 TeV, the running energy of the Large Hadron Collider (LHC) accelerator at CERN can investigate the structure of a target at a scale
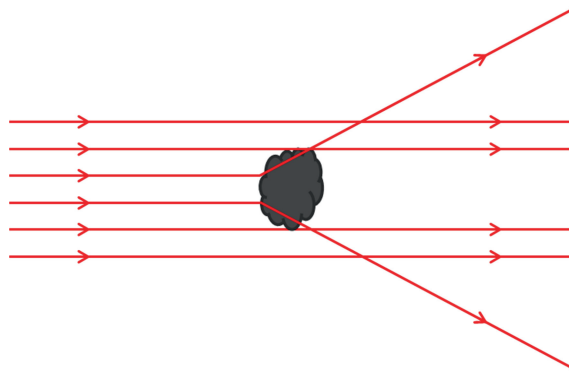
Fig. 2.4 Interaction of a particle beam with a single object target. Lines represent different particles in the beam.

$$\Delta x > \frac{\hbar c}{E} \simeq 3 \times 10^{-20}\,\text{m}. \tag{2.19}$$

Since one can extract only a finite energy from finite regions of the Universe (and maybe the Universe itself has a finite energy), there is an intrinsic limit to the investigation of the structure of matter, below which the quest makes no more sense. However, as we shall see, there are practical limits much more stringent than that. Does the concept of elementary particle have a meaning below these limits? The question is more philosophical than physical, since one cannot access infinite energies.

The maximum energies attainable by human-made accelerators are believed to be of the order of some 1 PeV. However, Nature gives us for free beams of particles with much larger energies, hitting the Earth from extraterrestrial sources: cosmic rays.

2.5 The Description of Scattering: Cross Section and Interaction Length

Particle physicists observe and count particles, as pioneered by the Rutherford experiment. They count, for instance, the number of particles of a certain type with certain characteristics (energy, spin, scattering angle) that result from the interaction of a given particle beam at a given energy with a given target. It is then useful to express the results as quantities independent from the number of particles in the beam, or in the target. These quantities are called cross sections.

2.5.1 Total Cross Section

The total cross section σ measured in a collision of a beam with a single object (Fig. 2.4) is defined as

$$\sigma_{tot} = \frac{N_{int}}{n_{beam}} \tag{2.20}$$

where N_{int} is the total number of measured interactions and n_{beam} is, as previously defined, the number of beam particles per unit of transverse area.

A cross section has thus dimensions of an area. It represents the effective area with which the interacting particles "see" each other. The usual unit for cross section is the barn, b (1 b $=$ 10^{-24} cm^2) and its submultiples (millibarn – mb, microbarn – μb, nanobarn – nb, picobarn – pb, femtobarn – fb, etc.). To give an order of magnitude, the total cross section for the interaction of two protons at a center-of-mass energy of around 100 GeV is 40 mb (approximately the area of a circle with radius 1 fm).

We can write the total cross section with a single target as

$$\sigma_{tot} = \frac{W_{int}}{J}\,, \tag{2.21}$$

in terms of the interaction rate W_{int} (number of interactions per unit of time) and of the flux of incident particles J (number of beam particles that cross the unit of transverse area per unit of time). J is given as
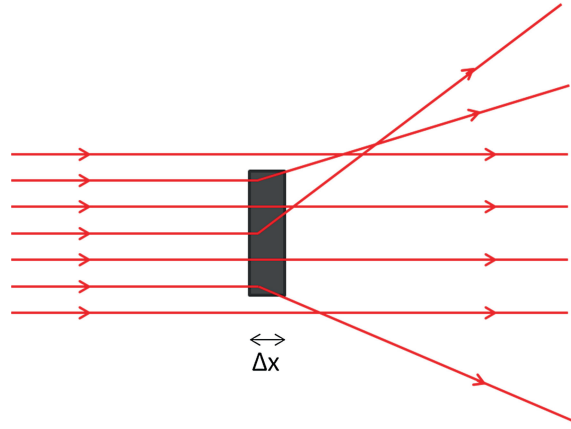
Fig. 2.5 Interaction of a particle beam with a target composed of many sub-targets.

$$J = \rho_{beam} v, \tag{2.22}$$

where ρ_{beam} is the density of particles in the beam and v is the beam particle velocity in the rest frame of the target.

In real life, most targets are composed of N_t small sub-targets (Fig. 2.5) within the beam incidence area. Considering as sub-targets the nuclei of the atoms of the target with depth Δx, and ignoring any shadowing between them, N_t is given by:

$$N_t = \mathcal{N} \frac{\rho \Delta x}{w_a}, \tag{2.23}$$

where $\mathcal{N}$ is Avogadro's number, ρ is the specific mass of the target, w_a is its atomic weight. Note that N_t is a dimensionless number: it is just the number of sub-targets that are hit by a beam that has one unit of transverse area. In the case of several sub-targets, the total cross section can thus be written as:

$$\sigma_{tot} = \frac{W_{int}}{J N_t} = \frac{W_{int}}{\mathcal{L}}, \tag{2.24}$$

where $\mathcal{L}$ is the luminosity.

The total number of interactions occurring in an experiment is then simply the product of the total cross section by the integral of the luminosity over the run time T of the experiment:

$$N_{tot} = \sigma_{tot} \int_T \mathcal{L} dt. \tag{2.25}$$

The units of integrated luminosity are therefore inverse barn, b^{-1}.

In this simplified model we are neglecting the interactions between the scattered particles, the interactions between beam particles, the binding energies of the target particles, the absorption, and the multi-scattering of the beam within the target.

2.5.2 Differential Cross Sections

In practice, detectors often cover only a given angular region and we do not measure the total cross section in the full solid angle. It is therefore useful to introduce the differential cross section

$$\frac{d\sigma(\theta, \phi)}{d\Omega} = \frac{1}{\mathcal{L}} \frac{dW_{int}(\theta, \phi)}{d\Omega} \tag{2.26}$$

and
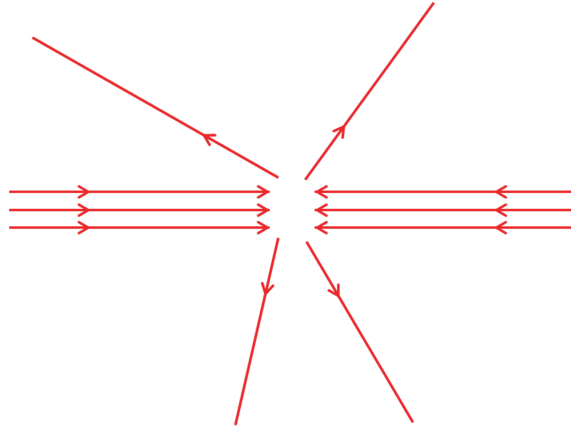
Fig. 2.6 Beam-beam interaction.

$$\sigma_{tot} = \int \int \frac{d\sigma(\theta, \phi)}{d\Omega} d\phi \, d\cos\theta \, . \tag{2.27}$$

The Rutherford formula (2.5) expressed as a differential cross section is then

$$\frac{d\sigma}{d\Omega} = \left(\frac{1}{4\pi\epsilon_0} \frac{Q_1 Q_2}{4E_0} \right)^2 \frac{1}{\sin^4 \frac{\theta}{2}} \, . \tag{2.28}$$

2.5.3 Cross Sections at Colliders

In colliders, beam–target collisions are replaced by beam–beam collisions (Fig. 2.6). Particles in the beams come in bunches. The luminosity is thus defined as

$$\mathcal{L} = \frac{N_1 N_2}{A_T} N_b \, f \tag{2.29}$$

where N_1 and N_2 are the number of particles in the crossing bunches, N_b is the number of bunches per beam, A_T is the intersection transverse area, and f is the beam revolution frequency. In case of two Gaussian beams, 1 and 2, one can approximate

$$A_T \simeq 2\pi \sqrt{\sigma_{x_1}^2 + \sigma_{x_2}^2} \sqrt{\sigma_{y_1}^2 + \sigma_{y_2}^2} \tag{2.30}$$

where x and y are othornormal coordinates transverse to the beam. In case of equal and symmetric beams

$$A_T \simeq 4\pi \sigma_B^{\,2} \, . \tag{2.31}$$

2.5.4 Partial Cross Sections

When two particles collide, it is often the case that there are many possible outcomes. Quantum mechanics allows us to compute the occurrence probability for each specific final state. Total cross section is thus a sum over all possible specific final states

$$\sigma_{tot} = \sum_i \sigma_i \tag{2.32}$$

where σ_i is defined as the partial cross section for channel i.

A relevant partial cross section is the elastic cross section, σ_{el}. In an elastic process, the particles in the final state and in the initial state are the same – there is simply an exchange of energy-momentum. Whenever there is no available energy to create new particles, $\sigma_{tot} = \sigma_{el}$. This is shown in Fig. 2.7 for the case of proton–proton and antiproton–proton interactions.
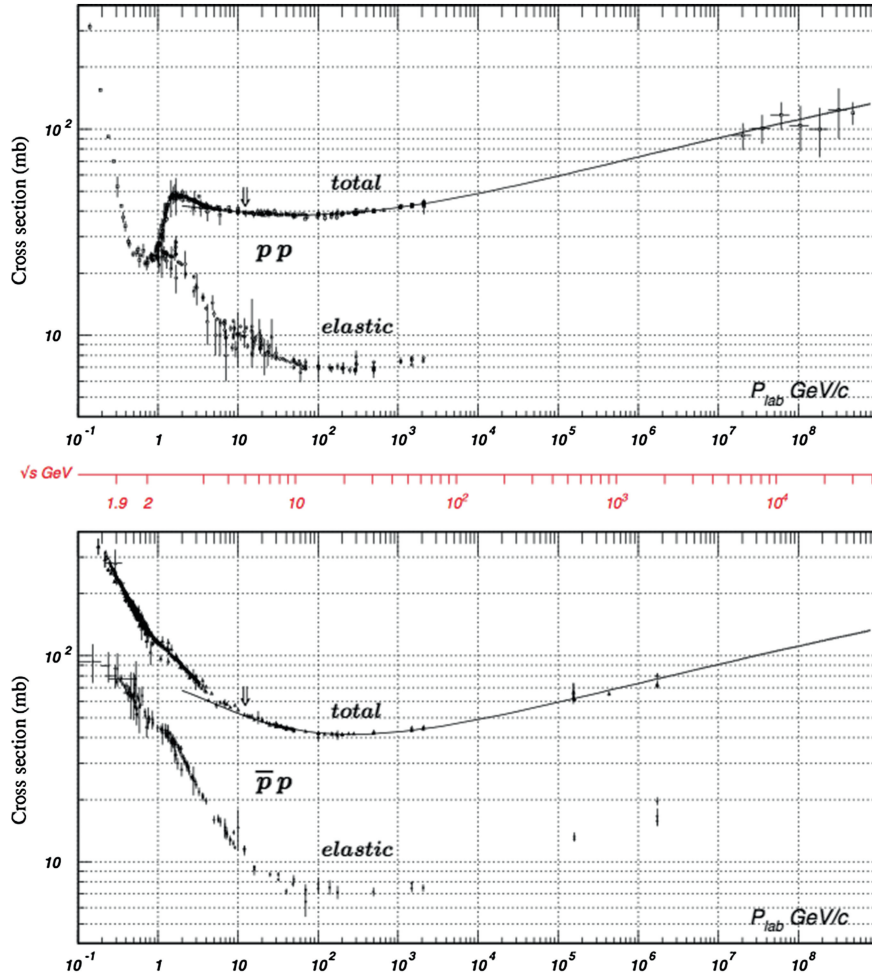
Fig. 2.7 Total and elastic cross sections for pp and $\bar{p}p$ collisions as a function of beam momentum in the laboratory reference frame and total center-of-mass energy. From the Review of Particle Physics, K.A. Olive et al. (Particle Data Group), Chin. Phys. C 38 (2014) 090001.

2.5.5 Interaction Length

When a beam of particles crosses matter, its intensity is reduced. Using the definition of total cross section (Eq. 2.21 and Eq. 2.24), the reduction when crossing a slice of thickness Δx is:

$$\frac{\Delta N}{N} = \frac{W_{int}}{J} = \left(\mathcal{N} \frac{\rho}{w_A} \Delta x \right) \sigma_{tot} \tag{2.33}$$

where w_A is the atomic weight of the target. Defining the interaction length L_{int} as

$$L_{int} = \frac{w_A}{\sigma_{tot} \mathcal{N} \rho} \tag{2.34}$$

then

$$\frac{dN}{dx} = -\frac{1}{L_{int}} N \tag{2.35}$$

and

$$N = N_0 \, e^{-x/L_{int}}. \tag{2.36}$$

L_{int} has units of length (usually cm). However, this quantity is often redefined as
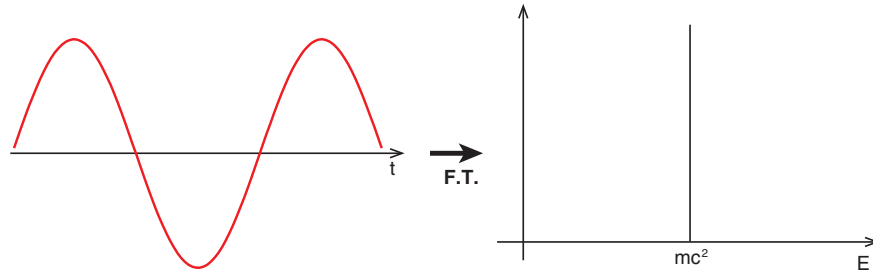
Fig. 2.8 The wavefunction of a stable particle and its energy spectrum.
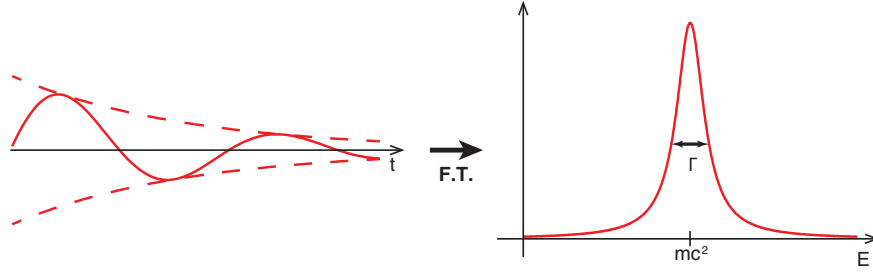
Fig. 2.9 The wavefunction of an unstable particle and its energy spectrum.

$$L'_{int} = L_{int} \ \rho = \frac{w_A}{\sigma_{tot} \ \mathcal{N}} \tag{2.37}$$

and its units will then be g cm^{-2}. This way of expressing L_{int} is widely used in cosmic ray physics. In fact, the density of the atmosphere has a strong variation with height. For this reason, to study the interaction of cosmic particles in their path in the atmosphere, the relevant quantity is not the path length but rather the amount of matter that has been traversed, $\int \rho dx$.

In a rough approximation, the atmosphere is isothermal; under this hypothesis, its depth x in g cm^{-2} varies exponentially with height h (km), according to the formula

$$x = Xe^{-h/H} \tag{2.38}$$

where $H \simeq 6.5$ km, and $X \simeq 1030$ g/cm^2 is the total vertical atmospheric depth.

2.6 Description of Decay: Width and Lifetime

Stable particles like (as far as we know) the proton and the electron are the exception, not the rule. The lifetime of most particles is finite and its value spans many orders of magnitude from, for instance, 10^{-25} s for the electroweak massive bosons (Z and W) to around 900 s for the neutron, depending on the strength of the relevant interaction and on the size of the decay phase space.

In order to describe decays we must use quantum mechanical language, given that they are a genuine quantum process whose statistical nature cannot be properly explained by classical physics. We shall use, thus, the language of wavefunctions. $|\Psi(x, y, z, t)|^2 \, dV$ is the probability density for finding a particle in a volume dV around point (x, y, z) at time t.

Stable particles are described by pure harmonic wavefunctions and their Fourier transforms are functions centered in well-defined proper energies – in the rest frame, $E = mc^2$ (Fig. 2.8):

$$\Psi(t) \propto \Psi(0) \ e^{-i\frac{E}{\hbar}t} \tag{2.39}$$

$$\Psi(E) \propto \delta(E - mc^2) \,. \tag{2.40}$$

Unstable particles are described by damped harmonic wavefunctions and therefore their proper energies are not well-defined (Fig. 2.9):

$$\Psi(t) \propto \Psi(0)e^{-i\,\frac{E}{\hbar}t}e^{-\frac{\Gamma}{2\hbar}t} \quad \Longrightarrow \quad |\Psi(t)|^2 \propto |\Psi(0)|^2 e^{-t/\tau} \tag{2.41}$$

$$\Psi(E) \propto \frac{1}{(E-mc^2)+i\Gamma/2} \Longrightarrow |\Psi(E)|^2 \propto \frac{1}{(E-mc^2)^2+\Gamma^2/4} \tag{2.42}$$

which is a Cauchy function (physicists call it a Breit-Wigner function) for which the width Γ is directly related to the particle lifetime τ:

$$\tau = \frac{\hbar}{\Gamma}. \tag{2.43}$$

If a particle can decay through different channels, its total width will be the sum of the partial widths Γ_i of each channel:

$$\Gamma_t = \sum \Gamma_i. \tag{2.44}$$

An unstable particle may thus have several specific decay rates, but it has just one lifetime:

$$\tau = \frac{\hbar}{\sum \Gamma_i}. \tag{2.45}$$

Therefore, all the Breit-Wigner functions related to the decays of the same particle have the same width Γ_t but different normalization factors, which are proportional to the fraction of the decays in each specific channel, also called the branching ratio, BR_i, defined as

$$BR_i = \frac{\Gamma_i}{\Gamma_t}. \tag{2.46}$$

2.7 Fermi Golden Rule and Rutherford Scattering

Particles interact like corpuscles but propagate like waves. This was the turmoil created in physics in the early twentieth century by Einstein's photoelectric effect theory. In the microscopic world, deterministic trajectories were no longer possible. Newton's laws had to be replaced by wave equations. Rutherford formulae, classically deduced, agree anyway with calculations based on quantum mechanics.

In quantum mechanics, the scattering of a particle due to an interaction that acts only during a finite time interval can be described as the transition between an initial and a final stationary states characterized by well-defined momenta. The probability λ of such a transition is given, if the perturbation is small, by Fermi's[4] "golden rule" (see [F2.1] among the recommended readings at the end of the chapter):

$$\lambda = \frac{2\pi}{\hbar}|H'_{if}|^2 \rho(E_i) \tag{2.47}$$

where H'_{if} is the transition amplitude[5] between states i and f ($H'_{if} = \langle f|H'_{int}|i\rangle$, where H'_{int} is the interaction Hamiltonian) and $\rho(E_i)$ is the density of final states for a given energy $E_i = E_f$. The cross section is, as it was seen above, the interaction rate per unit of flux J. Thus:

$$\sigma_{tot} = \frac{\lambda}{J}. \tag{2.48}$$

To compute the cross section one then needs to determine the transition amplitude, the flux, and the density of final states.

---

[4] Enrico Fermi (Rome 1901–Chicago 1954) studied in Pisa and became full professor of Analytical Mechanics in Florence in 1925, and then of Theoretical Physics in Rome from 1926. Soon he surrounded himself by a group of brilliant young collaborators, the so-called "via Panisperna boys" (E. Amaldi, E. Majorana, B. Pontecorvo, F. Rasetti, E. Segré, O. D'Agostino). For Fermi, theory and experiment were inseparable. In 1934, he discovered that slow neutrons catalyzed a certain type of nuclear reactions, which made it possible to derive energy from nuclear fission. In 1938, Fermi went to Stockholm to receive the Nobel Prize, awarded for his fundamental work on neutrons, and from there he emigrated to the USA, where he became an American citizen in open dispute with the Italian racial laws. He actively participated in the Manhattan Project for the use of nuclear power for the atomic bomb, but spoke out against the use of this weapon on civilian targets. Immediately after the end of World War II, he devoted himself to theoretical physics of elementary particles and to the origin of cosmic rays. Few scientists of the twentieth century impacted as profoundly as Fermi in different areas of physics: Fermi stands for elegance and power of thought in the group of immortal geniuses like Einstein, Landau, Heisenberg, and later Feynman.

[5] Depending on the textbook, you might encounter the notation H_{if} or H_{fi}.
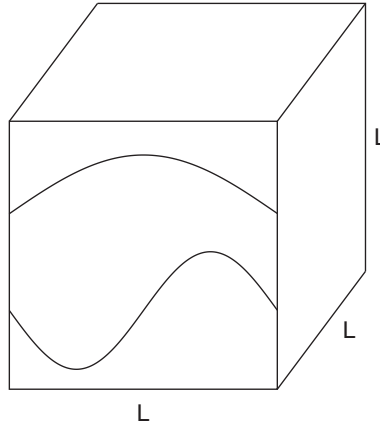
Fig. 2.10 Normalization box.

2.7.1 Transition Amplitude

Rutherford scattering can be, to a first approximation, treated as the nonrelativistic elastic scattering of a single particle by a fixed static Coulomb potential. The initial and final time-independent state amplitudes may be written as plane waves normalized in a box of volume L^3 (Fig. 2.10) and with linear momenta $\mathbf{p_i} = \hbar\,\mathbf{k_i}$ and $\mathbf{p_f} = \hbar\,\mathbf{k_f}$, respectively ($k = |\mathbf{k_i}| = |\mathbf{k_f}|$):

$$u_i = L^{-\frac{3}{2}}\exp(i\,\mathbf{k_i}\cdot\mathbf{r}) \tag{2.49}$$

and

$$u_f = L^{-\frac{3}{2}}\exp(i\,\mathbf{k_f}\cdot\mathbf{r}). \tag{2.50}$$

Assuming a scattering center at the origin of coordinates, the Coulomb potential is written as

$$V(r) = \frac{1}{4\pi\varepsilon_0}\frac{Q_1 Q_2}{r} \tag{2.51}$$

where ε_0 is the vacuum dielectric constant and Q_1 and Q_2 are the charges of the beam and of the target particles. The transition amplitude can thus be written as

$$H'_{if} = L^{-3}\int \exp\left(-i\,\mathbf{k_f}\cdot\mathbf{r}\right) V(r)\exp\left(-i\,\mathbf{k_i}\cdot\mathbf{r}\right) d^3 x. \tag{2.52}$$

Introducing the momentum transfer:

$$\mathbf{q} = \hbar\ (\mathbf{k_f} - \mathbf{k_i}) \tag{2.53}$$

the transition amplitude given by:

$$H'_{if} = L^{-3}\int V(r)\exp\left(-\frac{i}{\hbar}\,\mathbf{q}\cdot\mathbf{r}\right) d^3 x \tag{2.54}$$

is just the Fourier transform of $V(r)$ and then

$$H'_{if} = -\frac{4\,\pi\hbar^2}{L^3}\left(\frac{1}{4\pi\varepsilon_0}\frac{Q_1 Q_2}{|\mathbf{q}|^2}\right). \tag{2.55}$$

Expressing $|\mathbf{q}|^2$ as a function of the scattering angle θ as

$$|\mathbf{q}|^2 = 4\,\hbar^2\,k^2\sin^2\frac{\theta}{2}, \tag{2.56}$$

the transition amplitude may finally be written as

$$H'_{if} = -\frac{4\pi\hbar^2}{L^3} \left(\frac{1}{4\pi\varepsilon_0} \frac{Q_1\,Q_2}{4\hbar^2\,k^2\mathrm{sin}^2\frac{\theta}{2}} \right).$$ (2.57)

2.7.2 Flux

The flux, as seen in Eq. 2.22, is $J = \rho_{beam}v$, which in the present case may be written as

$$J = \frac{v}{L^3} = \frac{\hbar\,k}{m\,L^3}.$$ (2.58)

2.7.3 Density of States

The density of final states $\rho(E_i)$ is determined by the dimension of the normalization box. At the boundaries of the box, the wavefunction should be zero and so only harmonic waves are possible in the case of free particles. Therefore, the projections of the wave number vector $\boldsymbol{\kappa}$ along each axis should also obey

$$k_x = \frac{2\pi\,n_x}{L} \; ; \; k_y = \frac{2\pi\,n_y}{L} \; ; \; k_z = \frac{2\pi\,n_z}{L}$$ (2.59)

where n_x, n_y and n_z are the integer harmonic numbers.

Considering now a given wave number vector in its vector space, the volume associated to each possible state defined by a particular set of harmonic numbers is just

$$\frac{dk_x}{dn_x}\,\frac{dk_y}{dn_y}\,\frac{dk_z}{dn_z} = \left(\frac{2\pi}{L}\right)^3,$$ (2.60)

while the elementary volume d^3k in spherical coordinates is

$$d^3k = k^2\,dk\,d\Omega.$$ (2.61)

Then, the number of states dn in the volume d^3k is

$$dn = \left(\frac{L}{2\pi}\right)^3 k^2\,dk\,d\Omega.$$ (2.62)

Remembering that in nonrelativistic quantum mechanics

$$E = \frac{(\hbar k)^2}{2m},$$ (2.63)

the density of states $\rho\,(E_i)$ is therefore given as

$$\rho\,(E_i) = \frac{dn}{dE} = \left(\frac{L}{2\pi\hbar}\right)^3 \frac{(\hbar k)^2}{v}d\Omega,$$ (2.64)

where v is the velocity of the particle.

2.7.4 Rutherford Cross Section

Replacing all the terms in 2.47 and 2.48:

$$\frac{d\sigma}{d\Omega} = \left(\frac{1}{4\pi\varepsilon_0}\frac{Q_1Q_2}{4E_0}\right)^2 \frac{1}{\mathrm{sin}^4\frac{\theta}{2}}$$ (2.65)
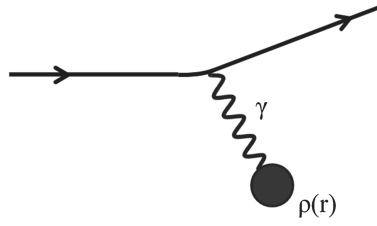
Fig. 2.11 Scattering by an extended source.

and this is exactly the Rutherford formula.

In fact, the minimum distance at which a nonrelativistic beam particle with energy E_0 can approach the target nucleus is:

$$d_{\min} = \frac{Q_1 Q_2}{4\pi\varepsilon_0 E_0} \tag{2.66}$$

while the de Broglie wavelength associated to that particle is

$$\lambda = \frac{h}{\sqrt{2mE_0}}. \tag{2.67}$$

In the particular case of the Rutherford experiment (α particles with a kinetic energy of $7.7\,\text{MeV}$ against a golden foil) $\lambda \ll d_{\min}$ and the classical approximation is, by chance, valid.

2.8 Particle Scattering in Static Fields

The Rutherford formula was deduced assuming a static Coulomb field created by a fixed point charge. These assumptions can be either too crude or just not valid in many cases. Hereafter, some generalizations of the Rutherford formula are discussed.

2.8.1 Extended Charge Distributions (Non Relativistic)

Let us assume that the source of the static Coulomb field has some spatial extension $\rho(r')$ (Fig. 2.11) with

$$\int_0^\infty \rho(r')\ dr' = 1. \tag{2.68}$$

Then

$$H'_{if} = L^{-3} \int\int \left(\frac{1}{4\pi\varepsilon_0} \frac{Q_1 Q_2\ \rho(\mathbf{r}')}{|\mathbf{r}' - \mathbf{r}|} \right) \exp\left(-\frac{i}{\hbar}\ \mathbf{q}\cdot\mathbf{r} \right) d^3x\, d^3x' = \tag{2.69}$$

$$= L^{-3} \int\int \left(\frac{1}{4\pi\varepsilon_0} \frac{Q_1 Q_2\ \rho(\mathbf{r}')}{|\mathbf{r}' - \mathbf{r}|} \right) \exp\left(-\frac{i}{\hbar}\ \mathbf{q}\cdot(\mathbf{r} - \mathbf{r}') \right) \exp\left(-\frac{i}{\hbar}\ \mathbf{q}\cdot\mathbf{r}' \right) d^3x\, d^3x'$$

and defining the electric form factor $F(q)$ as

$$F(q) = \int \rho(\mathbf{r}') \exp\left(-\frac{i}{\hbar}\ \mathbf{q}\cdot\mathbf{r}' \right) d^3x' \tag{2.70}$$

the modified scattering cross section is

$$\frac{d\sigma}{d\Omega} = |F(\mathbf{q})|^2 \left(\frac{d\sigma}{d\Omega} \right)_0 \tag{2.71}$$

where $\left(\frac{d\sigma}{d\Omega} \right)_0$ is the Rutherford cross section.

In the case of the proton, the differential *ep* cross section at low transverse momentum is described by such a formula, and the form factor is given by the *dipole formula*

$$F(q) \propto \left(1 + \frac{|\mathbf{q}|^2}{\hbar^2 b^2}\right)^{-2}. \tag{2.72}$$

The charge distribution is the Fourier transform $\rho(r) \propto e^{-r/a}$, where $a = 1/b \simeq 0.2$ fm corresponds to a root mean square charge radius of 0.8 to 0.9 fm. The size of the proton is then determined to be at the scale of 1 fm.

2.8.2 Finite Range Interactions

The Coulomb field, as the Newton gravitational field, has an infinite range. Let us now consider a field with an exponential attenuation (Yukawa potential)

$$V(r) = \frac{g}{4\pi r} \exp\left(-\frac{r}{a}\right) \tag{2.73}$$

where g is the interaction strength, and a is the interaction range scale. Then,

$$H'_{if} = L^{-3} \int \left(\frac{g}{4\pi r} \exp(-\frac{r}{a})\right) \exp\left(-\frac{i}{\hbar} \mathbf{q} \cdot \mathbf{r}\right) d^3 x, \tag{2.74}$$

giving

$$H'_{if} = -\frac{\hbar^2}{L^3} \left(\frac{g}{\mathbf{q}^2 + \frac{\hbar^2}{a^2}}\right). \tag{2.75}$$

Using now the Fermi golden rule,

$$\frac{d\sigma}{d\Omega} = g^2 \left(\frac{\mathbf{q}^2}{\mathbf{q}^2 + M^2 c^2}\right)^2 \left(\frac{d\sigma}{d\Omega}\right)_0, \tag{2.76}$$

where $\left(\frac{d\sigma}{d\Omega}\right)_0$ is the Rutherford cross section. $M = \hbar/(a\,c)$ was interpreted by Hideki Yukawa,[6] as it will be discussed in Sect. 3.2.4, as the mass of a particle exchanged between nucleons and responsible for the strong interaction which ensures the stability of nuclei. The scale $a = 1$ fm corresponds to the size of nucleons, and the mass of the exchanged particle comes out to be $M \simeq 200$ MeV/c^2 (see Sect. 2.9 for the conversion).

2.8.3 Electron Scattering

Electrons have nonzero spin $\left(S = \frac{1}{2}\hbar\right)$, and thus a nonzero magnetic moment

$$\boldsymbol{\mu} = \frac{Q_e}{m_e}\mathbf{S} \tag{2.77}$$

where Q_e and m_e are, respectively, the charge and the mass of the electron.

The electron scattering cross section is given by the Mott cross section (its derivation is beyond the scope of the present chapter as it implies relativistic quantum mechanics):

$$\frac{d\sigma}{d\Omega} = \left(\frac{d\sigma}{d\Omega}\right)_0 \left(1 - \beta^2 \sin^2\frac{\theta}{2}\right). \tag{2.78}$$

When the velocity $\beta \to 0$, the Rutherford scattering formula is recovered as

---

[6] Hideki Yukawa (Tokyo, 1907–Kyoto, 1981), professor at Kyoto University, gave fundamental contributions to quantum mechanics. For his research he won the prize Nobel Prize for Physics in 1949.
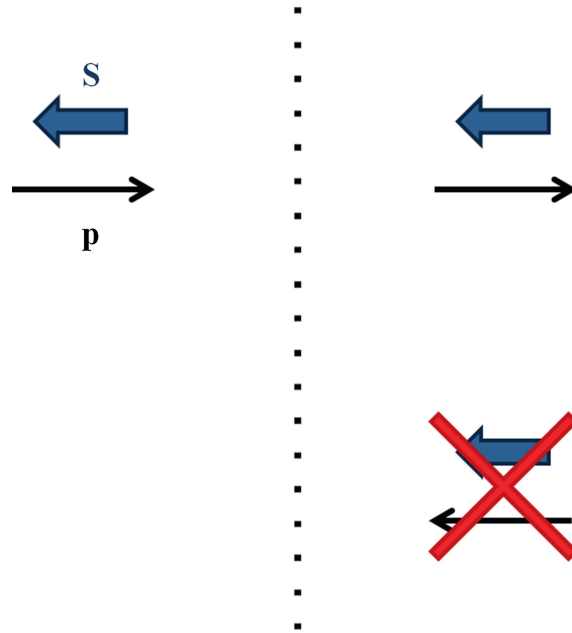
Fig. 2.12 Schematic representation of helicity conservation in the limit $\beta = 1$.

$$\frac{d\sigma}{d\Omega} = \left(\frac{d\sigma}{d\Omega}\right)_0 . \tag{2.79}$$

When $\beta \to 1$,

$$\frac{d\sigma}{d\Omega} = \left(\frac{d\sigma}{d\Omega}\right)_0 \cos^2\frac{\theta}{2} , \tag{2.80}$$

which translates the fact that, for massless particles, the projection of the spin $\mathbf{S}$ over the direction of the linear momentum $\mathbf{p}$ is conserved, as it will be discussed in Sect. 6.2.4 (Fig. 2.12). The helicity quantum number h is defined as

$$h = \mathbf{S} \cdot \frac{\mathbf{p}}{|\mathbf{p}|} . \tag{2.81}$$

A massless electron, thus, could not be backscattered.

2.9 Natural Units

The international system of units (SI) can be constructed on the basis of four fundamental units: a unit of length (the meter, m), a unit of time (the second, s), a unit of mass (the kilogram, kg) and a unit of charge (the coulomb, C).[7]

These units are inappropriate in the world of fundamental physics: the radius of a nucleus is of the order of 10^{-15} m (also called one femtometer or one fermi, fm); the mass of an electron is of the order of 10^{-30} kg; the charge of an electron is (in absolute value) of the order of 10^{-19} C. Using such units, we would carry along a lot of exponents. Thus, in particle physics, we prefer to use units like the electron charge for the electrostatic charge, and the electron-volt eV and its multiples (keV, MeV, GeV, TeV) for the energy:

Length	1 fm	10^{-15} m
Mass	1 MeV/c^2	$\sim 1.78 \times 10^{-30}$ kg
Charge	$|e|$	$\sim 1.602 \times 10^{-19}$ C.

[7] For reasons related only to metrology (reproducibility and accuracy of the definition) in the standard SI the unit of electric current, the ampere A, is used instead of the coulomb; the two definitions are however conceptually equivalent.

Note the unit of mass, in which the relation $E = mc^2$ is used implicitly: what one is doing here is to use $1\,\text{eV} \simeq 1.602 \times 10^{-19}$ J as the new fundamental unit of energy. In these new units, the mass of a proton is about $0.938\,\text{GeV}/c^2$, and the mass of the electron is about $0.511\,\text{MeV}/c^2$. The fundamental energy level of a hydrogen atom is about -13.6 eV.

In addition, nature provides us with two constants which are particularly appropriate in the world of fundamental physics: the speed of light $c \simeq 3.00 \times 10^8$ m/s $= 3.00 \times 10^{23}$ fm/s, and Planck's constant (over 2π) $\hbar \simeq 1.05 \times 10^{-34}$ J s $\simeq 6.58 \times 10^{-16}$ eV s.

It seems then natural to express speeds in terms of c, and angular momenta in terms of $\hbar$. We then switch to the so-called Natural Units (NU). The minimal set of natural units (not including electromagnetism) can then be chosen as

Speed	1 c	3.00×10^8 m/s
Angular momentum	1 $\hbar$	1.05×10^{-34} J s
Energy	1 eV	1.602×10^{-19} J.

After the convention $\hbar = c = 1$, one single unit can be used to describe the mechanical Universe: we choose energy, and we can thus express all mechanical quantities in terms of eV and of its multiples. It is immediate to express momenta and masses directly in NU. To express 1 m and 1 s, we can write[8]

$$1\ \text{m} = \frac{1\text{m}}{\hbar c} \simeq 5.10 \times 10^{12}\ \text{MeV}^{-1}$$

$$1\ \text{s} = \frac{1\text{s}}{\hbar} \simeq 1.52 \times 10^{21}\ \text{MeV}^{-1}$$

$$1\ \text{kg} = 1\text{J}/c^2 \simeq 5.62 \times 10^{29}\ \text{MeV}$$

Both length and time are thus, in natural units, expressed as inverse of energy. The first relation can also be written as $1\,\text{fm} \simeq 5.10\,\text{GeV}^{-1}$. Note that when you have a quantity expressed in MeV^{-1}, in order to express it in GeV^{-1}, you must multiply (and not divide) by a factor of 1000.

Let us now find a general rule to transform quantities expressed in natural units into SI, and vice versa. To express a quantity in NU back in SI, we first restore the $\hbar$ and c factors by dimensional arguments and then use the conversion factors $\hbar$ and c (or $\hbar c$) to evaluate the result. The dimensions of c are [m/s]; the dimensions of $\hbar$ are $[\text{kg}\,\text{m}^2\,\text{s}^{-1}]$.

The converse (from SI to NU) is also easy. A quantity with meter-kilogram-second [m k s] dimensions $M^p L^q T^r$ (where M represents mass, L length and T time) has the NU dimensions $[E^{p-q-r}]$, where E represents energy. Since $\hbar$ and c do not appear in NU, this is the only relevant dimension, and dimensional checks and estimates are very simple. The quantity Q in SI can be expressed in NU as

$$Q_{\text{NU}} = Q_{\text{SI}} \left(5.62 \times 10^{29} \frac{\text{MeV}}{\text{kg}}\right)^p \left(5.10 \times 10^{12} \frac{\text{MeV}^{-1}}{\text{m}}\right)^q$$
$$\times \left(1.52 \times 10^{21} \frac{\text{MeV}^{-1}}{\text{s}}\right)^r \text{MeV}^{p-q-r}$$

The NU and SI dimensions are listed for some important quantities in Table 2.1.

Table 2.1 Dimensions of different physical quantities in SI and NU

Quantity	SI $p\ q\ r$	NU n
Mass	1 0 0	1
Length	0 1 0	-1
Time	0 0 1	-1
Action ($\hbar$)	1 2 -1	0
Velocity (c)	0 1 -1	0
Momentum	1 1 -1	1
Energy	1 2 -2	1

---

[8] $\hbar c \simeq 1.97 \times 10^{-13} \text{MeV}\,\text{m} = 3.15 \times 10^{-26}\,\text{J}\,\text{m}$.

Note that, choosing natural units, all factors of $\hbar$ and c may be omitted from equations, which leads to considerable simplifications (we will profit from this in the next chapters). For example, the relativistic energy relation

$$E^2 = p^2 c^2 + m^2 c^4 \tag{2.82}$$

becomes

$$E^2 = p^2 + m^2. \tag{2.83}$$

Finally, let us discuss how to treat electromagnetism. To do so, we must introduce a new unit, of charge for example. We can redefine the unit charge by observing that

$$\frac{e^2}{4\pi\epsilon_0} \tag{2.84}$$

has the dimension of [J m], and thus is a pure, dimensionless, number in NU. Dividing by $\hbar c$ one has

$$\frac{e^2}{4\pi\epsilon_0 \hbar c} \simeq \frac{1}{137} \,. \tag{2.85}$$

Imposing for the electric permeability of vacuum $\epsilon_0 = 1$ (thus automatically $\mu_0 = 1$ for the magnetic permeability of vacuum, since from Maxwell's equations $\epsilon_0\mu_0 = 1/c^2$) we obtain the new definition of charge, and with this definition:

$$\alpha = \frac{e^2}{4\pi} \simeq \frac{1}{137} \,. \tag{2.86}$$

This is called the Lorentz-Heaviside convention. Elementary charge in NU becomes then a pure number

$$e \simeq 0.303 \,. \tag{2.87}$$

Let us make now some applications.

The Thomson cross section. Let us express a cross section in NU. The cross section for Compton scattering of a photon by a free electron is, for $E \ll m_e c^2$ (Thomson regime),

$$\sigma_T \simeq \frac{8\pi\alpha^2}{3m_e^2} \,. \tag{2.88}$$

The dimension of a cross section is, in SI, [m^2]. Thus we can write

$$\sigma_T \simeq \frac{8\pi\alpha^2}{3m_e^2} \hbar^a c^b \tag{2.89}$$

and determine a and b such that the result has the dimension of a length squared. We find $a = 2$ and $b = -2$; thus

$$\sigma_T \simeq \frac{8\pi\alpha^2}{3(m_e c^2)^2} (\hbar c)^2 \tag{2.90}$$

and thus $\sigma_T \simeq 6.65 \times 10^{-29} \ \mathrm{m}^2 = 665 \, \mathrm{mb}$.

The Planck mass, length, and time. According to quantum theory, a length called the Compton wavelength, λ_C, can be associated to any mass m. λ_C is defined as the wavelength of a photon with an energy equal to the rest mass of the particle:

$$\lambda_C = \frac{h}{mc} = 2\pi \frac{\hbar}{mc} \,. \tag{2.91}$$

The Compton wavelength sets the distance scale at which quantum field theory becomes crucial for understanding the behavior of a particle: wave and particle description become complementary at this scale.

On the other hand, we can compute for any mass m the associated Schwarzschild radius, R_S, such that compressing it to a size smaller than this radius we form a black hole. The Schwarzschild radius is the scale at which general relativity becomes crucial for understanding the behavior of the object:

$$R_S = \frac{2Gm}{c^2} \,, \tag{2.92}$$

where G is the gravitational constant[9].

We call Planck mass the mass at which the Schwarzschild radius of a particle becomes equal to its Compton length, and Planck length their common value when this happens. The probe that could locate a particle within this distance would collapse to a black hole, something that would make measurements very strange. In NU, one can write

$$\frac{2\pi}{m_P} = 2Gm_P \rightarrow m_P = \sqrt{\frac{\pi}{G}} \tag{2.93}$$

which can be converted into

$$m_P = \sqrt{\frac{\pi \hbar c}{G}} \simeq 3.86 \times 10^{-8} \text{kg} \simeq 2.16 \times 10^{19} \, \text{GeV/c}^2. \tag{2.94}$$

Since we are talking about orders of magnitude, the factor $\sqrt{\pi}$ is often neglected and we take as a definition:

$$m_P = \sqrt{\frac{\hbar c}{G}} \simeq 2.18 \times 10^{-8} \text{kg} \simeq 1.22 \times 10^{19} \, \text{GeV/c}^2. \tag{2.95}$$

Besides the Planck length ℓ_P, we can also define a Planck time $t_P = \ell_P/c$ (their value is equal in NU):

$$\ell_P = t_P = \frac{1}{m_P} = \sqrt{G} \tag{2.96}$$

(this corresponds to a length of about 1.6×10^{-20} fm, and to a time of about 5.4×10^{-44} s).

Both general relativity and quantum field theory are needed to understand the physics at mass scales about the Planck mass or distances about the Planck length, or times comparable to the Planck time. Traditional quantum physics and gravitation certainly fall short at this scale; since this failure should be independent of the reference frame, many scientists think that the Planck scale should be an invariant irrespective of the reference frame in which it is calculated (this fact would of course require important modifications to the theory of relativity).

Note that the shortest length you may probe with the energy of a particle accelerated by LHC is about 10^{15} times larger than the Planck length scale. Cosmic rays, which can reach center of mass energies beyond 100 TeV, are at the frontier of the exploration of fundamental scales.

Further Reading

- [F2.1] J.S. Townsend, "A modern approach to quantum mechanics", McGraw-Hill 2012. An excellent quantum mechanics course at an advanced undergraduate level.
- [F2.2] W. Rindler, "Introduction to Special Relativity", Second Edition, Oxford University Press 1991. A classic textbook on special relativity for undergraduates.

Exercises

1. *Rutherford formula.* Consider the Rutherford formula.

   (a) Determine the distance of closest approach of an α particle with an energy of 7.7 MeV to a gold target.
   (b) Determine the de Broglie wavelength of that α particle.
   (c) Explain why the classical Rutherford formula survived the revolution of quantum mechanics.

   You can find the numerical values of particle data and fundamental constants in the Appendices, or in your Particle Data Book(let).

---

[9] A classical derivation of this formula proceeds by computing the radius for which the escape velocity from a spherical distribution of mass with zero angular momentum is equal to c.

2. *Cross section at fixed target.* Consider a fixed target experiment with a monochromatic proton beam with an energy of 20 GeV and a 2 m long liquid hydrogen (H_2) target ($\rho = 60\,\text{kg/m}^3$). In the detector placed just behind the target beam fluxes of 7×10^6 protons/s and 10^7 protons/s are measured, respectively, with the target full and empty. Determine the proton–proton total cross section at this energy and its statistical error:

   (a) without taking into account the attenuation of the beam inside the target;
   (b) taking into account the attenuation of the beam inside the target.

3. *LHC collisions.* The LHC running parameters in 2012 were, for a c.m. energy $\sqrt{s} \simeq 8$ TeV: number of bunches = 1400; time interval between bunches $\simeq 50$ ns; number of protons per bunch $\simeq 1.1 \times 10^{11}$; beam width at the crossing point $\simeq 16\,\mu$m.

   (a) Determine the maximum instantaneous luminosity of the LHC in 2012.
   (b) Determine the number of interactions per collision ($\sigma_{pp} \sim 100$ mb).
   (c) As you probably heard, LHC found a particle called Higgs boson, which Leon Lederman called the "God particle" (a name the news like very much). If Higgs bosons are produced with a cross section $\sigma_H \sim 21$ pb, determine the number of Higgs bosons decaying into 2 photons ($BR(H \to \gamma\gamma) \simeq 2.28 \times 10^{-3}$) which might have been produced in 2012 in the LHC, knowing that the integrated luminosity of the LHC (luminosity integrated over the time) during 2012 was around 20 fb^{-1}. Compare it to the real number of detected Higgs in this particular decay mode reported by the LHC collaborations (about 400). Discuss the difference.

4. *Experimental determination of cross sections.* A thin ($1.4\,\text{mg/cm}^2$) target made of ^{22}Na is bombarded with a 5 nA beam of α particles. A detector with area 16 cm^2 is placed at 1 m from the target perpendicular to the line between the detector and the target. The detector records 45 protons/s, independently of the angular position (θ, ϕ) of the detector. Find the cross section in mb for the ^{22}Na $+\alpha \to p + X$–also written as ^{22}Na(α, p)– reaction.

5. *Uncertainty relations.* Starting from Eq. 2.15, demonstrate the uncertainty principle for position and momentum.

6. *Classical electromagnetism is not a consistent theory.* Consider two electrons at rest, and let r be the distance between them. The (repulsive) force between the two electrons is the electrostatic force

$$F = \frac{1}{4\pi\epsilon_0} \frac{e^2}{r^2},$$

   where e is the charge of the electron; it is directed along the line joining the two charges. But an observer is moving with a velocity v perpendicular to the line joining the two charges will measure also a magnetic force (still directed as F)

$$F' = \frac{1}{4\pi\epsilon_0} \frac{e^2}{r^2} - \frac{\mu_0}{2\pi r} v^2 e^2 \neq F.$$

   The expression of the force is thus different in the two frames of reference. But masses, charges, and accelerations are classically invariant. Comment.

7. *Classical momentum is not conserved in special relativity.* Consider the completely inelastic collision of two particles, each of mass m, in their c.m. system (the two particles become one particle at rest after the collision). Now observe the same collision in the reference frame of one particle. What happens if you assume that the classical definition of momentum holds in relativity as well?

8. *Energy is equivalent to mass.* How much more does a hot potato weigh than a cold one (in kg)?

9. *Mandelstam variables.* Demonstrate that, in the $1+2 \to 3+4$ scattering, $s+t+u = m_1^2 + m_2^2 + m_3^2 + m_4^2$.

10. *GZK threshold.* The Cosmic Microwave Background fills the Universe with photons with a peak energy of 0.37 meV and a density of $\rho \sim 400/\text{cm}^3$. Determine:

    (a) The minimal energy (known as the GZK threshold) that a proton should have in order that the reaction $p\gamma \to \Delta$ may occur.
    (b) The interaction length of such protons in the Universe considering a mean cross section above the threshold of 0.6 mb.

11. *$\bar{p}$ production at the Bevatron.* Antiprotons were first produced in laboratory in 1955, in proton–proton fixed target collisions at an accelerator called Bevatron (it was named for its ability to impart energies of

billions of eV, i.e., Billions of eV Synchrotron), located at Lawrence Berkeley National Laboratory, US . The discovery resulted in the 1959 Nobel Prize in physics for Emilio Segrè and Owen Chamberlain.

(a) Describe the minimal reaction able to produce antiprotons in such collisions.
(b) When a proton is confined in a nucleus, it cannot have arbitrarily low momenta, as one can understand from the Heisenberg principle; the actual value of its momentum is called the "Fermi momentum." Determine the minimal energy that the proton beam must have in order that antiprotons were produced considering that the target protons have a Fermi momentum of around 150 MeV/c.

12. *Photon conversion.* Consider the conversion of one photon in one electron–positron pair. Determine the minimal energy that the photon must have for this conversion to be possible if the photon is in the presence of:

(a) one proton;
(b) one electron;
(c) when no charged particle is around.

13. π^- *decay.* Consider the decay of a flying π^- into $\mu^- \bar{\nu}_\mu$ and suppose that the μ^- was emitted along the line of flight of the π^-. Determine:

(a) The energy and momentum of the μ^- and of the $\bar{\nu}_\mu$ in the π^- frame.
(b) The energy and momentum of the μ^- and of the $\bar{\nu}_\mu$ in the laboratory frame, if the momentum $P_\pi^- = 100$ GeV/c.
(c) Same as the previous question but considering now that was the $\bar{\nu}_\mu$ that was emitted along the flight line of the π^-.

14. π^0 *decay.* Consider the decay of a π^0 into $\gamma\gamma$ (with pion momentum of 100 GeV/c). Determine:

(a) The minimal and the maximal angles between the two photons in the laboratory frame.
(b) The probability of having one of the photons with an energy smaller than an arbitrary value E_0 in the laboratory frame.
(c) Same as (a) but considering now that the decay of the π^0 is into $e^+ e^-$.
(d) The maximum momentum that the π^0 may have in order that the maximal angle in its decay into $\gamma\gamma$ and in $e^+ e^-$ would be the same.

15. *Three-body decay.* Consider the decay $K^+ \to \pi^+ \pi^+ \pi^-$. Determine:

(a) the minimum and maximum values of the π^- energy and momentum in the K^+ rest system;
(b) the maximum value of the momentum in the laboratory system, assuming a K^+ with a momentum $p_K = 100$ GeV/c.

Do the same for the electron in the decay $n \to pe\bar{\nu}_e$.

16. *A classical model for the electron.* Suppose we interpret the electron as a classical solid sphere of radius r and mass m, spinning with angular momentum $\hbar/2$. What is the speed, v, of a point on its "equator"? Experimentally, it is known that r is less than 10^{-18} m. What is the corresponding equatorial speed? What do you conclude from this?

17. *Invariant flux.* In a collision between two particles a and b the incident flux is given by $F = 4|\mathbf{v_a} - \mathbf{v_b}|E_a E_b$ where $\mathbf{v_a}$, $\mathbf{v_b}$, E_a and E_b are, respectively, the vectorial speeds and the energies of particles a and b.

(a) Verify that the above formula is equivalent to: $F = 4\sqrt{(P_a P_b)^2 - (m_a m_b)^2}$ where P_a and P_b are, respectively, the four-vectors of particles a and b, and m_a and m_b their masses.
(b) Relate the expressions of the flux in the center-of-mass and in the laboratory reference frames.

18. *Lifetime and width of a particle.* The lifetime of the π^0 meson is $\simeq 0.085$ fs. What is the width of the π^0 (absolute, and relative to its mass)?

19. *Width and lifetime of a particle.* The width of the $\rho(770)$ meson is $\simeq 149$ MeV. What is the lifetime of the $\rho(770)$?

20. *Classical Schwarzschild radius for a Black Hole.* Compute the radius of a spherical planet of mass M for which the escape velocity is equal to c.

21. *Units.* Determine in Natural Units:

(a) Your own dimensions (height, weight, mass, age).
(b) The mean lifetime of the muon ($\tau_\mu = 2.2\,\mu s$).

Chapter 3
Cosmic Rays and the Development of Particle Physics

Alessandro De Angelis and Mário Pimenta

This chapter illustrates the path which led to the discovery that particles of extremely high energy, up to a few joule, come from extraterrestrial sources and collide with Earth's atmosphere. The history of this discovery started in the beginning of the twentieth century, but many of the techniques then introduced are still in use. A relevant part of the progress happened in recent years and has a large impact on the physics of elementary particles and fundamental interactions.

By 1785, Coulomb found that electroscopes (Fig. 3.1) can discharge spontaneously, and not simply due to defective insulation. The British physicist Crookes, in 1879, observed that the speed of discharge decreased when the pressure of the air inside the electroscope itself was reduced. The discharge was then likely due to the ionization of the atmosphere. But what was the cause of atmospheric ionization?

The explanation came in the early twentieth century and led to the revolutionary discovery of cosmic rays. We know today that cosmic rays are particles of extraterrestrial origin which can reach high energy (much larger than we shall ever be able to produce). They were the only source of high energy beams till the 1940s. World War II and the Cold War provided new technical and political resources for the study of elementary particles; technical resources included advances in microelectronics and the capability to produce high energy particles in human-made particle accelerators. By 1955, particle physics experiments would be largely dominated by accelerators, at least until the beginning of the 1990s, when explorations possible with the energies one can produce on Earth started showing signs of saturation, so that nowadays cosmic rays are again at the edge of physics.

3.1 The Puzzle of Atmospheric Ionization and the Discovery of Cosmic Rays

Spontaneous radioactivity (i.e., the emission of particles from nuclei as a result of nuclear instability) was discovered in 1896 by Becquerel. A few years later, Marie and Pierre Curie discovered that Polonium and Radium (the names Radium A, Radium B, ... indicated several isotopes of the element today called radon, and also some different elements) underwent transmutations by which they generated radioactivity; these processes were called "radioactive decays." A charged electroscope promptly discharges in the presence of radioactive materials. It was concluded that the discharge was due to the emission of charged particles, which induce the formation of ions in the air, causing the discharge of electroscopes. The discharge rate of electroscopes was used to gauge the radioactivity level. During the first decade of the twentieth century, several researchers in Europe and in the New World presented progress on the study of ionization phenomena.

Around 1900, C.T.R. Wilson[1] in Britain and Elster and Geitel in Germany improved the sensitivity of the electroscope, by improving the technique for its insulation in a closed vessel (Fig. 3.2). This improvement allowed the quantitative measurement of the spontaneous discharge rate, and led to the conclusion that the radiation causing this discharge came from outside the vessel. Concerning the origin of such radiation, the simplest hypothesis was that it was related to radioactive material in the surrounding of the apparatus. Terrestrial origin was thus a commonplace assumption, although experimental confirmation could not be achieved. Wilson did suggest that atmospheric ionization could be caused by a very penetrating radiation of extraterrestrial origin. His investigations in tunnels, with solid rock for shielding overhead, however could not support the idea, as no reduction in ionization was observed. The hypothesis of an extraterrestrial origin, though now and then discussed, was dropped for many years.

---

[1] Charles Thomson Rees Wilson, (1869–1959), a Scottish physicist and meteorologist, received the Nobel Prize in Physics for his invention of the cloud chamber; see the next chapter.
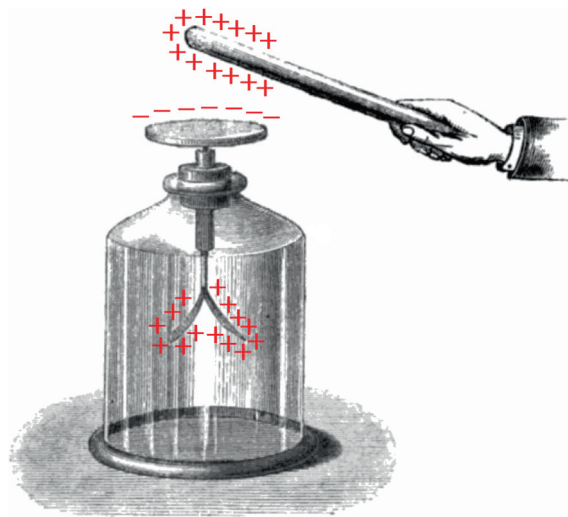
Fig. 3.1 The electroscope is a device for detecting electric charge. A typical electroscope (the configuration in the figure was invented at the end of the eighteenth century) consists of a vertical metal rod from the end of which two gold leaves hang. A disk or ball is attached to the top of the rod. The leaves are enclosed in a glass vessel, for protection against air movements. The test charge is applied to the top, charging the rod, and the gold leaves repel and diverge. By Sylvanus P. Thompson [public domain], via Wikimedia Commons.
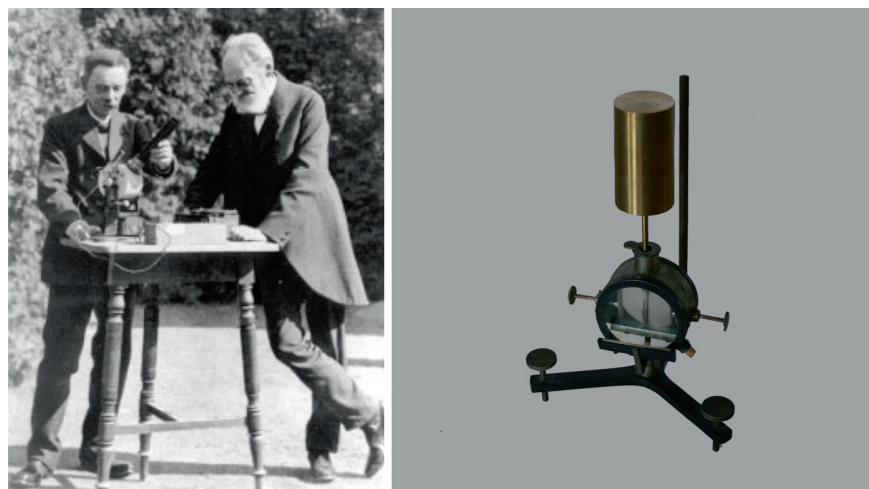
Fig. 3.2 Left: The two friends Julius Elster and Hans Geitel, gymnasium teachers in Wolfenbuttel, around 1900. Credit http://www.elster-geitel.de. Right: an electroscope developed by Elster and Geitel in the same period (private collection R. Fricke; photo by A. De Angelis).

By 1909, measurements on the spontaneous discharge had proved that the discharging background radiation was also present in insulated environments and could penetrate metal shields. It was thus difficult to explain it in terms of α (He nuclei) or β (electron) radiation; it was thus assumed to be γ radiation, i.e., made of photons, which was the most penetrating among the three kinds of radiation known at the time. Three possible sources were then hypothesized for this radiation: it could be extraterrestrial (possibly from the Sun), it could be due to radioactivity from the Earth crust, or to radioactivity in the atmosphere. It was generally assumed that there had to be large contribution from radioactive materials in the crust, and calculations of its expected decrease with height were performed.

3.1.1 Underwater Experiments and Experiments Carried Out at Altitude

Father Theodor Wulf, a German scientist and a Jesuit priest, thought of checking the variation of ionization with height to test its origin. In 1909, using an improved electroscope in which the two leaves had been
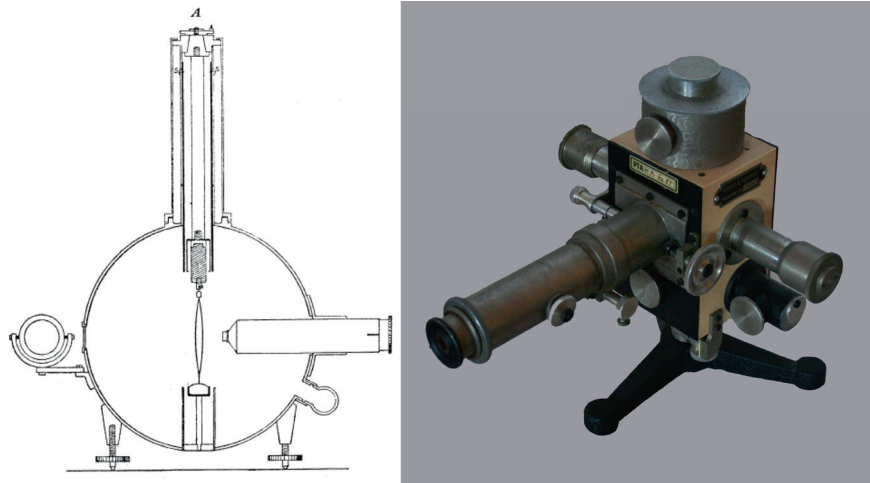
Fig. 3.3 Left: Scheme of the Wulf electroscope (drawn by Wulf himself; reprinted from Z. Phys. [public domain]). The main cylinder was made of zinc, 17 cm in diameter and 13 cm deep. The distance between the two silicon glass wires (at the center) was measured using the microscope to the right. The wires were illuminated using the mirror to the left. According to Wulf, the sensitivity of the instrument was 1 V, as measured by the decrease of the inter-wire distance. Right: an electroscope used by Wulf (private collection R. Fricke; photo by A. De Angelis).

replaced by metal coated silicon glass wires, making it easier to transport than previous instruments (Fig. 3.3), he measured the ionization rate at the top of the Eiffel tower in Paris, about 300 m high. Under the hypothesis that most of the radiation was of terrestrial origin, he expected the ionization rate to be significantly smaller than the value on the ground. The measured decrease was, however, too small to confirm the hypothesis: he observed that the radiation intensity "decrease at nearly 300 m [altitude] was not even to half of its ground value," while "just a few percent of the radiation" should remain if it did emerge from ground. Wulf's data, coming from experiments performed for many days at the same location and at different hours of the day, were of great value, and for a long time were considered the most reliable source of information on the altitude variation of the ionization rate. However, his conclusion was that the most likely explanation for this unexpected result was still emission from ground.

The conclusion that atmospheric ionization was mostly due to radioactivity from the Earth's crust was challenged by the Italian physicist Domenico Pacini. Pacini developed a technique for underwater measurements and conducted experiments in the sea of the Gulf of Genova and in the Lake of Bracciano (Fig. 3.4). He found a significant decrease in the discharge rate in electroscopes placed three meters underwater. He wrote: "Observations carried out on the sea during the year 1910 led me to conclude that a significant proportion of the pervasive radiation that is found in air has an origin that is independent of direct action of the active substances in the upper layers of the Earth's surface. [...] [To prove this conclusion] the apparatus [...] was enclosed in a copper box so that it could immerse in depth. [...] Observations were performed with the instrument at the surface, and with the instrument immersed in water, at a depth of 3 m." Pacini measured the discharge of the electroscope for 3 h, and repeated the measurement seven times. At the surface, the average ionization rate was 11.0 ions per cubic centimeter per second, while he measured 8.9 ions per cubic centimeter per second at a depth of 3 m in the 7 m deep sea (the depth of the water guaranteed that radioactivity from the soil was negligible). He concluded that the decrease of about 20 % was due to a radiation not coming from the Earth.

After Wulf's observations on the altitude effect, the need for balloon experiments (widely used for atmospheric electricity studies since 1885) became clear. The first high-altitude balloon with the purpose of studying the penetrating radiation was flown in Switzerland in December 1909 with a balloon from the Swiss aeroclub. Albert Gockel, professor at the University of Fribourg, ascended to 4500 m above sea level (a.s.l.). He made measurements up to 3000 m and found that ionization rate did not decrease with altitude as expected under the hypothesis of terrestrial origin. His conclusion was that "a non-negligible part of the penetrating radiation is independent of the direct action of the radioactive substances in the uppermost layers of the Earth."

In spite of Pacini's conclusions, and of Wulf's and Gockel's puzzling results on the altitude dependence, the issue of the origin of the penetrating radiation still raised doubts. A series of balloon flights by the
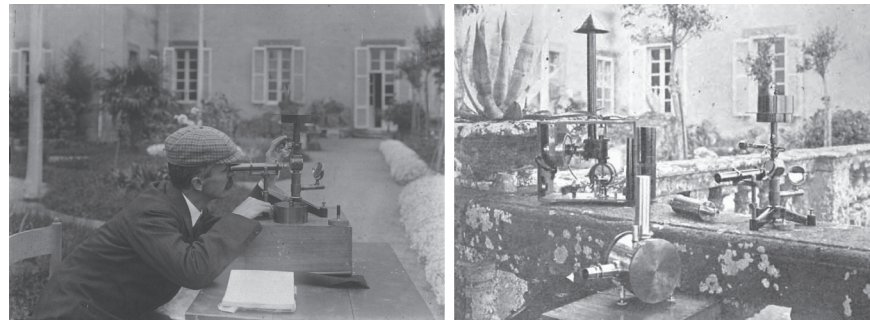
Fig. 3.4 Left: Pacini making a measurement in 1910. Courtesy of the Pacini family, edited by A. De Angelis [public domain, via Wikimedia Commons]. Right: the instruments used by Pacini for the measurement of ionization. By D. Pacini (Ufficio Centrale di Meteorologia e Geodinamica), edited by A. De Angelis [public domain, via Wikimedia Commons].
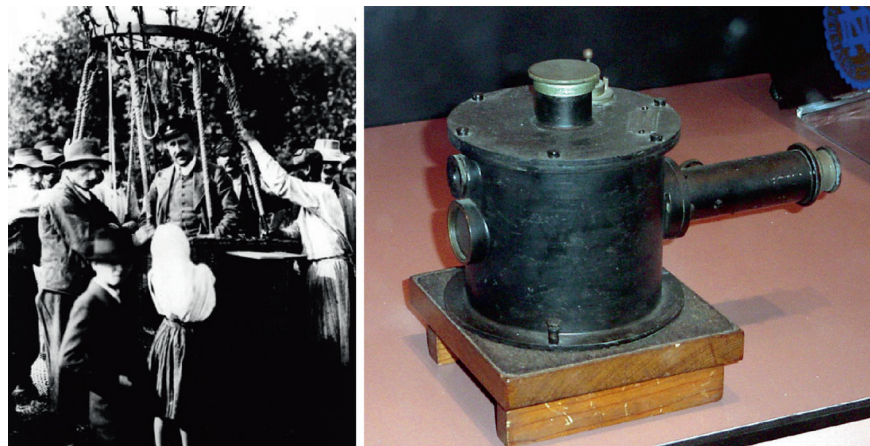
Fig. 3.5 Left: Hess during the balloon flight in August 1912. [public domain], via Wikimedia Commons. Right: one of the electrometers used by Hess during his flight. This instrument is a version of a commercial model of a Wulff electroscope especially modified by its manufacturer, Günther and Tegetmeyer, to operate under reduced pressure at high altitudes (Smithsonian National Air and Science Museum, Washington, DC). Photo by P. Carlson.

Austrian physicist Victor Hess[2] settled the issue, firmly establishing the extraterrestrial origin of at least part of the radiation causing the atmospheric ionization.

Hess started by studying Wulf's results. He carefully checked the data on gamma-ray absorption coefficients (due to the large use of radioactive sources he will loose a thumb) and, after careful planning, he finalized his studies with balloon observations. The first ascensions took place in August 1911. From April 1912 to August 1912, he flew seven times, with three instruments (one of them with a thin wall to estimate the effect of β radiation, as for a given energy electrons have a shorter range than heavier particles). In the last flight, on August 7, 1912, he reached 5200 m (Fig. 3.5). The results clearly showed that the ionization rate first passied through a minimum and then increased considerably with height (Fig. 3.6). "(i) Immediately above ground the total radiation decreases a little. (ii) At altitudes of 1000–2000 m there occurs again a noticeable growth of penetrating radiation. (iii) The increase reaches, at altitudes of 3000–4000 m, already 50 % of the total radiation observed on the ground. (iv) At 4000–5200 m the radiation is stronger [more than 100 %] than on the ground."

Hess concluded that the increase in the ionization rate with altitude was due to radiation coming from above, and he thought that this radiation was of extraterrestrial origin. His observations during the day and during the night showed no variation and excluded the Sun as the direct source of this hypothetical radiation.

The results by Hess would later be confirmed by Kolhörster. In flights up to 9200 m, Kolhörster found an increase in the ionization rate up to ten times its value at sea level. The measured attenuation length of

---

[2] Hess was born in 1883 in Steiermark, Austria, and graduated from Graz University in 1906 where he became professor of Experimental Physics in 1919. In 1936 Hess was awarded the Nobel Prize in Physics for the discovery of cosmic rays. He moved to the USA in 1938 as a professor at Fordham University. Hess became an American citizen in 1944 and lived in New York until his death in 1964.
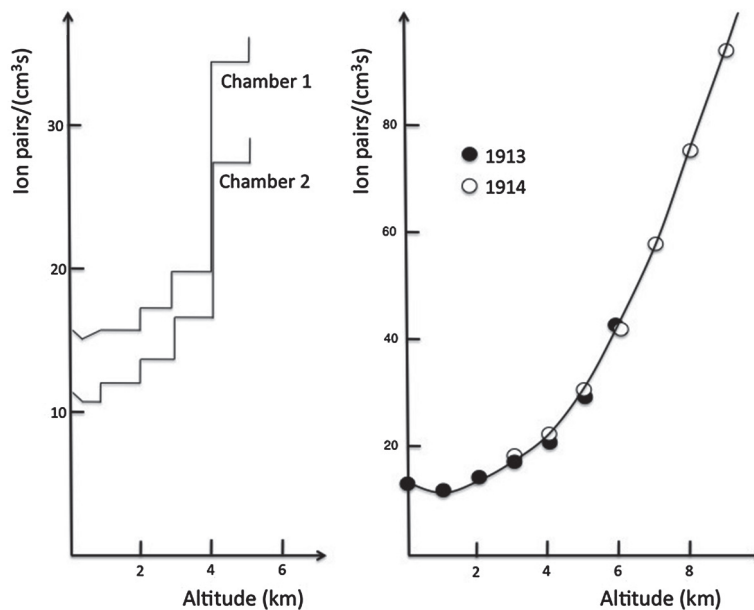
Fig. 3.6 Variation of ionization with altitude. Left panel: Final ascent by Hess (1912), carrying two ion chambers. Right panel: Ascents by Kolhörster (1913, 1914).

about 1 km in air came as a surprise, as it was eight times smaller than the absorption coefficient of air for γ rays as known at the time.

After the 1912 flights, Hess coined the name "Höhenstrahlung." Several other names were used for the extraterrestrial radiation: Ultrastrahlung, Ultra-X-Strahlung, kosmische Strahlung. The latter, used by Gockel and Wulf in 1909, inspired Millikan[3] who suggested the name "cosmic rays," which became generally accepted.

The idea of cosmic rays, despite the striking experimental evidence, was not immediately accepted (the Nobel prize for the discovery of cosmic rays was awarded to Hess only in 1936). During the 1914–1918 war and the years that followed, very few investigations of the penetrating radiation were performed. In 1926, however, Millikan and Cameron performed absorption measurements of the radiation at different depths in lakes at high altitudes. They concluded that the radiation was made up of high energy γ rays and that "these rays shoot through space equally in all directions," and called them "cosmic rays."

3.1.2 The Nature of Cosmic Rays

Cosmic radiation was generally believed to be γ radiation because of its penetrating power (the penetrating power of relativistic charged particles was not known at the time). Millikan had launched the hypothesis that these γ rays were produced when protons and electrons formed helium nuclei in the interstellar space.

A key experiment on the nature of cosmic rays was the measurement of the intensity variation with geomagnetic latitude. During two voyages between Java and Genova in 1927 and 1928, the Dutch physicist Clay found that ionization increased with latitude; this proved that cosmic rays interacted with the geomagnetic field and, thus, they were mostly charged particles.

In 1928, the Geiger-Müller counter tube[4] was introduced, and soon confirmation came that cosmic radiation is indeed electrically charged. In 1933, three independent experiments by Alvarez and Compton, Johnson,

---

[3] Robert A. Millikan (Morrison 1868—Pasadena 1953) was an American experimental physicist, Nobel Prize in Physics in 1923 for his measurements of the electron charge and his work on the photoelectric effect. A scholar of classical literature before turning physics, he was president of the California Institute of Technology (Caltech) from 1921 to 1945. He was not famous for his deontology: a common saying at Caltech was "Jesus saves, and Millikan takes the credit."

[4] The Geiger-Müller counter is a cylinder filled with a gas, with a charged metal wire inside. When a charged particle enters the detector, it ionizes the gas, and the ions and the electrons can be collected by the wire and by the walls. The electrical signal of the wire can be amplified and read by means of an amperometer. The tension V of the wire is large (a few thousand volts), in such a way that the gas is completely ionized; the signal is then a short pulse of height independent of the energy of the

and Rossi, discovered that close to the equator there were more cosmic rays coming from West than from East. This effect, due to the interaction with the geomagnetic field, showed that cosmic rays are mostly positively charged—and thus most probably protons, as some years later it was possible to demonstrate thanks to more powerful spectrometers.

3.2 Cosmic Rays and the Beginning of Particle Physics

With the development of cosmic ray physics, scientists knew that astrophysical sources provided high energy particles which entered the atmosphere. The obvious next step was to investigate the nature of such particles, and to use them to probe matter in detail, much in the same way as in the experiment conducted by Marsden and Geiger in 1909 (the Rutherford experiment, described in Chap. 2). Particle physics thus started with cosmic rays, and many of the fundamental discoveries were made thanks to cosmic rays.

In parallel, the theoretical understanding of the Universe was progressing quickly: at the end of the 1920s, scientists tried to put together relativity and quantum mechanics, and the discoveries following these attempts changed completely our view of nature. A new window was going to be opened: antimatter.

3.2.1 Relativistic Quantum Mechanics and Antimatter: from the Schrödinger Equation to the Klein-Gordon and Dirac Equations

Schrödinger's equation has evident limits. Since it contains derivatives of different order with respect to space and time, it cannot be relativistically covariant, and thus, it cannot be the "final" equation. How can it be extended to be consistent with Lorentz invariance? We must translate relativistically covariant Hamiltonians in the quantum language, i.e., into equations using wavefunctions. We shall see in the following two approaches.

3.2.1.1 The Klein–Gordon Equation

In the case of a free particle ($V = 0$), the simplest way to extend Schrödinger's equation to take into account relativity is to write the Hamiltonian equation

$$\hat{H}^2 = \hat{p}^2 c^2 + m^2 c^4$$
$$\implies -\hbar^2 \frac{\partial^2 \Psi}{\partial t^2} = -\hbar^2 c^2 \boldsymbol{\nabla}^2 \Psi + m^2 c^4 \Psi \,,$$

or, in natural units,

$$\left(-\frac{\partial^2}{\partial t^2} + \boldsymbol{\nabla}^2 \right) \Psi = m^2 \Psi \,.$$

This equation is known as the Klein-Gordon equation,[5] but it was first considered as a quantum wave equation by Schrödinger; it was found in his notebooks from late 1925. Schrödinger had also prepared a manuscript applying it to the hydrogen atom; however, he could not solve some fundamental problems related to the form of the equation (which is not linear in energy, so that states are not easy to combine), and thus he went back to the equation today known by his name. In addition, the solutions of the Klein-Gordon equation do not allow for statistical interpretation of $|\Psi|^2$ as a probability density—its integral would in general not remain constant in time.

The Klein-Gordon equation displays one more interesting feature. Solutions of the associated eigenvalue equation

---

particle. Geiger-Müller tubes can be also appropriate for detecting γ radiation, since a photoelectron or a Compton-scattered electron can generate an avalanche.

[5] Oskar Klein (1894–1977) was a Swedish theoretical physicist; Walter Gordon (1893–1939) was a German theoretical physicist, former student of Max Planck.

$$\left(-m^2 + \boldsymbol{\nabla}^2\right)\psi = E_p^2\psi$$

have both positive and negative eigenvalues for energy. For every plane wave solution of the form

$$\Psi(\mathbf{r}, t) = Ne^{i(\mathbf{p}\cdot\mathbf{r} - E_p t)}$$

with momentum $\mathbf{p}$ and positive energy

$$E_p = \sqrt{p^2 + m^2} \geq m,$$

there is a solution

$$\Psi^*(\mathbf{r}, t) = N^* e^{i(-\mathbf{p}\cdot\mathbf{r} + E_p t)}$$

with momentum $-\mathbf{p}$ and negative energy

$$E = -E_p = -\sqrt{p^2 + m^2} \leq -m.$$

Note that one cannot simply drop the solutions with negative energy as "unphysical": the full set of eigenstates is needed, because, if one starts from a given wavefunction, this could evolve with time into a wavefunction that, in general, has projections on all eigenstates (including those one would like to get rid of). We remind the reader that these are solutions of an equation describing a free particle.

A final comment about notation. The (classical) Schrödinger equation for a single particle in a time-independent potential can be decoupled into two equations: one (the so-called eigenvalue equation) depending only on space, and the other depending only on time. The solution of the eigenvalue equation is normally indicated by a lowercase Greek symbol, $\psi(\mathbf{r})$ for example, while the time part has a solution independent of the potential, $e^{-(E/\hbar)t}$. The wavefunction is indicated by a capital letter:

$$\Psi(\mathbf{r}, t) = \psi(\mathbf{r})e^{-i\frac{E}{\hbar}t}.$$

This distinction makes no sense for relativistically covariant equations and in particular for the Klein-Gordon equation and for the Dirac equation which will be discussed later. Both $\Psi(x)$ and $\psi(x)$ are now valid notations for indicating a wavefunction which is function of the 4-vector $x = (ct, x, y, z)$.

3.2.1.2 The Dirac Equation

Dirac[6] in 1928 searched for an alternative relativistic equation starting from the generic form describing the evolution of a wavefunction, in the familiar form:

$$i\hbar\frac{\partial\Psi}{\partial t} = \hat{H}\Psi$$

with a Hamiltonian operator linear in $\hat{\mathbf{p}}$, t (Lorentz invariance requires that if the Hamiltonian has first derivatives with respect to time also the spatial derivatives should be of first order):

$$\hat{H} = c\boldsymbol{\alpha}\cdot\mathbf{p} + \beta mc^2.$$

This must be compatible with the Klein-Gordon equation, and thus

$$\alpha_i^2 = 1 \;\; ; \;\; \beta^2 = 1$$
$$\alpha_i\beta + \beta\alpha_i = 0$$
$$\alpha_i\alpha_j + \alpha_j\alpha_i = 0.$$

---

[6] Paul Adrien Maurice Dirac (Bristol, UK, 1902—Tallahassee, US, 1984) was one of the founders of quantum physics. After graduating in engineering and later studying physics, he became professor of mathematics in Cambridge. In 1933 he shared the Nobel Prize with Schrödinger. He assigned to the concept of "beauty in mathematics" a prominent role among the basic aspects intrinsic to the nature so far as to argue that "a mathematically beautiful theory is more likely to be right and proper to an unpleasant as it is confirmed by the data."
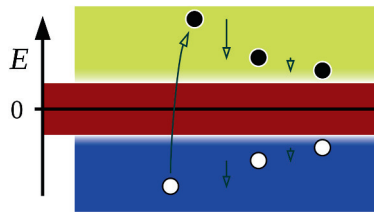
Fig. 3.7 Dirac picture of the vacuum. In normal conditions, the sea of negative energy states is totally occupied with two electrons in each level. By Incnis Mrsi [own work, public domain], via Wikimedia Commons.

Therefore, parameters $\boldsymbol{\alpha}$ and β cannot be numbers. However, it works if they are matrices (and if these matrices are Hermitian it is guaranteed that the Hamiltonian is also Hermitian). It can be demonstrated that the lowest order is 4×4.

Using the explicit form of the momentum operator $\mathbf{p} = -i\hbar\boldsymbol{\nabla}$ the Dirac equation becomes

$$i\hbar\frac{\partial \Psi}{\partial t} = \left(i\boldsymbol{\alpha} \cdot \boldsymbol{\nabla} + \beta mc^2\right)\Psi\,.$$

The wavefunctions Ψ must thus be four-component vectors:

$$\Psi(\mathbf{r}, t) = \begin{pmatrix} \Psi_1(\mathbf{r}, t) \\ \Psi_2(\mathbf{r}, t) \\ \Psi_3(\mathbf{r}, t) \\ \Psi_4(\mathbf{r}, t) \end{pmatrix}.$$

We arrived at an interpretation of the Dirac equation, as a four-dimensional matrix equation in which the solutions are four-component wavefunctions called bispinors (sometimes just spinors).[7] Plane wave solutions are

$$\Psi(\mathbf{r}, t) = u(\mathbf{p})e^{i(\mathbf{p}\cdot\mathbf{r}-Et)}$$

where $u(\mathbf{p})$ is also a four-component spinor satisfying the eigenvalue equation

$$(c\boldsymbol{\alpha} \cdot \mathbf{p} + \beta m)\,u(\mathbf{p}) = Eu(\mathbf{p}).$$

This equation has four solutions: two with positive energy $E = +E_p$ and two with negative energy $E = -E_p$. We discuss later the interpretation of the negative energy solutions.

Dirac's equation was a success. First, it accounted "for free" for the existence of two spin states (we remind the reader that spin had to be inserted by hand in Schrödinger equation of nonrelativistic quantum mechanics). In addition, since spin is embedded in the equation, Dirac's equation:

- allows the correct computation of the energy splitting of atomic levels with the same quantum numbers due to the spin–orbit interaction in atoms (fine and hyperfine splitting);
- explains the magnetic moment of point-like fermions.

The predictions of the values of the above quantities were incredibly precise and have passed every experimental test to date.

3.2.1.3 Hole Theory and the Positron

Negative energy states must be occupied: if they were not, transitions from positive to negative energy states would occur, and matter would be unstable. Dirac postulated that the negative energy states are completely filled under normal conditions. In the case of electrons, the Dirac picture of the vacuum is a "sea" of negative energy states, while the positive energy states are mostly free (Fig. 3.7). This condition cannot be distinguished from the usual vacuum.

---

[7] The term spinor indicates in general a vector which has definite transformation properties for a rotation in the proper angular momentum space—the spin space. The properties of rotation in spin space will be described in greater detail in Chap. 5.
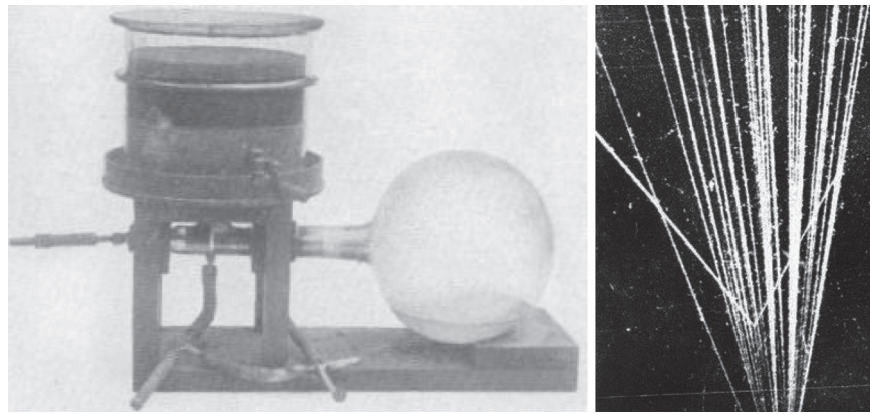
Fig. 3.8 Left: A cloud chamber built by Wilson in 1911. By C.T.R. Wilson [public domain], via Wikimedia Commons. Right: a picture of a collision in a cloud chamber [CC BY 4.0 http://creativecommons.org/licenses/by/4.0] via Wikimedia Commons.
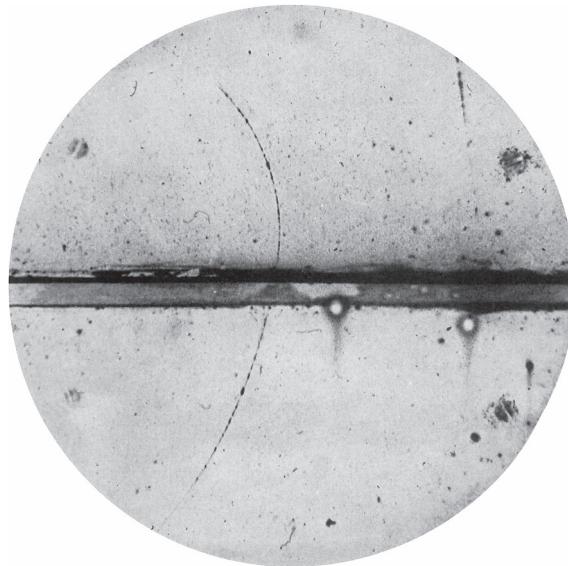
Fig. 3.9 The first picture by Anderson showing the passage of a cosmic antielectron, or positron, through a cloud chamber immersed in a magnetic field. One can understand that the particle comes from the bottom in the picture by the fact that, after passing through the sheet of material in the medium (and therefore losing energy), the radius of curvature decreases. The positive charge is inferred from the direction of bending in the magnetic field. The mass is measured by the bubble density (a proton would lose energy faster). Since most cosmic rays come from the top, the first evidence for antimatter comes thus from an unconventional event. From C.D. Anderson, "The Positive Electron," Physical Review 43 (1933) 491.

If an electron is added to the vacuum, it finds, in general, place in the positive energy region since all the negative energy states are occupied. If a negative energy electron is removed from the vacuum, however, a new phenomenon happens: removing such an electron with $E < 0$, momentum $-\mathbf{p}$, spin $-\mathbf{S}$ and charge $-e$ leaves a "hole" indistinguishable from a particle with positive energy $E > 0$, momentum $\mathbf{p}$, spin $\mathbf{S}$ and charge $+e$. This is similar to the formation of holes in semiconductors. The two cases are equivalent descriptions of the same phenomena. Dirac's sea model thus predicts the existence of a new fermion with mass equal to the mass of the electron, but opposite charge. This particle, later called the positron, is the antiparticle of the electron, and is the prototype of a new family of particles: antimatter.

3.2.2 The Discovery of Antimatter

During his doctoral thesis (supervised by Millikan), Anderson was studying the tracks of cosmic rays passing through a cloud chamber[8] in a magnetic field (Fig. 3.8). In 1933 he discovered antimatter in the form of a positive particle of mass consistent with the electron mass, later called the positron (Fig. 3.9). Dirac's equation prediction was confirmed; this was a great achievement for cosmic ray physics. Anderson shared with Hess the Nobel Prize for Physics in 1936; they were nominated by Compton, with the following motivation:

> The time has now arrived, it seems to me, when we can say that the so-called cosmic rays definitely have their origin at such remote distances from the Earth that they may properly be called cosmic, and that the use of the rays has by now led to results of such importance that they may be considered a discovery of the first magnitude. [...] It is, I believe, correct to say that Hess was the first to establish the increase of the ionization observed in electroscopes with increasing altitude; and he was certainly the first to ascribe with confidence this increased ionization to radiation coming from outside the Earth.

Why so late a recognition to the discovery of cosmic rays? Compton writes:

> Before it was appropriate to award the Nobel Prize for the discovery of these rays, it was necessary to await more positive evidence regarding their unique characteristics and importance in various fields of physics.

3.2.3 Cosmic Rays and the Progress of Particle Physics

After Anderson's fundamental discovery of antimatter, new experimental results in the physics of elementary particles with cosmic rays were guided and accompanied by the improvement of the tools for detection, in particular by the improved design of the cloud chambers and by the introduction of the Geiger-Müller tube. According to Giuseppe Occhialini, one of the pioneers of the exploration of fundamental physics with cosmic rays, the Geiger-Müller counter was like the Colt revolver in the Far West: a cheap instrument usable by everyone on one's way through a hard frontier.

At the end of the 1920s, Bothe and Kolhörster introduced the coincidence technique to study cosmic rays with the Geiger counter. A coincidence circuit activates the acquisition of data only when signals from predefined detectors are received within a given time window. The coincidence technique is widely used in particle physics experiments, but also in other areas of science and technology. Walther Bothe shared the Nobel Prize for Physics in 1954 "for the coincidence method and his discoveries made therewith." Coupling a cloud chamber to a system of Geiger counters and using the coincidence technique, it was possible to take photographs only when a cosmic ray traversed the cloud chamber (we call today such a system a "trigger"). This increased the chances of getting a significant photograph and thus the efficiency of cloud chambers.

Soon after the discovery of the positron by Anderson, a new important observation was made in 1933: the conversion of photons into pairs of electrons and positrons. Dirac's theory not only predicted the existence of antielectrons, but it also predicted that electron–positron pairs could be created from a single photon with energy large enough; the phenomenon was actually observed in cosmic rays by Blackett (Nobel Prize for Physics in 1948) and Occhialini, who further improved in Cambridge the coincidence technique. Electron–positron pair production is a simple and direct confirmation of the mass-energy equivalence and thus of what is predicted by the theory of relativity. It also demonstrates the behavior of light, confirming the quantum concept which was originally expressed as "wave-particle duality": the photon can behave as a particle.

In 1934, the Italian Bruno Rossi[9] reported the observation of the near-simultaneous discharge of two widely separated Geiger counters during a test of his equipment. In the report, he wrote: "[...] it seems

---

[8] The cloud chamber (see also next chapter), invented by C.T.R. Wilson at the beginning of the twentieth century, was an instrument for reconstructing the trajectories of charged particles. The instrument is a container with a glass window, filled with air and saturated water vapor; the volume could be suddenly expanded, bringing the vapor to a supersaturated (metastable) state. A charged cosmic ray crossing the chamber produces ions, which act as seeds for the generation of droplets along the trajectory. One can record the trajectory by taking a photographic picture. If the chamber is immersed in a magnetic field, momentum and charge can be measured by the curvature. The working principle of bubble chambers is similar to that of the cloud chamber, but here the fluid is a liquid. Along the tracks' trajectories, a trail of gas bubbles condensates around the ions. Bubble and cloud chambers provide a complete information: the measurement of the bubble density and the range, i.e., the total track length before the particle eventually stops, provide an estimate for the energy and the mass; the angles of scattering provide an estimate for the momentum.

[9] Bruno Rossi (Venice 1905—Cambridge, MA, 1993) graduated from Bologna, and then moved to Arcetri near Florence before becoming full professor of physics at the University of Padua in 1932. In Padua he was charged of overseeing the design and construction of the new Physics Institute, which was inaugurated in 1937. He was exiled in 1938, as a consequence of the Italian

that once in a while the recording equipment is struck by very extensive showers of particles, which causes coincidences between the counters, even placed at large distances from one another." In 1937 Pierre Auger, who was not aware of Rossi's report, made a similar observation and investigated the phenomenon in detail. He concluded that extensive showers originate when high energy primary cosmic rays interact with nuclei high in the atmosphere, leading to a series of interactions that ultimately yield a shower of particles that reach ground. This was the explanation of the spontaneous discharge of electroscopes due to cosmic rays.

3.2.4 The μ Lepton and the π Mesons

In 1935 the Japanese physicist Yukawa, 28 years old at that time, formulated his innovative theory explaining the "strong" interaction ultimately keeping together matter (strong interaction keeps together protons and neutrons in the atomic nuclei). This theory has been sketched in the previous chapter, and requires a "mediator" particle of intermediate mass between the electron and the proton, thus called meson—the word "meson" meaning "middle one."

To account for the strong force, Yukawa predicted that the meson must have a mass of about one-tenth of a GeV, a mass that would explain the rapid weakening of the strong interaction with distance. The scientists studying cosmic rays started to discover new types of particles of intermediate masses. Anderson, who after the Nobel Prize had become a professor, and his student Neddermeyer, observed in 1937 a new particle, present in both positive and negative charge, more penetrating than any other particle known at the time. The new particle was heavier than the electron but lighter than the proton, and they suggested for it the name "mesotron." The mesotron mass, measured from ionization, was between 200 and 240 times the electron mass; this matched Yukawa's prediction for the meson. Most researchers were convinced that these particles were the Yukawa's carrier of the strong nuclear force, and that they were created when primary cosmic rays collided with nuclei in the upper atmosphere, in the same way that electrons emit photons when colliding with a nucleus.

The lifetime of the mesotron was measured studying its flow at various altitudes, in particular by Rossi in Colorado; the result was of about two microseconds (a hundred times larger than predicted by Yukawa for the particle that transmits the strong interaction). Rossi found also that at the end of its life the mesotron decays into an electron and other neutral particles (neutrinos) that did not leave tracks in bubble chamber—the positive mesotron decays into a positive electron plus neutrinos.

Beyond the initial excitement, however, the picture did not work. In particular, the Yukawa particle is the carrier of strong interactions, and therefore it cannot be highly penetrating—the nuclei of the atmosphere would absorb it quickly. Many theorists tried to find complicated explanations to save the theory. The correct explanation was however the simplest one: the mesotron was not the Yukawa particle, as it was demonstrated in 1945/46 by three young Italian physicists, Conversi, Pancini, and Piccioni.

The experiment by Conversi, Pancini and Piccioni exploits the fact that slow negative Yukawa particles can be captured by nuclei in a time shorter than the typical lifetime of the mesotron, about $2\,\mu$s, and thus are absorbed before decaying; conversely, slow positive particles are likely to be repelled by the potential barrier of nuclei and thus have the time to decay. The setup is shown in Fig. 3.10; a magnetic lens focuses particles of a given charge, thus allowing charge selection. The Geiger counters A and B are in coincidence—i.e., a simultaneous signal is required; the C counters under the absorber are in "delayed coincidence," and it is requested that one of them fires after a time between 1 and $4.5\,\mu$s after the coincidence (AB). This guarantees that the particle selected is slow and, in case of decay, has a lifetime consistent with the mesotron. The result was that when carbon was used as an absorber, a substantial fraction of the negative mesons decayed. The mesotron was not the Yukawa particle.

There were thus two particles of similar mass. One of them (with a mass of about $140\,\mathrm{MeV}/c^2$), corresponding to the particle predicted by Yukawa, was later called pion (or π meson); it was created in the interactions of cosmic protons with the atmosphere, and then interacted with the nuclei of the atmosphere,

---

racial laws, and he moved to Chicago and then to Cornell. In 1943 he joined the Manhattan project in Los Alamos, working at the development of the atomic bomb, and after the end of the second World War moved to MIT. At MIT Rossi started working on space missions as a scientific consultant for the newborn NASA, and proposed together with his former student Riccardo Giacconi, physics Nobel prize in 2002, the rocket experiment that discovered the first extra-solar source of X-rays. Many fundamental contributions to modern physics, for example the electronic coincidence circuit, the discovery and study of extensive air showers, the East–West effect, and the use of satellites for the exploration of the high-energy Universe, are due to Bruno Rossi.
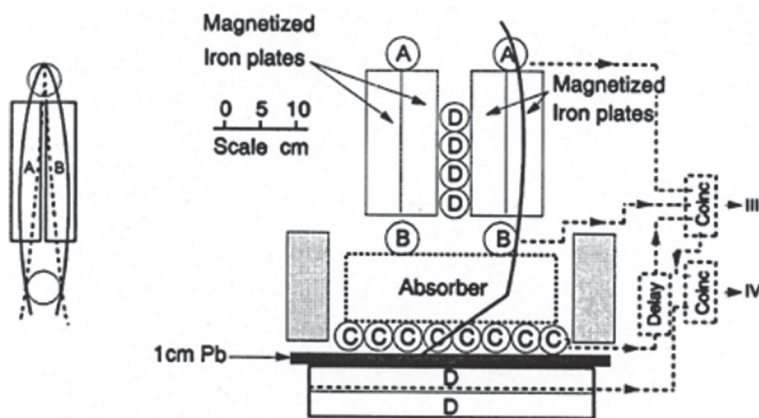
Fig. 3.10 Left: a magnetic lens (invented by Rossi in 1930). Right: setup of the Conversi, Pancini and Piccion experiment. From M. Conversi, E. Pancini, O. Piccioni, "On the disintegration of negative mesons", Physical Review 71 (1947) 209.

Fig. 3.11 The pion and the muon: the decay chain $\pi \to \mu \to e$. The pion travels from bottom to top on the left, the muon horizontally, and the electron from bottom to top on the right. The missing momentum is carried by neutrinos. From C.F. Powell, P.H. Fowler and D.H. Perkins, "The Study of Elementary Particles by the Photographic Method," Pergamon Press 1959.

or decayed. Among its decay products there was the mesotron, since then called the muon (or μ lepton), which was insensitive to the strong force.

In 1947, Powell, Occhialini and Lattes, exposing nuclear emulsions (a kind of very sensitive photographic plates, with space resolutions of a few μm; we shall discuss them in the next chapter) to cosmic rays on Mount Chacaltaya in Bolivia, finally proved the existence of charged pions, positive and negative, while observing their decay into muons and allowing a precise determination of the masses. For this discovery Cecil Powell, the group leader, was awarded the Nobel Prize in 1950.

Many photographs of nuclear emulsions, especially in experiments on balloons, clearly showed traces of pions decaying into muons (the muon mass was reported to be about 106 MeV/c^2), decaying in turn into electrons. In the decay chain $\pi \to \mu \to e$ (Fig. 3.11) some energy is clearly missing, and can be attributed to neutrinos.

At this point, the distinction between pions and muons was clear. The muon looks like a "heavier brother" of the electron. After the discovery of the pion, the muon had no theoretical reason to exist (the physicist Isidor Rabi was attributed in the 1940s the famous quote: "Who ordered it?"). However, a new family was initiated: the family of leptons—including for the moment the electron and the muon, and their antiparticles.

3.2.4.1 The Neutral Pion

Before it was even known that mesotrons were not the Yukawa particle, the theory of mesons was developed in great detail. In 1938, a theory of charge symmetry was formulated, conjecturing the fact that the forces between protons and neutrons, between protons and protons and between neutrons and neutrons are similar. This implies the existence of positive, negative and also neutral mesons.

The neutral pion was more difficult to detect than the charged one, due to the fact that neutral particles do not leave tracks in cloud chambers and nuclear emulsions—and also to the fact, discovered only later, that it lives only approximately 10^{-16} s before decaying mostly into two photons. However, between 1947 and 1950, the neutral pion was identified in cosmic rays by analyzing its decay products in showers of particles. So, after 15 years of research, the theory of Yukawa had finally complete confirmation.
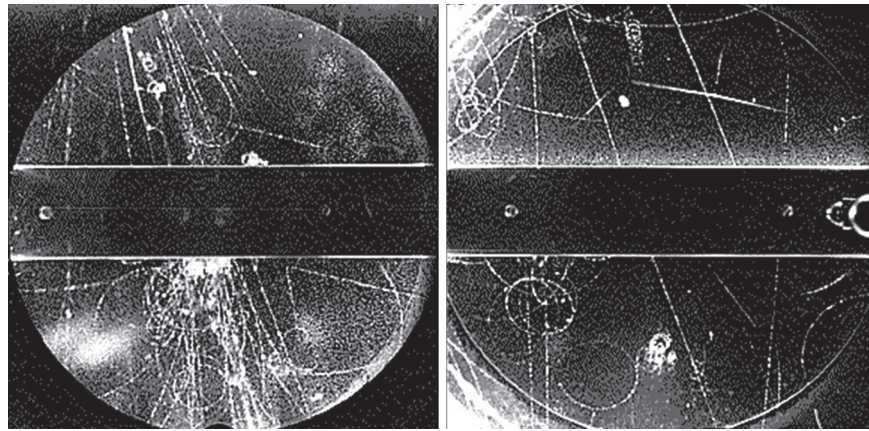
Fig. 3.12 The first images of the decay of particles known today as K mesons or kaons—the first examples of "strange" particles. The image on the left shows the decay of a neutral kaon. Being neutral it leaves no track, but when it decays into two lighter charged particles (just below the central bar to the right), one can see a "V". The picture on the right shows the decay of a charged kaon into a muon and a neutrino. The kaon reaches the top right corner of the chamber and the decay occurs where the track seems to bend sharply to the left. From G.D. Rochester, C.C. Butler, "Evidence for the Existence of New Unstable Elementary Particles" Nature 160 (1947) 855.

3.2.5 Strange Particles

In 1947, after the thorny problem of the meson had been solved, particle physics seemed to be a complete science. Fourteen particles were known to physicists (some of them at the time were only postulated, and were going to be found experimentally later): the proton, the neutron (proton and neutron together belong to the family of baryons, the Greek etymology of the word referring to the concept of "heaviness") and the electron, and their antiparticles; the neutrino that was postulated because of an apparent violation of the principle of energy conservation; three pions; two muons; and the photon.

Apart from the muon, a particle that appeared unnecessary, all the others seemed to have a role in nature: the electron and the nucleons constitute the atom, the photon carries the electromagnetic force, and the pion the strong force; neutrinos are needed for energy conservation. But, once more in the history of science, when everything seemed understood a new revolution was just around the corner.

Since 1944, strange topologies of cosmic particles were photographed from time to time in cloud chambers. In 1947, G.D. Rochester and the C.C. Butler from the University of Manchester observed clearly in a photograph a couple of tracks from a single point with the shape of a "V"; the two tracks were deflected in opposite directions by an external magnetic field. The analysis showed that the parent neutral particle had a mass of about half a GeV (intermediate between the mass of the proton and that of the pion), and disintegrated into a pair of oppositely charged pions. A broken track in a second photograph showed the decay of a charged particle of about the same mass into a charged pion and at least one neutral particle (Fig. 3.12).

These particles, which were produced only in high energy interactions, were observed only every few hundred photographs. They are known today as K mesons (or kaons); kaons can be positive, negative, or neutral. A new family of particles had been discovered. The behavior of these particles was somehow strange: the cross section for their production could be understood in terms of strong interactions; however, their lifetime was inconsistent with strong interaction, being too long. These new particles were called "strange mesons". Later analyses indicated the presence of particles heavier than protons and neutrons. They decayed with a "V" topology into final states including protons, and they were called strange baryons, or hyperons (Λ, Σ, ...). Strange particles appear to be always produced in pairs, indicating the presence of a new conserved quantum number—thus called strangeness.

3.2.5.1 The τ-θ Puzzle

In the beginning, the discovery of strange mesons was made complicated by the so-called τ-θ puzzle. A strange charged meson was disintegrating into two pions, and was called the θ meson; another particle called the τ meson was disintegrating into three pions. Both particles disintegrated via the weak force and, apart

from the decay mode, they turned out to be indistinguishable from each other, having identical masses within the experimental uncertainties. Were the two actually the same particle? It was concluded that they were (we are talking about the K meson); this opened a problem related to the so-called parity conservation law, and we will discuss it better in Chaps. 5 and 6.

3.2.6 Mountain-Top Laboratories

The discovery of mesons, which had put the physics world in turmoil after World War II, can be considered as the origin of the "modern" physics of elementary particles.

The following years showed a rapid development of the research groups dealing with cosmic rays, along with a progress of experimental techniques of detection, exploiting the complementarity of cloud and bubble chambers, nuclear emulsions, and electronic coincidence circuits. The low cost of emulsions allowed the spread of nuclear experiments and the establishment of international collaborations.

It became clear that it was appropriate to equip laboratories on top of the mountains to study cosmic rays. Physicists from all around the world were involved in a scientific challenge of enormous magnitude, taking place in small laboratories on the tops of the Alps, the Andes, the Rocky Mountains, the Caucasus.

Particle physicists used cosmic rays as the primary tool for their research until the advent of particle accelerators in the 1950s, so that the pioneering results in this field are due to cosmic rays. For the first 30 years since their discovery, cosmic rays allowed physicists to gain information on the physics of elementary particles. With the advent of particle accelerators, in the years since 1950, most physicists went from hunting to farming.

3.3 Particle Hunters Become Farmers

In 1953, the Cosmic Ray Conference at Bagnères de Bigorre in the French Pyrenees was a turning point for high energy physics. The technology of artificial accelerators was progressing, and many cosmic ray physicists were moving to this new frontier. CERN, the European Laboratory for Particle Physics, was soon to be founded.

Also from the sociological point of view, important changes were in progress, and large international collaborations were formed. Only 10 years earlier, articles for which the preparation of the experiment and the data analysis had been performed by many scientists were signed only by the group leader. But the recent G-stack experiment, an international collaboration in which cosmic ray interactions were recorded in a series of balloon flights by means of a giant stack of nuclear emulsions, had introduced a new policy: all scientists contributing to the result were authors of the publications. At that time the number of signatures in one of the G-stack papers, 35, seemed enormous; in the twenty-first century things have further evolved, and the two articles announcing the discovery of the Higgs particle by the ATLAS and CMS collaborations have 2931 and 2899 signatures respectively.

In the 1953 Cosmic Ray Conference contributions coming from accelerator physics were not accepted: the two methods of investigation of the nature of elementary particles were kept separated. However, the French physicist Leprince-Ringuet, who was going to found CERN in 1954 together with scientists of the level of Bohr, Heisenberg, Powell, Auger, Edoardo Amaldi, and others, said in his concluding remarks:

> Let's point out first that in the future we must use particle accelerators. [...T]hey will allow the measurement of certain fundamental curves (scattering, ionization, range) which will permit us to differentiate effects such as the existence of π mesons among the secondaries of K mesons. [...]

> I would like to finish with some words on a subject that is dear to my heart and is equally so to all the 'cosmicians', in particular the 'old timers'. [...] We have to face the grave question: what is the future of cosmic rays? Should we continue to struggle for a few new results or would it be better to turn to the machines? One can with no doubt say that the future of cosmic radiation in the domain of nuclear physics depends on the machines [...]. But probably this point of view should be tempered by the fact that we have the uniqueness of some phenomena, quite rare it is true, for which the energies are much larger.

It should be stressed that, despite the great advances of the technology of accelerators, the highest energies will always be reached by cosmic rays. The founding fathers of CERN, in their Constitution (Convention
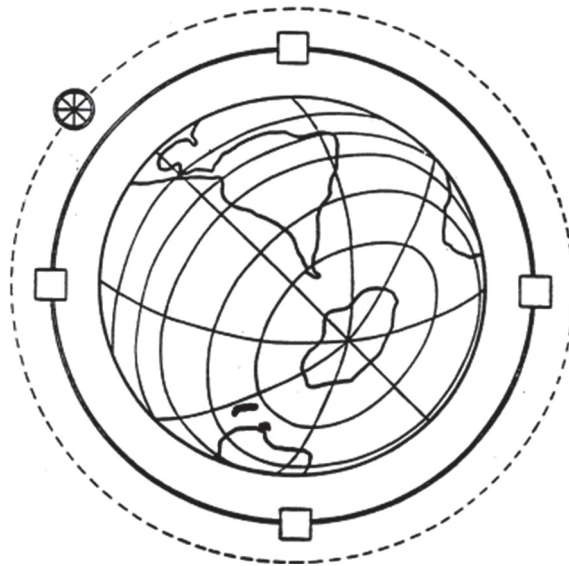
Fig. 3.13 The so-called "maximum accelerator" by Fermi (original drawing by Enrico Fermi reproduced from his 1954 speech at the annual meeting of the American Physical Society). Courtesy of Fermi National Laboratory, Batavia, Illinois.

for the Establishment of a European Organization for Nuclear Research, 1953) explicitly stated that cosmic rays are one of the research items of the Laboratory.

A calculation made by Fermi about the maximum reasonably (and even *unreasonably*) achievable energy by terrestrial accelerators is interesting in this regard. In his speech "What can we learn from high energy accelerators") held at the American Physical Society in 1954 Fermi had considered a proton accelerator with a ring as large as the maximum circumference of the Earth (Fig. 3.13) as the maximum possible accelerator. Assuming a magnetic field of 2 tesla (Fermi assumed that this was the maximum field attainable in stable conditions and for long magnets; the conjecture is still true unless new technologies will appear), it is possible to obtain a maximum energy of 5000 TeV: this is the energy of cosmic rays just under the "knee," the typical energy of galactic accelerators. Fermi estimated with great optimism, extrapolating the rate of progress of the accelerator technology in the 1950s, that this accelerator could be constructed in 1994 and cost approximately 170 million dollars (the cost of LHC is some 50 times larger, and its energy is 700 times smaller).

3.4 The Recent Years

Things went more or less as predicted by Leprince-Ringuet.

Between the 1950s and the 1990s most of the progress in fundamental physics was due to accelerating machines. Still, however, important experiments studying cosmic rays were alive, and were an important source of knowledge.

Cosmic rays are today central in the field of astroparticle physics, which has grown considerably in the last 20 years. Many large projects are active, with many different goals, including for example the search for dark matter in the Universe.

Gamma-ray space telescopes on satellites like the *Fermi* Large Area Telescope (*Fermi*-LAT) and AGILE, and the PAMELA and AMS-02 magnetic spectrometers, provided cutting-edge results; PAMELA in particular observed a yet unexplained anomalous yield of cosmic positrons, with a ratio between positrons and electrons growing with energy, which might point to new physics, in particular related to dark matter. The result was confirmed and extended to higher energies and with unprecedented accuracy by the AMS-02 detector onboard the International Space Station.

The study of very highest energy cosmic-ray showers, a century after the discovery of air showers by Rossi and Auger, is providing fundamental knowledge of the spectrum and sources of cosmic rays. In particular the region near the GZK cutoff is explored. The present day largest detector, the Pierre Auger Observatory, covers a surface of about $3000 \, \text{km}^2$ in Argentina,

The ground-based very-high energy gamma telescopes HAWC, H.E.S.S., MAGIC and VERITAS are mapping the cosmic sources of gamma rays in the TeV and multi-TeV region. Together with the *Fermi* satellite, they are providing indications of a link between the photon accelerators and the cosmic ray accelerators in the Milky Way, in particular supernova remnants. Studying the propagation of very energetic photons traveling through cosmological distances, they are also sensitive to possible violations of the Lorentz invariance at very high energy, and to photon interactions with the quantum vacuum, which in turn are sensitive to the existence of yet unknown fields. A new detector, CTA, is planned and will outperform the present detectors by at least an order of magnitude.

The field of study of cosmic neutrinos registered impressive results. In the analysis of the fluxes of solar neutrinos and then of atmospheric neutrinos, studies performed using large neutrino detectors in Japan, US, Canada, China, and Italy have demonstrated that neutrinos can oscillate between different flavors; this phenomenon requires that neutrinos have nonzero mass—present indications favor masses of the order of tenths of meV. Recently the IceCube South Pole Neutrino Observatory, a km^3 detector buried in the ice of Antarctica, has discovered the first solid evidence for astrophysical neutrinos from cosmic accelerators (some with energies greater than 1 PeV). With IceCube, some 10 astrophysical neutrinos per year (with a $\sim 20\%$ background) have been detected in the last 5 years; they do not appear within the present statistics to cluster around a particular astrophysical source.

Finally, a handful of gravitational wave events have been detected in very recent years. In 2015, the LIGO/Virgo project directly detected gravitational waves using laser interferometers. The LIGO detectors observed gravitational waves from the merger of two stellar-mass black holes, matching predictions of general relativity. These observations demonstrated the existence of binary stellar-mass black hole systems, and were the first direct detection of gravitational waves and the first observation of a binary black hole merger. Together with the detection of astrophysical neutrinos, the observations of gravitational waves paved the way for multimessenger astrophysics: combining the information obtained from the detection of photons, neutrinos, charged particles, and gravitational waves, can shed light on completely new phenomena and objects.

Cosmic rays and cosmological sources are thus again in the focus of very high energy particle and gravitational physics. This will be discussed in greater detail in Chap. 10.

Further Reading

[F3.1] P. Carlson, A. de Angelis, "Nationalism and internationalism in science: the case of the discovery of cosmic rays", The European Physical Journal H 35 (2010) 309.
[F3.2] A. de Angelis, "Atmospheric ionization and cosmic rays: studies and measurements before 1912", Astroparticle Physics 53 (2014) 19.
[F3.3] D.H. Griffiths, "Introduction to Quantum Mechanics, 2nd edition," Addison-Wesley, Reading, MA, 2004.
[F3.4] J. Björken and S. Drell, "Relativistic Quantum Fields," McGraw-Hill, New York, 1969.

Exercises

1. *The measurement by Hess.* Discuss why radioactivity decreases with elevation up to some 1000 m, and then increases. Can you make a model? This was the subject of the thesis by Schrödinger in Wien in the beginning of twentieth century.
2. *Klein-Gordon equation.* Show that in the nonrelativistic limit $E \simeq mc^2$ the positive energy solutions Ψ of the Klein-Gordon equation can be written in the form

$$\Psi(\mathbf{r}, t) \simeq \Phi(\mathbf{r}, t) e^{-\frac{mc^2}{\hbar}t},$$

   where Φ satisfies the Schrödinger equation.
3. *Antimatter.* The total number of nucleons minus the total number of anti nucleons is believed to be constant in a reaction—you can create nucleon–antinucleon pairs. What is the minimum energy of a proton hitting a proton at rest to generate an antiproton?

4. *Fermi maximum accelerator.* According to Enrico Fermi, the ultimate human accelerator, the "Globatron," would be built around 1994 encircling the entire Earth and attaining an energy of around 5000 TeV (with an estimated cost of 170 million US dollars at 1954 prices...). Discuss the parameters of such an accelerator.

5. *Cosmic pions and muons.* Pions and muons are produced in the high atmosphere, at a height of some 10 km above sea level, as a result of hadronic interactions from the collisions of cosmic rays with atmospheric nuclei. Compute the energy at which charged pions and muons respectively must be produced to reach on average the Earth's surface.

   You can find the masses of the lifetimes of pions and muons in Appendix D or in your Particle Data Booklet.

6. *Very-high-energy cosmic rays.* Justify the sentence "About once per minute, a single subatomic particle enters the Earth's atmosphere with an energy larger than 10 J" in Chap. 1.

7. *Very-high-energy neutrinos.* The IceCube experiment in the South Pole can detect neutrinos crossing the Earth from the North Pole. If the cross section for neutrino interaction on a nucleon is $(6.7 \times 10^{-39} E)$ cm^2 with E expressed in GeV (note the linear increase with the neutrino energy E), what is the energy at which half of the neutrinos interact before reaching the detector? Comment on the result.

8. If a π^0 from a cosmic shower has an energy of 2 GeV:

   (a) Assuming the two γ rays coming from its decay are emitted in the direction of the pion's velocity, how much energy does each have?

   (b) What are their wavelengths and frequencies?

   (c) How far will the average neutral pion travel, in the laboratory frame, from its creation to its decay? Comment on the difficulty to measure the pion lifetime.

Chapter 4
Particle Detection

Alessandro De Angelis and Mário Pimenta

After reading this chapter, you should be able to manage the basics of particle detection, and to understand the sections describing the detection technique in a modern article of high-energy particle or astroparticle physics.

Particle detectors measure physical quantities related to the result of a collision; they should ideally identify all the outcoming (and the incoming, if unknown) particles, and measure their kinematic characteristics (momentum, energy, velocity).

In order to detect a particle, one must make use of its interaction with a sensitive material. The interaction should possibly not destroy the particle that one wants to detect; however, for some particles this is the only way to obtain information.

In order to study the properties of detectors, we shall thus first need to review the characteristics of the interaction of particles with matter.

4.1 Interaction of Particles with Matter

4.1.1 Charged Particle Interactions

Charged particles interact basically with atoms, and the interaction is mostly electromagnetic: they might expel electrons (ionization), promote electrons to upper energy levels (excitation), or radiate photons (bremsstrahlung, Cherenkov radiation, transition radiation). High-energy particles may also interact directly with the atomic nuclei.

4.1.1.1 Ionization Energy Loss

This is one of the most important sources of energy loss by charged particles. The average value of the specific (i.e., calculated per unit length) energy loss due to ionization and excitation whenever a particle goes through a homogeneous material of density ρ is described by the so-called Bethe formula.[1] This expression has an accuracy of a few % in the region $0.1 < \beta\gamma < 1000$ for materials with intermediate atomic number.

$$-\frac{dE}{dx} \simeq \rho D \left(\frac{Z}{A}\right) \frac{(z_p)^2}{\beta^2} \left[\frac{1}{2} \ln\left(\frac{2m_e c^2 \beta^2 \gamma^2}{I}\right) - \beta^2 - \frac{\delta(\beta, \rho)}{2}\right] , \qquad (4.1)$$

where

- ρ is the material density, in g/cm^3;
- Z and A are the atomic and mass number of the material, respectively;
- z_p is the charge of the incoming particle, in units of the electron charge;

---

[1] The 24-year-old Hans Bethe, Nobel Prize in 1967 for his work on the theory of stellar nucleosynthesis, published this formula in 1930; the formula—not including the density term, added later by Fermi—was derived using quantum mechanical perturbation theory up to z_p^2. The description can be improved by considering corrections which correspond to higher powers of z_p: Felix Block obtained in 1933 a higher-order correction proportional to z_p^4, not reported in this text, and sometimes the formula is called "Bethe-Block energy loss"—although this naming convention has been discontinued by the Particle Data Group since 2008.
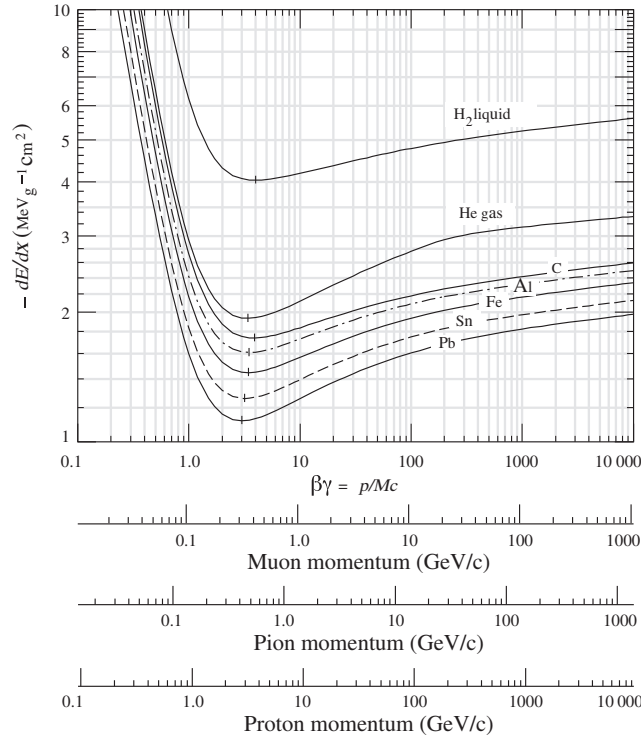
Fig. 4.1 Specific ionization energy loss for muons, pions, and protons in different materials. From K.A. Olive et al. (Particle Data Group), Chin. Phys. C 38 (2014) 090001.

- $D \simeq 0.307$ MeV cm^2/g;
- $m_e c^2$ is the energy corresponding to the electron mass, ~ 0.5 MeV;
- I is the mean excitation energy in the material; it can be approximated as $I \simeq 16$ eV $\times Z^{0.9}$ for $Z > 1$;
- δ is a correction term that becomes important at high energies. It accounts for the reduction in energy loss due to the so-called *density effect*. As the incident particle velocity increases, media become polarized and their atoms can no longer be considered as isolated.

The energy loss by ionization (Fig. 4.1) in first approximation is:

- independent of the particle's mass;
- typically small for high-energy particles (about 2 MeV/cm in water; one can roughly assume a proportionality to the density of the material);
- proportional to $1/\beta^2$ for $\beta\gamma \leq 3$ (the minimum of ionization: minimum ionizing particle, often just called a "mip");
- basically constant for $\beta > 0.96$ (logarithmic increase after the minimum);
- proportional to Z/A (Z/A being about equal to 0.5 for all elements but hydrogen and the heaviest nuclei).

In practice, most relativistic particles (such as cosmic-ray muons) have mean energy loss rates close to the minimum; they can be considered within less than a factor of two as minimum ionizing particles. The loss from a minimum ionizing particle is well approximated as

$$\frac{1}{\rho}\frac{dE}{dx} \simeq -3.5\left(\frac{Z}{A}\right) \text{ MeV cm}^2/\text{g}.$$

In any case, as we shall see later, the energy loss in the logarithmic increase region can be used by means of appropriate detectors for particle identification.

Due to the statistical nature of the ionization process, large fluctuations on the energy loss arise when fast charged particles pass through absorbers which are thin compared to the particle range. The energy loss is distributed around the most probable value according to an asymmetric distribution (named the Landau[2]

---

[2] Lev Davidovich Landau (1908 –1968) was a Soviet physicist who made fundamental contributions to many areas of theoretical physics, in particular quantum mechanics, particle physics, and the structure of matter. He received the 1962 Nobel Prize in Physics for his development of a mathematical theory of superfluidity.
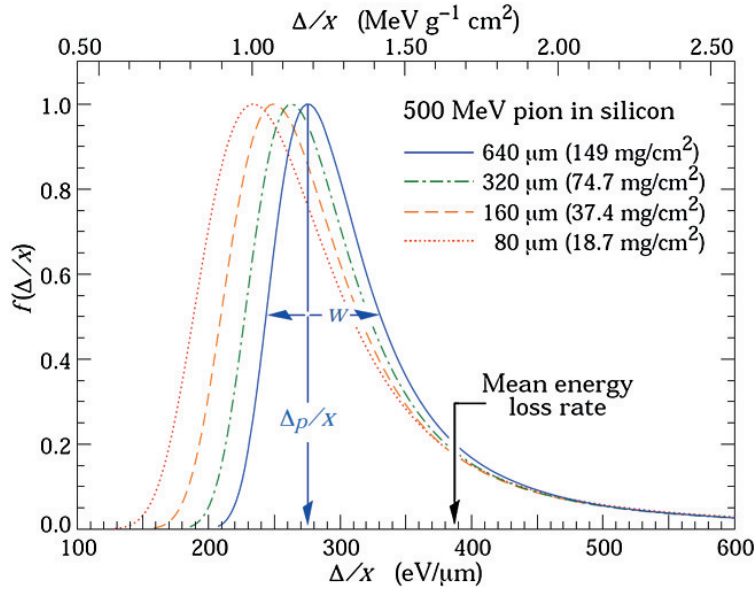
Fig. 4.2 Distribution of the energy loss (Landau distribution) in silicon for 500 MeV pions, normalized to unity at the most probable value. w is the full width at half maximum. From K.A. Olive et al. (Particle Data Group), Chin. Phys. C 38 (2014) 090001.

distribution). The average energy loss, represented by the Bethe formula, is larger than the most probable energy loss, since the Landau distribution has a long tail (as the width of the material increases, the most probable energy loss becomes however closer to the average, as one can see in Fig. 4.2).

Although its nature is quantum mechanical, the main characteristics of Eq. 4.1 can be derived classically, as it was first done by Bohr. Let us suppose a charged particle of mass m and charge z_p passes at a distance b from a target of mass M and charge Z. The momentum Δp transferred to the target depends on the electric field $\mathcal{E}$ produced by the charged traveling particle. Given the symmetry of the problem only the transverse component of the electric field with the respect to the particle track $\mathcal{E}_\perp$ matters. Relating the interaction time t with the velocity of the particle, $dt = dx/v$, one can write for the momentum transfer:

$$\Delta p = \int_{-\infty}^{+\infty} F \, dt = \int_{-\infty}^{+\infty} e \, \mathcal{E} \, dt = \frac{e}{v} \int_{-\infty}^{+\infty} \mathcal{E}_\perp \, dx.$$

The electric field integral can be calculated using the Gauss's law. In fact, the flux of the electric field passing through a cylinder of radius b is given by $\int \mathcal{E}_\perp \, 2\pi b \, dx = z_p \, e/\varepsilon_0$. Therefore, the momentum transferred to the target particle can be written as

$$\Delta p = \frac{z_p \, e^2}{2 \, \pi \, \varepsilon_0 \, v \, b}$$

or still in terms of the energy and using the classical radius of the electron[3] $r_e = (e^2/4\pi\epsilon_0)/(m_e c^2) \simeq 0.003$ pm:

$$\Delta E = \frac{\Delta p^2}{2 \, m} = \left(\frac{1}{4\pi\varepsilon_0}\right)^2 \frac{1}{m \, c^2} \frac{2 \, z_p^2 \, Z^2 \, e^4}{b^2 \, \beta^2} = \frac{(m_e \, c^2)^2}{m \, c^2} \frac{2 \, z_p^2 \, Z^2}{\beta^2} \left(\frac{r_e}{b}\right)^2 .$$

From this expression one can see that close collisions ($\Delta E \propto 1/b^2$) and low mass particles ($\Delta E \propto 1/m$) are the most important with respect to energy loss; thus one can neglect the effect of nuclei.

Photoluminescence. In some transparent media, part of the ionization energy loss goes into the emission of visible or near-visible light by the excitation of atoms and/or molecules. This phenomenon is called photoluminescence; often it results into a fast ($<100 \, \mu$s) excitation/deexcitation—in this last case we talk of fluorescence, or scintillation. Specialists often use definitions which distinguish between fluorescence and scintillation; this separation is, however, not universally accepted. We shall discuss later fluorescence in the context of the detection of large showers induced in the atmosphere by high-energy cosmic rays.

---

[3] The classical electron radius is the size the electron would need to have for its mass to be completely due to its electrostatic potential energy, under the assumption that charge has a uniform volume density and that the electron is a sphere.
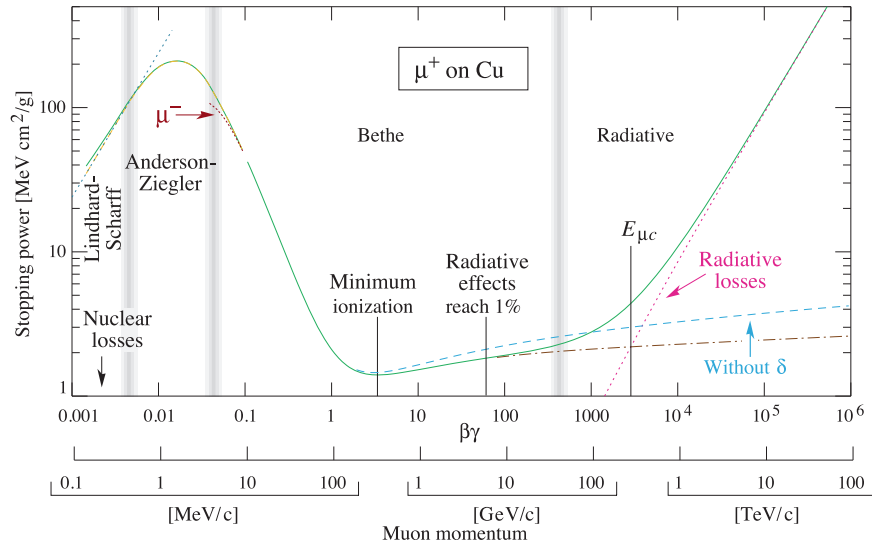
Fig. 4.3 The stopping power ($-dE/dx$) for positive muons in copper as a function of $\beta\gamma = p/Mc$ is shown over nine orders of magnitude in momentum (corresponding to 12 orders of magnitude in kinetic energy). From K.A. Olive et al. (Particle Data Group), Chin. Phys. C 38 (2014) 090001.

4.1.1.2 High-Energy Radiation Effects

According to classical electromagnetism, a charged particle undergoing acceleration radiates electromagnetic waves. The intensity of the emitted radiation from a dipole is proportional to the square of the acceleration.

Particles deflected by the electric field of the material traversed, thus, also emit photons. We speak in this case of bremsstrahlung, or braking radiation.

To first order, the emitted energy is (as in the classical case) proportional to the inverse of the square of the mass. On top of the ionization energy loss described by Eq. 4.1, above $\beta\gamma \sim 1000$ (which means an extremely high energy for a proton, $E \sim 1$ TeV, but just $E \sim 100$ GeV for a muon), such radiation effects become important (Fig. 4.3).

Bremsstrahlung is particularly relevant for electrons and positrons, particles for which the Bethe approximation starts to be inadequate even at lower energies. The average fractional energy loss by radiation for an electron of high energy ($E \gg m_e c^2$) is approximately independent of the energy itself, and can be described by

$$\frac{1}{E}\frac{dE}{dx} \simeq -\frac{1}{X_0} \tag{4.2}$$

where X_0 is called the radiation length, and is characteristic of the material—for example it is about 300 m for air at Normal Temperature and Pressure (NTP),[4] about 36 cm for water, about 0.5 cm for lead.

The radiation length has been tabulated for the different elements in Appendix B; a good approximation (for $Z > 4$) is

$$\frac{1}{X_0} = 4\left(\frac{\hbar}{m_e c}\right)^2 Z(Z+1)\alpha^3 n_a \ln\left(\frac{183}{Z^{1/3}}\right) , \tag{4.3}$$

where $\alpha = \frac{e^2}{4\pi}$ and n_a is the density of atoms per cubic centimeter in the medium, or more simply

$$\frac{1}{\rho}X_0 \simeq 180\frac{A}{Z^2}\text{cm} \ \left(\frac{\Delta X_0}{X_0} < \pm 20\,\% \text{ for } 12 < Z < 93\right) . \tag{4.4}$$

The total average energy loss by radiation increases rapidly (linearly in the approximation of Eq. 4.2) with energy, while the average energy loss by collision is practically constant. At high energies, radiation losses are thus much more important than collision losses (Fig. 4.4).

---

[4] NTP is commonly used as a standard condition; it is defined as air at $20\,^\circ$C (293.15 K) and 1 atm (101.325 kPa). Density is 1.204 kg/m^3. Standard Temperature and Pressure STP, another condition frequently used in physics, is defined by IUPAC (International Union of Pure and Applied Chemistry) as air at $0\,^\circ$C (273.15 K) and 100 kPa.
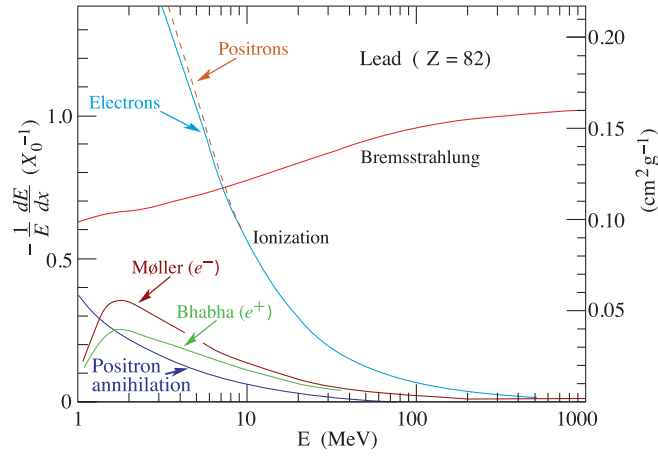
Fig. 4.4 Fractional energy loss per radiation length in lead as a function of the electron or positron energy. From K.A. Olive et al. (Particle Data Group), Chin. Phys. C 38 (2014) 090001.

The energy at which the radiation energy loss overtakes the collision energy loss (called the critical energy, E_c) decreases with increasing atomic number:

$$E_c \simeq \frac{550\,\text{MeV}}{Z}\ \left(\frac{\Delta E_c}{E_c} < \pm 10\,\% \text{ for } 12 < Z < 93\right). \tag{4.5}$$

The critical energy for air at NTP is about 84 MeV; for water it is about 74 MeV.

The photons radiated by bremsstrahlung are distributed at leading order in such a way that the energy loss per unit energy is constant, i.e.,

$$\frac{dN_\gamma}{dE_\gamma} \propto \frac{1}{E_\gamma}$$

between 0 and E. This results in a divergence for $E_\gamma \to 0$, which anyway does not contradict energy conservation: the integral of the energy released for each energy bin is constant.

The emitted photons are collimated: the typical angle of emission is $\sim m_e c^2 / E$.

4.1.1.3 Cherenkov Radiation

The Vavilov–Cherenkov[5] radiation (commonly called just Cherenkov radiation) occurs when a charged particle moves through a medium faster than the speed of light in that medium. The total energy loss due to this process is negligible; however, Cherenkov radiation is important related to the possibility of use in detectors.

The light is emitted in a coherent cone (Fig. 4.5) at an angle such that

$$\cos\theta_c = \frac{1}{n\beta} \tag{4.6}$$

from the direction of the emitting particle. The threshold velocity is thus $\beta = 1/n$, where n is the refractive index of the medium. The presence of a coherent wavefront can be easily derived by using the Huygens–Fresnel principle.

The number of photons produced per unit path length and per unit energy interval of the photons by a particle with charge $z_p e$ at the maximum (limiting) angle is

$$\frac{d^2N}{dEdx} \simeq \frac{\alpha z_p^2}{\hbar c}\sin^2\theta_c \simeq 370\sin^2\theta_c\,\text{eV}^{-1}\text{cm}^{-1} \tag{4.7}$$

or equivalently

---

[5] Pavel Cherenkov (1904–1990) was a Soviet physicist who shared the Nobel Prize in physics in 1958 with compatriots Ilya Frank (1908–1990) and Igor Tamm (1895–1971) for the discovery of Cherenkov radiation, made in 1934. The work was done under the supervision of Sergey Vavilov, who died before the recognition for the discovery by the Nobel committee.
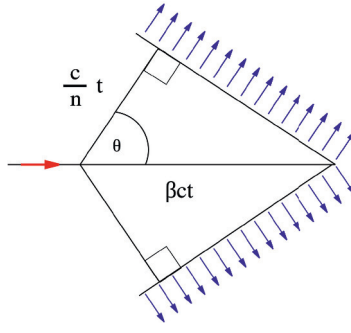
Fig. 4.5 The emission of Cherenkov radiation by a charged particle. User Harp, Creative Commons Attribution-Share Alike 2.5 Generic license via Wikimedia Commons.

$$\frac{d^2 N}{d\lambda dx} \simeq \frac{2\pi\alpha z_p^2}{\lambda^2} \sin^2\theta_c \tag{4.8}$$

(the index of refraction n is in general a function of photon energy E; Cherenkov radiation is relevant when $n > 1$ and the medium is transparent, and this happens close to the range of visible light).

The total energy radiated is small, some 10^{-4} times the energy lost by ionization. In the visible range (300–700 nm), the total number of emitted photons is about 40/m in air, about 500/cm in water. Due to the dependence on λ, it is important that Cherenkov detectors be sensitive close to the ultraviolet region.

Dense media can be transparent not only to visible light, but also to radio waves. The development of Cherenkov radiation in the radiowave region due to the interactions with electrons in the medium is often referred to as the Askar'yan effect. This effect has been experimentally confirmed for different media (namely sand, rock salt and ice) in accelerator experiments at SLAC; presently attempts are in progress to use this effect for in particle detectors.

4.1.1.4 Transition Radiation

X-ray transition radiation (XTR) occurs when a relativistic charged particle crosses from one medium to another with different dielectric permittivity.

The energy radiated when a particle with charge $z_p e$ and $\gamma \simeq 1000$ crosses the boundary between vacuum and a different transparent medium is typically concentrated in the soft X-ray range 2 keV–40 keV.

The process is closely related to Cherenkov radiation, and also in this case the total energy emitted is low (typically the expected number of photons per transition is smaller than unity; one thus needs several layers to build a detector).

4.1.2 Range

From the specific energy loss as a function of energy, we can calculate the fraction of energy lost as a function of the distance x traveled in the medium. This is known as the Bragg curve. For charged particles, most of the energy loss is due to ionization and occurs near the end of the path, where the particle speed is low. The Bragg curve has a pronounced peak close to the end of the path length, and then falls rapidly to zero. The range R for a particle of energy E is the average distance traveled before reaching the energy at which the particle is absorbed (Fig. 4.6):

$$R(E') = \int_E^{Mc^2} \frac{1}{dE/dx} dE\,.$$
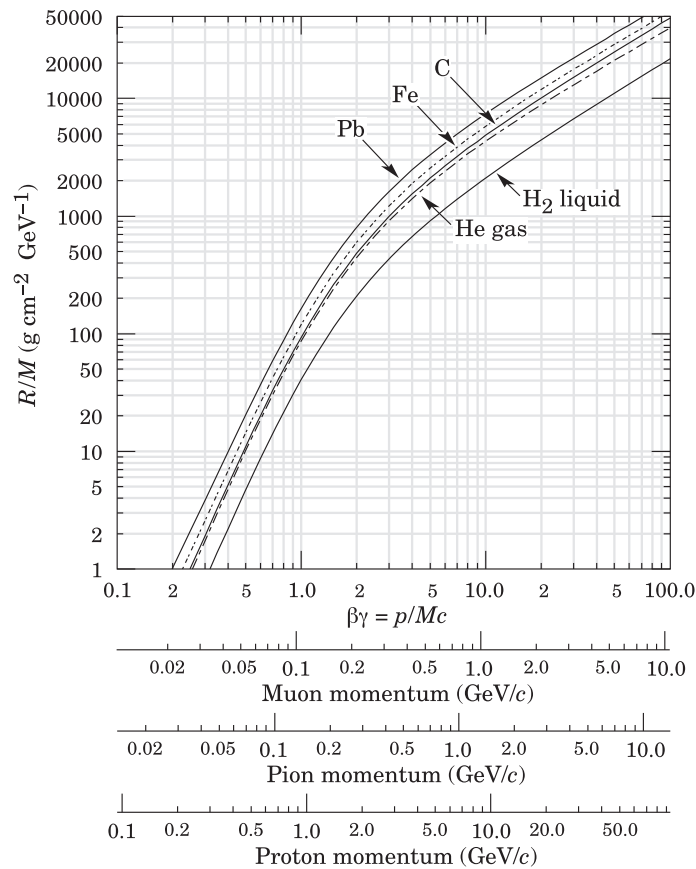
Fig. 4.6 Range per unit of density and of mass for heavy charged particles in liquid (bubble chamber) hydrogen, helium gas, carbon, iron, and lead. Example: a K^+ with momentum 700 MeV/c, $\beta\gamma \simeq 1.42$, and we read $R/M \simeq 396$, in lead, corresponding to a range of 195 g/cm^2. From K.A. Olive et al. (Particle Data Group), Chin. Phys. C 38 (2014) 090001.
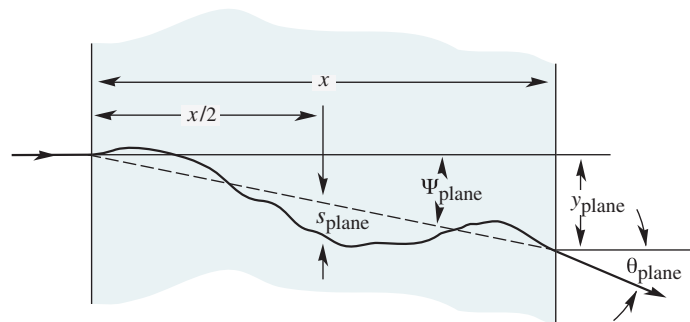
Fig. 4.7 Multiple Coulomb scattering. From K.A. Olive et al. (Particle Data Group), Chin. Phys. C 38 (2014) 090001.

4.1.3 Multiple Scattering

A charged particle passing near a nucleus undergoes deflection, with an energy loss that is in most cases negligible. This phenomenon is called elastic scattering and is caused by the interaction between the particle and the Coulomb field of the nucleus. The global effect is that the path of the particle becomes a random walk (Fig. 4.7), and information on the original direction is partly lost—this fact can create problems for the reconstruction of direction in tracking detectors. For very-high-energy hadrons, also hadronic cross section can contribute to the effect.

Summing up many relatively small random changes on the direction of flight of a particle of unit charge traversing a thin layer of material, the distribution of its projected scattering angle can be approximated by a Gaussian distribution of standard deviation projected on a plane (one has to multiply by $\sqrt{2}$ to determine the standard deviation in space):

$$\theta_0 \simeq \frac{13.6\,\text{MeV}}{\beta c p} z_p \sqrt{\frac{x}{X_0}} \left[1 + 0.038 \ln \frac{x}{X_0} \right] .$$

X_0 is the radiation length defined before. The above expression comes from the so-called Molière theory, and is accurate to some $10\,\%$ or better for $10^{-3} < x/X_0 < 100$. For an ultrarelativistic particle of absolute charge 1 it simplifies to

$$\theta_0 \simeq \frac{13.6\,\text{MeV}}{E} \sqrt{\frac{x}{X_0}} .$$

In some collisions however, deflections due to Rutherford scattering can be large and contribute to a sizable non-Gaussian tail.

4.1.4 Photon Interactions

High-energy photons mostly interact with matter via photoelectric effect, Compton scattering, and electron–positron pair production. Other processes, like Rayleigh scattering and photonuclear interactions, have in general much smaller cross sections.

4.1.4.1 Photoelectric Effect

The photoelectric effect is the ejection of an electron from a material that has just absorbed a photon. The ejected electron is called a *photoelectron.*

The photoelectric effect was pivotal in the development of quantum physics (for the explanation of this effect Albert Einstein was awarded the Nobel Prize). Due to photoelectric effect, a photon of angular frequency $\omega > V/e$ can eject from a metal an electron which pops up with a kinetic energy $\hbar\omega - V$, where V is the minimum gap of energy of electrons trapped in the metal (V is frequently called the *work function* of the metal).

No simple relationship between the attenuation of the incident electromagnetic wave and the photon energy E can be derived, since the process is characterized by the interaction with the (quantized) orbitals. The plot of the attenuation coefficient (the distance per unit density at which intensity is reduced by a factor $1/e$) as a function of the photon energy displays sharp peaks at the binding energies of the different orbital shells and depends strongly on the atomic number. Neglecting these effects, a reasonable approximation for the cross section σ is

$$\sigma \propto \frac{Z^\nu}{E^3} ,$$

with the exponent ν varying between 4 and 5 depending on the energy. The cross section rapidly decreases with energy above the typical electron binding energies (Fig. 4.8).

The photoelectric effect can be used for detecting photons below the MeV; a photosensor (see later) sensitive to such energies can "read" the signal generated by a photoelectron, possibly amplified by an avalanche process.

4.1.4.2 Compton Scattering

Compton scattering is the collision between a photon and an electron. Let E be the energy of the primary photon (corresponding to a wavelength λ) and suppose that the electron is initially free and at rest. After the collision, the photon is scattered at an angle θ and comes out with a reduced energy E', corresponding to a wavelength λ'; the electron acquires an energy $E - E'$. The conservation laws of energy and momentum yield the following relation (Compton formula):

$$\lambda' - \lambda = \lambda_C (1 - \cos\theta) \longrightarrow E' = \frac{E}{1 + \frac{E}{m_e c^2}(1 - \cos\theta)}$$

where θ is the scattering angle of the emitted photon; $\lambda_C = h/m_e c \simeq 2.4$ pm is the Compton wavelength of the electron.
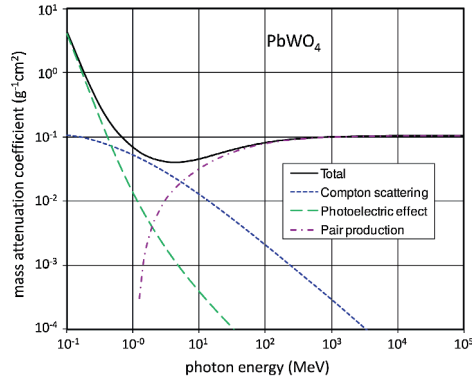
Fig. 4.8 Photon mass attenuation coefficient (cross section per gram of material) as a function of energy in lead tungstate (data from the NIST XCOM database.)

It should be noted that, in the case when the target electron is not at rest, the energy of the scattered photon can be larger than the energy of the incoming one. This regime is called *inverse Compton,* and it has great importance in the emission of high-energy photons by astrophysical sources: in practice, thanks to inverse Compton, photons can be "accelerated."

The differential cross section for Compton scattering was calculated by Klein and Nishina around 1930. If the photon energy is much below $m_e c^2$ (so the scattered electrons are non-relativistic) then the total cross section is given by the Thomson cross section. This is known as the Thomson limit. The cross section for $E \ll m_e c^2$ (Thomson regime) is about

$$\sigma_T \simeq \frac{8\pi\alpha^2}{3m_e^2} = \frac{8\pi r_e^2}{3} \,, \tag{4.9}$$

where $r_e = (e^2/4\pi\epsilon_0)/(m_e c^2) \simeq 0.003$ pm is the classical radius of the electron. If the photon energy is $E \gg m_e c^2$, we are in the so-called Klein-Nishina regime and the total cross section falls off rapidly with increasing energy (Fig. 4.8):

$$\sigma_{KN} \simeq \frac{3\sigma_T}{8} \frac{\ln 2E}{E} \,. \tag{4.10}$$

As in the case of the photoelectric effect, the ejected electron can be detected (possibly after multiplication) by an appropriate sensor.

4.1.4.3 Pair Production

Pair production is the most important interaction process for a photon above an energy of a few tens of MeV. In the electric field in the neighborhood of a nucleus, a high-energy photon has a non-negligible probability of transforming itself into a negative and a positive electron—the process being kinematically forbidden unless an external field, regardless of how little, is present.

Energy conservation yields the following relation between the energy E of the primary photon and the total energies U and U' of the electrons:

$$E = U + U'.$$

With reasonable approximation, for 1 TeV$> E >$ 100 MeV the fraction of energy $u = U/E$ taken by the secondary electron/positron is uniformly distributed between 0 and 1 (becoming peaked at the extremes as the energy increases to values above 1 PeV).

The cross section grows quickly from the kinematic threshold of about 1 MeV to its asymptotic value reached at some 100 MeV:

$$\sigma \simeq \frac{7}{9} \frac{1}{n_a X_0} \,,$$

where n_a is the density of atomic nuclei per unit volume, in such a way that the interaction length is

$$\lambda \simeq \frac{9}{7} X_0 \,.$$

The angle of emission for the particles in the pair is typically ~ 0.8 MeV$/E$.

4.1.4.4 Rayleigh Scattering and Photonuclear Interactions

Rayleigh scattering (the dispersion of electromagnetic radiation by particles with radii $\lesssim 1/10$ the wavelength of the radiation) is usually of minor importance for the conditions of high-energy particle and astroparticle physics, but it can be important for light in the atmosphere, and thus for the design of instruments detecting visible light. The photonuclear effect, i.e., the excitation of nuclei by photons, is mostly restricted to the region around 10 MeV, and it may amount to as much as 10 percent of the total cross section due to electrodynamic effects.

4.1.4.5 Comparison Between Different Processes for Photons

The total Compton scattering probability decreases rapidly when the photon energy increases. Conversely, the total pair production probability is a slowly increasing function of energy. At large energies, most photons are thus absorbed by pair production, while photon absorption by the Compton effect dominates at low energies (being the photoelectric effect characteristic of even smaller energies). The absorption of photons by pair production, Compton, and photoelectric effect is compared in Fig. 4.8.

As a matter of fact, above about 30 MeV the dominant process is pair production, and the interaction length of a photon is, to an extremely good approximation, equal to $9X_0/7$.

At extremely high matter densities and/or at extremely high energies (typically above 10^{16}–10^{18} eV, depending on the medium composition and density) collisions cannot be treated independently, and the result of the collective quantum mechanical treatment is a reduction of the cross section. The result is the so-called Landau-Pomeranchuk-Migdal effect, or simply LPM effect, which entails a reduction of the pair production cross section, as well as of bremsstrahlung.

4.1.5 Nuclear (Hadronic) Interactions

The nuclear force is felt by hadrons, charged and neutral; at high energies (above a few GeV) the inelastic cross section for hadrons is dominated by nuclear interaction.

High-energy nuclear interactions are difficult to model. A useful approximation is to describe them by an inelastic interaction length λ_H. Values for $\rho\lambda_H$ are typically of the order of $100\,\mathrm{g/cm^2}$; a listing for some common materials is provided in Appendix B—where the inelastic length λ_I and the total length λ_T are separately listed, and the rule for the composition is $1/\lambda_T = 1/\lambda_H + 1/\lambda_I$.

The final state products of inelastic high-energy hadronic collisions are mostly pions, since these are the lightest hadrons. The rate of positive, negative, and neutral pions is more or less equal—as we shall see, this fact is due to an approximate symmetry of hadronic interactions, called the *strong isospin* symmetry.

4.1.6 Interaction of Neutrinos

The case of neutrinos is a special one. Neutrinos have a very low interaction cross section. High-energy neutrinos mainly interact with nucleons, being the neutrino-lepton cross section smaller – with the exception of the peak corresponding to the production of the $W^\pm$ boson in neutrino-lepton interactions at $E_\nu \sim 10^{16}$ eV.

The neutrino-nucleon cross section grows with energy. It can be parameterized for intermediate energies, $1\,\mathrm{MeV} \lesssim E \lesssim 10\,\mathrm{TeV}$ (Fig. 4.9) as

$$\sigma_{\nu N} \simeq (0.67 \times 10^{-38} E)\,\mathrm{cm^2} = (6.7\,E)\,\mathrm{fb}\,, \tag{4.11}$$

E being the neutrino energy in GeV. At energies between 10 TeV and 10^7 TeV (10^{19} eV), a parametrization is
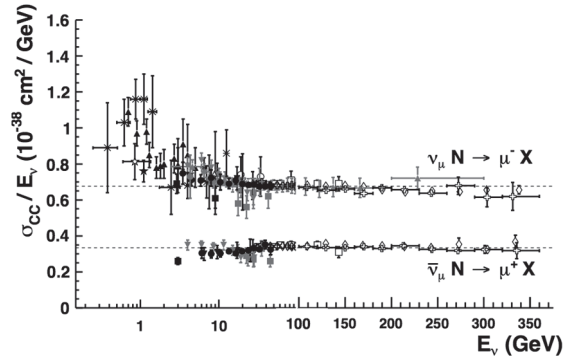
Fig. 4.9 Measurements of muon neutrino and antineutrino inclusive scattering cross sections divided by neutrino energy as a function of neutrino energy; different symbols represent experimental measurements by different experiments. Note the transition between logarithmic and linear scales at 100 GeV. From K.A. Olive et al. (Particle Data Group), Chin. Phys. C 38 (2014) 090001.

$$\sigma_{\nu N} \simeq \left(0.67 \times 10^{-34} \sqrt{\frac{E}{10\,\mathrm{TeV}}} \right) \mathrm{cm}^2 \,. \tag{4.12}$$

Solar neutrinos, which have MeV energies, typically cross the Earth undisturbed (see a more complete discussion in Chap. 9).

The low value of the interaction cross section makes the detection of neutrinos very difficult.

4.1.7 Electromagnetic Showers

High-energy electrons lose most of their energy by radiation. Thus, in their interaction with matter, most of the energy is spent in the production of high-energy photons and only a small fraction is dissipated. The secondary photons, in turn, undergo pair production (or, at lower energies, Compton scattering); secondary electrons and positrons can in turn radiate. This phenomenon continues generating cascades (showers) of electromagnetic particles; at each step the number of particles increases while the average energy decreases, until the energy falls below the critical energy.

Given the characteristics of the interactions of electrons/positrons and of photons with matter, it is natural to describe the process of electromagnetic cascades in terms of the scaled distance

$$t = \frac{x}{X_0}$$

(where X_0 is the radiation length), and of the scaled energy

$$\epsilon = \frac{E}{E_c}$$

(where E_c is the critical energy); the radiation length and the critical energy have been defined in Sect. 4.1.1.2. Since the opening angles for bremsstrahlung and pair production are small, the process can be in first approximation (above the critical energy) considered as one-dimensional (the lateral spread will be discussed at the end of this section).

A simple approximation (a "toy model"), proposed by Heitler in the late 1930s, assumes that

- the incoming charged particle has an initial energy E_0 much larger than the critical energy E_c;
- each electron travels one radiation length and then gives half of its energy to a bremsstrahlung photon;
- each photon travels one radiation length and then creates an electron–positron pair; the electron and the positron each carry half of the energy of the original photon.

In the above model, asymptotic formulas for radiation and pair production are assumed to be valid; the Compton effect and the collision processes are neglected. The branching stops abruptly when $E = E_c$, and then electrons and positrons lose their energy by ionization.
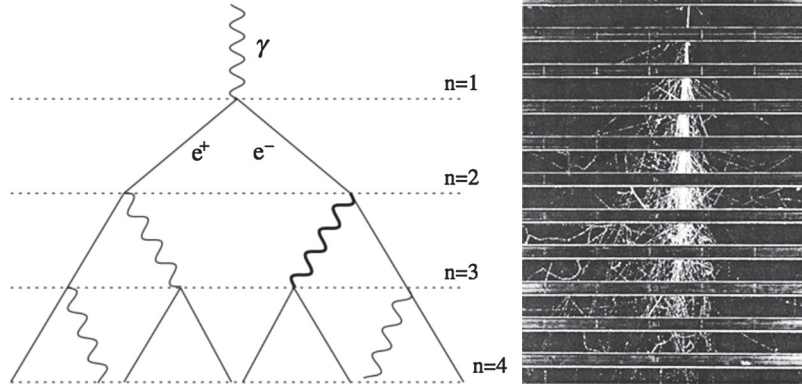
Fig. 4.10 Left: Scheme of the Heitler approximation for the development of an electromagnetic shower. From J. Matthews, Astropart. Phys. 22 (2005) 387. Right: Image of an electromagnetic shower developing through a number of brass plates 1.25 cm thick placed across a cloud chamber (from B. Rossi, "Cosmic rays", McGraw-Hill 1964.)

This simple branching model is schematically shown in Fig. 4.10, left. It implies that after t radiation lengths the shower will contain 2^t particles and there will be roughly the same number of electrons, positrons, and photons, each with an average energy

$$E(t) = E_0/2^t .$$

The cascading process will stop when $E(t) = E_c$, at a thickness of absorber $t_{\max}$, that can be written in terms of the initial and critical energies as

$$t_{\max} = \log_2(E_0/E_c) ,$$

with the number of particles at this point given by

$$N_{\max} = \frac{E_0}{E_c} \equiv y .$$

The model suggests that the shower depth at its maximum varies as the logarithm of the primary energy. This emerges also from more sophisticated shower models and is observed experimentally. A real image of an electromagnetic shower in a cloud chamber is shown in Fig. 4.10, right.

An improved model was formulated by Rossi in the beginning of the 1940s. Rossi (see for example reference [F4.1]) computed analytically the development of a shower in the so-called "approximation B," in which: electrons lose energy by ionization and bremsstrahlung (described by asymptotical formulae); photons undergo pair production, also described by asymptotical formulae. All the process is one-dimensional. The results of the "Rossi approximation B" are summarized in Table 4.1. Under this approximation, the number of particles grows exponentially in the beginning up to the maximum, and then decreases as shown in Figs. 4.11 and 4.12.

A common parameterization of the longitudinal profile for a shower of initial energy E_0 is

$$\frac{dE}{dt} = E_0 \frac{\beta}{\Gamma(\alpha)} (\beta t)^{\alpha - 1} e^{-\beta t} , \tag{4.13}$$

where Γ is Euler's Gamma function $\Gamma(z) = \int_0^{+\infty} t^{z-1} e^{-t} dt$. In the above approximation, $t_{\max} = (\alpha - 1)/\beta$, which should be thus equal to $\ln(E_0/E_c) - C$ with $C = 1$ for an electron and $C = 0.5$ for a photon.

Table 4.1 Shower parameters for a particle on energy E_0 according to Rossi's approximation B ($y = E_0/E_c$).

	Incident electron	Incident photon
Peak of shower $t_{\max}$	$1.0 \times (\ln y - 1)$	$1.0 \times (\ln y - 0.5)$
Center of gravity t_{med}	$t_{\max} + 1.4$	$t_{\max} + 1.7$
Number of e^+ and e^- at peak	$0.3y/\sqrt{\ln y - 0.37}$	$0.3y/\sqrt{\ln y - 0.31}$
Total track length	y	y
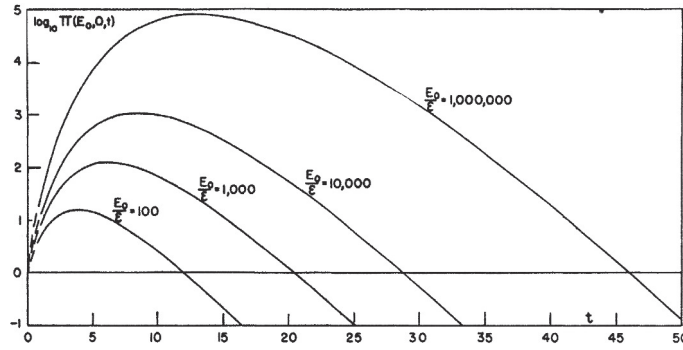
Fig. 4.11 Logarithm of the number of electrons for electron-initiated showers, calculated under Rossi approximation B, as a function of the number of radiation lengths traversed. Multiplication by E_c/I (E_c is called ε in the Figure) yields the specific ionization energy loss [F4.1].
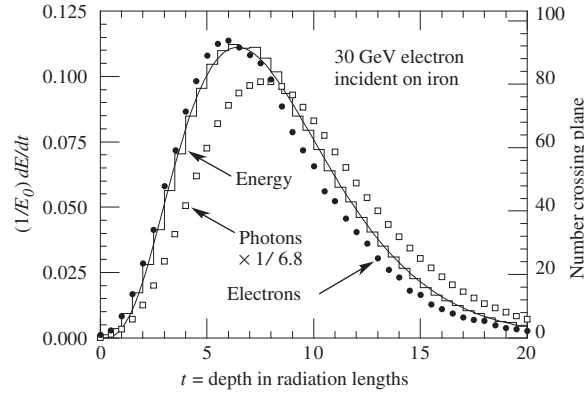
Fig. 4.12 A Monte Carlo simulation of a 30 GeV electron-induced cascade in iron. The histogram shows the fractional energy deposition per radiation length, and the curve is a fit to the distribution using Eq. 4.13. The circles indicate the number of electrons with total energy greater than 1.5 MeV crossing planes at $X_0/2$ intervals (scale on the right) and the squares the number of photons above the same energy crossing the planes (scaled down to have the same area as the electron distribution). From K.A. Olive et al. (Particle Data Group), Chin. Phys. C 38 (2014) 090001.

Fluctuations on the total track length are dominated by the fluctuations on the total number of particles, and thus they grow as $\sqrt{E_0}$. An incomplete longitudinal containment of the shower badly increases fluctuations on the deposited energy. A rule of thumb for the longitudinal containment of 95 % of the shower is

$$T(95\,\%) = (t_{\max} + 0.08Z + 9.6)\,,$$

expressed in radiation lengths.

Despite the elegance of Rossi's calculations, one can do better using computers, and most calculations are performed nowadays by Monte Carlo methods.[6] Monte Carlo calculations of electromagnetic cascades have the advantages of using accurate cross sections for bremsstrahlung and pair production, the correct energy dependence of ionization loss, and including all electromagnetic interactions. Monte Carlo calculations, in addition, give correct account for the fluctuations in the shower development, as well as for the angular and lateral distribution of the shower particles. Rossi's approximation B, however, is faster and represents a rather accurate model.

The description of the transverse development of a shower is more complicated. Usually the normalized lateral density distribution of electrons is approximated by the Nishimura-Kamata-Greisen (NKG) function, which depends on the "shower age" s, being 0 at the first interaction, 1 at the maximum and 3 at the death [F4.1]:

$$s = \frac{3t}{t + 2t_{\max}}\,. \tag{4.14}$$

The NKG function:

---

[6] Monte Carlo methods are computational algorithms based on repeated random sampling. The name is due to its resemblance to the act of playing in a gambling casino.
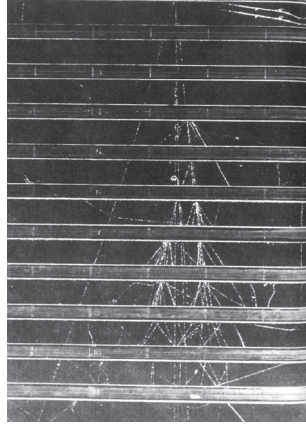
Fig. 4.13 Image of a hadronic shower developing through a number of brass plates 1.25 cm thick placed across a cloud chamber (from B. Rossi, "Cosmic rays," McGraw-Hill 1964). To be compared to Fig. 4.10, right.

$$\rho_{\mathrm{NKG}}(r, s, N_e) = \frac{N_e}{R_M^2} \frac{\Gamma(4.5 - s)}{2\pi \Gamma(s)\Gamma(4.5 - 2s)} \left(\frac{r}{R_M}\right)^{s-2} \left(1 + \frac{r}{R_M}\right)^{s-4.5} \tag{4.15}$$

where N_e is the electron shower size, r is the distance from the shower axis, and R_M is a transverse scale called the Molière radius described below, is accurate for a shower age $0.5 < s < 1.5$. A variety of transverse distribution functions can be found in the literature (Greisen, Greisen–Linsley, etc.) and are mostly specific modifications of the NKG function.

In a crude approximation, one can assume the transverse dimension of the shower to be dictated by the Molière radius:

$$R_M \simeq \frac{21\,\mathrm{MeV}}{E_c} X_0\,.$$

About 90 % of the shower energy is deposited in a cylinder of radius R_M; about 95 % is contained in a radius of $2R_M$, and about 99 % in a radius of $3R_M$. In air at NTP, $R_M \simeq 80\,\mathrm{m}$; in water $R_M \simeq 9\,\mathrm{cm}$.

4.1.8 Hadronic Showers

The concept of hadronic showers is similar to the concept of electromagnetic showers: primary hadrons can undergo a sequence of interactions and decays creating a cascade. However, on top of electromagnetic interactions one has now nuclear reactions. In addition, in hadronic collisions with the nuclei of the material, a significant part of the primary energy is consumed in the nuclear processes (excitation, emission of low-energy nucleons, etc.). One thus needs ad-hoc Monte Carlo corrections to account for the energy lost, and fluctuations are larger. The development of appropriate Monte Carlo codes for hadronic interactions has been a problem in itself, and still the calculation requires huge computational "loads." At the end of a hadronic cascade, most of the particles are pions, and one-third of the pions are neutral and decay almost instantaneously ($\tau \sim 10^{-16}$ s) into a pair of photons; thus on average one-third of the hadronic cascade is indeed electromagnetic (but it can be more or less, subject to fluctuations). As an example, the image of a hadronic shower in a cloud chamber is shown in Fig. 4.13.

To a first approximation, the development of the shower can be described by the inelastic hadronic interaction length λ_H; however, the approximation is less accurate than the one we did when we assumed electromagnetic reactions to scale with the radiation length X_0, and intrinsic fluctuations are larger.
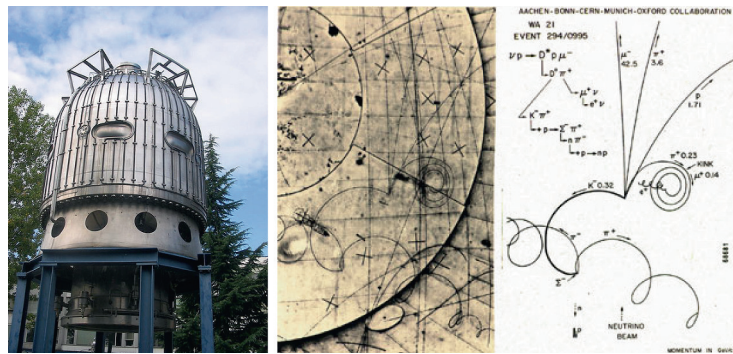
Fig. 4.14 Left: The BEBC bubble chamber. Center: A picture taken in BEBC, and right: its interpretation. Credits: CERN.

4.2 Particle Detectors

The aim of a particle detector is to measure the momenta and to identify the particles that pass through it after being produced in a collision or a decay; this is called an "event." The position in space where the event occurs is known as the interaction point.

In order to identify every particle produced by the collision, and plot the paths they have taken—i.e., to "completely reconstruct the event"—it is necessary to know the masses and momenta of the particles themselves. The mass can be computed by measuring the momentum and either the velocity or the energy.

The characteristics of the different instruments that allow these measurements are presented in what follows.

4.2.1 Track Detectors

A tracking detector reveals the path taken by a charged particle by measurements of sampled points (hits). Momentum measurements can be made by measuring the curvature of the track in a magnetic field, which causes the particle to curve into a spiral orbit with a radius proportional to the momentum of the particle. This requires the determination of the best fit to a helix of the hits (particle fit). For a particle of unit charge

$$p \simeq 0.3 B_\perp R\,,$$

where $B_\perp$ is the component of the magnetic field perpendicular to the particle velocity, expressed in tesla (which is the order of magnitude of typical fields in detectors), the momentum p is expressed in GeV/c, and R is the radius of curvature (Larmor radius) of the helix in meters.

A source of uncertainty for this determination is given by the errors in the measurement of the hits; another (intrinsic) noise is given by multiple scattering. In what follows we shall review some detectors used to determine the trajectory of charged tracks.

4.2.1.1 Cloud Chamber and Bubble Chamber

The cloud chamber was invented by C.T.R. Wilson in the beginning of the 20th century, and was used as a detector for reconstructing the trajectories of charged cosmic rays. The instrument, already discussed in the previous chapter, is a container with a glass window, filled with air and saturated water vapor (Fig. 3.8); the volume can be suddenly expanded, and the adiabatic expansion causes the temperature to decrease, bringing the vapor to a supersaturated (metastable) state. A charged particle crossing the chamber produces ions, which act as seeds for the generation of droplets along the trajectory. One can record the trajectory by taking a photographic picture. If the chamber is immersed in a magnetic field B, momentum and charge can be measured by the curvature.

The working principle of bubble chambers (Fig. 4.14) is similar to that of the cloud chamber, but here the fluid is a liquid. Along the trajectory of the particle, a trail of gas bubbles evaporates around the ions.
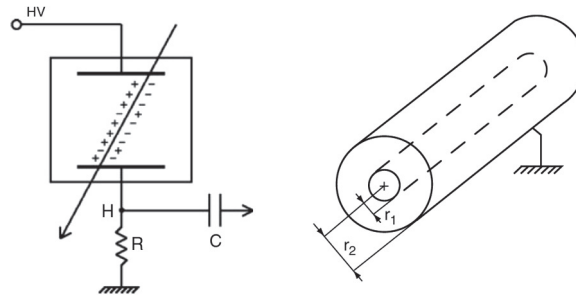
Fig. 4.15 Left: Operational scheme of a ionization chamber. Right: A chamber made in a "tube" shape, using coaxial cylindrical electrodes. From Braibant, Giacomelli and Spurio, "Particles and fundamental interactions," Springer 2014.

Due to the higher density of liquids compared with gases, the interaction probability is larger for bubble chambers than for gas chambers, and bubble chambers act at the same time both as an effective target and as a detector. Different liquids can be used, depending on the type of experiment: hydrogen to have protons as a target nucleus, deuterium to study interactions on neutrons, etc. From 1950 to the mid 1980s, before the advent of electronic detectors, bubble chambers were the reference tracking detectors. Very large chambers were built (the Big European Bubble Chamber BEBC now displayed at the entrance of the CERN exhibition is a cylinder with an active volume of 35 cubic meters), and wonderful pictures were recorded.

Bubble and cloud chambers provide a complete information: the measurement of the bubble density (their number per unit length) provides an estimate of the specific ionization energy loss dE/dx, hence $\beta\gamma = p/Mc$; the range, i.e., the total track length before the particle eventually stops (if the stopping point is recorded), provides an estimate for the initial energy; the multiple scattering (see below) provides an estimate for the momentum.

A weak point of cloud and bubble chambers is their dead time: after an expansion, the fluid must be recompressed. This might take a time ranging from about 50 ms for small chambers (LEBC, the LExan Bubble Chamber, used in the beginning of the 1980s for the study of the production and decay of particles containing the quark charm, had an active volume of less than a liter) to several seconds. Due to this limitation and to the labor-consuming visual scanning of the photographs, bubble chambers were abandoned in the mid 1980s—cloud chambers had been abandoned much earlier.

4.2.1.2 Nuclear Emulsions

A nuclear emulsion is a photographic plate with a thick emulsion layer and very uniform grain size. Like bubble chambers and cloud chambers they record the tracks of charged particles passing through, by changing the chemical status of grains that have absorbed photons (which makes them visible after photographic processing). They are compact, have high density, but have the disadvantages that the plates must be developed before the tracks can be observed, and they must be visually examined.

Nuclear emulsion have very good space resolution of the order of about 1 μm. They had great importance in the beginning of cosmic-ray physics, and they are still used in neutrino experiments (where interactions are rare) due to the lower cost per unit of volume compared to semiconductor detectors and to the fact that they are unsurpassed for what concerns to the single-point space resolution. They recently had a revival with the OPERA experiment at the LNGS underground laboratory in Gran Sasso, Italy, detecting the interactions of a beam of muon neutrinos sent from the CERN SPS in Geneva, 730 km away.

4.2.1.3 Ionization Counter, Proportional Counter and Geiger-Müller Counter

These three kinds of detectors have the same principle of operation: they consist of a tube filled with a gas, with a charged metal wire inside (Fig. 4.15). When a charged particle enters the detector, it ionizes the gas, and the ions and the electrons can be collected by the wire and by the walls (the mobility of electrons being larger than the mobility of ions, it is convenient that the wire's potential is positive). The electrical signal of the wire can be amplified and read by means of an amperometer. The voltage V of the wire must be larger than a threshold below which ions and electrons spontaneously recombine.

Depending on the voltage V of the wire, one can have three different regimes (Fig. 4.16):
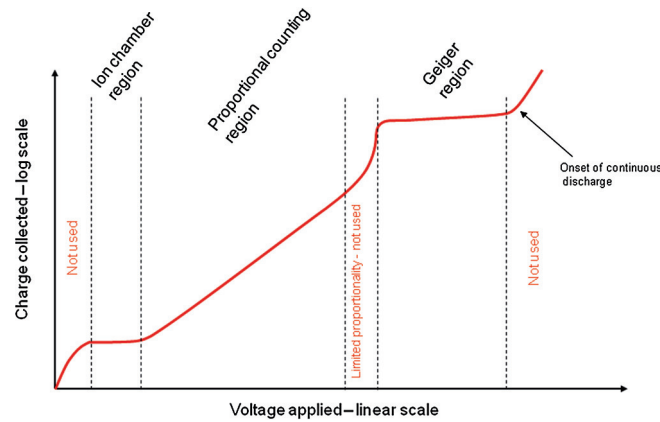
Fig. 4.16 Practical gaseous ionization detector regions: variation of the ion charge with applied voltage in a counter, for a constant incident radiation. By Doug Sim (own work) [CC BY-SA 3.0 http://creativecommons.org/licenses/by-sa/3.0], via Wikimedia Commons.
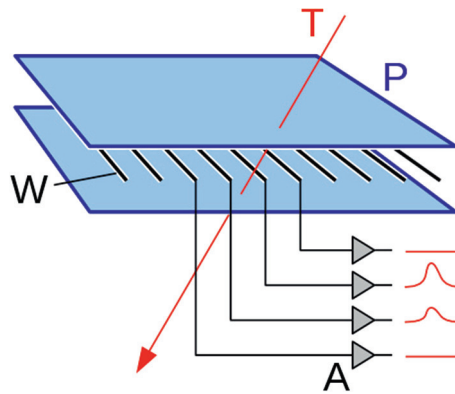
Fig. 4.17 Scheme of a multiwire chamber. By Michael Schmid (own work) [GFDL http://www.gnu.org/copyleft/fdl.html], via Wikimedia Commons.

- The ionization chamber regime when $V < I/e$ (I is the ionization energy of the gas, and e the electron charge). The primary ions produced by the track are collected by the wire, and the signal is then proportional to the energy released by the particle.
- The proportional counter regime when $V > I/e$, but V is smaller than a breakdown potential V_{GM} (see below). The ions and the electrons are then accelerated at an energy such that they can ionize the gas. The signal is thus amplified and it generates an avalanche of electrons around the anode. The signal is then proportional to the wire tension.
- Above a potential V_{GM}, the gas is completely ionized; the signal is then a short pulse of height independent of the energy of the particle (Geiger-Müller regime). Geiger-Müller tubes are also appropriate for detecting gamma radiation, since a photoelectron can generate an avalanche.

4.2.1.4 Wire Chamber

The multiwire chamber[7] is basically a sequence of proportional counters. Tubes are replaced by two parallel cathodic planes; the typical distance between the planes is 1–2 cm and the typical distance between the anodic wires is 1 mm (Fig. 4.17). A charged particle deposits the ionization charge on the closest wire, inducing an electric current; by a sequence of two parallel detectors with the wires aligned perpendicularly one can determine the position of a particle. The typical response time is of the order of 30 ns.

---

[7] Jerzy ("Georges") Charpak (1924–2010) was awarded the Nobel Prize in Physics in 1992 "for his invention and development of particle detectors, in particular the multiwire proportional chamber." Charpak was a Polish born, French physicist. Coming from a Jewish family, he was deported to the Nazi concentration camp in Dachau. After the liberation he studied in Paris and, from 1959, worked at CERN, Geneva.

Fig. 4.18 The flash chamber built by the Laboratório de Instrumentação e Partículas (LIP) in Lisbon for didactical purposes records a shower of cosmic rays.

4.2.1.5 Streamer Chamber and Flash Chamber

These are typically multianode (can be multiwire) chambers operating in the Geiger-Müller regime. Short electric pulses of the order of $10\,kV/cm$ are sent between subsequent planes; when a particle passes in the chamber, it can generate a series of discharges which can be visible—a sequence of flashes along the trajectory, Fig. 4.18.

4.2.1.6 Drift Chamber

The drift chamber is a multiwire chamber in which spatial resolution is achieved by measuring the time electrons need to reach the anode wire. This results in wider wire spacing with respect to what can be used in multiwire proportional chambers. Fewer channels have to be equipped with electronics in order to obtain a comparable overall space resolution; in addition, drift chambers are often coupled to high-precision space measurement devices like silicon detectors (see below).

Drift chambers use longer drift distances than multiwire chambers, hence their response can be slower. Since the drift distance can be long and drift velocity needs to be well known, the shape and constancy of the electric field need to be carefully adjusted and controlled. To do this, besides the anode wires (also called "signal" or "sense" wires), thick field-shaping cathode wires called "field wires" are often used.

An extreme case is the time projection chamber (TPC), for which drift lengths can be very large (up to $2\,m$), and sense wires are arranged at one end; signals in pads or strips near the signal wire plane are used to obtain three-dimensional information.

4.2.1.7 Semiconductor Detectors

Silicon detectors are solid-state particle detectors, whose principle of operation is similar to that of a ionization chamber: the passage of ionizing particles produces in them a number of electron–hole pairs proportional to the energy released. The detector is like a diode (p-n junction) with reverse polarization, the active area being the depleted region. The electron–hole pairs are collected thanks to the electric field, and generate an electrical signal.

The main feature of silicon detectors is the small energy required to create a electron–hole pair—about $3.6\,eV$, compared with about $30\,eV$ necessary to ionize an atom in an Ar gas ionization chamber.

Furthermore, compared to gaseous detectors, they are characterized by a high density and a high stopping power, much greater than that of the gaseous detectors: they can thus be very thin, typically about $300\,\mu m$.

An arrangement of silicon detectors is the so-called microstrip arrangement. A microstrip is a conducting strip separated from a ground plane by a dielectric layer known as the substrate. The general pattern of a
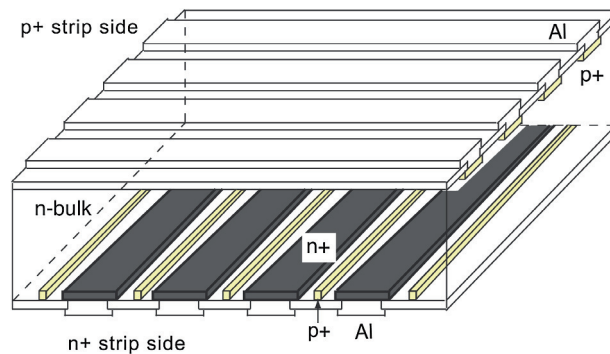
Fig. 4.19 Scheme of a silicon microstrip detector, arranged in a double-side geometry (strips are perpendicular). Source: http://spie.org/x20060.xml.
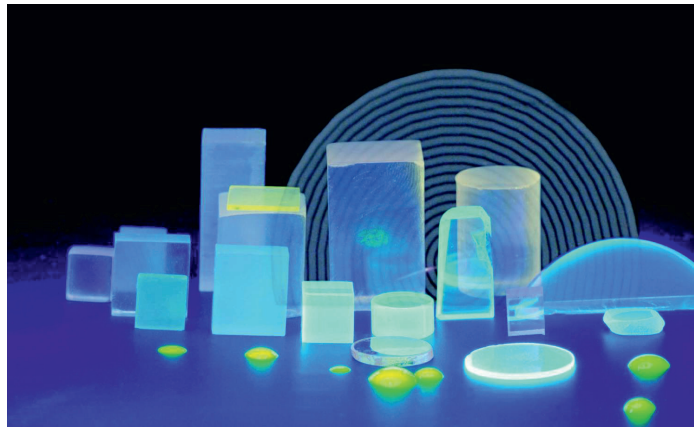
Fig. 4.20 A scintillator. From http://www.tnw.tudelft.nl/fileadmin/Faculteit/TNW.

silicon microstrip detector is shown in Fig. 4.19. The distance between two adjacent strips, called the pitch, can be of the order of 100 μm, as the width of each strip.

From the signal collected on the strip one can tell if a particle has passed through the detector. The accuracy can be smaller than the size and the pitch: the charge sharing between adjacent strips improves the resolution to some 10 μm. As in the case of multiwire chambers, the usual geometry involves adjacent parallel planes of mutually perpendicular strips.

A recent implementation of semiconductor detectors is the silicon pixel detector. Wafers of silicon are segmented into little squares (pixels) that are as small as 100 μm on a side. Electronics is more expensive (however with modern technology it can be bonded to the sensors themselves); the advantage is that one can measure directly the hits without ambiguities.

4.2.1.8 Scintillators

Scintillators are among the oldest particle detectors. They are slabs of transparent material, organic or inorganic; the ionization induces fluorescence, and light is conveyed towards a photosensor (photosensors will be described later). The light yield is large – can be as large as 10^4 photons per MeV of energy deposited – and the time of formation of the signal is very fast, typically less than 1 ns: they are appropriate for trigger[8] systems.

To make the light travel efficiently towards the photosensor (photomultiplier), light guides are frequently used (Fig. 4.20). Sometimes the fluorescence is dominated by low wavelengths; in this case it is appropriate to match the photosensor optical efficiency with a *wavelength shifter* (a material inducing absorption of light and re-emission in an appropriate wavelength).

---

[8] A trigger is an electronic system that uses simple criteria to rapidly decide which events in a particle detector to keep in cases where only a small fraction of the total number of events can be recorded.

The scintillators can be used as tracking devices, in the so-called "hodoscope" configuration (from the Greek "hodos" for path, and "skope" for observation) as in the case of silicon strips. Hodoscopes are characterized by being made up of many detecting planes, made in turn by segments; the combination of which segments record a detection is then used to reconstruct the particle trajectory. Detecting planes can be arranged in pairs of layers. The strips of the two layers should be arranged in perpendicular directions (let us call them horizontal and vertical). A particle passing through hits a strip in each layer; the vertical scintillator strip reveals the horizontal position of the particle, and the horizontal strip indicates its vertical position (as in the case of two wire chambers with perpendicular orientation of the wires, but with poorer resolution). Scintillator hodoscopes are among the cheapest detectors for tracking charged particles.

Among scintillators, some are polymeric (plastic); plastic scintillators are particularly important due to their good performance at low price, to their high light output and relatively quick (few ns) signal, and in particular to their ability to be shaped into almost any desired form.

4.2.1.9 Resistive-Plate Chambers

The resistive-plate chamber (RPC) is a lower-cost alternative to large scintillator planes. A RPC is usually constructed from two parallel high-resistivity glass or melaminic plates with a gap of a few millimeters between them, which is filled with gas at atmospheric pressure. A high potential (of the order of $10\,\mathrm{kV}$) is maintained between the plates.

A charged particle passing through the chamber initiates an electric discharge, whose size and duration are limited by the fact that the current brings the local potential below the minimum required to maintain it. The signal induced is read by metallic strips on both sides of the detector and outside the gas chamber, which are separated from the high voltage coatings by thin insulating sheets.

RPC detectors combine high efficiency (larger than 95 %) with excellent time resolution (about 1 ns), and they are therefore a good choice for trigger systems.

4.2.1.10 Comparison of the Performance of Tracking Detectors

The main characteristics of tracking detectors are summarized in Table 4.2.

4.2.2 Photosensors

Most detectors in particle physics and astrophysics rely on the detection of photons near the visible range, i.e., in the eV energy range. This range covers scintillation and Cherenkov radiation as well as the light detected in many astronomical observations.

Essentially, one needs to extract a measurable signal from a (usually very small) number of incident photons. This goal can be achieved by generating a primary photoelectron or electron–hole pair by an incident photon (typically by photoelectric effect), amplifying the signal to a detectable level (usually by a sequence of avalanche processes), and collecting the secondary charges to form the electrical signal.

The important characteristics of a photodetector include:

- the quantum efficiency QE, namely the probability that a primary photon generates a photoelectron;

Table 4.2 Typical characteristics of different kinds of tracking detectors. Data come from K.A. Olive et al. (Particle Data Group), Chin. Phys. C 38 (2014) 090001.

Detector type	Spatial resolution	Time resolution	Dead time
RPC	≤10mm	∼1ns (down to ∼50 ps)	–
Scintillation counter	10 mm	0.1 ns	10 ns
Emulsion	1 μm	−	−
Bubble chamber	10–100 μm	1 ms	50 ms–1 s
Proportional chamber	50–100 μm	2 ns	20–200 ns
Drift chamber	50–100 μm	few ns	20–200 ns
Silicon strip	Pitch/5 (few μm)	few ns	50 ns
Silicon pixel	10 μm	few ns	50 ns
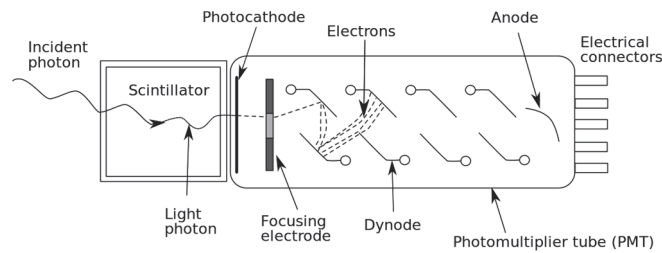
Fig. 4.21 Scheme of a photomultiplier attached to a scintillator. Source: Colin Eberhardt [public domain], via Wikimedia Commons.

- the collection efficiency C related to the overall acceptance;
- the gain G, i.e., the number of electrons collected for each photoelectron generated;
- the dark noise DN, i.e., the electrical signal when there is no incoming photon;
- the intrinsic response time of the detector.

Several kinds of photosensor are used in experiments.

4.2.2.1 Photomultiplier Tubes

Photomultiplier tubes (photomultipliers or PMTs) are detectors of light in the ultraviolet, visible, and near-infrared ranges of the electromagnetic spectrum; they are the oldest photon detectors used in high-energy particle and astroparticle physics.

They are constructed (Fig. 4.21) from a glass envelope with a high vacuum inside, housing a photocathode, several intermediate electrodes called dynodes, and an anode. As incident photons hit the photocathode material (a thin deposit on the entry window of the device) electrons are produced by photoelectric effect and directed by the focusing electrode toward the electron multiplier chain, where they are multiplied by secondary emission.

The electron multiplier consists of several dynodes, each held at a higher positive voltage than the previous one (the typical total voltage in the avalanche process being of 1–2 kV). The electrons produced in the photocathode have the energy of the incoming photon (minus the work function of the photocathode, i.e., the energy needed to extract the electron itself from the metal, which typically amounts to a few eV). As the electrons enter the multiplier chain, they are accelerated by the electric field. They hit the first dynode with an already much higher energy. Low-energy electrons are then emitted, which in turn are accelerated towards the second dynode. The dynode chain is arranged in such a way that an increasing number of electrons are produced at each stage. When the electrons finally reach the anode, the accumulation of charge results in a sharp current pulse. This is the result of the arrival of a photon at the photocathode.

Photocathodes can be made of a variety of materials with different properties. Typically materials with a low work function are chosen.

The typical quantum efficiency of a photomultiplier is about 30 % in the range from 300 to 800 nm of wavelength for the light, and the gain G is in the range 10^5–10^6.

A recent improvement to the photomultiplier was obtained thanks to hybrid photon detectors (HPD), in which a vacuum PMT is coupled to a silicon sensor. A photoelectron ejected from the photocathode is accelerated through a potential difference of about $V \simeq 20$ kV before it hits a silicon sensor/anode. The number of electron–hole pairs that can be created in a single acceleration step is $G \sim V/(3.6\,\mathrm{V})$, the denominator being the mean voltage required to create an electron–hole pair. The linear behavior of the gain is helpful because, unlike exponential gain devices, high voltage stability translates in gain stability. HPD detectors can work as single-photon counters.

4.2.2.2 Gaseous Photon Detectors

In gaseous photomultipliers (GPM) a photoelectron entering a suitably chosen gas mixture (a gas with low photoionization work function, like the tetra dimethyl-amine ethylene TMAE) starts an avalanche in a high-field region. Similarly to what happens in gaseous tracking detectors, a large number of secondary ionization electrons are produced and collected.

Since GPMs can have a good space resolution and can be made into flat panels to cover large areas, they are often used as position-sensitive photon detectors. Many of the ring imaging Cherenkov (RICH) detectors (see later) use GPM as sensors.

4.2.2.3 Solid-State Photon Detectors

Semiconductor photodiodes were developed during World War II, approximately at the same time photomultiplier tubes became a commercial product. Only in recent years, however, a technique which allows the Geiger-mode avalanche in silicon was engineered, and the semiconductor photodetectors reached sensitivities comparable to photomultiplier tubes. Solid-state photodetectors (often called SiPM) are more compact, lightweight, and they might become cheaper than traditional PMTs in the near future. They also allow fine pixelization, of the order of $1\,\text{mm} \times 1\,\text{mm}$, are easy to integrate in large systems and can operate at low-electric potentials.

One of the recent developments in the field was the construction of large arrays of tiny avalanche photodiodes (APD) packed over a small area and operated in Geiger mode.

The main advantages of SiPM with respect to the standard PMT are compact size, low power consumption, low operating voltage (less than $100\,\text{V}$), and immunity to electromagnetic field. The main disadvantages of SiPM are dark current caused by thermally generated avalanches even in the absence of an incoming photon, cross-talk between different channels, and the dependence of gain on temperature, of the order of 1% per kelvin at standard temperatures (temperature needs thus to be stabilized, or at least monitored).

4.2.3 Cherenkov Detectors

The main ingredients of Cherenkov detectors are a medium to produce Cherenkov radiation (usually called the radiator) and a system of photodetectors to detect Cherenkov photons. The yield of Cherenkov radiation is usually generous so as to make these detectors perform well.

If one does not need particle identification, a cheap medium (radiator) with large refractive index n can be used so to have a threshold for the emission as low as possible. A typical radiator is water, with $n \simeq 1.33$. The IceCube detector in Antarctica uses ice as a radiator (the photomultipliers are embedded in the ice).

Since the photon yield and the emission angle depend on the mass of the particle, some Cherenkov detectors are also used for particle identification.

Threshold Cherenkov detectors make a yes/no decision based on whether a particle velocity is or not above the Cherenkov threshold velocity c/n—this depends exclusively on the velocity and, if the momentum has been measured, provides a threshold measurement of the value of the mass. A more advanced version uses the number of detected photoelectrons to discriminate between particle species.

Imaging Cherenkov detectors measure the ring-correlated angles of emission of the individual Cherenkov photons. Low-energy photon detectors measure the position (and sometimes the arrival time) of each photon. These must then be "imaged" onto a detector so that the emission angles can be derived. Typically the optics maps the Cherenkov cone onto (a portion of) a conical section at the photodetector.

Among imaging detectors, in the so-called Ring Imaging Cherenkov (RICH) detectors, the Cherenkov light cone produced by the passage of a high-speed charged particle in a suitable gaseous or liquid radiator is detected on a position-sensitive planar photon detector. This allows for the reconstruction of a conical section (can be a ring), and its parameters give a measurement of the Cherenkov emission angle (Fig. 4.22). Both focusing and proximity-focusing detectors are used. In focusing detectors, photons are collected by a parabolic mirror and focused onto a photon detector at the focal plane. The result is a conic section (a circle for normal incidence); it can be demonstrated that the radius of the circle is independent of the emission point along the particle track. This scheme is suitable for low refractive index radiators such as gases, due to the large radiator length needed to accumulate enough photons. In proximity-focusing detectors, more compact, the Cherenkov light emitted in a thin volume traverses a short distance (the proximity gap) and is detected in the photon detector plane. The image is a ring of light, with radius defined by the Cherenkov emission angle and the proximity gap.

Atmospheric Cherenkov telescopes for high-energy γ astrophysics are also in use. If one uses a parabolic telescope, again the projection of the Cherenkov emission by a particle along its trajectory is a conical section in the focal plane. If the particle has generated through a multiplicative cascade a shower of secondary
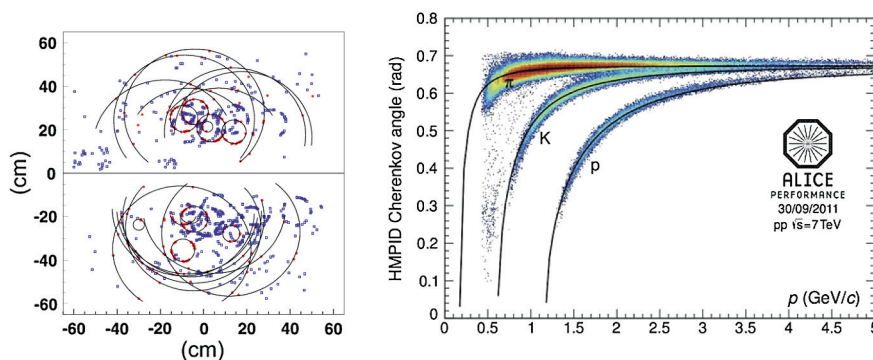
Fig. 4.22 Left: Image of the hits on the photon detectors of the RICHs of the LHCb experiment at CERN with superimposed rings. Credit: LHCb collaboration. Right: Dependence of the Cherenkov angle measured by the RICH of the ALICE experiment at CERN on the particle momentum; the angle can be used to measure the mass through Eq. 4.6 ($\beta = p/E$). Credit: ALICE Collaboration

particles (see later), the projection is a spot, whose shape can enable us to distinguish whether if the primary particle was a hadron or an electromagnetic particle (electron, positron, or photon).

4.2.4 Transition Radiation Detectors

Similar to Cherenkov detectors, transition radiation detectors (TRD) couple interfaces between different media (used as radiators) to photon detectors. Thin foils of lithium, polyethylene, or carbon are common; randomly spaced radiators are also in use, like foams. The main problem in the TRD is the low number of photons. In order to intensify the photon flux, periodic arrangements of a large number of foils are used, interleaved with X-ray detectors such as multiwire proportional chambers filled with xenon or a Xe/CO_2 mixture.

4.2.5 Calorimeters

Once entering an absorbing medium, particles undergo successive interactions and decays, until their energy is degraded, as we have seen in Sect. 4.1.7. Calorimeters are blocks of matter in which the energy of a particle is measured through the absorption to the level of detectable atomic ionizations and excitations. Such detectors can be used to measure not only the energy, but also the position in space, the direction, and in some cases the nature of the particle.

4.2.5.1 Electromagnetic Calorimeters

An ideal material used for an electromagnetic calorimeter – a calorimeter especially sensitive to electrons/positrons and photons – should have a short radiation length, so that one can contain the electromagnetic shower in a compact detector, and the signal should travel unimpeded through the absorber (homogeneous calorimeters). However, sometimes materials which can be good converters and conductors of the signals are very expensive: one then uses *sampling* calorimeters, where the degraded energy is measured in a number of sensitive layers separated by passive absorbers.

The performance of calorimeters is limited both by the unavoidable fluctuations of the elementary phenomena through which the energy is degraded and by the technique chosen to measure the final products of the cascade processes.

Homogeneous Calorimeters. Homogeneous calorimeters may be built with heavy (high density, high Z) scintillating crystals, i.e., crystals in which ionization energy loss results in the emission of visible light, or Cherenkov radiators such as lead glass and lead fluoride. The material acts as a medium for the development of

the shower, as a transducer of the electron signal into photons, and as a light guide towards the photodetector. Scintillation light and/or ionization can be detected also in noble liquids.

Sampling Calorimeters. Layers of absorbers are typically interspersed with layers of active material (sandwich geometry). The absorber helps the development of the electromagnetic shower, while the active material transforms part of the energy into photons, which are guided towards the photodetector. Different geometries can be used: for example sometimes rods of active material cross the absorber (spaghetti geometry).

Converters have high density, short radiation length. Typical materials are iron (Fe), lead (Pb), uranium, tungsten (W). Typical active materials are plastic scintillator, silicon, liquid ionization chamber gas detectors.

Disadvantages of sampling calorimeters are that only part of the deposited particle energy is detected in the active layers, typically a few percent (and even one or two orders of magnitude less in the case of gaseous detectors). These sampling fluctuations typically result in a worse energy resolution for sampling calorimeters.

Electromagnetic Calorimeters: Comparison of the Performance. The fractional energy resolution $\Delta E/E$ of a calorimeter can be parameterized as

$$\frac{\Delta E}{E} = \frac{a}{\sqrt{E}} \oplus b \oplus \frac{c}{E} \, ,$$

where the symbol $\oplus$ represents addition in quadrature. The stochastic term a originates from statistics-related effects such as the intrinsic fluctuations in the shower, number of photoelectrons, dead material in front of the calorimeter, and sampling fluctuations—we remind that the number of particles is roughly proportional to the energy, and thus the Poisson statistics gives fluctuations proportional to $\sqrt{E}$. The a term is at a few percent level for a homogeneous calorimeter and typically $10\,\%$ for sampling calorimeters. The systematic or constant b term represents contributions from the detector non-uniformity and calibration uncertainty, and from incomplete containment of the shower. In the case of hadronic cascades (discussed below), the different response of the instrument to hadrons and leptons, called non-compensation, also contributes to the constant term. The constant term b can be reduced to below one percent. The c term is due to electronic noise. Some of the above terms can be negligible in calorimeters.

The best energy resolution for electromagnetic shower measurement is obtained with total absorption, homogeneous calorimeters, such as those built with heavy crystal scintillators like $\text{Bi}_4\text{Ge}_3\text{O}_{12}$, called BGO. They are used when optimal performance is required. A relatively cheap scintillator with relatively short X_0 is the caesium iodide CsI, which becomes more luminescent when activated with thallium, and is called CsI(Tl); this is frequently used for dosimetry in medical applications, and in space applications, where high technological readiness and reliability are needed.

Energy resolutions for some homogeneous and sampling calorimeters are listed in Table 4.3.

4.2.5.2 Hadronic Calorimeters

We have examined the main characteristics of hadronic showers in Sect. 4.1.8.

Detectors capable of absorbing hadrons and detecting a signal were developed around 1950 for the measurement of the energy of cosmic rays. It can be assumed that the energy of the incident particle is proportional to the multiplicity of charged particles.

Most large hadron calorimeters are sampling calorimeters installed as part of complex detectors at accelerator experiments. The basic structure typically consists of absorber plates (Fe, Pb, Cu, or occasionally U or W) alternating with plastic scintillators (shaped as plates, tiles, bars), liquid argon (LAr) chambers, or gaseous detectors (Fig. 4.23). The ionization is measured directly, as in LAr calorimeters, or via scintillation light observed in photodetectors (usually photomultipliers).

The fluctuations in the invisible energy and in the hadronic component of a shower affect the resolution of hadron calorimeters.

A hadron with energy E generates a cascade in which there are repeated hadronic collisions. In each of these, neutral pions are also produced which immediately ($\tau \sim 0.1$ fs) decay into photons: a fraction of the energy is converted to a potentially observable signal with an efficiency which is in general different, usually larger, than the hadronic detection efficiency. The response of the calorimeters to hadrons is thus not compensated with respect to the response to electromagnetic particles (or to the electromagnetic part of the hadronic shower).

Due to all these problems, typical fractional energy resolutions are in the order of 30–$50\,\%/\sqrt{E}$.

Table 4.3 Main characteristics of some electromagnetic calorimeters. Data from K.A. Olive et al. (Particle Data Group), Chin. Phys. C 38 (2014) 090001. The accelerators quoted in the table are discussed in the next Section.

Technology (experiment)	Depth (X_0)	Energy resolution (relative)
BGO (L3 at LEP)	22	$2\,\%/\sqrt{E} \oplus 0.7\,\%$
CsI (kTeV at the FNAL K beam)	27	$2\,\%/\sqrt{E} \oplus 0.45\,\%$
PbWO$_4$ (CMS at LHC)	25	$3\,\%/\sqrt{E} \oplus 0.5\,\% \oplus 0.2\,\%/E$
Lead glass (DELPHI, OPAL at LEP)	20	$5\,\%/\sqrt{E}$
Scintillator/Pb (CDF at the Tevatron)	18	$18.5\,\%/\sqrt{E}$
Liquid Ar/Pb (SLD at SLC)	21	$12\,\%/\sqrt{E}$
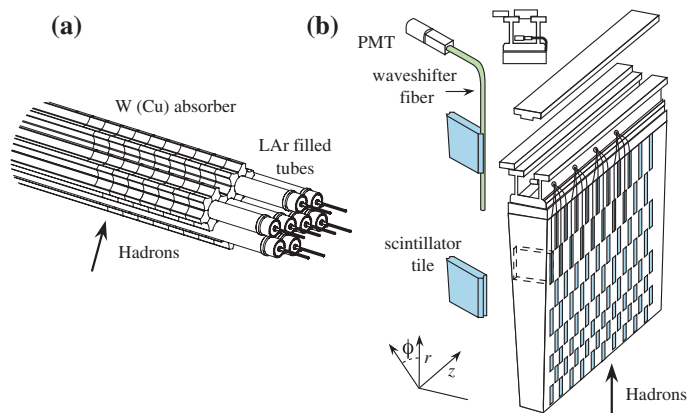
Fig. 4.23 The hadronic calorimeters of the ATLAS experiments at LHC. Credit: CERN

What is the difference between electromagnetic and hadronic calorimeters? Electromagnetic calorimeters are designed to stop photons and electrons and prevent the electromagnetic shower from leaking into the hadronic calorimeter, which in complex detectors is normally located downstream the electromagnetic calorimeter. Many hadrons still lose most of there energy in the electromagnetic calorimeter via strong interactions. Two prerequisites for a good electromagnetic calorimeter are a large Z and a large signal. Due to intrinsic fluctuations of hadronic showers, a hadronic calorimeter, for which large mass number A is the main requirement in order to maximize the hadronic cross section, is less demanding. In principle, however, you can have also a single calorimeter both for "electromagnetic" particles and for hadrons – in this case cost will be a limitation.

4.3 High-Energy Particles

We have seen that when we use a beam of particles as a microscope, like Rutherford did in his experiment, the minimum distance we can sample (for example, to probe a possible substructure in matter) decreases with increasing energy. According to de Broglie's equation, the relation between the momentum p and the wavelength λ of a wave packet is given by

$$\lambda = \frac{h}{p}\,.$$

Therefore, larger momenta correspond to shorter wavelengths, and allow us to access to smaller structures. Particle acceleration is thus a fundamental tool for research in physics.

In addition, we might be interested in using high-energy particles to produce new particles in collisions. This requires more energy, the more massive the particles we want to produce.

4.3.1 Artificial Accelerators

A particle accelerator is an instrument using electromagnetic fields to accelerate charged particles at high energies.

There are two schemes of collision:

- collision with a fixed target (fixed-target experiments);
- collision of a beam with another beam running in the opposite direction (collider experiments).

We also distinguish two main categories of accelerators depending on the geometry: linear accelerators and circular accelerators. In linear accelerators the bremsstrahlung energy loss is much reduced since there is no centripetal acceleration, but particles are wasted after a collision, while in circular accelerators the particles which did not interact can be re-used.

The center-of-mass energy E_{CM} sets the scale for the maximum mass of the particles we can produce (the actual value of the available energy being in general smaller due to constraints related to conservation laws).

We want now to compare fixed target and colliding beam experiments concerning the available energy.

In the case of beam–target collisions between a particles of energy E much larger than its mass, and a target of mass m,

$$E_{\mathrm{CM}} \simeq \sqrt{2mE}\,.$$

This means that, in a fixed target experiment, the center-of-mass energy grows only with the square root of E. In beam–beam collisions, instead,

$$E_{\mathrm{CM}} = 2E\,.$$

It is therefore much more efficient to use two beams in opposite directions. As a result, most of the recent experiments at accelerators are done at colliders.

Making two beams collide, however, is not trivial: one must control the fact that the beams tend to defocus due to mutual repulsion of the particles. In addition, Liouville's theorem states that the phase space volume (the product of the spread in terms of the space coordinates times the spread in the momentum coordinate) of an isolated beam is constant: reducing the momentum dispersion is done at the expense of the space dispersion—and one needs small space dispersion in order that the particles in the beam actually collide. Beating Liouville's theorem requires feedback on the beam itself.[9]

Since beams are circulated for several hours, circular accelerators are based on beams of stable particles and antiparticles, such as electrons, protons, and their antiparticles. In the future, muon colliders are an interesting candidate: as "clean" as electrons, since they are not sensitive to the hadronic interaction, muons have a lower energy dissipation (due to synchrotron radiation and bremsstrahlung) thanks to their mass being 200 times larger than electrons.

Particle accelerators and detectors are often situated underground in order to provide the maximal shielding possible from natural radiation such as cosmic rays that would otherwise mask the events taking place inside the detector.

4.3.1.1 Acceleration Methods

A particle of charge q and speed $\mathbf{v}$ in an electric field $\boldsymbol{\mathcal{E}}$ and a magnetic field $\mathbf{B}$ feels a force

$$\mathbf{F} = q(\boldsymbol{\mathcal{E}} + \mathbf{v} \times \mathbf{B})\,.$$

The electric field can thus accelerate the particle; the work by the magnetic field is zero, nevertheless the magnetic field can be used to control the particle's trajectory. For example, a magnetic field perpendicular to $\mathbf{v}$ can constrain the particle along a circular trajectory perpendicular to $\mathbf{B}$.

If a single potential were applied, increasing energy would demand increasing voltages. The solution is to apply multiple times a limited potential.

An acceleration line (which corresponds roughly to a linear accelerator) works as follows. In a beam pipe (a cylindrical tube in which vacuum has been made) cylindrical electrodes are aligned. A pulsed radiofrequency (RF) source of electromotive force V is applied. Thus particles are accelerated when passing in the RF cavity (Fig. 4.24); the period is adjusted in such a way that half of the period corresponds of the time needed to the particle to cross the cavity. The potential between the cylinders is reversed when the particle is located within them.

---

[9] The Nobel Prize for physics in 1984 was awarded to the Italian physicist Carlo Rubbia (1934 –) and to the Dutch Simon van der Meer (1925–2011) "for their decisive contributions to the large project, which led to the discovery of the field particles W and Z, communicators of weak interaction." In short, Rubbia and van der Meer used feedback signals sent in the ring to reduce the entropy of the beam; this technique allowed the accumulation of focalized particles with unprecedented efficiency, and is at the basis of all modern accelerators.
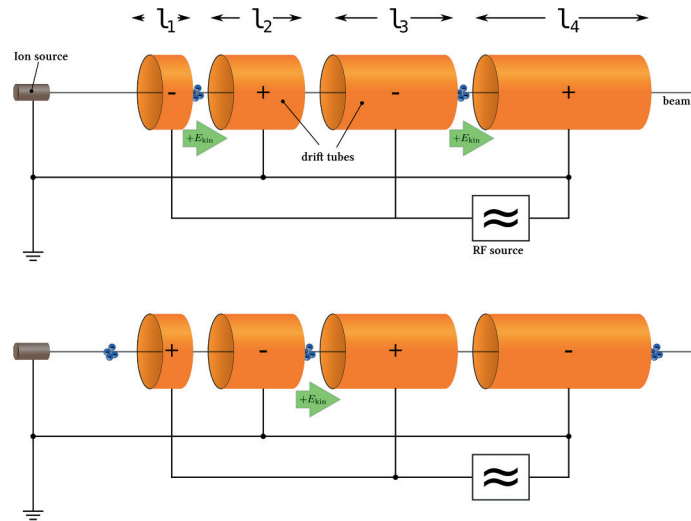
Fig. 4.24 Scheme of an acceleration line displayed at two different times. By Sgbeer (own work) [GFDL http://www.gnu.org/copyleft/fdl.html], via Wikimedia Commons.

To have a large number of collisions, it is useful that particles are accelerated in bunches. This introduces an additional problem, since the particles tend to diverge due to mutual electrostatic repulsion. Divergence can be compensated thanks to focusing magnets (for example quadrupoles, which squeeze beams in a plane).

A collider consists of two circular or almost circular accelerator structures with vacuum pipes, magnets and accelerating cavities, in which two beams of particles travel in opposite directions. The particles may be both protons, or protons and antiprotons, or electrons and positrons, or electrons and protons, or also nuclei and nuclei. The two rings intercept each other at a few positions along the circumference, where bunches can cross and particles can interact. In a particle–antiparticle collider (electron–positron or proton-antiproton), as particles and antiparticles have opposite charges and the same mass, a single magnetic structure is sufficient to keep the two beams circulating in opposite directions.

4.3.1.2 Parameters of an Accelerator

An important parameter for an accelerator is the maximum center-of-mass (c.m.) energy $\sqrt{s}$ available, since this sets the maximum mass of new particles that can be produced.

Another important parameter is *luminosity,* already discussed in Chap. 2. Imagine a physical process has a cross section σ_{proc}; the number of outcomes of this process per unit time can be expressed as

$$\frac{dN_{\text{proc}}}{dt} = \frac{dL}{dt}\sigma_{\text{proc}} \,.$$

dL/dt is called *differential luminosity* of the accelerator, and is measured in cm^{-2} s^{-1}; however, for practical reasons it is customary to use "inverse barns" and its multiples instead of cm^{-2} (careful: due to the definition, 1 mbarn^{-1} = 1000 barn^{-1}).

The integrated luminosity can be obtained by integrating the differential luminosity over the time of operation of an accelerator:

$$L = \int_{\text{time of operation}} \frac{dL(t)}{dt} dt \,.$$

In a collider, the luminosity is proportional to the product of the numbers of particles, n_1 and n_2, in the two beams. Notice that in a proton–antiproton collider the number of antiprotons is in general smaller than that of protons, due to the "cost" of the antiprotons (antiprotons are difficult to store and to accumulate, since they easily annihilate). The luminosity is also proportional to the number of crossings in a second f and inversely proportional to the transverse section $\mathcal{A}$ at the intersection point

$$\frac{dL}{dt} = f\frac{n_1 n_2}{\mathcal{A}} \,.$$

4.3.2 Cosmic Rays as Very-High-Energy Beams

As we have already shown, cosmic rays can attain energies much larger than the particles produced at human-made accelerators. The main characteristics of cosmic rays have been explained in Sect. 1.4 and in Chap. 3.

We just recall here that the distribution in energy (the so-called spectrum) of cosmic rays is quite well described by a power law E^{-p}, with the so-called spectral index p around 3 in average (Fig. 1.8), extending up to about 10^{21} eV (above this energy the GZK cutoff, explained in the previous chapters, stops the cosmic travel of particles; a similar mechanism works for heavier nuclei, which undergo photo-disintegration during their cosmic travel). The majority of the high-energy particles in cosmic rays are protons (hydrogen nuclei); about 10 % are helium nuclei (nuclear physicists call them usually "alpha particles"), and 1 % are neutrons or nuclei of heavier elements. These together account for 99 % of the cosmic rays, and electrons, photons and neutrinos dominate the remaining 1 %. The number of neutrinos is estimated to be comparable to that of high-energy photons, but it is very high at low energy because of the nuclear processes that occur in the Sun: such processes involve a large production of neutrinos. Cosmic rays hitting the atmosphere (called primary cosmic rays) generally produce secondary particles that can reach the Earth's surface, through multiplicative showers.

The reason why human-made accelerators cannot compete with cosmic accelerators from the point of view of the maximum attainable energy is that with the present technologies acceleration requires confinement within a radius R by a magnetic field B, and the final energy is proportional to the product of R times B. On Earth, it is difficult to imagine reasonable radii of confinement larger than one hundred kilometers and magnetic fields stronger than ten tesla (one hundred thousand times the Earth's magnetic field). This combination can provide energies of a few tens of TeV, such as those of the LHC accelerator at CERN. In nature there are accelerators with much larger radii, as the remnants of supernovae (hundreds of light years) and active galactic nuclei (tens of thousands of light years): one can thus reach energies as large as 10^{21} eV, i.e., 1 ZeV (the so-called Extremely-High-Energy, EHE, cosmic rays; cosmic rays above 10^{18} eV, i.e., 1 EeV, are often called Ultra-High-Energy, UHE). Of course terrestrial accelerators have great advantages like luminosity and the possibility of knowing the initial conditions.

The conditions are synthetically illustrated in the so-called Hillas plot (Fig. 10.32), a scatter plot in which different cosmic objects are grouped according to their sizes and magnetic fields; this will be discussed in larger detail in Chap. 10. UHE can be reached in the surroundings of active galactic nuclei, or in gamma-ray bursts. The product of R times B in supernova remnants are such that particles can reach energies of some PeV.

4.4 Detector Systems and Experiments at Accelerators

Detectors at experimental facilities are in general hybrid, i.e., they combine many of the detectors discussed so far, such as the drift chambers, Cherenkov detectors, electromagnetic, and hadronic calorimeters. They are built up in a sequence of layers, each one designed to measure a specific aspect of the particles produced after the collision.

Starting with the innermost layer the successive layers are typically as follows:

- A tracking system: this is designed to track all the charged particles and allow for complete event reconstruction. It is in general the first layer crossed by the particles, in such a way that their properties have not yet been deteriorated by the interaction with the material of the detector. It should have as little material as possible, so as to preserve the particles for the subsequent layer.
- A layer devoted to electromagnetic calorimetry.
- A layer devoted to hadronic calorimetry.
- A layer of muon tracking chambers: any particle releasing signal on these tracking detectors (often drift chambers) has necessarily traveled through all the other layers and is very likely a muon (neutrinos have extremely low interaction cross sections, and most probably they cross also the muon chambers without leaving any signal).

A layer containing a solenoid can be inserted after the tracking system, or after the calorimeter. Tracking in a magnetic field allows momentum measurement.
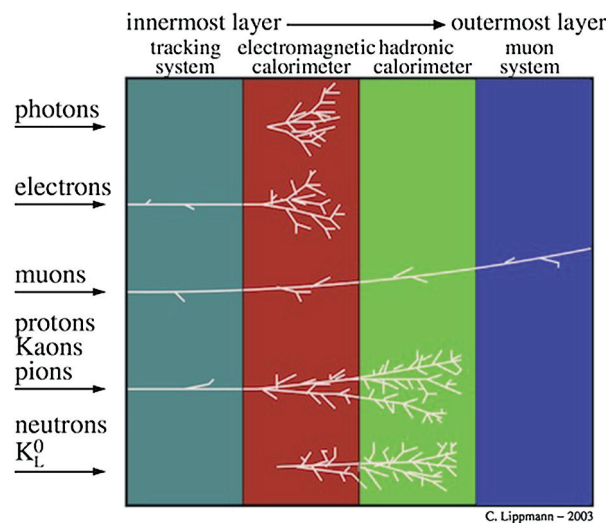
Fig. 4.25 Overview of the signatures by a particle in a multilayer hybrid detector. Credit: CERN.

The particle species can be identified for example by energy loss, curvature in magnetic field, and Cherenkov radiation. However, the search for the identity of a particle can be significantly narrowed down by simply examining which parts of the detector it deposits energy in:

- Photons leave no tracks in the tracking detectors (unless they undergo pair production) but produce a shower in the electromagnetic calorimeter.
- Electrons and positrons leave a track in the tracking detectors and produce a shower in the electromagnetic calorimeter.
- Muons leave tracks in all the detectors (likely as a minimum ionizing particle in the calorimeters).
- Long-lived charged hadrons (protons for example) leave tracks in all the detectors up to the hadronic calorimeter where they shower and deposit all their energy.
- Neutrinos are identified by missing energy-momentum when the relevant conservation law is applied to the event.

These signatures are summarized in Fig. 4.25.

4.5 Cosmic-Ray Detectors

The strong decrease in the flux Φ of cosmic rays with energy, in first approximation $\Phi \propto E^{-3}$, poses a big challenge to the dimensions and the running times of the experimental installations when high energies are studied. Among cosmic rays, a small fraction of about 10^{-3} are photons, which are particularly interesting since they are not deflected by intergalactic magnetic fields, and thus point directly to their sources; the large background from charged cosmic rays makes the detection even more complicated. Neutrinos are expected to be even less numerous than photons, and their detection is even more complicated due to the small cross section.

We shall examine first the detectors of cosmic rays which have a relatively large probability of interactions with the atmosphere: nuclei, electrons/positrons, and photons. We shall then discuss neutrinos, for which a severe limitation is given by the extremely low interaction cross sections, and finally the recently discovered gravitational waves, for which detection techniques are completely different.

Balloon and satellite-borne detectors operate at an altitude of above 15 km where they can detect the interaction of the primary particle inside the detector, but they are limited in detection area and therefore also limited in the energy range they can measure. The maximum primary energy that can be measured by means of direct observations is of the order of 1 PeV; above this energy the observations are performed by exploiting the cascades induced in atmosphere by the interactions of cosmic rays.
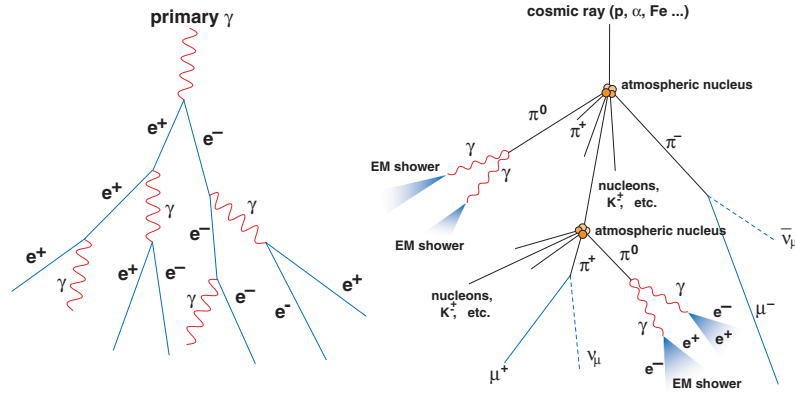
Fig. 4.26 Schematic representation of two atmospheric showers initiated by a photon (left) and by a proton (right). From R.M. Wagner, dissertation, MPI Munich 2007.

4.5.1 Interaction of Cosmic Rays with the Atmosphere: Extensive Air Showers

The physics of electromagnetic and hadronic showers has been described before; here we particularize the results obtained to the development of the showers due to the interaction of high-energy particles with the atmosphere. These are called extensive air showers (EAS).

High-energy hadrons, photons, and electrons interact in the high atmosphere. As we have seen, the process characterizing hadronic and electromagnetic showers is conceptually similar (Fig. 4.26).

For photons and electrons above a few hundred MeV, the cascade process is dominated by the pair production and the bremsstrahlung mechanisms: an energetic photon scatters on an atmospheric nucleus and produces an e^+e^- pair, which emits secondary photons via bremsstrahlung; such photons produce in turn a pair, and so on, giving rise to a shower of charged particles and photons, degrading the energy down to the critical energy E_c where the ionization energy loss of charged particles starts dominating over bremsstrahlung.

The longitudinal development of typical photon-induced extensive air showers is shown in Fig. 4.27 for different values of the primary energies. The maximum shower size occurs approximately after $\ln(E/E_c)$ radiation lengths, the radiation length for air being about 37 g/cm^2 (approximately 300 m at sea level and NTP). The critical energy E_c is about 80 MeV in air.[10]

The hadronic interaction length in air is about 61 g/cm^2 for protons (500 meters for air at NTP), being shorter for heavier nuclei—the dependence of the cross section on the mass number A is approximately $A^{2/3}$. The transverse profile of hadronic showers is in general wider than for electromagnetic showers, and fluctuations are larger.

Particles release energy in the atmosphere, which acts like a calorimeter, through different mechanisms—which give rise to a measurable signal. We have discussed these mechanisms in Sect. 4.1.1; now we reexamine them in relation to their use in detectors.

4.5.1.1 Fluorescence

As the charged particles in an extensive air shower go through the atmosphere, they ionize and excite the gas molecules (mostly nitrogen). In the de-excitation processes that follow, visible and ultraviolet (UV) radiations are emitted. This is the so-called fluorescence light associated to the shower.
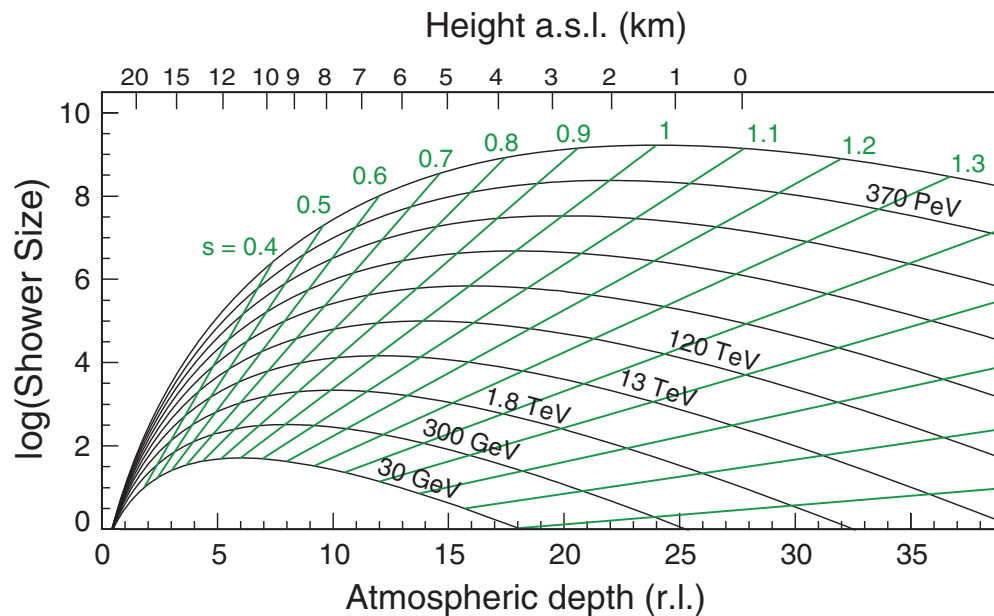
The number of emitted fluorescence photons is small—of the order of a few photons per electron per meter in air. This implies that the fluorescence technique can be used only at high energies. However, it is

---

[10] In the isothermal approximation, the depth x of the atmosphere at a height h (i.e., the amount of atmosphere above h) can be approximated as

$$x \simeq X e^{-h/7\,\mathrm{km}},$$

with $X \simeq 1030$ g/cm^2.

Fig. 4.27 Longitudinal shower development from a photon-initiated cascade. The parameter s describes the shower age. From R.M. Wagner, dissertation, MPI Munich 2007; adapted from reference [F4.1] in the "Further reading".

not directional as in the case of Cherenkov photons (see below), and thus it can be used in serendipitous observations.

4.5.1.2 Cherenkov Emission

Many secondary particles in the EAS are superluminal, and they thus emit Cherenkov light that can be detected. The properties of the Cherenkov emission have been discussed in Sect. 4.1.1 and 4.2.

At sea level, the value of the Cherenkov angle θ_C in air for a speed $\beta = 1$ is about 1.3°, while at 8 km a.s.l. it is about 1°. The energy threshold for Cherenkov emission at sea level is 21 MeV for a primary electron and 44 GeV for a primary muon.

Half of the emission occurs within 20 m of the shower axis (about 70 m for a proton shower). Since the intrinsic angular spread of the charged particles in an electromagnetic shower is about 0.5°, the opening of the light cone is dominated by the Cherenkov angle. As a consequence, the ground area illuminated by Cherenkov photons from a shower of 1 TeV (the so-called "light pool" of the shower) has a radius of about 120 m, with an approximately constant density of photons per unit area. The height of maximal emission for a primary photon of energy of 1 TeV is approximately 8 km a.s.l., and about 150 photons per m² arrive at 2000 m a.s.l. (where typically Cherenkov telescopes are located, see later) in the visible and near UV frequencies. This dependence is not linear, being the yield of about 10 photons per square meter at 100 GeV.

The atmospheric extinction of light drastically changes the Cherenkov light spectrum (originally proportional to $1/\lambda^2$) arriving at the detectors, in particular suppressing the UV component (Fig. 4.28) which is still dominant. There are several sources of extinction: absorption bands of several molecules, molecular (Rayleigh), scattering from aerosol (Mie).

Radio Emission. Cosmic-ray air showers also emit radio waves in the frequency range from a few to a few hundred MHz, an effect that opens many interesting possibilities in the study of UHE and EHE extensive air showers. At present, however, open questions still remain concerning both the emission mechanism and its strength.
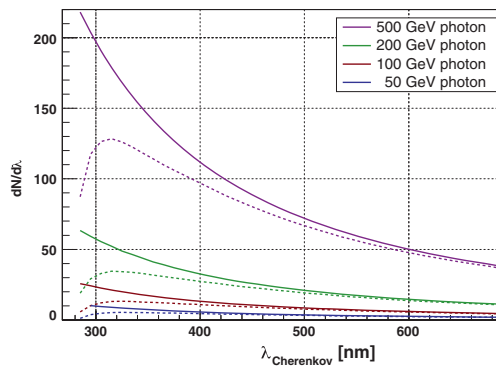
Fig. 4.28 Spectrum of the Cherenkov radiation emitted by gamma-ray showers at different energies initiated at 10 km a.s.l. (solid curves) and the corresponding spectra detected at 2200 meters a.s.l. (lower curve). From R.M. Wagner, dissertation, MPI Munich 2007.

4.5.2 Detectors of Charged Cosmic Rays

The detection of charged cosmic rays may be done above the Earth's atmosphere in balloon or satellite-based experiments whenever the fluxes are large enough (typically below tens or hundreds of GeV) and otherwise in an indirect way by the observation of the extensive air showers produced in their interaction with the atmosphere (see Sect. 4.5.1).

In the last thirty years, several experiments to detect charged cosmic rays in space or at the top of the Earth's atmosphere were designed and a few were successfully performed. In particular:

- The Advanced Composition Explorer (ACE) launched in 1997 and still in operation (with enough propellant to last until ∼2024) has been producing a large set of measurements on the composition (from H to Ni) of solar and Galactic Cosmic rays covering energies from the 1 keV/nucleon to 500 MeV/nucleon. ACE has several instruments which are able to identify the particle charge and mass using different types of detectors (for example silicon detectors, gas proportional counters, fiber-optics hodoscopes) and techniques (for example the specific energy loss dE/dx, the time-of-flight, electrostatic deflection). The total mass at launch (including fuel) was about 800 kg.
- The Balloon-borne Experiment with Superconducting Spectrometer (BESS) performed successive flights starting in 1993 with the main aim to measure the low-energy anti-proton spectrum and to search for anti-matter, namely anti-helium. The last two flights (BESS-Polar) were over Antarctica and had a long duration (8.5 days in 2004 and 29.5 days in 2007/2008). The instrument, improved before every flight, had to ensure a good charge separation and good particle identification. It had a horizontal cylindrical configuration and its main components were as follows: a thin-wall superconducting magnet; a central tracker composed of drift chambers; time-of-flight scintillation counter hodoscopes; an aerogel (an ultra-light porous material derived from a gel by replacing its liquid component with a gas) Cherenkov counter.
- The PAMELA experiment launched in June 2006 measured charged particle and anti-particles out of the Earth's atmosphere during a long (six years)-time period. A permanent magnet of 0.43 T and a microstrip silicon tracking system ensured a good charge separation between electrons and positrons up to energies of the order of the hundred of GeV measured by a silicon/tungsten electromagnetic calorimeter complemented by a neutron counter to enhance the electromagnetic/hadronic discrimination power. The trigger was provided by a system of plastic scintillators which were also used to measure the time-of-flight and an estimation of the specific ionization energy loss (dE/dX).
- The Alpha Magnetic Spectrometer (AMS-02) was installed in May 2011 on the International Space Station. Its concept is similar to PAMELA but with a much larger acceptance and a more complete set of sophisticated and higher performing detectors. Apart from the permanent magnet and the precision silicon tracker it consists of a transition radiation detector, time-of-flight and anti-coincidence counters, a ring imaging Cherenkov detector, and an electromagnetic calorimeter (Fig. 4.29). Its total weight is 8500 kg and its cost was over 2 billion euros.
- ISS-CREAM (Cosmic Ray Energetics and Mass for the International Space Station) is in orbit since 2017. It uses a Si detector, timing detectors, and scintillating fiber hodoscopes to detect the charge of incident particles up to iron at energies up to the knee. Energies are measured with a transition radiation detector (TRD), and with a calorimeter. The mission follows successful balloon flights of the CREAM detector.
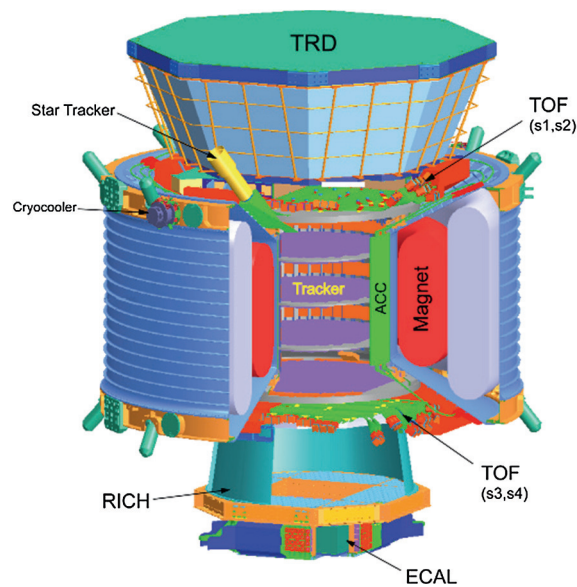
Fig. 4.29 The AMS-02 detector layout. Credit: AMS Collaboration.

Extensive air showers produced by high-energy cosmic rays in their interaction with the atmosphere are detected using three different techniques:

- The measurement of a fraction of the EAS particles arriving at the Earth's surface through an array of surface detectors (SD);
- The measurement in moonless nights of the fluorescence light emitted mainly by the excitation of the atmosphere nitrogen molecules by the shower low energetic electrons through an array of ultra-violet fluorescence detectors (FD) placed on the Earth surface or even in satellites; and
- The measurement of the Cherenkov light emitted by the ultra-relativistic air shower particles in a narrow cone around the shower axis, through telescopes as the Imaging Atmosphere Cherenkov Telescopes (IACTs), which will be discussed in the next section in the context of gamma-ray detection.

Other possible techniques (radio detection for example) might be exploited in the future.

Surface detectors measure at specific space locations the time of arrival of individual particles. The most widely used surface detectors are scintillation counters and water Cherenkov counters. More sophisticated tracking detectors as resistive plate chambers, drift chambers, and streamer tube detectors have been also used or proposed.

The arrival direction of an air shower is determined from the arrival time at the different surface detectors of the shower front (Fig. 4.30). To a first approximation, the front can be described by a thin disk propagating at the speed of light; second-order corrections can be applied to improve the measurement.

The impact point of the air shower axis at the Earth's surface (the air shower core) is defined as the point of maximum particle density and is determined from the measured densities at the different surface detectors using, to a first approximation, a modified center-of-mass algorithm. In Fig. 4.31, right, the particle density pattern of the highest energy event at the AGASA array experiment[11] is shown. The energy of the event was estimated to be about 2×10^{20} eV. The measured densities show a fast decrease with the distance of the core and are usually parameterized by empirical or phenomenological inspired formulae—the most popular being the NKG function, introduced in Sect. 4.1.7—which depend also on the shower age (the level of development of the shower when reaches ground). Such functions allow for a better determination of the shower core and for the extrapolation of the particle density to a reference distance of the core which is then used as an estimator of the shower size and thus of the shower energy. The exact function and the reference distance depend on the particular experimental setup.

Fluorescence telescopes record the intensity and arrival time of light emitted in the atmosphere in specific solid angle regions and thus allow reconstructing the shower axis and the shower longitudinal profile. Fig. 4.32

---

[11] The Akeno Giant Air-Shower Array (AGASA) is a very large surface array covering an area of $100\,\mathrm{km}^2$ in Japan and consisting of 111 surface detectors (scintillators) and 27 muon detectors (proportional chambers shielded by Fe/concrete).
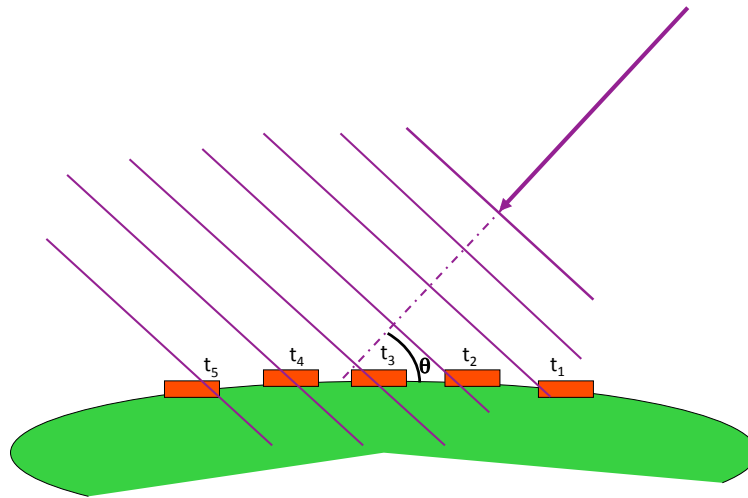
Fig. 4.30 Air shower front arriving at the Earth surface; arrival times are measured by surface detectors and allow the determination of the direction.
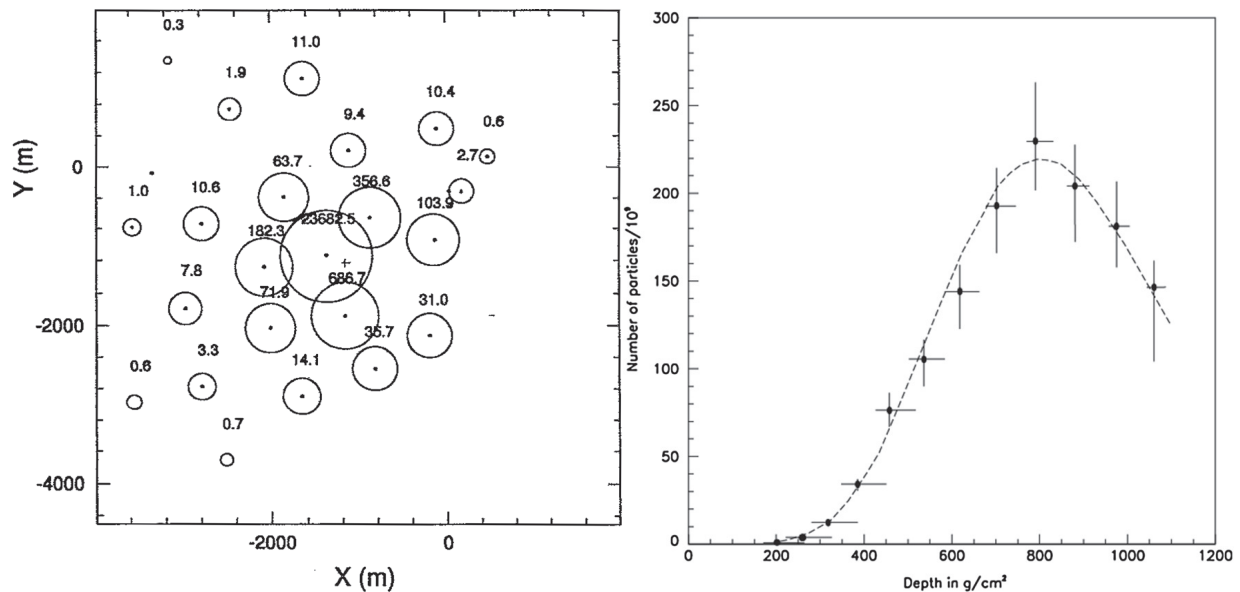

Fig. 4.31 *Left:* Map of the observed particle density pattern of the highest energy event at the AGASA array experiment. The cross corresponds to the fitted position of the shower core. From http://www.icrr.u-tokyo.ac.jp. *Right:* Shower longitudinal profile of the most energetic event observed by the Fly's Eye experiment. From D.J. Bird et al., Astrophys. J. 441 (1995) 144.

shows the image of a shower in the focal plane of one of the Pierre Auger fluorescence telescopes (see later). The third dimension, time, is represented in a color code.

The geometry of the shower (Fig. 4.33) is then reconstructed in two steps: first the shower detector plane (SDP) is found by minimizing the direction of the SDP perpendicular to the mean directions of the triggered pixels, and then the shower axis parameters within the SDP are found from the measured arrival time of the light in each pixel, assuming that the shower develops along a line at the speed of light.

Simultaneous observations of the shower by two (stereo) or more fluorescence detectors or by a surface detector array (hybrid detection) provide further geometric constrains improving considerably the resolution of the shower geometric reconstruction.

The intensity of collected light along the shower axis is corrected for the detector efficiency, the solid angle seen by each detector pixel, the attenuation in the atmosphere, the night sky background, and the contributions of fluorescence (dominant unless the shower axis points in the direction of the telescope) and of Cherenkov light are estimated. Finally, the shower longitudinal profile (Fig. 4.31, right) is obtained assuming proportionality between the fluorescence light emitted and the number of particles in the shower. The integral
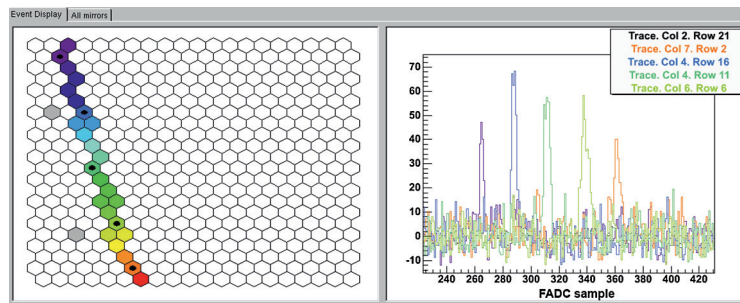
Fig. 4.32 Display of one shower in the focal plane of one of the Pierre Auger fluorescence telescopes. Left: Pattern of the pixels with signal; right response (signal versus time, with a time bin of 100 ns) of the selected pixels (marked with a black dot in the left panel). The development of the shower in the atmosphere can be qualitatively pictured. From https://www.auger.org.
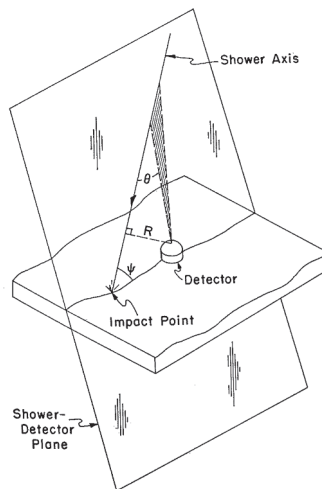
Fig. 4.33 The shower geometry as seen by a fluorescence telescope. From K.-H. Kampert and A. Watson, "Extensive Air Showers and Ultra High Energy Cosmic Rays: A Historical Review," EPJ-H 37 (2012) 359.

of such a profile is a good estimator of the energy of the shower (small "missing energy" corrections due to low interacting particles in the atmosphere, like muons and neutrinos, have to be taken into account).

The Pierre Auger Observatory. The Pierre Auger Observatory in Malargue, Argentina, is the largest cosmic-ray detector ever built. It covers a surface of about 3000 square kilometers with 1600 surface detector stations (Cherenkov water tanks) arranged in a grid of 1.5 km side complemented by 24 fluorescence telescopes, grouped into four locations to cover the atmosphere above the detector area (Fig. 4.34).

Each water tank is a cylinder of 10 m^2 base by 1.5 m height filled with 12 tons of water (Fig. 4.35). The inner walls of the tank are covered with a high reflectivity material. The Cherenkov light, produced by the charged particles crossing the water, is collected by three PMTs placed at the top of the tank. Each tank is autonomous being the time given by a GPS unit and the power provided by a solar panel; it communicates via radio with the central data acquisition system.

Each fluorescence detector is a Schmidt telescope[12] with a field of view of 30° in azimuth and 29° in elevation (Fig. 4.35). Light enters the telescope through an ultra-violet filter installed over the telescope and is collected in a 3.5 m diameter spherical mirror which focuses it in a 440 PMT camera.

The signal by an event of extremely high energy is shown in Fig. 4.36.

The Telescope Array. The largest cosmic-ray detector in the Northern hemisphere is the Telescope Array (TA) in Utah, US. Similar to Auger, it is also a hybrid detector composed of a surface array of 507 scintillator detectors, each 3 m in size, located on a 1.2 km square grid, plus three fluorescence stations each one with a dozen of telescopes, each instrumented with a 256 PMT camera covering 3°–33° in elevation. The total surface covered is about 800 km^2.

Future Prospects: Detection from Space. An innovative approach to detect extremely-high energy cosmic rays has been proposed by several collaborations as the "EUSO concept": increasing the effective

---

[12] In a Schmidt telescope, a spherical mirror receives light that passed through a thin aspherical lens that compensates for the image distortions that will occur in the mirror. Light is then reflected in the mirror into a detector that records the image.
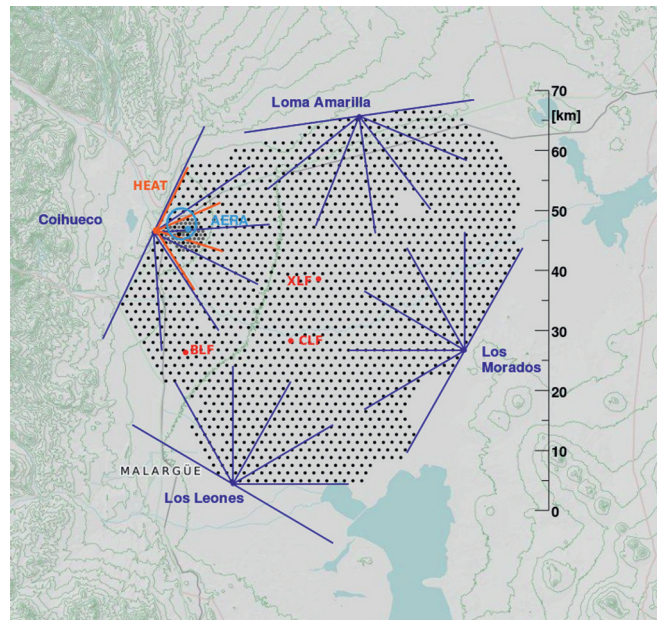
Fig. 4.34 The Pierre Auger Observatory near Malargue, Argentina. The radial lines point to the fluorescence detectors (FD, $4 \times 6 = 24$). The black dots are the 1600 ground stations (SD). Sites with specialized equipment are also indicated. By Darko Veberic [GFDL http://www.gnu.org/copyleft/fdl.html], via Wikimedia Commons.
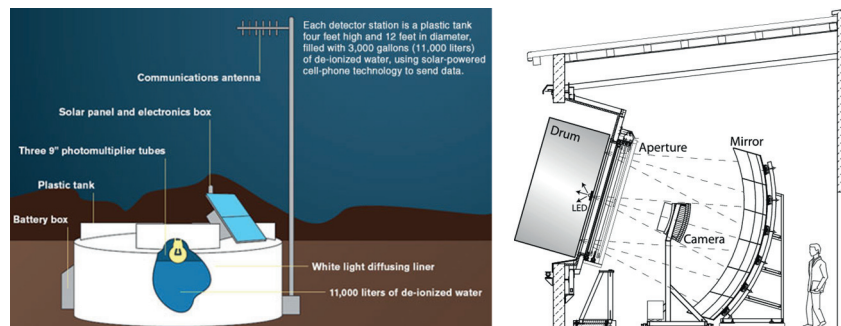
Fig. 4.35 Sketch of one of the Pierre Auger surface detectors (left); a fluorescence telescope (right). From https://www.auger.org.
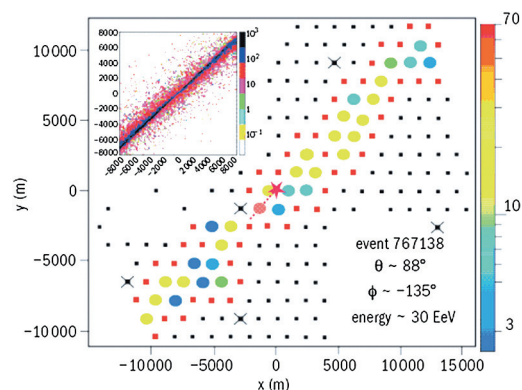
Fig. 4.36 A 30 EeV event at a zenith angle of about $88°$ recorded by the Auger detector. The inset shows a simulation of an event of the same energy and angle. From https://www.auger.org.

area by looking to a large volume of the atmosphere from a satellite. A space telescope equipped with a Fresnel lens can detect the fluorescence light emitted by the extended air showers (Fig. 4.37). Observing the Earth from 400 km above and having a large field of view ($\pm 30°$), one can cover a large surface on Earth (above 1.9×10^5 km^2), but the energy threshold is high (around 3×10^{19} eV).

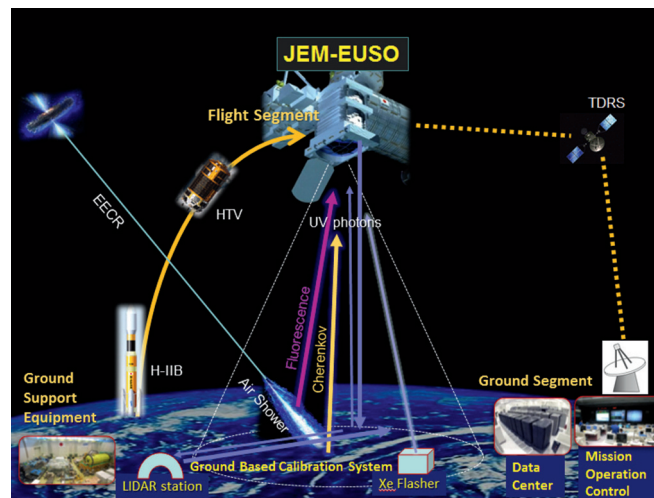**Fig. 4.37** EUSO observational principle. From http://jemeuso.riken.jp/en/.
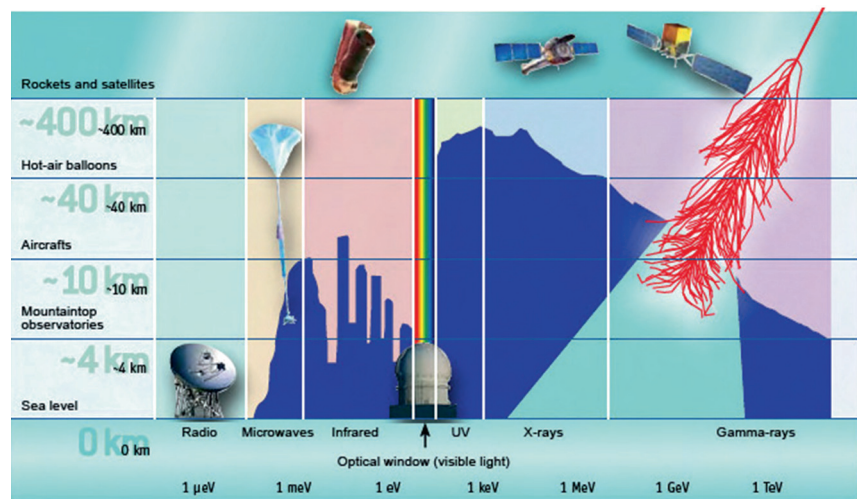

Fig. 4.38 Transparency of the atmosphere for different photon energies and possible detection techniques. Source: A. De Angelis and L. Peruzzo, "Le magie del telescopio MAGIC," Le Scienze, April 2007.

4.5.3 Detection of Hard Photons

Most photons in astrophysics are produced by systems near thermal equilibrium, approximately blackbodies. The bulk of astrophysical photons is due to CMB at a temperature of about 2.7 K (corresponding to an energy of about 0.1 meV). The highest-energy thermalized systems emit at energies of about a keV, i.e., in the X-ray range. We are interested in this book mainly on nonthermal processes, and thus, on photons in the keV range and above.

Nonthermal photons, in the keV range and above, are expected to be generated in astrophysical objects mostly by leptonic acceleration mechanisms (see Chap. 10), and by the decays of neutral pions produced in cosmic-ray interactions with radiation or gas – as these pions decay, they produce photons with typical energies one order of magnitude smaller than those of the cosmic-ray nucleons generating them. Photons in the MeV range can come also from nuclear de-excitation processes.

The detection of photons above the UV range is complicated by the absorption in the atmosphere (see Fig. 4.38) and by the faintness of the signal, in particular when compared to the corresponding charged particles of similar energy—being the latter three to four orders of magnitude more frequent. They interact with matter mostly due to photoelectric effect and by Compton mechanism at energies up to about 20 MeV–30 MeV, while e^+e^- pair production dominates above these energies.

Although arbitrary, a classification of hard photons as a function of their energy can be useful. We define as:

1. Hard X-ray region (or keV region) the energy region between 3 keV and 300 keV.
2. Low-energy gamma-ray region (or MeV region) the energy region between 0.3 MeV and 30 MeV. This is the region in which the Compton interaction probability is comparable with the pair production probability.
3. High-energy (HE) gamma-ray region (or GeV region) the energy region between 30 MeV and 30 GeV. The pair production process becomes dominant.
4. Very-high-energy (VHE) gamma-ray region (or TeV region) the energy region between 30 GeV and 30 TeV. Electromagnetic showers in the atmosphere start becoming visible.
5. PeV region the energy region between 30 TeV and 30 PeV. Charged particles from electromagnetic showers in the atmosphere can reach instruments at mountain-top altitudes. As we shall see in Chap. 10, however, the mean free path of photons at these energies is such that we expect photons from very few extragalactic sources to reach the Earth.

This classification, in particular, corresponds to different detection techniques, as we shall see now. The MeV, GeV and TeV regions are especially important related to the physics of cosmic rays and to fundamental physics. Note the difference in range with respect to highest-energy charged cosmic rays – do not forget that the flux in the latter case is three orders of magnitude larger in the MeV–GeV region.

Main figures of merit for a detector are its effective area (i.e., the product of the area times the detection efficiency), the energy resolution, the space or angular resolution (called as well point-spread function, or PSF). In particular the effective area has to be appropriate for the flux one wants to measure.

Due to the conversion probability in the atmosphere (whose thickness is about 28 radiation lengths at sea level) only satellite-based detectors can detect primary X/γ-rays - and thus gamma rays below the TeV region. Satellites are small, about 1 m^2 in area at maximum, because of the cost of space technology. The area sampled by ground-based detectors can be much larger than this. Since the fluxes of high-energy photons are low and decrease rapidly with increasing energy, TeV and PeV gamma rays can be detected only from the atmospheric showers they produce, i.e., by means of ground-based detectors. This fact clarifies another meaning of the division between HE and VHE photons: HE photons are detected using satellites, while for VHE photons the detection using ground-based instruments becomes possible.

4.5.3.1 Satellites

Satellite-based telescopes for hard photons can detect the primary particles at energies lower than ground-based telescopes. They have a small effective area, of order of 1 m^2 maximum, which limits their sensitivity. They have a large duty cycle, and they suffer a low rate of background events, since they can be coupled to anticoincidence systems rejecting the charged cosmic rays. They have a large cost, dominated by the costs of launch and by the strong requirements of instruments which must be sent into space, with little or no possibility of intervention to fix possible bugs.

1. Satellites operational in the keV regime use different focal plane detectors and optical system. Optical systems (Fig. 4.39) are constituted by focusing grazing incident mirrors or by collimating elements such as for example coded mask systems (grids of materials opaque to various wavelengths of light: by blocking light in a known pattern, a coded "shadow" is cast upon a sensitive plane, and the properties of the original light sources can then be mathematically reconstructed from this shadow).
   1a. In the energy band of a few keV, satellites in use today include NASA's Chandra mission and ESA's XMM-Newton observatory, both launched in 1999; they both use X-ray grazing incident mirrors. Chandra has an effective area of 800 and 400 cm^2 at 0.25 and 5 keV respectively. Different instruments can be inserted in the focal plane; at 1 keV, typically FoV is 30' $\times$ 30' and space resolution is as good as 0.5 arcsec; the spectral resolving power $E/\Delta E$ is between 30 and 2000. ESA's X-ray Multi-Mirror Mission (XMM-Newton) uses three co-aligned grazing incidence gold-coated imaging X-ray telescopes each with an effective area of $\sim$ 1500 cm^2 at 1 keV with a spatial resolution of 6 arcsec. Also in this case there are different instruments. Typical effective area is of the order of 1000 cm^2 at 1 keV for a spectral resolving power of 20; of the order of 200 cm^2 for a resolving power of 1000. The maximum energy detected by these detectors is around 15 keV.
   NASA's NuSTAR (Nuclear Spectroscopic Telescope Array), launched in 2012, is a space-based X-ray telescope that operates in the range of 3 to 80 keV. NuSTAR is the first telescope using imaging techniques at energies above 15 keV. The NuSTAR grazing mirrors have a focal length of 10.15 m and are held at the end of a long deployable mast. The point spread function for the flight mirrors is 43 arc-seconds, an unprecedentedly good resolution for focusing hard X-ray optics.
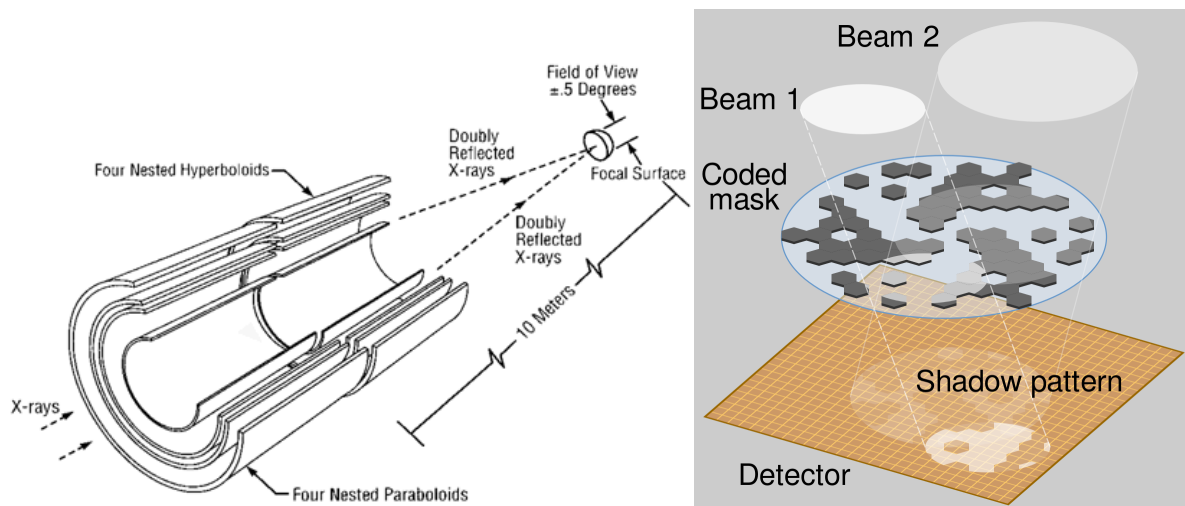
Fig. 4.39 Principles of operation of focusing grazing incident mirrors (left, credits: NASA) and of coded mask apertures (right, credits: Wikimedia Commons).

In the future (launch is planned for 2028), the ATHENA (Advanced Telescope for High Energy Astrophysics) satellite, one hundred times more sensitive than the best existing X-ray telescopes, will fly within ESA's Cosmic Vision program.

1b. At higher energies, collimating elements are used to image photons of energy in the range from 100 keV to few MeV. Coded mask systems are used both by the Swift Burst Alert Telescope (BAT) and by the main instruments on board the INTEGRAL satellite.

The Neil Gehrels Swift Observatory (shortly Swift) is a NASA international mission launched in 2004. The primary scientific objectives are to determine the origin of Gamma Ray Bursts (GRB) and to pioneer their use as probes of the early universe. Swift is a multiwavelength observatory carrying three instruments. The Burst Alert Telescope (BAT; 15-150 keV) is a wide field-of-view coded-aperture imager with an effective area 5240 cm^2 and a FoV of 1.4 sr half coded and a position accuracy of $\sim 4'$. The X-Ray Telescope (XRT; 0.2-10.0 keV) uses a X-ray grazing mirror system and has a CCD Imaging spectrometer with an effective area of 110 cm^2 at 1.5 keV, a FOV of $23.6' \times 23.6'$ and a ~ 5" position accuracy. The UV/Optical Telescope (UVOT; 170-650 nm) is a CCD detector with a FoV of $17' \times 17'$ and 0.3 arcsec position accuracy. The key characteristics of Swift are the rapid response to newly detected GRB and rapid data dissemination. As soon as the BAT discovers a new GRB, Swift rapidly releases its first position estimate, with (1-4) arcmin accuracy, to the ground and triggers and an autonomous trigger allows the burst entering within the field of view of XRT and UVOT to follow-up the afterglow.

ESA's International Gamma-Ray Astrophysics Laboratory (INTEGRAL) was launched in 2002. It is producing a complete map of the sky in the soft gamma-ray waveband and it is capable of performing high spectral and spatial observations in gamma rays. The observatory is also equipped with X-ray and optical detectors to provide simultaneous observations in these wavebands. The payload hosts several gamma-ray instruments. The Spectrometer (SPI; 20 keV - 8 MeV) has a coded aperture mask with a FOV of 16° and a detection plane made of a Germanium array with a detector area of 500 cm^2, a spectral resolution ($E/\Delta E$) of 500 at 1 MeV and a spatial resolution of 2°. The Imager (IBIS; 15 keV - 10 MeV) is also equipped with a coded aperture mask. Its FoV is 9° $\times$ 9°, a detector area of 2600 cm^2 (CdTe array - ISGRI) and of 3100 cm^2 (CsI array - PICSIT) with a spatial resolution of 12′. The Joint European X-Ray Monitor (JEM-X) makes observations simultaneously with the main gamma-ray instruments and provides images in the 3 - 35 keV prime energy band with an angular resolution of 3 arcmin.

In this energy range not collimated systems use scintillation materials to detect photons up to tens of MeV. The *Fermi* (see later) Gamma-ray Burst Monitor (GBM) is equipped with 12 NaI detectors sensitive from a few keV to about 1 MeV and two BGO detectors operating up to 40 MeV.

2. In the MeV regime, the state of the art for Compton imaging is mostly frozen at the COMPTEL instrument on the Compton Gamma Ray Observatory (CGRO), launched in 1991 aboard the space shuttle Atlantis, and safely deorbited in 2000. CGRO had four instruments that covered six decades of the electromagnetic spectrum, from 30 keV to 30 GeV. In order of increasing spectral energy coverage, these instruments were the Burst And Transient Source Experiment (BATSE), the Oriented Scintillation Spectrometer

Experiment (OSSE), the Imaging Compton Telescope (COMPTEL), and the Energetic Gamma Ray Experiment Telescope (EGRET). The Imaging Compton Telescope (COMPTEL) utilizes the Compton Effect and two layers of gamma-ray detectors to reconstruct an image of a gamma-ray source in the energy range 1 to 30 MeV. COMPTEL's upper layer of detectors are filled with a liquid scintillator which scatters an incoming gamma-ray photon according to the Compton Effect. This photon is then absorbed by NaI crystals in the lower detectors. The instrument records the time, location, and energy of the events in each layer of detectors which makes it possible to determine the direction and energy of the original gamma-ray photon and reconstruct an image and energy spectrum of the source.

The silicon detector technology allows today improving the sensitivity of COMPTEL by two orders of magnitude, and also crucially improving the localization accuracy. Two detectors are under evaluation, e-ASTROGAM by ESA and AMEGO by NASA, which use silicon detector planes without converter to build a hodoscope sensitive to both Compton interaction and pair production (Fig. 4.40).
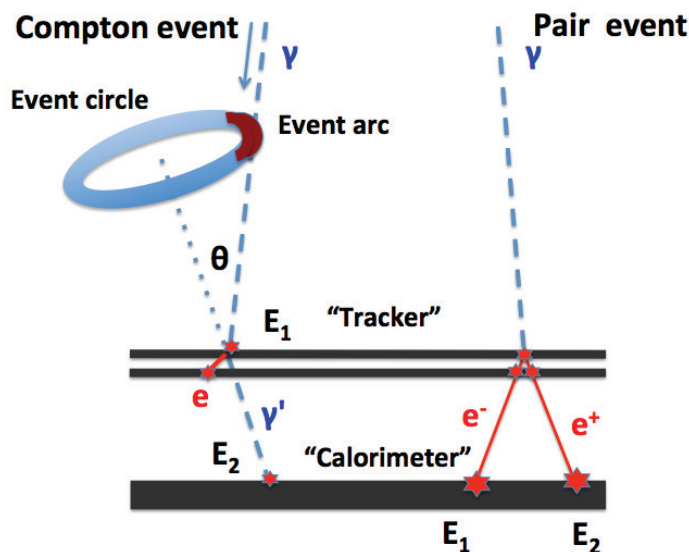

Fig. 4.40 Representative event topologies for a Compton event (left) and for a pair event (right). Photon tracks are shown in pale blue, dashed, and electron and/or positron tracks in red, solid. Courtesy of Alex Moiseev.

3. In the GeV regime, pair production is mostly used to detect photons. Three modern gamma-ray telescopes sensitive to photons in the HE region are in orbit; they are called AGILE, *Fermi* Large Area Telescope (LAT) (Fig. 4.41), and DAMPE.

   Their technology has been inherited from the smaller and less technological EGRET instrument, operational in the years 1991–2000 on the Compton Gamma-Ray Observatory, and from particle physics. The direction of an incident photon is determined through the geometry of its conversion into an e^+e^- pair in foils of heavy materials which compose the instrument, and detected by planes of silicon detectors. The presence of an anticoincidence apparatus realizes a veto against unwanted incoming charged particles. The principle of operation is illustrated in Fig. 4.41, right.

   The angular resolution of these telescopes is limited by the opening angle of the e^+e^- pair, approximately $0.8\,\mathrm{MeV}/E$, and especially by the effect of multiple scattering. To achieve a good energy resolution, in this kind of detector, a calorimeter in the bottom of the tracker is possibly used, depending on the weight that the payload can comply with. Due to weight limitations, however, it is difficult to fit in a calorimeter that completely contains the showers; this leakage downgrades the energy resolution. Since at low energies multiple scattering is the dominant process, the optimal detector design is a tradeoff between small radiation length (which decreases the conversion efficiency) and large number of samplings (which increases the power consumption, limited by the problems of heat dissipation in space).

   Fermi. The largest gamma-ray space-based detector ever built is up to now the *Fermi* observatory, launched in June 2008—and called GLAST before the successful positioning in orbit. It is composed
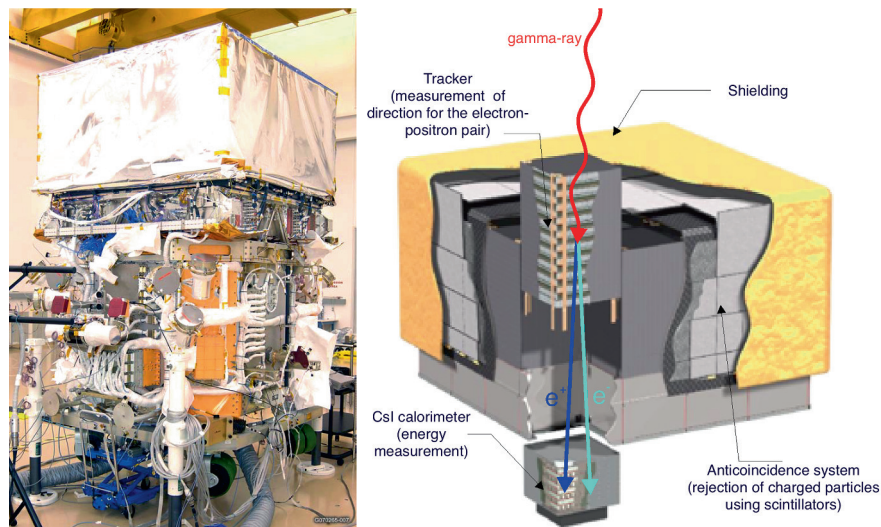
Fig. 4.41 On the left, the *Fermi* satellite. On the right, the layout of the Large Area Telescope (LAT), and principle of operation. Credits: NASA.

of the spacecraft and two instruments: the Large Area Telescope (LAT) and the *Fermi* Gamma Burst Monitor (GBM); the two instruments are integrated and they work as a single observatory.

The structure of the LAT consists mainly of a tracker, an anticoincidence apparatus and a calorimeter (see Fig. 4.41). Its energy range goes from 20 MeV to about 300 GeV and above, while the energy range explored by the GBM is 10–25 MeV. *Fermi* was built and it is operated by an international collaboration with contributions from space agencies, high-energy particle physics institutes, and universities in France, Italy, Japan, Sweden, and the United States; it involves about 600 scientists. After the first year, data are public, i.e., every scientist in the world can in principle analyze them.

The scientific objectives of the LAT include the understanding of the nature of unidentified gamma-ray sources and origins of diffuse Galactic emission; of particle acceleration mechanisms at the sources, particularly in active galactic nuclei, pulsars, supernova remnants, and the Sun; of the high-energy behavior of gamma-ray burst and transient sources. The observations will also be used to probe dark matter and, at high-energy, the early universe and the cosmic evolution of high-energy sources to redshift $z \sim 6$.

The characteristics and performance of the LAT are enabling significant progress in the understanding of the high-energy sky. In particular, it has good angular resolution for source localization and multi-wavelength study, high sensitivity in a broad field-of-view to detect transients and monitor variability, good calorimetry over an extended energy band for detailed emission spectrum studies, and good calibration and stability for absolute, long term flux measurements.

The LAT tracker is composed of 16 planes of high-Z material (W) in which incident γ rays can convert to an e^+e^- pair. The converter planes are interleaved with 18 two-layer planes of silicon detectors that measure the tracks of the particles resulting from pair-conversion. This information is used to reconstruct the directions of the incident γ rays. After the tracker, a calorimeter can measure the energy. It is made of CsI(Tl) crystals with a total depth of 8.6 radiation lengths, arranged in a hodoscope configuration in order to provide longitudinal and transverse information on the energy deposition. The depth and the segmentation of the calorimeter enable the high-energy reach of the LAT and significantly contribute to background rejection. The aspect ratio of the tracker (height/width) is 0.4 (the width being about 1.7 m), resulting in a large field-of-view (2.4 sr) and ensuring that most pair-conversion showers initiated in the tracker will reach the calorimeter for energy measurement. Around the tracker, an anticoincidence detector (ACD) made of plastic scintillator provides charged particle background rejection.

The overall performance of *Fermi* can be summarized as follows in the region of main interest (30 MeV–30 GeV):

- Effective area of about 1 m^2;
- Relative energy resolution decreasing between 10 % at 100 MeV and 5 % at 1 GeV, increasing again to 10 % at 30 GeV; and
- Angular resolution of 0.1° at 10 GeV, and approximately varying as $1/\sqrt{E}$.

AGILE, the precursor of *Fermi*, is a completely Italian satellite launched in April 2007. Its structure is very similar to *Fermi*, but its effective area is about one order of magnitude smaller. However, many remarkable physics results were obtained thanks to the AGILE data.

Finally DAMPE, launched in 2015, has also a structure and an effective area similar to AGILE. It is however characterized by an imaging calorimeter of about 31 radiation lengths thickness, made up of 14 layers of Bismuth Germanium Oxide (BGO) bars in a hodoscopic arrangement – this is the deepest calorimeter ever used in space.

4.5.3.2 Ground-Based Gamma-Ray Detectors

Ground-based VHE gamma-ray detectors–such as HAWC, H.E.S.S., MAGIC, and VERITAS–detect the atmospheric showers produced by primary photons and cosmic rays of energy higher than those observed by satellites.

The two kinds of detectors (on satellite and at the ground) are complementary. At energies below $1\,\text{GeV}$ or so, the showers generated by photons do not have the time to develop properly, and thus the only way to detect such photons below this energy is with the use of satellites. At TeV energies, however, the flux is too low to be detected with satellite-based detectors: due to their cost, and in particular to the cost of the launch, the satellites have areas of the order of $1\,\text{m}^2$ at most, and at these energies even the most luminous gamma-ray sources have a flux smaller than one photon per square meter every ten hours. Ground-based detectors have a huge effective area, so their sensitivity is high; they detect a huge amount of background events, but they have low cost.

The main problem of ground-based detection is the rejection of the background from showers generated by protons. As an example to evaluate the entity of the problem, we consider a source with an emission energy distribution like the Crab Nebula, a nearby (~ 2 kpc away) pulsar wind nebula and the first source detected in VHE gamma rays, and the brightest VHE gamma-ray source visible from both hemispheres–therefore it has become the so-called *standard reference* in VHE gamma-ray astronomy.
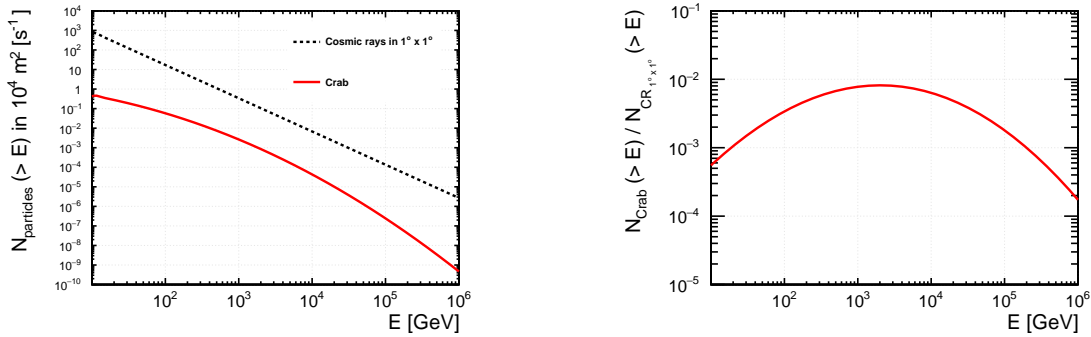
Fig. 4.42 Left: Signal above a given energy on an effective area of 10000 m^2, integrated over 1 second: Crab (solid line) and background from charged cosmic rays within one square degree (dashed line). Right: ratio signal/background from the plot on the left.
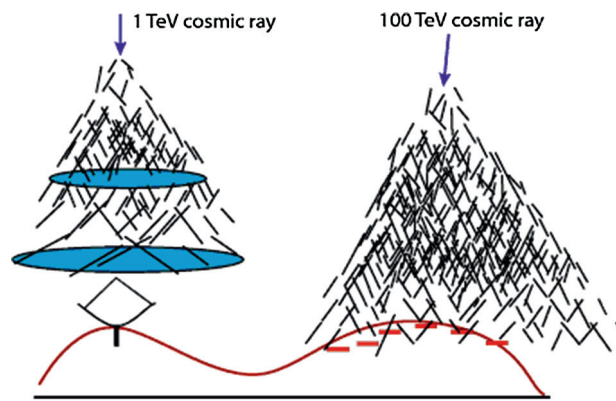
The *stationary* flux from the Crab Nebula in the region from some 20 GeV to about 100 TeV follows approximately a function

$$\frac{dN_\gamma}{dE} \simeq 3.23 \times 10^{-11} \left(\frac{E}{\text{TeV}}\right)^{-2.47-0.24\left(\frac{E}{\text{TeV}}\right)} \text{TeV}^{-1}\text{s}^{-1}\text{cm}^{-2}\,. \tag{4.16}$$

The spectral energy distribution of background cosmic rays can be approximated as

$$\frac{dN}{dE} \simeq 1.8 \times 10^4 \left(\frac{E}{\text{GeV}}\right)^{-2.7} \text{GeV}^{-1}\text{s}^{-1}\text{sr}^{-1}\text{m}^{-2}\,; \tag{4.17}$$

the approximation is valid from some 10 GeV to about 1 PeV.

Fig. 4.43 Sketch of the operation of Cherenkov telescopes and of EAS detectors.

The number of photons from the Crab per m^2 per second above a given threshold are shown in Fig. 4.42, and compared to the background from cosmic rays in a square degree. From this it becomes clear that in order to separate the gamma-ray signal from the background the angular resolution should be of one degree or better, and possibly there should be a way to distinguish electromagnetic showers from hadronic showers (e.g., by their topology or by the presence of muons in hadronic showers).

There are two main classes of ground-based VHE gamma-ray detectors: the EAS arrays and the Cherenkov telescopes (see Fig. 4.43).

EAS Detectors. The EAS detectors, such as MILAGRO, Tibet-AS and ARGO-YBJ in the past, and HAWC which is presently in operation, are large arrays of detectors sensitive to charged secondary particles generated in the atmospheric showers. They have a high duty cycle and a large field-of-view, but a relatively poor sensitivity. The energy threshold of such detectors is rather large—a shower initiated by a 1 TeV photon typically has its maximum at about 8 km a.s.l.

The principle of operation is the same as the one for the UHE cosmic rays detectors like Auger, i.e., direct sampling of the charged particles in the shower. This can be achieved:

- either using a sparse array of scintillator-based detectors, as for example in Tibet-AS (located at 4100 m a.s.l. to reduce the threshold; for an energy of 100 TeV there are about 50 000 electrons at mountain-top altitudes);
- or by effective covering of the ground, to ensure efficient collection and hence lower the energy threshold.
  - The ARGO-YBJ detector at the Tibet site followed this approach. It was of an array of resistive plate counters. Its energy threshold was in the 0.5 TeV-1 TeV range. The Crab Nebula with a significance of about 5 standard deviations (σ) in 50 days of observation.
  - MILAGRO was a water-Cherenkov instrument located in New Mexico (at an altitude of about 2600 m a.s.l.). It detected the Cherenkov light produced by the secondary particles of the shower when they enter the water pool instrumented with photomultipliers. MILAGRO could detect the Crab Nebula with a significance of about 5 σ in 100 days of observation, at a median energy of about 20 TeV.

The energy threshold of EAS detectors is at best in the 0.5–1 TeV range, so they are built to detect UHE photons as well as the most energetic VHE gamma rays. At such energies fluxes are small and large effective areas of order of 10^4 m^2 are required. We remind here that the effective area is the product of the collection area times the detection efficiency; the collection area can be larger than the area covered by the detector, since one can detect showers partially contained – this fact is more relevant for Cherenkov telescopes, see later.

Concerning the discrimination from the charged cosmic ray background, muon detectors devoted to hadron rejection may be present. Otherwise, this discrimination is based on the reconstructed shower shape. The direction of the detected primary particles is computed from the arrival times with an angular precision of about 1° to 2°. The calibration can be performed by studying the shadow in the reconstructed directions caused by the Moon. Energy resolution is poor.

Somehow, the past generation EAS detectors were not sensitive enough and just detected a handful of sources. This lesson lead to a new EAS observatory with much better sensitivity: the High Altitude Water Cherenkov detector HAWC, inaugurated in 2015.

HAWC (Fig. 4.44) is a very high-energy gamma-ray observatory located in Mexico at an altitude of 4100 m. It consists of 300 steel tanks of 7.3 m diameter and 4.5 m deep, covering an instrumented area of about 22 000 m². Each tank is filled with purified water and contains three PMTs of 20 cm diameter, which observe the Cherenkov light emitted in water by superluminal particles in atmospheric air showers. Photons traveling through the water typically undergo Compton scattering or produce an electron–positron pair, also resulting in Cherenkov light emission. This is an advantage of the water Cherenkov technique, as photons constitute a large fraction of the electromagnetic component of an air shower at ground.

HAWC improves the sensitivity for a Crab-like spectrum by a factor of 15 compared to MILAGRO. The sensitivity should be good enough to possibly detect gamma-ray burst emissions at high energy.
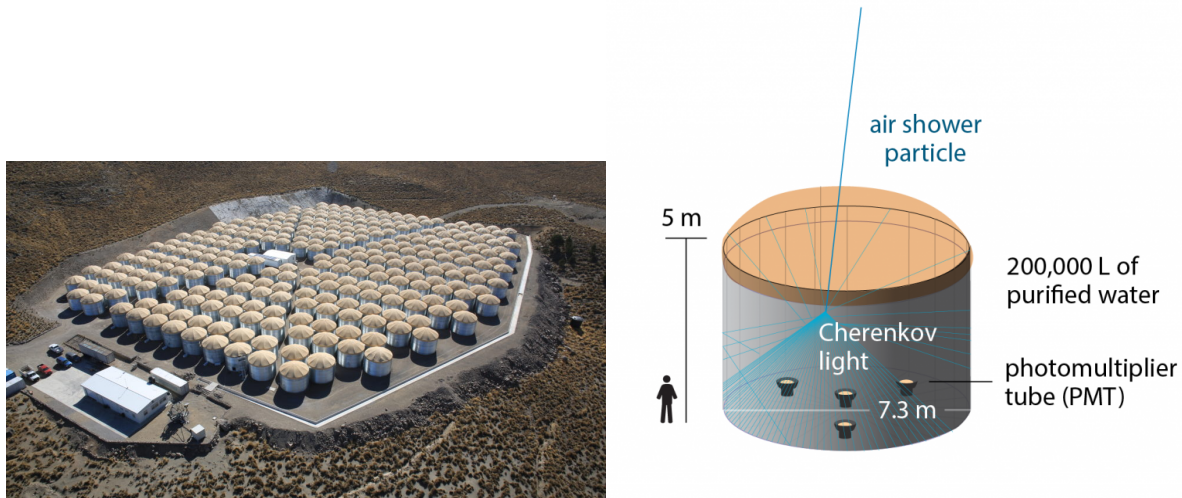
Fig. 4.44 Left: The HAWC detector. Right: Sketch of a water tank. Credit: HAWC Collaboration.

A future installation in the Northern hemisphere, a hybrid detector called LHAASO, is in construction in China. LHAASO covers a total area of about 10^6 m² with more than 5000 scintillation detectors, each of 1 m² area. A central detector of 80 000 square meters (four times the HAWC detector) of surface water pools is equipped with PMTs to study gamma-ray astronomy in the sub-TeV/TeV energy range. About 1200 water tanks underground, with a total sensitive area of about 42 000 m², pick out muons, to separate gamma-ray initiated showers from hadronic showers. 18 wide field-of-view Cherenkov telescopes will complete the observatory. LHAASO will have the best sensitivity on gamma-ray initiated showers above some 10 TeV. One quarter of the observatory should be ready by 2018, and completion is expected in 2021.

Cherenkov Telescopes. Most of the experimental results on VHE photons are presently due to Imaging Atmospheric Cherenkov Telescopes (IACTs), which detect the Cherenkov photons produced in air by charged, locally superluminal particles in atmospheric showers.

WHIPPLE in Arizona was the first IACT to see a significant signal (from the Crab Nebula, in 1989). The second generation instruments HEGRA and CANGAROO, improved the technology, and presently the third generation instruments H.E.S.S. in Namibia, MAGIC in the Canary Islands and VERITAS in Arizona are running smoothly and detecting tens of sources every year. For reasons explained below, these instruments have a low duty cycle (about 1000–1500 h/year) and a small field-of-view (FoV), but they have a high sensitivity and a low energy threshold.

The observational technique used by the IACTs is to project the Cherenkov light collected by a large optical reflector onto a focal camera which is basically an array of photomultipliers, with a typical quantum efficiency of about 30 %, in the focal plane of the reflector (see Fig. 4.45). The camera has a typical diameter of about 1 m, and covers a FoV of about 5° × 5°. The signal collected by the camera is analogically transmitted to trigger systems, similar to the ones used in high-energy physics. The events which pass the trigger levels are sent to the data acquisition system, which typically operates at a frequency of a few hundreds Hz. The typical resolution on the arrival time of a signal on a photomultiplier is better than 1 ns.

The shower has a duration of a few ns (about 2–3) at ground; this duration can be maintained by an isochronous (parabolic) reflector.
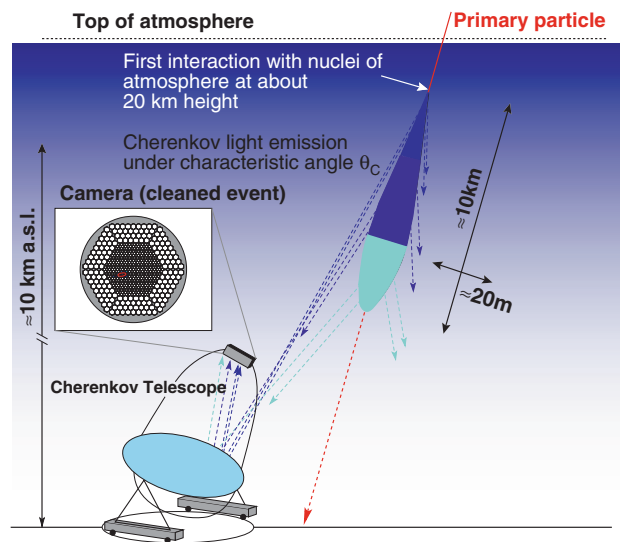
Fig. 4.45 The observational technique adopted by Cherenkov telescopes. From R.M. Wagner, dissertation, MPI Munich 2007.

Since, as discussed above, about 10 photons per square meter arrive in the light pool for a primary photon of 100 GeV, a light collector of area $100 \, \text{m}^2$ is sufficient to detect gamma ray showers if placed at mountain-top altitudes. Due to the faintness of the signal, data can typically be taken only in moonless time, or with moderate moonlight, and without clouds, which limits the total observation time to some 1000-1500 h/year.

In the GeV-TeV region, the background from charged particles is three orders of magnitude larger than the signal. Hadronic showers, however, have a different topology, being larger and more subject to fluctuations than electromagnetic showers. Showers induced by gamma rays can thus be separated from the hadronic ones on the basis of the shower shape. Most of the present identification techniques rely on a technique pioneered by Hillas in the 1980s; the discriminating variables are called "Hillas parameters." The intensity (and area) of the image produced provide an estimate of the shower energy, while the image orientation is related to the shower direction (photons "point" to emission sources, while hadrons are in first approximation isotropic). The shape of the image is different for events produced by photons and by other particles; this characteristic can be used to reject the background from charged particles (Figs. 4.46 and 4.47).

The time structure of Cherenkov images provides an additional discriminator against the hadronic background, which can be used by isochronous detectors (with parabolic shape) and with a signal integration time smaller than the duration of the shower (i.e., better than 1–2 GHz).

Systems of more than one Cherenkov telescope provide a better background rejection, and a better angular and energy resolution than a single telescope.

There are three large operating IACTs: H.E.S.S., MAGIC, and VERITAS; the first located in the Southern hemisphere and the last two in the Northern hemisphere.

- The H.E.S.S. observatory (Fig. 4.48) in Namibia is composed of four telescopes with a diameter of 12 m each, working since early 2003. A fifth large telescope, a surface of about $600 \, \text{m}^2$, is located in the center; it was inaugurated in 2012.
- The MAGIC observatory (Fig. 4.49) in the Canary Island of La Palma is a twin telescope system; each parabola has a diameter of 17 m and a reflecting surface of $236 \, \text{m}^2$.
- VERITAS is constituted by an array of four telescopes with a diameter of 12 m and is located near Tucson, Arizona. It is operational since April 2007.

These instruments are managed by international collaborations of some 150 scientists.

Typical sensitivities of H.E.S.S., MAGIC, and VERITAS are such that a source less than 1 % of the flux of the Crab Nebula can be detected at a 5σ significance in 50 hours of observation.

An overlap in the regions of the sky explored by the IACTs allows an almost continuous observation of sources placed at mid-latitude; there is however space for two more installations, one in South America and one (MACE, in construction) in India.

Agreements between the Cherenkov telescopes and *Fermi* allow a balance between competition and cooperation.
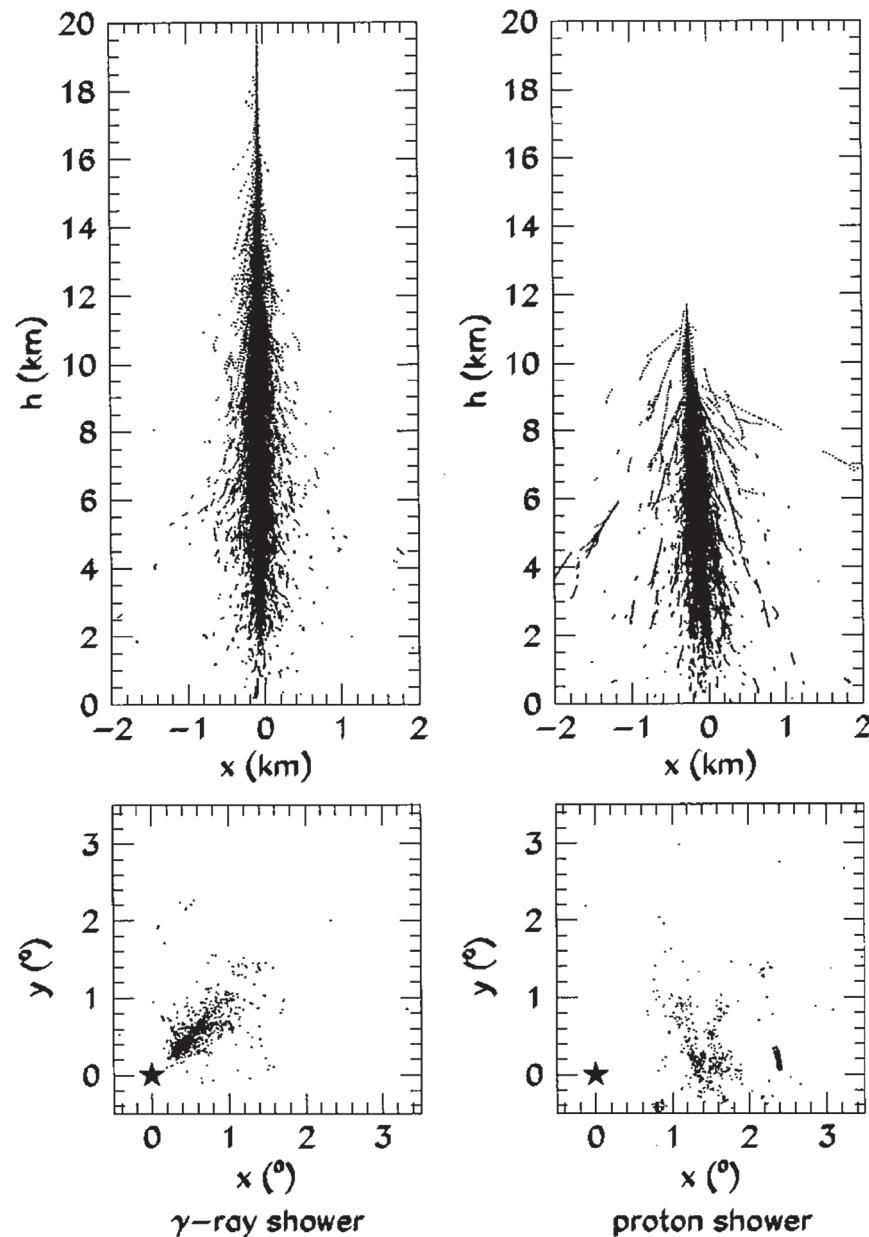
Fig. 4.46 Development of a vertical 1 TeV photon (left) and proton (right) showers in the atmosphere. The upper panels show the positions in the atmosphere of all shower electrons above the Cherenkov threshold; the lower panels show the resulting Cherenkov images in the focal plane of a 10 m reflecting mirror when the showers fall 100 m from the detector (the center of the focal plane is indicated by a star). From C.M. Hoffmann et al., "Gamma-ray astronomy at high energies," Reviews of Modern Physics 71 (1999) 897.

### 4.5.3.3 Summary of the Performance of Gamma-Ray Detectors

A simplified comparison of the characteristics of the *Fermi* LAT satellite detector, of the IACTs and of the EAS detectors (ground-based), is shown in Table 4.4. The sensitivities of the above described high-energy detectors are shown in Fig. 4.50.

A Cherenkov Telescope: MAGIC. We shall now describe in larger detail one of the Cherenkov telescopes: MAGIC. The MAGIC experiment, located at a height of 2200 m a.s.l. on the Canary island of La Palma, is composed of two 17 m diameter IACTs devoted to the observation of VHE gamma rays whith a lower energy threshold of 30 GeV. The first of the MAGIC telescopes started operations in 2004; the second was built some years later allowing stereo observations since autumn 2009.
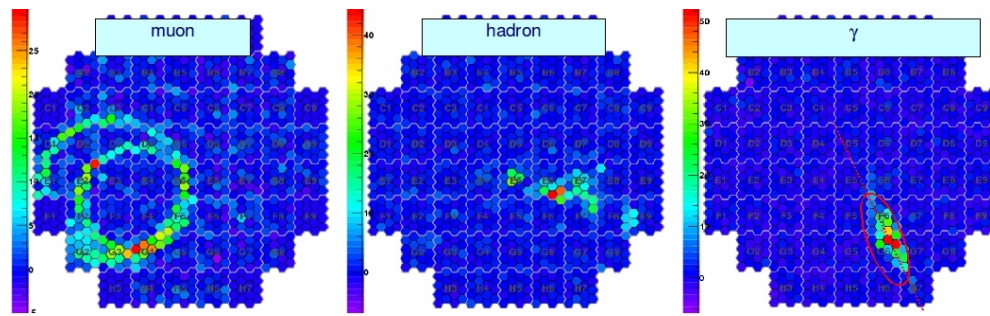
Fig. 4.47 Images from the focal camera of a Cherenkov telescope. The electromagnetic events differ from the hadronic events by several features: the envelope of the electromagnetic shower can be quite well described by an ellipse whereas the important fraction of large transverse momentum particles in hadronic showers will result in a more scattered reconstructed image. Muons are characterized by a conical section. From http://www.isdc.unige.ch/cta/images/outreach/.
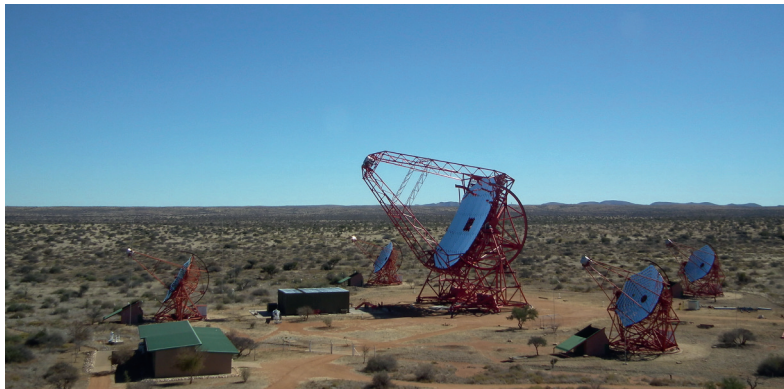
**Fig. 4.48** The H.E.S.S. telescopes. Credit: H.E.S.S. Collaboration.

Fig. 4.49 One of the MAGIC telescopes. Credit: Robert Wagner, University of Stockholm.

MAGIC II was constructed like a copy of MAGIC I with a few improvements–both are built using a light-weight carbon-fiber structure, and the size of the mirror dish (17 m diameter) and the camera field of view (3.5°) are the same. Each MAGIC camera is composed of 1039 0.1° hexagonal pixels (a hexagonal reflecting cone, called Winston cone, collecting the light onto a photomultiplier).

The reflectors are made of square mirrors with a curved surface; each mirror is $1\,\mathrm{m}^2$ in size. Their position can be corrected thanks to an automatic mirror control (AMC) in such a way that they point to the focal camera.

Table 4.4 A comparison of the characteristics of *Fermi*, the IACTs and of the EAS particle detector arrays. Sensitivity computed over one year for *Fermi* and the EAS, and over 50 h for the IACTs.

| Quantity	*Fermi*	IACTs	EAS
Energy range	20 MeV−200 GeV	100 GeV−50 TeV	400 GeV−100 TeV
Energy res.	5–10 %	15–20 %	∼ 50 %
Duty cycle	80 %	15 %	> 90 %
FoV	$4\pi/5$	5 deg × 5 deg	$4\pi/6$
PSF (deg)	0.1	0.07	0.5
Sensitivity	1 % Crab (1 GeV)	1 % Crab (0.5 TeV)	0.5 Crab (5 TeV)
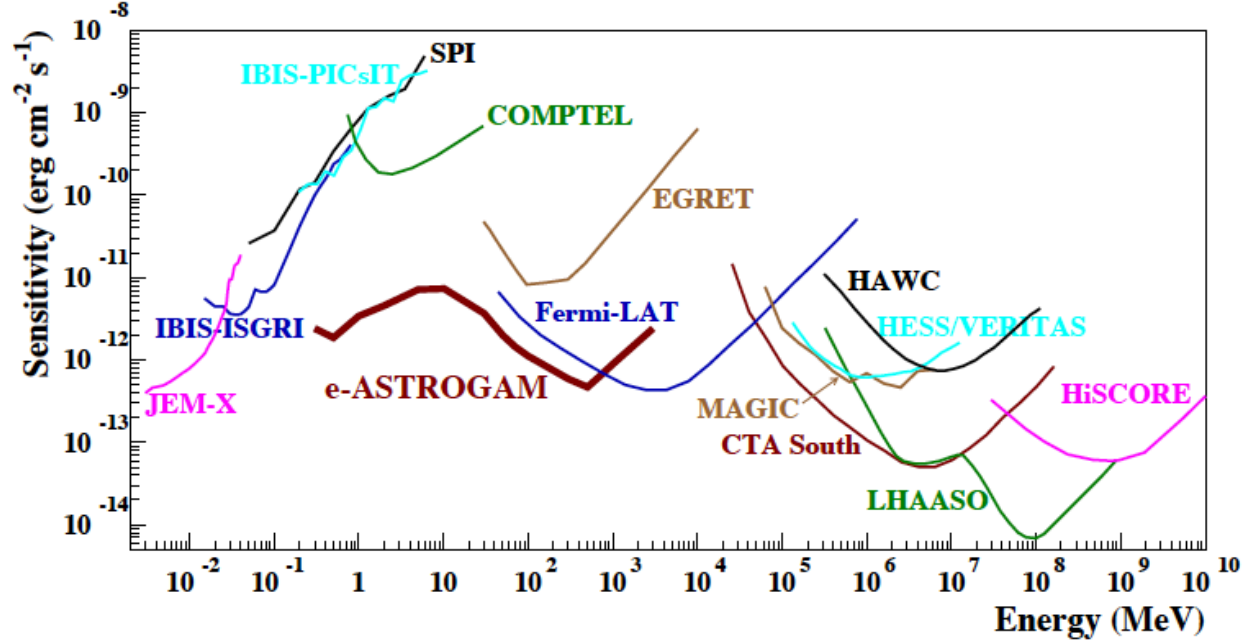
Fig. 4.50 Point source continuum differential sensitivity of different X- and γ-ray instruments. The curves for *INTEGRAL*/JEM-X, IBIS (ISGRI and PICsIT), and SPI are for an effective observation time $T_{obs} = 1$ Ms. The COMPTEL and EGRET sensitivities are given for the typical observation time accumulated during the ∼9 years of the CGRO mission. The *Fermi*/LAT sensitivity is for a high Galactic latitude source in 10 years of observation in survey mode. For MAGIC, H.E.S.S./VERITAS, and CTA, the sensitivities are given for $T_{obs} = 50$ hours. For HAWC $T_{obs} = 5$ yr, for LHAASO $T_{obs} = 1$ yr, and for HiSCORE $T_{obs} = 1000$ h. The e-ASTROGAM sensitivity is calculated at 3σ for an effective exposure of 1 year and for a source at high Galactic latitude.

In both telescopes the signals from the PMT in each pixel are optically transmitted to the counting house where trigger and digitization of the signals take place. The signals of both telescopes are digitized using a frequency of 2 GSample/s.

Regular observations are performed in stereoscopic mode. Only events that trigger both telescopes are recorded. The trigger condition for the individual telescope (level-0 trigger) is that at least 3 neighboring pixels must be above their pixel threshold. The stereo trigger makes a tight time coincidence between both telescopes taking into account the delay due to the relative position of the telescopes and their pointing direction. Although the individual telescope trigger rates are of several kHz, the stereo trigger rate is in the range of 150–200 Hz with just a few Hz being accidental triggers. The lower observational threshold can be reduced to 30 GeV thanks to a dedicated low-energy trigger.

4.5.3.4 Future Detectors for High-Energy Photons

It is difficult to think for this century of an instrument for GeV photons improving substantially the performance of the *Fermi* LAT: the cost of space missions is such that the size of *Fermi* cannot be reasonably overcome with present technologies. New satellites already approved (like the the Chinese-Italian mission
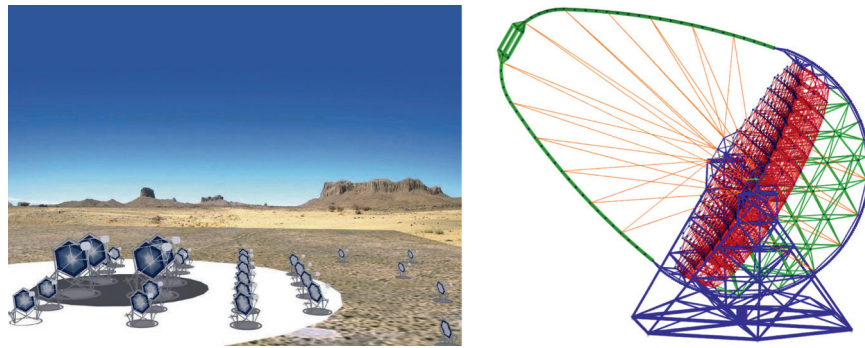
Fig. 4.51 Left: Possible layout of the CTA. Right: Project of the large telescope (LST). Credit: CTA Collaboration.

HERD, for which launch is expected after 2024) will improve some of the aspects of $Fermi$, – in this particular case, calorimetry.

Improvements are possible in the sectors of:

- **keV astrophysics.** The launch of ATHENA is foreseen in 2028, and will improve the sensitivity by two orders of magnitude.
- **MeV astrophysics.** The possible launches of e-ASTROGAM and/or AMEGO in 2028/29 will improve the sensitivity by two orders of magnitude, with a comparable improvement in the quality of data (localization accuracy, measurement of polarization, etc.).
- **TeV gamma-ray astrophysics.** VHE gamma-ray astrophysics in the current era has been dominated by Cherenkov telescopes. We know today that the previous generation EAS telescopes were underdimensioned in relation to the strength of the sources.

  The research in the future will push both on EAS and IACT, which have mutual advantages and disadvantages. The sensitivities of the main present and future detectors are illustrated in Fig. 4.50. We have already seen the characteristics of HAWC, which is under upgrade with the construction of an outtrigger; a very large Cherenkov Telescope Array (CTA) is also in construction.

  The CTA is a future observatory for VHE gamma-ray astrophysics that is expected to provide an order of magnitude improvement in sensitivity over existing instruments.

  An array of tens of telescopes will detect gamma-ray-induced showers over a large area on the ground, increasing the efficiency and the sensitivity, while providing a much larger number of views of each cascade. This will result in both improved angular resolution and better suppression of charged cosmic-ray background events. Three types of telescopes are foreseen:

  - The low energy (the goal is to detect showers starting from an energy of 20 GeV) instrumentation will consist of 23 m large-size telescopes (LST) with a FoV of about 4–5 degrees.
  - The medium energy range, from around 100 GeV–1 TeV, will be covered by medium-size telescopes (MST) of the 12 m class with a FoV of 6–8 degrees.
  - The high-energy instruments, dominating the performance above 10 TeV, will be small size (SST, 4–6 m in diameter) telescopes with a FoV of around 10 degrees.

  CTA will be deployed in two sites. The Southern hemisphere site is less than 10 km from the Paranal Observatory in the Atacama Desert in Chile; it will cover about three square kilometers of land with telescopes that will monitor all the energy ranges in the center of the Milky Way's Galactic plane. It will consist of all three types of telescopes with different mirror sizes (4 LSTs, 25 MSTs and 70 SSTs in the present design). The Northern hemisphere site is located on the existing Roque de los Muchachos Observatory on the Canary island of La Palma, close to MAGIC; only the two larger telescope types (4 LSTs and 15 MSTs in the present design) would be deployed, on a surface of about one square kilometer. These telescopes will be mostly targeted at extragalactic astronomy. The telescopes of different sizes will be arranged in concentric circles, the largest in the center (Fig. 4.51).

  Different modes of operation will be possible for CTA: deep field observation; pointing mode; scanning mode – also pointing to different targets.

- **PeV gamma-ray astrophysics.** Besides LHAASO, already in construction in the Northern hemisphere, another large-FoV detector is in construction in Russia, called HiSCORE (Hundred Square-km Cosmic

ORigin Explorer). Together with a system of Cherenkov telescopes, HiSCORE should form the hybrid array TAIGA.

There is a strong case for a PeV wide-FoV detector in the Southern hemisphere in order to study the highest-energy emissions of accelerators in the Galaxy. Several collaborations are proposing designs for such a detector, and convergence could be reached in the next years.

4.5.4 Neutrino Detection

The energy spectrum of neutrinos interesting for particle and astroparticle physics spans more than 20 orders of magnitude, from the ~ 2 K (~ 0.2 meV) of relic neutrinos from the big bang, to the MeV of reactors, to the few MeV of the solar neutrinos, to the few GeV of the neutrinos produced by the interaction of cosmic rays with the atmosphere (atmospheric neutrinos), to the region of extremely high energy where the production from astrophysical sources is dominant. We concentrate here on the detection of neutrinos of at least some MeV, and we present some of the most important neutrino detectors operating.

Since neutrino cross section is small, it is important that neutrino detectors be located underground or under water to shield from cosmic rays.

4.5.4.1 MeV Neutrinos

Detectors of neutrinos in the MeV range mostly use the detection of the products of induced β decays. The first setups used a solution of cadmium chloride in water and two scintillation detectors as a veto against charged cosmic rays. Antineutrinos with an energy above the 1.8 MeV threshold can cause charged inverse beta-decay interactions with the protons in the water, producing a positron which in turn annihilates, generating photon pairs that can be detected.

Radiochemical chlorine detectors consist instead of a tank filled with a chlorine solution in a fluid. A neutrino converts a ^{37}Cl atom into a ^{37}Ar; the threshold neutrino energy for this reaction is 0.814 MeV. From time to time the argon atoms are counted to measure the number of radioactive decays. The first detection of solar neutrinos was achieved using a chlorine detector containing 470 tons of fluid in the former Homestake Mine near Lead, South Dakota. This measurement evidenced a deficit of electron neutrinos from what expected by the power radiated from the Sun. For this discovery the leader of the experiment, Ray Davis, won the Nobel Prize in physics.[13] A similar detector design, with a lower detection threshold of 0.233 MeV, uses the Ga $\rightarrow$ Ge transition.

4.5.4.2 MeV to GeV Neutrinos

Probably the most important results in the sector of MeV to GeV neutrinos in the recent years are due to a Cherenkov-based neutrino detector, Kamiokande, in Japan. We give here a short description of this detector in its present version, called Super-Kamiokande.

The Super-Kamiokande Detector. Super-Kamiokande (often abbreviated to Super-K or SK) is a neutrino observatory located in a mine 1000 m underground under Mount Kamioka near the city of Hida, Japan. The observatory was initially designed to search for proton decay, predicted by several unification theories (see Sect. 7.6.1).

Super-K (Fig. 4.52) consists of a cylindrical tank about 40 m tall and 40 m in diameter containing 50 000 tons of ultra-pure water. The volume is divided by a stainless steel structure into an inner detector (ID) region (33.8 m in diameter and 36.2 m in height) and an outer detector (OD) consisting of the remaining tank volume. Mounted on the structure are about 11000 PMT 50 cm in diameter that face the ID and 2000 20 cm PMT facing the OD.

The interaction of a neutrino with the electrons or nuclei in the water can produce a superluminal charged particle generating Cherenkov radiation, which is projected as a ring on the wall of the detector and recorded

---

[13] One half of the Nobel Prize in physics 2002 was awarded jointly to the US physicist Raymond Davis Jr. (Washington 1914— New York 2006) and to the leader of the Kamiokande collaboration (see later) Masatoshi Koshiba (Aichi, Japan, 1926) "for pioneering contributions to astrophysics, in particular for the detection of cosmic neutrinos."
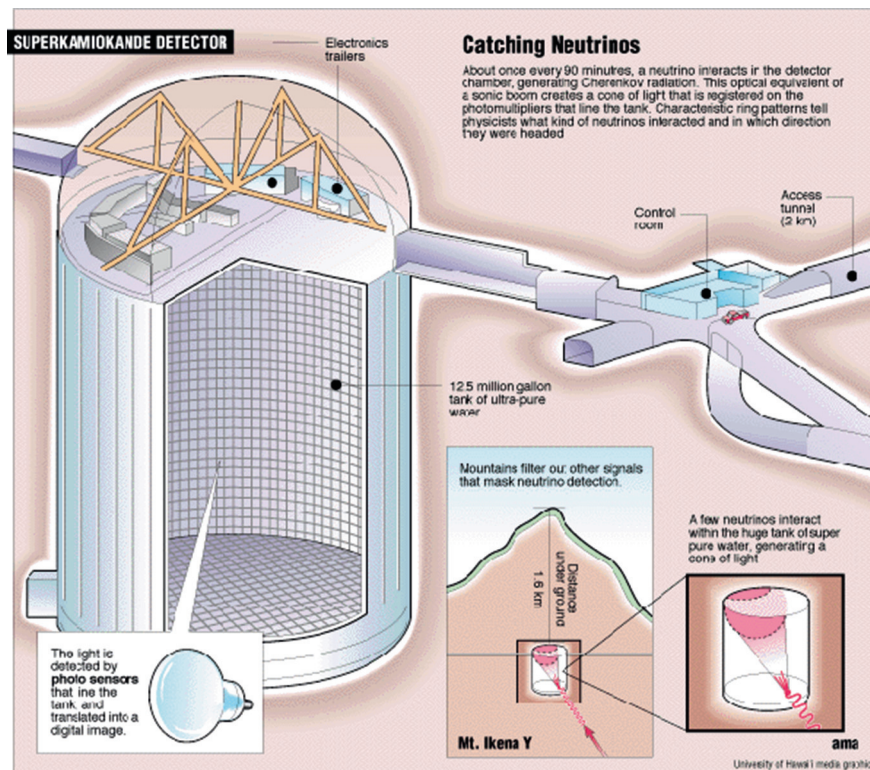
Fig. 4.52 The Super-Kamiokande detector. Credit: Super-Kamiokande Collaboration.

by a PMT. The information recorded is the timing and charge information by each PMT, from which one can reconstruct the interaction vertex, the direction and the size of the cone.

Typical threshold for the detection of electron neutrinos is of about 6 MeV. Electrons lose quickly their energy, and, if generated in the ID, are likely to be fully contained (not penetrating inside the OD). Muons instead can penetrate, and the muon events can be partially contained (or not) in the detector. The threshold for the detection of muon neutrinos is about 2 GeV.

A new detector called Hyper-Kamiokande is envisaged, with a volume 20 times larger than Super-Kamiokande. Construction is expected to start in 2018, and observations might start in 2025.

The SNO Detector. The Sudbury Neutrino Observatory (SNO) uses 1000 tons of heavy water (D_2O) contained in a 12 m diameter vessel surrounded by a cylinder of ordinary water, 22 m in diameter and 34 m high. In addition to the neutrino interactions visible in a detector as SK, the presence of deuterium allows the reaction producing a neutron, which is captured releasing a gamma-ray that can be detected.

4.5.4.3 Very-High-Energy Neutrinos

Very-high-energy neutrinos are expected to be produced in astrophysical objects by the decays of charged pions made in primary cosmic ray interactions with radiation or molecular clouds in astrophysical objects (this is called "hadronic" mechanism). As these pions decay, they produce neutrinos with typical energies one order of magnitude smaller than those of the cosmic-ray nucleons—more or less the same energies as photons. These neutrinos can travel long distances undisturbed by either the absorption experienced by high-energy photons or the magnetic deflection experienced by charged particles, making them a unique tracer of cosmic-ray acceleration. Additional sources can be the interactions of cosmic rays with the atmosphere (atmospheric neutrinos), and decays of heavier particles formed by the interaction of cosmic rays with the CMB, or decay of new, heavy particles.

Above an energy of 100 TeV, the expected atmospheric neutrino background falls to the level of one event per year per cubic kilometer, and any (harder) astrophysical flux can be clearly seen.

The challenge in the field of UHE neutrinos is to build telescopes with good enough sensitivity to see events, since the flux is expected to be lower than the photon flux (the main mechanism for the production
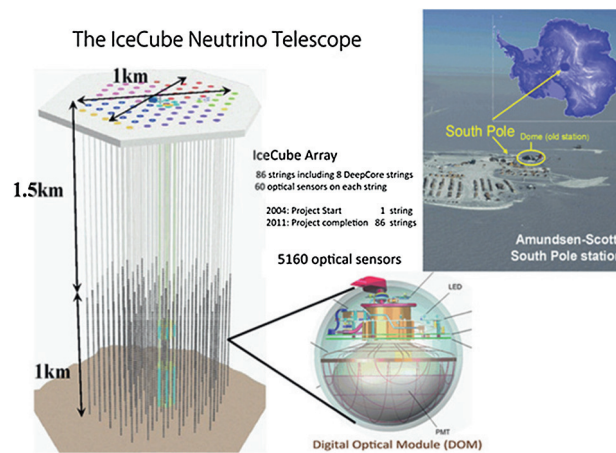
Fig. 4.53 The IceCube detector. Credit: http://www.icehap.chiba-u.jp/en/frontier/.

of neutrinos, i.e., the hadronic mechanism, is common to photons, which in addition can be produce via a "leptonic" mechanism as we shall see in Chap. 10). This requires instrumenting very large volumes. Efforts to use large quantities of water and ice as detectors are ongoing. Several experiments are completed, operating, or in development using Antarctic ice, the oceans, and lakes, with detection methods including optical and coherent radio detection as well as particle production.

Among the experiments in operation, the largest sensitivity detectors are Baikal NT-200 and IceCube.

Baikal NT-200 Detector. The underwater neutrino telescope NT-200 is located in the Siberian lake Baikal at a depth of approximately 1 km and is taking data since 1998. It consists of 192 optical sensors deployed in eight strings, with a total active volume of 5 million cubic meters. Deployment and maintenance are carried out during winter, when the lake is covered with a thick ice sheet and the sensors can easily be lowered into the water underneath. Data are collected over the whole year and permanently transmitted to the shore over electrical cables.

The IceCube Experiment. IceCube, a cube of $1 \, km^3$ instrumented in the Antarctica ices, has been in operation at the South Pole since 2010 (Fig. 4.53). The telescope views the ice through approximately 5160 sensors called digital optical modules (DOMs). The DOMs are attached to vertical strings, frozen into 86 boreholes, and arrayed over a cubic kilometer from 1 450 meters to 2 450 meters depth. The strings are deployed on a hexagonal grid with 125 meters spacing and hold 60 DOMs each. The vertical separation of the DOMs is 17 meters. Eight of these strings at the center of the array were deployed more compactly, with a horizontal separation of about 70 meters and a vertical DOM spacing of 7 meters. This denser configuration forms the DeepCore subdetector, which lowers the neutrino energy threshold to about 10 GeV, creating the opportunity to study neutrino oscillations. At the surface, an air-shower array is coupled to the detector. As the Earth is opaque to UHE neutrinos, detection of extremely high-energy neutrinos must come from neutrinos incident at or above the horizon, while intermediate energy neutrinos are more likely to be seen from below.

IceCube detects a dozen of very-high-energy events per year consistent with astrophysical sources. The IceCube sensitivity will soon reach the high-energy neutrino fluxes predicted in cosmogenic neutrino models.

KM3NeT. A large underwater neutrino detector, KM3NeT, is planned. KM3NeT will host a neutrino telescope with a volume of several cubic kilometers at the bottom of the Mediterranean sea. This telescope is foreseen to contain of the order of 12 000 pressure-resistant glass spheres attached to about 300 detection units—vertical structures with nearly one kilometer in height. Each glass sphere will contain 31 photomultipliers and connected to shore via a high-bandwidth optical link. At shore, a computer farm will perform the first data filtering in the search for the signal of cosmic neutrinos. KM3NeT builds on the experience of three pilot projects in the Mediterranean sea: the ANTARES detector near Marseille, the NEMO project in Sicily, and the NESTOR project in Greece. ANTARES was completed in 2008 and is the largest neutrino telescope in the Northern hemisphere.
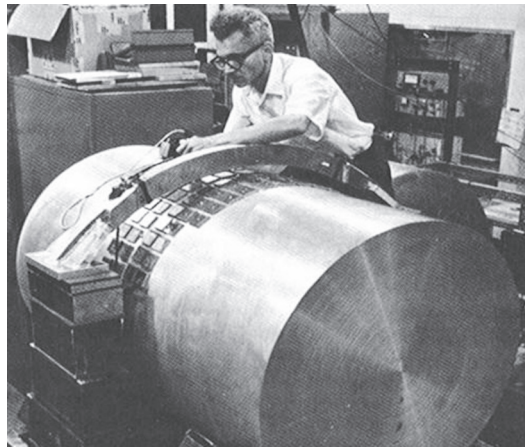
Fig. 4.54 Joseph Weber working on his gravitational antenna (1965). From http://www.physics.umd.edu/.

4.6 Detection of Gravitational Waves

Gravitational waves are generated by aspherical motions of matter distributions; they propagate at the speed of light, bringing curvature of space time information. Their effect on matter is to change the relative distances. This effect is however small, and even the most violent astrophysical phenomena (e.g., colliding black holes or neutron stars, collapsing stars) emit gravitational waves which, given the typical distance to the event, are expected to cause relative shifts on distances of only 10^{-20} on Earth. In fact, gravitational waves were predicted by Albert Einstein in his theory of general relativity roughly 100 years ago, but only recently has technology enabled us to detect them.

A figure of merit for a detector is the space strain ℓ:

$$\Delta L/L \sim \ell$$

where L is the distance between the two masses and ΔL is its variation. Another one is the horizon distance, i.e., the maximum range out to which it could see the coalescence of two 1.4 $M_\odot$ neutron stars.

The idea explored first to detect gravitational waves was to detect the elastic energy induced by the compression/relaxation of a metal bar due to the compression/relaxation of distance. Detectors were metal cylinders, and the energy converted to longitudinal oscillations of the bar was measured by piezoelectric transducers. The first large gravitational wave detector, built by Joseph Weber in the early 1960s, was a 1.2 ton aluminum cylindrical bar of 1.5 m length and 61 cm diameter (Fig. 4.54) working at room temperature and isolated as much as possible from acoustic and ground vibrations. The mechanical oscillation of the bar was translated into electric signals by piezoelectric sensors placed in its surface close to the central region. The detector behaved as a narrow band high$-Q$ (quality factor) mechanical resonator with a central frequency of about 1600 Hz. The attenuation of the oscillations is, in such devices, very small and therefore the bar should oscillate for long periods well after the excitation induced by the gravitational waves. The sensitivity of Weber's gravitational antenna was of the order of $\ell \sim 10^{-16}$ over timescales of 10^{-3} s. Bar detectors (ALLEGRO, AURIGA, Nautilus, Explorer, Niobe) reached sensitivities of $\ell \sim 10^{-21}$, thanks to the introduction of cryogenic techniques which allow for a substantial reduction in the thermal noise as well as the use of very performing superconducting sensors. However, their frequency bandwidths remain very narrow ($\sim$tens of Hz) and the resonant frequencies ($\sim$1 kHz) correspond typically to acoustic wavelengths of the order of the detector length. A further increase in sensitivity implies a particular attention to the quantum noise, and thus a considerable increase of the detector mass (bars with hundred tons of mass are being considered).

Nowadays the most sensitive interferometers are Michelson-type interferometers with kilometer-long arms and very stable laser beams (see Fig. 4.55). Resonant Fabry-Perot cavities are installed along their arms in a way that the light beams suffer multiple reflections increasing by a large factor the effective arm lengths. The lengths of the perpendicular arms of the interferometer will be differently modified by the incoming gravitational wave and the interference pattern will change accordingly. These detectors are per nature broadband, being their sensitivity limited only by the smallest time difference they are able to measure. Thanks to the Fabry-Perot cavities, the present and the aimed sensitivities ($\ell \sim 10^{-22} - 10^{-24}$) correspond
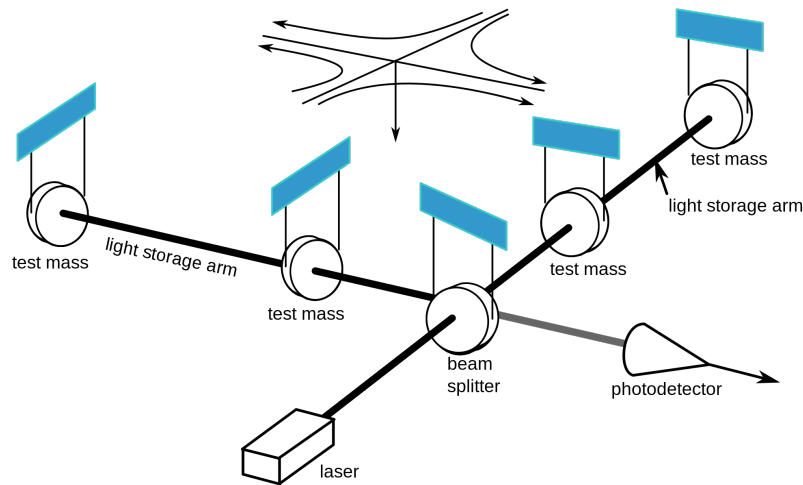
Fig. 4.55 Sketch of a Michelson interferometer. A monochromatic laser light is split into two beams by the beam splitter which travel along the two perpendicular arms. The laser light moves back and forth in the two arms between the two mirrors depicted as test masses (Fabry-Perot cavity) and is then made to combine again to form an interference pattern. A gravitational wave passing through (also depicted in the figure) will change the length of one arm with respect to another, causing relative phase shift of the laser light and thus in the interference pattern. Credit: LIGO Collaboration.

to interferences over distances many orders of magnitude ($\sim 10^{14} - 10^{16}$) smaller than the dimension of an atom, and thus both the stability of the laser beam and the control of all possible noise sources are critical. These noise sources may be classified as thermal, readout, and seismic:

- The thermal noise is associated to the Brownian motion of the test masses due to the impact of the surrounding air molecules, to their internal vibrations, and to the morror suspensions. To minimize such effects the rest masses should be placed in a high vacuum environment and the frequencies of the intrinsic resonances of the system should be set as far as possible from the target signal frequency band.
- The intrinsic readout noise is due to the fluctuations induced by the quantum nature of the interaction of the laser light beams with the mirrors. The light beams may be modeled as discrete set of photons obeying in their arrival time to the mirror to Poisson statistics. The number of photons measured in a time window has a statistical intrinsic fluctuation ("shot noise"); its effects on sensitivity decrease with the increasing of the laser power. On the other hand, the increase of the laser power increases the momentum transfer to the mirrors ("radiation pressure"), which will change the phase of the beams. To minimize such contradictory effects, the tests masses should be as heavy as possible and the Heisenberg uncertainties relations (the quantum limit) carefully handled.
- The seismic noise accounts for all the natural or human-made perturbations comprising a large range of diversified phenomena like earthquakes, environment perturbations or nearby automobile traffic. The measured spectrum of such noise, in a quiet location, decreases with the frequency and imposes already an important sensitivity constraint to the next generation of laser interferometer detectors. To minimize such effects, the test masses are isolated from ground through several attenuation stages characterized by resonance frequencies much lower than the expected signal frequencies. To access lower frequencies (1–10 Hz), the possibility to build large interferometers underground in a low seismic region are being studied. To go further into the 10^{-4}–10^{-1} Hz region it will be necessary to build large arm interferometer in space.

The largest gravitational wave observatories operating at present are the Laser Interferometer Gravitational Wave Observatory (LIGO) and Virgo. LIGO is built over two sites in the US (at Hanford, Washington, and at Livingston, Louisiana, 3 000 km apart), each one with a 4 km arm interferometer, while Virgo is installed near Pisa, Italy, and consists of a 3 km arm interferometer. A Japanese underground detector known as KAGRA which is 3 km in arm length is being commissioned right now and should start operating in 2019. A third LIGO detector is planned to be built in India before 2024. A close collaboration among all of the gravitational waves observatories is in place.

The first detection of gravitational waves was performed by LIGO in 2015; the signal was generated by two black holes with respectively 36 and 29 solar masses that merged into a 62 solar masses BH, thus releasing
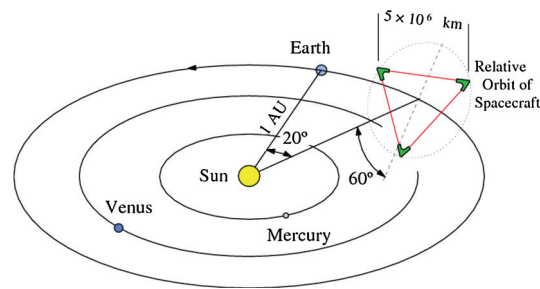
Fig. 4.56 The proposed LISA detector (the size is increased by a factor of 10). From M. Pitkin et al., "Gravitational Wave Detection by Interferometry (Ground and Space)," http://www.livingreviews.org/lrr-2011-5.
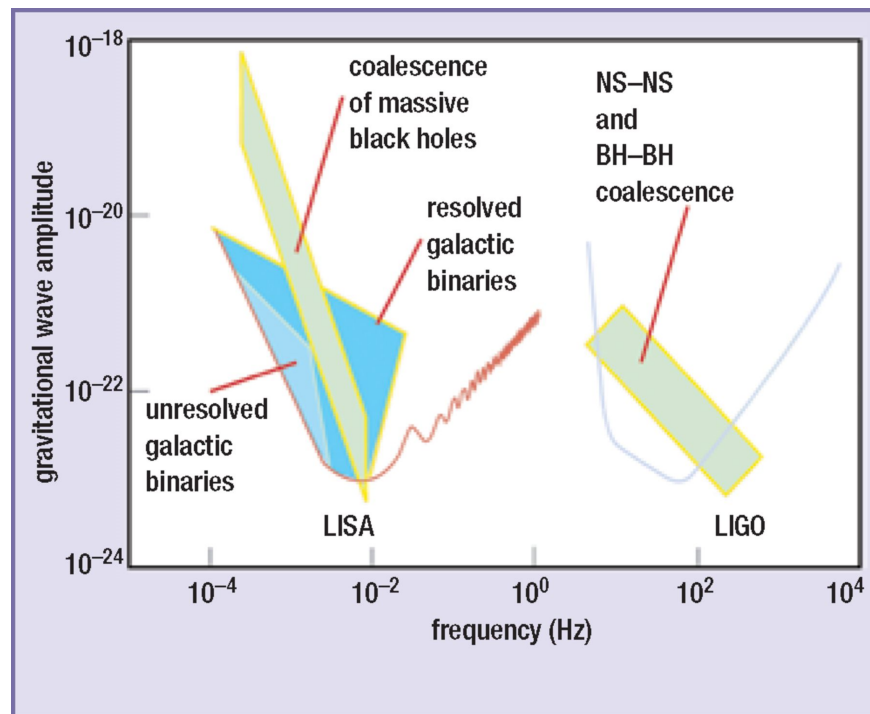
Fig. 4.57 Present and expected sensitivities of gravitational wave detectors. From M. Hendry and G. Woan, Astronomy & Geophysics 48 (2007) 1.

an energy corresponding to releasing 3 $M_\odot c^2$ - mostly in gravitational waves. Now we have a handful of signals of different phenomena, as we shall discuss in Chap. 10.

The development of new detectors (for example interferometers in space) will allow us to explore different frequency bands, and to detect gravitational waves generated by different astrophysical processes. In a more distant future a space observatory will be built extending the detection sensitivity to a much lower frequency range (10^{-4}–10^{-1} Hz). The LISA project, comprising three satellite detectors spaced by more than 2.5 million kilometers (Fig. 4.56), has been approved by ESA; launch is scheduled in the year 2034.

The present and expected sensitivities of gravitational wave detectors are summarized in Fig. 4.57.

Further Reading

- [F4.1] B. Rossi, "High-Energy Particles," Prentice-Hall, New York 1952. Still a fundamental book on particle detection, in particular related to the interaction of particles with matter and to multiplicative showers.
- [F4.2] K. Kleinknecht, "Detectors for Particle Radiation" Cambridge University Press 1986.
- [F4.3] W.R. Leo, "Techniques for Nuclear and Particle Physics Experiments," Springer Verlag 1994.

Exercises

1. *Muon energy loss.* A muon of 100 GeV crosses a layer of 1 m of iron. Determine the energy loss and the expected scattering angle.

2. *Energy loss in a water Cherenkov detector.* In the Pierre Auger Observatory the surface detectors are composed of water Cherenkov tanks 1.2 m high, each containing 12 tons of water. These detectors are able to measure the light produced by charged particles crossing them. Consider one tank crossed by a single vertical muon with an energy of 5 GeV. The refraction index of water is $n \simeq 1.33$ and can be in good approximation considered constant for all the relevant photon wavelengths. Determine the energy lost by ionization and compare it with the energy lost by Cherenkov emission.

3. *Cherenkov radiation.* A proton with momentum 1.0 GeV/c passes through a gas at high pressure. The index of refraction of the gas can be changed by changing the pressure. Compute: (a) the minimum index of refraction at which the proton will emit Cherenkov radiation; (b) the Cherenkov radiation emission angle when the index of refraction of the gas is 1.6.

4. *Pair production and multiple scattering.* What is the optimal thickness (in radiation lengths) of a layer of silicon in a gamma-ray telescope with hodoscopic structure in order that the multiple scattering does not deteriorate the information from the opening angle of the electron-positron pair in a photon conversion?

5. *Compton scattering.* A photon of wavelength λ is scattered off a free electron initially at rest. Let λ' be the wavelength of the photon scattered in the direction θ. Compute: (a) λ' as a function of λ, θ and universal parameters; (b) the kinetic energy of the recoiling electron.

6. *Reconstruction of a Compton interaction event.* Detecting gamma rays by Compton scattering in a gamma-ray telescope with hodoscopic structure (Fig. 4.40) is more complicated than for pair production. The Compton scattering of the incident photon occurs in one of the tracker planes, creating an electron and a scattered photon. The tracker measures the interaction location, the electron energy, and in some cases the electron direction. The scattered photon can be absorbed in the calorimeter where its energy and absorption position are measured.

   Suppose that an incident gamma-ray Compton scatters by an angle Θ in one layer of the tracker, transferring energy E_1 to an electron. The scattered photon is then absorbed in the calorimeter, depositing its energy E_2, Demonstrate that the scattering angle is given by $\cos \Theta = m_e c^2/E_2 + m_e c^2/(E_1 + E_2)$, where m_e is the electron mass. With this information, one can derive an "event circle" from which the original photon arrived – this sort of Compton events are called "untracked". Multiple photons from the same source enable a full deconvolution of the image, using probabilistic techniques.

   For energetic incident gamma rays (above ∼1 MeV), measurement of the track of the scattered electron might in addition be possible, resulting in a reduction of the event circle to a definite direction. If the scattered electron direction is measured, the event circle reduces to an event arc with length due to the uncertainty in the electron direction reconstruction, allowing improved source localization. This event is called "tracked", and its direction reconstruction is somewhat similar to that for pair event – the primary photon direction is reconstructed from the direction and energy of two secondary particles: scattered electron and photon. Comment.

7. *Nuclear reactions.* The mean free path of fast neutrons in lead is of the order of 5 cm. What is the total fast neutron cross section in lead?

8. *Range.* Compare approximately the ranges of two particles of equal velocity and different mass and charge traveling through the same medium.

9. *Hadron therapy.* The use of proton and carbon ion beams for cancer therapy can reduce the complications on the healthy tissue compared to the irradiation with MeV gamma rays. Discuss why.

10. *Neutrino interaction in matter.* For neutrinos produced in nuclear reactors typical energies are $E_\nu \sim 1$ MeV. What is the probability to interact in a water detector with the thickness of one meter? What is the probability to interact inside the Earth traveling along a trajectory that passes through its center? Answer the same questions for a neutrino of energy of 1 PeV.

11. *Electromagnetic showers.* How does an electromagnetic shower evolve as a function of the penetration depth in a homogeneous calorimeter? What is the difference between an incoming photon and an incoming electron/positron?

12. *Hadronic showers.* Let us approximate the effective cross section for protons on nucleons in air with a value of 20 mb. Calculate the interaction length of a proton (in g/cm^2, and in meters at NTP). What is the average height above the sea level where this interaction takes place? In hadronic showers we find also an electromagnetic component, and muons. Where do these come from?

13. *Tracking detectors.* Could you build a tracking detector for photons? And for neutrinos?

14. *Photodetectors.* What gain would be required from a photomultiplier in order to resolve the signal produced by three photoelectrons from that due to two or four photoelectrons? Assume that the fluctuations in the signal are described by Poisson statistics, and consider that two peaks can be resolved when their centers are separated by more than the sum of their standard deviations.

15. *Cherenkov counters.* Estimate the minimum length of a gas Cherenkov counter used in the threshold mode to be able to distinguish between pions and kaons with momentum 20 GeV. Assume that 200 photons need to be radiated to ensure a high probability of detection and that radiation covers the whole visible spectrum (neglect the variation with wavelength of the refractive index of the gas).

16. *Electromagnetic calorimeters.* Electromagnetic calorimeters have usually 20 radiation lengths of material. Calculate the thickness (in cm) for calorimeters made of of BGO, $PbWO_4$ (as in the CMS experiment at LHC), uranium, iron, tungsten, and lead. Take the radiation lengths from Appendix B or from the Particle Data Book.

17. *The HERA collider.* The HERA accelerator collided protons at energy $E_p \simeq 820$ GeV with electron at $E_e \simeq 820$ GeV. Which value of E_e would be needed to obtain the same center-of-mass energy at an *ep* fixed target experiment?

18. *The LHC collider.* What is the maximum energy for a tunnel 27 km long with a maximum magnetic field in the vacuum tube of 8.36 T?

19. *Focusing in the LHC.* The diameter of the vacuum tube in LHC is 18 mm. How many turns and for how long can a proton beam stay vertically in the tube if you do not focus it?

20. *Collisions in the LHC.* In the LHC ring there are 2835 bunches in each ring which collide which each other once in each detector. How many collisions of bunches are there in

   (a) one second,
   (b) one run which will last about 10 hours.

21. *Luminosity.* How much integrated luminosity does an experiment need to collect in order to measure at better than 1% the rate of a process with cross section of 1 pb ?

24. *Synchrotron radiation.* Consider a circular synchrotron of radius R_0 which is capable of accelerating charged particles up to an energy E_0. Compare the radiation emitted by a proton and an electron and discuss the difficulties to accelerate these particles with this technology.

26. *Bending radius of cosmic rays from the Sun.* What is the bending radius of a solar proton, 1 MeV kinetic energy, in the Earth's magnetic field (0.5 G), for vertical incidence with respect to the field?

27. *Low Equatorial Orbit.* Low-Earth Orbits (LEOs) are orbits between 300 km and 2000 km from the ground; the altitude is optimal in order to protect them from cosmic rays, thanks to the Van Allen radiation belts. Due to atmospheric drag, satellites do not usually orbit below 300 km. What is the velocity of an Earth satellite in a LEO and how does it compare to the escape velocity from Earth? How many revolutions per day does it make? Suppose that the satellite sees a solid angle of $2\pi/5$, and that it rolls: after how many hours it will observe all the sky?

28. *Electromagnetic showers in the atmosphere.* If a shower is generated by a gamma ray of $E = 1$ TeV penetrating the atmosphere vertically, considering that the radiation length X_0 of air is approximately 37 g/cm^2 and its critical energy E_c is about 88 MeV, calculate the height h_M of the maximum of the shower in the Heitler model and in the Rossi's approximation B.

29. *Extensive electromagnetic air showers.* The main characteristic of an electromagnetic shower (say, initiated by a photon) can be obtained using a simple Heitler model. Let E_0 be the energy of the primary particle and consider that the electrons, positrons and photons in the cascade always interact after traveling a certain atmospheric depth $d = X_0$, and that the energy is always equally shared between the two particles. With this assumptions, we can schematically represent the cascade as in Fig. 4.10.

   (a) Write the analytical expressions for the number of particles and for the energy of each particle at depth X as a function of d, n and E_0.
   (b) The multiplication of the cascade stop when the particles reach a critical energy, E_c (when the decay probability surpasses the interaction probability). Using the expressions obtained in the previous question, write as a function of E_0, E_c and $\lambda = d/\ln(2)$, the expressions, at the shower maximum, for:
      i. the average energy of the particles,
      ii. the number of particles, $N_{\max}$,
      iii. the atmospheric depth $X_{\max}$.

30. *Extensive hadronic air showers.* Consider a shower initiated by a proton of energy E_0. We will describe it with a simple Heitler-like model: after each depth d an equal number of pions, n_π, and each of the 3

types is produced: π^0, π^+, π^-. Neutral pions decay through $\pi^0 \to \gamma\gamma$ and their energy is transferred to the electromagnetic cascade. Only the charged pions will feed the hadronic cascade. We consider that the cascade ends when these particles decay as they reach a given decay energy E_{dec}, after n interactions, originating a muon (plus an undetected neutrino).

(a) How many generations are needed to have more that 90 % of the primary energy, E_0 in the electromagnetic component?
(b) Assuming the validity of the superposition principle, according to which a nucleus of mass number A and energy E_0 behaves like A nucleons of energy E_0/A, derive expressions for:
  i. the depth where this maximum is reached, $X_{\max}$,
  ii. the number of particles at the shower maximum,
  iii. the number of muons produced in the shower, N_μ.

31. *Cherenkov telescopes.* Suppose you have a Cherenkov telescope with 7 m diameter, and your camera can detect a signal only when you collect 100 photons from a source. Assuming a global efficiency of 0.1 for the acquisition system (including reflectivity of the surface and quantum efficiency of the PMT), what is the minimum energy (neglecting the background) that such a system can detect at a height of 2 km a.s.l.?

32. *Cherenkov telescopes and muon signals.* Show that the image of the Cherenkov emission from a muon in the focal plane of a parabolic IACT is a conical section (approximate the Cherenkov angle as a constant).

33. *Imaging Array Cherenkov Telescopes.* In the isothermal approximation, the depth x of the atmosphere at a height h (i.e., the amount of atmosphere above h) can be approximated as

$$x \simeq X e^{-h/7\,\mathrm{km}},$$

with $X \simeq 1030$ g/cm^2. If a shower is generated by a gamma ray of $E = 1$ TeV penetrating the atmosphere vertically, considering that the radiation length X_0 of air is approximately 36.6 g/cm^2 (440 m) and its critical energy E_c is about 88 MeV and using Rossi's approximation B (Table 4.1):

(a) Calculate the height h_M of the maximum of the shower in the Heitler model and in the Rossi's approximation B.
(b) If 2000 useful Cherenkov photons per radiation length are emitted by charged particles in the visible and near UV, compute the total number N_γ of Cherenkov photons generated by the shower (note: the critical energy is larger than the Cherenkov threshold).
(c) Supposing that the Cherenkov photons are all emitted at the center of gravity of the shower—that in the Heitler approximation is just the maximum of the shower minus one radiation length, compute how many photons per square meter arrive to a detector at a height h_d of 2000 m, supposing that the average attenuation length of photons in air is 3 km, and that the light pool can be derived by a opening of $\sim 1.3°$ from the shower maximum (1.3° is the Cherenkov angle and 0.5°, to be added in quadrature, comes from the intrinsic shower spread). Comment on the size of a Cherenkov telescope, considering an average reflectivity of the mirrors (including absorption in transmission) of 70 %, and a photodetection efficiency (including all the chains of acquisition) of 20 %.
(d) Redo the calculations for $E = 50$ GeV, and comment.

Chapter 8
The Standard Model of Cosmology and the Dark Universe

Alessandro De Angelis and Mário Pimenta

This chapter introduces the observational data on the structure, composition, and evolution of the Universe, within the framework of the theory of general relativity, and describes the model currently providing the best quantitative description. In particular, we will illustrate the experimental evidence suggesting the existence of new forms of matter of energy, and describe the expansion, the chemical evolution, and the formation of structures, from the beginning of time—that, we believe, started with a phase transition from a singularity: the "big bang".

The origin and fate of the Universe is, for many researchers, the fundamental question. Many answers were provided over the ages, a few of them built over scientific observations and reasoning. During the last century important scientific theoretical and experimental breakthroughs occurred after Einstein's proposal of the General Theory of Relativity in 1915, with precise and systematic measurements establishing the expansion of the Universe, the existence the Cosmic Microwave Background, and the abundances of light elements in the Universe. The fate of the Universe can be predicted from its energy content—but, although the chemical composition of the Universe and the physical nature of its constituent matter have occupied scientists for centuries, we do not know yet this energy content well enough.

We are made of protons, neutrons, and electrons, combined into atoms in which most of the energy is concentrated in the nuclei (baryonic matter); and we know a few more particles (photons, neutrinos, ...) accounting for a limited fraction of the total energy of atoms. However, the motion of stars in galaxies, as well as results about background photons in the Universe (both will be discussed in the rest of this chapter) are inconsistent with the presently known laws of physics, unless we assume that a new form of matter exists. This matter is not visible, showing little or no interaction with photons—we call it "dark matter". It is, however, important in the composition of the Universe, because its energy is a factor of five larger than the energy of baryonic matter.

Recently, the composition of the Universe has become even more puzzling, as observations imply an accelerated expansion. Such an acceleration can be explained by a new, unknown, form of energy—we call it "dark energy"—generating a repulsive gravitational force. Something is ripping the Universe apart.

The current view on the distribution of the total budget between these forms of energy is shown in Fig. 1.8. Note that we are facing a new Copernican revolution: we are not made of the same matter that most of the Universe is made of. Moreover, the Universe displays a global behavior difficult to explain, as we shall see in Sect. 8.1.1.

Today, at the beginning of the twenty-first century, the Big Bang model with a large fraction of dark matter (DM) and dark energy is widely accepted as "the standard model of cosmology", but no one knows what the "dark" part really is, and thus the Universe and its ultimate fate remain basically unknown.

8.1 Experimental Cosmology

About one century ago, we believed that the Milky Way was the only galaxy; today, we have a more-refined view of the Universe, and the field of experimental cosmology probably grows at a faster rate than any other field in physics. In the last century, we obtained unexpected results about the composition of the Universe, and its global structure.

8.1.1 The Universe is Expanding

As introduced in Chap. 1, striking evidence that the Universe is expanding comes from the observation that most galaxies are receding in all directions with radial velocities v proportional to their distance d from us. This is the famous Hubble law

$$v = H_0 \, d, \tag{8.1}$$

where $H_0 \simeq 68$ km s^{-1}Mpc^{-1} is the so-called Hubble constant (we shall see that it is not at all constant, and can change during the history of the Universe) which is often expressed as a function of a dimensionless parameter h defined as

$$h = \frac{H_0}{100 \text{ km s}^{-1} \text{ Mpc}^{-1}} \, . \tag{8.2}$$

However, velocity and distance are not directly measured. The main observables are the redshift z—i.e., the fractional wavelength shift observed in specific absorption lines (hydrogen, sodium, magnesium, ...) of the measured spectra of objects (Fig. 8.1)

$$z = \frac{\lambda_{\text{observed}} - \lambda_{\text{emitted}}}{\lambda_{\text{emitted}}} = \frac{\Delta\lambda}{\lambda_{\text{emitted}}}, \tag{8.3}$$

and the apparent luminosity of the celestial objects (stars, galaxies, supernovae, ...), for which we assume we know the intrinsic luminosity.

A redshift occurs whenever $\Delta\lambda > 0$ which is the case for the large majority of galaxies. There are notable exceptions ($\Delta\lambda < 0$, a blueshift) as the one of M31, the nearby Andromeda galaxy, explained by a large intrinsic velocity (peculiar velocity) oriented toward us.

Wavelength shifts were first observed by the US astronomer James Keeler at the end of the nineteenth century in the spectrum of the light reflected by the rings of Saturn, and later on, at the beginning of 20th century, by the US astronomer Vesto Slipher, in the spectral lines of several galaxies. In 1925 spectral lines had been measured for around 40 galaxies.

These wavelength shifts were (and still often are) incorrectly identified as simple special relativistic Doppler shifts due to the movement of the sources. In this case z would be given by

$$z = \sqrt{\frac{1+\beta}{1-\beta}} - 1, \tag{8.4}$$

which in the limit of small β becomes

$$z \simeq \beta \, ; \tag{8.5}$$

in terms of z the Hubble law can then be written as:

$$z \simeq \frac{H_0}{c} d \, . \tag{8.6}$$

However, the limit of small β is not valid for high redshift objects with z as high as 11 that have been observed in the last years—the list of the most distant object comprises more than 100 objects with $z > 7$ among galaxies (the most abundant category), black holes, and even stars. On the other hand, high redshift supernovae (typically $z \sim 0.1$ to 1) have been extensively studied. From these studies an interpretation of the expansion based on special relativity is clearly excluded: one has to invoke general relativity.

In terms of general relativity (see Sect. 8.2) the observed redshift is not due to any movement of the cosmic objects but to the expansion of the proper space between them. This expansion has no center: an observer at any point of the Universe will see the expansion in the same way with all objects in all directions receding with radial velocities given by the same Hubble law and not limited by the speed of light (in fact for $z \gtrsim 1.5$ radial velocities are, in a large range of cosmological models, higher than c): it is the distance scale in the Universe that is changing.

Let us now write the distance between two objects as

$$d = a(t)x, \tag{8.7}$$

where $a(t)$ is a scale that may change with time and x by definition is the present ($t = t_0$) distance between the objects ($a(t_0) = 1$) that does not change with time (comoving distance). Then
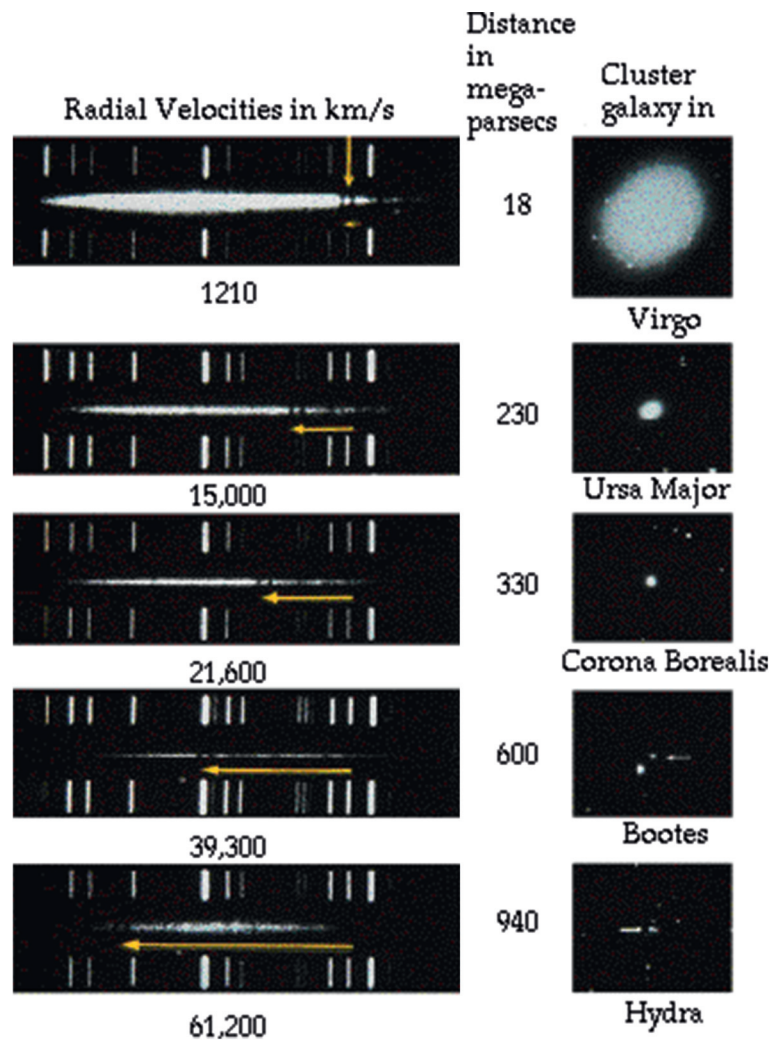
Fig. 8.1 Wavelength shifts observed in spectra of galaxies depending on their distance. From J. Silk, "The big bang", Times Books 2000.

$$\dot{d} = \dot{a}x \; ; \; v = H_0 d$$

with

$$H_0 = \frac{\dot{a}}{a} \, . \tag{8.8}$$

In this simple model the Hubble constant is just the expansion rate of the distance scale in the Universe.

Let us come back to the problem of the measurement of distances. The usual method to measure distances is to use reference objects (standard candles), for which the absolute luminosity L is known. Then, assuming isotropic light emission in an Euclidean Universe (see Sect. 8.2) and measuring the corresponding light flux f on Earth, the distance d can be estimated as

$$d = \sqrt{\frac{L}{4\pi f}} \, . \tag{8.9}$$
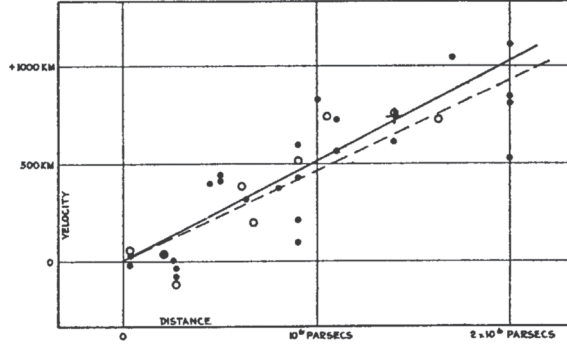
Fig. 8.2 The velocity–distance relation measured by Hubble (the original "Hubble plot"). From E. Hubble, Proceedings of the National Academy of Sciences 15 (1929) 168.

In his original plot shown in Fig. 8.2 Hubble used as standard candles Cepheid[1] stars, as well as the brightest stars in the Galaxy, and even entire galaxies (assuming the absolute luminosity of the brightest stars and of the Galaxies to be approximately constant).

The original Hubble result showed a linear correlation between v and d but the slope (the Hubble constant) was wrong by a factor of 7 due to an overall calibration error caused mainly by a systematic underestimate of the absorption of light by dust.

A constant slope would mean that the scale distance $a(t)$ discussed above would increase linearly with time:

$$a(t) = a(t_0) + \dot{a}(t - t_0),$$

i.e.,

$$\frac{a(t)}{a(t_0)} = 1 + H_0(t - t_0). \tag{8.10}$$

Hubble suggested in his original article, under the influence of a model by de Sitter, that this linear behavior could be just a first-order approximation. In fact until recently (1998) most people were convinced that at some point the expansion should be slowed down under the influence of gravity which should be the dominant (attractive) force at large scale. This is why the next term added to the expansion is usually written by introducing a deceleration parameter q_0 (if $q_0 > 0$ the expansion slows down) defined as

$$q_0 = -\frac{\ddot{a}a}{\dot{a}^2} = -\frac{\ddot{a}}{H_0{}^2 a}, \tag{8.11}$$

and then

$$\frac{a(t)}{a(t_0)} \simeq 1 + H_0(t - t_0) - \frac{1}{2} q_0 H_0{}^2 (t - t_0)^2. \tag{8.12}$$

The relation between z and d must now be modified to include this new term.

However, in an expanding Universe the computation of the distance is much more subtle. Two distances are usually defined between two objects: the proper distance d_p and the luminosity distance d_L.

- d_p is defined as the length measured on the spatial geodesic connecting the two objects at a fixed time (a geodesic is defined to be a curve whose tangent vectors remain parallel if they are transported along it. Geodesics are (locally) the shortest path between points in space, and describe locally the infinitesimal path of a test inertial particle). It can be shown (see Ref. [F8.2]) that

$$d_p \simeq \frac{c}{H_0} z \left(1 - \frac{1 + q_0}{2} z\right); \tag{8.13}$$

for small z the usual linear Hubble law is recovered.

[1] Cepheids are variable red supergiant stars with pulsing periods strongly correlated with their absolute luminosity. This extremely useful propriety was discovered by the US astronomer Henrietta Leavitt at the beginning of twentieth century and has been used by Hubble to demonstrate in 1924 that the Andromeda Nebula M31 was too far to be part of our own galaxy, the Milky Way.
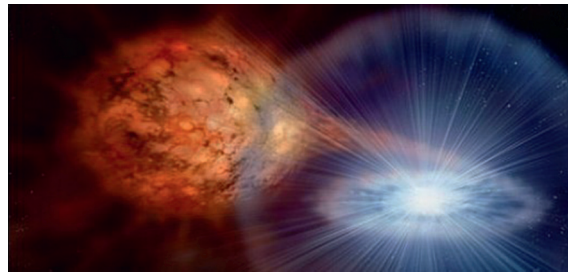
Fig. 8.3 Artistic representation of the formation and explosion of a supernova Ia (Image from A. Hardy, David A. Hardy/www.astroart.org).

- d_L is defined as the distance that is experimentally determined using a standard candle assuming a static and Euclidean Universe as noted above:

$$d_L = \sqrt{\frac{L}{4\pi f}} \, . \tag{8.14}$$

The relation between d_p and d_L depends on the curvature of the Universe (see Sect. 8.2.3). Even in a flat (Euclidean) Universe (see Sect. 8.2.3 for a formal definition; for the moment, we rely on an intuitive one, and think of flat space as a space in which the sum of the internal angles of a triangle is always π) the flux of light emitted by an object with a redshift z and received at Earth is attenuated by a factor $(1 + z)^2$ due to the dilation of time ($\gamma \simeq (1 + z)$) and the increase of the photon's wavelength ($a^{-1} = (1 + z)$). Then if the Universe was basically flat

$$d_L = d_p \, (1 + z) \simeq \frac{c}{H_0} z \left[1 + \frac{1 - q_0}{2} z \right] \, . \tag{8.15}$$

To experimentally determine q_0 one needs to extend the range of distances in the Hubble plot by a large amount. New and brighter standard candles are needed.

8.1.2 Expansion is Accelerating

Type Ia supernovae have been revealed themselves as an optimal option to extend the range of distances in the Hubble plot. Supernovae Ia occur whenever, in a binary system formed by a white dwarf (a compact Earth-size stellar endproduct of mass close to the solar mass) and another star (for instance a red giant, a luminous giant star in a late phase of stellar evolution), the white dwarf accretes matter from its companion reaching a total critical mass of about 1.4 solar masses. At this point a nuclear fusion reaction starts, leading to a gigantic explosion (with a luminosity about 10^5 times larger than the brightest Cepheids; see Fig. 8.3 for an artistic representation).

The results obtained by the "Supernova Cosmology Project" and by the "High-z Supernova Search Team" resulted in extended Hubble plots (Fig. 8.4) that were a surprise and triggered a revolution in our understanding of the content and evolution of the Universe.[2] The striking point is that the fit to the experimental supernova (z, d) data leads to negative values of q_0 meaning that, contrary to what was expected, the expansion of the Universe is nowadays accelerating.

An alternative method to the use of standard candles to determine extragalactic distances is the use of "standard rulers". Let us suppose that we know the absolute length l of an object (the standard ruler) that is placed at some distance transversally to the observation line. Then the distance of the object can be obtained from its angular size $\delta\theta$ by the simple formula:

---

[2] The Supernova Cosmology Project is a collaboration, led by Saul Perlmutter, dedicated to the study of distant supernovae of type Ia, that started collecting data in 1988. Another collaboration also searching for distant supernovae of type Ia was formed by Brian Schmidt Adam Riess in 1994, the High-z Supernova Search Team. These teams found over 50 distant supernovae of type Ia for which the light received was weaker than expected—which implied that the rate of expansion of the Universe was increasing. Saul Perlmutter, born in 1959 in Champaign–Urbana, IL, US, Ph.D. from University of California, Berkeley; Brian P. Schmidt, US and Australian citizen, born in 1967 in US, Ph.D. from Harvard; Adam G. Riess, born in 1969 in Washington, DC, US. Ph.D. from Harvard, all professors in the US, were awarded the 2011 Nobel Prize in Physics "for the discovery of the accelerating expansion of the Universe through observations of distant supernovae."
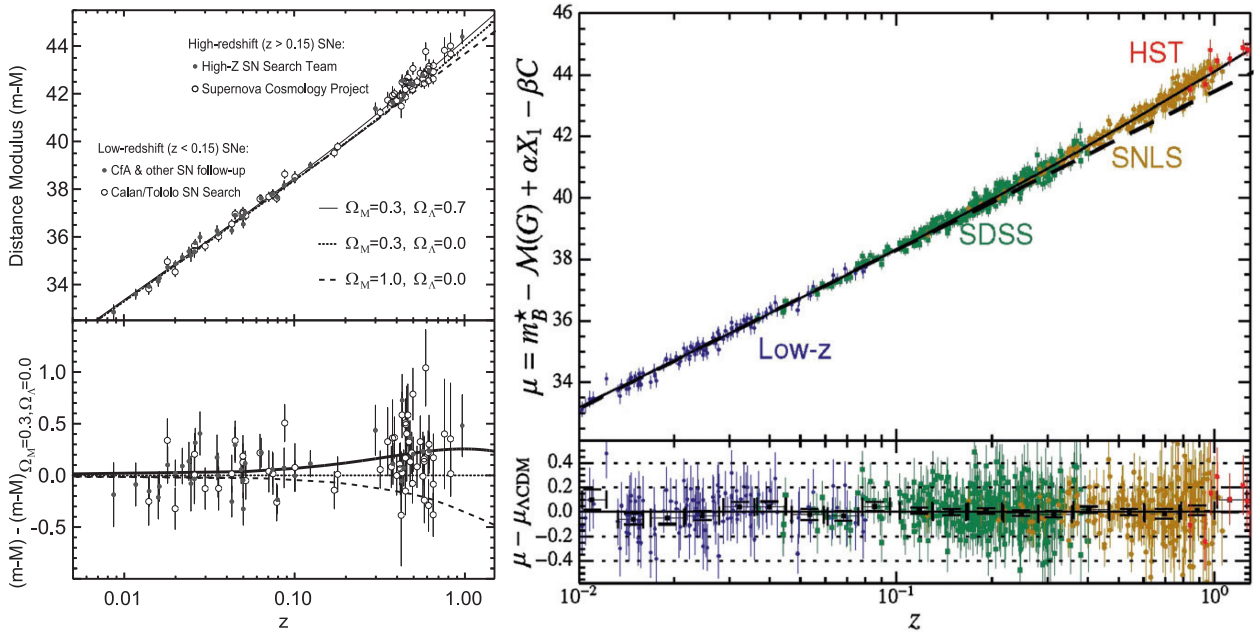
Fig. 8.4 Left: The "Hubble plot" obtained by the "High-z Supernova Search Team" and by the "Supernova Cosmology Project". The lines represent the prediction of several models with different energy contents of the Universe (see Sect. 8.4). The best fit corresponds to an accelerating expansion scenario. From "Measuring Cosmology with Supernovae", by Saul Perlmutter and Brian P. Schmidt; Lecture Notes in Physics 2003, Springer. Right: an updated version by the "Supernova Legacy Survey" and the "Sloan Digital Sky Survey" projects, M. Betoule et al. arXiv:1401.4064.

$$d_A = \frac{l}{\delta\theta}\,, \qquad (8.16)$$

where d_A is known as the angular diameter distance. In a curved and/or expanding Universe d_A does not coincide with the proper (d_p) and the luminosity (d_L) distances defined above but it can be shown (see Ref. [8.2]) that:

$$d_A = \frac{d_L}{(1+z)^2}\,. \qquad (8.17)$$

Several candidates for standard rulers have been discussed in the last years and, in particular, the observation of Baryon Acoustic Oscillations (BAO) opened a new and promising path. BAO use the Fourier transform of the distance correlation function between specific astrophysics objects (for instance luminous red galaxies, blue galaxies, etc.) to discover, as function of the redshift z, possible clustering scales of the baryonic matter. These scales may be related to the evolution of initial density perturbations in the early Universe (see Sect. **??**). The correlation function ξ between pairs of galaxies is just the probability that the two galaxies are at the distance r and thus a sharp peak in $\xi(r)$ will correspond in its Fourier transform to an oscillation spectrum with a well-defined frequency.

8.1.2.1 Dark Energy

There is no classical explanation for the accelerated expansion of the Universe. A new form of energy is invoked, permeating the space and exerting a negative pressure. This kind of energy can be described in the general theory of relativity (see later) and associated, e.g., to a "cosmological" term Λ; it is called "dark" energy—and to the present knowledge has the largest energy share in the Universe.

In Sect. 8.4 the current overall best picture able to accommodate all present experimental results (the so-called ΛCDM model) will be discussed.
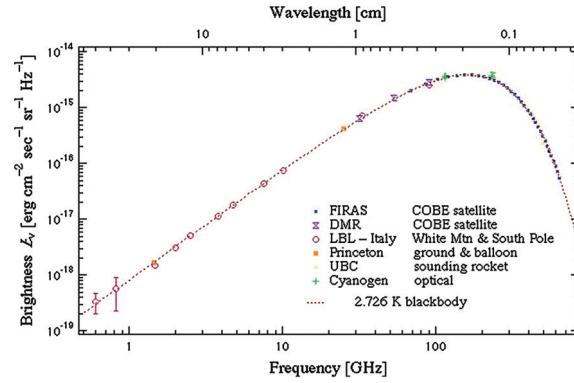
Fig. 8.5 The CMB intensity plot as measured by COBE and other experiments (from http://aether.lbl.gov/www/projects/cobe/CMB_intensity.gif).

8.1.3 Cosmic Microwave Background

In 1965 Penzias and Wilson,[3] two radio astronomers working at Bell Laboratories in New Jersey, discovered by accident that the Universe is filled with a mysterious isotropic and constant microwave radiation corresponding to a blackbody temperature around 3 K.

Penzias and Wilson were just measuring a small fraction of the blackbody spectrum. Indeed they were measuring the region in the tail around wavelength $\lambda \sim 7.5$ cm while the spectrum peaks around $\lambda \sim 2$ mm. To fully measure the density spectrum it is necessary to go above the Earth's atmosphere, which absorbs wavelengths lower than $\lambda \sim 3$ cm. These measurements were eventually performed in several balloon and satellite experiments. In particular, the Cosmic Background Explorer (COBE), launched in 1989, was the first to show that in the 0.1 to 5 mm range the spectrum, after correction for the proper motion of the Earth, is well described by the Planck blackbody formula

$$\varepsilon_\gamma\left(\nu\right)d\nu = \frac{8\pi h}{c^3}\frac{\nu^3 d\nu}{e^{\frac{h\nu}{k_B T}}-1}\,,\tag{8.18}$$

where k_B is the Boltzmann constant. Other measurements at longer wavelengths confirmed that the cosmic microwave background (CMB) spectrum is well described by the spectrum of a single temperature blackbody (Fig. 8.5) with a mean temperature of

$$T = \left(2.726 \pm 0.001\right)\mathrm{K}\,.$$

The total photon energy density is then obtained by integrating the Planck formula over the entire frequency range, resulting in the Stefan–Boltzmann law

$$\varepsilon_\gamma = \frac{\pi^2}{15}\frac{\left(k_B T\right)^4}{\left(\hbar c\right)^3} \simeq 0.26\,\mathrm{eV\ cm^{-3}}\,;\tag{8.19}$$

moreover, the number density of photons is given by

$$n_\gamma \simeq \frac{2.4}{\pi^2}\left(\frac{k_B T}{\hbar c}\right)^3 \simeq 410\,\mathrm{cm^{-3}}\,.\tag{8.20}$$

The existence of CMB had been predicted in the 1940s by George Gamow, Robert Dicke, Ralph Alpher, and Robert Herman in the framework of the Big Bang model.

---

[3] Arno Penzias (1933–) was born in Munich, Germany. In 1939 his family was rounded up for deportation, but they managed to escape to the US, where he could graduate in Physics at Columbia University. Robert Wilson (1936–) grew up in Huston, Texas, and studied at Caltech. They shared the 1978 Nobel prize in Physics "for their discovery of the cosmic microwave background radiation."

8.1.3.1 Recombination and Decoupling

In the Big Bang model the expanding Universe cools down going through successive stages of lower energy density (temperature) and more complex structures. Radiation materializes into pairs of particles and antiparticles, which, in turn, give origin to the existing objects and structures in the Universe (nuclei, atoms, planets, stars, galaxies, . . .). In this context, the CMB is the electromagnetic radiation left over when electrons and protons combine to form neutral atoms (the, so-called, *recombination* phase). After this stage, the absence of charged matter allows photons to be basically free of interactions, and evolve independently in the expanding Universe (*photon decoupling*).

In a simple, but reasonable, approximation (neglecting heavier elements, in particular helium) recombination occurs as the result of the balance between the formation and the photodisintegration of hydrogen atoms:

$$p + e^- \to H + \gamma \; ; \; H + \gamma \to p \; e^-.$$
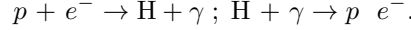
If these reactions are in equilibrium at a given temperature T (high enough to allow the photodisintegration and low enough to consider e, p, H as nonrelativistic particles) the number density of electrons, protons, and hydrogen atoms may be approximated by the Maxwell–Boltzmann distribution (see Sect. **??**)

$$n_x = g_x \left(\frac{m_x k_B T}{2\pi \; \hbar^2} \right)^{\frac{3}{2}} e^{-\frac{m_x c^2}{k_B T}} , \tag{8.21}$$

where g_x is a statistical factor accounting for the spin (the subscript x refers to each particle type).

The ratio $n_H / (n_p n_e)$ can then be approximately modeled by the] equation

$$\frac{n_H}{n_p n_e} \simeq \left(\frac{m_e k_B \; T}{2\pi \hbar^2} \right)^{-\frac{3}{2}} e^{\frac{Q}{k_B T}} , \tag{8.22}$$

where

$$Q = (m_p + m_e - m_H) \, c^2 \simeq 13.6 \text{ eV} \tag{8.23}$$

is the hydrogen binding energy.

Defining X as the fractional ionization ($X = 1$ for complete ionization, whereas, $X = 0$ when all protons are inside neutral atoms),

$$X = \frac{n_p}{n_p + n_H}, \tag{8.24}$$

and assuming that there is zero total net charge, ($n_p = n_e$), the Saha equation can be rewritten as

$$\frac{1-X}{X} \simeq n_p \left(\frac{m_e k_B T}{2\pi \hbar^2} \right)^{-\frac{3}{2}} e^{\left(\frac{Q}{k_B T} \right)} . \tag{8.25}$$

On the other hand at thermal equilibrium, the energy density of photons as a function of the frequency ν follows the usual blackbody distribution corresponding, as we have seen before, to a photon density number of:

$$n_\gamma \simeq \frac{2.4}{\pi^2} \left(\frac{k_B T}{\hbar c} \right)^3 . \tag{8.26}$$

For the typical photodisintegration temperatures ($k_B \; T \sim 13.6$ eV)
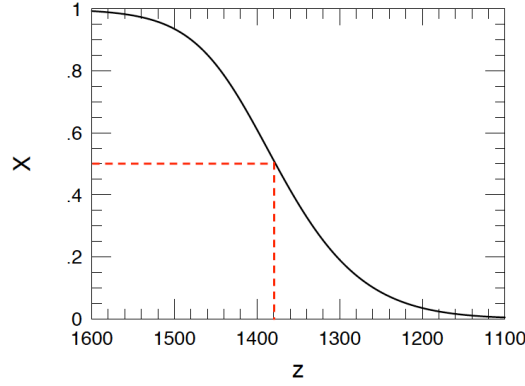
$$n_\gamma \gg n_B,$$

where n_B is the total number of baryons, which in this simple approximation is defined as

$$n_B = n_p + n_H = \frac{n_p}{X} . \tag{8.27}$$

The baryon to photon ratio is thus

$$\eta = \frac{n_B}{n_\gamma} = \frac{n_p}{X \; n_\gamma} \ll 1 . \tag{8.28}$$

Fig. 8.6 X as a function of z in the Saha equation. Time on the abscissa increases from left to right (as z decreases). Adapted from B. Ryden, lectures at ICTP Trieste, 2006.

After decoupling, n_B and n_γ evolve independently both as $a(t)^{-3}$, where $a(t)$ is the scale factor of the Universe, see Sect. 8.1.1. Thus, η is basically a constant, which can be measured at the present time through the measurement of the content of light elements in the Universe (see Sect. 8.1.4):

$$\eta \sim (5 - 6) \times 10^{-10} . \tag{8.29}$$

The Saha equation can then be written as a function of η and T, and used to determine the recombination temperature (assuming $X \sim 0.5$):

$$\frac{1 - X}{X^2} = 2 \simeq 3.84 \, \eta \left(\frac{k_B T}{m_e c^2} \right)^{\frac{3}{2}} e^{\frac{Q}{k_B T}} . \tag{8.30}$$

The solution of this equation gives a remarkably stable value of temperature for a wide range of η. For instance $\eta \sim 5.5 \times 10^{-10}$ results into

$$k_B T_{rec} \simeq 0.323 \, \text{eV} \Longrightarrow T_{rec} \simeq 3740 \, \text{K} . \tag{8.31}$$

This temperature is much higher than the measured CMB temperature reported above. The difference is attributed to the expansion of the Universe between the recombination epoch and the present. Indeed, as discussed in Sect. 8.1.1, the photon wavelength increases during the expansion of a flat Universe by a factor $(1 + z)$. The entire CMB spectrum was expanded by this factor, and then it could be estimated that recombination had occurred (see Fig. 8.6) at

$$z_{rec} \sim 1300 - 1400 . \tag{8.32}$$

After recombination the Universe became substantially transparent to photons. The photon decoupling time is defined as the moment when the interaction rate of photons Γ_{γ_scat} equals the expansion rate of the Universe (which is given by the Hubble parameter)

$$\Gamma_{\gamma\_scat} \sim H . \tag{8.33}$$

The dominant interaction process is the photon–electron Thomson scattering. Then

$$\Gamma_{\gamma_{scat}} \simeq n_e \sigma_T c ,$$

where n_e and σ_T are, respectively, the free electron density number and the Thomson cross section.

Finally, as n_e can be related to the fractional ionization $X(z)$ and the baryon density number ($n_e = X(z) \, n_B$), the redshift at which the photon decoupling occurs (z_{dec}) is given by

$$X(z_{dec}) \, n_B \sigma_T c \sim H . \tag{8.34}$$

However, the precise computation of z_{dec} is subtle. Both n_B and H evolve during the expansion (for instance in a matter-dominated flat Universe, as it will be discussed in Sect. 8.2, $n_B(z) \propto n_{B,0}(1+z)^3$ and $H(z) \propto H_0(1+z)^{3/2}$). Furthermore, the Saha equation is not valid after recombination once electrons and photons are no longer in thermal equilibrium. The exact value of z_{dec} depends thus on the specific model for the evolution of the Universe and the final result is of the order of

$$z_{dec} \sim 1100. \tag{8.35}$$

After decoupling the probability of a further scattering is extremely low except at the so-called *reionization* epoch. After the formation of the first stars, there was a period $(6 < z < 20)$ when the Universe was still small enough for neutral hydrogen formed at recombination to be ionized by the radiation emitted by stars. Still, the scattering probability of CMB photons during this epoch is small. To account for it, the reionization optical depth parameter τ is introduced, in terms of which the scattering probability is given by

$$P \sim 1 - e^{-\tau}.$$

The CMB photons follow then spacetime geodesics until they reach us. These geodesics are slightly distorted by the gravitational effects of the mass fluctuations close to the path giving rise to microlensing effects, which are responsible for a typical total deflection of ~ 2 arcminutes.

The spacetime points to where the last scattering occurred thereby define a region called the *last scattering surface* situated at a redshift, z_{lss}, very close to z_{dec}

$$z_{lss} \sim z_{dec} \sim 1100. \tag{8.36}$$

Beyond z_{lss} the Universe is opaque to photons and to be able to observe it other messengers, e.g., gravitational waves, have to be studied. On the other hand, the measurement of the primordial nucleosynthesis (Sect. 8.1.4) allows to indirectly test the Big Bang model at times well before the recombination epoch.

8.1.3.2 Temperature Fluctuations

The COBE satellite[4] measured the temperature fluctuations in sky regions centered at different points with galactic coordinates (θ, Φ)

$$\frac{\delta T(\theta, \Phi)}{\langle T \rangle} = \frac{T(\theta, \Phi) - \langle T \rangle}{\langle T \rangle} \tag{8.37}$$

and found that, apart from a dipole anisotropy of the order of 10^{-3}, the temperature fluctuations are of the order of 10^{-5}: the observed CMB spectrum is remarkably isotropic.

The dipole distortion (a slight blueshift in one direction of the sky and a redshift in the opposite direction—Fig. 8.7) observed in the measured average temperature can be attributed to a global Doppler shift due to the peculiar motion (COBE, Earth, Solar system, Milky way, local Group, Virgo cluster, ...) with respect to a hypothetical CMB isotropic reference frame characterized by a temperature T. Indeed

$$T^* = T\left(1 + \frac{v}{c}\cos\theta\right) \tag{8.38}$$

with

$$v = (371 \pm 1)\,\text{km/s}.$$

---

[4] Three satellite missions have been launched so far to study the cosmic background radiation. The first was COBE in 1989, followed by WMAP (Wilkinson Microwave Anisotropy Probe) in 2001, both of which were NASA missions. The latest (with the best angular resolution and sensitivity), called Planck, has been launched by the European Space Agency (ESA) with a contribution from NASA in 2009, and is still in orbit. In terms of sensitivity and angular resolution, WMAP improved COBE by a factor of 40, and Planck gave a further improvement by a factor of 4; in addition Planck measures polarization. The instruments onboard Planck are a low frequency (solid state) instrument from 30 GHz, and a bolometer—a device for measuring the power of incident electromagnetic radiation via the heating of a material with a temperature-dependent electrical resistance—for higher frequencies (up to 900 GHz). The total weight of the payload is 2 tons (it is thus classified as a large mission); it needs to be kept at cryostatic temperatures. John Mather, from the Goddard Space Flight Center, and George Smoot, at the University of California, Berkeley, shared the 2006 Nobel Prize in Physics "for their discovery of the blackbody form and anisotropy of the cosmic microwave background radiation".
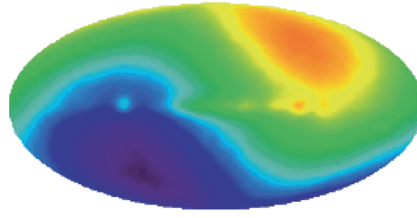
Fig. 8.7 Sky map (in galactic coordinates) of CMB temperatures measured by COBE after the subtraction of the emission from our Galaxy. A dipole component is clearly visible. (from http://apod.nasa.gov/apod/ap010128.html).
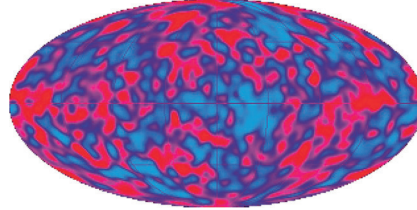
Fig. 8.8 CMB temperature fluctuations sky map as measured by COBE after the subtraction of the dipole component and of the emission from our Galaxy. http://lambda.gsfc.nasa.gov/product/cobe.
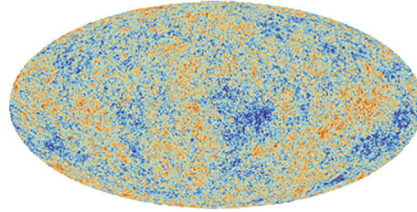
Fig. 8.9 CMB temperature fluctuations sky map as measured by the Planck mission after the subtraction of the dipole component and of the emission from our Galaxy. http://www.esa.int/spaceinimages.

After removing this effect, the remaining fluctuations reveal a pattern of tiny inhomogeneities at the level of the last scattering surface. The original picture from COBE (Fig. 8.8), with an angular resolution of 7°, was confirmed and greatly improved by the Wilkinson Microwave Anisotropy Probe WMAP, which obtained full sky maps with a 0.2° angular resolution. The Planck satellite delivered more recently sky maps with three times higher resolution and ten times higher sensitivity (Fig. 8.9), also covering a larger frequency range.

Once these maps are obtained it is possible to establish two-point correlations between any two spatial directions.

Technically, the temperature fluctuations are expanded using spherical harmonics

$$\frac{\delta T}{\langle T \rangle}(\theta, \Phi) = \sum_{l=0}^{\infty} \sum_{m=-l}^{l} a_{lm} Y_{lm}^*(\theta, \Phi), \tag{8.39}$$

with

$$a_{lm} = \int_{\theta=-\pi}^{\pi} \int_{\Phi=0}^{2\pi} \frac{\delta T}{\langle T \rangle}(\theta, \Phi) Y_{lm}^*(\theta, \Phi)\, d\Omega. \tag{8.40}$$

Then the correlation between two directions $\hat{n}$ and $\hat{n}^*$ separated by an angle α is defined as
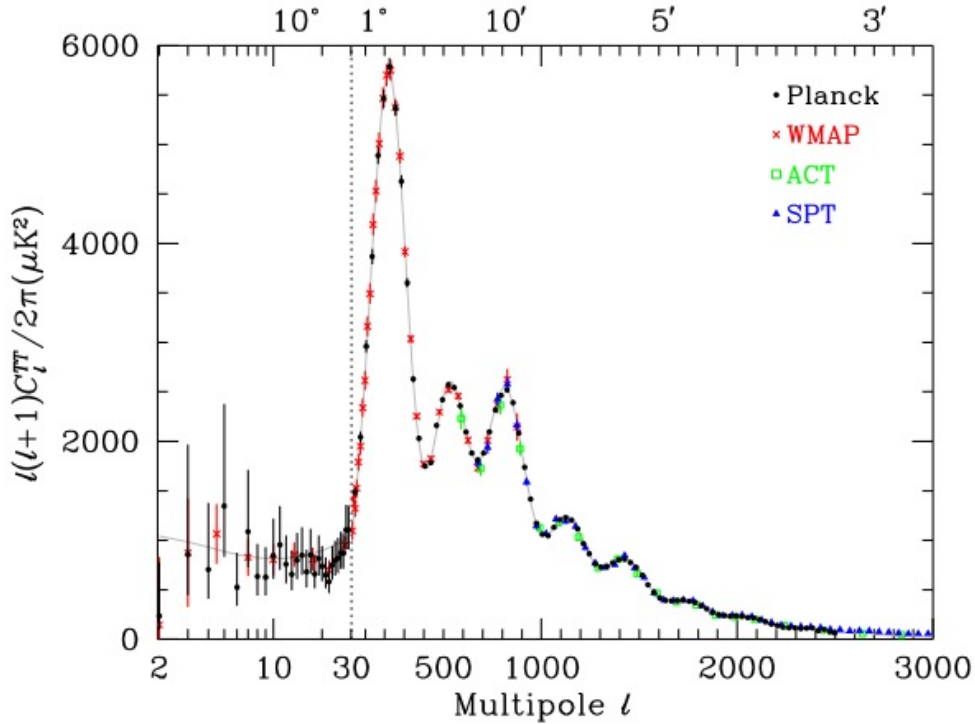
$$C(\alpha) = \left\langle \frac{\delta T}{\langle T \rangle}(\hat{n}) \frac{\delta T}{\langle T \rangle}(\hat{n}^*) \right\rangle_{\hat{n} \cdot \hat{n}^* = \cos \alpha}$$

and can be expressed as

$$C(\alpha) = \frac{1}{4\pi} \sum_{l=0}^{\infty} (2l+1)\, C_l P_l(\cos \alpha),$$

where P_l are the Legendre polynomials and the C_l, the multipole moments, are given by the variance of the harmonic coefficients a_{lm}:

Fig. 8.10 Temperature power spectrum from the Planck, WMAP, ACT, and SPT experiments. The abscissa is logarithmic for l less then 30, linear otherwise. The curve is the best-fit Planck model. From C. Patrignani et al. (Particle Data Group), Chin. Phys. C, 40, 100001 (2016).

$$C_l = \frac{1}{2l+1} \sum_{m=-l}^{l} \left\langle \mid a_{lm} \mid^2 \right\rangle. \tag{8.41}$$

Each multipole moment corresponds to a sort of angular frequency l, whose conjugate variable is an angular scale α such that

$$\alpha = \frac{180°}{l}. \tag{8.42}$$

The total temperature fluctuations (temperature powers spectrum) can be then expressed as a function of the multipole moment l (Fig. 8.10, top)

$$\left\langle \varDelta T^2 \right\rangle = \left(\frac{l(l+1)}{2\pi} C_l \right) \left\langle T \right\rangle^2. \tag{8.43}$$

Such a function shows a characteristic pattern with a first peak around $l \sim 200$ followed by several smaller peaks.

The first peak at an angular scale of $1°$ defines the size of the horizon at the time of last scattering (see Sect. 8.1.4) and the other peaks (acoustic peaks) are extremely sensitive to the specific contents and evolution model of the Universe at that time. The observation of very tiny fluctuations at large scales (much greater than the horizon, $l \ll 200$) leads to the hypothesis that the Universe, to be casually connected, went a through a very early stage of exponential expansion, called *inflation*.

Anisotropies can also be found studying the polarization of CMB photons. Indeed at the recombination and reionization epochs the CMB may be partially polarized by Thomson scattering with electrons. It can be shown that linear polarization may also be originated by quadrupole temperature anisotropies. In general the polarization pattern is decomposed in two orthogonal modes, respectively, called B-mode (curl-like) and E-mode (gradient-like). Thomson scattering only originates the E-mode while primordial gravitational waves are expected to display both polarization modes. Gravitational lensing of the CMB E-modes may also be a source of B-modes. E-modes were first measured in 2002 by the DASI telescope in Antarctica and later on the Planck collaboration published high resolution maps of the CMB polarization over the full sky. The detection and the interpretation of B-modes are very challenging since the signals are tiny and foreground

contaminations, as the emission by Galactic dust, are not always easy to estimate. The arrival angles of CMB photons are smeared, due to the microlensing effects, by dispersions that are function of the integrated mass distribution along the photon paths. It is possible, however, to deduce these dispersions statistically from the observed temperature angular power spectra and/or from polarized E- and B-mode fields. The precise measurement of these dispersions will give valuable information for the determination of the cosmological parameters. It will also help constraining parameters, such as the sum of the neutrino masses or the dark energy content, that are relevant for the growth of structures in the Universe, and evaluating contaminations in the B-mode patterns from possible primordial gravity waves.

The detection of gravitational lensing was reported by several experiments such as the Atacama Cosmology Telescope, the South Pole Telescope, and the POLARBEAR experiment. The Planck collaboration has measured its effect with high significance using temperature and polarization data, establishing a map of the lensing potential.

Some of these aspects will be discussed briefly in Sect. **??** but a detailed discussion of the theoretical and experimental aspects of this fast-moving field is far beyond the scope of this book.
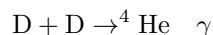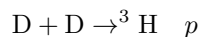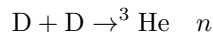
8.1.4 Primordial Nucleosynthesis

The measurement of the abundances of light elements in the Universe (H, D, ^{3}He, ^{4}He, ^{6}Li, ^{7}Li) is the third observational "pillar" of the Big Bang model, after the Hubble expansion and the CMB. As it was proposed, and first computed, by the Russian American physicists Ralph Alpher and George Gamow in 1948, the expanding Universe cools down, and when it reaches temperatures of the order of the nuclei binding energies per nucleon ($\sim 1-10$ MeV) nucleosynthesis occurs if there are enough protons and neutrons available. The main nuclear fusion reactions are

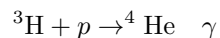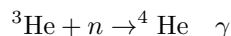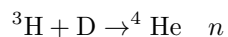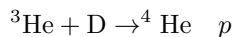- proton–neutron fusion:
$$p + n \rightarrow D \; \gamma$$
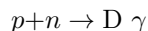
- deuterium–deuterium fusion:
$$D + D \rightarrow\!^3He \quad n$$
$$D + D \rightarrow\!^3H \quad p$$
$$D + D \rightarrow\!^4He \quad \gamma$$

- other ^{4}He formation reactions:
$$^3He + D \rightarrow\!^4He \quad p$$
$$^3H + D \rightarrow\!^4He \quad n$$
$$^3He + n \rightarrow\!^4He \quad \gamma$$
$$^3H + p \rightarrow\!^4He \quad \gamma$$

- and finally the lithium and beryllium formation reactions (there are no stable nuclei with $A = 5$):
$$^4He + D \rightarrow\!^6Li \quad \gamma$$
$$^4He +^3H \rightarrow\!^7Li \quad \gamma$$
$$^4He +^3He \rightarrow\!^7Be \quad \gamma$$
$$^7Be + \gamma \quad \rightarrow\!^7Li \quad p.$$
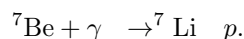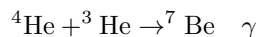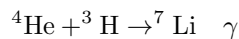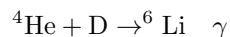
The absence of stable nuclei with $A = 8$ basically stops the primordial big bang nucleosynthesis chain. Heavier nuclei are produced in stellar (up to Fe) or supernova nucleosynthesis.[5]

The relative abundance of neutrons and protons, in case of thermal equilibrium at a temperature T, is fixed by the ratio of the usual Maxwell–Boltzmann distributions (similarly to what was discussed for the recombination—Sect. 8.1.3):

---

[5] Iron (^{56}Fe) is the stable element for which the binding energy per nucleon is largest (about 8.8 MeV); it is thus the natural endpoint of fusion processes of lighter elements, and of fission of heavier elements.

$$\frac{n_n}{n_p} = \left(\frac{m_n}{m_p}\right)^{\frac{3}{2}} \exp\left(-\frac{(m_n - m_p)\,c^2}{kT}\right).$$ (8.44)

If $k_B T \gg (m_n - m_p)\,c^2 \longrightarrow n_n/n_p \sim 1$; if $k_B T \ll (m_n - m_p)\,c^2 \longrightarrow n_n/n_p \sim 0$.

Thermal equilibrium is established through the weak processes connecting protons and neutrons:

$$n + \nu_e \rightleftharpoons p + e^-$$

$$n + e^+ \rightleftharpoons p + \overline{\nu}_e$$

as long as the interaction rate of these reactions $\Gamma_{n,p}$ is greater than the expansion rate of the Universe,

$$\Gamma_{n,p} \geq H.$$

Γ and H diminish during the expansion, the former much faster than the latter. Indeed in a flat Universe dominated by radiation (Sect. 8.2)

$$\Gamma_{n,p} \sim G_F T^5,$$ (8.45)

$$H \sim \sqrt{g^*}T^2,$$ (8.46)

where G_F is the Fermi weak interaction constant and g^* the number of degrees of freedom that depends on the relativistic particles content of the Universe (namely, on the number of generations of light neutrinos n_μ, which, in turn, allows to set a limit on n_μ).

The exact calculation of the freeze-out temperature T_f at which

$$\Gamma_{n,p} \sim H$$

is out of the scope of this book. The values obtained for T_f are a little below the MeV scale:

$$k_B T_f \sim 0.8 \text{ MeV}.$$ (8.47)

At this temperature

$$\frac{n_n}{n_p} \sim 0.2.$$

After the freeze-out this ratio would remain constant if neutrons were stable. However, as we know, neutrons decay via beta decay,

$$n \to p e^- \overline{\nu}_e.$$

Therefore, the n_n/n_p ratio will decrease slowly while all the neutrons will not be bound inside nuclei, so that

$$\frac{n_n}{n_p} \sim 0.2\, e^{-t/\tau_n}$$ (8.48)

where $\tau_n \simeq 885.7$ s is the neutron lifetime.

The first step of the primordial nucleosynthesis is, as we have seen, the formation of deuterium via proton–neutron fusion

$$p + n \rightleftharpoons \text{D}\gamma$$

Although the deuterium binding energy, 2.22 MeV, is higher than the freeze-out temperature, the fact that the baryons to photons ratio η is quite small ($\eta \sim (5-6) \times 10^{-10}$) makes photodissociation of the deuterium nuclei possible at temperatures lower than the blackbody peak temperature T_f (the Planck function has a long tail). The relative number of free protons, free neutrons, and deuterium nuclei can be expressed, using a c8sps6-like equation (Sect. 8.1.3), as follows:

$$\frac{n_\text{D}}{n_p n_n} \simeq \frac{g_\text{D}}{g_p g_n} \left(\frac{m_\text{D}}{m_p\,m_n}\right)^{\frac{3}{2}} \left(\frac{k_B T}{2\pi\hbar^2}\right)^{-\frac{3}{2}} e^{\frac{Q}{k_B T}},$$ (8.49)

where Q is now given by

$$Q = (m_p + m_n - m_\text{D})\,c^2 \sim 2.22 \text{ MeV}.$$

Expressing n_p as a function of η and n_γ and performing an order of magnitude estimation, we obtain
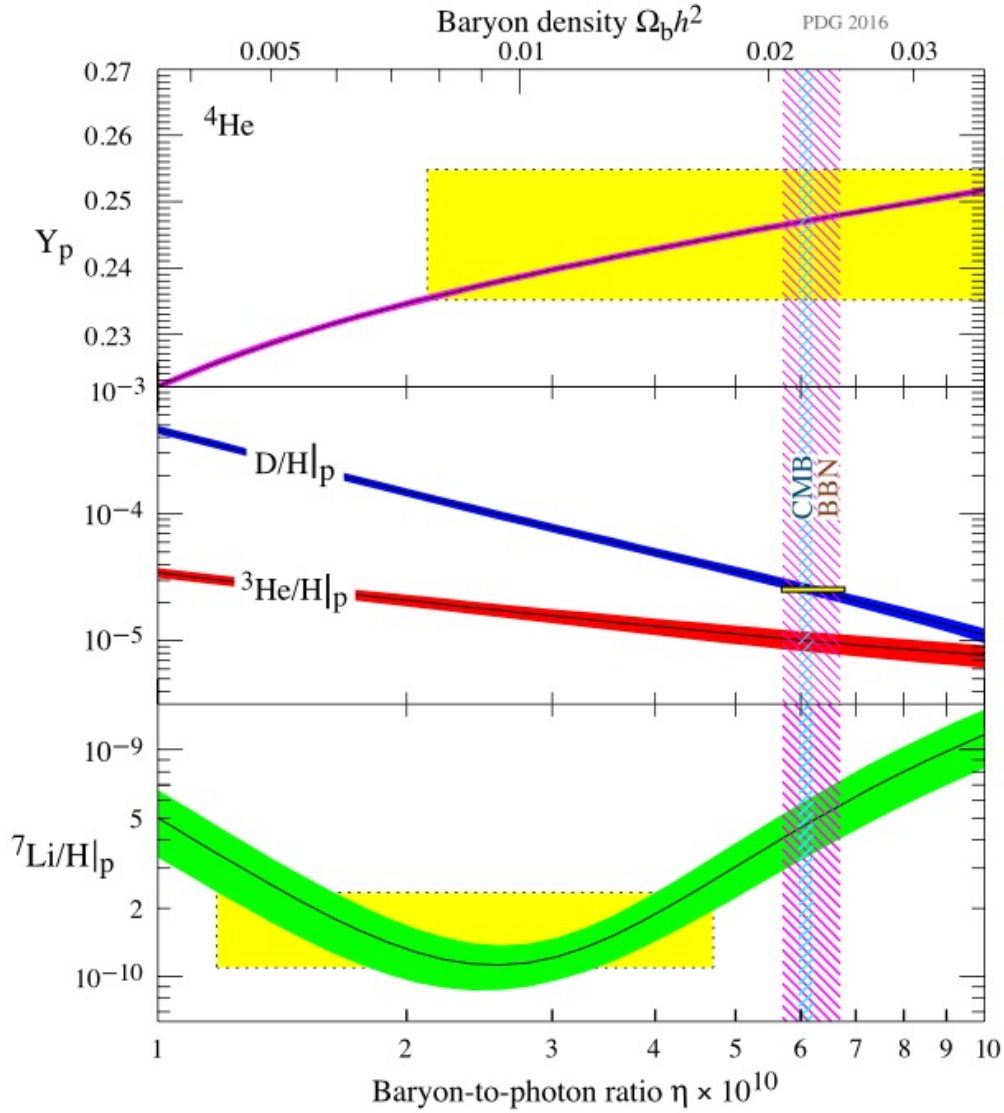
Fig. 8.11 The observed and predicted abundances of ^{4}He, D, ^{3}He, and ^{7}Li. The bands show the 95% CL range. Boxes represent the measured abundances. The narrow *vertical* band represents the constraints at 95% CL on η (expressed in units of 10^{10}) from the CMB power spectrum analysis while the wider is the Big-Bang nucleosynthesis concordance range From C. Patrignani et al. (Particle Data Group), Chin. Phys. C, 40, 100001 (2016).

$$\frac{n_{\mathrm{D}}}{n_n} \propto \eta n_\gamma \left(\frac{m_p \; c^2 k_B T}{\pi \hbar^2} \right)^{-\frac{3}{2}} e^{\frac{Q}{k_B T}} . \qquad (8.50)$$

Replacing now n_γ by the Planck distribution

$$\frac{n_{\mathrm{D}}}{n_n} \propto \eta \left(\frac{k_B \; T}{m_p \; c^2} \right)^{\frac{3}{2}} e^{\frac{Q}{k_B T}} . \qquad (8.51)$$

This is analogous to the formulation of the Saha equation used to determine the recombination temperature (Sect. 8.1.3). As we have shown its solution (for instance for $(n_{\mathrm{D}}/n_n) \sim 1$) gives a remarkably stable value of temperature. In fact there is a sharp transition around $k_B T_{\mathrm{D}} \sim 0.1$ MeV: above this value neutrons and protons are basically free; below this value all neutrons are substantially bound first inside D nuclei and finally inside ^{4}He nuclei, provided that there is enough time before the fusion rate of nuclei becomes smaller than the expansion rate of the Universe. Indeed, since the ^{4}He binding energy per nucleon is much higher than those of D, ^{3}H, and ^{3}He, and since there is no stable nuclei with $A = 5$, then ^{4}He is the favorite final state.

The primordial abundance of ^{4}He, Y_p, is defined usually as the fraction of mass density of ^{4}He nuclei, $\rho(^4\text{He})$, over the total baryonic mass density, $\rho\,(\text{Baryons})$

$$Y_p = \frac{\rho\left(^4\text{He}\right)}{\rho\,(\text{Baryons})}. \tag{8.52}$$

In a crude way let us assume that after nucleosynthesis all baryons are H or ^{4}He, i.e., that

$$\rho\,(\text{H}) + \rho\left(^4\text{He}\right) \simeq 1.$$

Thus

$$Y_p = 1 - \frac{\rho\,(\text{H})}{\rho\,(\text{Baryons})} = 1 - \frac{n_p - n_n}{n_p + n_n} = \frac{2\frac{n_n}{n_p}}{1 + \frac{n_n}{n_p}}. \tag{8.53}$$

For $(n_n/n_p) \sim 0.2$, $Y_p = 0.33$.

In fact due to the decay of neutrons between $k_B T_f \sim 0.8$ MeV and $k_B T_D \sim 0.1$ MeV

$$\frac{n_n}{n_p} \sim 0.13 - 0.15$$

and the best estimate for Y_p is in the range

$$Y_p \sim 0.23 - 0.26\,. \tag{8.54}$$

Around one quarter of the primordial baryonic mass of the Universe is due to ^{4}He and around three quarters is made of hydrogen. There are however small fractions of D, ^{3}He, and ^{3}H that did not turn into ^{4}He, and there are, thus, tiny fractions of ^{7}Li and ^{7}Be that could have formed after the production of ^{4}He and before the dilution of the nuclei due to the expansion of the Universe. Although their abundances are quantitatively quite small, the comparison of the expected and measured ratios are important because they are rather sensitive to the ratio of baryons to photons, η.

In Fig. 8.11 the predicted abundances of ^{4}He, D, ^{3}He, and ^{7}Li computed in the framework of the standard model of Big Bang nucleosynthesis as a function of η are compared with measurements (for details see the Particle Data Book). An increase in η will increase slightly the deuterium formation temperature T_D (there are less γ per baryon available for the photodissociation of the deuterium), and therefore, there is more time for the development of the chain fusion processes ending at the formation of the ^{4}He. Therefore, the fraction of ^{4}He will increase slightly, in relative terms, and the fraction of D and ^{3}He will decrease much more significantly, again in relative terms. The evolution of the fraction of ^{7}Li is, on the contrary, not monotonous; it shows a minimum due to the fact that it is built up from two processes that have a different behavior (the fusion of ^{4}He and ^{3}H is a decreasing function of η; the production via ^{7}Be is an increasing function of η).

Apart from the measured value for the fraction of ^{7}Li all the other measurements converge to a common value of η that is, within the uncertainties, compatible with the value indirectly determined by the study of the acoustic peaks in the CMB power spectrum (see Sect. 8.4).

8.1.5 Astrophysical Evidence for Dark Matter

Evidence that the Newtonian physics applied to visible matter does not describe the dynamics of stars, galaxies, and galaxy clusters was well established in the 20th century.

As a first approximation, one can estimate the mass of a galaxy based on its brightness: brighter galaxies contain more stars than dimmer galaxies. However, there are other ways to assess the total mass of a galaxy. In spiral galaxies, for example, stars rotate in quasi-circular orbits around the center. The rotational speed of peripheral stars depends, according to Newton's law, on the total mass of the galaxy, and one has thus an independent measurement of this mass. Do these two methods give consistent results?

In 1933 the Swiss astronomer Fritz Zwicky applied for the first time the virial theorem to the Coma cluster of galaxies;[6] his choice was motivated by the fact that Coma is a regular and nearly spherical well-studied

---

[6] The word *virial* comes from the latin *vis*, i.e., strength, or force; the term was coined by German physicist and mathematician Rudolf Clausius, one of the founders ofthe science of thermodynamics, around 1870.

cluster. We recall that the virial theorem states that, for a stationary self-gravitating system, twice its total kinetic energy K plus its potential energy U vanishes. Explicitly, denoting by v the total velocity of a galaxy in the cluster, we have $K = M\,v^2/2$ and for a spherical system $U = -\,\alpha G\,M^2/R$, where the constant α depends on the density profile and it is generally of order one. Since any astronomical object is not at rest with respect to the Sun (because of the expansion of the Universe, of the peculiar motion, etc.), the application of the virial theorem to Coma requires the velocity to be measured with respect to its center-of-mass. Accordingly, v^2 should be replaced by σ^2, where σ is the three-dimensional velocity dispersion of the Coma galaxies. Further, since only the line-of-sight velocity dispersion $\sigma_\parallel$ of the galaxies can be measured, Zwicky made the simplest possible assumption that Coma galaxies are isotropically distributed, so that $\sigma = \sqrt{3}\,\sigma_\parallel$. As far as the potential energy is concerned, Zwicky assumed that galaxies are uniformly distributed inside Coma, which yields $\alpha = 3/5$. Thus, the virial theorem now reads

$$\sigma^2_{\parallel,\mathrm{vir}} = \frac{G\,M_{\mathrm{gal}}}{5\,R_{\mathrm{Coma}}} \;, \tag{8.55}$$

where M_{gal} is the total mass of Coma in term of galaxies (no intracluster gas was known at that time). Zwicky was able to measure the line-of-sight of only seven galaxies of the cluster; assuming them to be representative of the whole galaxy population of Coma he found $\langle v_\parallel \rangle \simeq 7.31 \times 10^8\,\mathrm{cm\,s^{-1}}$ and $\sigma_{\parallel,\mathrm{obs}} \simeq 6.57 \times 10^7\,\mathrm{cm\,s^{-1}}$. Further, from the measured angular diameter of Coma and its distance as derived from the Hubble law he estimated $R_{\mathrm{Coma}} \simeq 10^{24}\,\mathrm{cm}$. Finally, Zwicky supposed that Coma contains about N = 800 galaxies with mass $m_{\mathrm{gal}} \simeq 10^9\,M_\odot$ – which at that time was considered typical for galaxies – thereby getting $M_{\mathrm{Coma}} \simeq 8 \times 10^{11}\,M_\odot$. Therefore Eq. (8.55) yields $\sigma_\parallel \simeq 4.62 \times 10^6\,\mathrm{cm\,s^{-1}}$. Since $\sigma^2_\parallel \propto M_{\mathrm{gal}}$, in order to bring $\sigma_{\parallel,\mathrm{vir}}$ in agreement with $\sigma_{\parallel,\mathrm{obs}}$, Zwicky had to increase m_{gal} by a factor of about 200 (he wrote 400), thereby obtaining for the Coma galaxies $M_{\mathrm{gal}} \simeq 2 \times 10^{11}\,M_\odot$ (he wrote $4 \times 10^{11}\,M_\odot$). Thus, Zwicky ended up with the conclusion that Coma galaxies have a mass about two orders of magnitudes larger than expected: his explanation was that these galaxies are totally dominated by dark matter.

Despite this early evidence, it was only in the 1970s that scientists began to explore this discrepancy in a systematic way and that the existence of dark matter started to be quantified. It was realized that the discovery of dark matter would not only have solved the problem of the lack of mass in clusters of galaxies, but would also have had much more far-reaching consequences on our prediction of the evolution and fate of the Universe.

An important observational evidence of the need for dark matter was provided by the rotation curves of spiral galaxies—the Milky Way is one of them. Spiral galaxies contain a large population of stars placed on nearly circular orbits around the Galactic center. Astronomers have conducted observations of the orbital velocities of stars in the peripheral regions of a large number of spiral galaxies, and found that the orbital speeds remain constant, contrary to the expected prediction of reduction at larger radii. The mass enclosed within the orbits radius must therefore gradually increase in regions even beyond the edge of the visible galaxy.

Later, another independent confirmation of Zwicky's findings came from gravitational lensing. Lensing is the effect that bends the light coming from distant objects, due to large massive bodies in the path to the observer. As such it constitutes another method of measuring the total content of gravitational matter. The obtained mass-to-light ratios in distant clusters match the dynamical estimates of dark matter in those clusters.

8.1.5.1 How Is Dark Matter Distributed in Galaxies?

The first systematic investigation of the distribution of DM contained in spiral galaxies was carried out by Vera Rubin and collaborators between 1980 and 1985 using stars as DM tracers. Since in spiral galaxies stars move on nearly circular orbits, the gravitational acceleration equals the centripetal force. Thus, by denoting by μ the mass of a star, we have $\mu\,v^2/r = G\mu\,M(r)/r^2$ where $M(r)$ is the total mass inside the radius r of the orbit of the star:

$$v(r) = \sqrt{\frac{GM(r)}{r}} \;. \tag{8.56}$$

Thus, from the kinematic measurements of the *rotation curve* $v(r)$ one can infer the dynamics of the galaxy. If all galactic mass were luminous, then at large enough distance from the center most of the mass would be well inside r, thereby implying that $M(r) \simeq$ constant; Eq. 8.56 yields $v(r) \propto 1/\sqrt{r}$. This behavior is called
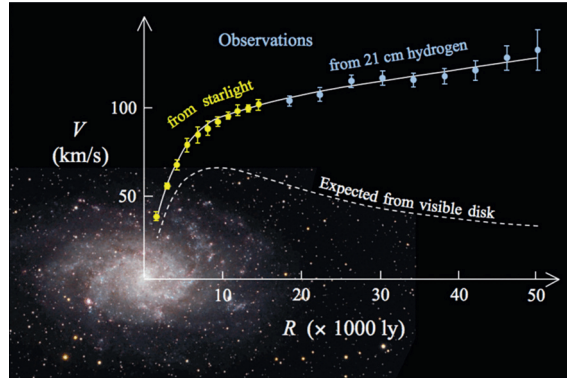
Fig. 8.12 Rotation curve of the galaxy M33 (from Wikimedia Commons, public domain).

Keplerian because it is identical to that of the rotation velocity of the planets orbiting the Sun. Yet, the observations of Rubin and collaborators showed that $v(r)$ rises close enough to the center, and then reaches a maximum and stays constant as r increases, failing to exhibit the expected Keplerian fall-off. According to Eq. 8.56 the observed behavior implies that in order to have $v(r) = $ constant it is necessary that $M(r) \propto r$. But since

$$M(r) = 4\pi \int_0^r dr' \ \rho(r') \ , \tag{8.57}$$

where $\rho(r)$ is the mass density, the conclusion is that al large enough galactocentric distance the mass density goes like $\rho(r) \propto 1/r^2$. In analogy with the behavior of a self-gravitating isothermal gas sphere, the behavior is called *singular isothermal.* As a consequence, spiral galaxies turn out to be surrounded in first approximation by a singular isothermal halo made of dark matter. In order to get rid of the central singularity, it is often assumed that the halo profile is pseudo-isothermal, assuming a density:

$$\text{Pseudo} - \text{Isothermal} : \rho_{\text{iso}}(r) = \frac{\rho_0}{1 + (r/r_s)^2} \ . \tag{8.58}$$

While strongly suggestive of the existence of dark halos around spiral galaxies, optical studies have the disadvantage that typically at the edge of the stellar disk the difference between a constant rotation curve and a Keplerian one is about 15 %, too small to draw waterproof conclusion when errors are taken into account. Luckily, the disks of spirals also contain neutral atomic hydrogen (HI) clouds; like stars they move on nearly circular orbits, but the gaseous disk extends typically twice, and in some cases even more. According to relativistic quantum mechanics, the non-relativistic ground state of hydrogen at $E \simeq -13.6\,\text{eV}$ splits into a pair of levels, depending on the relative orientation of the spins of the proton and the electron; the energy splitting is only $\delta E \simeq 5.9\,\mu\text{eV}$ (hyperfine splitting). Both levels are populated thenks to collisional excitation and interaction with the CMB; thus, HI clouds can be detected by radio-telescopes since photons emitted during the transition to the ground state have a wavelength of about 21 cm. In 1985 Van Albada, Bahcall, Begeman and Sancisi performed this measurement for the spiral NGC 3198, whose gaseous disks is more extended than the stellar disk by a factor of 2.7, and could construct the rotation curve out to 30 kpc. They found that the flat behavior persists, and this was regarded as a clear-cut evidence for dark matter halos around spiral galaxies. Measurements now include a large set of galaxies (Fig. 8.12), including the Milky Way (Fig. 8.13).

Profiles obtained in numerical simulations of dark matter including baryons are steeper in the center than those obtained from simulations with dark matter only. The Navarro, Frenk, and White (NFW) profile, often used as a benchmark, follows a r^{-1} distribution at the center. On the contrary, the Einasto profile does not follow a power law near the center of galaxies, is smoother at kpc scales, and seems to fit better more recent numerical simulations. A value of about 0.17 for the shape parameter α in Eq. 8.59 is consistent with present data and simulations. Moore and collaborators have suggested profiles steeper than NFW.

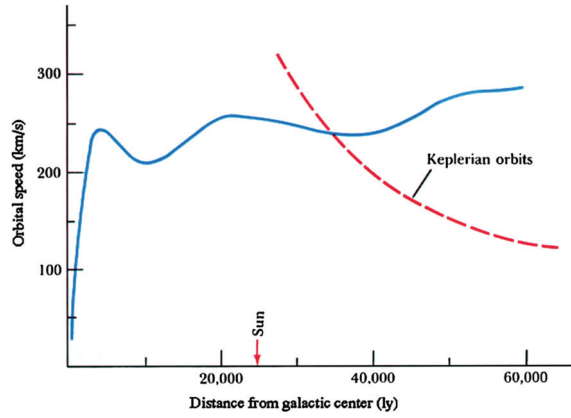The analytical expression of these profiles are

Fig. 8.13 Rotation curve of the Milky Way (from http://abyss.uoregon.edu).
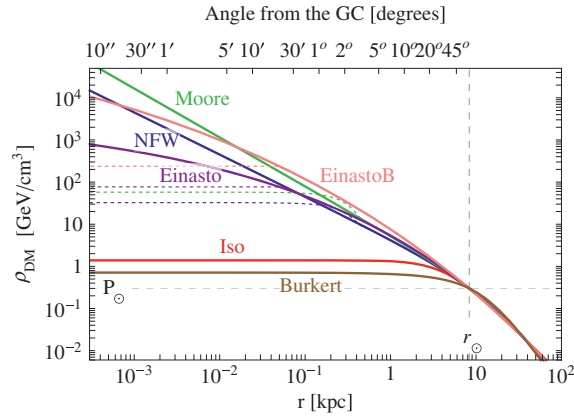

Fig. 8.14 Comparison of the densities as a function of the radius for DM profiles used in the literature, with values adequate to fit the radial distribution of velocities in the halo of the Milky Way. The curve EinastoB indicates an Einasto curve with a different α parameter. From M. Cirelli et al., "PPPC 4 DM ID: A Poor Particle Physicist Cookbook for Dark Matter Indirect Detection", arXiv:1012.4515, JCAP 1103 (2011) 051.

$$
\begin{aligned}
\text{NFW}: \quad & \rho_{\text{NFW}}(r) = \rho_s \frac{r_s}{r}\left(1 + \frac{r}{r_s}\right)^{-2} \\
\text{Einasto}: \ & \rho_{\text{Einasto}}(r) = \rho_s \exp\left\{-\frac{2}{\alpha}\left[\left(\frac{r}{r_s}\right)^{\alpha} - 1\right]\right\} \\
\text{Moore}: \quad & \rho_{\text{Moore}}(r) = \rho_s \left(\frac{r_s}{r}\right)^{1.16}\left(1 + \frac{r}{r_s}\right)^{-1.84}.
\end{aligned}
\tag{8.59}
$$

Presently, there are no good observational measurements of the shape of the Milky Way near the Galactic Center; this is why one usually assumes a spherically symmetrical distribution. Figure 8.14 compares these different profiles with the constraint to fit the velocities in the halo of our galaxy.

In the neighborood of the Solar System one has a DM density

$$
\rho_{DM,\,local} \simeq 0.4 \, \text{GeV/cm}^3 \,,
$$

i.e., five orders of magnitude larger than the total energy density of the Universe.

To distinguish between the functional forms for the halos is not easy. They vary among each other only in the central region, where the luminous matter is dominant. Needless to say, the high-density, central region is the most crucial for detection—and uncertainties there span three orders of magnitude. Also because of this, one of the preferred targets for astrophysical searches for DM are small satellite galaxies of the Milky Way, the so-called dwarf spheroidals (dSph), which typically have a number of stars $\sim 10^3 - 10^8$, to be compared with the $\sim 10^{11}$ of our Galaxy. For these galaxies the ratio between the estimate of the total mass M inferred from the velocity dispersion (velocities of single stars are measured with an accuracy of a few kilometers per second thanks to optical measurements) and the luminous mass L, inferred from the count
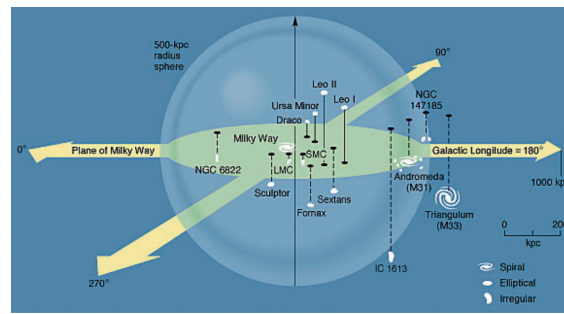
Fig. 8.15 The Local Group of galaxies around the Milky Way (from http://abyss.uoregon.edu/ js/ast123/lectures/lec11.html). The largest galaxies are the Milky Way, Andromeda, and M33, and have a spiral form. Most of the other galaxies are rather small and with a spheroidal form. These orbit closely the large galaxies, as is also the case of the irregular Magellanic Clouds, best visible in the southern hemisphere, and located at a distance of about 120,000 ly, to be compared with the Milky Way radius of about 50 000 ly.

of the number of stars, can be very large. The dwarf spheroidal satellites of the Milky Way could become tidally disrupted if they did not have enough dark matter. In addition these objects are not far from us: a possible DM signal should not be attenuated by distance dimming. Table 8.1 shows some characteristics of dSph in the Milky Way; their position is shown in Fig. 8.15.

The observations of the dynamics of galaxies and clusters of galaxies, however, are not the only astrophysical evidence of the presence of DM. Cosmological models for the formation of galaxies and clusters of galaxies indicate that these structures fail to form without DM.

8.1.5.2 An Alternative Explanation: Modified Gravity

The dependence of v^2 on the mass $M(r)$ on which the evidence for DM is based relies on the virial theorem, stating that the kinetic energy is on average equal to the absolute value of the total energy for a bound state, defining zero potential energy at infinite distance. The departure from this Newtonian prediction could also be related to a departure from Newtonian gravity.

Alternative theories do not necessarily require dark matter, and replace it with a modified Newtonian gravitational dynamics. Notice that, in a historical perspective, deviations from expected gravitational dynamics already led to the discovery of previously *unknown matter* sources. Indeed, the planet Neptune was discovered following the prediction by Le Verrier in the 1840s of its position based on the detailed observation of the orbit of Uranus and Newtonian dynamics. In the late nineteenth century, the disturbances to the expected orbit of Neptune led to the discovery of Pluto. On the other hand, the precession of the perihelion of Mercury, which could not be *quantitatively* explained by Newtonian gravity, confirmed the prediction of general relativity—and thus a modified dynamics.

The simplest model of modified Newtonian dynamics is called MOND; it was proposed in 1983 by Milgrom, suggesting that for extremely small accelerations the Newton's gravitational law may not be valid—indeed Newton's law has been verified only at reasonably large values of the gravitational acceleration. MOND postulates that the acceleration a is not linearly dependent on the gradient of the gravitational field ϕ_N at

Table 8.1 A list of dSph satellites of the Milky Way that may represent the best candidates for DM searches according to their distance from the Sun, luminosity, and inferred M/L ratio

dSph	$D_\odot$ (kpc)	L (10^3 $L_\odot$)	M/L ratio
Segue 1	23	0.3	>1000
UMa II	32	2.8	1100
Willman 1	38	0.9	700
Coma Berenices	44	2.6	450
UMi	66	290	580
Sculptor	79	2200	7
Draco	82	260	320
Sextans	86	500	90
Carina	101	430	40
Fornax	138	15500	10

Fig. 8.16 The matter in the "bullet cluster" is shown in this composite image (from http://apod.nasa.gov/apod/ap060824.html, credits: NASA/CXC/CfA/ M. Markevitch et al.). In this image depicting the collision of two clusters of galaxies, the bluish areas show the distributions of dark matter in the clusters, as obtained with gravitational lensing, and the red areas correspond to the hot X-ray emitting gases. The individual galaxies observed in the optical image data have a total mass much smaller than the mass in the gas, but the sum of these masses is far less than the mass of dark matter. The clear separation of dark matter and gas clouds is a direct evidence of the existence of dark matter.

small values of the acceleration, and proposes the following modification:

$$\mu\left(\frac{a}{a_0}\right) a = |-\boldsymbol{\nabla}\phi_N| \ . \tag{8.60}$$

The function μ is positive, smooth, and monotonically increasing; it is approximately equal to its argument when the argument takes small values compared to unity (deep MOND limit), but approaches unity when that argument is large. a_0 is a constant with dimensions, approximately equal to $10^{-10}\,\mathrm{m\,s^{-2}}$.

Let us now consider again stars orbiting a galaxy with speed $v(r)$ at radius r. For large r values, a will be smaller than a_0 and we can approximate $\mu(x) \simeq x$. One has then

$$\frac{v^4}{r^2} \simeq a_0 \frac{GM}{r^2} \ .$$

In this limit, the rotation curve flattens at a typical value v_f given by

$$v_f = (MGa_0)^{1/4} \ . \tag{8.61}$$

MOND explains well the shapes of rotation curves; for clusters of galaxies one finds an improvement but the problem is not completely solved.

The likelihood that MOND is the full explanation for the anomaly observed in the velocities of stars in the halo of galaxies is not strong. An explanation through MOND would require an *ad hoc* theory to account for cosmological evidence as well. In addition the observation in 2004 of the merging galaxy cluster 1E0657-58 (the so-called bullet cluster), has further weakened the MOND hypothesis. The bullet cluster consists of two colliding clusters of galaxies, at a distance of about 3.7 Gly. In this case (Fig. 8.16), the distance of the center of mass to the center of baryonic mass cannot be explained by changes in the gravitational law, as indicated by data with a statistical significance of 8σ.

One could also consider the fact that galaxies may contain invisible matter of known nature, either baryons in a form which is hard to detect optically, or massive neutrinos—MOND reduces the amount of invisible matter needed to explain the observations.

8.1.6 Age of the Universe: a First Estimate

The age of the Universe is an old question. Has the Universe a finite age? Or is the Universe eternal and always equal to itself (steady state Universe)?

For sure the Universe must be older than the oldest object that it contains and the first question has been then: how old is the Earth? In the eleventh century, the Persian astronomer Abu Rayhan al-Biruni had already realized that Earth should have a finite age, but he just stated that the origin of Earth was too far away to possibly measure it. In the nineteenth century the first quantitative estimates finally came. From considerations, both, on the formation of the geological layers, and on the thermodynamics of the formation and cooling of Earth, it was estimated that the age of the Earth should be of the order of tens of millions of years. These estimates were in contradiction with both, some religious beliefs, and Darwin's theory of evolution. Rev. James Ussher, an Irish Archbishop, published in 1650 a detailed calculation concluding that according to the Bible "God created Heaven and Earth" some six thousand years ago, more precisely "at the beginning of the night of October 23rd in the year 710 of the Julian period", which means 4004 B.C.. On the other hand, tens or even a few hundred million years seemed to be a too short time to allow for the slow evolution advocated by Darwin. Only the discovery of radioactivity at the end of nineteenth century provided precise clocks to date rocks and meteorite debris with, and thus to allow for reliable estimates of the age of the Earth. Surveys in the Hudson Bay in Canada found rocks with ages of over four billion ($\sim 4.3 \times 10^9$) years. On the other hand measurements on several meteorites, in particular on the Canyon Diablo meteorite found in Arizona, US, established dates of the order of $(4.5-4.6) \times 10^9$ years. Darwin had the time he needed!

The proportion of elements other than hydrogen and helium (defined as the metallicity) in a celestial object can be used as an indication of its age. After primordial nucleosynthesis (Sect. 8.1.4) the Universe is basically composed by hydrogen and helium. Thus the older (first) stars should have lower metallicity than the younger ones (for instance our Sun). The measurement of the age of low metallicity stars imposes, therefore, an important constraint on the age of the Universe. Oldest stars with a well-determined age found so far are, for instance, HE 1523-0901, a red giant at around 7500 light years away from us, and HD 140283, denominated the Methuselah star, located around 190 light years away. The age of HE 1523-0901 was measured to be 13.2 Gyr, using mainly the decay of uranium and thorium. The age of HD 140283 was determined to be (14.5 ± 0.8) Gyr.

The "cosmological" age of the Universe is defined as the time since the Big Bang, which at zeroth order is just given by the inverse of the Hubble constant:

$$t_0 \simeq \frac{1}{H_0} \simeq 14 \, \text{Gyr} \,. \tag{8.62}$$

A more precise value is determined by solving the equations of evolution of the Universe, the so-called Friedmann equations (see Sect. 8.2), for a given set of the cosmological parameters. Within the ΛCDM model (see Sect. 8.4) the best fit value, taking into account the present knowledge of such parameters, is

$$t_0 = (13.80 \pm 0.04) \, \text{Gyr} \,. \tag{8.63}$$

Within uncertainties both the cosmological age and the age of the first stars are compatible, but the first stars had to be formed quite early in the history of the Universe.

Finally, we stress that a Universe with a finite age and in expansion will escape the nineteenth century Olbers' Paradox: "How can the night be dark?" This paradox relies on the argument that in an infinite static Universe with uniform star density (as the Universe was believed to be by most scientists until the mid of last century) the night should be as bright as the day. In fact, the light coming from a star is inversely proportional to the square of its distance, but the number of stars in a shell at a distance between r and $(r + dr)$ is proportional to the square of the distance r. From this it seems that any shell in the Universe should contribute the same amount light. Apart from some too crude approximations (such as, not taking into account the finite life of stars), redshift and the finite size of the Universe solve the paradox.

8.2 General Relativity

Special relativity, introduced in Chap. 2, states that one cannot distinguish on the basis of the laws of physics between two inertial frames moving at constant speed one with respect to the other. Experience tells that it is possible to distinguish between an inertial frame and an accelerated frame. Can the picture change if we include gravity?

In classical mechanics, gravity is a force and determines the movement of a body according to Newton's second law. The gravitational force is proportional to the body's gravity charge, which is the gravitational mass m_g; this, in turn, is proportional to the inertial mass m_I, that characterizes the body's inertia to be accelerated by a force. The net result is that the local acceleration of a body, g, due to a gravitational field created by a mass M at a distance r, is proportional to the ratio m_g/m_I

$$F_g = m_g \; G\frac{M}{r^2} = F_g = m_I \; g \, ,$$

and

$$g = \frac{m_g}{m_I} \; G\frac{M}{r^2} \, ,$$

where G is the universal gravitational constant.

Thus if m_g were proportional to m_I the movement of a body in a gravitational field would be independent of its mass and composition. In fact the experiments of Galilei on inclined planes showed the universality of the movement of rolling balls of different compositions and weights. Such universality was also found by measuring the period of pendulums with different weights and compositions but identical lengths, first again by Galilei, and later on with a much higher precision (better than 0.1%) by Newton. Nowadays, m_g/m_I is experimentally known to be constant for all bodies, independent of their nature, mass, and composition, up to a relative resolution of 5×10^{-14}. We then *choose* G in such a way that $m_g/m_I \equiv 1$. Space-based experiments, allowing improved sensitivities up to 10^{-17} on m_g/m_I, are planned for the next years.

8.2.1 Equivalence Principle

It is difficult to believe that such a precise equality is just a coincidence. This equality has been thus promoted to the level of a principle, named the *weak equivalence principle*, and it led Einstein to formulate the *strong equivalence principle* which is a fundamental postulate of General Relativity (GR). Einstein stated that it is not possible to distinguish infinitesimal movements occurring in an inertial frame due to gravity (which are proportional to the gravitational mass), from movements occurring in an accelerated frame due to "fictitious" inertial forces (which are proportional to the inertial mass).

A ball dropped in a gravitational field has, during an infinitesimal time interval, the same behavior that a free ball has in an accelerated frame if the acceleration a of the accelerated frame is opposite to the local acceleration g of gravity (Fig. 8.17). No experiment can distinguish between the two scenarios.

8.2.2 Light and Time in a Gravitational Field

In the same way, if an observer is inside a free-falling elevator, gravity is locally canceled out by the "fictitious" forces due to the acceleration of the frame. Free falling frames are equivalent to inertial frames. A horizontal light beam in such a free falling elevator then moves in a straight line for an observer inside the elevator, but it curves down for an observer outside the elevator (Fig. 8.18). Light therefore curves in a gravitational field.

The bending of light passing near the Sun was discussed by Newton himself and computed by Cavendish and Soldner to be of about 0.9 arcsecond for a light ray passing close to the Sun's limb; this result in its deduction assumes the Newton corpuscular theory of light. However, Einstein found, using the newborn equations of GR, a double value and then a clear test was in principle possible through the observation of the apparent position of stars during a total solar eclipse. In May 1919 Eddington and Dyson led two independent expeditions, respectively, to the equatorial islands of São Tomé e Príncipe and to Sobral, Brazil. The observations were perturbed by clouds (Príncipe) and by instrumental effects (Sobral) but nevertheless the announcement by Eddington that Einstein's predictions were confirmed had an enormous impact on public opinion and made general relativity widely known. Further and more robust observations were carried on in the following years and the predictions of general relativity on light deflection were firmly confirmed.
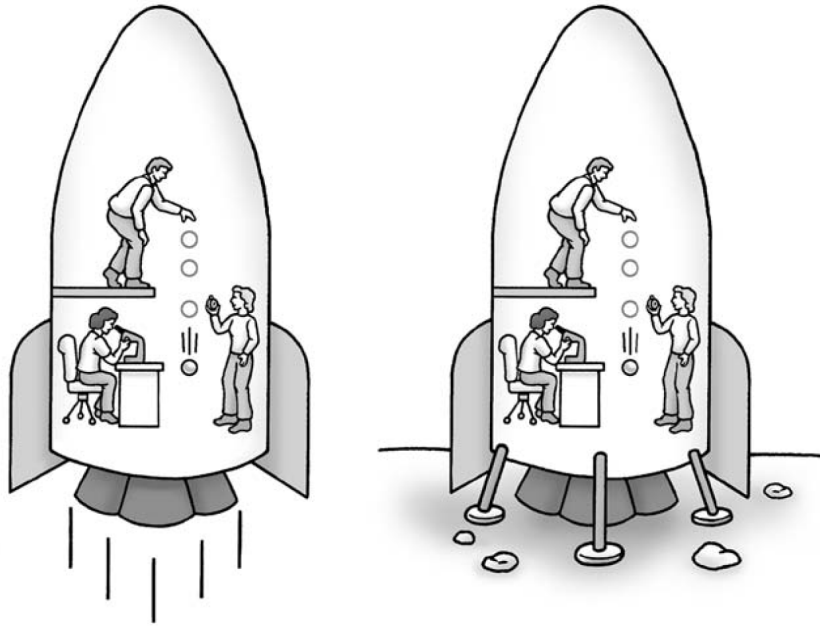
Fig. 8.17 Scientists performing experiments in an accelerating spaceship moving with an upward acceleration g (left) obtain the same results as if they were on a planet with gravitational acceleration g (right). From A. Zimmerman Jones, D. Robbins, "String Theory For Dummies", Wiley 2009.
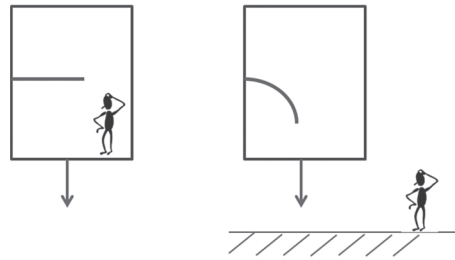
Fig. 8.18 Trajectory of a light beam in an elevator freely falling seen by an observer inside (left) and outside (right).

Now we want to use the principle of equivalence for predicting the influence of the gravitational field on the measurement of time intervals. We shall follow the line of demonstration by Feynman in his famous Lectures on Physics.
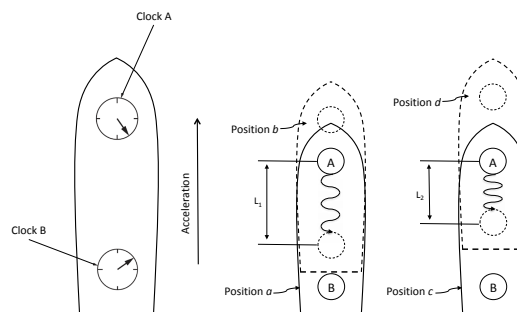
Fig. 8.19 Rocket on the left: Two clocks onboard an accelerating rocket. Two rockets on the right: Why the clock at the head appears to run faster than the clock at the tail.

Suppose we put a clock A at the "head" of a rocket uniformly accelerating, and another identical clock B at the "tail," as in Fig. 8.19, left. Imagine that the front clock emits a flash of light each second, and that you are sitting at the tail comparing the arrival of the light flashes with the ticks of clock B. Assume that the rocket is in the position a of Fig. 8.19, right, when clock A emits a flash, and at the position b when the flash arrives at clock B. Later on the ship will be at position c when the clock A emits its next flash, and at position d when you see it arrive at clock B. The first flash travels the distance L_1 and the second flash travels the shorter distance L_2, because the ship is accelerating and has a higher speed at the time of the second flash. You can see, then, that if the two flashes were emitted from clock A one second apart, they would arrive at clock B with a separation somewhat less than one second, since the second flash does not spend as much time on the way. The same will also happen for all the later flashes. So if you were sitting in the tail you would conclude that clock A was running faster than clock B. If the rocket is at rest in a gravitational field, the principle of equivalence guarantees that the same thing happens. We have the relation

$$\text{(Rate at the receiver)} = \text{(Rate of emission)} \left(1 + \frac{g\text{H}}{c^2} \right)$$

where H is the height of the emitter above the receiver. This time dilation due to the gravitational field can also be seen as due to the differences in the energy losses of the photons emitted in both elevators by "climbing" out the gravitational field. In fact in a weak gravitational field the variation of the total energy of a particle of mass m, assuming the equivalence principle, is independent of m:

$$\frac{\Delta E}{E} \simeq \frac{mg\text{H}}{mc^2} = \frac{g\text{H}}{c^2} .$$

Since, for a photon, energy and frequency are related by the Planck formula $E = h\nu$:

$$\frac{\Delta E}{E} = \frac{\Delta \nu}{\nu} \sim \frac{\Delta \lambda}{\lambda} \sim \frac{g\text{H}}{c^2} .$$

8.2.3 Flat and Curved Spaces

Gravity in GR is no longer a force (whose sources are the masses) acting in a flat spacetime Universe. Gravity is embedded in the geometry of spacetime that is determined by the energy and momentum contents of the Universe.

Classical mechanics considers that we are living in a Euclidean three-dimensional space (flat, i.e., with vanishing curvature), where through each point outside a "straight" line (a geodesic) there is one, and only one, straight line parallel to the first one; the sum of the internal angles of a triangle is 180°; the circumference of a circle of radius R is $2\pi R$, and so on. However, it is interesting to consider what would happen if this were not the case.

To understand why a different approach could be interesting, let us consider that we are living on the surface of a sphere (the Earth is approximately a sphere). Such a surface has positive (ideally constant) curvature at all points (i.e., the spherical surface stays on just one side of the tangent planes to the surface at any given point): the small distance between two points is now the length of the arc of circle connecting the two points and whose center coincides with the center of the sphere (geodesic line in the sphere), and this is as close as we can get to a *straight line*; the sum of the angles of a triangle is greater than 180°; the circumference of a circle of radius R is less than $2\pi R$. Alternatively, let us imagine that we were living on a saddle, which has a negative curvature (the surface can curve away from the tangent plane in two different directions): then the sum of the angles of a triangle is less than 180°; the perimeter of a circumference is greater than $2\pi R$, and so on. The three cases are visualized in Fig. 8.20. The metric of the sphere and of the saddle are not Euclidean.
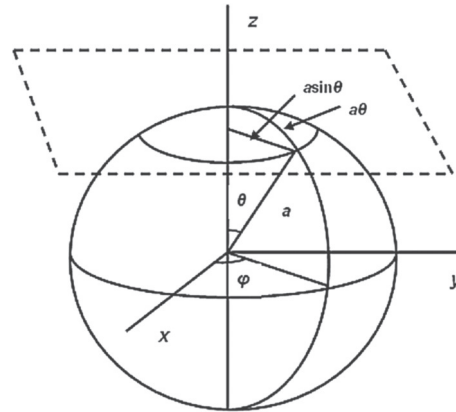
8.2.3.1 2D Space

In a flat 2D surface (a plane) the square of the distance between two points is given in Cartesian coordinates by

$$ds^2 = dx^2 + dy^2 \tag{8.64}$$
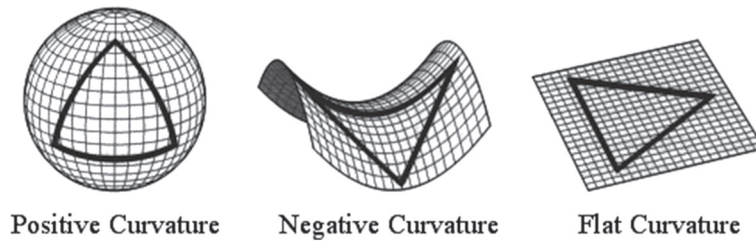
Fig. 8.20 2D surfaces with positive, negative, and null curvatures (from http://thesimplephysicist.com, ©2014 Bill Halman/tdotwebcreations).

Fig. 8.21 Distances on a sphere of radius a. From A. Tan et al. DOI:10.5772/50508.

or

$$ds^2 = g_{\mu\nu}dx^\mu dx^\nu \tag{8.65}$$

with

$$g_{\mu\nu} = \begin{pmatrix} 1 & 0 \\ 0 & 1 \end{pmatrix} . \tag{8.66}$$

The metric $g_{\mu\nu}$ of the 2D flat surface is constant and the geodesics are straight lines.

The metric of a 2D spherical surface is a little more complex. The square of the distance between two neighboring close points situated on the surface of a sphere with radius a embedded in our usual 3D Euclidean space (Fig. 8.21) is given in spherical coordinates by

$$ds^2 = a^2 d\theta^2 + a^2\sin^2\theta \; d\varphi^2. \tag{8.67}$$

The maximum distance between two points on the sphere is bounded by $d = \sqrt{s^2} = \pi \, a$: the two points are the extrema of a half great circle.

Now the matrix representing the metric in spherical coordinates,

$$g_{\mu\nu} = \begin{pmatrix} a^2 & 0 \\ 0 & a^2\sin^2\theta \end{pmatrix} , \tag{8.68}$$

is no longer constant, because of the presence of the $\sin^2\theta$ term. It is not possible to cover the entire sphere with one unique plane without somewhat distorting the plane, although it is always possible to define locally at each point one tangent plane. The geodesics are not straight lines; they are indeed part of great circles, as it can be deduced directly from the metrics and its derivatives.

This metric can now be written introducing a new variable $r = \sin\theta$ as

$$ds^2 = a^2 \left(\frac{dr^2}{1 - Kr^2} + r^2 \; d\varphi^2 \right) \tag{8.69}$$

with

$$K = 1$$

for the case of the sphere.[7] Indeed, the sphere has a positive $(K = 1)$ curvature at any point of its surface. However, the above expressions are valid both for the case of negative $(K = -1)$ and null $(K = 0)$ curvature. In the case of a flat surface, indeed, the usual expression in polar coordinates is recovered:

$$ds^2 = a^2 \left(dr^2 + r^2 \, d\varphi^2 \right) . \tag{8.70}$$

The distance between two points with the same φ and, respectively, $r_1 = 0$ and $r_2 = R/a$, is given by:

$$s = \int_0^{\frac{R}{a}} a \, \frac{dr}{\sqrt{1 - Kr^2}} = a \, S_k \tag{8.71}$$

with

$$S_k = \begin{cases} \arcsin(R/a) & \text{if } K = 1 \\ R/a & \text{if } K = 0 \\ \text{arcsinh}(R/a) & \text{if } K = -1 \end{cases} . \tag{8.72}$$

The area of the sphere is now given by

$$A = 4 \, \pi \, a^2 {S_k}^2 . \tag{8.73}$$

The relation between the proper distance and the luminosity distance (Sect. 8.1.1) is now

$$d_L = d_p \frac{a}{R} S_k (1 + z) , \tag{8.74}$$

and the metric can also be written in a more compact form using the function S_k:

$$ds^2 = a^2 \left(dr^2 + {S_k}^2 d\varphi^2 \right) . \tag{8.75}$$

8.2.3.2 3D Space

For a homogeneous and isotropic 3D space the previous formula can be generalized (now r and θ are independent variables) leading to:

$$ds^2 = a^2 \left[\frac{dr^2}{1 - Kr^2} + r^2 \left(d\theta^2 + \sin^2\theta \, d\varphi^2 \right) \right] .$$

8.2.3.3 4D Spacetime

For a spatially homogeneous and isotropic 4D spacetime the generalization leads to the so-called Robertson–Walker metric $(c = 1)$:

$$ds^2 = dt^2 - a^2(t) \left[\frac{dr^2}{1 - Kr^2} + r^2 \left(d\theta^2 + \sin^2\theta \, d\varphi^2 \right) \right] \tag{8.76}$$

where $a(t)$ is a radial scale factor which may depend on t (allowing for the expansion/contraction of the Universe).

Introducing the solid angle, $d\Omega^2 = d\theta^2 + \sin^2\theta \, d\varphi^2$, the Robertson–Walker metric can be written as

$$ds^2 = dt^2 - a^2 t \left(\frac{dr^2}{1 - Kr^2} + r^2 \, d\Omega^2 \right) . \tag{8.77}$$

Finally, the Robertson–Walker metric can also be written using the functions S_k introduced above as

$$ds^2 = dt^2 - a^2 t \left(dr^2 + {S_k}^2 \, d\Omega^2 \right) . \tag{8.78}$$

---

[7] r is dimensionless, with range $[0, 1]$; K is the curvature, which, in general, can be -1, 0, or $+1$. The more general change of coordinates $r' = a \sin\theta$ does not result in anything new, and can be recast in the form used above after setting $r = r'/a$. Of course with the r' coordinate, the curvature is not normalized, and can be, generically, negative, zero, or positive.

The special relativity Minkowski metric is a particular case ($K = 0$, $at = $ constant) of the Robertson–Walker metric.

The geodesics in a 4D spacetime correspond to the extremal (maximum or minimum depending on the metric definition) world lines joining two events in spacetime and not to the 3D space paths between the two points. The geodesics are determined, as before, just from the metric and its derivatives.

8.2.4 Einstein's Equations

In GR the world lines of freely falling test particles are just the geodesics of the 4D spacetime of the Universe we are living in, whose geometry is locally determined by its energy and momentum contents as expressed by Einstein's equations (which, below, are in the form where we neglect a cosmological constant term)

$$G_{\mu\nu} = R_{\mu\nu} - \frac{1}{2} g_{\mu\nu} \mathcal{R} = \frac{8\pi}{c^4} T_{\mu\nu}.$$

In the equations above $G_{\mu\nu}$ and $R_{\mu\nu}$ are, respectively, the Einstein and the Ricci tensors, which are built from the metric and its derivatives; $\mathcal{R}$ is the Ricci scalar ($\mathcal{R} = g^{\mu\nu} R_{\mu\nu}$) and $T_{\mu\nu}$ is the energy–momentum tensor.

The energy and the momentum of the particles determine the geometry of the Universe which then determines the trajectories of the particles. Gravity is embedded in the geometry of spacetime. Time runs slower in the presence of gravitational fields.

Einstein's equations are tensor equations and thus independent on the reference frame (the covariance of the physics laws is automatically ensured). They involve 4D symmetric tensors and represent in fact 10 independent nonlinear partial differential equations whose solutions, the metrics of spacetime, are in general difficult to sort out. However, in particular and relevant cases, exact or approximate solutions can be found. Examples are the Minkowski metric (empty Universe); the Schwarzschild metric (spacetime metric outside a noncharged spherically symmetric nonrotating massive object—see Sect. 8.2.8); the Kerr metric (a cylindrically symmetric vacuum solution); the Robertson–Walker metric (homogeneous and isotropic Universe—see Sect. 8.2.5).

Einstein introduced at some point a new metric proportional term in his equations (Λ, the so-called "cosmological constant"):

$$G_{\mu\nu} + g_{\mu\nu} \Lambda = \frac{8\pi}{c^4} T_{\mu\nu}. \tag{8.79}$$

His motivation was to allow for static cosmological solutions, as this term can balance gravitational attraction. Although later on Einstein discarded this term (the static Universe would be unstable), the recent discovery of the accelerated expansion of the Universe might give it again an essential role (see Sects. 8.2.5 and 8.4).

The energy–momentum tensor $T^{\mu\nu}$ in a Universe of free noninteracting particles with four-momentum p_i^μ moving along trajectories $r_i t$ is defined as

$$T^{\mu 0} = \sum_i p_i^\mu t \, \delta^3 (r - r_i t) \tag{8.80}$$

$$T^{\mu k} = \sum_i p_i^\mu t \frac{dx_i^k}{dt} \, \delta^3 (r - r_i t) \ . \tag{8.81}$$

The $T^{\mu 0}$ terms can be seen as "charges" and the $T^{\mu k}$ terms as "currents", which then obey a continuity equation which ensures energy–momentum conservation. In general relativity local energy–momentum conservation generalizes the corresponding results in special relativity,

$$\frac{\partial}{\partial x^0} T^{\mu 0} + \nabla_i T^{\mu i} = 0 \, , \text{or } \frac{\partial}{\partial x^\nu} T^{\mu\nu} = 0 \, . \tag{8.82}$$

To get an intuitive grasp of the physical meaning of the energy–momentum tensor, let us consider the case of a special relativistic perfect fluid (no viscosity). In the rest frame of a fluid with energy density ρ and pressure $\mathcal{P}$

$$T^{00} = c^2 \rho \, ; \ T^{0i} = 0 \, ; \ T^{ij} = \mathcal{P} \, \delta_{ij} \, . \tag{8.83}$$

Pressure has indeed the dimension of an energy density ($\delta W = F \cdot dx = \mathcal{P} \; dV$) and accounts for the "kinetic energy" of the fluid.

To appreciate a fundamental difference from the Newtonian case, we quote that for a perfect fluid with energy density ρ and pressure $\mathcal{P}$ the weak gravity field predicted by Newton is given by

$$\nabla^2 \phi = 4 \; \pi G \; \rho, \tag{8.84}$$

from which we see that pressure does not contribute. On the contrary, the weak field limit of Einstein's equations is

$$\nabla^2 \phi = 4 \; \pi G \; \left(\rho + \frac{3 \; \mathcal{P}}{c^2} \right) . \tag{8.85}$$

Remembering that, in the case of a relativistic fluid

$$\mathcal{P} \sim \frac{1}{3} \; \rho \; c^2 \tag{8.86}$$

the weak gravitational field is then determined by

$$\nabla^2 \phi = 8 \; \pi G \; \rho, \tag{8.87}$$

which shows that the gravitational field predicted by general relativity is twice the one predicted by Newtonian gravity. Indeed, the observed light deflection by Eddington in 1919 at S. Tomé and Príncipe islands in a solar eclipse was twice the one expected according to classical Newtonian mechanics.

Once the metric is known, the free fall trajectories of test particles are obtained "just" by solving the geodesic equations

$$\frac{d^2 x^\sigma}{d\tau^2} + \Gamma^\sigma_{\mu\nu} \frac{dx^\mu}{d\tau} \frac{dx^\nu}{d\tau} = 0, \tag{8.88}$$

where $\Gamma^\sigma_{\mu\nu}$ are the Christoffel symbols given by

$$\Gamma^\sigma_{\mu\nu} = \frac{g^{\rho\sigma}}{2} \left(\frac{\partial g_{\nu\rho}}{\partial x^\mu} + \frac{\partial g_{\mu\rho}}{\partial x^\nu} - \frac{\partial g_{\mu\nu}}{\partial x^\rho} \right) . \tag{8.89}$$

In the particular case of flat space in Cartesian coordinates the metric tensor is everywhere constant, $\Gamma^\sigma_{\mu\nu} = 0$, and then

$$\frac{d^2 x^\mu}{d\tau^2} = 0 \, .$$

The free particles classical straight world lines are then recovered.

8.2.5 The Friedmann–Lemaitre–Robertson–Walker Model (Friedmann Equations)

The present standard model of cosmology assumes the so-called cosmological principle, which in turn assumes a homogeneous and isotropic Universe at large scales. Homogeneity means that, in Einstein's words, "all places in the Universe are alike" and isotropic just means that all directions are equivalent.

The Robertson–Walker metric discussed before (Sect. 8.2.3) embodies these symmetries leaving two independent functions, $a(t)$ and $K(t)$, which represent, respectively, the evolution of the scale and of the curvature of the Universe. The Russian physicist Alexander Friedmann in 1922, and independently the Belgian Georges Lemaitre in 1927, solved Einstein's equations for such a metric leading to the famous Friedmann equations, which are still the starting point for the standard cosmological model, also known as the Friedmann–Lemaitre–Robertson–Walker (FLRW) model.

The Friedmann equations can be written (with the convention $c = 1$) as

$$\left(\frac{\dot{a}}{a} \right)^2 + \frac{K}{a^2} = \frac{8\pi G}{3} \; \rho + \frac{\Lambda}{3} \tag{8.90}$$

$$\left(\frac{\ddot{a}}{a}\right) = -\frac{4\pi G}{3}\left(\rho + 3\mathcal{P}\right) + \frac{\Lambda}{3}\,. \tag{8.91}$$

These equations can be combined into a thermodynamics like equation

$$\frac{d}{dt}\left(\rho\, a^3\right) = -\mathcal{P}\,\frac{d}{dt}\left(a^3\right), \tag{8.92}$$

where by identifying a^3 with the volume V we can recognize adiabatic energy conservation

$$dE = -\mathcal{P}\, dV\,.$$

Moreover, remembering that the Hubble parameter is given by (Eq. 8.8):

$$H = \frac{\dot{a}}{a}\,,$$

the first Friedmann equation is also often written as

$$H^2 + \frac{K}{a^2} = \frac{8\pi G}{3}\,\rho + \frac{\Lambda}{3}, \tag{8.93}$$

which shows that the Hubble constant is not a constant but a parameter that evolves with the evolution of the Universe.

8.2.5.1 Classical Newtonian Mechanics

"Friedmann-like" equations can also be formally deduced in the framework of classical Newtonian mechanics, as follows:

1. From Newton law of gravitation and from the Newton second law of motion we can write

$$m\ddot{R} = -\frac{GMm}{R^2} \implies \left(\frac{\ddot{a}}{a}\right) = -\frac{4\pi G}{3}\,\rho\,. \tag{8.94}$$

2. From energy conservation

$$\frac{1}{2}m\,\dot{R}^2 - \frac{GMm}{R} = \text{constant} \implies \left(\frac{\dot{a}}{a}\right)^2 - \frac{\text{constant}}{a^2} = \frac{8\pi G}{3}\,\rho\,. \tag{8.95}$$

The two Friedmann equations are "almost" recovered. The striking differences are that in classical mechanics the pressure does not contribute to the "gravitational mass", and that the Λ term must be introduced by hand as a form of repulsive potential.

The curvature of spacetime is, in this "classical" version, associated to (minus) the total energy of the system, which can somehow be interpreted as a "binding energy".

8.2.5.2 Single Component Universes

The two Friedmann equations determine, once the energy density ρ and the pressure $\mathcal{P}$ are known, the evolution of the scale $a(t)$ and of the curvature $K(t)$ of the Universe. However, ρ and $\mathcal{P}$ are nontrivial quantities, depending critically on the amount of the different forms of energy and matter that exist in the Universe at each evolution stage.

In the simplest case of a Universe with just nonrelativistic particles (ordinary baryonic matter or "cold"— i.e., nonrelativistic—dark matter) the pressure is negligible with respect to the energy density ($\mathcal{P} \ll \rho_m\, c^2$) and the Friedmann equations can be approximated as

$$\frac{d}{dt}\left(\rho_m\, a^3\right) = 0\,;\ \left(\frac{\ddot{a}}{a}\right) = -\frac{4\pi G}{3}\,\rho_m. \tag{8.96}$$

Solving these equations one finds

$$\rho_m \propto \frac{1}{a^3} \; ; \; a(t) \propto t^{\frac{2}{3}} \, . \tag{8.97}$$

In general for a Universe with just one kind of component characterized by an equation of state relating ρ and $\mathcal{P}$ of the type $\mathcal{P} = \alpha \rho$, the solutions are

$$\rho \propto a^{-3(\alpha+1)} \; ; \; a(t) \propto t^{\frac{2}{3(\alpha+1)}} \, . \tag{8.98}$$

For instance, in the case of a Universe dominated by relativistic particles (radiation or hot matter), $\alpha = 1/3$, and we obtain

$$\rho_\gamma \propto \frac{1}{a^4} \; ; \; a(t) \propto t^{\frac{1}{2}} \, . \tag{8.99}$$

This last relation can be interpreted by taking, as an example, a photon-dominated Universe, where the decrease in the density number of photons ($n_\gamma \propto a^{-3}$) combines with a decrease in the mean photon energy ($E_\gamma \propto a^{-1}$) corresponding to wavelength dilation.

8.2.5.3 Static Universe and Vacuum Energy Density

To model a static Universe ($\dot{a} = 0$, $\ddot{a} = 0$) one should have:

$$\frac{K}{a^2} = \frac{8\pi G}{3} \rho \; ; \; \rho + 3\mathcal{P} = 0 \, . \tag{8.100}$$

K should then be positive ($K = 1$) and $\mathcal{P} = -\frac{1}{3}\rho$. This requires a "new form of energy" with negative α, which can be related to the "cosmological" constant term. By reading this term on the right-hand side of Einstein's equations, we can formally include it in the energy–momentum tensor, thus defining a "vacuum" tensor as

$$T_{\mu\nu}^\Lambda = g_{\mu\nu}\Lambda = \begin{pmatrix} \rho_\Lambda & 0 & 0 & 0 \\ 0 & -\rho_\Lambda & 0 & 0 \\ 0 & 0 & -\rho_\Lambda & 0 \\ 0 & 0 & 0 & -\rho_\Lambda \end{pmatrix} \tag{8.101}$$

with

$$\rho_\Lambda = \frac{\Lambda}{8\pi G} \, . \tag{8.102}$$

This implies an equation of state of the form ($\alpha = -1$):

$$\mathcal{P}_\Lambda = -\rho_\Lambda \, . \tag{8.103}$$

Therefore, in a static Universe we would have

$$\rho = \rho_m + \rho_\Lambda \tag{8.104}$$

and

$$\rho_m = 2 \, \rho_\Lambda \, . \tag{8.105}$$

8.2.5.4 De Sitter Universe

In a Universe dominated by the cosmological constant ($\rho \equiv \rho_\Lambda$), as first discussed by de Sitter,

$$\frac{d}{dt}\left(\rho_\Lambda \, a^3\right) = \rho_\Lambda \frac{d}{dt}\left(a^3\right) \tag{8.106}$$

and

$$H^2 + \frac{K}{a^2} = \frac{\Lambda}{3} \tag{8.107}$$

implying

$$\rho_\Lambda = \text{constant} \; ; \; a(t) \sim e^{Ht} \tag{8.108}$$

with

$$H = \sqrt{\frac{\Lambda}{3}}. \tag{8.109}$$

Thus the de Sitter Universe has an exponential expansion while its energy density remains constant.

8.2.6 Critical Density of the Universe; Normalized Densities

The curvature of the Universe depends, according to Friedmann equations, on the energy density of the Universe according to

$$\frac{K}{a^2} = \frac{8\pi G}{3}\rho - H^2. \tag{8.110}$$

Therefore, if

$$\rho = \rho_{crit} = \frac{3H^2}{8\pi G} \tag{8.111}$$

one obtains

$$K = 0$$

and the Universe is, in this case, spatially flat.

For the present value of H_0 this corresponds to

$$\rho_{crit} \sim 5\,\text{GeV}/\text{m}^3, \tag{8.112}$$

i.e., less than 6 hydrogen atoms per cubic meter. The number of baryons per cubic meter one obtains from galaxy counts is, however, twenty times smaller—consistently with the result of the fit to CMB data.

8.2.6.1 Normalized Densities Ω_i, H, and q_0

The energy densities of each type of matter, radiation, and vacuum are often normalized to the critical density as follows:

$$\Omega_i = \frac{\rho_i}{\rho_{crit}} = \frac{8\pi G}{3\,H^2}\,\rho_i. \tag{8.113}$$

By defining also a normalized "curvature" energy density as

$$\Omega_K = -\frac{K}{H^2 a^2} = -\frac{K}{\dot{a}^2}, \tag{8.114}$$

the first Friedmann equation

$$\frac{8\pi G}{3H^2}\,\rho - \frac{K}{H^2 a^2} = 1 \tag{8.115}$$

takes then a very simple form

$$\Omega_m + \Omega_\gamma + \Omega_\Lambda + \Omega_K = 1. \tag{8.116}$$

On the other hand, it can be shown that taking into account the specific evolution of each type of density with the scale parameter a, the evolution equation for the Hubble parameter can be written as

$$H^2 = H_0^2\left(\Omega_{0\Lambda} + \Omega_{0K}a^{-2} + \Omega_{0m}a^{-3} + \Omega_{0\gamma}a^{-4}\right), \tag{8.117}$$

where the subscripts 0 indicate the values at present time ($t = t_0$, $a_0 = 1$).

Since the scale factor a is related to the redshift z, as discussed in Sect. 8.1.1, by

$$(1 + z) = a^{-1},$$

the Hubble evolution equation can be written as

$$H^2(z) = H_0^2\left(\Omega_{0\Lambda} + \Omega_{0K}(1+z)^2 + \Omega_{0m}(1+z)^3 + \Omega_{0\gamma}(1+z)^4\right). \tag{8.118}$$

Finally, the deceleration parameter q_0 can also be expressed as a function of the normalized densities Ω_i. In fact q_0 was defined as (Sect. 8.1.1)

$$q_0 = -\frac{\ddot{a}}{H_0{}^2 a} \,. \tag{8.119}$$

Now, using the second Friedmann equation

$$\left(\frac{\ddot{a}}{a}\right) = -\frac{4\pi G}{3} \ (\rho + 3\mathcal{P})$$

and the equations of state

$$\mathcal{P}_i = \alpha_i \ \rho_i,$$

one obtains

$$q_0 = -\frac{\ddot{a}}{H_0{}^2 a} = \frac{1}{2}\frac{8\pi G}{3H_0{}^2} \ \sum_i \rho_i \left(1 + 3\alpha_i\right)$$

$$q_0 = \frac{1}{2} \ \sum_i \Omega_i \left(1 + 3\alpha_i\right)$$

$$q_0 = \frac{1}{2}\Omega_{0m} + \Omega_{0\gamma} - \Omega_{0\Lambda} \,. \tag{8.120}$$

These equations in H and q_0 are of the utmost importance, since they connect directly the experimentally measured quantities H_0 and q_0 to the densities of the various energy species in the Universe.

8.2.6.2 Experimental Determination of the Normalized Densities

The total density of baryons, visible or invisible, as inferred from nucleosynthesis, is about 0.26 baryons per cubic meter, i.e.,

$$\Omega_b \sim 0.049 \pm 0.003 \,. \tag{8.121}$$

A small fraction of this is luminous—i.e., visible energy.

The currently most accurate determination of the overall densities comes from global fits of cosmological parameters to recent observations (see later). Using measurements of the anisotropy of the CMB and of the spatial distribution of galaxies, as well as the measured acceleration, the data indicate a fraction of nonbaryonic DM over the total energy content of the Universe given by

$$\Omega_{DM, nonbaryonic} \sim 0.258 \pm 0.011 \,. \tag{8.122}$$

According to the same fits, the total baryonic matter density is

$$\Omega_b \sim 0.048 \pm 0.002 \,. \tag{8.123}$$

Part of the baryonic matter may contribute to DM in form of nonluminous Dark Matter, e.g., massive compact objects or cold molecular gas clouds (see later).

In summary, a remarkable agreement of independent astrophysical observations with cosmological global fits indicates that the energy content of DM in the Universe could be about 25 % of the total energy of the Universe, compared to some 5 % due to ordinary matter.

The dark energy density can be measured from the observed curvature in the Hubble plot and from the position of the "acoustic peaks" in the angular power spectrum of the temperature fluctuations in the CMB:

$$\Omega_\Lambda \sim 0.692 \pm 0.012 \,. \tag{8.124}$$

Dark energy dominates thus the energy content of the Universe.

The Friedmann equation 8.90 can also be rewritten as

$$\Omega = \frac{\rho}{\rho_{crit}} = 1 + \frac{K}{H^2 a^2} \,, \tag{8.125}$$

where the *closure parameter* Ω is the sum of Ω_m, Ω_γ and Ω_Λ, with $\Omega_\gamma \simeq 5 \times 10^{-5}$ being negligible. This means that, in general, Ω is a function of time, unless $\Omega = 1$ and thus $K = 0$ (flat Universe).

The resent experimental data indicate a value

$$\Omega \sim 1.0002 \pm 0.0026 : \tag{8.126}$$

it would look very strange if this were a coincidence, unless Ω is identically one. For this reason this fact is at the heart of the standard model of cosmology, the ΛCDM model, which *postulates* $\Omega = 1$.

8.2.7 Age of the Universe from the Friedmann Equations and Evolution Scenarios

The evolution of the Hubble parameter can be used to estimate the age of the Universe for different composition of the total energy density. Indeed

$$H = \frac{\dot{a}}{a} = \frac{1}{a}\frac{da}{dt} = -\left(\frac{dz/dt}{1+z}\right)$$

$$dt = -\frac{dz}{(1+z)\ H}$$

$$(t_0 - t) = \frac{1}{H_0} \int_0^Z \frac{dz}{(1+z)\left(\Omega_\Lambda + \Omega_K(1+z)^2 + \Omega_m(1+z)^3 + \Omega_\gamma(1+z)^4\right)^{1/2}}. \tag{8.127}$$

The solution to this equation has to be obtained numerically in most realistic situations. However, in some simplified scenarios, an analytical solution can be found. In particular for matter ($\Omega_m = 1$) and radiation ($\Omega_\gamma = 1$) dominated Universes the solutions are, respectively,

$$(t_0 - t) = \frac{2}{3H_0} \tag{8.128}$$

and

$$(t_0 - t) = \frac{1}{2H_0}. \tag{8.129}$$

In a flat Universe with matter and vacuum energy parameters close to the ones presently measured ($\Omega_m = \Omega_{DM,nonbaryonic} + \Omega_B \simeq 0.3$, $\Omega_\Lambda \simeq 0.7$) we obtain

$$(t_0 - t) \sim \frac{0.96}{H_0}. \tag{8.130}$$

8.2.7.1 Evolution Scenarios

Friedmann equations have four independent parameters which can be chosen as:

- the present value of the Hubble parameter, H_0;
- the present value of the energy density of radiation, Ω_γ (we shall omit the subscript 0);
- the present value of the energy density of matter, Ω_m;
- the present value of the energy density of vacuum, Ω_Λ.

If we know these parameters, the geometry and the past and future evolutions of the Universe are determined provided the dynamics of the interactions, annihilations and creations of the different particle components (see Sect. **??**) are neglected. The solutions to these equations, in the general multicomponent scenarios, cannot be expressed in closed, analytical form, and require numerical approaches.
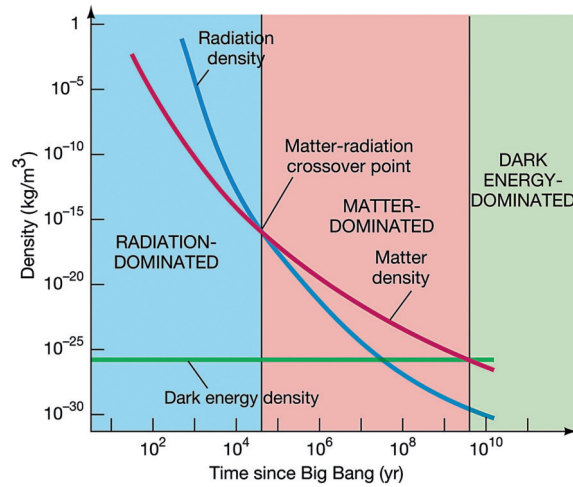
Fig. 8.22 The different ages the Universe passed through since the Big Bang (from http://scienceblogs.com/startswithabang/files/2013/06/AT_7e_Figure_27_01.jpeg, ©2011 Pearson education, Pearson Addison Wesley).

However, as we have discussed above, the evolution of the energy density of the different components scales with different powers of the scale parameter of the Universe a. Therefore, there are "eras" where a single component dominates. It is then reasonable to suppose that, initially, the Universe was radiation dominated (apart for a very short period where it is believed that inflation occurred—see Sect. **??**), then that it was matter dominated and finally, at the present time, that it is the vacuum energy (mostly "dark" energy, i.e., not coming from quantum fluctuations of the vacuum of the known interactions) that is starting to dominate (Fig. 8.22).

The crossing point ($a = a_{cross}$) between the matter and radiation ages can be obtained, in first approximation, by just equalizing the corresponding densities:

$$\Omega_\gamma \left(a_{cross}\right) = \Omega_m \left(a_{cross}\right)$$

$$\Omega_\gamma \left(a_0\right) \ \left(\frac{a_{cross}}{a_0}\right)^{-4} = \Omega_m \left(a_0\right) \ \left(\frac{a_{cross}}{a_0}\right)^{-3}$$

$$\left(\frac{a_{cross}}{a_0}\right)^{-1} = 1 + z_{cross} = \frac{\Omega_m \left(a_0\right)}{\Omega_\gamma \left(a_0\right)}. \tag{8.131}$$

The time after the Big Bang when this crossing point occur can approximately be obtained from the evolution of the scale factor in a radiation dominated Universe

$$a_{cross} \sim \left(2 \ H_0 \ \sqrt{\Omega_\gamma \left(a_0\right)} \ t_{cross}\right)^{\frac{1}{2}}, \tag{8.132}$$

or

$$t_{cross} \sim a_{cross}^2 \left(2 \ H_0 \ \sqrt{\Omega_\gamma \left(a_0\right)} \ \right)^{-1}. \tag{8.133}$$

Using the current best fit values for the parameters (see Sect. 8.4), we obtain

$$z_{cross} \ \sim 3\,200 \Longrightarrow t_{cross} \sim 7 \times 10^4 \text{ years}. \tag{8.134}$$

After this time (i.e., during the large majority of the Universe evolution) a two-component (matter and vacuum) description should be able to give a reasonable, approximate description. In this case the geometry and the evolution of the Universe are determined only by Ω_m and Ω_Λ. Although this is a restricted parameter phase space, there are several different possible evolution scenarios as shown in Fig. 8.23:

1. If $\Omega_m + \Omega_\Lambda = 1$ the Universe is flat but it can expand forever ($\Omega_\Lambda > 0$) or eventually recollapses ($\Omega_\Lambda < 0$).
2. If $\Omega_m + \Omega_\Lambda > 1$ the Universe is closed (positive curvature).
3. If $\Omega_m + \Omega_\Lambda < 1$ the Universe is open (negative curvature).
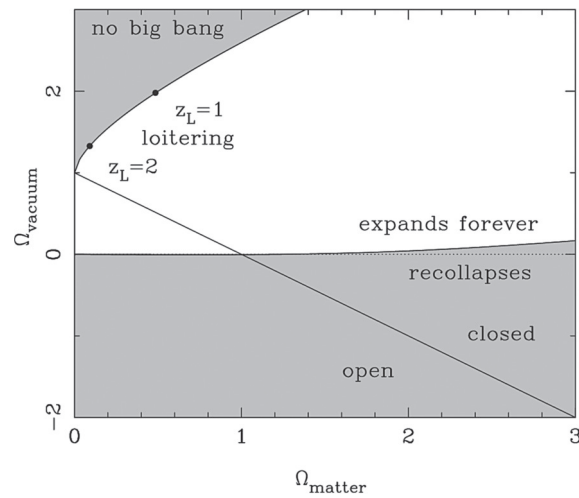
Fig. 8.23 Different scenarios for the expansion of the Universe. The Hubble constant was fixed to $H_0 = 70$ (km/s)/Mpc. From J.A. Peacock, "Cosmological Physics", Cambridge University press 1998.
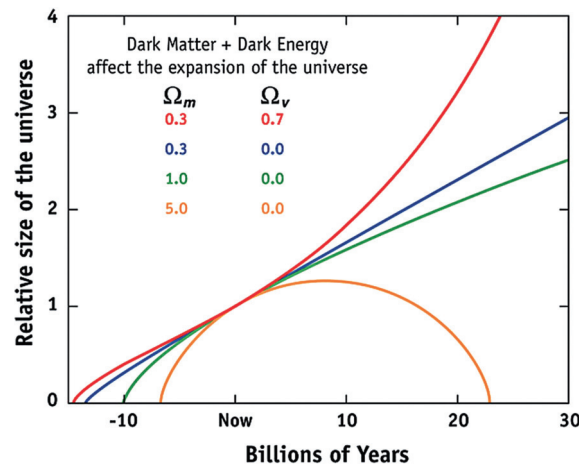
Fig. 8.24 Evolution of the Universe in a two-component model (matter and vacuum) for different $(\Omega_m, \Omega_\Lambda)$ values. (from http://map.gsfc.nasa.gov/universe/uni_fate.html).

4. In a small phase space region with $\Omega_m + \Omega_\Lambda > 1$ and $\Omega_\Lambda > 0$ there is a solution for which the Universe bounces between a minimum and a maximum scale factor.

Some of these evolution scenarios are represented as functions of time in Fig. 8.24 for selected points in the parameter space discussed above. The green curve represents a flat, matter-dominated, critical density Universe (the expansion rate is slowing down forever). The blue curve shows an open, low density, matter-dominated Universe (the expansion is slowing down, but not as much). The orange curve shows a closed, high-density Universe (the expansion reverts to a "big crunch"). The red curve shows a Universe with a large fraction of "dark energy" (the expansion of the Universe accelerates).

The present experimental evidence (see Sect. 8.4) highly favors the "dark energy" scenario, leading to a cold thermal death of the Universe.

8.2.8 Black Holes

The first analytical solution of Einstein's equations was found in 1915, just a month after the publication of Einstein's original paper, by Karl Schwarzschild, a German physicist who died one year later from a disease contracted on the First World War battle field.

Schwarzschild's solution describes the gravitational field in the vacuum surrounding a single, spherical, nonrotating massive object. In this case the spacetime metric (called the Schwarzschild metric) can be expressed as

$$ds^2 = \left(1 - \frac{r_S}{r}\right) c^2 dt^2 - \left(1 - \frac{r_S}{r}\right)^{-1} dr^2 - r^2(d\theta^2 + \sin^2\theta d\phi^2), \tag{8.135}$$

with

$$r_S = \frac{2GM}{c^2} \simeq 2.7\,\mathrm{km}\,\frac{M}{M_\odot}\,. \tag{8.136}$$

In the weak field limit, $r \to \infty$, we recover flat spacetime. According to this solution, a clock with period τ^* placed at a point r is seen by an observer placed at $r = \infty$ with a period τ given by:

$$\tau = \left(1 - \frac{r_S}{r}\right)^{-1} \tau^*\,. \tag{8.137}$$

In the limit $r \to r_S$ (the Schwarzschild radius) the metric shows a coordinate singularity: the time component goes to zero and the radial component goes to infinity. From the point of view of an asymptotic observer, the period τ^* is seen now as infinitely large. No light emitted at $r = r_S$ is able to reach the $r > r_S$ world. This is what is usually called, following John Wheeler, a "black hole".

The existence of objects so massive that light would not be able to escape from them, was already predicted in the end of the eighteenth century by Michell in England and independently by Laplace in France. They just realized that, if the escape velocity from a massive object would have been greater than the speed of light, then the light could not escape from the object:

$$v_{esc} = \sqrt{\frac{2\,G\,M}{r}} > c\,. \tag{8.138}$$

Thus an object with radius R and a mass M would be a "black hole" if:

$$M > \frac{Rc^2}{2G}\ : \tag{8.139}$$

the "classical" radius and the Schwarzschild radius coincide.

The singularity observed in the Schwarzschild metric is not in fact a real physics singularity; it depends on the reference frame chosen (see [F8.3] for a discussion). An observer in free fall frame will cross the Schwarzschild surface without feeling any discontinuity; (s)he will go on receiving signals from the outside world but (s)he will not be able to escape from the unavoidable, i.e., from crunching, at last, at the center of the black hole (the real physical singularity).

Schwarzschild black holes are however just a specific case. In 1963, New Zealand mathematician Roy Kerr found an exact solution to Einstein's equations for the case of a rotating noncharged black hole and two years later the US Ezra Newman extended it to the more general case of rotating charged black holes. In fact it can be proved that a black hole can be completely described by three parameters: mass, angular momentum, and electric charge (the so-called no-hair theorem).

Black holes are not just exotic solutions of the General Theory of Relativity. They may be formed either by gravitational collapse or particle high-energy collisions. While so far there is no evidence of their formation in human-made accelerators, there is striking indirect evidence that they are part of several binary systems and that they are present in the center of most galaxies, including our own (the Milky Way hosts in its center a black hole of roughly 4 million solar masses, as determined from the orbit of nearby stars). Extreme high-energy phenomena in the Universe, generating the most energetic cosmic rays, may also be caused by supermassive black holes inside AGNs (Active Galactic Nuclei—see Chap. 10).

8.2.9 Gravitational Waves

Soon after the discovery of the electromagnetic radiation the existence of gravitational waves was suggested. The analogy was appealing but it took a long way before a firm prediction by Einstein and only very recent direct the experimental detection has been possible (see Chap. 10). According to Einstein's equations the structure of spacetime is determined by the energy-momentum distributions but the solutions of such

equations are far from being trivial. In particular, in the case of gravitational waves, where the components of the spacetime metric have to be time dependent (contrary for instance to the cases discussed in the previous section where the metric was assumed to be static), general exact analytic solutions are, still nowadays, impossible to obtain.

The spacetime metric out of the gravitational sources is basically flat and small perturbation of the metric components may be considered (linearized gravity). Let us then write the space metric in free space (weak field approximation) as:

$$g_{\mu\nu} = \eta_{\mu\nu} + h_{\mu\nu}, \tag{8.140}$$

where $\eta_{\mu\nu}$ is the Minkowski metric and $h_{\mu\nu} \ll 1$ for all μ, ν .

Choosing the appropriate coordinate system, the "transverse traceless" (TT) gauge (for a detailed discussion see for example [F8.6]), Einstein's equations in vacuo can, in this approximation, be written as:

$$\left(\frac{\partial^2}{\partial^2 t} - \nabla^2\right) h_{\mu\nu} = 0 \text{ or more briefly } \Box h_{\mu\nu} = 0 . \tag{8.141}$$

This is a wave equation whose simplest solutions are plane waves:

$$h_{\mu\nu} = A_{\mu\nu} e^{i k_a x^a}, \tag{8.142}$$

where $A_{\mu\nu}$ and k_a are respectively the wave amplitude and the wave vector. These waves are transverse,

$$A_{\mu\nu} k^\mu = 0, \tag{8.143}$$

and they propagate along light rays, i.e., k_a is a null-vector:

$$k_\mu k^\mu = 0. \tag{8.144}$$

Their propagation velocity is thus the light velocity c (remember that $c=1$ in the metric we have chosen), which is a non trivial result. These equations were derived directly from Einstein's equations.

Assuming a propagation along the z axis with an energy w:

$$k_\mu = (w, 0, 0, w), \tag{8.145}$$

it can be shown that, in this gauge, only four components of $A_{\mu\nu}$ ($A_{xx} = -A_{yy}$; $A_{xy} = A_{yx}$), may be nonzero. The general solution for a propagation along the z axis with fixed frequency w can thus be written as:

$$h_{\mu\nu}(z,t) = \begin{pmatrix} 0 & 0 & 0 & 0 \\ 0 & A_{xx} & A_{xy} & 0 \\ 0 & A_{xy} & -A_{xx} & 0 \\ 0 & 0 & 0 & 0 \end{pmatrix} e^{iw(z-t)}. \tag{8.146}$$

Then, whenever $A_{xy} = 0$, the space-time metric produced by such a wave is given by:

$$ds^2 = dt^2 - ((1 + h_+)dx^2) + (1 - h_+)dy^2 + dz^2) \tag{8.147}$$

with

$$h_+ = A_{xx} e^{iw(z-t)} . \tag{8.148}$$

The effects of this wave in the transverse space axes x and y are opposite: while one expands, the other contracts and vice-versa. For instance, this gravitational wave would change the distance L between two masses placed on the x axis by $dL = L h_+$. This wave is said to be "plus" polarized (denoted by +). On the other hand, if $A_{xx} = 0$ a similar effects may be observed for axis rotated by 45^0 and then the wave is said to be "cross" polarized (denoted by ×). Such effects are graphically represented in Fig. 8.25.

The amplitudes of such effects are however quite tiny if the sources are quite far (h_+ is proportional to $1/R$ where R is the distance to the source). The relative change of the distance between two tests masses at Earth, the *strain*, which is the variable measured by gravitational wave detectors (see Sect. 4.6), is of the of the order of 10^{-23} for the Hulse-Taylor binary pulsar and of 10^{-21} for the coalescence of a binary stellar-mass black hole system (see Sect. 10.4.4).
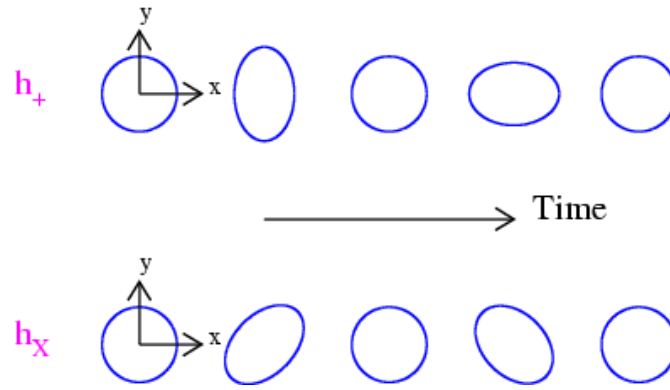
Fig. 8.25 Graphical representation of the effects of polarized waves (top, + polarization; bottom, ×polarization) From K. Riles, "Gravitational Waves: Sources, Detectors and Searches", Prog. Part. Nucl. Phys. 68 (2013) 1.

In summary, gravitational waves are "ripples in space-time" propagating in free space with the velocity of light and their effect on the relative distances between free mass particles have been detected, as it will be discussed in Chap. 10.

8.4 The ΛCDM Model

The ΛCDM model, also denominated as the *concordance model* or *the Standard Model of Cosmology*, is a parametrization of the Big Bang cosmological model based on general relativity with a reduced set of parameters. We can assume the evolution of the Universe under GR to be represented through the first Friedmann equation

$$\boxed{H^2 = \frac{8\pi G}{3}\left(\rho + \frac{\Lambda}{3}\right) - \frac{K}{a^2}} \tag{8.149}$$

K being the curvature of space and ρ the density. The ΛCDM model postulates that we live in a flat Universe ($K = 0$ and $\Omega_m + \Omega_\gamma + \Omega_\Lambda = 1$) with $\Omega_m = \Omega_b + \Omega_c$, Ω_b being the baryonic density and Ω_c the cold dark matter (CDM) density. The Universe is dominated by dark energy in the form of a nonzero cosmological constant Λ and cold dark matter, CDM. The ΛCDM model also assumes homogeneity, isotropy, and a power law spectrum of primordial fluctuations. It is the simplest model describing the existence and structure of the CMB, of the large-scale structure in the distribution of galaxies, of the abundances of nucleons, of the accelerating expansion of the universe.

The assumption that ($\Omega_m + \Omega_\gamma + \Omega_\Lambda = 1$) is motivated by the fact that observations are consistent with this value with extreme accuracy. Indeed

$$\Omega_m + \Omega_\gamma + \Omega_\Lambda = 1.0002 \pm 0.0026 \,. \tag{8.150}$$

Since at present $\Omega_\gamma \simeq 0$, then $\Omega_\Lambda \simeq 1 - (\Omega_b + \Omega_c)$. The minimal ΛCDM model has six free parameters, which can be chosen as:

1. H_0, the Hubble parameter;
2. Ω_b, the baryonic matter density in units of the critical density;
3. Ω_c, the cold dark matter density in units of the critical density;
4. τ, the optical depth to reionization (see Sect. 8.1.3.1);
5. A_s and n_s, related to the primordial fluctuation spectrum (we shall not make use of these parameters in the following).

The first evidence for a nonzero cosmological constant came from the observations by the "Supernova Cosmology Project" and by the "High-z Supernova Search Team", showing that the Universe is in a state of accelerated expansion (see Sect. 8.1.1). In 2003 it was already possible to conclude that $\Omega_m \simeq 0.3$ and $\Omega_\Lambda \simeq 0.7$ (Fig. 8.26). The present best fit for observational data by the PDG (2018) provides for the main ΛCDM parameters from 1 to 4 the following values:
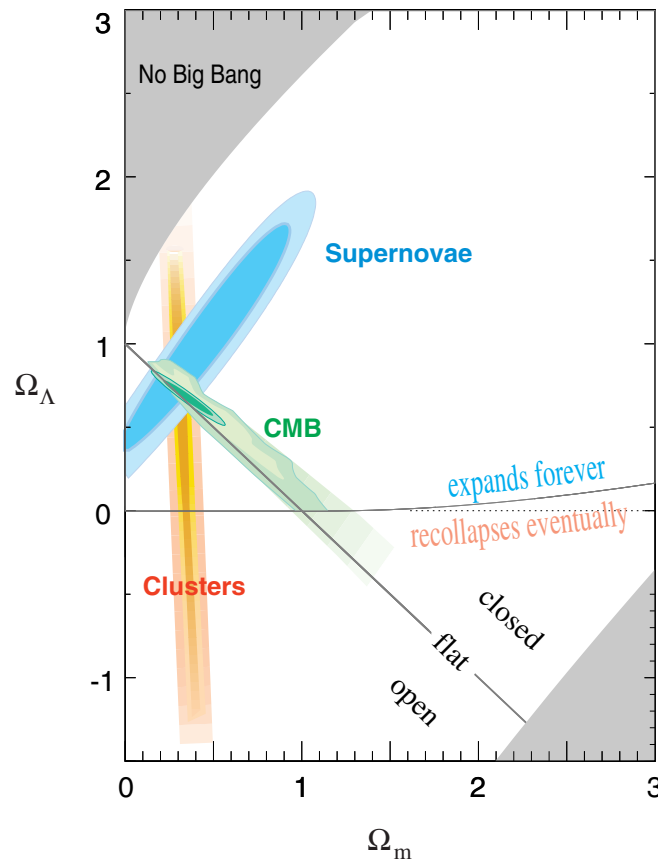
**Fig. 8.26** Confidence regions in the plane (Ω_m, Ω_Λ). Credit: http://supernova.lbl.gov.

1. $H_0 = (100 \times h)$ km s^{-1} Mpc^{-1}, with $h = 0.678 \pm 0.009$
2. $\Omega_b = (0.02226 \pm 0.00023)/h^2$
3. $\Omega_c = (0.1186 \pm 0.0020)/h^2$
4. $\tau = 0.066 \pm 0.016$.

Relaxing some of the assumptions of the standard ΛCDM model, extra parameters like, for example, the total mass of the neutrinos, the number of neutrino families, the dark energy equation of state, the spatial curvature, can be added.

As it is the case for particle physics, in the beginning of the twenty-first century we have a standard model also for cosmology that describes with remarkable precision the high quality data sets we were able to gather in the last years. Although we do not yet know how to deduce the parameters of this SM from first principles in a more complete theory, we do have, nevertheless, realized that a slight change in many of these parameters would jeopardize the chance of our existence in the Universe. Are we special?

At the same time, additional questions pop up. What is dark matter made of? And how about dark energy? Why the "particle physics" vacuum expectation value originated from quantum fluctuations is 120 orders of magnitude higher than what is needed to account for dark energy?

Finally, the standard model of cosmology gives us a coherent picture of the evolution of the Universe (Figs. 8.27 and 8.28) starting from close to Planck time, where even General Relativity is no longer valid. What happened before? Was there a single beginning, or our Universe is one of many? What will happen in
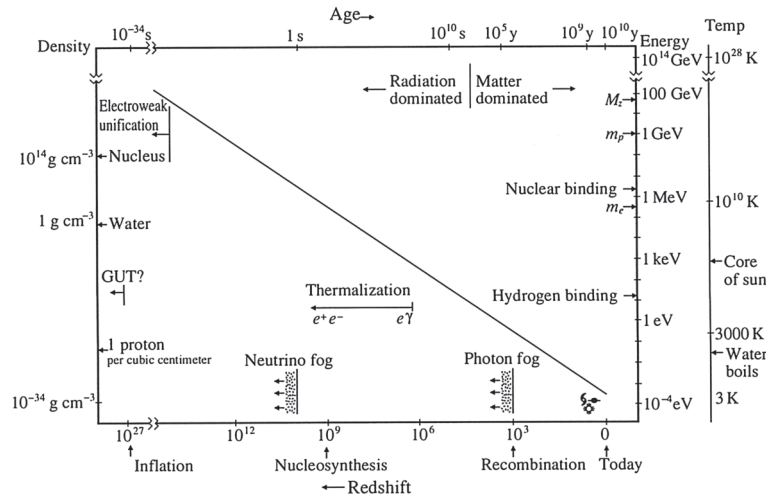
Fig. 8.27 The density, temperature, age, and redshift for the several Universe epochs. From E. Linder, "First principles of Cosmology", Addison-Wesley 1997.

the future? Is our Universe condemned to a thermal death? Questions for the twenty-first century. Questions for the present students and the future researchers.

8.4.1 Dark Matter Decoupling and the "WIMP Miracle"

The ΛCDM model assumes that dark matter is formed by stable massive nonrelativistic particles. These particles must have an interaction strength weaker than the electromagnetic one—otherwise they would have been found (see later); the acronym WIMP (Weakly Interactive Massive Particle) is often used to name them, since for several reasons that will be discussed below, the favorite theoretical guess compatible with experiment is that they are heavier than $M_Z/2 \sim 45$ GeV. The lightest supersymmetric particle, possibly one of the neutralinos χ (the lightest SUperSYmmetric particles, see the previous Chapter), is for many the most likely candidate; we shall use often the symbol χ to indicate a generic WIMP. WIMPs must be neutral and, if there is only one kind of WIMP, we can assume that they coincide with their antiparticle (as it is the case for the neutralino).

1. We can think that in the early Universe, in the radiation dominated era, WIMPs were produced in collisions between particles of the thermal plasma. Important reactions were the production and annihilation of WIMP pairs in particle-antiparticle collisions. At temperatures corresponding to energies much higher than the WIMP mass, $k_B T \gg m_\chi c^2$, the colliding particle-antiparticle pairs in the plasma had enough energy to create WIMP pairs, the rate of the process being

$$\Gamma_\chi = \langle \sigma v \rangle n_\chi$$

where n_χ is the number density of WIMPs, σ the annihilation cross section, and v the speed. The inverse reactions converting pairs of WIMPs into SM particles were in equilibrium with the WIMP-producing processes.

2. As the Universe expanded, temperature decreased, and the number of particles capable to produce a WIMP decreased exponentially as the Boltzmann factor

$$e^{-\left(\frac{m_\chi c^2}{k_B T}\right)}. \tag{8.151}$$

In addition, the expansion decreased the density n_χ, and with it the production and annihilation rates.

3. When the mean free path for WIMP-producing collisions became of the same order of the radius:

$$\lambda = \frac{1}{n_\chi \sigma} \sim \frac{v}{H}$$
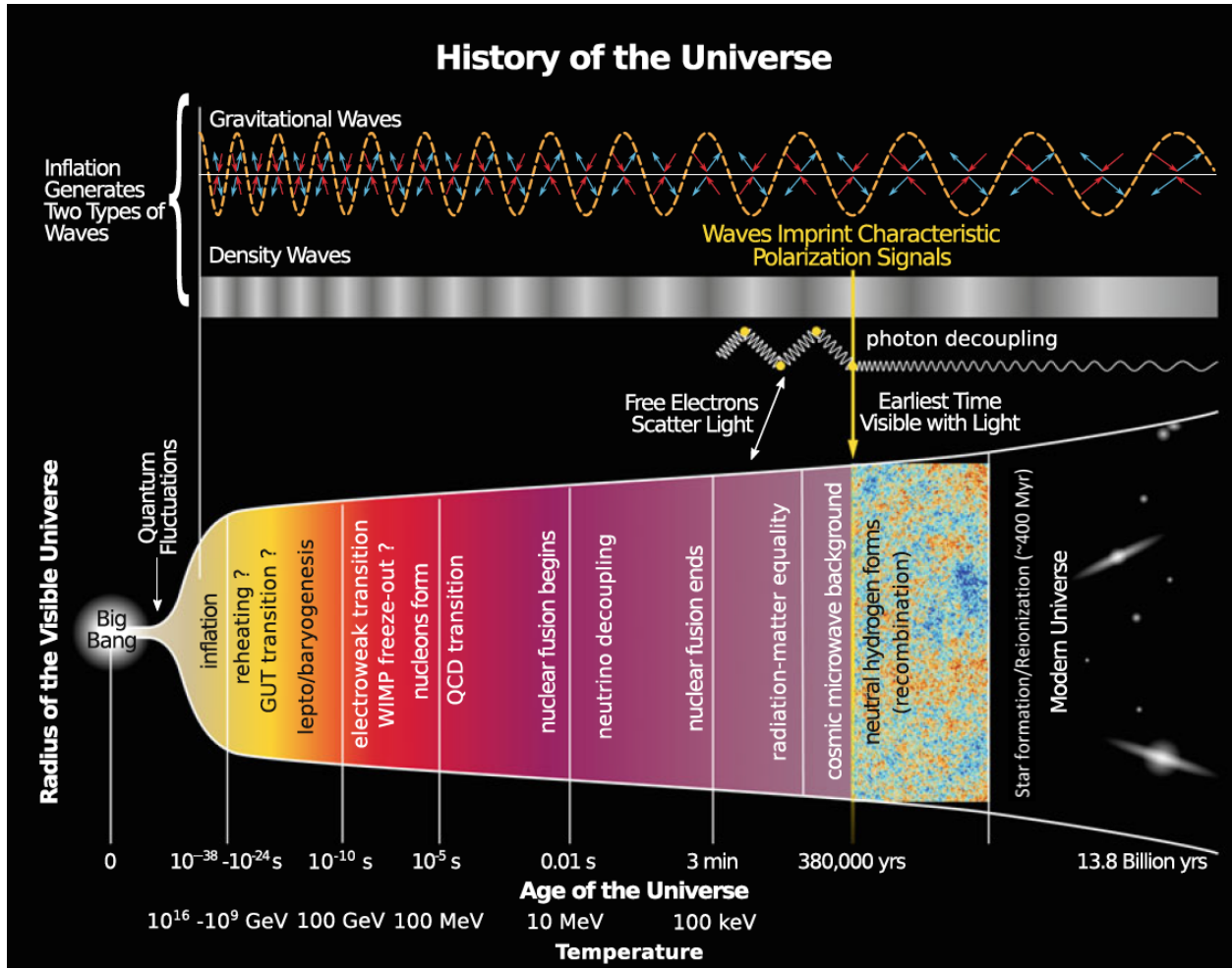
Fig. 8.28 Timeline of the Universe. Adapted from G. Sigl, "Astroparticle Physics: Theory and Phenomenology", Springer 2017. Taken from Yinweichen – Own work, CC BY-SA 3.0, Wikimedia Commons.

or equivalently the WIMP annihilation rate became smaller than the expansion rate of the universe H:

$$\Gamma_\chi \sim n_\chi \langle \sigma v \rangle \sim H \,, \tag{8.152}$$

production of WIMPs ceased (decoupling). After this, the number of WIMPs in a comoving volume remained approximately constant and their number density decreased as a^{-3}. The value of the decoupling density is therefore a decreasing function of $\langle \sigma v \rangle$, where the velocity v is small for a large mass particle. In Fig. 8.29 the number density of a hypothetical dark matter particle as a function of time (expressed in terms of the ratio $m_\chi c^2 / k_B T$) for different assumed values of $\langle \sigma \, v \rangle$ is shown.
A numerical solution provides

$$k_B T_{dec} \sim \frac{m_\chi c^2}{x} \tag{8.153}$$

with $x \sim 20 - 50$ in the range $10 \text{ GeV} \lesssim m_\chi c^2 \lesssim 10 \text{ TeV}$, and

$$\left(\frac{\Omega_\chi}{0.2} \right) \sim \frac{x}{20} \left(\frac{3 \text{ pb}}{\sigma} \right) \,. \tag{8.154}$$

An important property illustrated in Fig. 8.29 is that smaller annihilation cross sections lead to larger relic densities: the weakest wins. This fact can be understood from the fact that WIMPs with stronger interactions remain in thermodynamical equilibrium for a longer time: hence they decouple when the Universe is colder, and their density is further suppressed by a smaller Boltzmann factor. This leads to the inverse relation between Ω_χ and σ in Eq. 8.154.
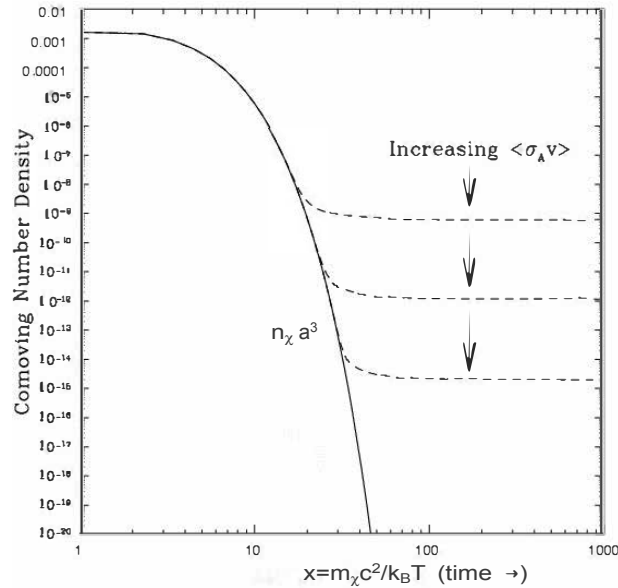
Fig. 8.29 The comoving number density of a nonrelativistic massive particle as a function of time (expressed in terms of the ratio $\frac{m_\chi c^2}{k_B T}$) for different values of $\langle \sigma\, v \rangle$. Adapted from D. Hooper, "TASI 2008 Lectures on Dark Matter", arXiv:0901.4090 [hep-ph]).

4. If the χ particle interacts via weak interactions (Chap. 6) its annihilation cross section for low energies can be expressed as

$$\sigma \sim \frac{g_W^4}{m_\chi^2} \tag{8.155}$$

where g_W is the weak elementary coupling constant, $g_W^4 \simeq 90$ nb GeV^2. Inserting for m_χ^2 a value of the order of 100 GeV in Eq. 8.154 one finds the right density of dark matter to saturate the energy budget of the Universe with just one particle, and no need for a new interaction.

Eq. 8.154 is often expressed using the thermally-averaged product of the cross section times velocity $\langle \sigma v \rangle$. For $x \sim 20$, $v \sim c/3$, and one has

$$\langle \sigma v \rangle \sim 3\,\mathrm{pb} \times 10^{10}\ \frac{\mathrm{cm}}{\mathrm{s}} = 3 \times 10^{-26}\ \frac{\mathrm{cm}^3}{\mathrm{s}}.$$

The value $\langle \sigma v \rangle \sim 3 \times 10^{-26}$ cm^3/s is a benchmark value for the velocity-averaged annihilation cross section of dark matter particles.

An appropriate relation between g_χ and m_χ can thus ensure a density of particles at decoupling saturating the total DM content of the Universe. In addition the expected values for a WIMP with $m_\chi \sim m_Z \sim 100$ GeV and $g_\chi \sim g_W \sim 0.6$, corresponding to the electroweak coupling, provides the right scale for the observed dark matter density ($\Omega_\chi \sim 0.2$–0.3, see Sect. 8.4); this coincidence is called the *WIMP miracle*. A WIMP can indeed be the mysterious missing dark particle, but the WIMP miracle is not the only possible solution: we take it just as a benchmark. In the opinion of Andrej Sacharov, dark matter could just be gravitationally coupled–and if he was right, it will be extremely difficult to detect it experimentally. A value $\langle \sigma v \rangle$ of the order of $\sim 3 \times 10^{-26}$ cm^3/s is the resulting benchmark value for the velocity-averaged annihilation cross section of dark matter particles in a range of weak interactions and of DM masses of the order[8] of 50 GeV-10 TeV.

---

[8] Strictly speaking, the Fermi model of the weak interactions entailing a cross section proportional to $1/s$ starts failing at energies $\gg 100$ GeV, since the squares of the masses of the vector bosons have to be considered. However, the "WIMP miracle" is still granted up to some 10 TeV.
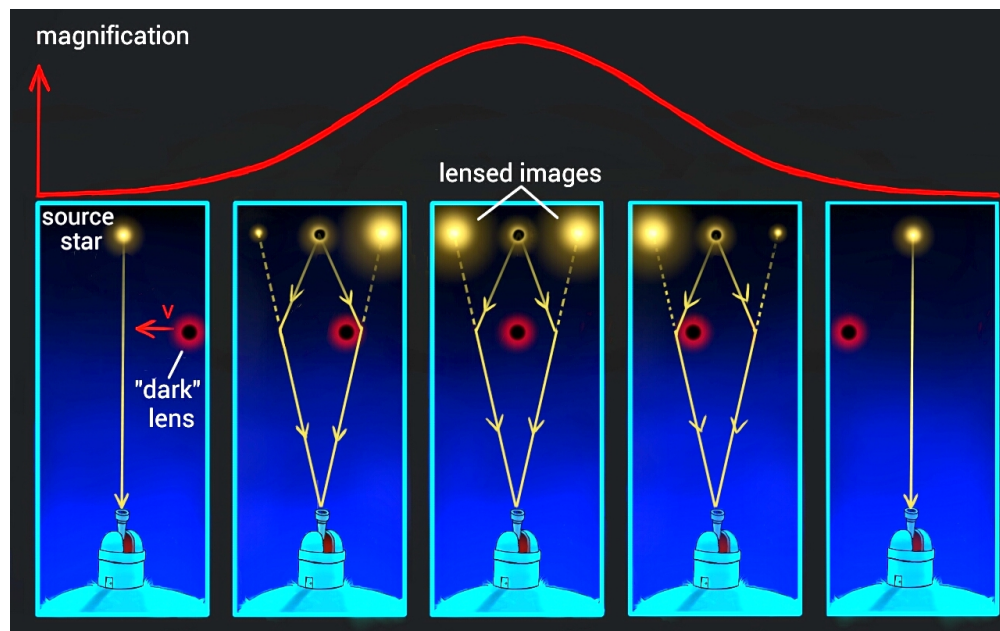
Fig. 8.30 Principle of gravitational microlensing. By Adam Rogers, blog "The Amateur Realist".

8.5 What Is Dark Matter Made Of, and How Can It Be Found?

Observations indicate a large amount of dark matter or substantial modifications of the standard theory of gravitation (see Sect. 8.1.5).

Dark matter is unlikely to consist of baryons.

- First, the ΛCDM model (Sect. 8.4) computes the total content of baryonic DM (i.e., nonluminous matter made by ordinary baryons) from the fit to the CMB spectrum, and the result obtained is only some 4 % of the total energy of the Universe; the structure of the Universe, computed from astrophysical simulations, is consistent with the fractions within the ΛCDM model.
- Second, the abundances of light elements depend on the baryon density, and the observed abundances are again consistent with those coming from the fit to Ω_b coming from the CMB data.

A direct search for baryonic dark matter has been however motivated by the fact that some of the hypotheses on which cosmological measurements are based might be wrong (as in the case of MOND, for example).

Baryonic DM should cluster into massive astrophysical compact objects, the so-called MACHOs,[9] or into molecular clouds.

Molecular clouds, when hot, are easily observable (for example in hot galaxy clusters); the result of observations is that the amount of DM due to molecular clouds is small.

The main baryonic component should be thus concentrated in massive objects (MACHOs), including black holes. We can estimate the amount of this component using the gravitational field generated by it: a MACHO may be detected when it passes in front of a star and the star light is bent by the MACHO's gravity. This causes more light to reach the observer and the star to look brighter, an effect known as gravitational microlensing (Fig. 8.30), very important also in the search for extrasolar planets (see Chap. 11). Several research groups have searched for MACHOs and found that only a few percent of the total DM can be attributed to them. Therefore, MACHOs do not solve the missing mass problem.

Candidates for nonbaryonic DM must interact very "weakly" with electromagnetic radiation (otherwise they would not be dark), and they must have the right density to explain about one-quarter of the energy content of the Universe. A new particle of mass above the eV and below some $M_Z/2$ would have been already found by LEP: DM particles must be very heavy or very light if they exist. They must also be stable on cosmological timescales (otherwise they would have decayed by now). We use the acronyms WIMP (weakly

---

[9] MACHO is a generic name for a compact structure composed of baryonic matter, which emits little or no radiation, and are thus very difficult to detect. MACHOs may be black holes or neutron stars, as well as brown or very faint dwarf stars, or large planets.

interacting massive particle) to indicate possible new "heavy" particles, and WISP (weakly interacting slim particle, or sub-eV particle) to indicate possible new light particles. Part of the rationale for WIMPs has been discussed in Sect. 8.4.1.

We shall present in this chapter the results of direct searches for dark matter, searches at accelerators, and shortly of indirect searches; a more detailed discussion of indirect signatures in the context of multimessenger astrophysics will be presented in Chap. 10.

8.5.1 WISPs: Neutrinos, Axions and ALPs

Among WISPs, neutrinos seem to be an obvious candidate. However, they have a free-streaming length larger than the size of a supercluster of galaxies (they thus enter in the category of the so-called "hot" dark matter). If neutrinos were the main constituent of dark matter, the first galaxies would have the sizes of superclusters; this is in contrast with the deep field observations from the Hubble Space Telescope (which looked in the past by sampling the Universe in depth). Observations from the Planck satellite allow to set an upper limit at 95 % CL

$$\Omega_\nu \leq 0.004.$$

After having excluded known matter as possible a DM candidate, we are only left with presently unknown—although sometimes theoretically hypothesized—matter.

The axion is a hypothetical light pseudoscalar (spin-parity 0^+) particle originally postulated to explain the so-called strong CP problem. In principle, CP should not be a symmetry of the QCD Lagrangian; however, CP (and T) appear to be conserved, as opposed to what happens for weak interactions; this fact has been verified with very good accuracy. To fix this problem, Peccei and Quinn (1977) proposed a new global symmetry, spontaneously broken at a very-high-energy scale, and giving rise to an associated boson called the axion (see Sect. 7.3.2). Being pseudoscalar (like the π^0), the axion can decay into two photons, at a rate determined by the (small) coupling $g_{A\gamma\gamma} = 1/M$—all quantities here are expressed in NU. The standard axion mass m_A is related to the coupling by the formula

$$\frac{m_A}{1\,\text{eV}} \simeq \frac{1}{M/6 \times 10^6\,\text{GeV}}\,. \tag{8.156}$$

The axion lifetime would then be proportional to $1/M^5$, which is larger than the age of the Universe for $m_A > 10$ eV. An axion below this mass would thus be stable.

Since the axion couples to two photons, in a magnetic or electric field it could convert to a photon; vice versa, a photon in an external magnetic or electric field could convert into an axion (Primakoff effect); the amplitude of the process would be proportional to $g_{A\gamma\gamma}$.

Axion-like particles (ALPs) are a generalization of the axion: while the axion is characterized by a strict relationship between its mass m_A and $g_{A\gamma\gamma} = 1/M$, these two parameters are unrelated for ALPs. Depending on the actual values of their mass and coupling constant, ALPs can play an important role in cosmology, either as cold dark matter particles or as quintessential dark energy.

In order to account for dark matter, that is, to reach an energy density of the order of the critical density, axion masses should be at least 0.1 meV. Light axions and ALPs could still be DM candidates, since they are produced nonthermally via Bose-Einstein condensation, and thus they can be "cold".

Axion and ALP Searches. Attempts are being made to directly detect axions mostly by:

1. Using the *light-shining-through-a-wall* (LSW) technique: a laser beam travels through a region of high magnetic field, allowing the possible conversion of photons into axions. These axions can then pass through a wall, and on the other side they can be converted back into photons in a magnetic field. An example is the OSQAR experiment at CERN.
2. Trying to spot *solar axions* using helioscopes: the CAST (CERN Axion Solar Telescope) experiment looks for the X-rays that would result from the conversion of solar axions produced in the Sun back into photons, using a 9-tons superconducting magnet.
3. Searching for axions in the local galactic dark matter halo (haloscopes). Axion conversion into photons is stimulated by strong magnetic field in a microwave cavity. When the cavity's resonant frequency is tuned to the axion mass, the interaction between local axions and the magnetic field is enhanced. The Axion Dark
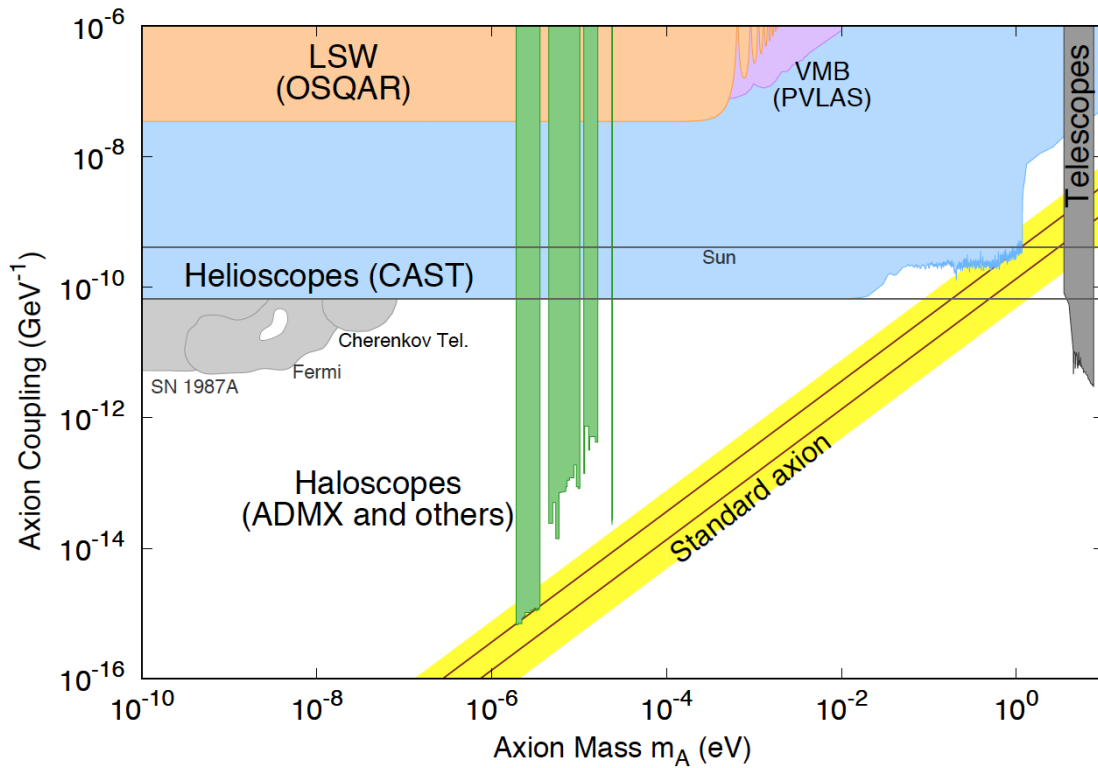
Fig. 8.31 Axion and ALP coupling to photons versus the ALP mass. The labels are explained in the text. Adapted from C. Patrignani et al. (Particle Data Group), Chin. Phys. C, 40, 100001 (2016) and 2017 update.

Matter eXperiment (ADMX) in Seattle uses a resonant microwave cavity within a 8 T superconducting magnet.

Indirect searches are also possible.

4. The vacuum magnetic birefringence (VMB) in high magnetic fields due to photon–axion mixing can be investigated. Different polarizations often experience a different refractive index in matter—a common example is a uniaxial crystal. The vacuum is also expected to become birefringent in presence of an external magnetic field perpendicular to the propagation direction, due to the orientation of the virtual e^+e^- loops. The magnitude of this birefringence could be enhanced by the presence of an axion field, which provides further magnetic-dependent mixing of light to a virtual field (experiment PVLAS by E. Zavattini and collaborators, 2006).

5. Study of possible anomalies in the cooling times of stars and of cataclusmic stellar events. An example is given by SNe, which produce vast quantities of weakly interacting particles, like neutrinos and possibly gravitons, axions, and other unknown particles. Although this flux of particles cannot be measured directly, the properties of the cooling depend on the ways of losing energy. The results on the cooling times and the photon fluxes (since photons are coupled to axions) constrain the characteristics of the invisible axions: emission of very weakly interacting particles would "steal energy from the neutrino burst and shorten it. The best limits come from SN1987A. However, significant limits come also from the cooling time of stars on the horizontal branch in the color-magnitude diagram, which have reached the helium burning phase.

6. ALPs can also directly affect the propagation of photons coming from astrophysical sources, by mixing to them. This possibility has been suggested in 2007 by De Angelis, Roncadelli, and Mansutti (DARMa), and by Simet, Hooper, and Serpico. The conversion of photons into axions in the random extragalactic magnetic fields, or at the source and in the Milky Way, could give rise to a sort of cosmic light-shining-through-a-wall effect. This might enhance the yield of very-high-energy photons from distant active galactic nuclei, which would be otherwise suppressed by the interaction of these photons with the background photons in the Universe (see Chap. 10). These effects are in the sensitivity range of *Fermi*-LAT and of the Cherenkov telescopes.

7. The line emission from the two-photon decay of axions in galaxy clusters can be searched with optical and near-optical telescopes.

With negative results, experimental searches have limited the region of mass and coupling allowed for ALPs. The limit

$$g_{A\gamma\gamma} < 6.6 \times 10^{-11} \, \text{GeV}^{-1} \qquad (8.157)$$

represents the strongest constraint for a wide mass range.

A hint for ALPs comes from possible anomalies in the propagation of very-high-energy photons from astrophysical sources (see Chap. 10).

A summary of exclusion limits, and of a possible observational window indicated by the cosmological propagation of VHE photons (see Chap. 10), is shown in Fig. 8.31. The topic is very hot and many new experimental results are expected in the next years.

8.5.2 WIMPs

If dark matter (DM) particles χ are massive they must be "weakly" (i.e., with a strength corresponding to the weak interaction or even weaker) interacting (WIMPs). A lower limit for the strength of the interaction is given by the gravitational strength. They must be neutral and, for a large range of interaction strengths, of mass larger than $M_Z/2$, otherwise they would have been found at the LEP e^+e^- collider.

The "WIMP miracle", discussed in Sect. 8.4.1, guarantees that a single type of WIMP of mass m_χ of the order of 50 GeV - few TeV, emerged from a standard thermal decoupling, can saturate the energy budget of the Universe for dark matter if the interaction characterizing WIMPs is the well-known electroweak interaction. WIMPs should be stable or should have a lifetime large enough in order to have survived from the early Universe until the present time.

If DM can be explained by just one particle χ, coincident with its antiparticle, we expect an annihilation cross section σ_{ann}

$$\sigma_{ann} \sim 3 \, \text{pb} . \qquad (8.158)$$

and a product of the cross section to the average velocity

$$\langle \sigma_{\text{ann}} | v_\chi | \rangle \simeq 3 \times 10^{-26} \, \text{cm}^3 \text{s}^{-1} . \qquad (8.159)$$

The results in Eqs. 8.158 and 8.159 are a natural benchmark for the behavior of WIMPs, and fit wells with the dynamics of electroweak interactions (Sect. 8.4.1).

Several extensions to the SM have proposed WIMP candidates, most notably supersymmetric models (SUSY) with $R-$parity conservation, in which the lightest supersymmetric particle, the putative neutralino χ, is stable and thus a serious candidate (Sect. 7.6.1) with a range of annihilation cross sections including the desired ones–the spectrum of cross section can vary in some 5 orders of magnitude depending on the many free parameters of SUSY. For this reason the neutralino is usually thought to be a "natural" DM candidate. However, more general models are also allowed.

WIMPs could be detected:

1. At accelerators, where they can be produced.
2. Directly, via elastic scattering with targets on Earth. If the DM conjecture is correct, we live in a sea of WIMPs. For a WIMP mass of 50 GeV, there might be in our surroundings some 10^5 particles per cubic meter, moving at a speed smaller than the revolution velocity of the Earth around the Sun. From astrophysical observations the local WIMP density about $0.4 \, \text{GeV/cm}^3$; the velocity distribution is Maxwellian, truncated by the Galactic escape velocity of 650 km/s. For a mass of 50 GeV, the RMS velocity is comparable to the speed of the solar system in the Galaxy, ~ 230 km/s. Direct detection relies on observation of the scattering or other interaction of the WIMPs inside low-background Earth-based detectors.
3. Indirectly, by their decay products if they are unstable (WIMPs can be unstable, provided their lifetime is larger than the Hubble time), or by their self-annihilation products in high-density DM environments. The annihilation products of pairs of WIMPs—for example, in the halo of the Galaxy, or as a result of their accumulation in the core of the Sun or of the Earth, is likely to happen if the WIMP is a boson or a Majorana fermion as the SUSY neutralino.

These three techniques are complementary (Fig. 8.32), but results are often difficult to compare. In this Chapter we shall discuss the techniques and summarize the main results on 1. and 2.; we shall explain the observables related to 3. and we shall discuss the experimental results in Chapter 10, in the context of multimessenger astrophysics.
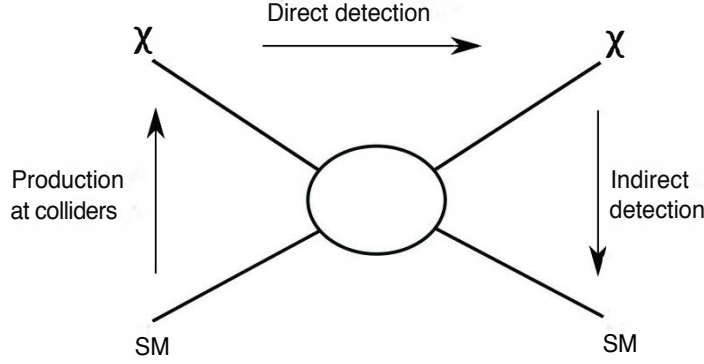
Fig. 8.32 Different proceses used to investigate on WIMPs.

8.5.2.1 Production and Detection of WIMPs at Accelerators

WIMPs can be created at colliders, but they are difficult to detect, since they are neutral and weakly interacting. However, it is possible to infer their existence. Their signature would be missing energy when one tries to reconstruct the dynamics of a collision into a final state involving dark matter particles and standard model particles—notice that a collision producing dark matter particles only would not be triggered. There has been a huge effort to search for the appearance of these new particles.

The production of WIMPs is severely constrained by LEP up to a mass close to $M_Z/2$. WIMPs with $m_\chi < m_H/2 \sim 63$ GeV can be constrained with the branching ratio for invisible Higgs boson decays which is measured at LHC to be < 0.2. This does not appear as a strong constraint, but in many scenarios the Higgs boson coupling to WIMPs is stronger than to SM particles.

Accelerator searches are complementary to the direct searches that will be described later; however, to compare with noncollider searches, the limits need to be translated via a theory into upper limits on WIMP-nucleon scattering or on WIMP annihilation cross sections, introducing model dependence–for example, the comparison can be done in the framework of SUSY (Fig. 8.35). In particular, searches at accelerators can exclude the region below 10 GeV and a cross section per nucleon of the order of 10^{-44} cm^2, where direct searches are not very sensitive.

8.5.2.2 Direct Detection of WIMPs in Underground Detectors

Experimental detection is based on the nuclear recoil that would be caused by WIMP elastic scattering.

WIMP velocities in the Earth's surroundings are expected to be of one order of magnitude smaller than the Galactic escape velocity, i.e., they are nonrelativistic: thermalized WIMPs have typical speeds

$$\sqrt{\langle v_\chi^2 \rangle} \simeq \sqrt{\frac{2k_B T}{m_\chi}} \simeq 27 \left(\frac{100 \,\text{GeV}}{m_\chi} \right)^{1/2} \text{m/s}\,.$$

These are smaller than the velocity $v_\odot$ of the Solar System with respect to the center of the Galaxy, which is of the order of $10^{-3} c$.

If the Milky Way's dark halo is composed of WIMPs, then, given the DM density in the vicinity of the Solar System and the speed of the Solar System with respect to the center of the Galaxy, the χ flux on the Earth should be about

$$\Phi_\chi \simeq v_\odot n_{\text{DM,local}} \simeq 10^5 \frac{100 \,\text{GeV}}{m_\chi} \text{cm}^{-2}\text{s}^{-1}$$

(a local dark matter density of 0.4 GeV/cm^3 has been used to compute the number density of DM particles). This flux is rather large and a potentially measurable fraction might scatter off nuclei.

The kinematics of the scattering is such that the transferred energy is in the keV range. The recoil energy E_K of a particle of mass M initially at rest after a nonrelativistic collision with a particle of mass m_χ traveling at a speed $10^{-3}c$ is approximately
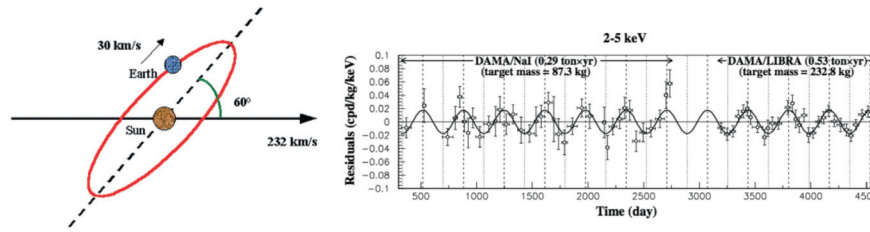
Fig. 8.33 Left: the directions of the Sun's and the Earth's motions during a year. Assuming the WIMPs to be on average at rest in the Galaxy, the average speed of the WIMPs relative to the Earth is modulated with a period of 1 year. Right: annual modulation of the total counting rate (background plus possible dark matter signal) in 7 years of data with the DAMA detector. A constant counting rate has been subtracted. From R. Bernabei et al., Riv. Nuovo Cim. 26 (2003) 1.

$$E_K \simeq 50 \, \text{keV} \left[\frac{M}{100 \, \text{GeV}} \left(\frac{2}{1 + M/m_\chi} \right)^2 \right]. \tag{8.160}$$

The expected number of collisions is some 10^{-3} per day in a kilogram of material for a 50 GeV particle weakly interacting.

Translating a number of collisions into a cross section per nucleon is not trivial in this case. The WIMP-nucleon scattering cross-section has a spin-dependent (SD) and a spin-independent (SI) part. When the scattering is coherent, the SI cross section has a quadratic dependence on the mass number A^2, which leads to strong enhancement for heavy elements. A nucleus can only recoil coherently for $A \ll 50$. SD scattering on the other hand depends on the total nuclear angular momentum. In the case of spin-dependent interaction the cross-section is smaller by a factor of order $A - A^2$ than for coherent scattering.

Detectors sensitive to WIMP interactions should have a low energy threshold, a low-background noise, and a large mass. The energy of a nucleus after a scattering from a WIMP is converted into a signal corresponding to (1) ionization, (2) scintillation light; (3) vibration quanta (phonons). The main experimental problem is to distinguish the genuine nuclear recoil induced by a WIMP from the huge background due to environmental radioactivity. It would be useful to do experiments which can measure the nuclear recoil energy and if possible the direction. The intrinsic rejection power of these detectors can be enhanced by the simultaneous detection of different observables (for example, heat and ionization or heat and scintillation).

The WIMP rate may be expected to exhibit some angular and time dependence. For example, there might be a daily modulation because of the shadowing effects of the Earth when turned away from the Galactic center (GC). An annual modulation in the event rate would also be expected as the Earth's orbital velocity around the Sun (about 30 km/s) adds to or subtracts from the velocity of the Solar System with respect to the GC (about 230 km/s), so that the number of WIMPs intercepted per unit time varies (Fig. 8.33, left).

The detectors have then to be well isolated from the environment, possibly shielded with active and passive materials, and constructed with very low activity materials. In particular, it is essential to operate in an appropriate underground laboratory to limit the background from cosmic rays and from natural radioactivity. There are many underground laboratories in the world, mostly located in mines or in underground halls close to tunnels, and the choice of the appropriate laboratory for running a low-noise experiment is of primary importance. Just to summarize some of the main characteristics,

- The thickness of the rock (to isolate from muons and from the secondary products of their interaction).
- The geology (radioactive materials produce neutrons that should be shielded) and the presence of Radon.
- The volume available (none of the present installations could host a megaton detector).
- The logistics.

Some of the largest underground detectors in the world are shown in Fig. 8.34.

As an example, the INFN Gran Sasso National Laboratory (LNGS), which is the largest underground European laboratory, hosts some 900 researchers from 30 different countries. LNGS is located near the town of L'Aquila, about 120 kilometers from Rome. The underground facilities are located on one side of the highway tunnel crossing the Gran Sasso mountain; there are three large experimental halls, each about 100 m long, 20 m wide, and 18 m high. An average 1400 m rock coverage gives a reduction factor of one million in the cosmic ray flux; the neutron flux is thousand times less than the one at the surface. One of the halls points to CERN, allowing long-baseline accelerator neutrino experiments.

Essentially three types of detectors operate searching directly for dark matter in underground facilities all around the world.
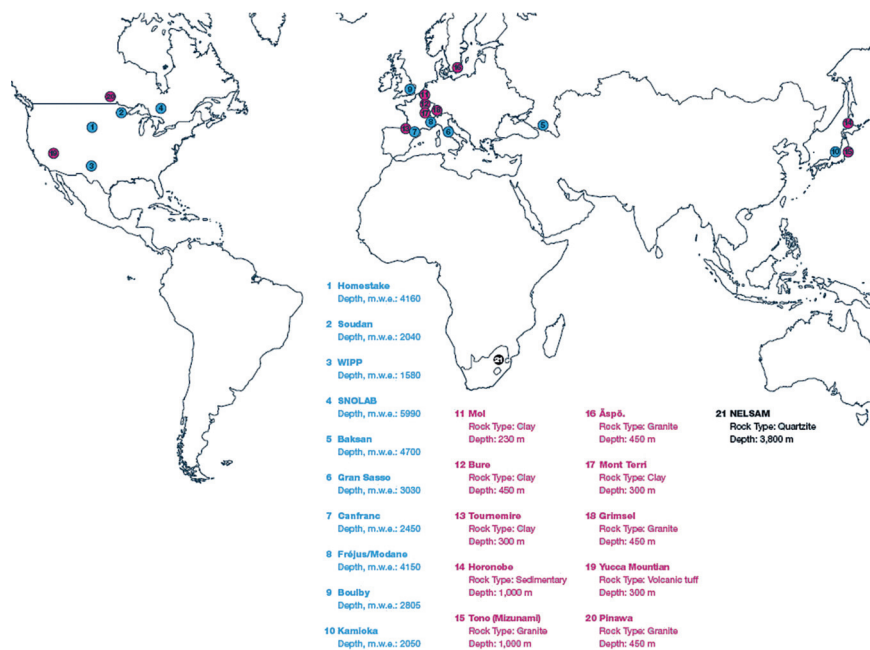
Fig. 8.34 Underground laboratories for research in particle physics (1–10) listed with their depth in meters water equivalent. Laboratories for research in the million-year scale isolation of nuclear waste are also shown (11–20). The NELSAM laboratory (21) is for earthquake research. From www.deepscience.org.

- Semiconductor detectors. The recoil nucleus or an energetic charged particle or radiation ionizes the traversed material and produces a small electric signal proportional to the deposited energy. Germanium crystals, which have a very small value of the gap energy (3 eV) and thus have a good resolution of 1 per thousand at 1 MeV, are commonly used as very good detectors since some years. The leading detectors are the CDMS, CoGeNT, CRESST, and EDELWEISS experiments. The bolometric technique (bolometers are ionization-sensitive detectors kept cold in a Wheatstone bridge; the effects measured are: the change in electric resistance consequent to the heating, i.e., the deposited energy, and ionization) increases the power of background rejection, and allows a direct estimate of the mass of the scattering particle.
- Scintillating crystals. Although their resolution is worse than Germanium detectors, no cooling is required. The scintillation technique is simple and well known, and large volumes can be attained because the cost per mass unit is low. However, these detectors are not performant enough to allow an event-by-event analysis. For this reason, some experiments are looking for a time-dependent modulation of a WIMP signal in their data. As the Earth moves around the Sun, the WIMP flux should be maximum in June (when the revolution velocity of the Earth adds to the velocity of the solar system in the Galaxy) and minimum in December, with an expected amplitude variation of a few percent. DAMA (now called in its upgrade DAMA/LIBRA) is the first experiment using this detection strategy. The apparatus is made of highly radio-pure NaI(Tl) crystals, each with a mass of about 10 kg, with two PMTs at the two opposing faces.
- Noble liquid detectors. Certainly the best technique, in particular in a low-background environment, it uses noble elements as detectors (this implies low background from the source itself) such as argon (A = 40) and xenon (A = 131). Liquid xenon (LXe) and liquid argon (LAr) are good scintillators and ionizers in response to the passage of radiation. Using pulse-shape discrimination of the signal, events induced by a WIMP can be distinguished from background electron recoil. The main technique is to the present knowledge the "double phase" technique. A vessel is partially filled with noble liquid, with the rest of the vessel containing the same element in a gaseous state. Electric fields of about 1 kV/cm and 10 kV/cm are established across the liquid and gas volumes, respectively. An interaction in the liquid produces excitation and ionization processes. Photomultiplier tubes are present in the gas volume and in the liquid. The double phase allows reconstruction of the topology of the interaction (the gas allowing a TPC reconstruction), thus helping background removal. The leading experiments are:
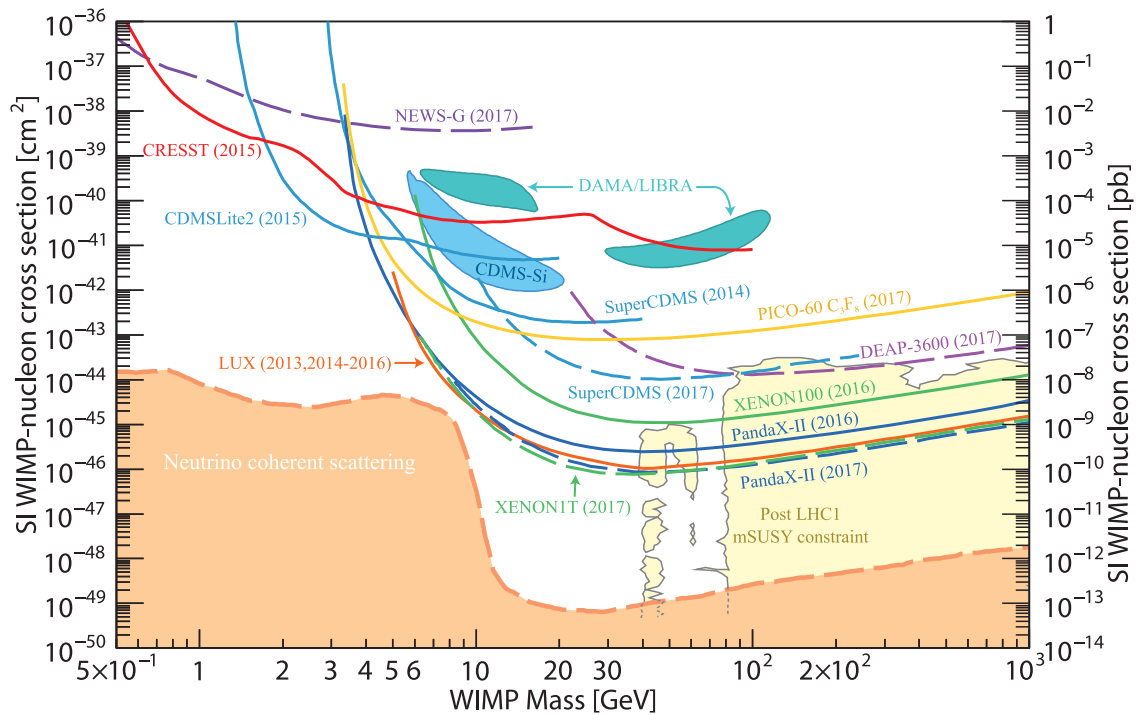
Fig. 8.35 Compilation of experimental results on cross sections of WIMPs versus masses. The areas labeled as DAMA/LIBRA and CDMS-Si indicate regions of possible signals from those experiments. Supersymmetry implications are also shown. New experiments to hunt for dark matter are becoming so sensitive that neutrino will soon show up as background; the "neutrino floor is shown in the plot. From C. Patrignani et al. (Particle Data Group), Chin. Phys. C, 40, 100001 (2016) and 2017 update, in which experiments are also described in detail.

- – The XENON100 detector, a 165 kg liquid xenon detector located in LGNS with 62 kg in the target region and the remaining xenon in an active veto together with high purity Germanium detectors. A new liquid xenon-based project, XENON1t, is planned in the LNGS, with 3.5 tons of liquid xenon.
- – The LUX detector, a 370 kg xenon detector installed in the Homestake laboratory (now called SURF) in the US. LUX was decommissioned in 2016 and a new experiment, LUX-ZEPLIN (LZ), with 7 tons of active liquid xenon is in preparation.

Whatever the detector is, the energy threshold is a limiting factor on the sensitivity at low WIMP masses; but for high values of m_χ the flux decreases as $1/m_\chi$ and the sensitivity for fixed mass densities also drops. The best sensitivity is attained for WIMP masses close to the mass of the recoiling nucleus.

The experimental situation is not completely clear (Fig. 8.35). Possible WIMP detection signals were claimed by the experiment DAMA, based on a large scintillator (NaI (Tl)) volume, and the CRESST and CoGeNT data show some stress with respect to experiments finding no signal. The data analyzed by DAMA corresponded to 7 years of exposure with a detector mass of 250 kg, to be added to 6 years of exposure done earlier with a detector mass of 100 kg. Based on the observation of a signal at 9.3 σ (Fig. 8.33, right) modulated with the expected period of 1 year and the correct phase (with a maximum near June 2, as expected from the Earth's motion around the Sun), DAMA proposes two possible scenarios: a WIMP with $m_\chi \simeq 50$ GeV and a cross section per nucleon $\sigma \simeq 7 \times 10^{-6}$ pb, and a WIMP with $m_\chi \simeq 8$ GeV and $\sigma \simeq 10^{-3}$ pb. The DAMA signal is controversial, as it has not presently been reproduced by other experiments with comparable sensitivity but with different types of detectors (we remind that there is some model dependence in the rescaling from the probability of interaction to the cross section per nucleon).

In the next years the sensitivity of direct DM detectors will touch the "neutrino floor" for WIMP masses above 10 GeV, in particular thanks to the DARWIN detector, a 50-ton LXe detector planned to start in the mid 2020s at LNGS.
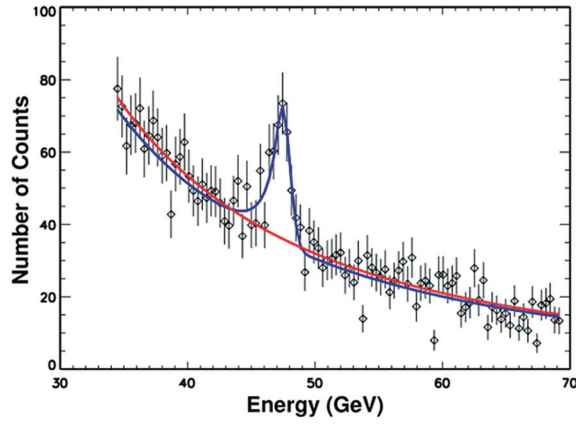
Fig. 8.36 γ-ray signature of neutralino self-annihilation or of neutralino decay. Simulation from the *Fermi*-LAT collaboration.

8.5.2.3 Indirect Detection of WIMPs

WIMPs are likely to annihilate in pairs; it is also possible that they are unstable, with lifetimes comparable with the Hubble time, or larger. In these cases one can detect secondary products of WIMP decays. Let us concentrate now on the case of annihilation in pairs—most of the considerations apply to decays as well.

If the WIMP mass is below the W mass, the annihilation of a pair of WIMPs should proceed mostly through $f\bar{f}$ pairs. The state coming from the annihilation should be mostly a spin-0 state (in the case of small mutual velocity the s-wave state is favored in the annihilation; one can derive a more general demonstration using the Clebsch–Gordan coefficients). Helicity suppression entails that the decay in the heaviest accessible fermion pair is preferred, similar to what seen in Chap. 6 when studying the $\pi^{\pm}$ decay (Sect. 6.3.4): the probability decay into a fermion–antifermion pair is proportional to the square of the mass of the fermion. In the mass region between 10 GeV and 80 GeV, the decay into $b\bar{b}$ pairs is thus preferred (this consideration does not hold if the decay is radiative, and in this case a generic $f\bar{f}$ pair will be produced). The $f\bar{f}$ pair will then hadronize and produce a number of secondary particles.

In the case of the annihilation in the cores of stars, the only secondary products which could be detected would be neutrinos. However, no evidence for a significant extra flux of high-energy neutrinos from the direction of the Sun or from the Earth's core has ever been found.

One could have annihilations in the halos of galaxies or in accretion regions close to black holes or generic cusps of dark matter density. In this case one could have generation of secondary particles, including gamma rays, or antimatter which would appear in excess to the standard rate.

We shortly present here the possible scenarios for detections, which will be discussed in larger details in Chap. 10, in the context of multimessenger astrophysics.

Gamma Rays. The self-annihilation of a heavy WIMP χ can generate photons (Fig. 8.36) in three main ways.

(a) Directly, via annihilation into a photon pair ($\chi\chi \to \gamma\gamma$) or into a photon—$Z$ pair ($\chi\chi \to \gamma Z$) with $E_\gamma = m_\chi$ or $E_\gamma = (m_\chi - m_Z)^2/(4m_\chi)$, respectively; these processes give a clear signature at high energies, as the energy is monochromatic, but the process is suppressed at one loop, so the flux is expected to be very faint.

(b) Via annihilation into a quark pair which produces jets emitting in turn a large number of γ photons ($qq \to jets \to many\ photons$); this process produces a continuum of gamma rays with energies below the WIMP mass. The flux can be large but the signature might be difficult to detect, since it might be masked by astrophysical sources of photons.

(c) Via internal bremsstrahlung; also in this case one has an excess of low energy gamma rays with respect to a background which is not so well known. Besides the internal bremsstrahlung photons, one will still have the photons coming from the processes described at the two previous items.

The γ-ray flux from the annihilation of a pair of WIMPs of mass m_χ can be expressed as the product of a particle physics component times an astrophysics component:

$$\frac{dN}{dE} = \frac{1}{4\pi} \underbrace{\frac{\langle \sigma_{\mathrm{ann}} v \rangle}{2m_\chi^2} \frac{dN_\gamma}{dE}}_{\text{Particle Physics}} \times \underbrace{\int_{\Delta\Omega - l.o.s.} dl(\Omega) \rho_\chi^2}_{\text{Astrophysics}} \; . \tag{8.161}$$

The particle physics factor contains $\langle \sigma_{\mathrm{ann}} v \rangle$, the velocity-weighted annihilation cross section (there is indeed a possible component from cosmology in v), and dN_γ/dE, the γ-ray energy spectrum for all final states convoluted with the respective branching rations. The part of the integral over line of sight ($l.o.s.$) in the observed solid angle of the squared density of the dark matter distribution constitutes the astrophysical contribution.

It is clear that the expected flux of photons from dark matter annihilations, and thus its detectability, depend crucially on the knowledge of the annihilation cross section σ_{ann} (which even within SUSY has uncertainties of one to two orders of magnitude for a given WIMP mass) and of ρ_χ, which is even more uncertain, and enters squared in the calculation. Cusps in the dark matter profile, or even the presence of local clumps, could make the detection easier by enhancing ρ_χ—and we saw that the density in the cusps is uncertain by several orders of magnitude within current models (Sect. 8.1.5.1). In the case of WIMP decays, the density term will be linear.

The targets for dark matter searches should be not extended, with the highest density, with no associated astrophysical sources, close to us, and possibly with some indication of small luminosity/mass ratio from the stellar dynamics.

- The Galactic center is at a distance of about 8 kpc from the Earth. A black hole of about 3.6×10^6 solar masses, Sgr A*, lies there. Because of its proximity, this region might be the best candidate for indirect searches of dark matter. Unfortunately, there are other astrophysical γ-ray sources in the field of view (e.g., the supernova remnant Sgr A East), and the halo core radius makes it an extended rather than a point-like source.
- The best observational targets for dark matter detection outside the Galaxy are the Milky Way's dwarf spheroidal satellite galaxies (for example, Carina, Draco, Fornax, Sculptor, Sextans, Ursa Minor). For all of them (e.g., Draco), there is observational evidence of a mass excess with respect to what can be estimated from luminous objects, In addition, the gamma-ray signal expected in the absence of WIMP annihilation is zero. i.e., a high M/L ratio.

The results of the experimental searches will be discussed in Sect. 10.5.3.

Neutrinos. Neutrino–antineutrino pairs can also be used for probing WIMP annihilation or decay, along the same line discussed for gamma rays, apart from the fact that neutrino radiation is negligible. Besides the smaller astrophysical background, the advantage of neutrinos is that they can be observed even if the annihilation happens in the cores of opaque astrophysical objects (the Sun or compact objects in particular); apart form these cases the sensitivity of the gamma-ray channel is by far superior, due to the experimental difficulty of detecting neutrinos for the present and next generation of detectors.

Matter–Antimatter and Electron Signatures. Another indirect manifestation of the presence of WIMPs would be given by their decay (or self-annihilation) producing democratically antimatter and matter.

A possible observable could be related to electron and positron pairs. A smoking gun would be the presence of a peak in the energy of the collected electrons, indicating a two-body decay. A shoulder reaching $m_\chi/2$ could also be a signature, but, in this last case, one could hypothesize astrophysical sources as well.

An excess of antimatter with respect to the prediction of models in which antimatter is just coming from secondary interactions of cosmic rays and astrophysical sources could be seen very clearly in the positron and antiproton spectrum. The PAMELA space mission observed a positron abundance in cosmic radiation higher than that predicted by current models (see Chap. 10). This has been confirmed by the AMS-02 mission, reaching unprecedented accuracy. AMS-02 has also found an excess of antiprotons with respect to models in which only secondary production is accounted. A smoking gun signature for the origin of positrons from the decay of a χ or from a $\chi\chi$ annihilation would be a steep drop-off of the ratio at a given energy. A more detailed discussion of experimental data will be presented in Chap. 10.

8.5.3 Other Nonbaryonic Candidates

Additional candidates, more or less theoretically motivated, have been proposed in the literature. We list them shortly here; they are less economic than the ones discussed before (WIMPs in particular).

Sterile Neutrinos. A possible DM candidate is a "sterile" neutrino, i.e., a neutrino which does not interact via weak interactions. We know that such neutrino states exist: the right-handed component of neutrinos in the standard model are sterile. Constraints from cosmology make it, however, unlikely that light sterile neutrinos can be the main component of dark matter. Sterile neutrinos with masses of the order of the keV and above could be, with some difficulty, accommodated in the present theories.

Kaluza–Klein States. If particles propagate in extra spacetime dimensions, they will have an infinite spectroscopy of partner states with identical quantum numbers; these states could be a DM candidate.

Matter in Parallel Branes; Shadow or Mirror Matter. Some theories postulate the presence of matter in parallel branes, interacting with our world only via gravity or via a super-weak interaction. In theories popular in the 1960s, a "mirror matter" was postulated to form astronomical mirror objects; the cosmology in the mirror sector could be different from our cosmology, possibly explaining the formation of dark halos. This mirror-matter cosmology has been claimed to explain a wide range of phenomena.

Superheavy Particles (WIMPzillas). Superheavy particles above the GZK cutoff (WIMPzillas) could have been produced in the early Universe; their presence could be detected by an excess of cosmic rays at ultrahigh energies.

Further Reading

[F8.1] J. Silk, "The big bang", Times Books 2000.
[F8.2] B. Ryden, "Introduction to Cosmology", Cambridge 2016. This book provides a clear introduction to cosmology for upper level undergraduates.
[F8.3] E.F. Taylor and J.A. Wheeler, "Exploring Black Holes, introduction to general relativity", Addison Wesley 2000. This book provides an enlightening introduction to the physics of black holes emphasizing how they are "seen" by observers in different reference frames.
[F8.4] M.V. Berry, "Principles of Cosmology and Gravitation", Adam Hilger 1989. This book presents the fundamentals of general relativity and cosmology with many worked examples and exercises without requiring the use of tensor calculus.
[F8.5] V. Mukhanov, "Physical Foundations of Cosmology", Cambridge 2005. This book provides a comprehensive introduction to inflationary cosmology at early graduate level.
[F8.6] B. Schutz, "A first Course in General Relativity", second edition, Cambridge University Press 2009. This is a classic and comprehensive textbook.
[F8.7] R. Feynman, "The Feynman Lectures on Physics", www.feynmanlectures.caltech.edu. The classic book by Feynman on web.

Exercises

1. *Cosmological principle and Hubble law.* Show that the Hubble law does not contradict the cosmological principle (all points in space and time are equivalent).
2. *Olbers Paradox.* Why is the night dark? Does the existence of interstellar dust (explanation studied by Olbers himself) solve the paradox?
3. *Steady state Universe.* In a steady state Universe with Hubble law, matter has to be permanently created. Compute in that scenario the creation rate of matter.
4. *Blackbody form of the Cosmic Microwave Background.* In 1965 Penzias and Wilson discovered that nowadays the Universe is filled with a cosmic microwave background which follows an almost perfect Planck blackbody formula. Show that the blackbody form of the energy density of the background photons was preserved during the expansion and the cooling that had occurred in the Universe after photon decoupling.

5. *The CMB and our body.* If CMB photons are absorbed by the human body (which is a reasonable assumption), what is the power received by a human in space because of CMB?

6. *CMB, infrared and visible photons.* Estimate the number of near-visible photons (λ from 0.3 μm to 1 μm) in a cubic centimeter of interstellar space. Estimate the number of far-infrared photons in the region of λ from 1000 μm to 1 μm.

7. *Requirements for a cosmic neutrino background detector.* Let the typical energy of a neutrino in the Cosmic Neutrino Background be ~ 0.2 meV. What is the approximate interaction cross-section for cosmic neutrinos? How far would typically a cosmic neutrino travel in ice before interacting?

8. *Dark Matter and mini-BHs.* If BHs of mass $10^{-8} M_\odot$ made up all the dark matter in the halo of our Galaxy, how far away would the nearest such BH on average? How frequently would you expect such a BH to pass within 1 AU of the Sun?

9. *Nucleosynthesis and neutron lifetime.* The value of the neutron lifetime, which is anormaly long for weak decay processes (why?), is determinant in the evolution of the Universe. Discuss what would have been the primordial fraction of He if the neutron lifetime would have been one-tenth of its real value.

10. *GPS time corrections.* Identical clocks situated in a GPS satellite and at the Earth surface have different periods due general relativity effects. Compute the time difference in one day between a clock situated in a satellite in a circular orbit around Earth with a period of 12 h and a clock situated on the Equator at the Earth surface. Consider that Earth has a spherical symmetry and use the Schwarzschild metric.

11. *Asymptotically Matter-dominated Universe.* Consider a Universe composed only by matter and radiation. Show that whatever would have been the initial proportion of the matter and the radiation energy densities this Universe will be asymptotically matter dominated.

12. *Cosmological distances.* Consider a light source at a redshift of $z = 2$ in an Einstein-de Sitter Universe. (a) How far has the light from this object traveled to reach us? (b) How distant is this object today?

13. *Decoupling.* What are the characteristic temperatures (or energies) at which (a) neutrinos decouple; (b) electron-positron pairs annihilate; (c) protons and neutrons drop out of equilibrium; (d) light atomic nuclei form, (e) neutral He atoms form, (f) neutral hydrogen atoms form, (g) photons decouple from baryonic matter?

14. *Evolution of momentum.* How does the momentum of a free particle evolve with redshift (or scale factor)?

15. *ΛCDM and distances.* Estimate the expected apparent magnitude of a type Ia supernova (absolute magnitude $M \simeq -19$ at a redshift $z = 1$ in the ΛCDM Universe.

16. *Flatness of the Early Universe.* The present experimental data indicate a value for a total energy density of the Universe compatible with one within a few per mil. Compute the maximum possible value of $|\Omega - 1|$ at the scale of the electroweak symmetry breaking consistent with the measurements at the present time.

17. *WIMP "miracle".* Show that a possible Weak Interacting Massive Particle (WIMP) with a mass of the order of $m_\chi \sim 100$ GeV would have the relic density needed to be the cosmic dark matter (this is the so-called WIMP "miracle").

18. *Recoil energy in a DM detector.* Calculate the recoil energy of a target nucleus in a DM detector.

Chapter 9
The Properties of Neutrinos

Alessandro De Angelis and Mário Pimenta

This chapter deals with the physics of neutrinos, which are neutral particles, partners of the charged leptons in SU(2) *multiplets, subject to the weak interaction only—besides their negligible gravitational interaction. Due to their low interaction probability, they are very difficult to detect and as a consequence the neutrino sector is the less known in the standard model of particle physics. In the late 1990s it has been discovered that neutrinos of different flavors (electron, muon, or tau) "oscillate": neutrinos created with well-defined leptonic flavor may be detected in another flavor eigenstate. This phenomenon implies that neutrinos have a non-zero—although tiny even for the standards of particle physics—mass.*

Neutrinos have been important for the developments of particle physics since they were conjectured in the 1930s and are still at present at the center of many theoretical and experimental efforts. Their detection is difficult, since they are only subject to weak interactions (besides the even weaker gravitational interaction).

The existence of neutrinos was predicted by Wolfgang Pauli in 1930 in order to assure the energy momentum conservation in the β decay as it was recalled in Sect. 2.3. Then in 1933 Enrico Fermi established the basis of the theory of weak interactions in an analogy with QED but later on it was discovered that parity is not conserved in weak interactions: neutrinos should be (with probability close to one) left-handed, antineutrinos should be right-handed (see Chap. 6). The theory needed a serious update, which was performed by the electroweak unification (Chap. 7).

Neutrinos were experimentally discovered only in the second-half of the twentieth century: first the electron antineutrino in 1956 by Reines[1] and Cowan (Sect. 2.8); then in 1962 the muon neutrino by Lederman, Schwartz and Steinberger[2]; and finally, the tau neutrino in 2000 by the DONUT experiment at Fermilab (Sect. 5.6.2). Meanwhile it was established in 1991 in the LEP experiments at CERN that indeed there are only three kinds of light neutrinos (see Sect. 7.5.1).

Neutrinos are only detected through their interactions, and different neutrino flavors are defined by the flavors of the charged lepton they produce in weak interactions. The electron neutrino ν_e, for example, is the neutrino produced together with a positron, and its interaction will produce an electron. Similarly, for the muon and the tau neutrinos.

For many years it was thought that neutrinos were massless, and for the standard model of particle physics three generations of massless left-handed neutrinos were enough—a non-zero mass was not forbidden, but it implied new mass terms in the Lagrangian discussed in Chap. 7. There was anyway a "cloud": the so-called solar neutrino problem—in short, the number of solar electron neutrinos arriving to the Earth was measured to be much smaller (roughly between one-third and 60 %, depending on the experiment's threshold) of what it should have been according to the estimates based on the solar power. This problem was solved when it was demonstrated that neutrinos can change flavor dynamically: neutrino species "mix", and quantum mechanics implies that, since they mix, they cannot be massless.

---

[1] Frederick Reines (1918–1998) was a physicist from the US, professor at the University of California at Irvine and formerly employed in the Manhattan project. He won the Nobel Prize in Physics 1995 "for pioneering experimental contributions to lepton physics;" his compatriot and coworker Clyde Cowan Jr. (1919–1974) had already passed away at the time of the recognition.

[2] The Nobel Prize in Physics 1988 was awarded jointly to Leon Lederman (New York 1922), Melvin Schwartz (New York 1931—Ketchum, Idaho, 2006) and Jack Steinberger (Bad Kissingen 1921) "for the neutrino beam method and the demonstration of the doublet structure of the leptons through the discovery of the muon neutrino".
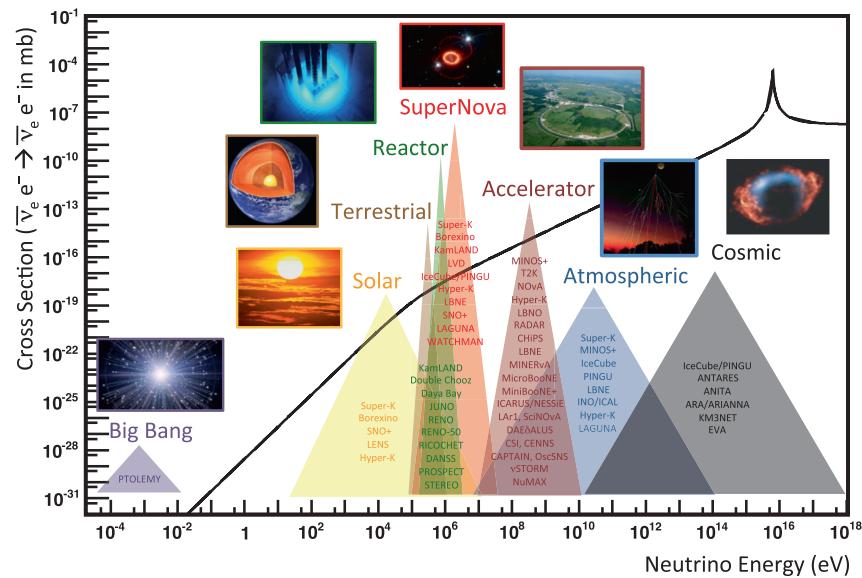
Fig. 9.1 Neutrino interaction cross section as a function of energy, showing typical energy regimes accessible by different neutrino sources and experiments. The curve shows the scattering cross section for an electron antineutrino on an electron. From A. de Gouvêa et al., arXiv:1310.4340v1.

9.1 Sources and Detectors; Evidence of the Transmutation of the Neutrino Flavor

Neutrinos are generated in several processes, and their energy spans a wide range (Fig. 9.1). Correspondingly, there are different kinds of detectors to comply with the different fluxes and cross sections expected.

Let us start by analyzing some neutrino sources. Solar, atmospheric, reactor, and accelerator neutrinos have been complementary in determining the neutrino oscillation parameters, and thus, constraining the masses and the mixing matrix. Other sources of neutrinos, more relevant for astrophysics, will be discussed in Chap. 10.

9.1.1 Solar Neutrinos, and the Solar Neutrino Problem

In the so-called "Standard Solar Model" (SSM), the Sun produces energy via thermonuclear reactions in its core, a region $< 10\%$ of the solar radius containing roughly $1/3$ of the total mass. Most of the energy is released via MeV photons, which originate the electromagnetic solar radiation through propagation and interaction processes that take a long time ($\sim$2 million years). The light emitted comes mostly from the thermal emission of the external region, the photosphere, which has a temperature of about 6000 K, and is heated by the moderation of these photons.

The fusion reactions in the Sun release about 26.7 MeV and produce also a large flux of electron neutrinos that can be detected at Earth (the expected flux at Earth predicted by John Bahcall and collaborators in the SSM is $\sim$6 $\times 10^{10}$ cm^{-2}s^{-1}). This flux is produced mainly by the nuclear reactions initiated by proton-proton (pp) fusions as sketched in Fig. 9.2. The contribution of the alternative CNO chain[3] is small.

The dominant pp reaction ($>$90 % of the total flux) produces ν_e which have a low energy endpoint ($<$0.42 MeV) as it is shown in Fig. 9.3. The ^{7}B line at 0.86 MeV is the second most relevant ν_e source (7–8 %) while the "pep" reaction producing ν_e with energy of 1.44 MeV contributes with just a 0.2 %.

^{8}B neutrinos are produced in the "$ppIII$" chain with energies $<$15 MeV and although their flux could appear marginal ($\sim$0.1 %) they have a major role in the solar neutrino detection experiments. In fact, they

---

[3] The CNO cycle (for carbon-nitrogen-oxygen) is a set of alternative chains of conversion of hydrogen to helium. In the CNO cycle, four protons fuse, giving origin to one alpha particle, two positrons and two electron neutrinos; the cycle uses C, N, and O as catalysts. While the threshold of the pp-chain is around temperatures of 4 MK, the threshold of a self-sustained CNO chain is at approximately 15 MK. The CNO chain becomes dominant at 17 MK.
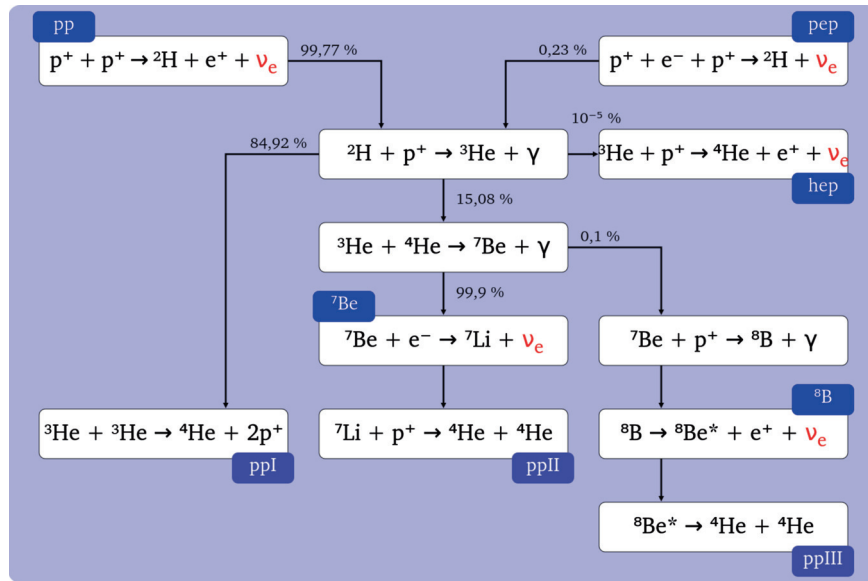
Fig. 9.2 Main nuclear fusion reactions that contribute to the solar neutrino flux. By Dorottya Szam [CC BY 2.5 http://creativecommons.org/licenses/by/2.5], via Wikimedia Commons.
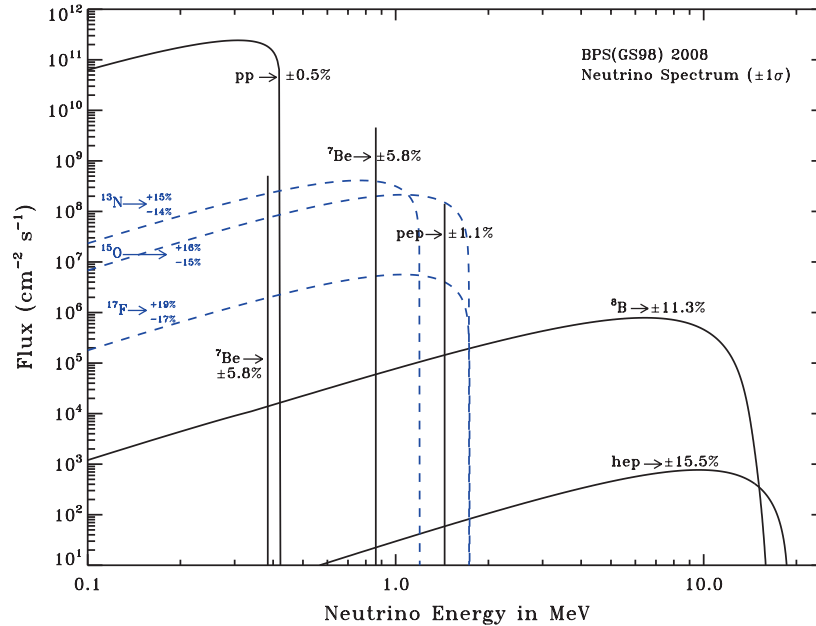
Fig. 9.3 The solar neutrino energy spectrum predicted by the SSM. For continuum sources, fluxes are expressed in units of $cm^{-2}s^{-1}$ MeV^{-1} at the Earth's surface. For line sources, the units are number of neutrinos $cm^{-2}s^{-1}$. The total theoretical errors are quoted for each source. From http://arxiv.org/abs/0811.2424.

were the dominant contribution in the historical Chlorine experiment and can be detected by Cherenkov experiments like Super-Kamiokande and SNO (Fig. 9.3).

The first solar neutrino experiment was done in the late 1960s by Ray Davis in the Homestake mine in South Dakota, USA, counting the number of ^{37}Ar atoms produced in 615 ton of C_2Cl_4 by the reaction involving chlorine:

$$\nu_e \ {}^{37}_{17}Cl \to {}^{37}_{18}Ar \ e^- \tag{9.1}$$

(Nobel prize for Davis, as we discussed in Chap. 4). The observed rate was just around one third of the expected number of interactions based on the energetics of the Sun. This unexpected result originated the so-called "solar neutrino problem" that for three decades led to a systematic and careful work of a large community of physicists, chemists, and engineers which finally confirmed both the predictions of the SSM
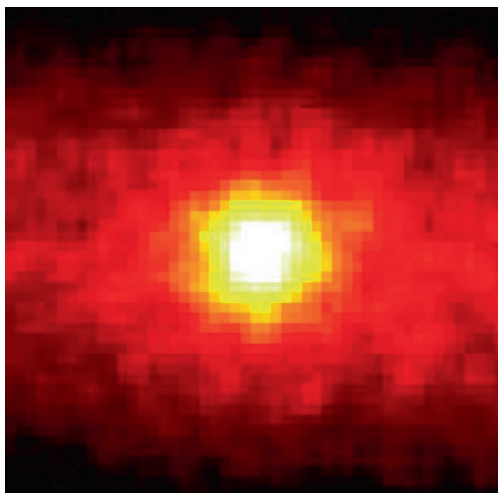
Fig. 9.4 Image of the Sun obtained in a 500 days run of Super-Kamiokande. Credit: R. Svoboda and K. Gordan (Louisiana State University, USA).

and the experimental results of Davis: the explanation was in a fundamental property of neutrinos. Indeed subsequent solar neutrino experiments based on different detection techniques also found a significant deficit in the observed ν_e fluxes; in particular, the GALLEX (at the INFN laboratories under Gran Sasso in Italy) and the SAGE (at Baksan in Russia) experiments used also a radiochemical technique with a lower threshold, choosing Gallium as the detection medium, enabling thus the detection of pp neutrinos.

The Kamiokande and the Super-Kamiokande (described in Chap. 4; also called Super-K, or SK) experiments at Kamioka in Japan used water as target material (50 000 tons in the case of Super-K) which allowed the detection, by Cherenkov radiation, of electrons produced in the interaction of MeV neutrinos on atomic electrons. The energy and the direction of the scattered electron could be measured determining respectively the number of photons and the orientation of the Cherenkov ring. In this way, as the electron keeps basically the direction of the incoming neutrino, it could be proved that indeed the neutrinos were coming from the Sun as it is shown by the beautiful "neutrino picture" of the Sun (Fig. 9.4) that was obtained.

Also in this experiment the total observed flux, when interpreted as only ν_e interactions, is significantly lower than expected by the SSM.

Was the SSM wrong, or some electron neutrinos were disappearing on their way to the Earth? The final answer was given by the Sudbury Neutrino Observatory (SNO) in Canada. SNO used 1000 tons of heavy water (D_2O) as target material. Both charged- and neutral-current neutrino interactions with deuterium nuclei were then observable:

- $\nu_e\, d \to e^- p\, p$ (charged current, CC);
- $\nu_x\, d \to \nu_x\, n\, p$ (neutral current, NC).

While in the first reaction only the ν_e can interact (the neutrino energy is below the kinematic threshold for tau production), the neutrinos of all flavors can contribute to the second one. The resulting e^- is detected by measuring the corresponding water Cherenkov ring. The neutron in the final state may be captured either with low efficiency in the deuterium nuclei or with higher efficiency in ^{35}Cl nuclei from 2 tons of salt (NaCl) that were added in the second phase of the experiment. In any case in those radiative captures γ photons are produced and these may produce, via Compton scattering, relativistic electrons which again originate Cherenkov radiation. In the third and final phase, an array of ^{3}He-filled proportional counters were deployed to provide an independent counting of the NC reaction. In addition to the two processes described above, the elastic scattering

$$\nu_x e^- \to \nu_x e^-$$

is also possible for all neutrino types—although with different cross sections, being the neutrino electron process favored with respect to the other neutrino types.

While ν_e, ν_μ, ν_τ can contribute to the NC, only ν_e contribute to the CC. Thus one has in SNO a clear way to separate the measurement of the ν_e flux from the measurement of the different active neutrino species (in a three-flavor model, $\nu_e + \nu_\mu + \nu_\tau$). SNO could determine that
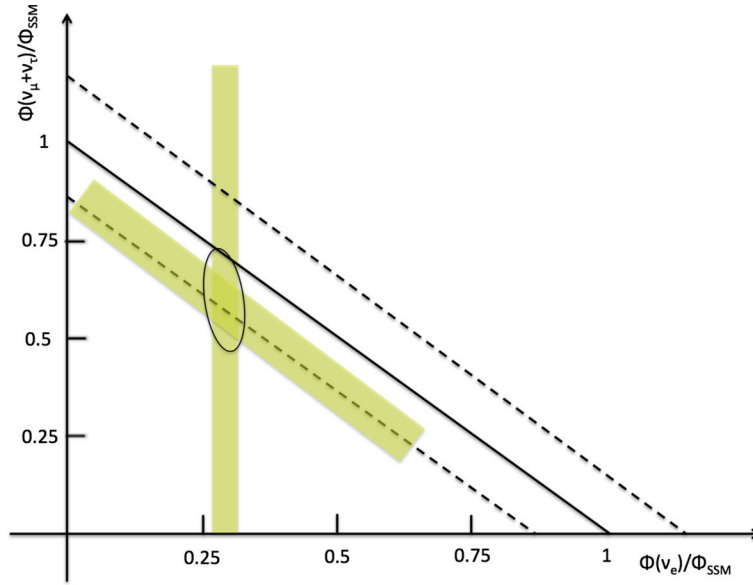
Fig. 9.5 The flux of muon plus tau neutrinos versus the flux of electron neutrinos as derived from the SNO data. The vertical band comes from the SNO charged-current analysis; the diagonal band from the SNO neutral-current analysis; the ellipse shows the 68 % confidence region from the best fit to the data. The predicted Standard Solar Model total neutrino flux is the solid line lying between the dotted lines.

$$\frac{\Phi(\nu_e)}{\Phi(\nu_x)} = 0.340 \pm 0.038 \,(\text{stat.} + \text{syst.})$$

and thus indicated that electron neutrinos might transform themselves into different neutrino flavors during their travel from the Sun to the Earth. The result is compatible with a value of $1/3$.

The results obtained by SNO are summarized in Fig. 9.5. The total measured neutrino flux is clearly compatible with the total flux expected from the SSM and the fraction of detected ν_e is consistent with being only one-third of the total number of the neutrinos.

The solar neutrino problem could be solved without modifying the SSM, and the solution was that solar neutrinos change their flavor during their way to the Earth; the mixing appears to be maximal, in the sense that electron neutrinos are only one third of the total.

Let us examine now the characteristics of the oscillation of neutrinos in the simplified hypothesis that there are only two flavors, and two eigenstates.

9.1.2 Neutrino Oscillation in a Two-Flavor System

The transmutation of neutrinos from one species to another implies in a quantum mechanical world an oscillation phenomenon, similar to what we have observed in the $K^0 - \bar{K}^0$ system. We examine now a simplified model of the neutrino oscillations, to see its implications.

In a world with two flavors (let us suppose for the moment they are ν_e, ν_μ) and two mass (ν_1, ν_2) eigenstates, the flavor eigenstates can be written as a function of a single real mixing angle θ as:

$$\nu_e = \nu_1 \cos\theta + \nu_2 \sin\theta \tag{9.2}$$

$$\nu_\mu = -\nu_1 \sin\theta + \nu_2 \cos\theta \tag{9.3}$$

or, using matrices,

$$\begin{pmatrix} \nu_e \\ \nu_\mu \end{pmatrix} = \begin{pmatrix} \cos\theta & \sin\theta \\ -\sin\theta & \cos\theta \end{pmatrix} \begin{pmatrix} \nu_1 \\ \nu_2 \end{pmatrix} . \tag{9.4}$$

Then, for instance, if a ν_e is produced at time $t = 0$ and position $\mathbf{x} = 0$, the space–time evolution of this quantum state ψ will be determined by the evolution of the corresponding mass eigenstates:

$$\psi = \nu_1 \cos\theta e^{-i(E_1 t - \mathbf{p_1}\cdot\mathbf{x})} + \nu_2 \sin\theta e^{-i(E_2 t - \mathbf{p_2}\cdot\mathbf{x})} \tag{9.5}$$

or, expressing this quantum state again in terms of the weak eigenstates:

$$\psi = \left(\cos^2\theta e^{-i(E_1 t - \mathbf{p_1}\cdot\mathbf{x})} + \sin^2\theta e^{-i(E_2 t - \mathbf{p_2}\cdot\mathbf{x})} \right) \nu_e -$$
$$\left(\cos\theta \sin\theta \left(e^{-i(E_1 t - \mathbf{p_1}\cdot\mathbf{x})} - e^{-i(E_2 t - \mathbf{p_2}\cdot\mathbf{x})} \right) \right) \nu_\mu \,.$$

Note that at $(t = 0, \mathbf{x} = 0)$, $\psi = \nu_e$ but, at later times, there will be usually a mixture between the two-flavor states ν_e, ν_μ.

It can be seen from the equations above that the probability to find a state ν_μ at a distance L from the production point is given by:

$$P(\nu_e \to \nu_\mu) = \sin^2(2\theta) \sin^2\left(\frac{\Delta m^2 L}{4 E_\nu} \right) \tag{9.6}$$

where

$$\Delta m^2 = \left(m_2^2 - m_1^2 \right) \,. \tag{9.7}$$

In order for the mixing to have an effect, the two masses must be different, i.e., at least one should be different from zero. The $\sin^2(2\theta)$ factor plays the role of the amplitude of the oscillation while the phase is given by $\Delta m^2 L/4 E_\nu$. A phase too small or too large makes the measurement of the oscillation parameters quite difficult. Typically, an experiment is sensitive to:

$$\left| \Delta m^2 \right| \sim \frac{E_\nu}{L} \,. \tag{9.8}$$

It is also usual to define an oscillation length L_ν as:

$$L_\nu = \frac{2\pi E_\nu}{\Delta m^2} \tag{9.9}$$

and then

$$P(\nu_e \to \nu_\mu) = \sin^2(2\theta) \sin^2\left(\frac{\pi}{2} \frac{L}{L_\nu} \right) \,. \tag{9.10}$$

We stress the fact that, whenever $L \sim n\, L_\nu$ (with $n = 1, 3, \dots$), the probability of oscillation is maximal.

The oscillation formula is often written using practical units:

$$P(\nu_e \to \nu_\mu) = \sin^2(2\theta) \sin^2\left(1.27 \frac{\Delta m^2 \left(\mathrm{eV}^2\right) L\,(\mathrm{km})}{E_\nu\,(\mathrm{GeV})} \right) \tag{9.11}$$

and the probability to find a state ν_e at the same distance L is by construction:

$$P(\nu_e \to \nu_e) = 1 - P(\nu_e \to \nu_\mu) \,. \tag{9.12}$$

The oscillation probabilities, in this two-flavor world, are just a function of two parameters: the mixing angle θ and the difference of the squares of the two masses $\Delta m^2 = \left(m_1^2 - m_2^2 \right)$.

Experiments that measure the possible depletion of the initial neutrino beam are called *disappearance* experiments. Experiments that search for neutrinos with a flavor different from the flavor of the initial neutrino beam are called *appearance* experiments. An appearance experiment is basically sensitive to a given oscillation channel $\nu_i \to \nu_j$ with $i \neq j$ while a disappearance experiment is sensitive to transitions to all possible different neutrino species, or to pure disappearance.

The determination of the parameters of neutrino oscillations has been one of the priorities of the research during the last years. If neutrinos oscillate, their masses, although small, cannot be zero. The direct measurement of such masses and of the mixing strengths has gained a renewed interest.

The theoretical origin of neutrino masses is not yet established: either it is the result of the Higgs mechanism as it is the case for all the other fermions (Dirac neutrino) or, as suggested by Majorana, the neutrino is its own antiparticle (Majorana neutrino). If the latter is the case, double beta decays—nuclear decays in which two neutrons become protons—could be neutrinoless (the simplest ways of viewing this fact is to think that the two neutrinos annihilate each other, or that the second neutron absorbs the neutrino emitted by the first one during its transition, and then undergoes the process $\nu n \to p$).

In addition, neutrinos travel a long way within the Sun, and most of the neutrino oscillation is likely to happen in matter.

The neutrino oscillations can be enhanced (or suppressed) whenever neutrinos travel through matter. In fact, while all neutrino flavors interact equally with matter through neutral currents, charged current interactions with matter are flavor dependent (at solar neutrino energies, basically only electron neutrinos can interact). This is called the MSW effect, as it comes from works by Lincoln Wolfenstein, Stanislav Mikheyev, and Alexei Smirnov. Thus, the time evolution in matter of the electron neutrino and of the other neutrinos can be different.

In the case of a constant density medium, this effect is translated, in a two-flavor approximation, into a modified oscillation probability the oscillation probability $\nu_e \to \nu_x$ to:

$$P\left(\nu_e \to \nu_x\right) = \sin^2\left(2\theta_m\right)\sin^2\left(\frac{\pi}{2}\frac{L}{L_\nu}F\right) \tag{9.13}$$

where

$$\sin\left(2\theta_m\right) = \sin\left(2\theta\right)/F, \tag{9.14}$$

$$F = \sqrt{\left(\cos\left(2\theta\right) - \frac{L_\nu}{L_e}\right)^2 + \sin^2\left(2\theta\right)} \tag{9.15}$$

and

$$L_e = \pm 2\pi/\left(2\sqrt{2}G_F N_e\right). \tag{9.16}$$

L_e, the electron neutrino interaction length, is positive for neutrinos, negative for antineutrinos. G_F is the Fermi constant and N_e the electron density in the medium. L_ν, the neutrino oscillation length in vacuum, is, as defined before, a function of the neutrino energy and of the difference of the square of the masses:

$$L_\nu = \frac{2\pi E_\nu}{\Delta m^2}. \tag{9.17}$$

Note that the sign of L_ν is determined by the sign of Δm^2. In fact as it will be discussed in Sect. 9.2 there are two possibilities in the hierarchy of the neutrino mass and thus the sign of Δm^2 can be positive or negative.

The values of the mass eigenstates are also changed. The new eigenstates are given by:

$$M_{2,1}^2 = \frac{1}{2}\left[m_1^2 + m_2^2 + \Delta m^2\left(\frac{L_\nu}{L_e} \pm F\right)\right] \tag{9.18}$$

where the $+$ sign is for M_2 and the $-$ is for M_1. Whenever $L_\nu = L_e \cos\left(2\theta\right)$ the amplitude of the oscillation is maximal ($\sin^2\left(2\theta_m\right) = 1$). Thus, for a given set of (E, N_e) values, resonant oscillations are possible and the oscillation probability may be strongly enhanced independently of the value of θ in vacuum.

In the center of the Sun $N_e \sim 3 \times 10^{31}$ m^{-3} and then the value of L_e is $\sim 3 \times 10^5$ m which is a small number when compared with the Sun radius (10^8–10^9 m). In this way, the suppression of the electron neutrinos is a function of the neutrino energy for given values of Δm^2 and θ.

How to determine the oscillation parameters? More information comes from different neutrino sources.

9.1.3 Long-Baseline Reactor Experiments

Nuclear reactors are abundant $\overline{\nu}_e$ sources via the β decays of several of the isotopes produced in the fission reactions. The $\overline{\nu}_e$ have an energy of a few MeV and can be detected by the inverse β decay reaction ($\overline{\nu}_e\ p \to e^+n$). The results from reactors can be combined with the results obtained in the solar experiments supposing that ν_e and $\overline{\nu}_e$ have the same behavior. In reactor experiments the energies and the distances are much better determined than in solar experiments.

The KamLAND experiment (again in Kamioka in Japan), a 1000-ton liquid scintillator detector, is placed at distances of the order of 100 km from several nuclear reactors (the weighted average distance being of 180 km) and thus, as discussed in the previous section, is sensitive to small Δm^2 oscillations.
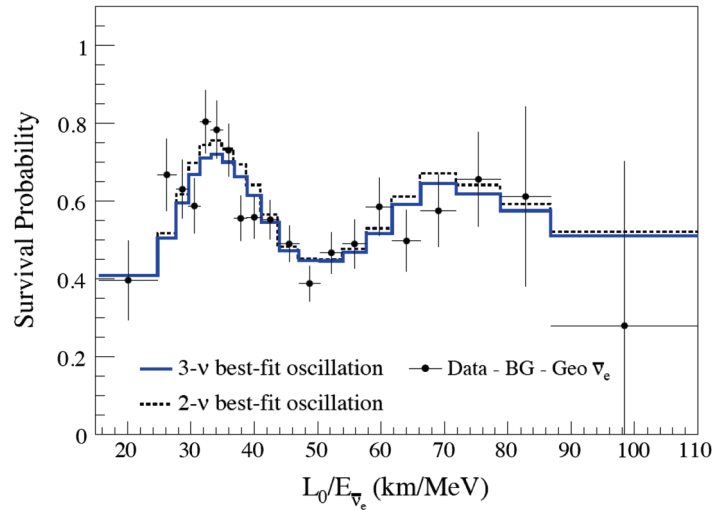
Fig. 9.6 The $\bar{\nu}_e$ survival probability as a function of L/E observed in the KamLAND experiment. Figure from A. Gando et al. (KamLAND Collab.), Phys. Rev. D83 (2011) 052002.

Electron antineutrinos are detected through the reaction $\bar{\nu}_e p \rightarrow e^+ n$, which has a 1.8 MeV energy threshold. The prompt scintillation light from the positron allows to estimate the energy of the incident antineutrino. The neutron recoil energy is only a few tens of keV; the neutron is captured on hydrogen and a characteristic 2.2 MeV gamma ray is emitted after some 200 μs. This delayed-coincidence between the positron and the gamma ray signals provides a very powerful signature for distinguishing antineutrinos from backgrounds produced by other sources.

KamLAND detects a clear pattern of oscillation as shown in Fig. 9.6.

9.1.4 Estimation of $\nu_e \rightarrow \nu_\mu$ Oscillation Parameters

KamLAND and the solar experiments provide the best determinations of the θ and Δm^2 parameters involved in the ν_e oscillations. The results taking into account all the data available at the end of 2017 are shown in Fig. 9.7, where these parameters are labelled, as it will be discussed later on, as θ_{12} and Δm_{21}^2. There is a perfect agreement in the obtained values of $\sin^2(\theta_{12})$ while the central value of KamLAND for Δm_{21}^2 is slightly higher (2σ) than the one from solar experiments. The effect of variations on the solar abundances, illustrated in the figure by the curves for two different versions of the SSM (GS98 and AGSS09 models), are quite small. The best fit values obtained for these parameters in the NuFIT[4] 3.1 (2017) (we shall call them for the moment θ_{Sun} and $\Delta m_{\mathrm{Sun}}^2$) are:

$$\sin^2(2\theta_{Sun}) \sim 0.85, \tag{9.19}$$

and

$$\Delta m_{Sun}^2 \sim 7.5 \times 10^{-5} \mathrm{eV}^2. \tag{9.20}$$

Note that it is not straightforward to obtain the "solar" parameters listed above from solar neutrino data: large part of the oscillation effect happens within the Sun, and needs a different mathematical treatment with respect to the oscillation *in vacuo*.

9.1.5 Atmospheric Neutrinos and the $\nu_\mu \rightarrow \nu_\tau$ Oscillation

Another solid evidence that neutrinos do oscillate came from the measurement at the Earth surface of the relative ratio of the ν_e and ν_μ produced in cosmic-ray showers (Fig. 9.8; see also Chap. 10) by the decays of

---

[4] The NuFIT group provides and regularly updates at the web site http://www.nu-fit.org/ a global analysis of neutrino oscillation measurements.
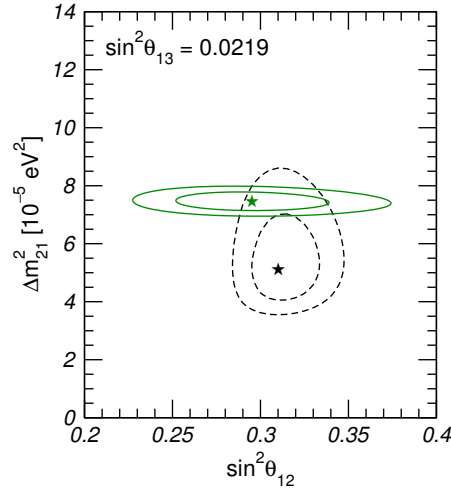
Fig. 9.7 Allowed parameter regions (at 1σ and 2σ) in the ($\sin^2\theta_{12}$, Δm^2_{21}) space for the combined analysis of solar neutrino data and for the analysis of KamLAND data. The result for KamLAND is illustrated by the ellipses with horizontal major axis, with the best fit marked by a green star. The two other ellipses and the other star indicate the corresponding values for solar neutrino data. Figure adapted from NuFIT 2017.

the $\pi^\pm$ and to a lesser extent of the $K^\pm$. The decay chains:

$$\pi^+ \to \mu^+ \nu_\mu \; ; \; \mu^+ \to e^+ \nu_e \overline{\nu}_\mu \tag{9.21}$$

$$\pi^- \to \mu^- \overline{\nu}_\mu \; ; \; \mu^- \to e^- \overline{\nu}_e \nu_\mu \tag{9.22}$$

imply that the ratio:

$$R = \frac{\nu_\mu + \overline{\nu}_\mu}{\nu_e + \overline{\nu}_e} \tag{9.23}$$

should be around 2. In fact the value of this ratio is slightly different from 2, because not all muons decay in their way to Earth and only around $63\,\%$ of the $K^\pm$ follow similar decay chains; this ratio is, thus, energy-dependent. Monte Carlo calculations allow the computation of these corrections.

The ratio measured by Kamiokande-II, Super-Kamiokande, and by several other experiments, was however quite different from 2. There was, as it is shown in Fig. 9.9, left, a clear deficit of muon neutrinos coming mainly from below the detector. Indeed upward muon neutrinos ($\cos\theta < 0$, see Fig. 9.8) which traveled longer distances showed a higher probability to disappear. As the interaction cross section in the Earth is too small to explain such disappearance (and no deficit was observed for electron neutrinos), this phenomenon is due to muon neutrino oscillation in particular into tau neutrinos.

Since the number of electron neutrinos was found not to deviate from expectations, oscillations were interpreted as indeed mainly involving tau neutrinos (any undetected type of neutrino would anyway explain the observations). In fact the observed modulation pattern as a function of the zenith angle (Fig. 9.9, left) and as a function of L/E (Fig. 9.9, right) is very well reproduced considering the same survival oscillation formula (Eq. 9.11) deduced in just a two-flavor scenario but now between the muon and the tau neutrinos.

The best fit to all available data provides:

$$\Delta m^2_{atm} \sim 2.5 \times 10^{-3} \text{eV}^2 \tag{9.24}$$

and a large mixing, consistent with unity:

$$\sin^2(2\theta_{atm}) \sim 1 \,. \tag{9.25}$$

We now need to extend the phenomenology of flavor oscillation to three families to see the global picture.
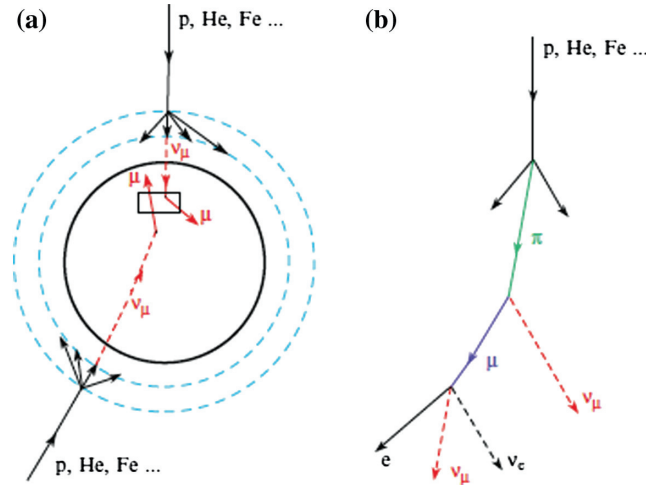
Fig. 9.8 The interaction of cosmic rays in the upper atmosphere generates particle showers comprising neutrinos (right picture), which originate from a 10–20 km thick atmospheric layer. A large volume detector placed underground, like Super-K, is used to detect them; downward-going neutrinos traveled only few tens of kilometers and had no "space" to oscillate, while upward-going neutrinos have traveled about 10 000 km and have likely oscillated. The detector (left picture) can distinguish between electron neutrinos and muon neutrinos: secondary muons are likely to escape the detector (non-contained or partially contained events), while secondary electrons formed by neutrino electrons interacting in the detector are likely to be absorbed (fully contained events). In the case of fully contained events the electron ring is "fuzzier" than the muon ring. From Braibant, Giacomelli and Spurio, "Particles and fundamental interactions," Springer 2014.
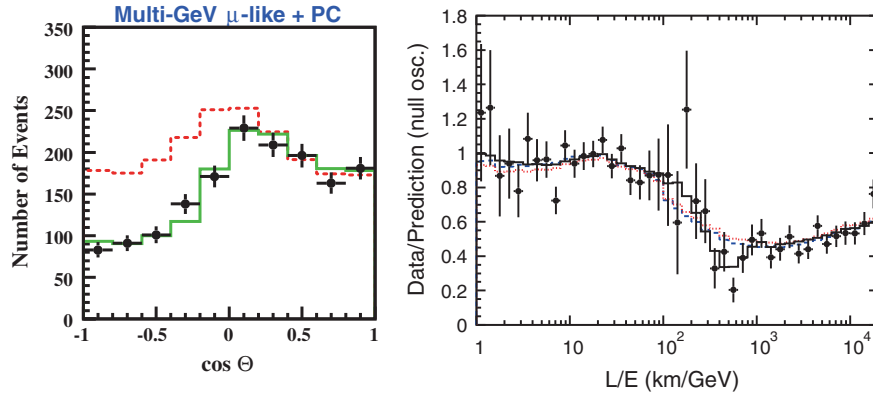
Fig. 9.9 Left: Zenith angle distribution of muon neutrinos in SK. The observed number of upward-going neutrinos was roughly half of the predictions. Right: Survival probability of ν_μ as a function of L/E. Black dots show the observations and the lines shows the prediction based on neutrino oscillation. Data show a dip around $L/E \simeq 500$ km/GeV. The prediction of two-flavor neutrino oscillations agrees well with the position of the dip. From http://www-sk.icrr.u-tokyo.ac.jp/sk/physics/atmnu-e.html and The Super-Kamiokande Collaboration, Y. Ashie et al., "Evidence for an Oscillatory Signature in Atmospheric Neutrino Oscillations," Phys. Rev. Lett. 93 (2004) 101801.

9.1.6 Phenomenology of Neutrino Oscillations: Extension to Three Families

Bruno Pontecorvo first suggested in 1957 that the neutrino may oscillate; in the 1960s it was suggested that the neutrino weak and mass eigenstates might have not been the same. Neutrinos would be produced in weak interactions in pure flavor states that would be a superposition of several mass states (preserving unitarity) which would determine their time-space evolution, giving rise to mixed flavor states.

We have shortly discussed in the beginning of this chapter a simplified model in which only two neutrinos and two mass eigenstates appear. Assuming three weak eigenstates (ν_e, ν_μ, ν_τ) and three mass eigenstates (ν_1, ν_2, ν_3), the mixing can be modeled, similarly to what seen for the CKM matrix, using a 3×3 unitary matrix, which we call today the Pontecorvo-Maki-Nakagawa-Sakata (PMNS) matrix

$$\begin{pmatrix} \nu_e \\ \nu_\mu \\ \nu_\tau \end{pmatrix} = \begin{pmatrix} U_{e1} & U_{e2} & U_{e3} \\ U_{\mu1} & U_{\mu2} & U_{\mu3} \\ U_{\tau1} & U_{\tau2} & U_{\tau1} \end{pmatrix} \begin{pmatrix} \nu_1 \\ \nu_2 \\ \nu_3 \end{pmatrix}. \tag{9.26}$$
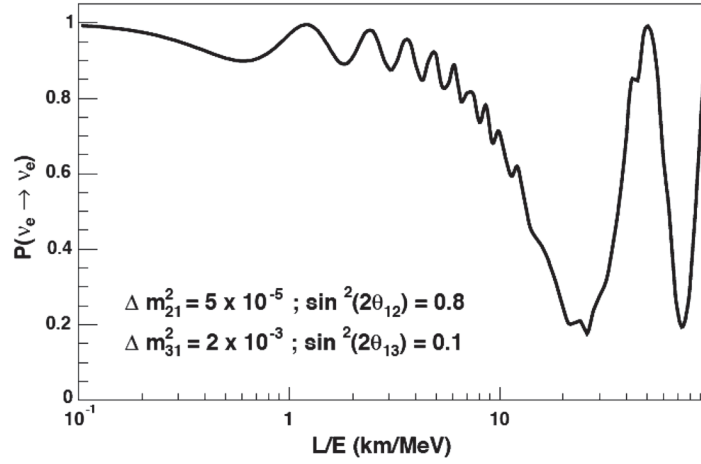
Fig. 9.10 The ν_e survival probability as a function of L/E for fixed oscillation parameters as indicated in the figure. From http://www.hep.anl.gov/minos.

Taking into account the relations imposed by unitarity and the fact that several phases can be absorbed in the definition of the fields (if the neutrinos are standard fermions) there are only three real parameters usually chosen as the mixing angles θ_{12}, θ_{13}, θ_{23} and a single complex phase written in the form $e^{i\delta}$. If the mixing angle $\theta 13$ and $\sin\delta$ are $\neq 0$, CP is violated.

The PMNS matrix can be decomposed as the product of three 3×3 matrices:

$$\begin{pmatrix} U_{e1} & U_{e2} & U_{e3} \\ U_{\mu 1} & U_{\mu 2} & U_{\mu 3} \\ U_{\tau 1} & U_{\tau 2} & U_{\tau 1} \end{pmatrix} = \tag{9.27}$$

$$= \begin{pmatrix} 1 & 0 & 0 \\ 0 & \cos\theta_{23} & \sin\theta_{23} \\ 0 & -\sin\theta_{23} & \cos\theta_{23} \end{pmatrix} \begin{pmatrix} \cos\theta_{13} & 0 & \sin\theta_{13}e^{-i\delta} \\ 0 & 1 & 0 \\ -\sin\theta_{13}e^{i\delta} & 0 & \cos\theta_{13} \end{pmatrix} \begin{pmatrix} \cos\theta_{12} & \sin\theta_{12} & 0 \\ -\sin\theta_{12} & \cos\theta_{12} & 0 \\ 0 & 0 & 1 \end{pmatrix} . \tag{9.28}$$

This format puts in evidence what we observed: in the first approximation, both the oscillation $\nu_e \to \nu_\mu$ and the oscillation $\nu_\mu \to \nu_\tau$ can be described as oscillations between two weak eigenstates and two mass eigenstates. Thus, we can identify the two most important parameters for solar neutrinos, θ_{Sun} and $\Delta m^2_{\mathrm{Sun}}$, with θ_{12} and Δm^2_{21}, respectively; while for atmospheric neutrinos we identify θ_{atm} and $\Delta m^2_{\mathrm{atm}}$, with θ_{23} and $\left| \Delta m^2_{32} \right| \simeq \left| \Delta m^2_{31} \right|$, respectively (experimentally it was observed that $\left| \Delta m^2_{32} \right| \simeq \left| \Delta m^2_{31} \right| \gg \left| \Delta m^2_{21} \right|$).

The survival probability, for example, $\nu_e \to \nu_e$, in the case of three families is given by:

$$P(\nu_e \to \nu_e) = 1 - 4 \left| U_{e1} \right|^2 \left| U_{e2} \right|^2 \sin^2 \left(\frac{\Delta m^2_{21} L}{4E_\nu} \right) +$$

$$-4 \left| U_{e1} \right|^2 \left| U_{e3} \right|^2 \sin^2 \left(\frac{\Delta m^2_{31} L}{4E_\nu} \right) - 4 \left| U_{e2} \right|^2 \left| U_{e3} \right|^2 \sin^2 \left(\frac{\Delta m^2_{32} L}{4E_\nu} \right) .$$

The fact that $\left| \Delta m^2_{32} \right| \simeq \left| \Delta m^2_{31} \right| \gg \left| \Delta m^2_{21} \right|$ leads to an oscillation characterized by two different length scales. Indeed assuming that $\left| \Delta m^2_{32} \right| = \left| \Delta m^2_{31} \right|$, imposing unitarity and expressing the matrix elements in terms of the PMNS parametrization reported above, one obtains:

$$P(\nu_e \to \nu_e) \simeq 1 - \cos^4(\theta_{13}) \sin^2(2\theta_{12}) \sin^2 \left(\frac{\Delta m^2_{21} L}{4E_\nu} \right) - \sin^2(2\theta_{13}) \sin^2 \left(\frac{\Delta m^2_{32} L}{4E_\nu} \right) . \tag{9.29}$$

In reactor experiments the energy of the neutrino (in fact $\overline{\nu}_e$) beams are of the order of a few MeV. Thus, as $\Delta m^2_{21} \sim 10^{-5} - 10^{-4}$ eV^2 and $\left| \Delta m^2_{32} \right| \sim 10^{-3}$ eV^2, experiments placed at distances of the order of the km are sensitive to θ_{13} while experiments placed at distances of the order of the hundreds of km are sensitive to θ_{12}.

This two-length behavior is illustrated in Fig. 9.10 where the probability of ν_e survival is shown for fixed oscillation parameters.
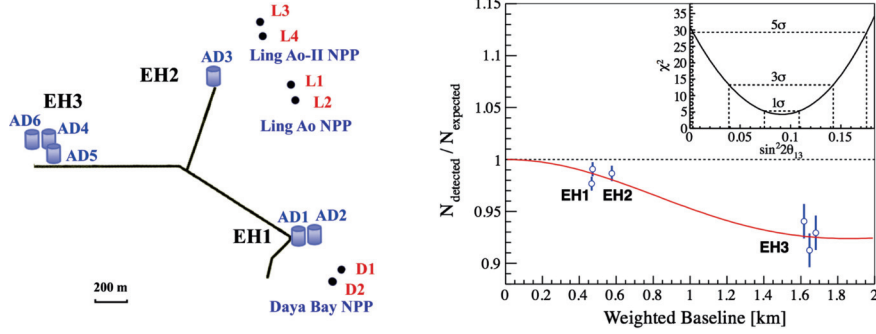
Fig. 9.11 Left: Layout of the Daya Bay experiment. The dots represent reactors, labeled as D1, D2, L1, L2, L3, and L4; the locations of the detectors are labeled EH1, EH2 and EH3. Right: The $\overline{\nu}_e$ disappearance as measured by the Daya Bay experiment. Ratio of the measured signal in each detector versus the signal expected assuming no oscillation. The oscillation survival probability at the best-fit $\sin^2 2\theta_{13}$ value is given by the smooth curve. The χ^2 versus $\sin^2 2\theta_{13}$ is shown in the inset. Figures from F.P. An et al., Phys. Rev. Lett. 108 (2012) 171803.

In the first case ($L \sim$ km) the above formula can be simplified to:

$$P\left(\overline{\nu}_e \to \overline{\nu}_e\right) \approx 1 - \sin^2\left(2\theta_{13}\right)\sin^2\left(\frac{\Delta m_{32}^2\, L}{4\, E_{\overline{\nu}}}\right) \tag{9.30}$$

while in the second case ($L \sim 100$ km) it can be simplified to:

$$P\left(\overline{\nu}_e \to \overline{\nu}_e\right) \approx 1 - \cos^4\left(\theta_{13}\right)\sin^2\left(2\theta_{12}\right)\sin^2\left(\frac{\Delta m_{21}^2\, L}{4\, E_{\overline{\nu}}}\right) . \tag{9.31}$$

9.1.7 Short-Baseline Reactor Experiments, and the Determination of θ_{13}

Close to a fission reactor, where the long wavelength oscillation did not develop yet, the electron antineutrino survival probability can be approximated as computed in Eq. 9.30.

The Daya Bay experiment in China is a system of six 20-ton liquid scintillator detectors (antineutrino detectors, AD) arranged in three experimental halls (EH), placed near six nuclear reactors (the geometry is shown in Fig. 9.11, left); as a consequence of the distances and of the geometry it is sensitive to short oscillations which may occur in a 3×3 mixing matrix scenario (see Sect. 9.1.6). In fact Daya Bay reported in March 2012 the first evidence of such short-scale oscillations (Fig. 9.11, right). Later, the RENO experiment in South Korea and Double Chooz in France confirmed such oscillations.

The best fit values to all available data, including accelerator data (see Sect. 9.1.8), provides:

$$\sin^2\theta_{13} = 0.02203 \pm 0.00083\,.$$

Although small, a nonzero value of θ_{13} allows the phase $\delta \neq 0$ to produce CP violation in the neutrino sector.

9.1.8 Accelerator Neutrino Beams

The results from atmospheric neutrino experiments and reactor experiments can be tested in accelerator experiments, building intense and collimated ν_μ and $\overline{\nu}_\mu$ beams from the decay of secondary $\pi^\pm$ (and in a smaller percentage of $K^\pm$), and placing detectors both near (100–1000 m) and far (100–1000 km) from the primary target. The oscillation distance L is then fixed and the neutrino flux and the energy spectrum can be well predicted and precisely measured at the near detectors, constraining the elements of the neutrino mixing matrix.

The K2K (KEK to Kamioka) experiment, in Japan, was the first such experiment (actually its construction started at the end of the 1990s before the discovery of the neutrino oscillations in Super-Kamiokande). The neutrino beam, with a mean energy of 1.3 GeV, was produced at KEK in Tsukuba and the interactions were
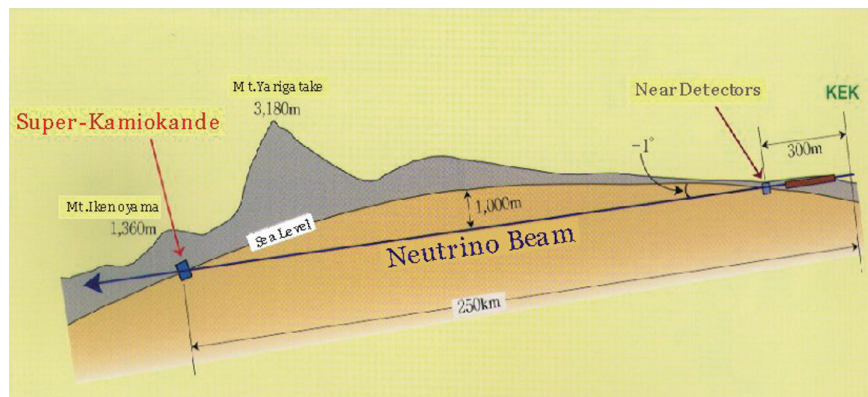
Fig. 9.12 Sketch of the neutrino path in the K2K long-baseline experiment. From http://neutrino.kek.jp.
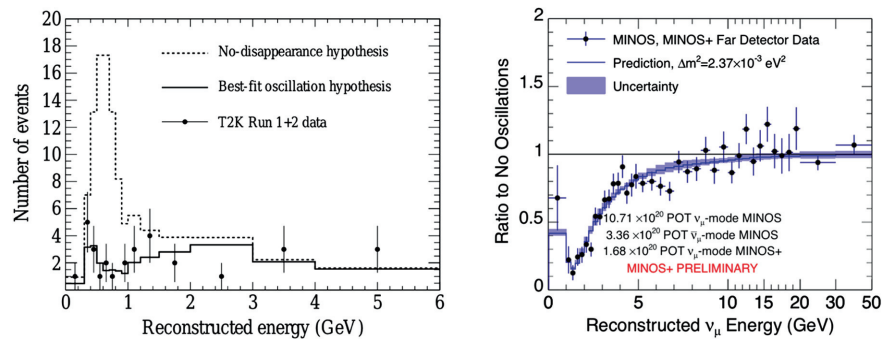
Fig. 9.13 Left: The first T2K study on the disappearance of muon neutrinos: muon-antineutrino events with well-reconstructed energy recorded before 2011. The energy distribution is compared to the calculations with and without oscillations. From Phys. Rev. D 85, 031103 (2012). Right: The ratio of the observed spectrum of muon neutrino interactions from MINOS to the predicted spectrum in the absence oscillations. The dark band represents the prediction assuming oscillations and its 1σ systematic uncertainty, using the best-fit oscillation parameters from MINOS. The observed data are well described by the oscillation model. From http://www-numi.fnal.gov/PublicInfo.

measured in a nearby detector at 300 m and in the Super-Kamiokande detector at 250 km (Fig. 9.12). 112 events were detected while 158 ± 9 where expected without considering oscillations; a neutrino oscillation pattern compatible with the atmospheric neutrino results was observed.

The T2K (Tokai to Kamioka) experiment followed K2K sending muon neutrinos to the Super-Kamiokande detector. It is a second generation experiment located at 295 km from the accelerator. The neutrino beam, produced in the the J-PARC facility in Tokai, Eastern Japan, has a narrow range of energies around 600 MeV, selected in order to maximize the neutrino oscillation probability in their way to Super-Kamiokande. The intensity of the beam is two orders of magnitude larger than in K2K. The near detector (ND280), 280 m downstream the neutrino beam, is a segmented detector composed of neutrino targets inside a tracking system surrounded by a magnet. ND280 can measure the energy spectrum of the ν beam, its flux, flavor content, and interaction cross sections before the neutrino oscillation. We shall see later that, on top of precise measurements of the $\overline{\nu}_\mu$ disappearance (Fig. 9.13, left), T2K detected for the first time explicitly the appearance of $\overline{\nu}_e$ in a $\overline{\nu}_\mu$ beam.

In the USA, the MINOS experiment started taking data in 2005. The beam line at Fermilab is optimized to produce both ν_μ and $\overline{\nu}_\mu$ beams with a mean energy of 3 GeV. The far detector is placed at a distance of 735 km in the Soudan mine. A distortion of the energy spectrum at the far detector compatible with the previous oscillation measurements was observed for ν_μ beams (Fig. 9.13, right). More recently the NOνA experiment announced its first two years results. NOνA is also a long-baseline (810 km) Fermilab experiment and is optimized to study ν_μ-disappearance and as ν_e-appearance in both neutrino and antineutrino channels.

These results can be once again interpreted in terms of oscillations in a two-flavor scenario (but now considering $\nu_\mu \to \nu_\tau$). They confirm and improve the result from the atmospheric neutrinos. The mixing is large and the mass difference is again much smaller than the normal fermion masses but much higher than the values measured in the case of the electron neutrino beam, i.e., in the "solar" neutrinos as discussed above. Accelerator and atmospheric experiments are complementary: in the former L is fixed and E known
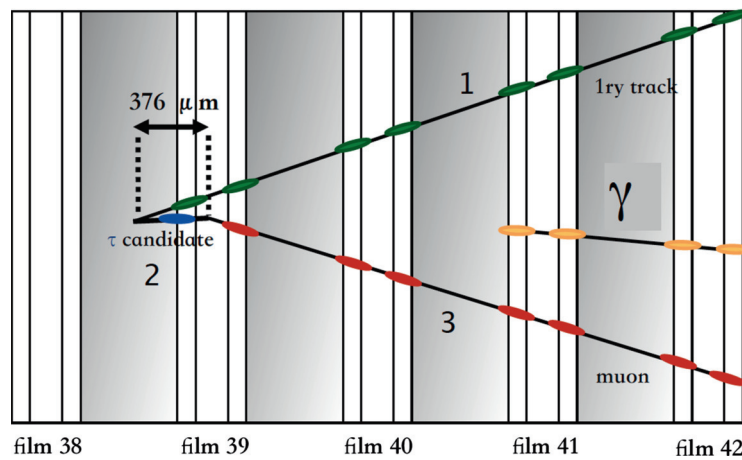
Fig. 9.14 One of the three tau neutrino candidate events observed by OPERA. From http://operaweb.lngs.infn.it.

assuring a good resolution in the measurement of $\left|\Delta m_{23}^2\right|$ while in the latter the fluxes are high assuring a good resolution in the measurement of θ_{23}.

9.1.9 Explicit Appearance Experiment

The SNO experiment was somehow an appearance experiment: the comparison of charged current events with neutral current events was an indication that μ plus τ neutrinos were present in the flux of solar neutrinos. However, two experiments made an explicit detection of neutrinos of different flavor from the muon neutrinos in an accelerator beam.

The OPERA experiment located at Gran Sasso, Italy, receives a 17 GeV muon neutrino beam produced at CERN located 730 km away. OPERA uses a sophisticated 1200 tons detector composed by a sandwich of photographic emulsion films and lead plates in order to be able to detect tau-leptons: it is thus an appearance experiment aiming to detect tau-neutrinos resulting from the oscillation of the initial muon neutrino beam. OPERA, which concluded data-taking, reported five tau-neutrino candidates corresponding to significance of about 5σ; one of them is shown in Fig. 9.14.

T2K can make use of both muon neutrino and antineutrino beams from the same accelerator. Recent observation of the ν_e appearance from a high-purity ν_μ beam recorded 89 electron neutrino events while 67 events were expected in case of no CP violation; on the other hand, in a $\overline{\nu}_\mu$ beam 7 electron anti-neutrino events were detected while 9 events were expected in the case of no CP violation. The observed excess in the electron neutrino appearance rate and the observed smaller rate in the electron anti-neutrino appearance provides a 2σ indication of a possible difference in the oscillation parameters for neutrinos and anti-neutrinos which would imply a CP violation in the neutrino sector; this fact is reflected in the present result on the δ parameter (see Sect. 9.2).

9.1.10 A Gift from Nature: Geo-Neutrinos

The interior of the Earth radiates heat at a rate of about 50 TW, which is about 0.1 % of the incoming solar energy. Part of this heat originates from the energy generated upon decays of radioactive isotopes, while another part is due to the cooling of the Earth.

The Earth's radioactive elements (in particular ^{238}U, ^{232}Th, ^{40}K) are β^- emitters and thus natural sources of $\overline{\nu}_e$, in this case designated as geo-neutrinos. The fluxes are small (as an example, around 21 events/year in KamLAND) but their measurement may provide important geological information on Earth's composition and structure that is not accessible by other means. The main backgrounds are due to nuclear reactors, since the contribution of atmospheric neutrinos is negligible and the Sun emits exclusively ν_e. KamLAND reported in 2013 a total observed signal of 116^{+28}_{-27} events and Borexino (a 280 ton liquid scintillator detector in Gran

Sasso) reported recently the detection of a signal with a significance as high as 5.9 standard deviations. The current estimates are that, although with large errors, some 20 TW of energy from the Earth comes from nuclear processes.

Thanks to neutrino detectors, a new highly interdisciplinary field, neutrino geophysics, has just been born.

9.2 Neutrino Oscillation Parameters

The simplified model in which neutrinos coming from two mass eigenstates oscillate between two flavors does not describe the full picture coming from the data. The large majority of the present experimental results are well-described assuming three weak eigenstates (ν_e, ν_μ, ν_τ) and three mass eigenstates (ν_1, ν_2, ν_3).

Some researchers evidence a possible tension in the data, which for the first time was announced as the "LSND[5] anomaly". LSND claimed an oscillation with $|\Delta m| \sim 1$ eV, which would imply the existence of a neutrino with mass of at least one eV. The only way to accommodate this with the LEP results in the number of neutrino families is that this particle is a new kind of neutrino, which should be sterile–or at least not coupled to $W^\pm$ and Z.

The mixing matrix between three states is the Pontecorvo-Maki-Nakagawa-Sakata (PMNS) matrix (see Sect. 9.1.6). However, it should be noted that a complete treatment of neutrino propagation requires subtle questions of field theory, and has close links to the foundation of quantum mechanics. Since different mass components travel at different speeds, the mixing spreads the neutrino wavefunction in space, with EPR-like[6] implications.

The parameters of the PMNS matrix are: two mass differences (we can choose Δm_{21}^2 and Δm_{31}^2); three angles (θ_{12}, θ_{23} and θ_{13}); one single complex phase written in the form $e^{i\delta}$.

Data show that $|\Delta m_{31}^2| \gg |\Delta m_{21}^2|$. The sign of

$$\Delta M^2 \equiv m_3^2 - \frac{m_2^2 + m_1^2}{2} \,. \tag{9.32}$$

is not presently known: only the sign of Δm_{21} is determined to be positive from the experimental measurements (solar neutrinos). There are two possibilities (Fig. 9.15):

- $m_1 < m_2 < m_3$ (the so-called "Normal" Hierarchy or Ordering, NH or NO, ΔM^2 positive);
- $m_3 < m_1 < m_2$ (the so-called "Inverted" Hierarchy or Ordering, IH or IO, ΔM^2 negative).

Results are usually presented in terms of the variable $\Delta m_{3\ell}^2$, with $\ell = 1$ for NH and $\ell = 2$ for IH. Hence, $\Delta m_{3\ell}^2 = \Delta m_{31}^2 > 0$ for NH and $\Delta m_{3\ell}^2 = \Delta m_{32}^2 < 0$ for IH, i.e., it corresponds to the mass splitting with the largest absolute value. Best fit values of the mass differences and of the mixing angles imposing unitarity of the mixing matrix and, in case the difference between the NH and the IH hypothesis is smaller than half the error, averaging the two values and increasing the error itself by the absolute half difference of the two values, are:

$$\Delta m_{21}^2 = \left(74.0^{+2.1}_{-2.0}\right) \times 10^{-6} \mathrm{eV}^2 = (8.60 \pm 0.12\,\mathrm{meV})^2 \tag{9.33}$$

$$|\Delta m_{3\ell}^2| = (24.99 \pm 0.50) \times 10^{-4} \mathrm{eV}^2 = (50.0 \pm 0.5\,\mathrm{meV})^2 \tag{9.34}$$

$$\sin^2 \theta_{12} = 0.307 \pm 0.013 \tag{9.35}$$

$$\sin^2 \theta_{23} = 0.568 \pm 0.028 \tag{9.36}$$

$$\sin^2 \theta_{13} = 0.02203 \pm 0.00083 \,. \tag{9.37}$$

The complex phase is

$$\delta = \left(228^{+51}_{-33}\right)^\circ \ (NH) \,; \ \delta = \left(281^{+30}_{-33}\right)^\circ \ (IH) \,. \tag{9.38}$$

Data give a marginal indication of violation of CP in the neutrino sector, but there is not yet sensitivity to confirm firmly this hypothesis–values of $\sin \delta$ are consistent with zero at 3σ. Anyhow, the current best fit

---

[5] The Liquid Scintillator Neutrino Detector (LSND) was a 167-tons scintillation counter at Los Alamos National Laboratory that measured the flux of neutrinos produced by a near neutrino source, an accelerator beam dump.

[6] The Einstein-Podolski-Rosen (EPR) paradox originally involved two particles, A and B, which interact briefly and then move off in opposite directions. The two particles are then entangled, and any measurement on A (projection of A on an eigenstate) would have *immediately* implications on the state of B; this would violate locality. In the case of neutrinos, the neutrino wavefunction itself spreads during the travel, with possible nonlocal effects.
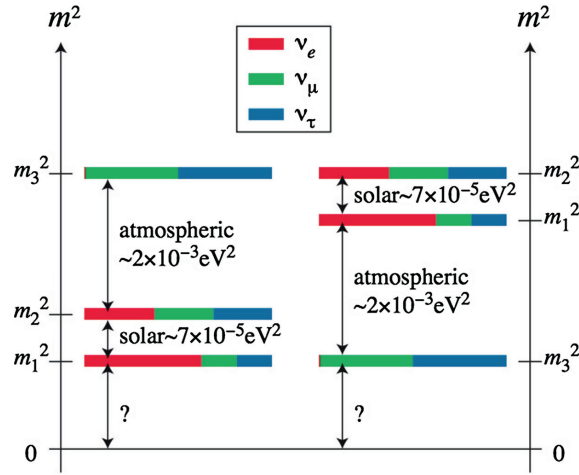
Fig. 9.15 Diagram of the relationship between the mass eigenstates (labeled 1, 2 and 3) for neutrinos and the flavor eigenstates (ν_e, ν_μ, ν_τ). Neutrinos from the Sun have been used to determine the relation between m_2 and m_1; m_3 may be greater or smaller than m_1 and m_2. The fractional contribution of each flavor to the mass eigenstates is indicted by the colored bars. From S.F. King, arXiv:0712.1750.

value for δ, even with these very large errors, is close to $(3/2)\pi$ which would imply a maximal CP violation. This could help, through the leptogenesis mechanisms, to explain the matter-antimatter asymmetry in the Universe.

The PMNS matrix is highly non-diagonal, which is very different from what it is observed in the quark sector (see Sect. 6.3.7). The best estimates of 3σ confidence intervals for its elements are (NuFIT 2017):

$$
\begin{pmatrix} \nu_e \\ \nu_\mu \\ \nu_\tau \end{pmatrix} = \begin{pmatrix} 0.799 \rightarrow 0.844 & 0.516 \rightarrow 0.582 & 0.140 \rightarrow 0.156 \\ 0.234 \rightarrow 0.502 & 0.452 \rightarrow 0.688 & 0.626 \rightarrow 0.784 \\ 0.273 \rightarrow 0.527 & 0.476 \rightarrow 0.705 & 0.604 \rightarrow 0.765 \end{pmatrix} \begin{pmatrix} \nu_1 \\ \nu_2 \\ \nu_3 \end{pmatrix} . \tag{9.39}
$$

Future facilities are planned to improve our knowledge of the mixing matrix and possibly discover new physics; in particular, high-precision and high-luminosity long-baseline neutrino oscillation experiments have been proposed in the US, in Japan, and in Europe.

9.3 Neutrino Masses

The discovery of neutrino oscillations showed, as discussed above, that the neutrino flavor eigenstates are not mass eigenstates and at least two of the mass eigenstates are different from zero.

Thanks to a huge experimental effort, we know quite well the neutrino mass differences. As of today we do not know, however, the absolute values of the neutrino masses: measurements of the endpoint energy in β decays are just not sensitive enough. The value of $\Delta m_{3\ell}^2$ (Eq. 9.34) suggests masses of the order of 1–100 meV; a lower limit

$$
\sum m_{\nu_i} > 60 \text{ meV} \tag{9.40}
$$

can be extracted at 95% C.L. from the data discussed in the previous Section.

However, the possibility that the mass of the lightest neutrino is much larger than this and that all three known neutrino masses are quasi-degenerate is not excluded.

Neutrino masses can only be directly determined via non-oscillation neutrino experiments. The most model-independent observable for the determination of the mass of the electron neutrino is the shape of the endpoint of the beta decay spectrum. Other probes of the absolute value of the neutrino masses include double beta decays, if neutrinos are of Majorana type, discussed below, and maps of the large-scale structure of the Universe, which is sensitive to the masses of neutrinos—although this sensitivity depends on cosmological models.

9.3.1 The Constraints from Cosmological and Astrophysical Data

The neutrino mass is constrained by cosmological data. Indeed neutrinos contribute to the energy density of the Universe playing the role of "hot dark matter". The combined analyses of the CMB data and of the surveys of the large-scale structures in the Universe (see Chap. 8) set a limit on the sum of the mass of the three neutrino species to

$$\sum m_{\nu_i} < 0.23 \text{ eV} \tag{9.41}$$

at 95 % C.L. A more conservative limit

$$\sum m_{\nu_i} < 0.68 \text{ eV} \tag{9.42}$$

can be extracted as follows, based on the density and sizes of structures in the Universe. Initial fluctuations seeded the present structures in the Universe, growing during its evolution. Neutrinos, due to their tiny masses, can escape from most structures being their speed larger than the gravitational escape velocity. As a net result, neutrinos can erase the structures at scales smaller than a certain value D_F called the free streaming distance. The smaller the sum of the neutrino masses, the larger is D_F. The relevant observable is the mass spectrum, i.e., the probability of finding a structure of a given mass as a function of the mass itself. Cosmological simulations predict the shape of the mass spectrum in terms of a small number of parameters; the limit in Eq. 9.42 is the limit beyond which the predicted distribution of structures is inconsistent with the observed one.

Data from astrophysical neutrino propagation over large distances are less constraining. So far the only reported upper limit on the neutrino velocity was obtained comparing the energy and the arrival time of a few tens of neutrinos by three different experiments from the explosion of the supernova 1987A in the Large Magellanic Cloud at around 50 kpc from Earth. From these results a limit of about 6 eV was obtained on the masses of the neutrinos reaching the Earth. The present long-baseline accelerator experiments are not sensitive enough to set competitive limits.

Further Reading

[F9.1] C. Giunti and C.W. Kim, "Fundamentals of Neutrino Physics and Astrophysics", Oxford 2007.

Exercises

1. *Neutrino interaction cross section.* Explain the peak in the cross section in Fig. 9.1.
2. *Neutrinos from the Sun.* Neutrinos from the Sun come mostly from reactions which can be simplified into

$$4p \to\,^4 \text{He} + 2e^+ + 2\nu_e\,.$$
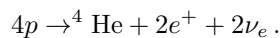
   The energy gain per reaction corresponds to the binding energy of He, $\sim$28.3 MeV. The power of the Sun at Earth (nominal solar constant) is P = 1361 W/m^2. How many solar neutrinos arrive at Earth per square meter per second?
3. *Radiation exposure due to solar neutrinos.* If the the neutrino-nucleon cross section in the energy range for solar neutrinos is approximately 10^{-45} cm^2/nucleon, (a) compute the rate of interactions of solar neutrinos in the human body, assuming that the human body has the density of water. (b) If neutrinos interact with nucleons N in the human body by the process $\nu N \to e N'$, and radiation damage is caused by electrons, estimate the annual dose for a human with mass of 80 kg under the assumption that on average 50% of the neutrino energy is transferred to the electron, and that the average energy of neutrinos is 100 keV.
4. *Neutrino oscillation probability.* Given a beam of a pure muon neutrino beam, with fixed energy E, derive the probability of observing another neutrino flavor at a distance L assuming two weak eigenstates related to two mass eigenstates by a simple rotation matrix.
5. *Tau neutrinos appearance.* OPERA is looking for the appearance of tau neutrinos in the CNGS (CERN neutrinos to Gran Sasso) neutrino beam. The average neutrino energy is 17 GeV and the baseline is about

730 km. Neglecting mass effects, calculate the oscillation probability

$$P(\nu_\mu \to \nu_\tau)$$

and comment.

6. *Neutrino mass differences.* One neutrino experiment detects, at 200 m from the nuclear reactor that the flux of a 3 MeV antineutrino beam is $(90 \pm 10)\%$ of what was expected in case of no oscillation. Assuming a maximal mixing determine the value of Δm_ν^2.

7. *Neutrino rotation angles.* Suppose there are three neutrino types (electron, muon, tau) and three mass values, related by the 3×3 PMNS matrix, usually factorized by three rotation matrices. Knowing that the three mass values are such that:

   - Δm^2 (solar) $= m_2^2 - m_1^2 \sim 10^{-5} \mathrm{eV}^2$
   - Δm^2 (atmospheric) $= \left| m_3^2 - m_2^2 \right| \sim 10^{-3} \mathrm{eV}^2$

   discuss the optimization of reactor and accelerator experiments to measure each of the three rotation angles and to confirm such mass differences. Compare, for example, the pairs of experiments (KamLAND, DayaBay), (T2K, OPERA).

8. *Neutrino from Supernova 1987A.* In 1987, a Supernova explosion was observed in the Magellanic Cloud, and neutrinos were measured in three different detectors. The neutrinos, with energies between 10 and 50 MeV, arrived with a time span of 10s, after a travel distance of 5×10^{12} s, and 3 h before photons at any wavelength.

   (a) Can this information be used to determine a neutrino mass? Discuss the quantitative mass limits that could be derived from the SN1987A.

   (b) This was the only SN observed in neutrinos, up to now, but the same reasoning can be used in pulsed accelerator beams. Derive the needed time and position precision to measure $\sim 1 \mathrm{eV}$ masses, given a beam energy E ~ 1 GeV and distance L.

Chapter 10
Messengers from the High-Energy Universe

Alessandro De Angelis and Mário Pimenta

By combining observations of a single phenomenon using different related particles, it is possible to achieve a more complete understanding of the properties of the sources; this approach is known as multi-messenger astrophysics. Multi-messenger astrophysics has developed in the beginning of the century using mostly information coming from charged particles and from photons at different wavelengths. In the very recent years simultaneous measurements involving also the detection of neutrinos and gravitational waves have been performed, expanding the horizon of astronomy.

Cosmic rays[1] were discovered at the beginning of the twentieth century (see Chap. 3). Since then an enormous number of experiments were performed on the Earth's surface, underground/underwater, on balloons, or on airplanes, or even on satellites. We know today that particles of different nature, spanning many decades in energy, are of cosmic origin, travel through the interstellar space and come to us. Their origin and composition is a challenging question. The combined study of charged and neutral cosmic rays of different nature and energies, called multi-messenger astrophysics, can solve fundamental problems, in particular related to physics in extreme environments, and unveil the presence of new particles produced in high-energy phenomena and/or in earlier stages of the Universe.

As we have seen in Chap. 1, we believe that the ultimate engine of the acceleration of cosmic rays is gravity. In gigantic gravitational collapses, such as those occurred in supernovae (energetic explosions following the collapse of stars) and in the accretion of supermassive black holes in the center of galaxies at the expense of the surrounding matter, part of the potential gravitational energy is transformed into kinetic energy of particles. The mechanism is not fully understood, although we can model part of it; we shall give more details in this chapter. The essential characteristics of regions near collapsed matter are for sure the presence of protons, electrons, hydrogen and helium atoms (and possibly heavier atoms and ions), photons, and variable magnetic fields. A high density kernel is likely to be the center of "shock waves", expanding boundaries between regions of different density.

As usual in physics, experimental data are the key to understand how these ingredients lead to the production of high-energy particles: we need to know as accurately as possible the origin, composition, and energy spectrum of cosmic rays. Different kinds of cosmic particles act as complementary messengers: the production and propagation mechanisms can be, in particular, different. This is the basis of multimessenger astrophysics, the "New Astronomy" for the XXI century.

Multimessenger astrophysics is based on the combined information from:

- Charged cosmic rays. We shall see that this study is extremely difficult, since they can "point" to their sources only when their energy exceeds tens of EeV.
- Gamma rays. We shall see that the Universe is essentially transparent to gamma rays in a region up to some 100 GeV; beyond this energy the interaction with background photons in the Universe entails an absorption effect through the interaction $\gamma\gamma \to e^+e^-$.
- Neutrinos. Because of their small interaction cross section they travel almost undisturbed through cosmic distances, but they are very difficult to detect,
- Gravitational waves. Astronomy with gravitational waves has just started.

Cosmic rays are mainly protons ($\sim$90 %) and heavier nuclei, with a small fraction of electrons, a few per mil of the total flux. Antiprotons fluxes are even smaller (about four orders of magnitude) and so far compatible with secondary production by hadronic interactions of primary cosmic rays with the interstellar

---

[1] In this textbook we define as *cosmic rays* all particles of extraterrestrial origin. It should be noted that other textbooks instead define as cosmic rays only nuclei, or only protons and ions – i.e., they separate gamma rays and neutrinos from cosmic rays.
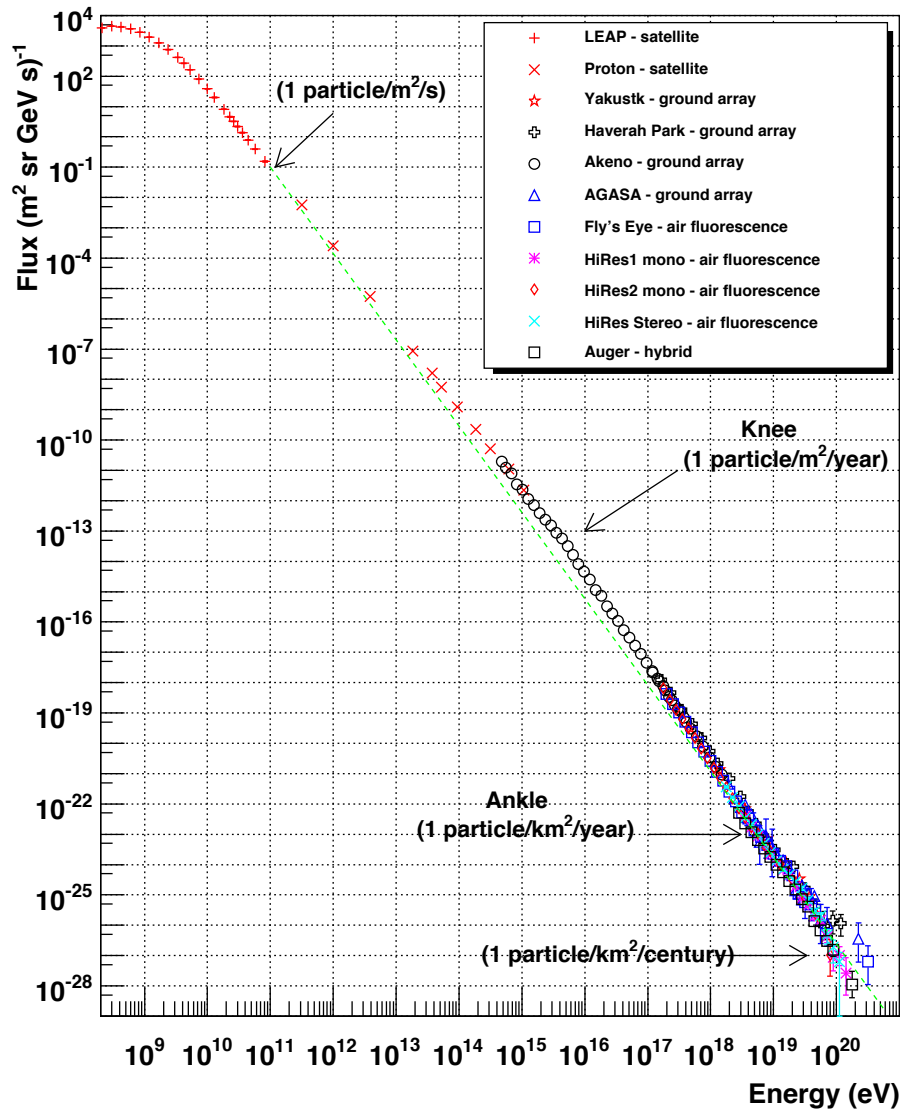
Fig. 10.1 Energy spectrum of charged cosmic rays. From http://www.physics.utah.edu/w̃hanlon/spectrum.html.

medium. Up to now there is no evidence for the existence of heavier anti-nuclei in cosmic rays. Photons and neutrinos are also a small fraction of the cosmic rays.

The energy spectrum of the charged cosmic rays reaching the atmosphere spans over many decades in flux and energy (Fig. 10.1). Above a few GeV the intensity of the cosmic ray flux follows basically a power law $E^{-\gamma}$, the differential spectral index γ being typically between 2.7 and 3.3, with two clear changes in the slope: the "knee" around $E \simeq 5 \times 10^{15}$ eV, and the "ankle" around $E \simeq 5 \times 10^{18}$ eV. A strong suppression of the flux at the highest energies, $E \gtrsim 5 \times 10^{19}$ eV, is nowadays clearly established; it may result from the destructive interaction of highly energetic particles with the Cosmic Microwave Background (CMB), or from a limit to the maximum energies of the cosmic accelerators (see Sect. 10.3.3.2 and Sect. 10.4.1.6).

Charged cosmic rays arrive close to the Solar System after being deflected from the Galactic magnetic fields (about 1 μG in intensity) and possibly by extragalactic magnetic fields (between 1 nG and 1 fG), if they are of extragalactic origin; when getting close to the Earth they start interacting with stronger magnetic fields—up to $\mathcal{O}(1\text{G})$ at the Earth's surface, although for shorter distances. The radius of curvature in the Galaxy
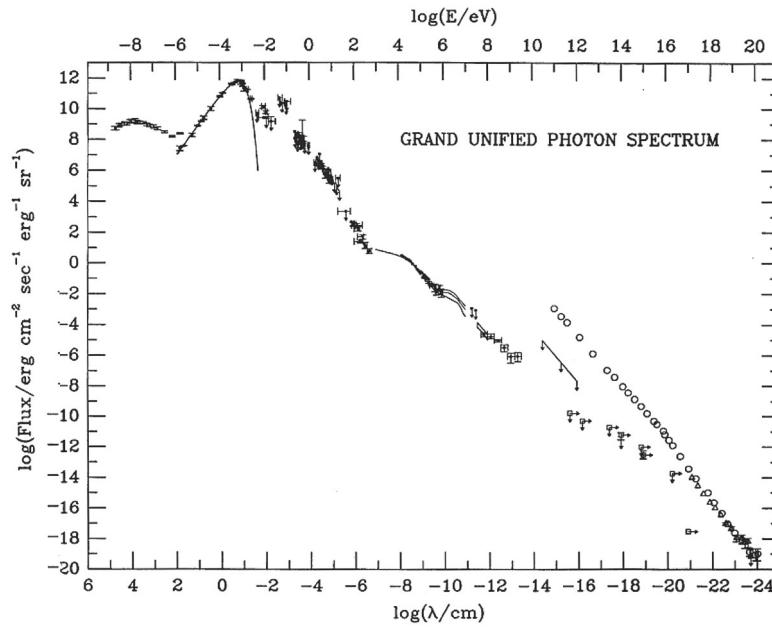
Fig. 10.2 Energy spectrum of photons measured at different energies. From M.T. Ressell and M.S. Turner 1989, "The grand unified photon spectrum: a coherent view of the diffuse extragalactic background radiation," Fermi National Accelerator Laboratory, http://purl.fdlp.gov/GPO/gpo48234.

$$\frac{R_L}{1\text{kpc}} \simeq \frac{E/1\text{EeV}}{B/1\mu\text{G}} \,, \tag{10.1}$$

is shorter than the distance to the Galactic center for energies smaller than $\sim 2 \times 10^{19}$ eV – much above the knee – and thus astronomy with charged cosmic rays is extremely difficult. To do astronomy with cosmic rays one must use photons. High-energy astrophysical processes generate photon radiation over a large range of wavelengths. Such photon radiation can be associated to the emitters, which is an advantage with respect to charged cosmic rays. In addition, photon radiation, besides being interesting in itself, can give insights on the acceleration of charged particles, being photons the secondary products of accelerated charged particles. In addition, photons are likely to be present in the decay chain of unstable massive particles, or in the annihilation of pairs of particles like dark matter particles.

Experimental data on cosmic photon radiation span some 30 energy decades (Fig. 10.2). The general behavior of the yield at high energies can be approximated by an energy dependence as a power law $E^{-2.4}$. There is little doubt on the existence of photons in the PeV–EeV range, but so far cosmic gamma rays have been unambiguously detected only in the low (MeV), high (GeV) and very (TeV) high-energy domains: upper limits are plotted above the TeV in the Figure.

A look at the sources of cosmic gamma rays in the HE region shows a diffuse background, plus a set of localized emitters. Some 5500 emitters above 100 MeV have been identified up to now, mostly thanks to the 4th catalog issued by the *Fermi*-LAT after 8 years of operation, and some 200 of them are VHE emitters as well (Fig. 10.3). About half of the gamma ray emitters are objects in our Galaxy; at VHE most of them can be associated to supernova remnants (SNRs), while at MeV to GeV energies they are mostly pulsars; the remaining half are extragalactic, and the space resolution of present detectors (slightly better than 0.1°) is not good enough to associate them with particular points in the host galaxies; we believe, however, that they are produced by accretion of supermassive (up to billion solar masses) black holes in the centers of the galaxies. These are the so-called Active Galactic Nuclei (AGN).

Among cosmic messengers, gamma rays are important because they point to the sources. Present gamma-ray detectors have imaged may sources of high-energy gamma rays, which might likely be also sources of charged cosmic rays, neutrinos and other radiation. Abrupt increases of luminosity ("flares") are sometimes detected, in particular in Galactic emitters and in active galactic nuclei (AGN); the most spectacular phenomenon is the explosion being of gamma ray bursts.

Gamma Ray Bursts (GRBs), recorded almost daily, are extremely intense shots of gamma radiation of extragalactic origin. They last from fractions of a second (the so-called "short" GRBs, recently associated to neutron star-neutron star mergers), to a few seconds and more ("long" GRBs), associated to the collapse
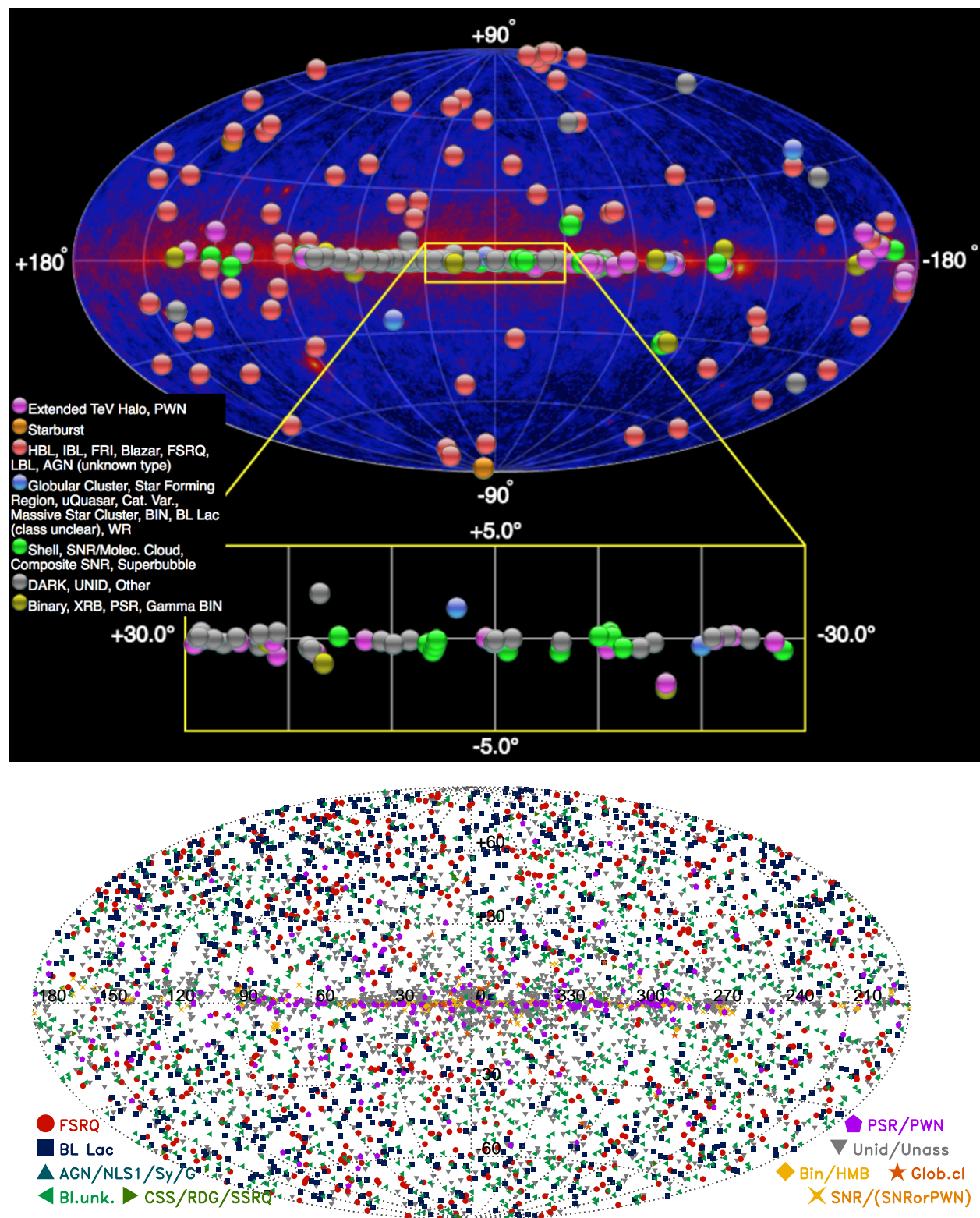
Fig. 10.3 On the top, sources of gamma-ray emission above 100 GeV plotted in galactic coordinates. The background represents the high-energy gamma ray sources detected by *Fermi*-LAT. The region near the Galactic Center is enlarged. From the TeVCat catalog, http://tevcat.uchicago.edu/, February 2018. The sources detected by the *Fermi* LAT above 100 MeV after 8 years of data taking are shown in detail on the bottom.

of a very large mass star (hundreds of solar masses), and a very energetic supernova (a "hypernova"). They are often followed by "afterglows" after minutes, hours, or days.

In the past few years the first observation of very-high-energy-neutrinos of astrophysical origin and the first direct detections of gravitation waves were announced. New channels to observe and understand the Universe and its evolution are now available. It has been possible to locate some sources of astrophysical neutrinos (Sect. 10.4.3.3) and of gravitational waves (Sect. 10.4.4).

10.1 How Are High-Energy Cosmic Rays Produced?

We shall discuss two basic scenarios for the production of cosmic rays: a top-down and a bottom-up scenario.

In top-down scenarios, cosmic rays come from the decays of heavier, exotic particles with masses ranging from the typical 100 GeV – 1 TeV scale of supersymmetry to the 10^{11} GeV scale of superheavy particles up to the GUT scale, $M_{GUT} \sim 10^{24}$ eV and beyond – in this last case the GZK cutoff can be avoided, since protons can be produced in the Earth's vicinity. We shall write more on this in Sect. 10.1.3.

The production of protons in particle acceleration processes in sources is instead referred to as the bottom-up scenario. At a scientific conference in 1933, Zwicky and Baade advanced a revolutionary conjecture: massive stars end their lives in explosions which blow them apart; such explosions produce cosmic rays, and leave behind a collapsed star made of densely packed neutrons. Many of the high-energy gamma-ray emitters correspond positionally to SNRs, thus indirectly confirming this conjecture–indeed we are convinced nowadays that most of the accelerators of cosmic rays in our galaxy are SNRs. But how can a supernova remnant (or whatever remnant of a gravitational collapse) accelerate particles? By which mechanisms cosmic rays are "reprocessed" interacting with molecular clouds in the universe? It took 16 years after the conjecture by Zwicky and Baade before Enrico Fermi could devise a model in which this conjecture could be explained.

10.1.1 Acceleration of Charged Cosmic Rays: the Fermi Mechanism

Charged cosmic rays produced by particle ejection in several possible astrophysical sources may be accelerated in regions of space with strong turbulent magnetic fields. Permanent magnetic fields are not a good candidate since they cannot accelerate particles; static electric fields would be quickly neutralized; variable magnetic fields may instead induce variable electric fields and thus accelerate, provided the particles are subject to many acceleration cycles.

In 1949 Fermi proposed a mechanism in which particles can be accelerated in stochastic collisions; this mechanism could model acceleration in shock waves which can be associated to the remnant of a gravitational collapse–for example, a stellar collapse, but also, as we know today, the surrounding of a black hole accreted in the center of a galaxy.

Let us suppose (see Fig. 10.4) that a charged particle with energy E_1 (velocity v) in the "laboratory" frame is scattering against a moving boundary between regions of different density (a partially ionized gas cloud). Due to the chaotic magnetic fields generated by its charged particles, the cloud will act as a massive scatterer. Let the cloud have a velocity $\beta = V/c$, and let θ_1 and θ_2 be the angles between, respectively, the initial and final particle momentum and the cloud velocity. Let us define $\gamma = 1/\sqrt{1-\beta^2}$.

The energy of the particle E_1^* (supposed relativistic) in the cloud reference frame is given by (neglecting the particle mass with respect to its kinetic energy):

$$E_1^* \simeq \gamma E_1 (1 - \beta \cos\theta_1).$$

The cloud has an effective mass much larger than the particle's mass, and thus it acts as a "magnetic mirror" in the collision. In the cloud reference frame $E_2^* = E_1^*$ (collision onto a wall), and in the laboratory frame the energy of the particle after the collision is:

$$E_2 \simeq \gamma E_2^*(1 + \beta \cos\theta_2^*) = \gamma^2 E_1 (1 - \beta \cos\theta_1)(1 + \beta \cos\theta_2^*).$$

Thus the relative energy change is given by:
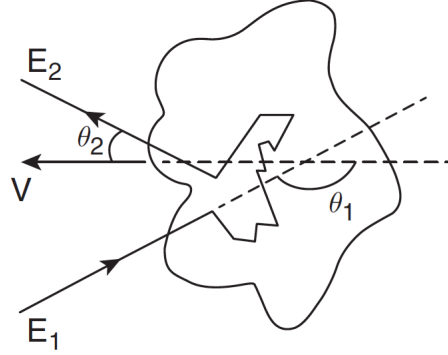
Fig. 10.4 Scattering of a cosmic ray by a moving gas cloud. From T. Gaisser, "Cosmic Rays and Particle Physics,", Cambridge University Press 1990.

$$\frac{\Delta E}{E} = \frac{1 - \beta \cos \theta_1 + \beta \cos \theta_2^* - \beta^2 \cos \theta_1 \cos \theta_2^*}{1 - \beta^2} - 1 \,. \tag{10.2}$$

The collision is the result of a large number of individual scatterings suffered by the particle inside the cloud, so the output angle in the c.m. is basically random. Then

$$\langle \cos \theta_2^* \rangle = 0 \,.$$

The probability P to have a collision between a cosmic ray and the cloud is not constant as a function of the relative angle θ_1; it is rather proportional to their relative velocity (it is more probable that a particle hits a cloud that is coming against it, than a cloud that it is running away from it):

$$P \propto (v - V \cos \theta_1) \propto (1 - \beta \cos \theta_1)$$

and thus

$$\langle \cos \theta_1 \rangle \simeq \frac{\int_{-1}^{1} \cos \theta_1 (1 - \beta \cos \theta_1) d \cos \theta_1}{\int_{-1}^{1} (1 - \beta \cos \theta_1) d \cos \theta_1} = -\frac{\beta}{3} \,. \tag{10.3}$$

The energy after the collision increases then on average by a factor

$$\left\langle \frac{\Delta E}{E} \right\rangle \simeq \frac{1 - \beta \langle \cos \theta_1 \rangle}{1 - \beta^2} - 1 \simeq \frac{1 + \beta^2/3}{1 - \beta^2} - 1 \simeq \frac{4}{3} \beta^2 \,. \tag{10.4}$$

This mechanism is known as the second-order Fermi acceleration mechanism. It is not very effective, since the energy gain per collision is quadratic in the cloud velocity, and the random velocities of interstellar clouds in the Galaxy are very small, $\beta \sim 10^{-4}$; also the diffusion velocities directly measured, for example, in the observations of supernova remnants (see Fig. 10.5), are small ($\beta \sim 10^{-3} - 10^{-2}$).

An energy gain linear in β (1st order Fermi acceleration) is needed instead to explain the cosmic ray spectrum, and we are going now to see that this happens in the Diffusive Shock Acceleration (DSA). What changes in this case is that the directions of the clouds, instead of being randomly distributed, are strongly correlated: they are approximately fronts of a plane wave. This is what occurs, for example, when a supernova ejects a sphere of hot gas into the interstellar medium, and rapidly moving gas, faster than the local speed of sound, i.e., of the speed of pressure waves, is ejected into a stationary gas, this last behaving as an obstacle for the expansion.

A shock wave creates a high-density region propagating with a locally plane wave front, acting like a piston. A shocked gas region runs ahead of the advancing piston into the interstellar medium. We assume that there is an abrupt discontinuity between two regions of fluid flow, and in the undisturbed region ahead of the shock wave, the gas is at rest. In the reference frame of the shock front, the medium ahead (upstream) runs into the shock itself with a velocity $\mathbf{u_u}$, while the shocked gas (downstream) moves away with a velocity $\mathbf{u_d}$ (Fig. 10.6); according to the kinetic theory of gases, in a supersonic shock propagating through a monoatomic gas $|u_u| \sim 4|u_d|$. In the laboratory system, a particle coming from upstream to downstream meets in a head-on collision a high-density magnetized gas. The particle inverts the direction
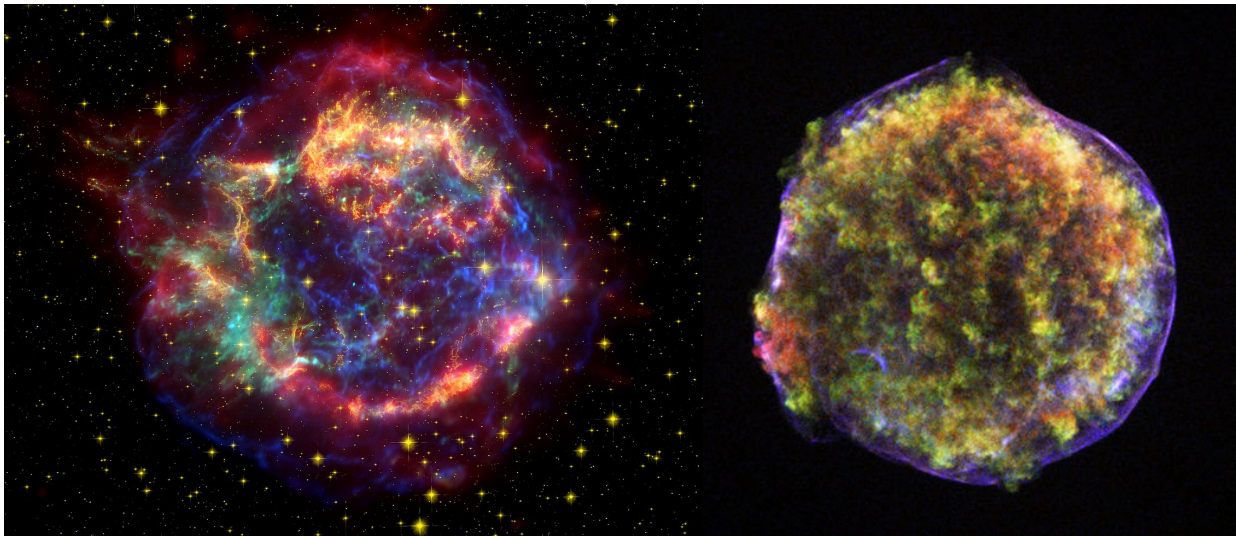
Fig. 10.5 Left: The Cassiopeia A supernova remnant is a bright remnant of a supernova occurred approximately 300 years ago (this is what we call a young SNR), 11 000 light-years away within the Milky Way. The expanding cloud of material left over from the supernova now appears approximately 10 light-years across; it is very likely a site of hadron acceleration. The image is a collage in false colors of data from the Spitzer Space Telescope (infrared, depicted in red), from the Hubble Space Telescope (visible, depicted in orange), and from the Chandra X-ray Observatory (blue and green). By Oliver Krause et al., Public Domain, https://commons.wikimedia.org/w/index.php?curid=4341500. Right: A Chandra image of another young SNR: Tycho, exploded in 1572 and studied by Tycho Brahe, at a distance of about 8000 ly and large ∼20 ly across. Shock heated gas (filamentary blue) expands with a 3000 km/s blast wave. By NASA/CXC/Chinese Academy of Sciences/F. Lu et al.
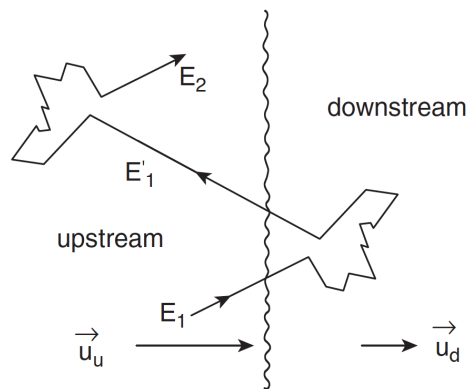
Fig. 10.6 Cosmic ray acceleration for a diffusing shock wave, in the reference frame of the shock. Adapted from T. Gaisser, "Cosmic Rays and Particle Physics,", Cambridge University Press 1990.

of the component of its initial velocity parallel to the shock front direction, crosses the shock front itself, and scatters with the gas upstream; it can bounce again and again within such a pair of parallel magnetic mirrors. Note that, although the system is equivalent from the point of view of the dynamics of the bouncing particle to a pair of mirrors approaching with a net relative velocity $V = |\mathbf{u_u} - \mathbf{u_d}|$, the two mirrors do not actually approach, since the molecules acting as mirrors belong for different rebounds to different regions of the gas, and the distance is approximately constant if the diffusion velocity does not vary.

If we put ourselves in the frame of reference of one of the clouds (upstream or downstream), each bound-rebound cycle is equivalent from the point of view of the energy gain to a collision in the laboratory with a head-on component into a cloud moving with speed V (see Fig. 10.4). Being the target gas coherently moving, the component of the velocity of the particle perpendicular to the direction of propagation of the shock wave will have a negligible change, while the component parallel to the direction itself will be inverted. If we call θ the angle between the (fixed) direction of the expansion and the direction of the incident particle, with the same convention as in Fig. 10.4, Eq. 10.2 becomes

$$\frac{\Delta E}{E} \simeq -2\beta \cos\theta \,, \tag{10.5}$$

the angle θ between the particle initial velocity and the magnetic mirror being now constrained to the specific geometry: $-1 \le \cos\theta \le 0$. The probability of crossing the wave front is proportional to $-\cos\theta$, and Eq. 10.3 becomes:

$$\langle \cos\theta \rangle \simeq \frac{\int_{-1}^{0} -\cos^2\theta \; d\cos\theta}{\int_{-1}^{0} -\cos\theta \; d\cos\theta} = -\frac{2}{3}. \tag{10.6}$$

The average energy gain for each bound-rebound cycle is:

$$\left\langle \frac{\Delta E}{E} \right\rangle \simeq -2\beta\langle \cos\theta \rangle \simeq \frac{4}{3}\beta \equiv \epsilon \,. \tag{10.7}$$

After n cycles the energy of the particle is:

$$E_n = E_0(1+\epsilon)^n \tag{10.8}$$

i.e., the number of cycles needed to a particle to attain a given energy E is:

$$n = \ln\left(\frac{E}{E_0}\right) / \ln(1+\epsilon) \,. \tag{10.9}$$

On the other hand, at each cycle a particle may escape from the shock region with some probability P_e, which can be considered to be proportional to the velocity V, and then the probability P_{E_n} that a particle escapes from the shock region with an energy greater or equal to E_n is:

$$P_{E_n} = P_e \sum_{j=n}^{\infty} (1-P_e)^j = (1-P_e)^n \,. \tag{10.10}$$

Replacing n by the formula 10.9 one has:

$$P_{E_n} = (1-P_e)^{\ln\left(\frac{E}{E_0}\right)/\ln(1+\epsilon)}$$

$$\ln P_{E_n} = \frac{\ln\left(\frac{E}{E_0}\right)}{\ln(1+\epsilon)} \ln(1-P_e) = \frac{\ln(1-P_e)}{\ln(1+\epsilon)} \ln\left(\frac{E}{E_0}\right) \,.$$

Then

$$\frac{N}{N_0} = P_{E_n} = \left(\frac{E}{E_0}\right)^{-\alpha} \implies \frac{dN}{dE} \propto \left(\frac{E}{E_0}\right)^{-\Gamma} \tag{10.11}$$

with

$$\alpha = -\frac{\ln(1-P_e)}{\ln(1+\epsilon)} \cong \frac{P_e}{\epsilon} \quad ; \quad \Gamma = \alpha + 1 \,. \tag{10.12}$$

The 1st order Fermi mechanism predicts then that the energy spectrum is a power law with an almost constant index (both ϵ and P_e are proportional to $\langle \beta \rangle$).

In the case of the supersonic shock of a monoatomic gas α is predicted by the kinetic theory of gases (see for example the volume on Fluid Mechanics by Landau and Lifshitz) to be around 1 ($\Gamma \sim 2$). The detected spectrum at Earth is steeper. In its long journey from the Galactic sources to the Earth the probability that the particle escapes from the Galaxy is proportional to its energy (see Sect. 10.3.3):

$$\left|\frac{dN}{dE}\right|_{\text{Earth}} \propto \left(\frac{dN}{dE}\right)_{\text{sources}} \times E^{-\delta} \propto \left(\frac{E}{E_0}\right)^{-\Gamma-\delta} \,. \tag{10.13}$$

δ is estimated, in most cosmic rays galactic transport models, to be between 0.3 and 0.6. The 1st order Fermi model provides thus a remarkable agreement with the observed cosmic ray spectrum; however, V has been assumed to be nonrelativistic, and a numerical treatment is needed to account for relativistic speeds.

Note that one can approximate

$$P_e \simeq \frac{T_{cycle}}{T_e} \,, \tag{10.14}$$

where T_e is the characteristic time for escape from the acceleration region, and T_{cycle} is the characteristic time for an acceleration cycle. Thus, if E_0 is the typical energy of injection into the accelerator,

$$E < E_0(1 - \epsilon)^{\tau/T_{cycle}} \;\; : \tag{10.15}$$

the maximum energy reachable by an accelerator is constrained by the lifetime τ of the accelerator (typically ~ 1000 years for the active phase of a SNR).

SNRs through Fermi first-order acceleration mechanisms are commonly recognized nowadays as responsible for most of the high-energy cosmic rays in the Galaxy. However, the proof that this mechanism can accelerate cosmic rays all the way up to the knee region is still missing.

To summarize, the main ingredients of acceleration are magnetic fields and shock waves. These can be present in several types of remnants of gravitational collapses, in particular SNRs, AGN, GRBs. In these objects, clouds of molecular species, dust, photon gas from bremsstrahlung and synchrotron radiation are likely to be present, and accelerated charged particles can interact with them.

10.1.2 Production of High-Energy Gamma Rays and Neutrinos

The study of sources of gamma rays and neutrinos is crucial for high-energy astrophysics: photons and neutrinos point back to their source allowing the identification of high-energy accelerators. Usually the spectrum of photons and neutrinos is measured as the energy flux in erg (or in eV or multiples) per unit area per unit time per unit frequency ν (in Hz), and fitted, where possible, to a power law; the spectral index characterizes the source. Another important quantity is the energy flux νF_ν, usually expressed in erg cm^{-2} s^{-1}, called the spectral energy distribution (SED). Equivalent formulations use the spectral photon (neutrino) flux dN/dE, and the relation holds:

$$\nu F_\nu = E^2 \frac{dN}{dE} \,. \tag{10.16}$$

High-energy photons can be produced by radiative and collisional processes, in particular those involving the interaction of high-energy charged particles (for example, electrons, protons, ions accelerated by the shock waves of remnants of gravitational collapses) with nuclear targets such as molecular clouds or radiation fields (magnetic fields, photon fields). We distinguish between purely leptonic mechanisms of production and models in which photons are secondary products of hadronic interactions; the latter provide a direct link between high-energy photon production and the acceleration of charged cosmic rays (Sect. 10.2.5), and produce, in general, also neutrinos. Since neutrinos cannot be practically absorbed nor radiated, and in bottom-up processes they come only through hadronic cascades, the neutrino is a unique tracer of hadronic acceleration.

Positron annihilation and nuclear processes associated with neutron capture and de-excitation of nuclei dominate the gamma-ray production at MeV energies.

An alternative mechanism (top-down scenario) could be the production via the decay of heavy particles; this mechanism works also for neutrinos.

10.1.2.1 Leptonic Gamma Ray Production Models

Photons cannot be directly accelerated; however, mechanisms exist such that photons of rather large energies are radiated. We examine in this subsection radiation processes just involving leptons (they are called "leptonic" photoproduction mechanisms). In particular, we shall sketch the simplest self-sustaining acceleration mechanism, the synchrotron self-Compton restricted to a single acceleration region.

Synchrotron Radiation. High-energy photon emission in a magnetic field is in the beginning generally due to synchrotron radiation. The dynamics of charged particles is strongly influenced through the Lorentz force by the magnetic fields present in astrophysical environments. Accelerated relativistic particles radiate synchrotron photons; the power loss for a charged particle of mass M and charge Ze can be expressed as
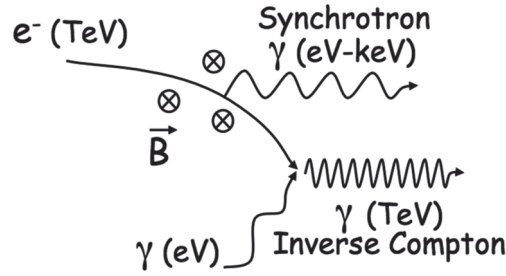
Fig. 10.7 Scheme of the SSC mechanism.

$$-\frac{dE}{dt} \simeq 2.6\,\frac{\text{keV}}{\text{s}}\left(\frac{Zm_e}{M}\right)^4\left(\frac{E}{1\,\text{keV}}\right)^2\left(\frac{B}{1\,\mu\text{G}}\right)^2. \tag{10.17}$$

It is immediately evident from Eq. 10.17 that synchrotron energy loss is by far more important for electrons than for protons.

Compton scattering and "inverse Compton" process. The Compton scattering of a photon by an electron is a relativistic effect, by which the frequency of a photon changes due to a scattering. In the scattering of a photon by an electron at rest, the wavelength shift of the photon can be expressed as

$$\frac{\lambda' - \lambda}{\lambda} = \frac{\hbar\omega}{m_e c^2}(1 - \cos\alpha),$$

where α is the angle of the photon after the collision with respect to its line of flight. As evident from the equation and from the physics of the problem, the energy of the scattered photon cannot be larger than the energy of the incident photon. However, when low-energy photons collide with high-energy electrons instead than with electrons at rest, their energy can increase: such process is called inverse Compton (IC) scattering. This mechanism is very effective for boosting (for this reason it is called "inverse") the photon energy, and is important in regions of high soft-photon energy density and energetic electron density.

Synchrotron Self-Compton. The simplest purely leptonic mechanism we can draw for photon "acceleration"—a mechanism we have seen at work in astrophysical objects—is the so-called self-synchrotron Compton (SSC) mechanism. In the SSC, ultrarelativistic electrons accelerated in a magnetic field—such as the field present in the accretion region of AGN, or in the surrounding of SNR—generate synchrotron photons. The typical values of the fields involved are such that the synchrotron photons have an energy spectrum peaked in the infrared/X-ray range. Such photons in turn interact via Compton scattering with their own parent electron population (Fig. 10.7); since electrons are ultrarelativistic (with a Lorentz factor $\gamma_e \sim 10^{4-5}$), the energy of the rescattered photon can be boosted by a large factor.

For a power law population of relativistic electrons with a differential spectral index q and a blackbody population of soft photons at a temperature T, mean photon energies and energy distributions can be calculated for electron energies in the Thomson regime and in the relativistic Klein-Nishina regime:

$$\langle E_\gamma \rangle \simeq \tfrac{4}{3}\gamma_e^2\langle\eta\rangle \quad \text{for } \gamma_e\eta \ll m_e c^2 \text{ (Thomson limit)} \tag{10.18}$$

$$\simeq \tfrac{1}{2}\langle E_e\rangle \quad \text{for } \gamma_e\eta \gg m_e c^2 \text{ (Klein-Nishina limit)} \tag{10.19}$$

$$\frac{dN_\gamma}{dE_\gamma} \propto E_\gamma^{-\frac{q+1}{2}} \quad\quad \text{for } \gamma_e\eta \ll m_e c^2 \text{ (Thomson limit)} \tag{10.20}$$

$$\propto E_\gamma^{-(q+1)}\ln(E_\gamma) \quad \text{for } \gamma_e\eta \gg m_e c^2 \text{ (Klein-Nishina limit)} \tag{10.21}$$

where E_γ denotes the scattered photon's energy, E_e denotes the energy of the parent electron, and η denotes the energy of the seed photon. Note that an observer sees a power-law synchrotron spectrum only if no absorption of photons happens. Sources in which all produced photons are not absorbed are called optically thin. In an optically thick source, significant self-absorption can happen, modifying the shape of the synchrotron spectrum and typically sharpening the cutoff.

A useful approximate relation linking the electron's energy and the Comptonized photon's energy is given by:
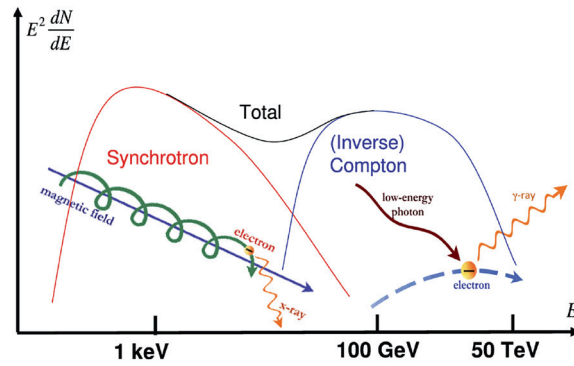
Fig. 10.8 Differential energy spectrum of photons in the SSC model.

$$E_\gamma \simeq 6.5 \left(\frac{E_e}{\mathrm{TeV}} \right)^2 \left(\frac{\eta}{\mathrm{meV}} \right) \, \mathrm{GeV} \, .$$

The Compton component can peak at GeV–TeV energies; the two characteristic synchrotron and Compton peaks are clearly visible on top of a general E_γ^{-2} dependence. Fig. 10.8 shows the resulting energy spectrum. This behavior has been verified with high accuracy on the Crab Nebula and on several other emitters, for example on active galactic nuclei. If in a given region the photons from synchrotron radiation can be described by a power law with spectral index p, in the first approximation the tails at the highest energies from both the synchrotron and the Compton mechanisms will have a spectral index p. Note, however, that since he Klein-Nishina cross section is smaller than the Thomson cross section, the Compton scattering becomes less efficient for producing gamma rays at energies larger than ~ 50 TeV.

A key charasteristics of the SSC model is a definite correlation between the yields from synchrotron radiation and from IC during a flare (it would be difficult to accommodate in the theory an "orphan flare," i.e., a flare in the IC region not accompanied by a flare in the synchrotron region). Although most of the flaring activities occur almost simultaneously with TeV gamma ray and X-ray fluxes, observations of 1ES 1959+650 and other AGN have exhibited VHE gamma ray flares without their counterparts in X-rays. The SSC model has been very successful in explaining the SED of AGN, but flares observed in VHE gamma rays with absence of high activity in X-rays are difficult to reconcile with the standard SSC.

10.1.2.2 Hadronic Models and the Production of Gamma Rays and Neutrinos

Alternative and complementary models of VHE emission involve cascades initiated by primary protons/nuclei that had been accelerated in the system. The beam of accelerated hadrons collides with a target of nucleons (for example, a molecular cloud) or with a sea of photons, coming from the synchrotron radiation or the bremsstrahlung of electrons accelerated or starlight (hadronic photoproduction).

In either case, the energy of the primary protons is expected by the physics of hadronic cascades to be one-two orders of magnitude larger than the energy of gamma rays, since the dominant mechanism for photon production is the decay of the secondary π^0 mesons into $\gamma\gamma$ pairs at the end of the hadronic cascade. The study of γ rays can thus provide insights on the acceleration of charged cosmic rays. Photons coming from π^0 decay have in general energies larger than photons from synchrotron radiation.

A characteristics of hadroproduction of gamma rays is a peak at $\simeq m_\pi c^2/2 \simeq 67.5$ MeV in the spectral energy distribution, which can be related to a component from π^0 decay; this feature, which is almost independent of the energy distribution of π^0 mesons and consequently of the parent protons, is called the "pion bump", and can be explained as follows. In the rest frame of the neutral pion, both photons have energy $E_\gamma = m_\pi c^2/2 \simeq 67.5$ MeV and momentum opposite to each other. Once boosted for the energy E of the emitting π^0, the probability to emit a photon of energy E_γ is constant over the range of kinematically allowed energies (the interval between $E(1 - v/c)/2$ and $E(1 + v/c)/2$, see Exercise 2). The spectrum of gamma rays for an arbitrary distribution of neutral pions is thus a superposition of rectangles for which only one point at $m_\pi c^2/2$ is always present. This should result in a spectral maximum independent of the energy distribution of parent pions.

The existence of a hadronic component has been demonstrated from the experimental data on Galactic SNRs and from the region of the Galactic center (see later), and could explain the production of cosmic

ray hadrons at energies up to almost the knee. The detection of orphan AGN flares and, more recently, of a simultaneous gamma ray-neutrino flare from an AGN, indicated evidence for hadronic production of gamma rays in such sources powered by supermassive black holes.

Let us shortly examine the relation between the high-energy part of the spectra of secondary photons and the spectra of primary cosmic rays (we shall assume protons) generating them. We shall in parallel examine the case of the spectra of secondary neutrinos, which are copiously produced in the decays of $\pi^\pm$, also present in the final states, and whose rate is closely related to the π^0 rate– neutrinos could become, if large enough detectors are built, another powerful tool for the experimental investigation. We shall follow here an analytical approach; it should be noted however that Monte Carlo approaches in specialized software programs called SIBYLL, QGSJet, EPOS and DPMJet provide much more precise results, and are normally used in scientific publications.

Proton-nucleon collisions. In beam dump processes of protons against molecular clouds, at c.m. energies much larger than the pion mass, the cross section is about 30 mb - 40 mb. The final state is dominated by particles emitted with small transverse momentum (soft or low-p_T processes). Almost the same number of π^0, π^- and π^+ are produced, due to isospin symmetry. The π^0s decay immediately into two gamma rays; the charged pions decay into $\mu\,\nu_\mu$, with the μ decaying into $e\nu_e\nu_\mu$ (charge conjugates are implicitly included). Thus, there are three neutrinos for each charged pion and three neutrinos for every gamma ray; each neutrino has approximately 1/4 of the $\pi^\pm$ energy in the laboratory, while each photon has on average half the energy of the π^0.

We assume the cross section for proton-proton interactions to be constant, $\sigma_{pp} \simeq 3 \times 10^{-26}$ cm^2. If generic hadrons of mass number A constitute the beam instead of protons, one can approximate $\sigma_{Ap} \sim A^{2/3}\sigma_{pp}$. The average pion multiplicity (shared democratically among each pion species π^0, π^- and π^+) is approximately proportional to the square root of the c.m. energy as modeled by Fermi and Landau (Chap. 6); we can approximate, for incident protons,

$$N_\pi \sim 3\left(\frac{E_p - E_{th}}{\text{GeV}}\right)^{1/4} \sim 3\left(\frac{E_p}{\text{GeV}}\right)^{1/4}, \tag{10.22}$$

where E_{th} is the threshold energy for pion production, less than 1 GeV - we can neglect it at large proton energies. Consequently, the average pion energy at the source is related to the proton energy, in the direction of flight of the proton, by

$$\langle E_\pi \rangle \sim \frac{1}{3}\left(\frac{E_p}{\text{GeV}}\right)^{3/4},$$

where γ_p is the Lorentz boost of the proton.

The generic pion distribution from the hadronic collision, assuming equipartition of energy among pions, can be written as

$$q_\pi \simeq n_H l \sigma_{pp} \int_{E_{th}}^\infty dE_p\, j_p \left(\frac{E_p}{\text{GeV}}\right)^{3/4} \delta(E_\pi - \langle E_\pi \rangle), \tag{10.23}$$

where n_H is the density of hadrons in the target, l is the depth ($N_H = n_H l$ is the column density), j_p is the proton rate. If the differential proton distribution per energy and time interval at the source is

$$j_p(E_p) = A_p E_p^{-p}, \tag{10.24}$$

making in the integral (10.23) the substitution $E_p \to E_\pi^{4/3}$ the pion spectrum at the source is

$$q_\pi(E_\pi) \propto E_p^{-\frac{4}{3}p + \frac{1}{3}}. \tag{10.25}$$

The photon spectrum is finally

$$q_\gamma(E_\gamma) = A_\gamma E_\gamma^{-\frac{4}{3}p + \frac{1}{3}}, \text{ with } A_\gamma \simeq 800 N_H A_p \sigma_{pp}. \tag{10.26}$$

This simple analytic result comes from an approximation of the interaction, but the result is not far from that of a complete calculation. Equation (10.26) provides us with an estimate of the total photon flux at the source. The spectral behavior of the protons can be estimated from diffusive shock acceleration and a spectral index -2 can be assumed.

The treatment of the neutrino case proceeds along the same line; one has

$$q_\nu(E_\nu) \simeq A_\nu (24E_\nu/\text{GeV})^{-\frac{4}{3}p+\frac{1}{3}} \; ; \; A_\nu \simeq 300 N_H A_p \sigma_{pp} \,. \tag{10.27}$$

Photoproduction interactions have a cross section of a fraction of mb, smaller than the proton-proton interaction by two orders of magnitude. They are thus important in environments where the target photon density is much higher than the matter density – this is the case of many astrophysical systems, like the neighborhood of SMBHs in AGN.

One can imagine that photoproduction of neutrinos and photons happens mainly via the Δ^+ resonance: $p\gamma \to N\pi$. The cross sections for the processes $p\gamma \to p\pi^0$ and $p\gamma \to n\pi^+$ at the Δ resonance are in the approximate ratio of 2:1, due to isospin balance (Chap. 5). The process happens beyond the threshold energy for producing a Δ^+:

$$4E_p\epsilon \gtrsim m_\Delta^2 \,, \tag{10.28}$$

where ϵ is the energy of the target photon. The cross section for this reaction peaks at photon energies of about 0.35 $m_p c^2$ in the proton rest frame. In the observer's frame the energy ϵ of the target photon is such that $\epsilon E_p \sim 0.35$, with E_p in EeV and ϵ in eV. For UV photons, with a mean energy of 40 eV, this translates into a characteristic proton energy of some 10 PeV.

The photon and neutrino energies are lower than the proton energy by two factors which take into account (i) the average momentum fraction carried by the secondary pions relative to the parent proton[2] ($\langle x_F \rangle \simeq 0.2$) and (ii) the average fraction of the pion energy carried by the photon in the decay chain $\pi^0 \to \gamma\gamma$ (1/2) and by the neutrinos in the decay chain $\pi^+ \to \nu_\mu \mu^+ \to e^+ \nu_e \bar{\nu}_\mu$ (roughly 3/4 of the pion energy because equal amounts of energy are carried by each lepton). Thus:

$$E_\gamma \sim \frac{E_p}{10} \; ; \; E_\nu \sim \frac{E_p}{20} \,. \tag{10.29}$$

The photon and neutrino spectra are related. All the energy of the π^0 ends up in photons and 3/4 of the π^+ energy goes to neutrinos, which corresponds to a ratio of neutrino to gamma luminosities (L_ν/L_γ)

$$\frac{L_\nu}{L_\gamma} \simeq \frac{3}{8} \,. \tag{10.30}$$

This ratio is somewhat reduced taking into account that some of the energy of the accelerated protons is lost to direct pair production ($p + \gamma \to e^+ e^- p$).

If a source is occulted by the presence of thick clouds or material along the line of sight to the Earth, however, gamma rays are absorbed while neutrinos survive.

An approximate expression for the relation between the neutrino and the gamma-ray fluxes produced from hadronic cascades holds if the proton energy spectrum can be described by a power law, or by an exponential:

$$E_\nu^2 \frac{dN_\nu}{dE_\nu}(E_\nu) \sim \frac{3}{4} K E_\gamma^2 \frac{dN_\gamma}{dE_\gamma}(E_\gamma) \,; \; K = 1/2 \; (2) \; \text{for} \; \gamma p \; (pp) \,. \tag{10.31}$$

The production rate of gamma rays is not necessarily the emission rate observed: photons can be absorbed, and the photon field reduces the pionic gamma rays via pair production.

10.1.2.3 Nuclear Processes and gamma rays in the MeV range

Protons at energies below the pion production threshold (about 300 MeV) can be at the origin of gamma rays through nuclear excitation of the ambient medium. De-excitation of the target nuclei leads to gamma ray lines in the energy region between several hundred keV to several MeV. The most distinct features in the overall nuclear gamma-ray spectrum appear around 4.4 MeV (from ^{12}C), 6.1 MeV (from ^{16}O), 0.85 MeV (from ^{56}Fe), etc.

Gamma ray line emission is expected also from radioactive isotopes synthesised in stellar interiors or during supernova explosions. Since nucleosynthesis can be effective only in very dense environments, to survive and be observed gamma-ray lines should be produced by abundant isotopes with long lifetimes. The

---

[2] The variable x_F (Feynman x), defined as the ratio between the longitudinal momentum of a particle and the maximum allowed value, is used in the discussion of hadronic interactions at large energies. It displays approximate scaling with energy.

best candidates are lines from ^{26}Al and ^{60}Fe for the production of diffuse galactic emission, and from ^{7}Be, ^{44}Ti and ^{56}Ni produced during transient phenomena.

10.1.3 Top-Down Mechanisms; Possible Origin from Dark Matter Particles

Finally, top-down mechanisms might be at the origin of high energy particles (hadrons, gamma rays, neutrinos, ...).

In the GeV-TeV region, photons and neutrinos might come from the decay of heavier particles (dark matter particles for example), or from blobs of energy coming from the annihilation of pairs of such particles. Experimental data collected up to now do not support the existence of such mechanisms—which are anyway searched for actively, especially for photons which are easier to detect, since they might shed light on new physics.

The top-down mechanism implies also an excess of antimatter: differently from the bottom-up mechanism, which privileges matter with respect to antimatter due to the abundance of the former in the Universe, decays of heavy particles should have approximately the same matter and antimatter content. An excess of antimatter at high energy with respect to what expected by standard production (mostly photon conversions and final states from collisions of CRs with the ISM) is also searched for as a "golden signature" for dark matter. Some even believe that at the highest energy cosmic rays are the decay products of remnant particles or topological structures created in the early universe. A topological defect from a phase transition in grand unified theories with typical energy scale of 10^{24} eV could suffer a chain decay into GUT mediators X and Y (see Chap. 7) that subsequently decay to known particles; in the long term the number of neutral pions (decaying into photons) is two orders of magnitude larger than the number of protons. Therefore, if the decay of topological defects is the source of the highest energy cosmic rays, the final state particles must be photons and neutrinos, which are difficult to detect.

Features in the spectra of known particles, in the GeV–TeV range, could show up if these particles originate in decays of exotic particles of very large mass possibly produced in the early Universe. Such long-lived heavy particles are predicted in many models, and the energy distribution of particles coming from their decay should be radically different from what predicted by the standard emission models from astrophysical sources.

Special care is dedicated to the products of the decays of particles in the 100-GeV mass range, since this is the order of magnitude of the mass we expect (Sect. 8.4.1) for candidate dark matter particles.

10.1.3.1 Origin from WIMPs

Dark matter candidates (WIMPs in particular, as discussed in Chap. 8) are possible sources of, e.g., photons, electrons and positrons, and neutrinos via a top-down mechanism.

As discussed in Chap. 8, the normalized relic density of dark matter (DM) particles χ can be expressed as

$$\frac{\Omega_\chi}{0.2} \simeq \frac{3 \times 10^{-26} \text{cm}^3 \text{s}^{-1}}{\langle \sigma_{ann} v \rangle} \ .$$

The value for the interaction rate $\langle \sigma_{ann} v \rangle$ corresponds to a cross section of the order of 10 pb, typical for weak interactions at a scale ~ 100 GeV. This is the so-called "WIMP miracle": a weakly interacting massive particle would be a good DM candidate. WIMP masses can be expected in the range between 10 GeV and a few TeV.

Given the expected amount of WIMP dark matter in the current Universe and the annihilation cross section, it is likely that DM is subject to self-annihilations. To be able to self-annihilate, the DM particle must either coincide with its antiparticle, or be present in both the particle and antiparticle states. In the annihilation (or decay) of the dark matter particles all allowed standard model particles and antiparticles could be produced, and gamma rays and/or charged particles are present in the final states (in the last case, with no preference between matter and antimatter, contrary to the standard sources of cosmic rays).

Where dark matter densities ρ are large, the probability that WIMPs encounter each other and annihilate is enhanced, being proportional to ρ^2. The problem is that we know the dark matter density in the halos of galaxies, while the extrapolation to big density cores (like, for example, galactic centers are expected to be)

Table 10.1 Typical values of radii and magnetic fields in acceleration sites, and the maximum attainable energy.

Source	Magnetic field	Radius	Maximum energy (eV)
SNR	30 μG	1 pc	3×10^{16}
AGN	300 μG	10^4 pc	$>10^{21}$
GRB	10^9 G	10^{-3} AU	0.2×10^{21}

relies on models – this fact holds also for the Milky Way. If one can trust the extrapolations of DM density, one can predict the expected annihilation signal when assuming a certain interaction rate $\langle \sigma v \rangle$ or put limits on this quantity in the absence of a signal (see Sect. 10.4.2.4).

10.2 Possible Acceleration Sites and Sources

In Sect. 10.1.1 we explained how a particle can be accelerated. In which astrophysical objects such acceleration process can take place?

In order to effectively accelerate a particle, the source must have at least a size R of the order of the particle *Larmor radius r_L*:

$$r_L = \frac{pc}{ZeBc} \tag{10.32}$$

where Z is the atomic number of the nucleus.

Note that the charged particle acceleration in a given magnetic field depends thus on the ratio of its linear momentum and of its electric charge, parameter defined usually as the *rigidity*:

$$\mathcal{R} = r_L Bc = \frac{pc}{Ze}. \tag{10.33}$$

The rigidity is measured in volt V and its multiples (GV, TV).

In convenient units, the energy of the accelerated particles, the magnetic field and the source size are related as:

$$\frac{E}{1\,\mathrm{PeV}} \simeq Z \frac{B}{1\,\mu\mathrm{G}} \times \frac{R}{1\,\mathrm{pc}} \simeq 0.2Z \frac{B}{1\,\mathrm{G}} \times \frac{R}{1\,\mathrm{AU}}. \tag{10.34}$$

This entails the so-called Hillas relation, which is illustrated in Table 10.1 and Fig. 10.9. We remind that the energies in the Hillas plot are maximum attainable energies: besides the containment, one must have an effective acceleration mechanism.

In the following, known possible acceleration sites are described.

10.2.1 Stellar Endproducts as Acceleration Sites

We have seen that most VHE gamma-ray emissions in the Galaxy can be associated to supernova remnants. More than 90 % of the TeV galactic sources discovered up to now are, indeed, SNRs at large (we include here in the set of "SNR" also pulsar wind nebulae, see later).

The term "supernova" indicates a very energetic "stella nova", a term invented by Galileo Galilei to indicate objects that appeared to be new stars, that had not been observed before in the sky. The name is a bit ironic, since Galilei's diagnosis was wrong: supernovae are actually stars at the end of their life cycle with an explosion. Five supernovae have been recorded during the last millennium by eye (in the year 1006; in the year 1054–this one was the progenitor of the Crab Nebula; in the year 1181; in 1572, by Tycho Brahe; and by Kepler in 1604); more than 5000 have been detected by standard observatories–nowadays, a few hundreds supernovae are discovered every year by professional and amateur astronomers. Only one core collapse supernova has been detected so far in neutrinos: SN1987a in the Large Magellanic Cloud at a distance of about 50 kpc. In modern times each supernova is named by the prefix SN followed by the year of discovery and a by a one- or two-letter designation (from A to Z, then aa, ab, and so on).

Supernovae are classified taxonomically into two "types". If a supernova's spectrum contains lines of hydrogen it is classified Type II; otherwise it is classified as Type I. In each of these two types there are subdivisions according to the presence of lines from other elements or the shape of the light curve (a graph
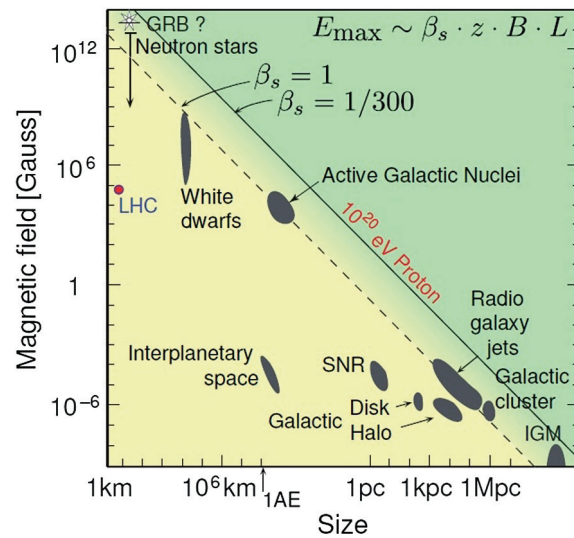
Fig. 10.9 The "Hillas plot" represents astrophysical objects which are potential cosmic ray accelerators on a two-dimensional diagram where on the horizontal axis the size R of the accelerator, and on the vertical axis the magnetic field strength B, are plotted. The maximal acceleration energy E is proportional to $ZRB\beta_s$, where β_s expresses the efficiency of the accelerator and depends on the shock velocity and on the geometry, and Z is the absolute value of the particle charge in units of the electron charge. Particular values for the maximal energy correspond to diagonal lines in this diagram and can be realized either in a large, low field acceleration region or in a compact accelerator with high magnetic fields. Typical β_s values go from ~ 1 in extreme environments down to $\sim 1/300$. From http://astro.uni-wuppertal.de/ kampert.

of the supernova's apparent magnitude as a function of time). It is simpler, however, to classify them by the dynamic of the explosion:

1. **Core-collapse supernovae (type II, Ib, Ic).** In the beginning, a massive star burns the hydrogen in its core. When the hydrogen is exhausted, the core contracts until the density and temperature conditions are reached such that the fusion $3\alpha \rightarrow {}^{12}C$ can take place, which continues until helium is exhausted. This pattern (fuel exhaustion, contraction, heating, and ignition of the ashes of the previous cycle) might repeat several times depending on the mass, leading finally to an explosive burning. Almost the entire gravitational energy of about 10^{53} erg is released in MeV neutrinos of all flavors in a burst lasting seconds. A 25-solar mass star can go through a set of burning cycles ending up in the burning of Si to Fe in a total amount of time of about 7 My (as discussed in Chap. 1, Fe is stable with respect to fusion), with the final stage taking a few days.
2. **Type Ia supernovae**, already discussed in Chap. 8 as "standard candles", occur whenever, in a binary system formed by a small white dwarf and another star (for instance a red giant), the white dwarf accretes matter from its companion reaching a total critical mass of about 1.4 solar masses. Beyond this mass, it re-ignites and can trigger a supernova explosion.

A supernova remnant (SNR) is the structure left over after a supernova explosion: a high-density neutron star (or a black hole) lies at the center of the exploded star, whereas the ejecta appear as an expanding bubble of hot gas that shocks and sweeps up the interstellar medium. A star with mass larger than 1.4 times the mass of the Sun cannot die into a white dwarf and will collapse; it will become a neutron star or possibly, if its mass is larger than 3–5 times the mass of the Sun, a black hole. The most frequent elements heavier than helium created by the fusion processes are carbon, nitrogen, oxygen (this set is just called "CNO"), and iron.

10.2.1.1 Neutron Stars; Pulsars

When a star collapses into a neutron star, its size shrinks to some 10–20 km, with a density of about 5×10^{17} kg/m^3. Since angular momentum is conserved, the rotation can become very fast, with periods of the order of a few ms up to 1 s. Neutron stars in young SNRs are typically pulsars (short for pulsating stars), i.e., they emit a pulsed beam of electromagnetic radiation. Since the magnetic axis is in general not aligned to the rotation axis, two peaks corresponding to each of the magnetic poles can be seen for each period (Fig. 10.10).
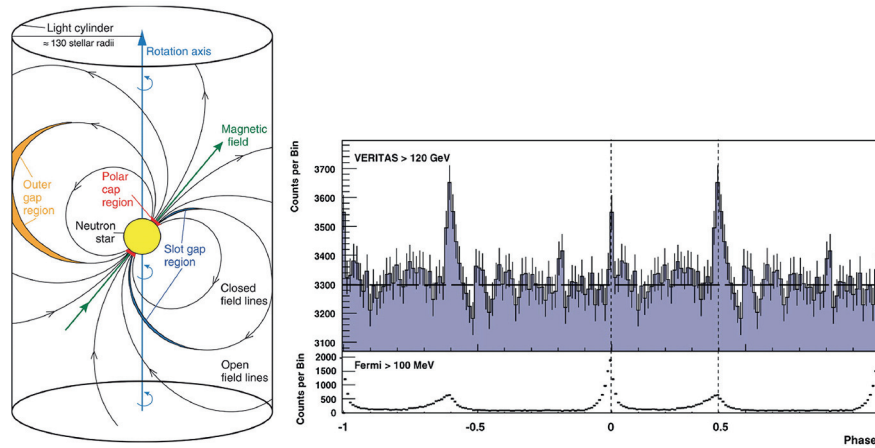
Fig. 10.10 Left: Schematic of the Crab Pulsar. Electrons are trapped and accelerated along the magnetic field lines of the pulsar and can emit electromagnetic synchrotron radiation. Vacuum gaps or vacuum regions occur at the "polar cap" close to the neutron star surface and in the outer region; in these regions density varies and thus one can have acceleration. From MAGIC Collaboration, Science 322 (2008) 1221. Right: Time-resolved emission from the Crab Pulsar at HE and VHE; the period is about 33 ms. From VERITAS Collaboration, Science 334 (2011) 69.

The rotating period for young pulsars can be estimated using basic physics arguments. A star like our Sun has a radius $R \sim 7 \times 10^5$ km and a rotation period of $T \simeq 30$ days, so that the angular velocity is $\omega \sim 2.5 \times \mu$rad/s. After the collapse, the neutron star has a radius $R_{NS} \sim 10$ km. From angular momentum conservation, one can write:

$$R^2 \omega \sim R_{NS}^2 \omega_{NS} \Longrightarrow \omega_{NS} = \omega \frac{R^2}{R_{NS}^2} \Longrightarrow T_{NS} \simeq 0.5 \,\mathrm{ms} \,.$$

The gravitational collapse amplifies the stellar magnetic field. As a result, the magnetic field B_{NS} near the NS surface is extremely high. To obtain an estimate of its magnitude, let us use the conservation of the magnetic flux during the contraction. Assuming the magnetic field to be approximately constant over the surface,

$$B_{\mathrm{star}} R^2 = B_{NS} R_{NS}^2 \Longrightarrow B_{NS} = B_{\mathrm{star}} \frac{R^2}{R_{NS}^2} \,.$$

For a typical value of $B_{\mathrm{star}} = 1$ kG, the magnetic fields on the surface of the neutron star is about 10^{12} G. This estimate has been experimentally confirmed by measuring energy levels of free electrons in the pulsar strong magnetic fields. In a class of neutron stars called *magnetars* the field can reach 10^{15} G.

Typical pulsars emitting high-energy radiation have cutoffs of the order of a few GeV. More than hundred HE pulsars emitting at energies above 100 MeV have been discovered by the *Fermi*-LAT until 2013. They are very close to the Solar System (Fig. 10.11, left), most of the ones for which the distance has been measured being less that a few kpc away. A typical spectral energy distribution is shown in Fig. 10.11, right. The pulsar in Crab Nebula is not typical, being one of the two (together with the Vela pulsar) firmly detected up to now in VHE (Fig. 10.12)—Crab and Vela were also the first HE pulsars discovered in the late 1970s.

10.2.1.2 Binary Systems

Neutron stars and BHs and other compact objects are frequently observed orbiting around a companion compact object or a non-degenerate star (like in the binary LS I +61 303). In binary systems mass can be transferred to the (more) compact object, accreting it. Shocks between the wind of the massive companion and the compact object can contribute to the production of non-thermal emission in X-rays or even in gamma rays. Due to the motion of ionized matter, very strong electromagnetic fields are produced in the vicinity of the compact object, and charged particles can be accelerated to high energies, generating radiation.
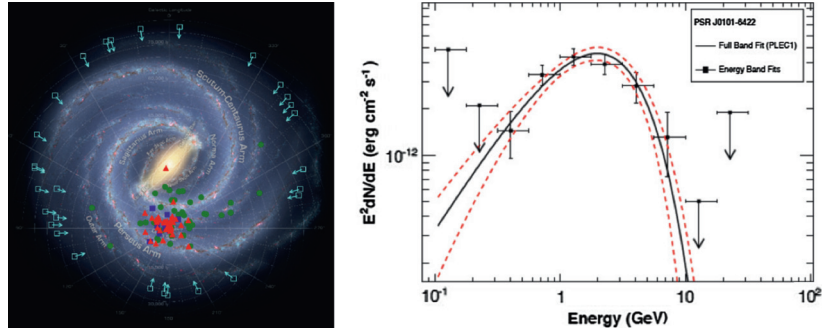
Fig. 10.11 Left: Map of the pulsars detected by the *Fermi*-LAT (the Sun is roughly in the center of the distribution). The open squares with arrows indicate the lines of sight toward pulsars for which no distance estimates exist. Credit: NASA. Right: Spectral energy distribution from a typical high-energy pulsar. Credit: NASA.
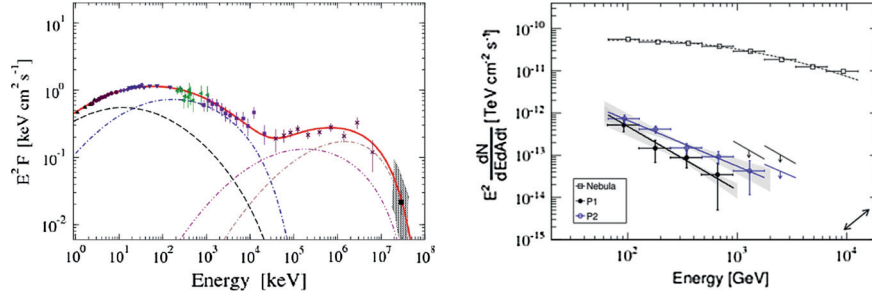
Fig. 10.12 Left: Spectral energy distribution of the Crab Pulsar. Right: The VHE energy emission, compared with the emission from the pulsar wind nebula powered by the pulsar itself. The two periodical peaks are separated. Credit: MAGIC Collaboration.

10.2.1.3 Supernova Remnants and Particle Acceleration

Supernova remnants (SNRs) are characterized by expanding ejected material interacting with ambient gas through shock fronts, with the generation of turbulent magnetic fields, of the order of $B \sim 10\,\mu G$ to 1 mG. Typical velocities for the expulsion of the material out of the core of the explosion are of the order of 3000 km/s to 10 000 km/s for a young (< 1000 yr) SNR. The shock slows down over time as it sweeps up the ambient medium, but it can expand over tens of thousands of years and over tens of parsecs before its speed falls below the local sound speed.[3]

Based on their emission and morphology (which are actually related), SNRs are generally classified under three categories: shell-type, pulsar wind nebulae (PWN), and composite (a combination of the former, i.e., a shell-type SNR containing a PWN). The best known case of a PWN is the Crab Nebula, powered by the central young ($\sim$1000 year) pulsar B0531+21. Crab Nebula emits radiation across a large part of the electromagnetic spectrum, as seen in Fig. 10.13 – and qualitatively one can see in this figure the SSC mechanism at work with a transition at ~ 30 GeV between the synchrotron and the IC emissions. One can separate the contribution of the pulsar itself to the photon radiation from the contribution of the PWN (Fig. 10.12).

Note that sometimes in the literature shell-type supernova remnants are just called SNRs and distinguished from PWN, but this is not the convention used in this book.

The evolution of a SNR can be described by a free expansion phase, an adiabatic phase, a radiative phase and a dissipation phase (Fig. 10.14).

1. In the free expansion phase, lasting up to few hundred years depending on the density of the surrounding gas, the shell expands at constant velocity and acts like an expanding piston, sweeping up the surrounding medium.
2. When the mass of the swept-up gas becomes comparable to the ejected mass, the Sedov-Taylor (adiabatic) phase starts. The ISM produces a strong pressure on the ejecta, reducing the expansion velocity, which remains supersonic for some 10^4 years, until all the energy is transferred to the swept-out material. During

---

[3] The speed of shock is the speed at which pressure waves propagate, and thus it determines the rate at which disturbances can propagate in the medium.
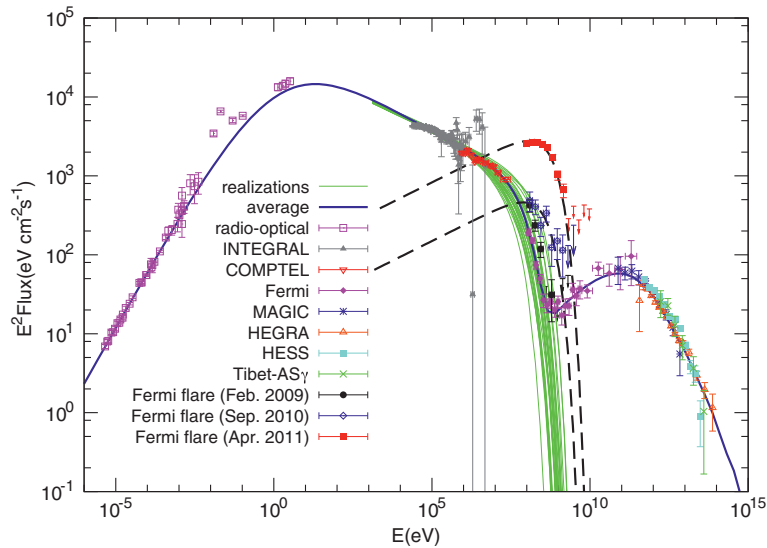
Fig. 10.13 Spectral energy distribution of the Crab Nebula (data from radio-optical up to 100 TeV). From Yuan, Yin et al., http://arxiv.org/abs/1109.0075/arXiv:1109.0075.
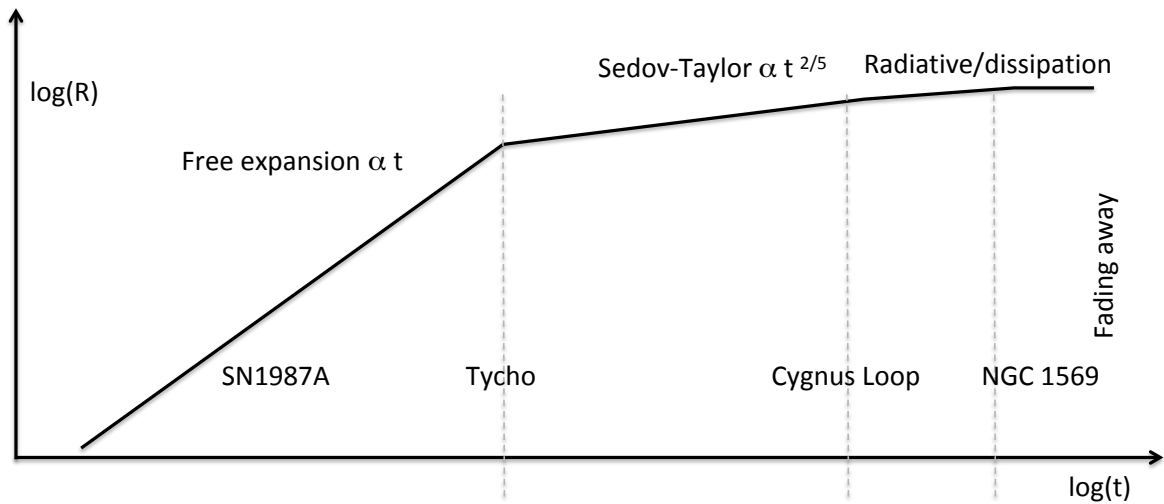
Fig. 10.14 Phases in the life of a supernova remnant.

this phase, the radius of the shock grows as $t^{2/5}$. Strong X-ray emission traces the strong shock waves and hot shocked gas.

3. As the expansion continues, it forms a thin ($\lesssim 1$ pc), dense (1-100 million atoms per cubic metre) shell surrounding the $\sim 10^4$K hot interior. The shell can be seen in optical emission from recombining ionized hydrogen and ionized oxygen atoms. Radiative losses become important, and the expansion slows down.
4. Finally, the hot interior starts cooling. The shell continues to expand from its own momentum, and $R \propto t^{1/4}$. This stage can be seen in the radio emission from neutral hydrogen atoms.

When the supernova remnant slows to the speed of the random velocities in the surrounding medium, after roughly 30 000 years, it merges into the general turbulent flow, contributing its remaining kinetic energy to the turbulence, and spreading around heavy atoms which can be recycled in the ISM.

A young supernova remnant has the ideal conditions for the Fermi 1st order acceleration. The maximum energy that a charged particle could achieve is given by the rate of energy gain, times the time T_e spent in the shock. In the Fermi first-order model,

$$\frac{dE}{dt} \simeq \beta \frac{E}{T_{cycle}} \qquad (10.35)$$

(Sec. 10.1.1); $\lambda_{cycle} \sim r_L \simeq E/(ZeB)$ is of the order of the Larmor radius (see Sect. 10.2).
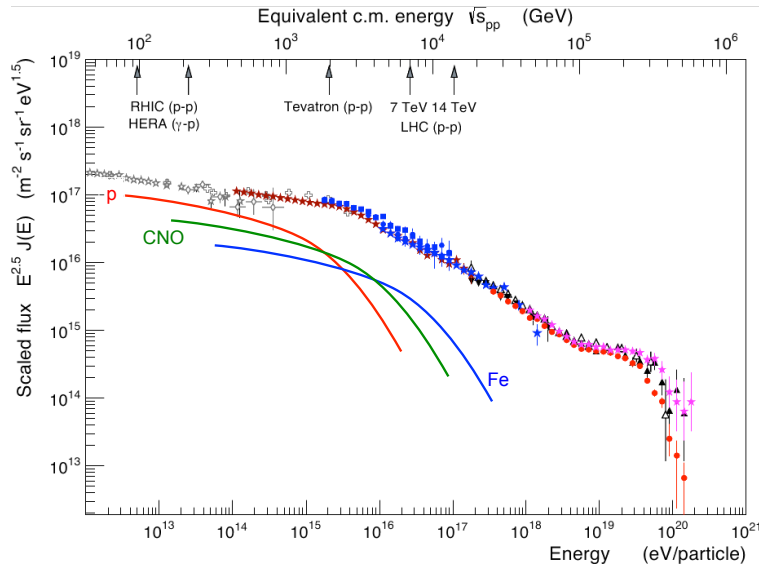
Fig. 10.15 The interpretation of the knee as due to the dependence of the maximum energy on the nuclear charge Z. The flux of each nuclear species decreases after a given cutoff. The behavior of hydrogen, CNO and iron ($Z = 26$) nuclei are depicted in figure.

$$T_{cycle} \simeq \frac{E}{ZeB\beta c} \implies \frac{dE}{dt} \simeq (\beta^2 c)ZeB\,. \tag{10.36}$$

Finally

$$E_{max} \simeq T_S \frac{dE}{dt} \simeq ZeBR_S\beta\,. \tag{10.37}$$

Inserting in Eq. 10.37 $4\,\mu$G as a typical value of the magnetic field B, and assuming $T_e \simeq R_S/(\beta c)$, where R_S is the radius of the supernova remnant, we obtain:

$$E_{max} \simeq \beta\,Ze\,B\,R_S \simeq 300\,Z\,\text{TeV}\,. \tag{10.38}$$

The shock acceleration of interstellar particles in SNR explains the spectrum of cosmic ray protons up to few hundreds of TeV, close to the region where the knee begins (see Fig. 10.1).

An important consequence of (10.38) is that the maximum energy is proportional to the charge Z of the ion, and it is thus higher for multiply ionized nuclei with respect to a single-charged proton. In this model, the knee is explained as a structure due to the different maximum energy reached by nuclei with different charge Z (Fig. 10.15). Note that the proportion to Z is an underestimate of the actual proportion, since in addition to the acceleration efficiency growing with Z the escape probability from the Galaxy decreases with Z.

10.2.2 Other Galactic Sources

Particle acceleration could be a more common phenomenon than indicated above, and be characteristic of many astrophysical objects. For example, we have seen that TeV emission has been found from binary sources.

The galactic zoo could be more varied at lower fluxes and energies; we shall discuss in the rest of the chapter some diffuse emitters up to ~ 10 GeV. Next generation detectors will tell if other classes of emitters exist.

However, most of the Galactic emitters of TeV gamma rays are SNRs at large. SNRs can, in principle, reach energies not larger than a few PeV, being limited by the product of radius time the magnetic field—see the Hillas plot. Photons above about 100 TeV have anyway never been observed, and the question is if this is due to the limited sensitivity of present detectors.

10.2.3 Extragalactic Acceleration Sites: Active Galactic Nuclei and Other Galaxies

Among the extragalactic emitters that may be observed from Earth, Active Galactic Nuclei (AGN) and Gamma Ray Bursts could fulfil the conditions (size, magnetic field, acceleration efficiency) to reach the highest energies.

Supermassive black holes of $\sim 10^6$–10^{10} solar masses ($M_\odot$) and beyond reside in the cores of most galaxies—for example, the center of our Galaxy, the Milky Way, hosts a black hole of roughly 4 million solar masses, its mass having been determined by the orbital motion of nearby stars. The mass of BHs in the center of other galaxies has been calculated through its correlation to the velocity dispersion of the stars in the galaxy.[4]

In approximately 1% of the cases such black hole is active, i.e., it displays strong emission and has signatures of accretion: we speak of an active galactic nucleus (AGN). Despite the fact that AGN have been studied for several decades, the knowledge of the emission characteristics up to the highest photon energies is mandatory for an understanding of these extreme particle accelerators.

Infalling matter onto the black hole can produce a spectacular activity. An AGN emits over a wide range of wavelengths from γ ray to radio: typical luminosities can be very large, and range from about 10^{37} to 10^{40} W (up to 10 000 times a typical galaxy). The energy spectrum of an AGN is radically different from an ordinary galaxy, whose emission is due to its constituent stars. The maximum luminosity (in equilibrium conditions) is set by requirement that gravity (inward) is equal to radiation pressure (outward); this is called the Eddington luminosity–approximately, the Eddington luminosity in units of the solar luminosity is 40 000 times the BH mass expressed in solar units. For short times, the luminosity can be larger than the Eddington luminosity.

Matter falling into the central black hole will conserve its angular momentum and will form a rotating accretion disk around the BH itself. In about 10% of AGN, the infalling matter turns on powerful collimated jets that shoot out in opposite directions, likely perpendicular to the disk, at relativistic speeds (see Fig. 10.16). Jets have been observed close to the BH having a transverse size of about 0.01 pc, orders of magnitude smaller than the radius of the black hole and a fraction 10^{-5} of the length of jets themselves.

Frictional effects within the disk raise the temperature to very high values, causing the emission of energetic radiation—the gravitational energy of infalling matter accounts for the power emitted. The typical values of the magnetic fields are of the order of 10^4 G close to the BH horizon, quickly decaying along the jet axis.

Many AGN vary substantially in brightness over very short timescales (days or even minutes). Since a source of light cannot vary in brightness on a timescale shorter than the time taken by light to cross it, the energy sources in AGN must be very compact, much smaller than their Schwarzschild radii—the Schwarzschild radius of the BH is $3\,\mathrm{km} \times (M/M_\odot)$, i.e., 20 AU (about 10^4 light seconds) for a supermassive black hole mass of $10^9 M_\odot$.

The so-called "unified model" accounts for all kinds of active galaxies within the same basic model. The supermassive black hole and its inner accretion disk are surrounded by matter in a toroidal shape, and according to the unified model the type of active galaxy we see depends on the orientation of the torus and jets relative to our line of sight. The jet radiates mostly along its axis, also due to the Lorentz enhancement—the observed energy in the observer's frame is boosted by a Doppler factor Γ which is obtained by the Lorentz transformation of a particle from the jet fluid frame into the laboratory frame; in addition the Lorentz boost collimates the jet.

- An observer looking very close to the jet axis will observe essentially the emission from the jet, and thus will detect a (possibly variable) source with no spectral lines: this is called a blazar.
- As the angle of sight with respect to the jet grows, the observer will start seeing a compact source inside the torus; in this case we speak generically of a quasar.
- From a line of sight closer to the plane of the torus, the BH is hidden, and one observes essentially the jets (and thus, extended radio-emitting clouds); in this case, we speak of a radio galaxy (Fig. 10.16).

---

[4] The so-called $M - \sigma$ relation is an empirical correlation between the stellar velocity dispersion σ of a galaxy bulge and the mass M of the supermassive black hole (SMBH) at its center:

$$\frac{M}{10^8 M_\odot} \simeq 1.9 \left(\frac{\sigma}{200 \ \mathrm{km/s}} \right)^{5.1}$$

where $M_\odot$ is the solar mass. A relationship exists also between galaxy luminosity and black hole (BH) mass, but with a larger scatter.
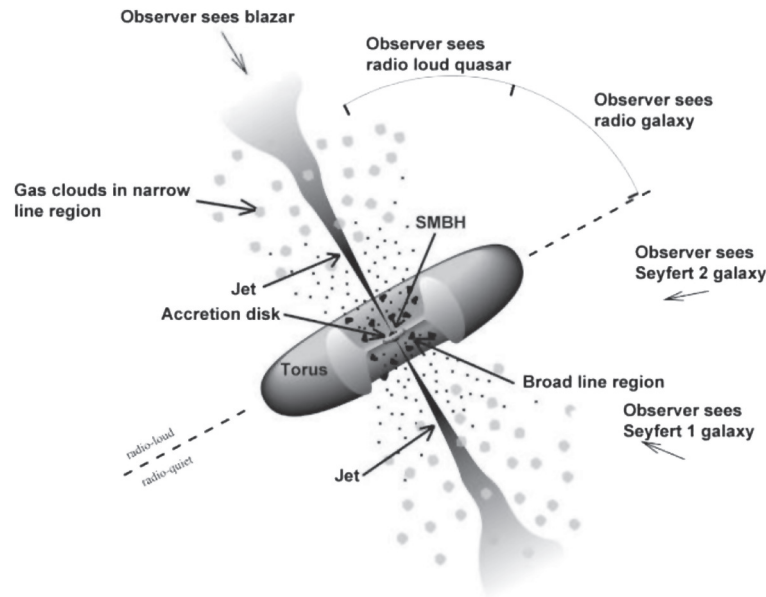
Fig. 10.16 Schematic diagram for the emission by an AGN. In the "unified model" of AGN, all share a common structure and only appear different to observers because of the angle at which they are viewed. Adapted from http://www.astro-photography.net.

The class of jet dominated AGN corresponds mostly to radio-loud AGN. These can be blazars or non-aligned AGN depending on the orientation of their jets with respect to the line of sight. In blazars, emission is modified by relativistic effects due to the Lorentz boost. Due to a selection effect, most AGN we observe at high energies are blazars.

10.2.3.1 Blazars

Blazars accelerate particles to the highest observed energies, and are therefore of high interest.

Observationally, blazars are divided into two main subclasses depending on their spectral properties.

- Flat Spectrum Radio Quasars, or FSRQs, show broad emission lines in their optical spectrum.
- BL Lacertae objects (BL Lacs) have no strong, broad lines in their optical spectrum.

Typically FSRQs have a synchrotron peak at lower energies than LBLs.

BL Lacs are further classified according to the energies of the synchrotron peak $\hat{\nu}_S$ of their SED; they are called accordingly:

- low-energy peaked BL Lacs (LBLs) if $\hat{\nu}_S \lesssim 10^{14}$ Hz (about 0.4 eV);
- intermediate-energy peaked BL Lacs (IBL);
- high-energy peaked BL Lacs (HBL) if $\hat{\nu}_S \gtrsim 10^{15}$ Hz (about 4 eV).

(note that the thresholds for the classification vary in the literature).

Blazar population studies at radio to X-ray frequencies indicate a redshift distribution for BL Lacs peaking at $z \sim 0.3$, with only few sources beyond $z \sim 0.8$, while the FSRQ population is characterized by a rather broad maximum at $z \sim 0.6$–1.5.

10.2.3.2 Non-AGN Extragalactic Gamma Ray Sources

At TeV energies, the extragalactic γ ray sky is completely dominated by blazars. At present, more than 50 objects have been discovered and are listed in the online TeV Catalog. Only 3 radio galaxies have been detected at TeV energies (Centaurus A, M87 and NGC 1275).

The two most massive closeby starburst (i.e., with an extremely large rate of star formation) galaxies NGC 253 and M82 are the only extragalactic sources detected at TeV energies for which the accretion disk-jet structure is not evidenced.

At GeV energies, a significant number (about 1/3 ot the total sample) of unidentified extragalactic objects has been detected by the *Fermi*-LAT (emitters that could not be associated to any known object), and few non-AGN objects have been discovered. Among non-AGN objects, there are several local group galaxies (LMC, SMC, M31) as well as galaxies in the star formation phase (NGC 4945, NGC 1068, NGC 253, and M82).

CRs might be accelerated by SNRs or other structures related to star formation activity.

10.2.3.3 The Gamma Ray Yield From Extragalactic Objects

The observed VHE spectra at high energies are usually described by a power law $dN/dE \propto E^{-\Gamma}$. The spectral indices Γ need to be fitted from a distribution deconvoluted from absorption in the Universe, since the transparency of the Universe depends on energy; they typically range in the interval from 2 to 4, with some indications for spectral hardening with increasing activity. Emission beyond 10 TeV has been established, for close galaxies like Mrk 501 and Mrk 421. Some sources are usually detected during high states (flares) only, with low states falling below current sensitivities.

Observed VHE flux levels for extragalactic objects range typically from 1 % of the Crab Nebula steady flux (for the average/steady states) up to 10 times as much when the AGN are in high activity phases. Since TeV instruments are now able to detect sources at the level of 1 % of the Crab, the variability down to few minute scale of the near and bright TeV-emitting blazars (Mrk 421 and Mrk 501) can be studied in detail. Another consequence of the sensitivity of Cherenkov telescopes is that more than one extragalactic object could be visible in the same field of view.

The study and classification of AGN and their acceleration mechanisms require observations from different instruments. The spectral energy distributions (SEDs) of blazars can span almost 20 orders of magnitude in energy, making simultaneous multiwavelength observations a particularly important diagnostic tool to disentangle the underlying nonthermal processes. Often, SEDs of various objects are obtained using nonsimultaneous data—which limits the accuracy of our models.

In all cases, the overall shape of the SEDs exhibits the typical broad double-hump distribution, as shown in Fig. 10.17 for three AGN at different distances. The SEDs of all AGN considered show that there are considerable differences in the position of the peaks of the two components and in their relative intensities. According to current models, the low-energy hump is interpreted as due to synchrotron emission from highly relativistic electrons, and the high-energy bump is related to inverse Compton emission of various underlying radiation fields, or π^0 decays, depending on the production mechanism in action (Sect. 10.1.2). Large variability is present, especially at optical/UV and X-ray frequencies.

Variability is also a way to distinguish between hadronic and leptonic acceleration modes. In a pure leptonic mode, one expects that in a flare the increase of the synchrotron hump is fully correlated to the increase of the IC hump; in a hadronic mode, vice versa, one can have a "orphan flare" of the peak corresponding to π^0 decay.

Studies on different blazar populations indicate a continuous spectral trend from FSRQ to LBL to IBL to HBL, called the "blazar sequence." The sequence is characterized by a decreasing source luminosity, increasing synchrotron peak frequency, and a decreasing ratio of high- to low-energy component (Fig. 10.17).

10.2.4 Extragalactic Acceleration Sites: Gamma Ray Bursts

Gamma ray bursts (GRBs) are another very important possible extragalactic acceleration site. GRBs are extremely intense and fast shots of gamma radiation. They last from fractions of a second to a few seconds and sometimes up to a thousand seconds, often followed by "afterglows" orders of magnitude less energetic than the primary emission after minutes, hours, or even days. GRBs are detected once per day in average, typically in X-rays and soft gamma rays. They are named GRByymmdd after the date on which they were detected: the first two numbers after "GRB" correspond to the last two digits of the year, the second two numbers to the month, and the last two numbers to the day. A progressive letter ("A," "B," ...) might be added—it is mandatory if more than one GRB was discovered in the same day, and it became customary after 2010. A historical curiosity: the first GRB was discovered in 1967 by one of the US satellites of the Vela series, but the discovery has been kept secret for six years. The Vela satellites had been launched to verify if Soviet Union was respecting the nuclear test ban treaty imposing non-testing of nuclear devices in space.
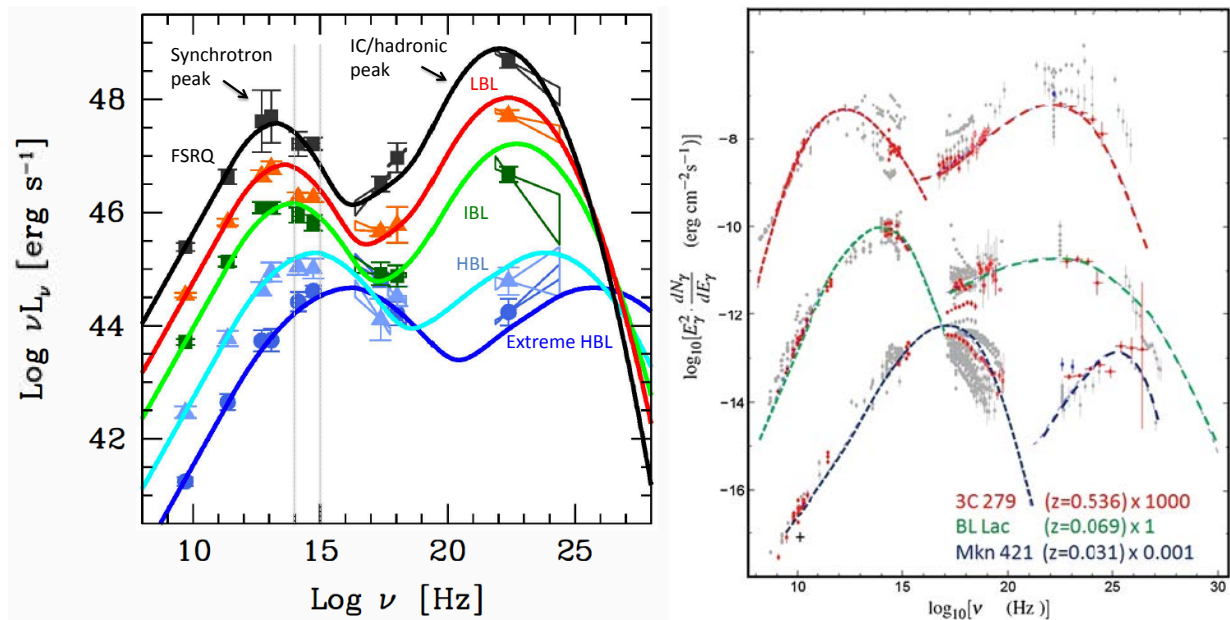
Fig. 10.17 Left: The blazar sequence. From G. Fossati et al., Mon. Not. Roy. Astron. Soc. 299 (1998) 433. Right: The SED of three different AGN at different distance from the Earth and belonging to different subclasses. To improve the visibility of the spectra, the contents of the farthest (3C 279) have been multiplied by a factor 1000, while that of the nearest (Mrk 421) by a factor 0.001. The dashed lines represent the best fit to the data assuming leptonic production. From D. Donato et al., Astron. Astrophys. 375 (2001) 739.
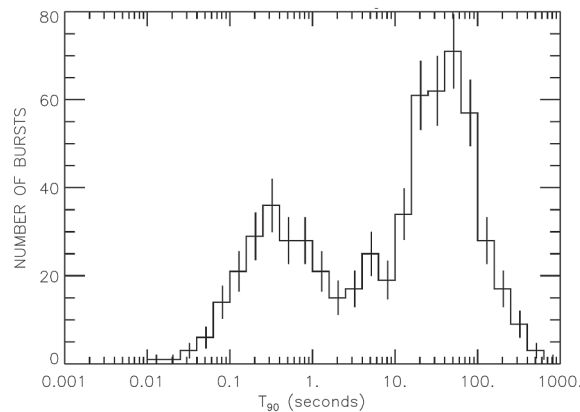
Fig. 10.18 Time distribution of GRBs detected by the BATSE satellite as a function of the time T90 during which 90 % of the photons are detected. It is easy to see "short" and "long" GRBs. Credit: NASA.

After the observation of the GRB, it took some time to be sure that the event was of astrophysical origin. Unfortunately, we do not know anything about possible similar discoveries by the Soviet Union.

GRBs are of extragalactic origin. The distribution of their duration is bimodal (Fig. 10.18), and allows a first phenomenological classification between "short" GRBs (lasting typically 0.3 s; duration is usually defined as the time T90 during which 90 % of the photons are detected) and "long" GRBs (lasting more than 2 s, and typically 40 s). Short GRBs are on average harder than long GRBs.

- Short GRBs have been associated to the coalescence of pairs of massive objects, neutron star-neutron star (NS-NS) or neutron star-black hole (NS-BH). The system loses energy due to gravitational radiation, and thus spirals closer and closer until tidal forces disintegrate it providing an enormous quantity of energy before the merger. This process can last only a few seconds, and has been recently proven by the simultaneous observation of gravitational waves and gamma rays in a NS-NS merger.
- For long GRBs in several cases the emission has been associated with a supernova from a very high mass progenitor, a "hypernova" (Sect. 10.2.4). The connection between large mass supernovae (from the explosion of hypergiants, stars with a mass of between 100 and 300 times that of the Sun) and long GRBs is proven by the observation of events coincident both in time and space, and the energetics would account
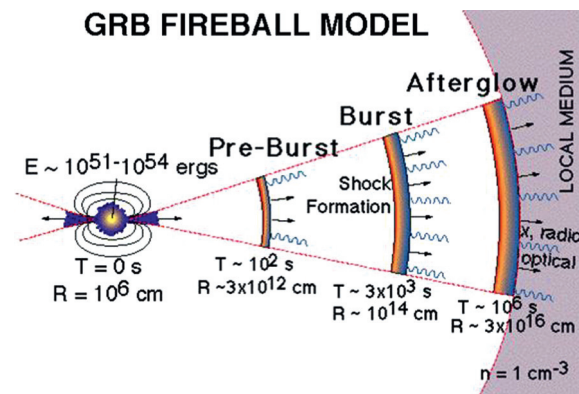
Fig. 10.19 The fireball model. Credit: http://www.swift.ac.uk/about/grb.php.

for the emission—just by extrapolating the energetics from a supernova. During the abrupt compression of such a giant star the magnetic field could be squeezed to extremely large values, of the order of 10^{12}–10^{14} G, in a radius of some tens of kilometers.

Although the two families of GRBs have different progenitors, the acceleration mechanism that gives rise to the γ rays themselves (and possibly to charged hadrons one order of magnitude more energetic, and thus also to neutrinos) can be the same.

The fireball model is the most widely used theoretical framework to describe the physics of GRBs. In this model, first the black hole formed (or accreted) starts to pull in more stellar material; quickly an accretion disk forms, with the inner portion spinning around the BH at a relativistic speed. This creates a magnetic field which blasts outward two jets of electrons, positrons and protons at ultrarelativisic speed in a plane out of the accretion disk. Photons are formed in this pre-burst.

Step two is the fireball shock. Each jet behaves in its way as a shock wave, plowing into and sweeping out matter like a "fireball". Gamma rays are produced as a result of the collisions of blobs of matter; the fireball medium does not allow the light to escape until it has cooled enough to become transparent—at which point light can escape in the direction of motion of the jet, ahead of the shock front. From the point of view of the observer, the photons first detected are emitted by a particle moving at relativistic speed, resulting in a Doppler blueshift to the highest energies (i.e., gamma rays). This is the gamma ray burst.

An afterglow results when material escaped from the fireball collides with the interstellar medium and creates photons. The afterglow can persist for months as the energies of photons decrease.

Fig. 10.19 shows a scheme of the fireball shock model.

10.2.5 Gamma Rays and the Origin of Cosmic Rays: the Roles of SNRs and AGN

10.2.5.1 Gamma Rays and the Origin of Cosmic Rays from SNRs

Among the categories of possible cosmic ray accelerators, several have been studied in an effort to infer the relation between gamma rays and charged particles. In the Milky Way in particular, SNRs are, since the hypothesis formulated by Baade and Zwicky in 1934, thought to be possible cosmic ray accelerators; according to the Hillas plot, this acceleration can go up to energies up to the order the PeV. The particle acceleration in SNRs is likely to be accompanied by production of gamma rays due to interactions of accelerated protons and nuclei with the ambient medium.

The conjecture has a twofold justification. From one side, SNRs are natural places in which strong shocks develop and such shocks can accelerate particles. On the other side, supernovae can easily account for the required energetics. In addition, there are likely molecular clouds and photon fields which allow the reprocessing of accelerated protons–thus one can expect sizable gamma-ray and neutrino emission. Nowadays, as a general remark, we can state that there is no doubt that SNR accelerate (part of the) Galactic CR, the open questions being: which kind of SNR; in which phase of their evolution SNR really do accelerate
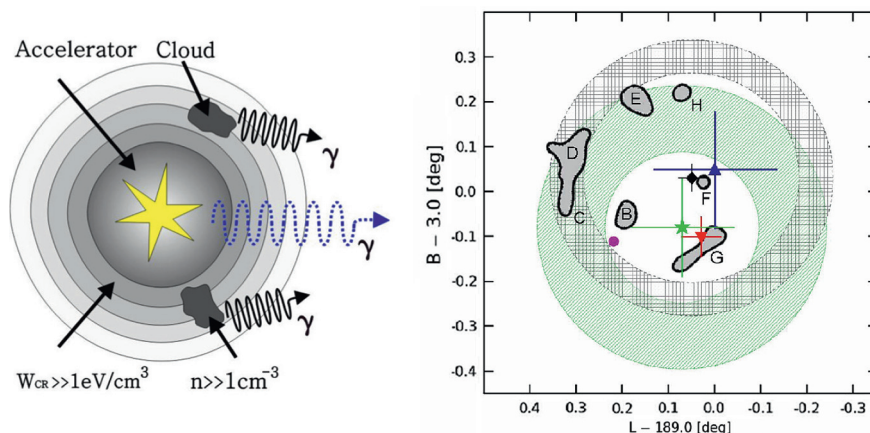
Fig. 10.20 On the left: Scheme of the generation of a hadronic cascade in the dump of a proton with a molecular cloud. On the right, IC443: centroid of the emission from different gamma detectors. The position measured by *Fermi*-LAT is marked as a diamond, that by MAGIC as a downwards oriented triangle; the latter is consistent with the molecular cloud G.

particles; and if the maximum energy of these accelerated particles can go beyond ~1 PeV, and thus get insights on the nature, the energy and the composition of the knee.

A very important step forward in this field of research was achieved in the recent years with an impressive amount of experimental data at TeV energies, by Cherenkov telescopes (H.E.S.S., MAGIC, VERITAS), and at GeV energies, by the *Fermi*-LAT and AGILE satellites.

In SNRs with molecular clouds, in particular, a possible mechanism involves a source of cosmic rays illuminating clouds at different distances, and generating hadronic showers by pp collisions. This allows to spot the generation of cosmic rays by the study of photons coming from π^0 decays in the hadronic showers.

Recent experimental results support the "beam dump" hypothesis of accelerated protons on molecular clouds or photon fields from the imaging of the emitter. An example is the SNR IC443. In Fig. 10.20, a region of acceleration at GeV energies is seen by the *Fermi*-LAT. It is significantly displaced from the centroid of emission detected at higher energies by the MAGIC gamma ray telescope–which, in turn, is positionally consistent with a molecular cloud. The spectral energy distribution of photons also supports a two-component emissions, with a rate of acceleration of primary electrons approximately equal to the rate of production of protons. Such a 2-region displaced emission morphology has been also detected in several other SNRs (W44 and W82 for example).

A characteristics of hadroproduction of gamma rays is the presence of a "pion bump" at $\simeq m_\pi/2 \simeq 67.5$ MeV in the spectral energy distribution, which can be related to π^0 decay; this feature has been observed in several SNRs, see for example Fig. 10.21. Unfortunately, present gamma-ray detectors are not very sensitive in the region of few tens of MeV, and the reconstruction of the pion bump is not very accurate.

Besides indications from the studies of the morphology and from the shape of the SED, the simple detection of photons of energies of the order of 100 TeV and above could be a direct indication of production via π^0 decay, since the emission via leptonic mechanisms should be strongly suppressed at those energies where the inverse Compton scattering cross section enters the Klein–Nishina regime. A cosmic-ray accelerator near the PeV has likely been found in the vicinity of the Galactic center.

10.2.5.2 Where Are the Galactic PeVatrons?

We saw that cosmic rays up to the knee are accelerated in the Galaxy; this implies that our Galaxy contains petaelectronvolt accelerators, often called PeVatrons.

Cosmic ray acceleration has been proven in particular in some stellar endproducts, as we have just seen; however, these sources display an exponential-like cutoff, or an index break, significantly below 100 TeV. This implies that none of these can be identified as a PeVatron. Now the question is: where are the PeVatrons?

Recent measurements of the Galactic center region by H.E.S.S. have shown that gamma-ray emission is compatible with a steady source accelerating CRs up to PeV energies within the central 10 pc of the Galaxy. The supermassive black hole Sagittarius A* could be linked to this possible PeVatron.
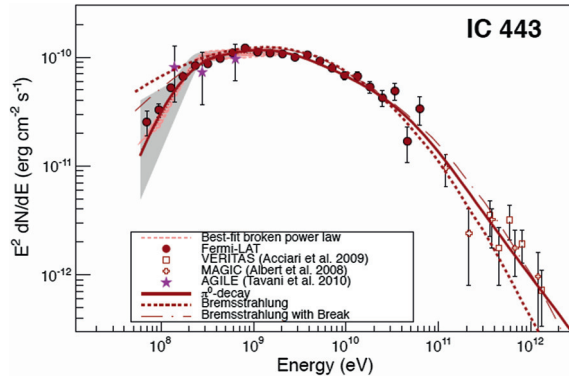
Fig. 10.21 Spectral energy distribution of photons emitted by the SNR IC443. The fit requires on top of photons coming from a leptonic acceleration mechanism also photons from π^0 decay. From *Fermi*-LAT Collaboration (M. Ackermann et al.), Science 339 (2013) 807.

From an annulus centered at Sagittarius (Sgr) A* (see Fig. 10.22, left) the energy spectrum of the diffuse γ-ray emission (Fig. 10.22, right) has been extracted. The best fit to the data is found for a spectrum following a power law extending with a photon index $\simeq 2.3$ to energies up to tens of TeV, without any indication of a cutoff. Since extremely-high energy γ-rays might result from the decay of neutral pions produced by *pp* interactions, the derivation of such hard power-law spectrum implies that the spectrum of the parent protons should extend to energies close to 1 PeV. The best fit of a γ-ray spectrum from neutral pion decays is found for a proton spectrum following a pure power-law with index ≈ 2.4. In the future, with larger and more sensitive neutrino detectors, *pp* interactions of 1 PeV protons could also be studied by the observation of emitted neutrinos.
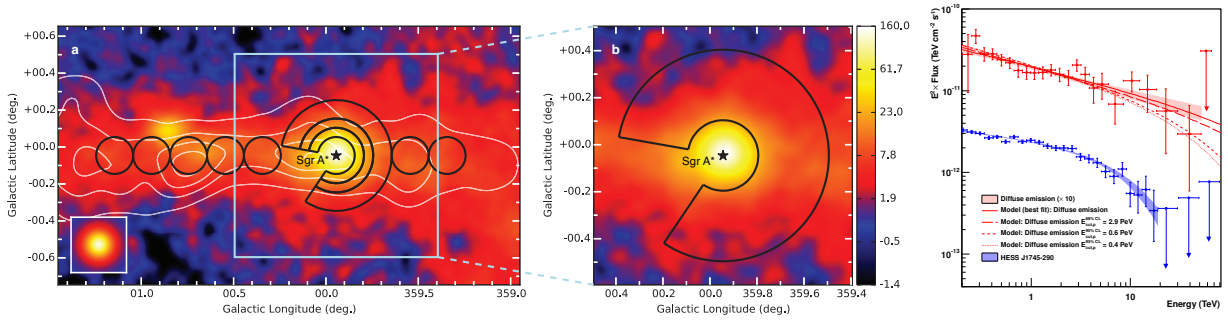
Fig. 10.22 Left: VHE γ-ray image of the Galactic Center region. The black lines show the regions used to calculate the CR energy density throughout the central molecular zone. White contour lines indicate the density distribution of molecular gas. The inset shows the simulation of a point-like source. The inner ~ 70 pc and the contour of the region used to extract the spectrum of the diffuse emission are zoomed. Right: VHE γ-ray spectra of the diffuse emission and of the source HESS J1745-290, positionally consistent with the Galectic Center. The Y axis shows fluxes multiplied by a factor E^2, in units of TeV cm^{-2}s^{-1}. Arrows represent 95% C.L. flux upper limits. The red lines show the numerical computations assuming that γ-rays result from the decay of neutral pions produced by proton-proton interactions. The fluxes of the diffuse emission spectrum and models are multiplied by 10.

Although its current rate of particle acceleration is not sufficient to provide a substantial contribution to Galactic CR, Sagittarius A* could have plausibly been more active over the last $\gtrsim 10^{6-7}$ years, and therefore should be considered as a sizable source of PeV Galactic cosmic rays. However, the hypothesis is speculative; moreover, the identification of the source remains unclear, since the GC region is very confused, and several other VHE gamma-ray sources exist.

Crab Nebula is a PWN currently showing no clear cutoff, and the gamma-ray emission reaches some 100 TeV and beyond, as shown by HEGRA, MAGIC and H.E.S.S.. Although there is no direct indication that it is a hadron accelerator from the morphology or from the SED, the fact itself that photon energies are so

high disfavors a purely leptonic origin of gamma rays, due to Klein-Nishina suppression: Crab could likely be a PeVatron as well.

10.2.5.3 Testing if Cosmic Rays Originate from AGN

As the energetics of SNRs might explain the production of galactic CR, the energetics of AGN might explain the production of CR up to the highest energies. In the Hillas relation, the magnetic field and the typical sizes are such that acceleration is possible (Table 10.1).

Where molecular clouds are not a likely target, as, for example, in the vicinity of supermassive black holes, proton–photon interactions can start the hadronic shower.

Although the spatial resolution of gamma ray telescopes is not yet good enough to study the morphology of extragalactic emitters, a recent study of a flare from the nearby galaxy M87 (at a distance of about 50 Mly, i.e., a redshift of 0.0004) by the main gamma telescopes plus the VLBA radio array has shown, based on the VLBA imaging power, that this AGN accelerates particles to very high energies in the immediate vicinity (less than 60 Schwarzschild radii) of its central black hole. This galaxy is very active: its black hole, of a mass of approximately 7 billion solar masses, accretes by 2 or 3 solar masses per year. A jet of energetic plasma originates at the core and extends outward at least 5000 ly.

Also Centaurus A, the near AGN for which some weak hint of correlation with the Auger UHE data exists, has been shown to be a VHE gamma emitter.

The acceleration of hadrons above 1 EeV has been proven very recently to correlate with the position of AGN, and in particular one blazar has been identified as a hadron accelerator at some tens of PeV. These two evidences will be discussed in detail later, in Sect. 10.4.1.7 and in Sect. 10.4.3.2 respectively.

10.2.6 Sources of Neutrinos

Neutrinos play a special role in particle astrophysics. Their cross section is very small and they can leave production sites without interacting. Differently from photons, neutrinos can carry information about the core of the astrophysical objects that produce them. Different from photons, they practically do not suffer absorption during their cosmic propagation.

1. Neutrinos can be produced in the nuclear reactions generating energy in stars. For example, the Sun emits about 2×10^{38} neutrinos/s. The first detection of neutrinos from the Sun happened in the 1960s. The deficit of solar neutrinos with respect to the flux expected from the energy released by the Sun paved the way to the discovery of neutrino oscillations and thus, ultimately, of a nonzero neutrino mass (see Chaps. 4 and 9).
2. Neutrinos should be produced in the most violent phenomena, including the Big Bang, supernovae, and the accretion of supermassive black holes. The burst of neutrinos produced in a galactic core-collapse supernova is detectable with detectors like Super-Kamiokande and SNO; however, this has been detected only once up to now. On February 23, 1987, a neutrino burst from a supernova in the LMC, some 0.2 Mly from Earth, was observed in the proton-decay detectors Kamiokande and IMB (see Sect. 10.4.3).
3. Neutrinos are the main output of the cooling of astrophysical objects, including neutron stars and red giants.
4. Neutrinos are produced as secondary by-products of cosmic ray collisions:

  (a) with photons or nuclei near the acceleration regions (these are "astrophysical" neutrinos, like the ones at items 2. and 3.);
  (b) with the CMB in the case of ultrahigh-energy cosmic rays suffering the GZK effect (these are called cosmogenic neutrinos, or also "GZK neutrinos," although the mechanism was proposed by Berezinsky and Zatsepin in 1969);
  (c) and also with the Earth atmosphere (they are called atmospheric neutrinos). When primary cosmic protons and nuclei hit the atmosphere, the hadronic reactions with atmospheric nuclei can produce in particular secondary pions, kaons and muons. Atmospheric neutrinos are generated then by the decay of these secondaries. The dominating processes are:

$$\pi^{\pm}(K^{\pm}) \to \mu^{\pm} + \nu_\mu(\overline{\nu}_\mu),$$
$$\mu^{\pm} \to e^{\pm} + \nu_e(\overline{\nu}_e) + \overline{\nu}_\mu(\nu_\mu). \tag{10.39}$$

For cases (a) and (b), coming gamma-rays and neutrinos both from pion decay, the gamma and neutrino fluxes are of the same order of magnitude at production – of course, the flux at the Earth might be different due to the absorption of gamma rays.

5. Finally, they are likely to be present in the decay chain of unstable massive particles, or in the annihilation of pairs of particles like dark matter particles.

Sources 2., 4. and 5. in the list above are also common to photons. However, detection of astrophysical neutrinos could help constraining properties of the primary cosmic ray spectrum more effectively than high-energy photons. Neutrinos produced by reactions of ultrahigh-energy cosmic rays can provide information on otherwise inaccessible cosmic accelerators.

Neutrino sources associated with some of nature's most spectacular accelerators however exist similar to photon sources. The program of experiments to map out the high-energy neutrino spectrum is now very active, guided by existing data on cosmic ray protons, nuclei, and γ rays, which constrain possible neutrino fluxes. In 2013, the IceCube Collaboration discovered a flux of astrophysical neutrinos with estimated energies above 1 PeV. They are the highest energy neutrinos ever observed, and they must come, directly or indirectly, from extra solar sources; at the present status, however, these events do not appear to cluster to a common source (see Sect. 10.4.3.2).

The neutrino sources just discussed are displayed in Fig. 10.23, left, according to their contributions to the terrestrial flux density. The figure includes low-energy sources, such as the thermal solar neutrinos of all flavors, and the terrestrial neutrinos—i.e., neutrinos coming from the Earth's natural radioactivity—not explicitly discussed here. Beyond the figure's high-energy limits there exist neutrino sources associated with some of nature's most energetic accelerators.

Very high energy cosmic ray protons should be, as discussed above, a source of very energetic neutrinos (10^{17}- 10^{19} eV) by, namely, its interaction with CMB photons. Theoretical predictions of the fluxes of such neutrinos as well as projected sensitivities of relevant experiments are shown in Fig. 10.23, right. Energetic nuclei may be also a source of neutrinos by its photo-desintegration ($A + \gamma \to A` + p$) followed by the interaction of the resulting protons with again the IR/optical/UV photon background. Existing data on the high-energy particle spectrum is thus one of the frontiers of neutrino astronomy.
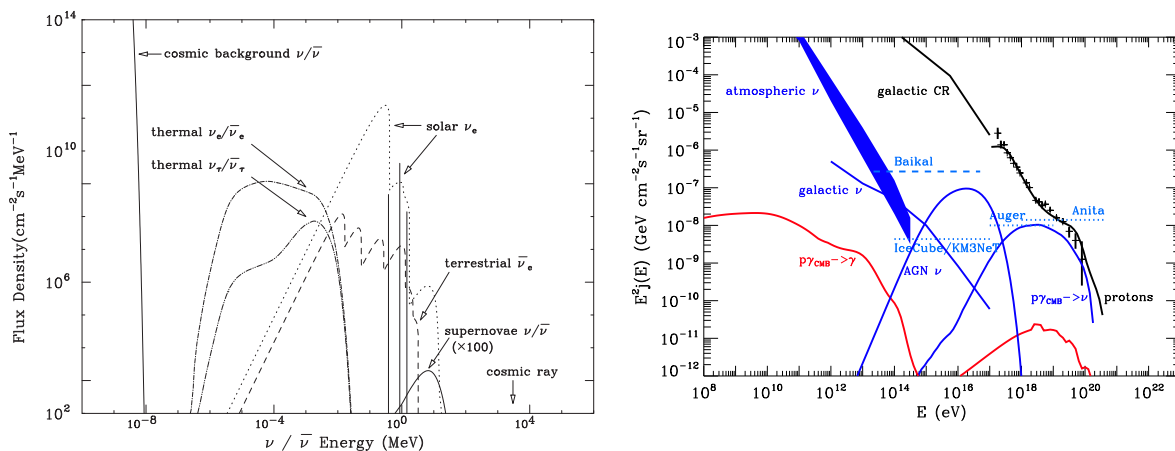
Fig.   10.23 Left: Sources   of   neutrinos   with   energies   below   1   TeV.   From   W.C.   Haxton, http://arxiv.org/abs/1209.3743/arXiv:1209.3743, to appear in Wiley's Encyclopedia of Nuclear Physics. Right: A theoretical model of high-energy neutrino sources. The figure includes experimental data, limits, and projected sensitivities to existing and planned telescopes. From G. Sigl, http://arxiv.org/abs/0612240/arXiv:0612240.

10.2.6.1 Testing if Ultra-High-Energy Cosmic Rays Originate from GRBs

IceCube has been searching for neutrinos arriving from the direction and at the time of a gamma-ray burst. After more than one thousand follow-up observations, none was found, resulting in a limit on the neutrino flux from GRBs of less than one per cent. This focuses to an alternative explanation for the sources of extragalactic cosmic rays: active galactic nuclei.

10.2.7 Sources of Gravitational Waves

The equations of Einstein's General Relativity (see Chap. 8) couple the metric of space–time with the energy and momentum of matter and radiation, thus providing the mechanism to generate gravitational waves as a consequence of radially asymmetric acceleration of masses at all scales. At the largest scales (extremely low frequencies 10^{-15}–10^{-18}Hz) the expected sources are the fluctuations of the primordial Universe. At lower scales (frequencies 10^{-4}–10^4Hz) the expected sources are:

- Stellar mass black hole binaries, of the type detected already by LIGO.
- Neutrons star binaries.
- Supernova, gamma-ray bursts, mini-mountains on neutron stars (caused by phase transitions on the crust, for example).
- Supermassive black hole binaries, formed when galaxies merge.
- Extreme mass-ratio inspirals, when a neutron stars or stellar-mass black hole collides with a supermassive black hole.

Gravitational waves are ripples in space-time propagating in free space at the velocity of light. In the weak-field approximation (linearized gravity), the local metric is deformed by the addition of a dynamical tensor term $h_{\mu\nu}$ fulfilling the equation

$$\Box h_{\mu\nu} = 0 \,. \tag{10.40}$$

This is a wave equation whose simplest solutions are transverse plane waves propagating along light rays at the speed of light. The effects of this wave in the space axes transverse to the propagation are opposite: while one expands, the other contracts and vice-versa. A gravitational wave changes the distance L between two masses placed on a transverse axis by an amount $\delta L = L\,h$, oscillating in time. The amplitude of the effect is quite tiny if the source is far (h is proportional to $1/R$ where R is the distance to the source). The relative change of the distance between two tests masses at Earth, the *strain*, which is the variable measured by gravitational wave detectors (see Sect. 4.6), is of the of the order of 10^{-23} for the Hulse-Taylor binary pulsar and of 10^{-21} for the coalescence of a binary stellar-mass black hole system (see Sect. 10.4.4).

The first gravitational wave signal (see Sect. 10.4.4), observed in 2015, was attributed to the coalescence of a stellar-mass binary black hole system. Before this detection and the following, the probability of formation of BH binaries with such masses (tens of solar masses) from the stellar collapse was believed to be quite small.

10.3 The Propagation

The propagation of cosmic messengers is influenced by the presence of magnetic fields in the Universe, and by the possible interaction with background photons and matter. The density of background photons, and of matter, can be extremely variable: it is larger within galaxies and even larger closer to acceleration sites than in the intergalactic space. We expect the same behavior for the magnetic field.

10.3.1 Magnetic Fields in the Universe

We know from studies of the Faraday rotation of polarization that the Galactic magnetic fields are of the order of a few μG; the structure is highly directional and maps exist.

Although these values may appear quite small, they are large enough to not allow galactic "charged particle astronomy". Indeed, since the Larmor radius of a particle (note that this is the same formula we previously used to compute the maximum energy reachable by a cosmic accelerator) of unit charge in a magnetic field can be written as (see Sect. 10.2),

$$\frac{R_L}{1\text{kpc}} \simeq \frac{E/1\text{EeV}}{B/1\mu\text{G}} \, , \qquad (10.41)$$

In order to "point" to the Galactic center, which is about 8 kpc from the Earth, for a Galactic field of 1μG one needs protons of energy of at least 2×10^{19} eV. The flux is very small at this energy; moreover, Galactic accelerators are not likely to accelerate particles up to this energy (remind the Hillas plot). There is thus a need to use neutral messengers to study the emission of charged cosmic rays. Unfortunately, the yield of photons at an energy of 1 TeV is only 10^{-3} times the yield of protons, and the yield of neutrinos is expected to be of the same order of magnitude or smaller. In addition, the detection of neutrinos is experimentally very challenging, as discussed in Chap. 4.

Different from Galactic magnetic fields, the origin and structure of cosmic (i.e., extragalactic) magnetic fields remain elusive. Observations have detected the presence of nonzero magnetic fields in galaxies, clusters of galaxies, and in the bridges between clusters. The determination of the strength and topology of large-scale magnetic fields is crucial also because of their role in the propagation of ultrahigh-energy cosmic rays and, possibly, on structure formation.

Large-scale magnetic fields are believed to have a cellular structure. Namely, the magnetic field B is supposed to have a correlation length λ, randomly changing its direction from one domain to another but keeping approximately the same strength. Correspondingly, a particle of unit charge and energy E emitted by a source at distance $d \gg \lambda$ performs a random walk and reaches the Earth with angular spread

$$\theta \simeq 0.25° \left(\frac{d}{\lambda}\right)^{1/2} \left(\frac{\lambda}{1\,\text{Mpc}}\right) \left(\frac{B}{1\,\text{nG}}\right) \left(\frac{10^{20}\,\text{eV}}{E}\right) \, . \qquad (10.42)$$

The present knowledge of the extragalactic magnetic fields (EGMF), also called intergalactic magnetic field (IGMF), allows setting the following constraints:

$$B \simeq 10^{-9}\text{G} - 10^{-15}\text{G} \; ; \; \lambda \simeq 0.1\,\text{Mpc} - 100\,\text{Mpc} \, . \qquad (10.43)$$

This estimate is consistent with various intergalactic magnetic field generation scenarios, including in particular generated outflows from the galaxies, and, from the experimental side, with the negative results of the search for the secondary gamma-ray emission from the e^+e^- pairs produced by the interaction of gamma rays from AGN with background photons in the Universe. In the presence of large magnetic fields, this would blur the image of distant galaxies.

10.3.2 Photon Background

The photon background in the Universe has the spectrum in Fig. 10.2. The maximum photon density corresponds to the CMB, whose number density is about 410 photons per cubic centimeter.

A region of particular interest is the so-called extragalactic background light (EBL), i.e., the light in the visible and near infrared regions. It is mainly composed by ultraviolet, optical, and near-infrared light emitted by stars throughout the whole cosmic history, and its re-emission to longer wavelengths by interstellar dust, which produces its characteristic double peak spectral energy distribution. This radiation is redshifted by the expansion of the Universe by a factor $(1 + z)$, and thus, the visible light from old sources is detected today as infrared. Other contributions to the EBL may exist such as those coming from the accretion on super-massive black holes, light from the first stars, or even more exotic sources such as products of the decay of relic dark matter particles.

The density of EBL photons in the region near the visible can be derived by direct deep field observations, and by constraints on the propagation of VHE photons (see later). A plot of the present knowledge on the density of photons in the EBL region is shown in Fig. 10.24, left. Fig. 10.24, right, shows a summary of the estimated photon number density of the background photons as composed by the radio background, the CMB, and the infrared/optical/ultraviolet background (EBL).
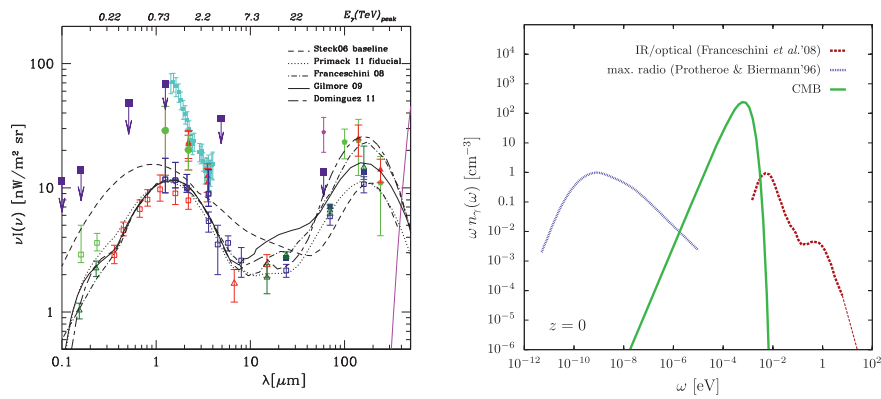
Fig. 10.24 Left: Spectral energy distribution of the EBL as a function of the wavelength and energy. Open symbols correspond to lower limits from galaxy counts while filled symbols correspond to direct estimates. The curves show a sample of different recent EBL models, as labeled. On the upper axis the TeV energy corresponding to the peak of the $\gamma\gamma$ cross section is plotted. From L. Costamante, IJMPD 22 (2013) 1330025. Right: A summary of our knowledge about the density of background photons in intergalactic space, from the radio region to the CMB, to the infrared/optical/ultraviolet region. From M. Ahlers et al., Astropart. Phys. 34 (2010) 106.
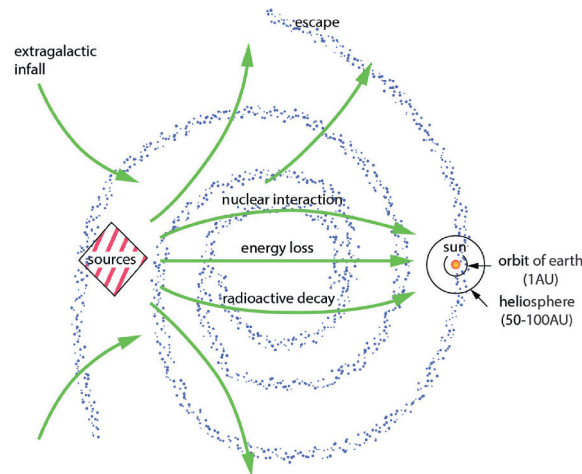
Fig. 10.25 Galactic cosmic ray propagation.

10.3.3 Propagation of Charged Cosmic Rays

The presence of magnetic fields in the Universe limits the possibility to investigate sources of emission of charged cosmic rays, as they are deflected by such fields. The propagation is affected as well by the interaction with backgroung photons and matter.

10.3.3.1 Propagation of Galactic Cosmic Rays and Interaction with the Interstellar Medium

Cosmic rays produced in distant sources have a long way to cross before reaching Earth. Those produced in our Galaxy (Fig. 10.25) suffer diffusion in magnetic fields of the order of a μG, convection by Galactic winds, spallation[5] in the interstellar medium, radioactive decays, as well as energy losses or gains (reacceleration). At some point they may arrive to Earth or just escape the Galaxy. Low-energy cosmic rays stay within the Galaxy for quite long times. Typical values of confinement times of 10^7 years are obtained measuring the ratios of the abundances of stable and unstable isotopes of the same element (for instance $^7Be/^{10}Be$, see below).

---

[5] The spallation (or fragmentation) process is the result of a nucleus-nucleus collision, in which the beam fragments into lighter nuclei.
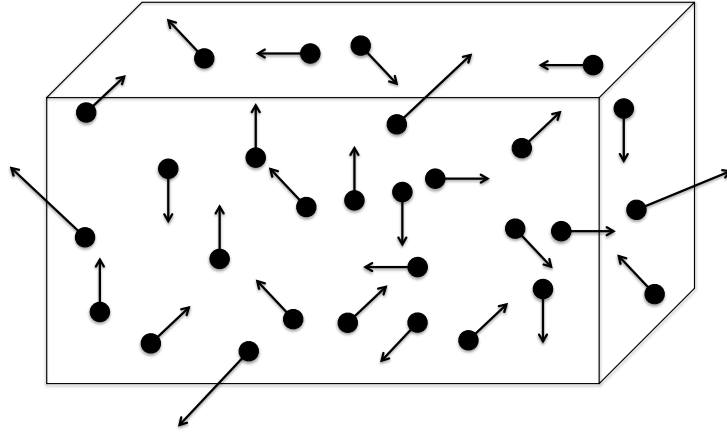
Fig. 10.26 The leaky box model: a sketch.

All these processes must be accounted in coupled transport equations involving the number density N_i of each cosmic ray species of atomic number Z_i and mass number A_i as a function of position, energy and time. These differential equations, can, for instance, be written as:

$$\frac{\partial N_i}{\partial t} = C_i + \boldsymbol{\nabla} \cdot (D\boldsymbol{\nabla} N_i - \mathbf{V} N_i) + \frac{\partial}{\partial E} \left(b\left(E\right) N_i \right) +$$

$$- \left(n\beta_i c\sigma_i^{\text{spall}} + \frac{1}{\gamma_i \tau_i^{\text{decay}}} + \frac{1}{\hat{\tau}_i^{\text{esc}}} \right) N_i +$$

$$+ \sum_{j>i} \left(n\beta_j c\sigma_{ji}^{\text{spall}} + \frac{1}{\gamma_j \tau_{ji}^{\text{decay}}} \right) N_j . \tag{10.44}$$

In the above equation:

- The term C_i on the right side accounts for the sources (injection spectrum).
- The second term accounts for diffusion and convection:

  - $\boldsymbol{\nabla} \cdot (D\boldsymbol{\nabla} N)$ describes diffusion: when at a given place N is high compared to the surroundings (a local maximum of concentration), particles will diffuse out and their concentration will decrease. The net diffusion is proportional to the Laplacian of the number density through a parameter D called diffusion coefficient or diffusivity, whose dimensions are a length squared divided by time;
  - $(\boldsymbol{\nabla} \cdot \mathbf{V})N$ describes convection (or advection), which is the change in density because of a flow with velocity $\mathbf{V}$.

- The third term accounts for the changes in the energy spectrum due to energy losses or reacceleration – we assume that energy is lost, or gained, at a rate $dE/dt = -b(E)$.
- The fourth term accounts for the losses due to spallation, radioactive decays, and probability of escaping the Galaxy. n is the number density of the interstellar medium (ISM).
- The fifth term accounts for the gains due to the spallation or decays of heavier elements.

These equations may thus include all the physics process and all spatial and energy dependence but the number of parameters is large and the constraints from experimental data (see below) are not enough to avoid strong correlations between them. The solutions can be obtained in a semi-analytical way or numerically using sophisticated codes (e.g., GALPROP), where three-dimensional distributions of sources and the interactions with the ISM can be included.

Simpler models, like for example "leaky box" models, are used to cope with the main features of the data. In the simplest version the leaky box model consists in a volume (box) where there are sources uniformly distributed and charged cosmic rays freely propagate with some probability of escaping from the walls (see Fig. 10.26). Diffusion and convection effects are incorporated in the escape probability (lifetime). The stationary equation of the leaky box can be written as:

$$0 \simeq C_i - N_i \left(n\beta_i c\sigma_i^{\text{spall}} + \frac{1}{\gamma_i \tau_i^{\text{decay}}} + \frac{1}{\tau_i^{\text{esc}}} \right) + \sum_{j>i} N_j \left(n\beta_j c\sigma_{ji}^{\text{spall}} + \frac{1}{\gamma_j \tau_{ji}^{\text{decay}}} \right) . \tag{10.45}$$

Here once again the first term on the right side accounts for the sources and the second and the third, respectively, for the losses (due to spallation, radioactive decays, and escape probability) and the gains (spallation or decays of heavier elements). In a first approximation, the dependence of the escape time on the energy and the charge of the nucleus can be computed from the diffusion equations, the result being $\tau_i^{\text{esc}} \underset{\sim}{\propto} E^{-\delta}/Z_i$. For the values of size and magnetic field typical of the Milky Way, $\delta \sim 0.6$.

All these models are adjusted to the experimental data and in particular to the energy dependence of the ratios of secondary elements (produced by spallation of heavier elements during their propagation) over primary elements (produced directly at the sources) as well as the ratios between unstable and stable isotopes of the same element (see Fig. 10.27). Basically all nuclei heavier than He (at primordial nucleosynthesis only H and He nuclei were present, with a ratio 3:1) are produced by nuclear fusion inside stars, generating energy to support them. Nuclear fusion proceeds up to the formation of nuclei with $A < 60$; stellar nucleosynthesis, while producing carbon, nitrogen and oxygen, does not increase the abundance of light nuclei (lithium, beryllium, and boron). Heavier elements up to iron are only synthesized in massive stars with $M > 8M_\odot$. Once Fe becomes the primary element in the core of a star, further compression does not ignite nuclear fusion anymore; the star is unable to thermodynamically support its outer envelope and initiates its gravitational collapse and its eventual explosion; nuclei formed during stellar nucleosynthesis are released in the Galaxy and can be recycled for the formation of new stars. The secondary abundances are tracers of spallation processes of primary CRs with the ISM. The unstable secondary nuclei that live long enough to be useful probes of CRs propagation are ^{10}Be ($\tau \sim 2.2$ Myr), ^{26}Al ($\tau \sim 1.2$ Myr), ^{36}Cl ($\tau \sim 0.4$ Myr), and ^{54}Mn ($\tau \sim 0.9$ Myr). The most used probe is ^{10}Be which has a lifetime similar to the escape time of 10^7 years from the Galaxy and which is produced abundantly in the fragmentation of C, N, and O.
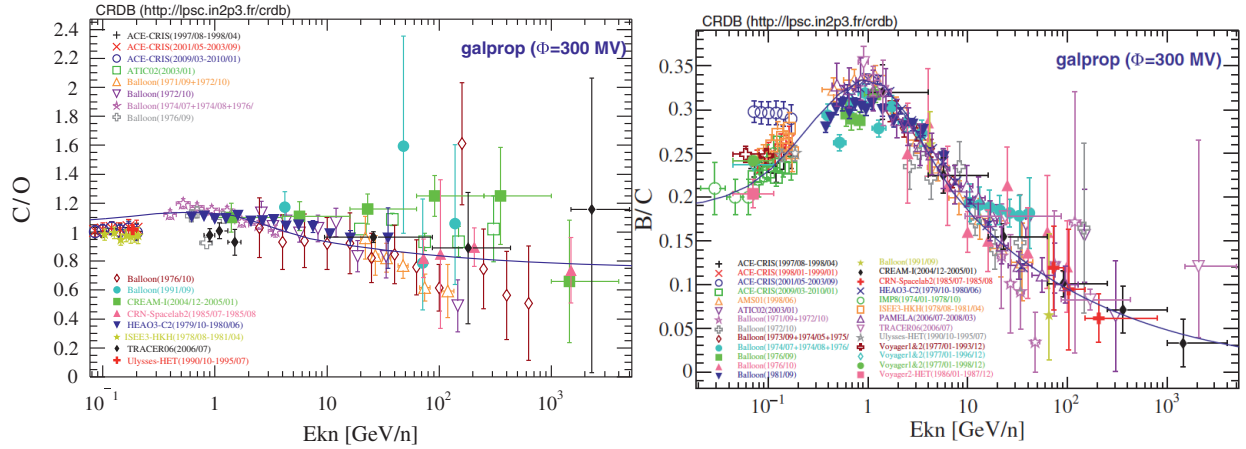
Fig. 10.27 Left:The C/O ratio (primary/primary) as a function of energy. Right: B/C (secondary over primary) as a function of the energy. Data points are taken from the Cosmic Ray database by Maurin et al. (2014) [http://arxiv.org/abs/1302.5525/arXiv:1302.5525]. The full lines are fits using the GALPROP model with standard parameters. Reference: http://galprop.stanford.edu.

We can further simplify the last equation depending if we are dealing with primary or secondary CR: for primaries we can neglect spallation feed-down (i.e., they are not produced by heavier CR), while for secondaries we can neglect production by sources ($C_i = 0$). For example, let us assume now a primary cosmic nucleus P at speed β and energy E, assumed stable (most nuclei are stable, one exception being Be which is unstable through beta decay). The equation can be written as:

$$\frac{N_P(E)}{\tau^{\text{esc}}(E)} \simeq C_P(E) - \frac{\beta c \rho_H N_P(E)}{\lambda_P(E)} \implies N_P(E) \simeq \frac{C_P(E)}{1/\tau^{\text{esc}}(E) + \beta c \rho_H / \lambda_P(E)}$$

where $\rho_H = nm_H$ is the density of targets and λ_P is the mean free path in g/cm^2.

While τ^{esc} is the same for all nuclei with same rigidity at the same energy, λ depends on the mass of the nucleus. The equation suggests that at low energies the spectra for different primary nuclei can be very

different (e.g. for Fe interaction losses dominate over escape losses), but ratios should be approximately constant at high energies if particles come from the same source.

For high-energy protons with interaction lengths λ_p much larger than the escape length, the equation can be even further simplified to

$$N_p(E) \simeq C_p(E)\tau^{\mathrm{esc}}(E)$$

and if $C_p(E) \propto E^{-2}$ (first order Fermi acceleration mechanism) we expect $N_p(E) \propto E^{-2.6}$.

Secondary/primary ratios (Fig. 10.27, right) show a strong energy dependence at high energies as a result of the increase of the escape probability, while primary/primary ratios (Fig. 10.27, left) basically do not depend on energy. By measuring primary/primary and secondary/primary ratios as a function of energy we can infer the propagation and diffusion properties of cosmic rays.

One should note that in the propagation of electrons and positrons the energy losses are much higher (dominated by synchrotron radiation and inverse Compton scattering) and the escape probability much higher. Thus leaky box models do not apply to electrons and positrons. Primary TeV electrons lose half their total energy within a distance smaller than few hundreds parsec from the source.

10.3.3.2 Extragalactic Cosmic Rays: The GZK Cutoff and the Photodisintegration of Nuclei

Extragalactic cosmic rays might cross large distances (tens or hundreds of Mpc) in the Universe. Indeed the Universe is full of CMB photons ($n_\gamma \sim 410$ photons/cm^3—see Chap. 8) with a temperature of $T \sim 2.73$ K ($\sim 2\times10^{-4}$ eV). Greisen and Zatsepin, and Kuzmin, realized independently early in 1966 that for high-energy protons the inelastic interaction

$$p \, \gamma_{CMB} \to \Delta^+ \to p \, \pi^0 \, (n \, \pi^+)$$
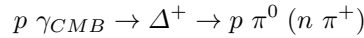
is likely leading to a strong decrease of the proton interaction length. The proton threshold energy for the process is called the "GZK cutoff"; its value is given by relativistic kinematics:

$$(p_p + p_\gamma)^2 = (m_p + m_\pi)^2 \implies E_p = \frac{m_\pi^2 + 2m_p m_\pi}{4 \, E_\gamma} \simeq 6 \times 10^{19} \text{ eV} \ . \tag{10.46}$$

The pion photoproduction cross section, $\sigma_{\gamma p}$, reaches values as large as $\sim$500 μb just above the threshold (with a plateau for higher energies slightly above $\sim$100 μb). The mean free path of the protons above the threshold is thus:

$$\lambda_p \simeq \frac{1}{n_\gamma \, \sigma_{\gamma p}} \simeq 10 \text{ Mpc} \,. \tag{10.47}$$

In each GZK interaction the proton looses on average around 20 % of its initial energy.

A detailed computation of the effect of such cutoff on the energy spectrum of ultrahigh-energy cosmic ray at Earth would involve not only the convolution of the full CMB energy spectrum with the pion photoproduction cross section but also the knowledge of the sources, their location and energy spectrum as well as the exact model of expansion of the Universe (CMB photons are redshifted). An illustration of the energy losses of protons as a function of their propagation distance is shown in Fig. 10.28 without considering the expansion of the Universe. Typically, protons with energies above the GZK threshold energy after 50–100 Mpc loose the memory of their initial energy and end up with energies below the threshold.

The decay of the neutral and charged pions produced in these GZK interactions will originate, respectively, high-energy photons and neutrinos which would be a distinctive signature of such processes.

At a much lower energy ($E_p \sim 2 \, 10^{18}$ eV) the conversion of a scattered CMB photon into an electron–positron pair may start to occur, what was associated by Hillas and Berezinsky to the existence of the ankle (this is the so-called "dip model", Sect. 10.4.1).

Heavier nuclei interacting with the CMB and Infrared Background (IRB) photons may disintegrate into lighter nuclei and typically one or two nucleons. The photodisintegration cross section is high (up to $\sim$100 mb) and is dominated by the Giant Dipole resonance with a threshold which is a function of the nuclei binding energy per nucleon (for Fe the threshold of the photon energy in the nuclei rest frame is $\sim$10 MeV). Stable nuclei thus survive longer. The interaction length of Fe, the most stable nucleus, is, at the GZK energy, similar to the proton GZK interaction length. Lighter nuclei have smaller interaction lengths and thus the probability of interaction during their way to Earth is higher.
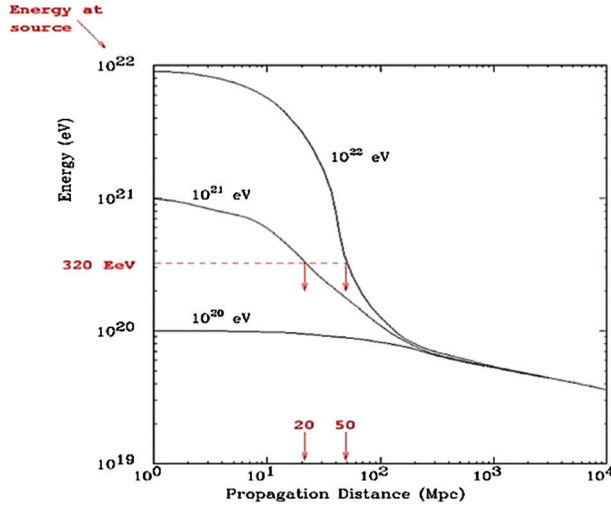
Fig. 10.28 Proton energy as a function of the propagation distance. From J.W. Cronin, Nucl. Phys. B Proc. Suppl. 28B (1992) 213.

10.3.4 Propagation of Photons

Once produced, VHE photons must travel towards the observer. Electron–positron (e^-e^+) pair production in the interaction of VHE photons off extragalactic background photons is a source of opacity of the Universe to γ rays whenever the corresponding photon mean free path is of the order of the source distance or smaller.

The dominant process for the absorption is pair-creation

$$\gamma + \gamma_{\text{background}} \to e^+ + e^- \; ;$$

the process is kinematically allowed for

$$\epsilon > \epsilon_{\text{thr}}(E, \varphi) \equiv \frac{2\, m_e^2\, c^4}{E\,(1 - \cos\varphi)} \; , \tag{10.48}$$

where φ denotes the scattering angle, m_e is the electron mass, E is the energy of the incident photon and ϵ is the energy of the target (background) photon. Note that E and ϵ change along the line of sight in proportion of $(1+z)$ because of the cosmic expansion. The corresponding cross section, computed by Breit and Wheeler in 1934, is

$$\sigma_{\gamma\gamma}(E, \epsilon, \varphi) = \frac{2\pi\alpha^2}{3m_e^2} W(\beta) \simeq 1.25 \cdot 10^{-25}\, W(\beta)\, \text{cm}^2 \; , \tag{10.49}$$

with

$$W(\beta) = \left(1 - \beta^2\right)\left[2\beta\left(\beta^2 - 2\right) + \left(3 - \beta^4\right)\ln\left(\frac{1+\beta}{1-\beta}\right)\right] \; .$$

The cross section depends on E, ϵ and φ only through the speed β—in natural units—of the electron and of the positron in the center-of-mass

$$\beta(E, \epsilon, \varphi) \equiv \left[1 - \frac{2\, m_e^2\, c^4}{E\epsilon\,(1 - \cos\varphi)}\right]^{1/2} \; , \tag{10.50}$$

and Eq. 10.48 implies that the process is kinematically allowed for $\beta^2 > 0$. The cross section $\sigma_{\gamma\gamma}(E, \epsilon, \varphi)$ reaches its maximum $\sigma_{\gamma\gamma}^{max} \simeq 1.70 \cdot 10^{-25}\, \text{cm}^2$ for $\beta \simeq 0.70$. Assuming head-on collisions ($\varphi = \pi$), it follows that $\sigma_{\gamma\gamma}(E, \epsilon, \pi)$ gets maximized for the background photon energy

$$\epsilon(E) \simeq \left(\frac{500\,\text{GeV}}{E}\right)\text{eV} \; , \tag{10.51}$$
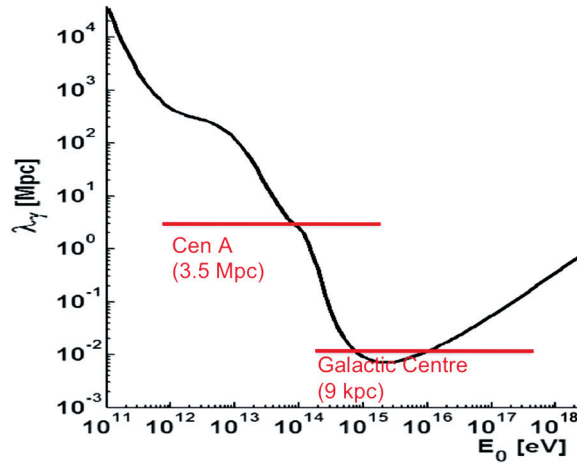
Fig. 10.29 Mean free path as a function of the photon energy, at $z = 0$. Adapted from A. de Angelis, G. Galanti, M. Roncadelli, MNRAS 432 (2013) 3245.

where E and ϵ correspond to the same redshift. For an isotropic background of photons, the cross section is maximized for background photons of energy:

$$\epsilon(E) \simeq \left(\frac{900 \, \text{GeV}}{E} \right) \, \text{eV} \,. \tag{10.52}$$

Explicitly, the situation can be summarized as follows:

- For $10 \, \text{GeV} \le E < 10^5 \, \text{GeV}$ the EBL plays the leading role in the absorption. In particular, for $E \sim 10 \, \text{GeV}$ $\sigma_{\gamma\gamma}(E, \epsilon)$—integrated over an isotropic distribution of background photons—is maximal for $\epsilon \sim 90 \, \text{eV}$, corresponding to far-ultraviolet soft photons, whereas for $E \sim 10^5 \, \text{GeV}$ $\sigma_{\gamma\gamma}(E, \epsilon)$ is maximal for $\epsilon \sim 9 \cdot 10^{-3} \, \text{eV}$, corresponding to soft photons in the far-infrared.
- For $10^5 \, \text{GeV} \le E < 10^{10} \, \text{GeV}$ the interaction with the CMB becomes dominant.
- For $E \ge 10^{10} \, \text{GeV}$ the main source of opacity of the Universe is the radio background.

The upper x-axis of Fig. 10.24, left, shows the energy of the incoming photon for which the cross section of interaction with a photon of the wavelength as in the lower x-axis is maximum.

From the cross section in Eq. 10.49, neglecting the expansion of the Universe, one can compute a mean free path (Fig. 10.29); for energies smaller than some 10 GeV this is larger than the Hubble radius, but it becomes comparable with the distance of observed sources at energies above 100 GeV.

The attenuation suffered by observed VHE spectra can thus be used to derive constraints on the EBL density. Specifically, the probability P for a photon of observed energy E to survive absorption along its path from its source at redshift z to the observer plays the role of an attenuation factor for the radiation flux, and it is usually expressed in the form:

$$P = e^{-\tau(E,z)} \,. \tag{10.53}$$

The coefficient $\tau(E, z)$ is called *optical depth*.

To compute the optical depth of a photon as a function of its observed energy E and the redshift z of its emission one has to take into account the fact that the energy E of a photon scales with the redshift z as $(1 + z)$; thus when using Eq. 10.49 we must treat the energies as function of z and evolve $\sigma\big(E(z), \epsilon(z), \theta\big)$ for $E(z) = (1 + z)E$ and $\epsilon(z) = (1 + z)\epsilon$, where E and ϵ are the energies at redshift $z = 0$. The optical depth is then computed by convoluting the photon number density of the background photon field with the cross section between the incident γ ray and the background target photons, and integrating the result over the distance, the scattering angle and the energy of the (redshifted) background photon:
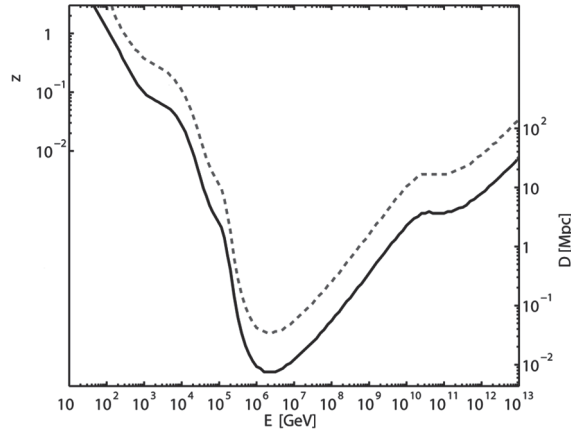
Fig. 10.30 Curves corresponding to the gamma ray horizon $\tau(E, z) = 1$ (lower) and to a survival probability of $e^{-\tau(E,z)} = 1\%$ (upper). Adapted from A. de Angelis, G. Galanti, M. Roncadelli, MNRAS 432 (2013) 3245.

$$\tau(E, z) = \int_0^z dl(z) \int_{-1}^1 d\cos\theta \frac{1 - \cos\theta}{2} \times$$
$$\times \int_{\frac{2(m_e c^2)^2}{E(1 - \cos\theta)}}^{\infty} d\epsilon(z) \; n_\epsilon\big(\epsilon(z), z\big) \; \sigma(E(z), \epsilon(z), \theta) \qquad (10.54)$$

where θ is the scattering angle, $n_\epsilon\big(\epsilon(z), z\big)$ is the density for photons of energy $\epsilon(z)$ at the redshift z, and $l(z) = c \, dt(z)$ is the distance as a function of the redshift, defined by

$$\frac{dl}{dz} \;=\; \frac{c}{H_0} \frac{1}{(1 + z) \left[(1 + z)^2 (\Omega_M \, z + 1) - \Omega_\Lambda \, z(z + 2)\right]^{\frac{1}{2}}} \;. \qquad (10.55)$$

In the last formula (see Chap. 8) H_0 is the Hubble constant, Ω_M is the matter density (in units of the critical density, ρ_c) and Ω_Λ is the "dark energy" density (in units of ρ_c); therefore, since the optical depth depends also on the cosmological parameters, its determination constrains the values of the cosmological parameters if the cosmological emission of galaxies is known.

The energy dependence of τ leads to appreciable modifications of the observed source spectrum (with respect to the spectrum at emission) even for small differences in τ, due to the exponential dependence described in Eq. 10.53. Since the optical depth (and consequently the absorption coefficient) increases with energy, the observed flux results steeper than the emitted one.

The *horizon* or *attenuation edge* for a photon of energy E is defined as the distance corresponding to the redshift z for which $\tau(E, z) = 1$, that gives an attenuation by a factor $1/e$ (see Fig. 10.30).

Other interactions than the one just described might change our picture of the attenuation of γ rays, and they are presently subject of intense studies, since the present data on the absorption of photons show some tension with the pure QED picture: from the observed luminosity of VHE photon sources, the Universe appears to be more transparent to γ rays than expected. One speculative explanation could be that γ rays might transform into sterile or quasi-sterile particles (like, for example, the axions which have been described in Chap. 8); this would increase the transparency by effectively decreasing the path length. A more detailed discussion will be given at the end of this chapter.

Mechanisms in which the absorption is changed through violation of the Lorentz invariance are also under scrutiny; such models are particularly appealing within scenarios inspired by quantum gravity (QG).

10.3.5 Propagation of Neutrinos

The neutrino cross section is the lowest among elementary particles. Neutrinos can thus travel with the smallest interaction probability and are the best possible astrophysical probe.
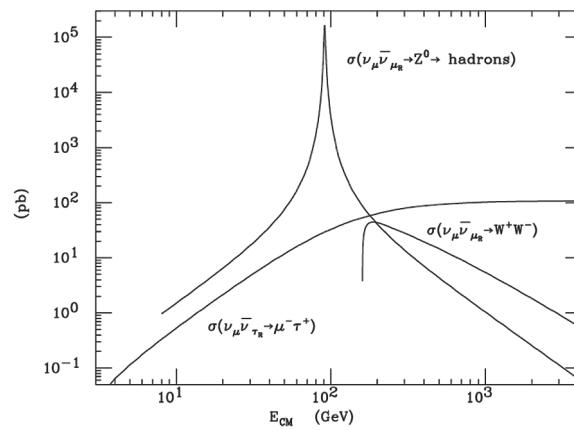
Fig. 10.31 $\nu\nu_c$ inelastic cross section as a function of the interaction center of mass. From D. Fargion and B. Mele, http://arxiv.org/abs/astro-ph/9902024/arXiv:astro-ph/9902024.

Neutrinos of energies up to 10^{16} eV (which is the largest possible detectable energy, given the hypothesis of fluxes comparable with the photon fluxes, and the maximum size of neutrino detectors, of the order of a cubic kilometer) in practice travel undisturbed to the Earth.

On the other hand extremely high energetic neutrinos, if ever they exist in the Universe, will suffer a GZK-like interaction with the cosmological neutrinos ν_c. Indeed, the $\nu\nu_c$ cross section increases by several orders of magnitude whenever the center-of-mass energy of this interaction is large enough to open the inelastic channels as it is shown in Fig. 10.31. For instance, at $E_\nu \sim 10^{21}(4eV/m_\nu)$ the s-channel $\nu\nu_c \to Z$ is resonant. Thus, the Universe for these neutrinos of extreme energies becomes opaque.

10.3.6 Propagation of Gravitational Waves

Gravitational waves are oscillations of the space–time metrics which, accordingly to general relativity, propagate in the free space with the speed of light in the vacuum. Their coupling with matter and radiation is extremely weak and they propagate without significant attenuation, scattering, or dispersion in their way through the Universe. By energy conservation their amplitude follows a $1/R$ dependence where R is the distance to the source. A very good reference for a detailed discussion is $[F10.4]]$ by K. S. Thorne.

Note that the speed of gravitational waves is not the speed of the gravitational field in the case, e.g., of a planet orbiting around the Sun. The speed of the propagation of the information on physical changes in the gravitational (or electromagnetic) field should not be confused with changes in the behavior of static fields that are due to pure observer effects. The motion of an observer with respect to a static charge and its extended static field does not change the field, which extends to infinity, and does not propagate. Irrespective of the relative motion the field points to the "real" direction of the charge, at all distances from the charge.

10.4 More Experimental Results

10.4.1 Charged Cosmic Rays: Composition, Extreme Energies, Correlation with Sources

Charged cosmic rays arrive close to the Solar System after being deflected from the galactic magnetic fields (about 1 μG in intensity) and possibly by extragalactic magnetic fields, if they are of extragalactic origin; when getting closer to the Earth they start interacting with stronger magnetic fields—up to $\mathcal{O}(1G)$ at the Earth's surface, although for shorter distances. Fluxes of charged particles at lower energies, below 1 GeV, can thus be influenced, e.g., by the solar cycle which affects the magnetic field from the Sun.

Cosmic rays are basically protons ($\sim$90 %) and heavier nuclei. The electron/positron flux at the top of the atmosphere is small (a few per mil of the total cosmic ray flux) but extremely interesting as it may be a
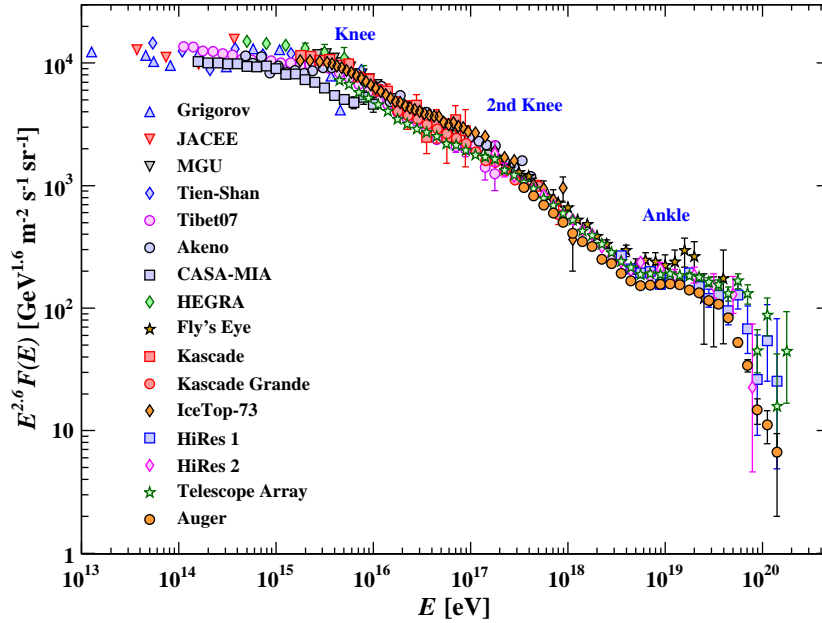
Fig. 10.32 Cosmic-ray spectrum coming from experimental measurements by different experiments; the spectrum has been multiplied by $E^{+2.6}$. The anthropomorphic interpretation should be evident. From Beatty, Matthews, and Wakely, "Cosmic Rays", in Review of Particle Physics, 2018.

signature of unknown astrophysical or Dark Matter sources (see Chap. 8). Antiprotons fluxes are even smaller (about four orders of magnitude) and so far compatible with secondary production by hadronic interactions of primary cosmic rays with the interstellar medium. Up to now there is no evidence for the existence of heavier anti-nuclei (in particular anti-deuterium and anti-helium) in cosmic rays.

10.4.1.1 Energy Spectrum

The energy spectrum of charged cosmic rays reaching the atmosphere spans over many decades in flux and energy, as we have seen in the beginning of this Chapter (Fig. 10.1).

At low energies, $E \lesssim 1$ GeV, the fluxes are high (thousands of particles per square meter per second) while there is a strong cutoff at about $10^{19.5}$ eV–at the highest energies ever observed, $E \gtrsim 10^{11}$ GeV, there is less than one particle per square kilometer per century. The cosmic rays at the end of the known spectrum have energies well above the highest beam energies attained in any human-made accelerator and their interactions on the top of the Earth atmosphere have center-of-mass energies of a few hundred TeV (the design LHC beam energy is $E = 7 \times 10^3$ GeV); at these energies, however, the flux of cosmic rays is highly suppressed. This fact affects the choice of experiments to detect cosmic rays: one can study the energies up to the knee with satellites, while above the knee one must rely on ground-based detectors. Above a few GeV the intensity of the cosmic rays flux follows basically a power law,

$$I(E) \propto E^{-\gamma}$$

with the differential spectral index γ being typically between 2.7 and 3.3. Below a few GeV, the flux is modulated by the solar activity and in particular by the magnetic field from the Sun–notice that these effects are variable in time.

The small changes in the spectral index can be clearly visualized multiplying the flux by some power of the energy. Fig. 10.32 shows a suggestive anthropomorphic representation of the cosmic ray energy spectrum

obtained multiplying the flux by $E^{+2.6}$. Two clear features corresponding to changes in the spectral index are observed. The first, called the knee, occurs around $E \simeq 5 \times 10^{15}$ eV, and it is sometimes associated to the transition from galactic to extragalactic cosmic rays; it corresponds to a steepening from a spectral index of about 2.7 to a spectral index of about 3.1. The second clear feature, denominated the "ankle," occurs around $E \simeq 5 \times 10^{18}$ eV and its nature is still controversial. Another feature, called the second knee, marks a steepening to from about 3.1 to about 3.3, at an energy of about 400 PeV.

The number of primary nucleons per GeV from about 10 GeV to beyond 100 TeV is approximately

$$\frac{dN}{dE} \simeq 1.8 \times 10^4 E^{-2.7} \frac{\text{nucleons}}{\text{m}^2\,\text{s}\,\text{sr}\,\text{GeV}} \tag{10.56}$$

where E is the energy per nucleon in GeV.

A strong suppression at the highest energies, $E \simeq 5 \times 10^{19}$ eV, is nowadays clearly established (Fig. 10.32); it may result, as explained in Sect. 10.3.3.2, from the so-called GZK mechanism due to the interaction of highly energetic protons with the Cosmic Microwave Background (CMB). However, a scenario in which an important part of the effect is a change of composition (from protons to heavier nuclei, which undergo nuclear photodisintegration[6]) and the exhaustion of the sources is not excluded as it will be discussed in Sect. 10.4.1.6.

10.4.1.2 Composition

The composition and energy spectrum of cosmic rays is not a well-defined problem: it depends on where experiments are performed. One could try a schematic separation between "primary" cosmic rays—as produced by astrophysical sources—and "secondaries"—those produced in interactions of the primaries with interstellar gas or with nuclei in the Earth's atmosphere. Lithium, beryllium and boron, for example, are very rare products in stellar nucleosynthesis, and thus are secondary particles, as well as antiprotons and positrons—if some antimatter is primary is a question of primary interest.

The interaction with the Earth's atmosphere is particularly important since it changes drastically the composition of cosmic rays. In the cases in which the flux of cosmic rays has to be measured at ground (for example, high-energy cosmic rays, at energies above hundreds GeV, where the low flux makes the use of satellites ineffective) one needs nontrivial unfolding operations to understand the primary composition. What one observes is a cascade shower generated by a particle interacting with the atmosphere, and the unfolding of the fundamental properties (nature and energy of the showering particle) requires the knowledge of the physics of the interaction at energies never studied at accelerators: experimental data are thus less clear.

Accessing the composition of cosmic rays can be done, in the region below a few TeV, at the top or above the Earth atmosphere by detectors placed in balloons or satellites able, for example, of combining the momentum measurement with the information from Cherenkov detectors, or transition radiation detectors.

The absolute and relative fluxes of the main hadronic components of cosmic rays measured directly is shown in Fig. 10.33, and compared to the relative abundances existing in the solar system. To understand this figure, one should take into account the fact that nuclei with even number of nucleons are more stable, having higher binding energy because of pairing effects.

Besides a clear deficit of hydrogen and helium in the cosmic rays compared to the composition of the Solar System, the main features from this comparison are the agreement on the "peaks" (more tightly bounded even-Z nuclei) and higher abundances for cosmic rays on the "valleys." These features can be explained within a scenario where primary cosmic rays are produced in stellar end-products, being the "valley" elements mainly secondaries produced in the interaction of the primaries cosmic rays with the interstellar medium ("spallation").

Direct composition measurements are not possible above a few hundred GeV. For extensive air shower (EAS, see Chap. 4) detectors, effective at higher energies, being able to distinguish between a shower generated by a proton or by a heavier particle is a more difficult task. Variables which may allow the disentangling between protons and heavier nuclei, as it will be discussed in Sect. 10.4.1.6, are: in ground sampling detectors,

---

[6] In the case of nuclei, the spallation cross section is enhanced due to the giant dipole resonance, a collective excitation of nucleons in nuclei due to the interaction with photons. For all nuclei but iron the corresponding mean free paths are, at these energies, much smaller than the proton GZK mean free path.
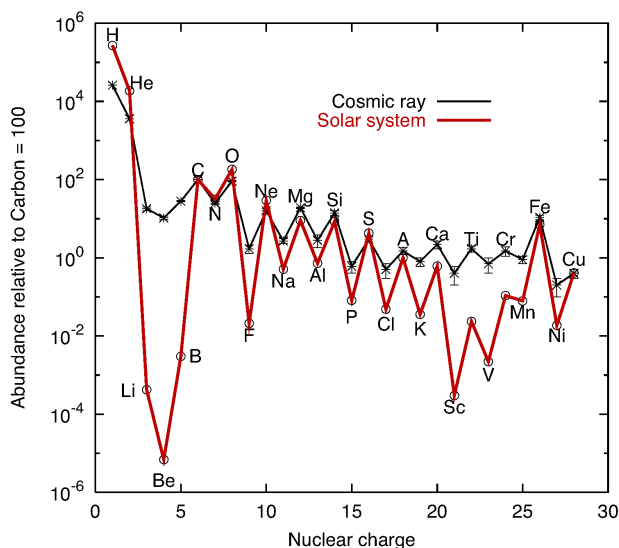
Fig. 10.33 Relative abundance of the main nuclear species present in Galactic cosmic rays and in the Solar System. Both are normalized to the abundance of C= 100, and the relevant energy range is a few hundred MeV/nucleon. From J.A. Aguilar, lectures at the Université Libre Bruxelles, 2016.

the muonic contents of the air shower; at high energies in shower detectors, the depth of the maximum of the shower (the so-called X_{max}). A summary plot including these higher energy is shown in Fig. 10.34.

There is experimental evidence that the chemical composition of cosmic rays changes after the knee region with an increasing fraction of heavy nuclei at higher energy, at least up to about 10^{18} eV (see Sect. 10.4.1.6).

10.4.1.3 Electrons and Positrons

High-energy electrons and positrons have short propagation distances (less than a few hundred parsec, as seen before) as they lose energy through synchrotron and inverse Compton processes while propagating through the Galaxy. Their spectra, which extend up to several TeV, are therefore expected to be dominated by local electron accelerators or by the decay/interactions of heavier particles nearby. Positrons in particular could be the signature of the decay of dark matter particles.

The experimental data on the flux of electrons plus positrons suggested in a recent past the possible evidence a bump-like structure (ATIC balloon experiment results) at energies between 250 and 700 GeV. These early results were not confirmed by later and more accurate instruments like the *Fermi* satellite Large Area Tracker (*Fermi*-LAT), AMS-02 and DAMPE, as it is shown in Fig. 10.35. However, either in the individual flux of positrons or in its fraction with respect to the total flux of electrons plus positrons (Fig. 10.36), an excess in the high-energy positron fraction with respect to what expected from known sources (basically the interactions of cosmic rays with the interstellar medium), first observed by PAMELA and thus called the PAMELA effect, was clearly confirmed by AMS-02.

This is indeed quite intriguing: in a matter-dominated Universe, one would expect this ratio to decrease with energy, unless specific sources of positrons are present nearby. If these sources are heavy particles decaying into final states involving positrons, one could expect the ratio to increase, and then steeply drop after reaching half of the mass of the decaying particle. If an astrophysical source of high-energy positrons is present, a smooth spectrum is expected. The present data is compatible with an hypothetical dark-matter particle with a mass of around 1 TeV, but there is not a definite answer yet. The most recent data on the abundance of high-energy pulsars nearby might justify an astrophysical explanation of this excess but not the results in antiproton observed also by AMS-02 as discussed in the next section.
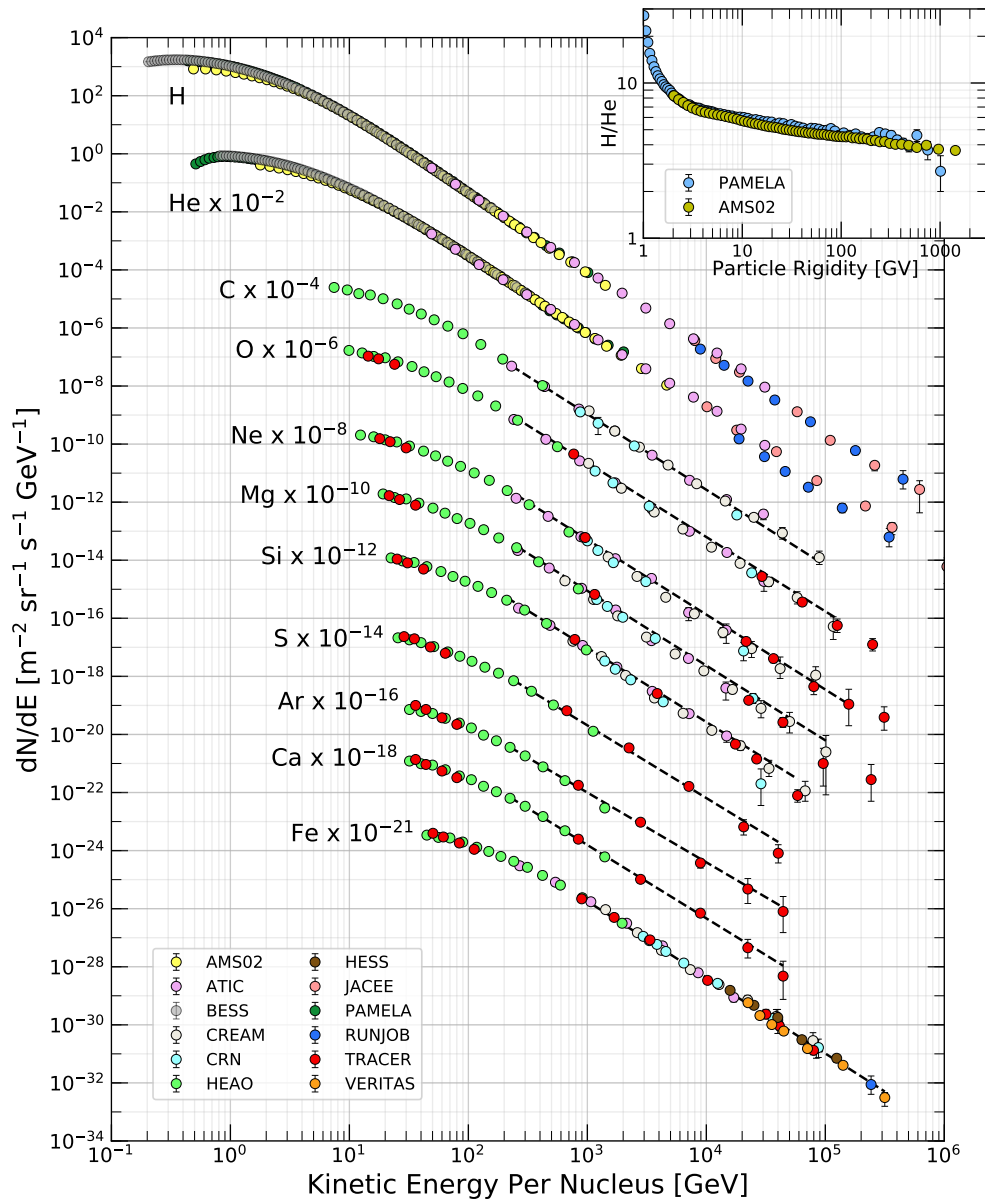
Fig. 10.34 Fluxes of nuclei of the primary cosmic radiation in particles per energy-per-nucleus plotted versus energy-per-nucleus. The inset shows the H/He ratio at constant rigidity. From Beatty, Matthews, and Wakely, "Cosmic Rays", in Review of Particle Physics, 2018.

10.4.1.4 Antiprotons

Data are shown in Fig. 10.37. The antiproton to proton ratio stays constant from 20 to 400 GeV. This behavior cannot be explained by secondary production of antiprotons from ordinary cosmic ray collisions. In contrast with the excess of positrons, the excess of antiprotons cannot be easily explained from pulsar origin. More study is needed, and this is certainly one of the next frontiers.

10.4.1.5 Cosmic Rays at the Earth's Surface: Muons

Most charged particles on the top of the atmosphere are protons; however, the interaction with the atoms of the atmosphere itself has the effect that the nature of particles reaching ground does not respect the composition of cosmic rays. Secondary muons, photons, electrons/positrons and neutrinos are produced by the interaction of charged cosmic rays in air, in addition to less stable particles. Note that the neutron/proton
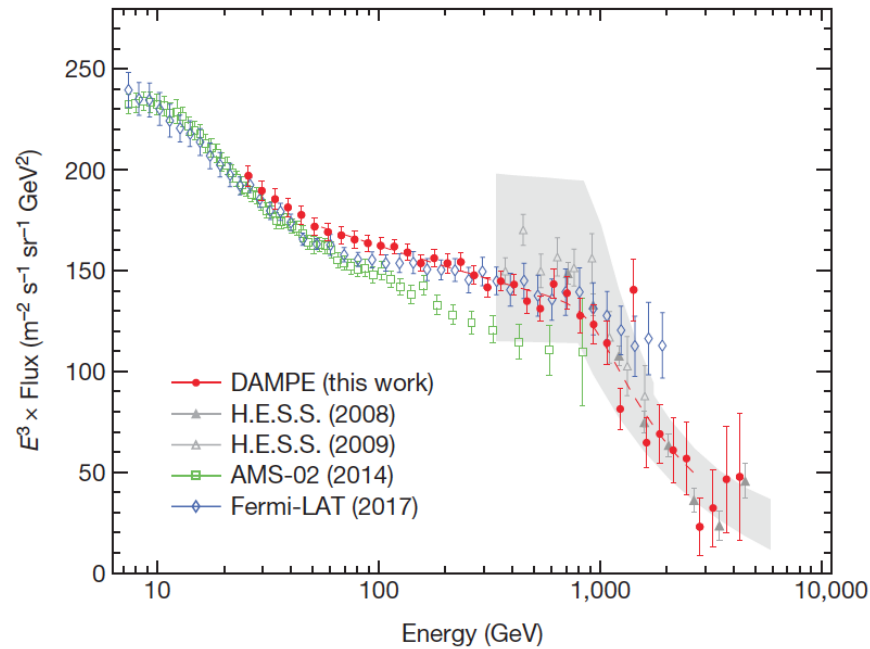
Fig. 10.35 Energy spectrum of e^+ plus e^-, multiplied by E^3. The dashed line represents a smoothly broken power-law model that best fits the DAMPE data in the range from 55 GeV to 2.63 TeV. The grey band represents the systematic error from HESS. From DAMPE Collaboration, Nature 2017, doi:10.1038/nature24475.
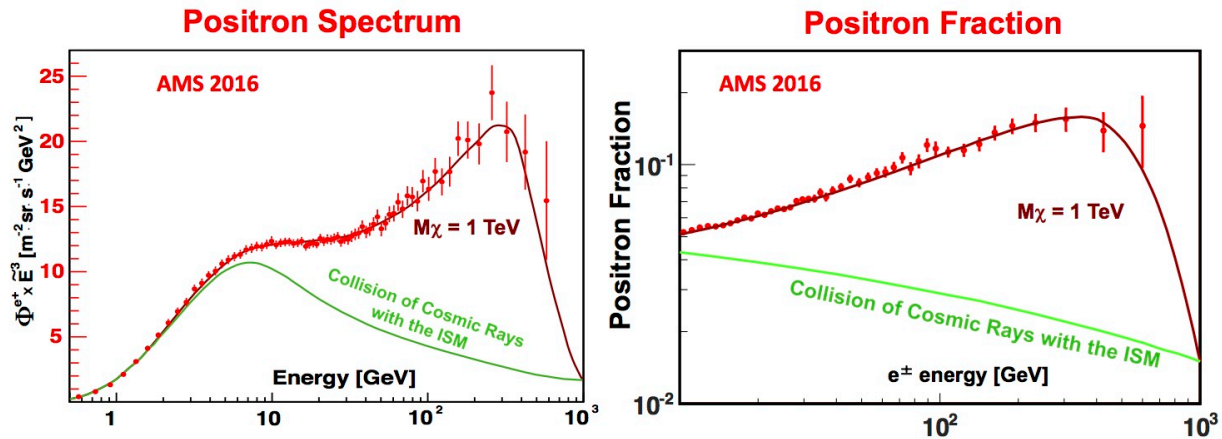
Fig. 10.36 Left: Energy spectrum of e^+ (multiplied by E^3) from AMS-02. Right: positron fraction in high-energy cosmic rays of the flux of positrons with respect to the total flux of electrons plus positrons measured from AMS-02.

ratio changes dramatically in such a way that neutrons, which are 10 % of the total at the atmosphere's surface, become roughly 1/3 at the Earth's surface.

Astrophysical muons can hardly reach the Earth's atmosphere due to their lifetime ($\tau \sim 2\,\mu$s); this lifetime is however large enough, that secondary muons produced in the atmosphere can reach the Earth's surface, offering a wonderful example of time dilation: the space crossed on average by such particles is $L \simeq c\gamma\tau$, and already for $\gamma \sim 50$ (i.e., an energy of about 5 GeV) they can travel 20, 30 km, which roughly corresponds to the atmospheric depth. Muons lose some 2 GeV by ionization when crossing the atmosphere.

Charged particles at sea level are mostly muons (see Fig. 10.38), with a mean energy of about 4 GeV.

The flux of muons from above 1 GeV at sea level is about 60 m^{-2}s^{-1}sr^{-1}. A detector looking at the horizon sees roughly one muon per square centimeter per minute. The zenith angular distribution for muons of $E \sim 3$ GeV is $\propto \cos^2\theta$, being steeper at lower energies and flatter at higher energies: low energy muons at large angles decay before reaching the surface. The ratio between μ^+ and μ^- is due to the fact that there
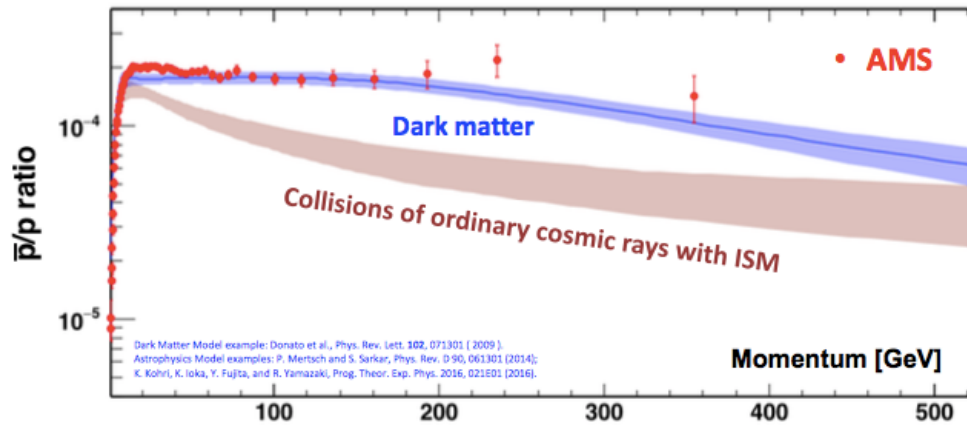
Fig. 10.37 Antiproton to proton ratio measured by AMS-02. Within the existing models of secondary production, the ratio lacks explanation.
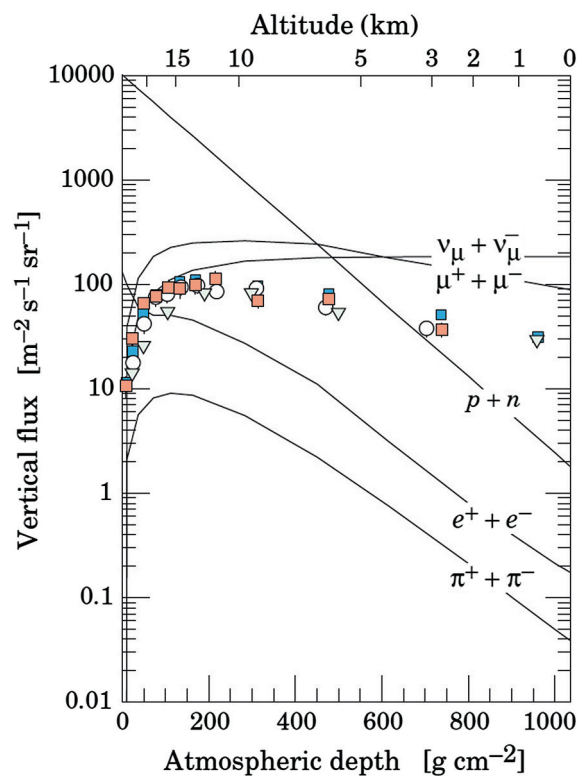
Fig. 10.38 Fluxes of cosmic rays with $E > 1$ GeV in the atmosphere as a function of height (simulation). The points show experimental measurements of negative muons. From K.A. Olive et al. (Particle Data Group), Chin. Phys. C 38 (2014) 090001.

are more π^+ than π^- in the proton-initiated showers; there are about 30 % more μ^+ than μ^- at momenta above 1 GeV/c.

A fortiori, among known particles only muons and neutrinos reach significant depths underground. The muon flux reaches 10^{-2} m^{-2} s^{-1} sr^{-1} under 1 km of water equivalent (corresponding to about 400 m of average rock) and becomes about 10^{-8} m^{-2} s^{-1} sr^{-1} at 10 km of water equivalent.

10.4.1.6 Ultrahigh-Energy Cosmic Rays

Ultra-High-Energy Cosmic Rays (UHECR) are messengers from the extreme Universe and a unique opportunity to study particle physics at energies well above those reachable at the LHC. However, their limited
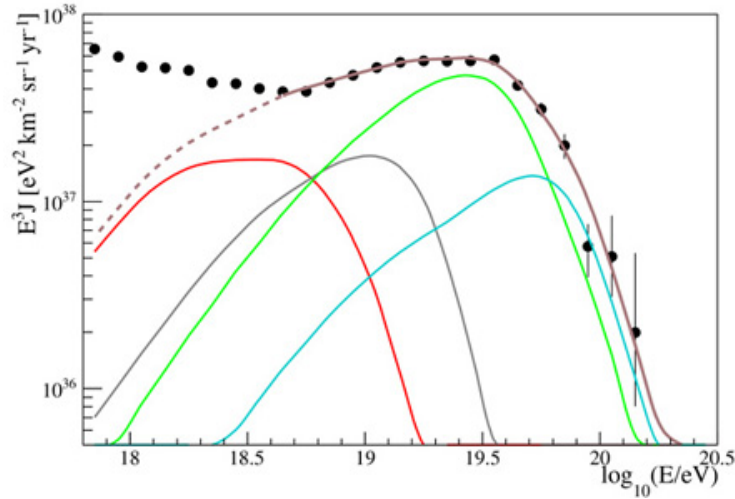
Fig. 10.39 UHECR Energy spectrum measured by the Pierre Auger Observatory (closed circles); the spectrum has been multiplied by E^3. Superposed is a fit to the sum of different components at the top of the atmosphere. The partial spectra are grouped as according to the mass number as follows: Hydrogen (red), Helium-like (grey), Carbon, Nitrogen, Oxygen (green), Iron-like (cyan), total (brown). Image credit: Pierre Auger Collaboration.

flux and their indirect detection have not yet allowed to answer to the basic, and always present, questions: Where are they coming from? What is their nature? How do they interact?

The energy spectrum of the UHECR is nowadays well measured up to 10^{20}eV (see Fig. 10.39). The strong GZK-like suppression at the highest energies may be interpreted assuming different CR composition and source scenarios. Indeed, both pure proton and mixed composition scenarios are able to describe the observed features. In the case of a pure proton scenario, the ankle would be described by the opening, at that energy, of the pair production channel in the interaction of the incoming protons with the CMB photons ($p \, \gamma_{CMB} \rightarrow p \, e^+ e^-$) (this is called the "dip model"), while the suppression at the highest energies would be described in terms of the predicted GZK effect. In the case of mixed composition scenarios such features may be described by playing with different source distributions and injection spectra, assuming that the maximum energy that each nucleus may attain, scales with its atomic number Z. An example of composition fit is given in Fig. 10.39, where the Pierre Auger Observatory data are fitted to a mixed composition scenario. The solution of such puzzle may only be found with the experimental determination of the cosmic ray composition from detailed studies on the observed characteristics of the extensive air showers.

The depth of the maximum number of particles in the shower, X_{max}, schematically represented in Fig. 10.40), is sensitive to the cross-section of the primary cosmic ray interaction in the air. Thus it can be used either to measure the cross-section, if the composition is known, or, since the cross section for a nucleus grows with its atomic number, to determine the composition, if the nuclei-air interaction cross-sections at these energies are assumed to be described correctly by the model extrapolations of the cross-sections measured at lower energies in the accelerators. Indeed, X_{max} may be defined as the sum of the depth of the first interaction X_1 and a shower development length ΔX (see Fig. 10.40):

$$X_{max} = X_1 + \Delta X \,.$$

The experimental X_{max} distribution is then the convolution of the X_1 distribution with the ΔX distribution (which has a shape similar to the X_{max} distribution) and a detector resolution function (see Fig. 10.41).The distribution of X_1, in the case of a single component composition, should be just a negative exponential, $\exp\left(-X_1/\Lambda_\eta\right)$, where Λ_η is the interaction length which is proportional to the inverse of the cosmic ray–air interaction cross section. Thus, the tail of the observed X_{max} distribution reflects the X_1 exponential distribution of the lighter cosmic ray component (smaller cross-section, deeper penetration).

The measured X_{max} distribution by the Pierre Auger collaboration in the energy bin 10^{18}–$10^{18.5}$eV for the 20 % of the most deeply penetrating showers is shown in Fig. 10.42. It follows the foreseen shape with a clear exponential tail. The selection of the most deeply penetrating showers strongly enhances the proton contents in the data sample since the proton penetrate deeply in the atmosphere than any other nuclei.

The conversion of the exponential index of the distribution tail to a value of proton-air cross section is performed using detailed Monte Carlo simulations. The conversion to proton–proton total and inelastic cross
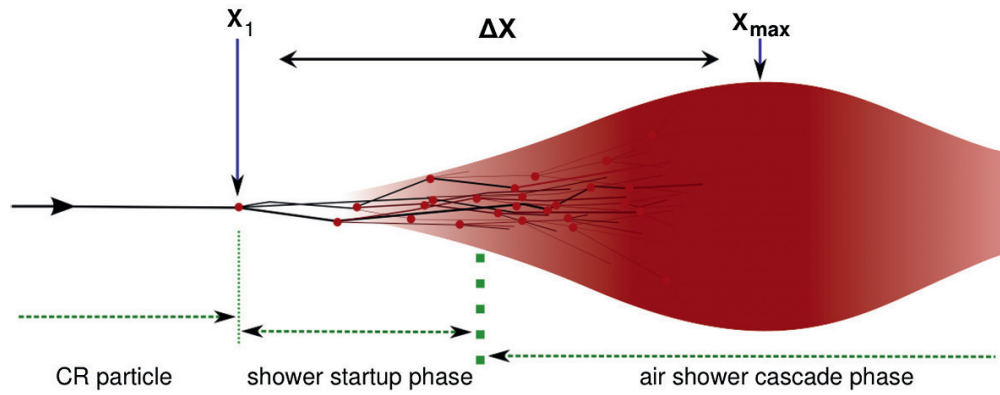
Fig. 10.40 Shower development scheme. Adapted from the Ph.D. thesis of R. Ulrich: "Measurement of the proton–air cross section using hybrid data of the Pierre Auger Observatory," http://bibliothek.fzk.de/zb/berichte/FZKA7389.pdf.
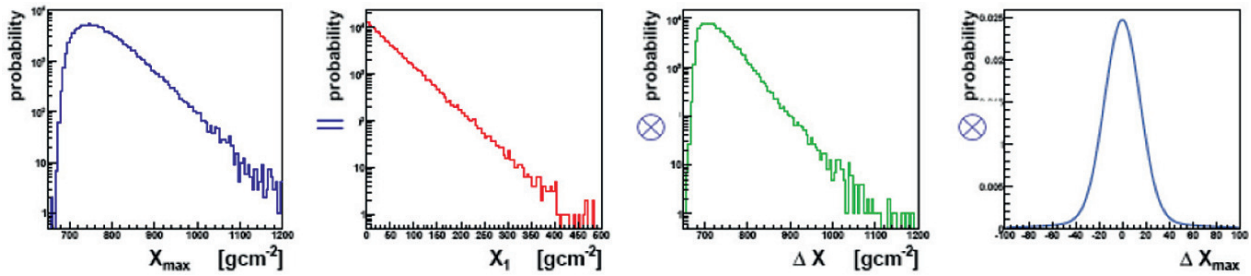
Fig. 10.41 Ingredients of the experimental X_{max} distribution. Adapted from the Ph.D. thesis of R. Ulrich: "Measurement of the proton–air cross section using hybrid data of the Pierre Auger Observatory," http://bibliothek.fzk.de/zb/berichte/FZKA7389.pdf.
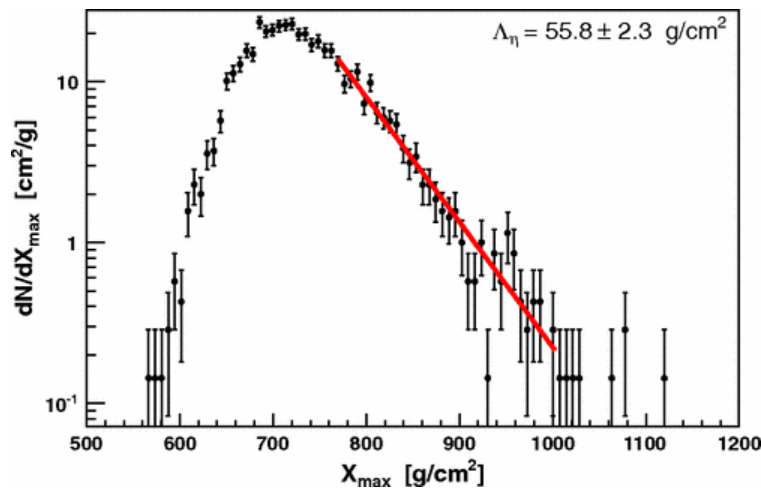
Fig. 10.42 X_{max} distribution expressed in g/cm^2 measured by the Pierre Auger Observatory in the energy interval 10^{18}–$10^{18.5}$eV. The line represents the likelihood fit performed to extract Λ_η. From P. Abreu et al., Phys. Rev. Lett. 109 (2012) 062002.

section is then done using the Glauber model which takes into account the multi-scattering probability inside the nuclei (Sect. 6.4.7). The Auger result is shown in Fig. 10.43 together with accelerator data–namely with the recent LHC results, as well as with the expected extrapolations of several phenomenological models. The experimental results confirm the evolution of the proton–proton cross section as a function of the energy observed so far, and give a strong indication that the fraction of protons in the cosmic ray "beam" is important at least up to 10^{18} eV.

The study of the first two momenta of the X_{max} distribution ($\langle X_{max} \rangle$ and the RMS) is nowadays the main tool to constrain hadronic interactions models and hopefully access the cosmic ray composition. The mean and the RMS of the X_{max} distributions measured by the Pierre Auger collaboration as a function
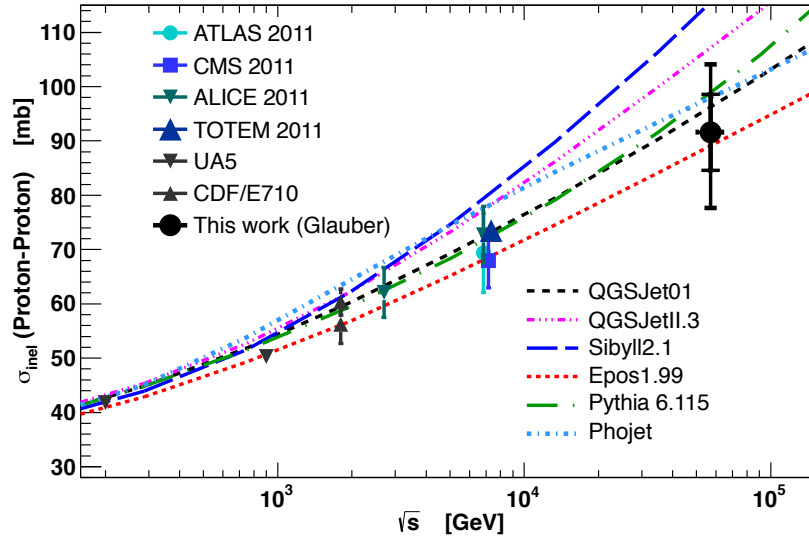
Fig. 10.43 Comparison of the inelastic proton–proton cross section derived by the Pierre Auger Observatory in the energy interval 10^{18}–$10^{18.5}$ eV to phenomenological model predictions and results from accelerator experiments at lower energies. From P. Abreu et al., Phys. Rev. Lett. 109 (2012) 062002.
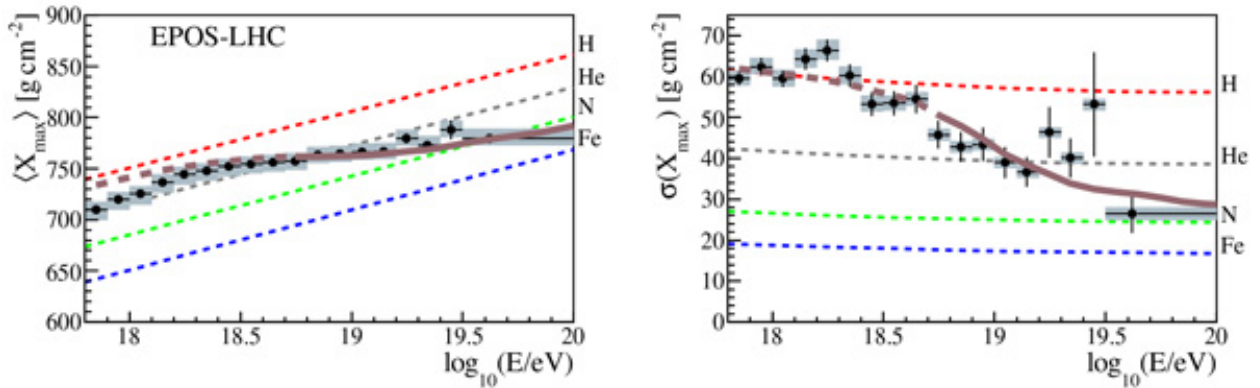
Fig. 10.44 Energy evolution of the mean (Left:) and the RMS (Right:) of the X_{max} distributions measured at the $Sp\bar{p}S$, at the LHC and by the Pierre Auger Observatory. The lines from top to bottom represent the expectations for pure proton, helium, nitrogen and iron from a simulation model tuned at the LHC energies. Credit: Auger Collaboration.

of the energy are shown in Fig. 10.44 and compared to the prediction for pure p, He, N and Fe. A fit to extract the fractions of each of these components as a function of the energy was then performed assuming several different hadronic interaction models. The results indicate evidence of a change of the cosmic ray composition from light elements (with a large fraction of protons) at lower energies to heavier elements (He or N depending on the hadronic model) but a negligible abundance of Fe at least until $10^{19.4}$ eV. However, none of the present simulation models is able to reproduce well the observed data. Combining the X_{max} results with variables related with the muonic contents of these extreme high energy EAS the tension between the measurements and the model predictions becomes even more evident.

Only qualitative and quantitative improvements in the understanding of the shower development, for example, accessing direct experimental information on the muon contents and improving the modelling of hadronic interactions in Monte Carlo simulations, may clarify this striking open question. The scenario in which the strong GZK-like suppression at the highest energies is due to the exhaustion of the sources and that the higher number of muons in the shower are due to bad modelling of the hadronic interactions is nowadays the most widely accepted. "New physics" scenarios providing, for instance, a sudden increase of the proton-proton cross section (related to the access of a new scale of interaction below the parton scale) are however not excluded.
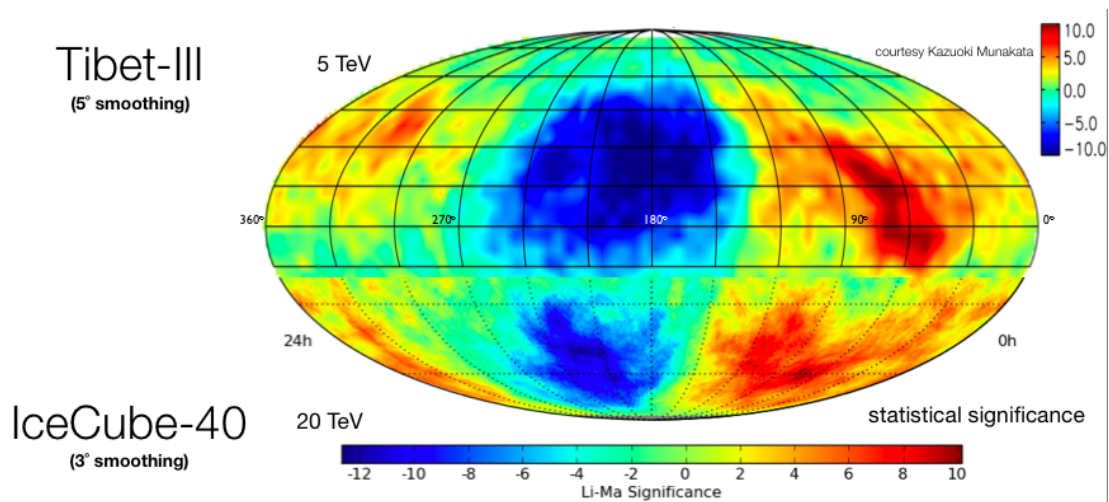
Fig. 10.45 Skymap in equatorial coordinates showing the relative intensity of multi-TeV cosmic rays arrival directions: the northern hemisphere data is from Tibet-III Air Shower Array, Amenomori M. et al., Science 314, 439, 2006, (map courtesy of Kazuoki Munakata); the southern hemisphere data is from the IceCube-40 string configuration from http://icecube.wisc.edu/ desiati/activity/anisotropy/large.

10.4.1.7 Correlation of charged cosmic rays with sources

When integrating over all energies, say, above a few GeV, the arrival direction of charged cosmic rays is basically isotropic—a fact which can find explanation in the effect of the galactic magnetic field smearing the directions–the Compton-Getting effect, a dipole anisotropy of about 0.6% resulting from the proper motion of Earth in the rest frame of cosmic ray sources, has to be subtracted. However, Milagro, IceCube, HAWC, ARGO-YBJ and the Tibet air shower array have observed additional small large-scale anisotropies (at the level of 10^{-3}), and small small-scale anisotropies (at the level of about $10^{-4}-10^{-5}$) in an energy range from a few tens of GeV to a few hundreds of TeV (see Fig. 10.45). Its origin is still under debate; the disentangling of its probable multiple causes is not easy. There is no simple correlation of anisotropies with known astrophysical objects.

At extremely high energies, instead, statistically significant anisotropies have been found – and their interpretation is straightforward.

To accelerate particles up to the ultra-high-energy region above the EeV, 10^{18} eV, one needs conditions that are present in astrophysical objects such as the surroundings of SMBHs in AGN, or transient high-energy events such as the ones generating gamma ray bursts. Galactic objects are not likely to be acceleration sites for particles of such energy, and coherently we do not observe a concentration of UHECRs in the galactic plane; in addition, the galactic magnetic field cannot confine UHECRs above 10^{18} eV within our galaxy.

Under the commonly accepted assumptions of a finite horizon (due to a GZK-like interaction) and of extragalactic magnetic fields in the range (1 nG - 1 fG), the number of sources is relatively small and thus some degree of anisotropy could be found studying the arrival directions of the cosmic rays at the highest energies. Such searches have been performed extensively in the last years either by looking for correlations with catalogs of known astrophysical objects or by applying sophisticated self-correlation algorithms at all angular scales. Indication for intermediate-scale anisotropy, namely correlated to Active Galactic Nuclei and Star-forming or Starburst Galaxies catalogs, have been reported by the Pierre Auger Observatory. At large scales,

- In about 30 000 cosmic rays with energies above 8 EeV recorded over a period of 12 years, corresponding to a total exposure of 76 800 km^2 sr year, the Pierre Auger Observatory has evidenced at more than 5.2σ a dipole anisotropy of about 6.5% towards $(\ell, b) \simeq (233°, -13°)$ (see Fig. 10.46).

  If ultrahigh-energy cosmic rays originate from an inhomogeneous distribution of sources and then diffuse through intergalactic magnetic fields, one can expect dipole amplitudes growing with energy, reaching 5% to 20% at 10 EeV. If the sources were distributed like galaxies, the distribution of which has a significant dipolar component, a dipolar cosmic-ray anisotropy would be expected in a direction similar to that of the dipole associated with the galaxies. For the infrared-detected galaxies in the 2MRS catalog[7], the flux-

---

[7] The 2MASS Redshift Survey (2MRS) maps the distribution of galaxies out to a redshift of $z \simeq 0.03$ (about 115 Mpc).
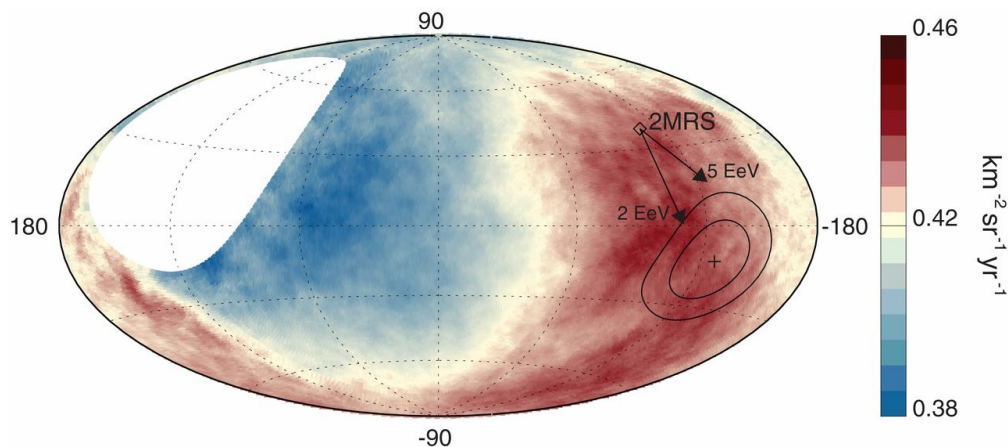
Fig. 10.46 Sky map in galactic coordinates showing the cosmic-ray flux for $E > 8$ EeV. The cross indicates the measured dipole direction; the contours denote the 68% and 95% confidence level regions. The dipole in the 2MRS galaxy distribution is indicated. Arrows show the deflections expected due to the galactic magnetic field on particles with $E/Z = 5$ and 2 EeV. Image credit: Pierre Auger collaboration.

weighted dipole points in galactic coordinates in the direction $(\ell, b) \simeq (251°, 38°)$, about 55° away from the dipole direction found by Auger. However, as shown in Fig. 10.46, the effect of Galactic magnetic fields is to get the two directions closer; in addition, the correlation between the visible flux and the cosmic ray flux is just qualitative.

The conclusion is that the anisotropy seen by Auger strongly supports, and probably demonstrates, the hypothesis of an extragalactic origin for large part of the highest-energy cosmic rays; the origin is in particular related to AGN.

- In 2007 the Pierre Auger collaboration claimed with a significance larger than 3σ a hot spot near the Centaurus A AGN, at a distance of about 5 Mpc. Cen A is also a VHE gamma-ray emitter. However, the data collected after 2007 have not increased the significance of the detection.
- the Telescope Array Project observes at energies above 57 EeV a hot spot, with best circle radius: 25°, near the region of the Ursa Major constellation.

10.4.2 Photons: Different Source Types, Transients, Fundamental Physics

High-energy astrophysical processes generate photon radiation over a large range of wavelengths. Such photon radiation can be easily associated to the emitters, which is an advantage with respect to charged cosmic rays. In addition, photon radiation, besides being interesting per itself, can give insights on the acceleration of charged particles, being photons secondary products of accelerated charged particles. In addition, they are likely to be present in the decay chain of unstable massive particles, or in the annihilation of pairs of particles like dark matter particles.

The experimental data on the diffuse cosmic photon radiation span some 30 energy decades; a compilation of the data is shown in Fig. 10.2. A bump is visible corresponding to the CMB, while the general behavior of the yield of gamma rays at high energies can be approximated by an energy dependence as a power law $E^{-2.4}$ (Fig. 10.47). A cutoff at energies close to 1 TeV might be explained by the absorption of higher energy photons by background photons near the visible populating the intergalactic medium—through creation of e^+e^- pairs.

There is little doubt on the existence of the so-called ultra- and extremely-high-energy photons (respectively in the PeV-EeV and in the EeV-ZeV range), but so far cosmic gamma rays have been unambiguously detected only in the low (MeV), high (GeV) and very high-energy (TeV) domains. The behavior above some 30 TeV is extrapolated from data at lower energies and constrained by experimental upper limits.

In Chap. 4 we have defined as high energy (HE) the photons above 30 MeV—i.e., the threshold for the production of e^+e^- pairs plus some phase space; as very high energy (VHE) the photons above 30 GeV. The HE—and VHE in particular—regions are especially important related to the physics of cosmic rays and to fundamental physics. One of the possible sources of HE gamma rays is indeed the generation as a secondary
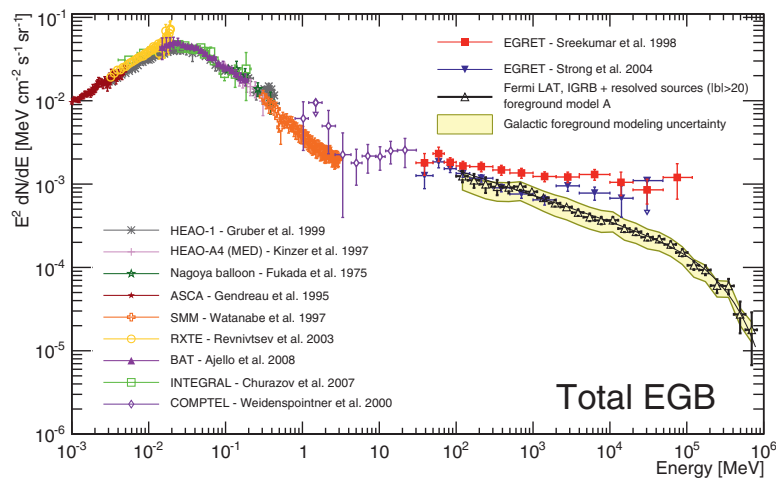
Fig. 10.47 Spectrum of the total extragalactic gamma ray emission measured by the *Fermi*-LAT. From M. Ackermann et al., The Astrophysical Journal 799 (2015) 86.

product in conventional scenarios of acceleration of charged particles; in this case cosmic gamma rays are a probe into cosmic accelerators. The VHE domain is sensitive to energy scales important for particle physics. One is the 100 GeV – 1 TeV scale expected for cold dark matter and for the lightest supersymmetric particles. A second scale is the scale of possible superheavy particles, at $\sim 10^{20}$ eV. Finally, it might be possible to access the GUT scale and the Planck scale, at energies $\sim 10^{24}$ eV – $\sim 10^{19}$ GeV. This last scale corresponds to a mass $\sqrt{\hbar c/G}$—which is, apart from factors of order 1, the mass of a black hole whose Schwarzschild radius equals its Compton wavelength.

Gamma rays provide at present the best window into the nonthermal Universe, being the "hottest" thermalized processes observed up to now in the accretion region of supermassive black holes at a temperature scale of the order of 10 keV, in the X-ray region. Tests of fundamental physics with gamma rays are much beyond the reach of terrestrial accelerators.

Besides the interest for fundamental physics, the astrophysical interest of HE and VHE photons is evident: for some sources such as the AGN—supermassive black holes in the center of galaxies, powered by infalling matter—the total power emitted above 100 MeV dominates the electromagnetic dissipation.

10.4.2.1 Hunting Different Sources and Source Types

The study of the galactic sources continues and their morphology and the SED of the emitted photons are telling us more and more, also in the context of multiwavelength analyses; in the future, the planned Cherenkov Telescope Array (CTA) will give the possibility to explore the highest energies, and to contribute, together with high-energy CR detectors and possibly with neutrino detectors, to the final solution of the CR problem.

One of the main results from the next-generation detectors will probably be the discovery of new classes of CR sources. The key probably comes from dedicating effort to surveys, which constitute an unbiased, systematic exploratory approach. Surveys of different extents and depths are amongst the scientific goals of all major planned facilities.

The key for such surveys are today gamma detectors (and in the future neutrino detectors as well).

More than half of the known VHE gamma-ray sources are located in the galactic plane. Galactic plane surveys are well suited to Cherenkov telescopes given the limited area to cover, as well as their low-energy thresholds and relatively good angular resolution (better than 0.1° to be compared to ∼1° for EAS detectors). CTA, investing 250 h (3 months) of observation, can achieve a 3 mCrab sensitivity (being the flux limit on a single pointing roughly proportional to $1/\sqrt{t_{obs}}$, where t_{obs} is the observation time) on the Galactic plane. More than 300 sources are expected at a sensitivity based on an extrapolation of the current "(log N − log S)" diagram[8] for VHE Galactic sources (Fig. 10.48).

---

[8] The number of sources as a function of flux "(log N − log S)" is an important tool for describing and investigating the statistical properties of various types of source populations. It is defined as the cumulative distribution of the number of sources brighter than a given flux density S, and it is based on some regularity properties like homogeneity and isotropy.
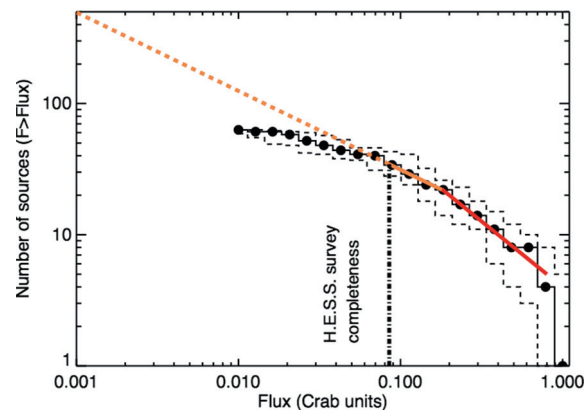
Fig. 10.48 "$(\log N - \log S)$" diagram of the VHE Galactic sources. From M. Renaud, http://arxiv.org/abs/0905.1287.

All-sky VHE surveys are well suited to EAS arrays that observe the whole sky with high duty cycles and large field of view. MILAGRO and the Tibet air shower arrays have carried out a survey for sources in the Northern hemisphere down to an average sensitivity of 600 mCrab above 1 TeV; HAWC has a sensitivity of 50 mCrab in a year, at median energy around 1 TeV. EAS detectors like HAWC can then "guide" the CTA. A combination of CTA and the EAS can reach sensitivities better than 30 mCrab in large parts of the extragalactic sky. The survey could be correlated with maps obtained by UHE cosmic ray and high-energy neutrino experiments.

Roughly, 5500 HE emitters above 100 MeV have been identified up to now, mostly by the *Fermi*-LAT, and some 200 of them are VHE emitters as well (Fig. 10.3).

About half of the gamma ray emitters are objects in our Galaxy; at TeV energies most of them can be associated to different kinds of supernova remnants (SNR), while at MeV to GeV energies they are mostly pulsars; the remaining half are extragalactic, and the space resolution of present detectors (slightly better than 0.1°) is not good enough to associate them with particular points in the host galaxies; we believe, however, that they are produced in the vicinity of supermassive black holes in the centers of the galaxies (see Sect. 10.2 and Sect. 10.4.1.7).

The strongest steady emitters are galactic objects; this can be explained by the fact that, being closer, they suffer a smaller attenuation. The observed strongest steady emitter at VHE is the Crab Nebula. The energy distribution of the photons from Crab Nebula is typical for gamma sources (see the explanation of the "double-hump" structure in Sect. 10.1.2.1), and it is shown in Fig. 10.13.

10.4.2.2 Transient Phenomena and Gamma Ray Bursts; Quasiperiodical Emissions

Among cosmic rays, gamma rays are important not only because they point to the sources, but also because the sensitivity of present instruments is such that transient events (in jargon, "transients") can be recorded. Sources of HE and VHE gamma rays (some of which might likely be also sources of charged cosmic rays, neutrinos and other radiation) were indeed discovered to exhibit transient phenomena, with timescales from few seconds to few days.

The sky exhibits in particular transient events from steady emitters ("flares") and burst of gamma rays from previously dark regions ("gamma ray bursts"). The phenomenology of such events is described in the rest of this section.

Short timescale variability has been observed in the gamma emission at high energies for several astrophysical objects, both galactic and extragalactic, in particular binary systems, and AGN. For binary systems the variability is quasiperiodical and can be related to the orbital motion, while for AGN it must be related to some cataclysmic events; this is the phenomenon of flares. Flares observed from Crab Nebula have, as today, no universally accepted interpretation.

Flares. Flares are characteristic mostly of extragalactic emitters (AGN). Among galactic emitters, the Crab Nebula, which was for longtime used as a "standard candle" in gamma astrophysics, has been recently discovered to be subject to dramatic flares on timescales of $\sim$10 h. The transient emission briefly dominates the flux from this object with a diameter of 10 light-years—which is the diameter of the shell including the pulsar remnant of the imploded star, and corresponds to roughly 0.1° as seen from Earth.
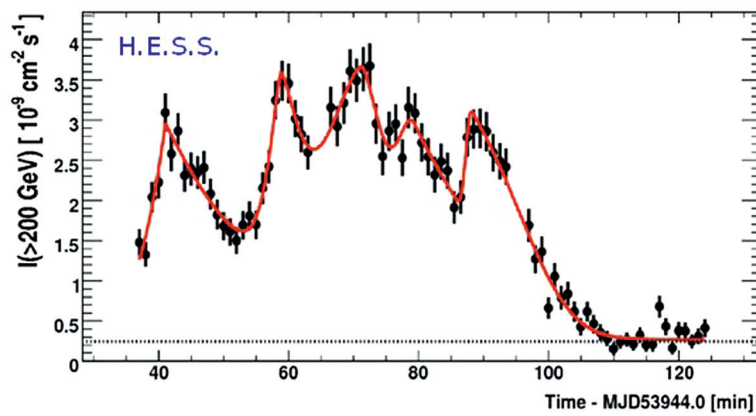
Fig. 10.49 Variability in the very-high-energy emission of the blazar PKS 2155-304. The dotted horizontal line indicates the flux from the Crab Nebula (from the H.E.S.S. experiment, http://www.mpi-hd.mpg.de/hfm/HESS.)
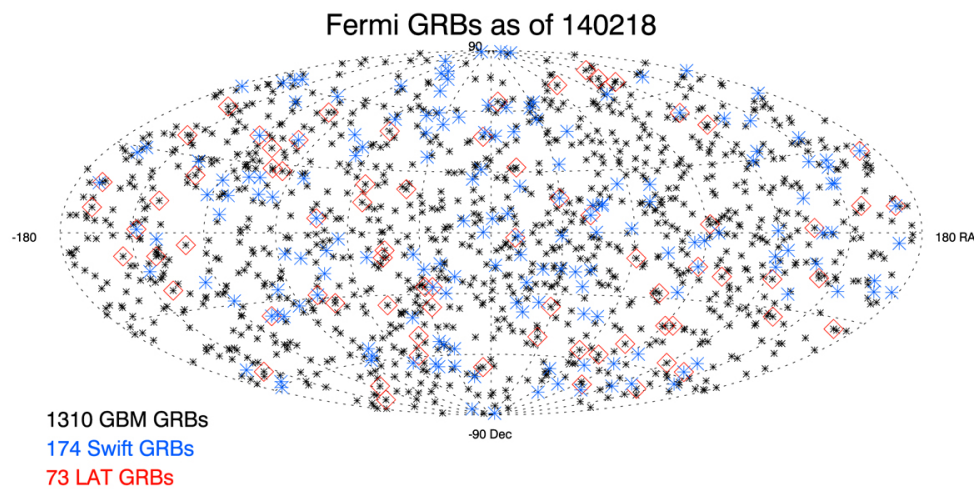
Fig. 10.50 Skymap of the GRBs located by the GRB monitor of *Fermi* and by the *Fermi*-LAT. Some events also seen by the Swift satellite are also shown. Credit: NASA.

Very short timescale emission from blazars have also been observed in the TeV band, the most prominent being at present the flare from the AGN PKS 2155-304 shown in Fig. 10.49: a flux increase by a factor larger than ten with respect to the quiescent state, with variability on timescales close to 1 min. Note that the Schwarzschild radius of the black hole powering PKS2155 is about 10^4 light seconds (corresponding to 10^9 solar masses), which has implications on the mechanisms of emission of gamma rays (see later).

Indeed the gamma ray sky looks like a movie rather than a picture, the most astonishing phenomenon being the explosion of gamma ray bursts.

Gamma Ray Bursts. Gamma Ray Bursts (GRBs) are extremely intense and fast shots of gamma radiation. They last from fractions of a second to a few seconds and sometimes up to a thousand seconds, often followed by "afterglows" orders of magnitude less energetic than the primary emission after minutes, hours, or even days. GRBs are detected once per day on average, typically in X-rays and soft gamma rays. They are named GRByymmdd after the date on which they were detected: the first two numbers after "GRB" correspond to the last two digits of the year, the second two numbers to the month, and the last two numbers to the day. A progressive letter ("A," "B," ...) might be added—it is mandatory if more than one GRB was discovered in the same day, and it became customary after 2010.

Their position appears random in the sky (Fig. 10.50), which suggests that they are of extragalactic origin. A few of them per year have energy fluxes and energies large enough that the *Fermi*-LAT can detect them (photons of the order of few tens of GeV have been detected in a few of them). Also in this case the sources appear to be isotropic.

The energy spectrum is nonthermal and varies from event to event, peaking at around a few hundred keV and extending up to several GeV. It can be roughly fitted by phenomenological function (a smoothly
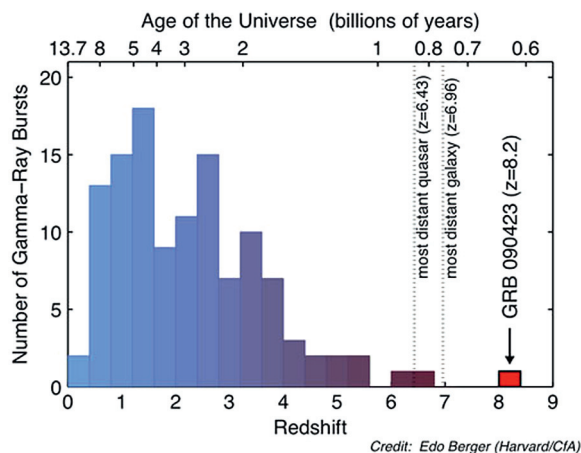
Fig. 10.51 Distribution of redshifts and corresponding age of the Universe for gamma ray bursts detected by NASA's Swift satellite. Credit: Edo Berger (Harvard), 2009.

broken power law) called "Band spectrum" (from the name of David Band who proposed it). The change of spectral slope from a typical slope of -1 to a typical slope of -2 occurs at a break energy E_b which, for the majority of observed bursts, is in the range between 0.1 and 1 MeV. Sometimes HE photons are emitted in the afterglows.

During fractions of seconds, their energy emission in the gamma ray band exceeds in some cases the energy flux of the rest of the Universe in the same band. The time integrated fluxes range from about 10^{-7} to about 10^{-4} erg/cm^2. If the emission were isotropic, the energy output would on average amount to a solar rest-mass energy, about 10^{54} erg; however, if the mechanism is similar to the one in AGN the emission should be beamed,[9] with a typical jet opening angle of a few degrees. Thus the actual average energy yield in γ rays should be $\sim 10^{51}$ erg. This value can be larger than the energy content of a typical supernova explosion, of which only 1 % emerges as visible photons (over a time span of thousands of years).

The distribution of their duration is bimodal (Fig. 10.18), and allows a first phenomenological classification between "short" GRBs (lasting typically 0.3 s; duration is usually defined as the time T90 during which 90 % of the photons are detected) and "long" GRBs (lasting more than 2 s, and typically 40 s). Short GRBs are on average harder than long GRBs.

GRBs are generally very far away, typically at $z \sim 1$ and beyond (Fig. 10.51). The farthest event ever detected is a 10-s long GRB at $z \simeq 8.2$, called GRB090423, observed by the Swift satellite (the burst alert monitor of Swift being sensitive to energies up to 0.35 MeV).

Short GRBs have been associated to the merging of pairs of compact objects. For long GRBs in several cases the emission has been associated with a formation of a supernova, presumably of very high mass (a "hypernova"). Possible mechanisms for GRBs will be discussed in Sect. 10.2.4.

Binary Systems. Binary stars (i.e., pairs of stars bound by gravitational interaction) are frequent in the Universe: most solar-size and larger stars reside in binaries. Binary systems in which one object is compact (a pulsar, a neutron star, or a black hole) have been observed to be periodical emitters of gamma radiation.

Finally, binary systems in which one object is compact (a pulsar, a neutron star, or a black hole) have been observed to be periodical emitters of gamma radiation.

A particular class of binary systems are microquasars, binary systems comprising a black hole, which exhibit relativistic jets (they are morphologically similar to the AGN). In quasars, the accreting object is a supermassive (millions to several billions of solar masses) BH; in microquasars, the mass of the compact object is only a few solar masses.

---

[9] Nuclear regions of AGN produce sometimes two opposite collimated jets, with a fast outflow of matter and energy from close to the disc. The direction of the jet is determined by the rotational axis of the accreting structure. The resolution of astronomical instruments is in general too poor, especially at high energies, to resolve jet morphology in gamma rays, and as a consequence observations cannot provide explanations for the mechanism yet. The limited experimental information available comes from the radio waveband, where very-long-baseline interferometry can image at sub-parsec scales the emission of synchrotron radiation near the black hole—but radiation should be present from the radio through to the gamma ray range.
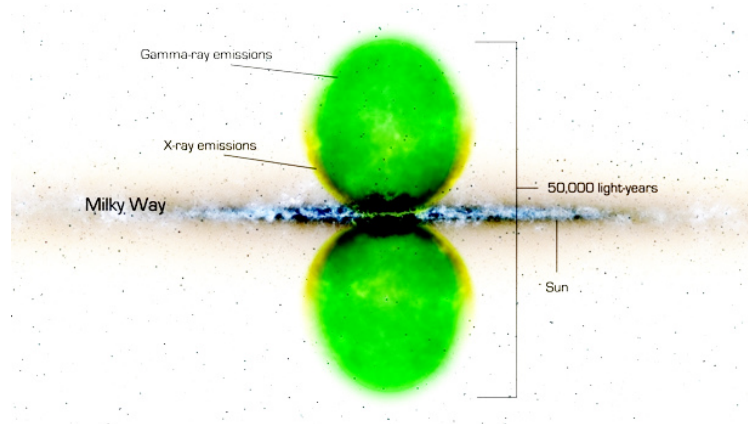
Fig. 10.52 The *Fermi* bubbles (smoothed). Credit: NASA.

10.4.2.3 Diffuse Regions of Photon Emission; The *Fermi* Bubbles

As the space resolution of the *Fermi*-LAT and of the Cherenkov telescopes are of the order of $0.1°$, we can image diffuse structure only in the Milky Way: the other galaxies will mostly appear like a point. Morphology studies at VHE are basically limited to structures within our galaxy.

Morphology of SNR is in particular one of the keys to understand physics in the vicinity of matter at high density—and one of the tools to understand the mechanism of acceleration of cosmic rays. Sometimes SNRs and the surrounding regions are too large to be imaged by Cherenkov telescopes, which typically have fields of view of $3°$–$4°$. A large field of view is also essential to understand the nature of primary accelerators in pulsar wind nebulae (PWN), as discussed in Sect. 10.2.1.3: it would be important to estimate the energy spectrum as a function of the angular distance to the center of the pulsar to separate the hadronic acceleration from the leptonic acceleration. The highest energy electrons lose energy quickly as they propagate away from the source; this is not true for protons.

Intermediate emission structures, a few degrees in radius, have been observed by MILAGRO and ARGO, which can be attributed to diffusion of protons within the interstellar medium.

A surprising discovery by *Fermi*-LAT was the existence of a giant structure emitting photons in our Galaxy, with size comparable to the size of the Galaxy itself: the so-called *Fermi* bubbles. These two structures, about 50 000-light-years across (Fig. 10.52), have quite sharp boundaries and emit rather uniformly in space with an energy spectrum peaking at a few GeV but yielding sizable amount of energy still up to 20 GeV.

Although the parts of the bubbles closest to the galactic plane shine in microwaves as well as gamma rays, about two-thirds of the way out the microwave emission fades and only X- and gamma rays are detectable.

Possible explanations of such a large structure are related to the past activity of the black hole in the center of our Galaxy. A large-scale structure of the magnetic field in the bubble region might indicate an origin from the center of the Galaxy, where magnetic fields are of the order of $100~\mu G$, and might also explain the mechanism of emission as synchrotron radiation from trapped electrons. However, this explanation is highly speculative, and as of today the reason for the emission is unknown.

10.4.2.4 Results on WIMPs

WIMPs are mostly searched in final states of their pair annihilation or decay involving antimatter and gamma rays. We shall refer in the following, unless explicitly specified, to a scenario in which secondary particles are produced in the annihilation of pairs of WIMPs.

Dark matter particles annihilating or decaying in the halo of the Milky Way could produce an excess of antimatter, and thus, an observable flux of cosmic positrons and/or antiprotons. This could explain the so-called PAMELA anomaly, i.e., the excess of positron with respect to models just accounting for secondary production (Fig. 10.36). Most DM annihilation or decay models can naturally reproduce the observed rise of the positron fraction with energy, up to the mass of the DM candidate (or half the mass, depending if the

self-annihilation or the decay hypothesis is chosen). This flux is expected not to be directional. The measured antiproton flux also shows unexpected features with respect to the hypothesis of pure secondary production.

It is plausible that both the positron excess and the excess observed in the electron/positron yield with respect to current models (see Sect. 10.4.1) can be explained by the presence of nearby sources, in particular pulsars, which have indeed been copiously found by the *Fermi*-LAT (Sect. 10.2.1.1). AMS-02 is steadily increasing the energy range over which positrons and electrons are measured, as well as the statistics. If the positron excess is originated from a few nearby pulsars, it would probably give an anisotropy in the arrival direction of cosmic rays at the highest energies—there is a tradeoff here between distance and energy, since synchrotron losses are important; in addition, the energy spectrum should drop smoothly at the highest energies. A sharp cutoff in the positron fraction would instead be the signature of a DM origin of the positron excess; the present data do not demonstrate such a scenario, but they cannot exclude it, either: the attenuation of the positron/electron ratio observed by AMS-02 at several hundred GeV is consistent with the production from a particle at the TeV scale .

For what concerns photons, the expected flux from dark matter annihilation can be expressed as

$$\frac{dN}{dE} = \frac{1}{4\pi} \underbrace{\frac{\langle\sigma_{ann}v\rangle}{2m_{DM}^2}\frac{dN_\gamma}{dE}}_{\text{Particle Physics}} \times \underbrace{\int_{\Delta\Omega-l.o.s.} dl(\Omega)\rho_{DM}^2}_{\text{Astrophysics}} \ . \tag{10.57}$$

The astrophysical factor, proportional to the square of the density, is also called the "boost factor". DM-induced gamma rays could present sharp spectral signatures, like for instance $\gamma\gamma$ or $Z\gamma$ annihilation lines, with energies strictly related to the WIMP mass. However, since the WIMP is electrically neutral, these processes are loop suppressed and therefore should be rare. WIMP-induced gamma rays are thus expected to be dominated by a relatively featureless continuum of by-products of cascades and decays (mostly from π^0) following the annihilation in pairs of quarks or leptons. The number of resulting gamma rays depends quadratically on the DM density along the line of sight of the observer. This motivates search on targets, where one expects DM density enhancements. Among these targets are the Galactic center, galaxy clusters, and nearby dwarf spheroidal galaxies. Of course, an additional proof is given by proximity, to reduce the $1/d^2$ attenuation.

Unfortunately, as said before, dark matter densities are not known in the innermost regions of galaxies, where most of the signal should come from: data allow only the computation in the halos, and models helping in the extrapolation to the centers frequently disagree (Sect. 8.1.4). Observations of galaxy rotation curves favor constant density cores in the halos; unresolved "cusp" substructures can have a very large impact, but their existence is speculative—however, since they exist for baryonic matter, they are also likely to exist for DM. This uncertainty is typically expressed by the so-called "boost factor," defined as the ratio of the true, unknown, line-of-sight integral to the one obtained when assuming a smooth component without substructure.

As a consequence of all uncertainties described above, the choice of targets is somehow related to guesses, driven by the knowledge of locations where one expects large ratios of gravitating to luminous mass. Remembering Chap. 8, the main targets are:

- *Galactic center.* The Galactic center (GC) is expected to be the brightest source of dark matter annihilation. However, the many astrophysical sources of gamma rays in that region complicate the identification of DM. In the GeV region the situation is further complicated by the presence of a highly structured and extremely bright diffuse gamma ray background arising from the interaction of the pool of cosmic rays with dense molecular material in the inner Galaxy. Finally, there is a huge uncertainty on the boost factor. To limit problems, searches for dark matter annihilation/decay are usually performed in regions $0.3°$–$1°$ away form the central black hole.

  At TeV energies, Cherenkov telescopes detected a point source compatible with the position of the supermassive black hole in the center of our Galaxy and a diffuse emission coinciding with molecular material in the Galactic ridge. The GC source has a featureless power law spectrum at TeV energies with an exponential cutoff at ∼10 TeV not indicating a dark matter scenario; the signal is usually attributed to the supermassive black hole Sgr A* or a to pulsar wind nebula in that region.

  Searches have been performed for a signal from the galactic dark matter halo close to the core; no signal has been found.

  There have been several claims of a signal in the galactic center region. An extended signal coinciding with the center of our Galaxy, corresponding to a WIMP of mass about 40 GeV/c^2 was reported above the galactic diffuse emission—however, the interaction of freshly produced cosmic rays with interstellar

material is a likely explanation. The second claimed signal was the indication of a photon line at ∼130 GeV in regions of interest around the GC, but this has not been confirmed.

- *Dwarf Spheroidal Galaxiess.* Dwarf spheroidal galaxies (dSph) are a clean environment to search for dark matter annihilation: astrophysical backgrounds that produce gamma rays are expected to be negligible. The DM content can be determined from stellar dynamics and these objects have been found to be the ones with the largest mass-to-light ratios in the Universe, and uncertainties on the boost factor are within one order of magnitude. Some three-four dozens of dwarf satellite galaxies of the Milky Way are currently known and they are observed both by ground-based and by satellite-based gamma detectors. No signal has been found, and stringent limits have been calculated. In particular, a combined ("stacked") analysis of all known dwarf satellites with the *Fermi*-LAT satellite has allowed a limit to be set below the canonical thermal relic production cross section of 3×10^{-26}cm^{3}s^{-1} for a range of WIMP masses (around 10 GeV) in the case of the annihilation into $b\bar{b}$ (the $b\bar{b}$ is used as a template due to the result obtained in Sect. 8.4.2).

- *Galaxy clusters.* Galaxy clusters are groups of hundreds to thousands galaxies bound by gravity. Galaxy clusters nearby (10–100 Mpc) include the Virgo, Fornax, Hercules, and Coma clusters. A very large aggregation known as the Great Attractor, is massive enough to locally modify the trajectories in the expansion of the Universe.

  Galaxy clusters are much more distant than dwarf spheroidal galaxies or any of the other targets generally used for dark matter searches with gamma rays; however, like dwarf spheroidals, astrophysical dynamics shows that they are likely to be dark matter dominated—and if DM exists, one of the largest accumulators. The range of likely boost factors due to unresolved dark matter substructure can be large; however, when making conservative assumptions, the sensitivity to DM is several orders of magnitude away from the canonical thermal relic interaction rate.

- *Line Searches.* The annihilation of WIMP pairs into γX would lead to monochromatic gamma rays with $E_\gamma = m_\chi(1 - m_X/4M_\chi^2)$. Such a signal would provide a smoking gun since astrophysical sources could very hardly produce it, in particular if such a signal is found in several locations. This process is expected to be loop suppressed being possible only at $\mathcal{O}(\alpha^2)$.

A summary of the present results from searches in the photon channel is plotted in Fig. 10.53 together with extrapolation to the first three years of data collection by the next generation detector CTA, and with a collection of 10 years of data by *Fermi* (to be reached in 2019). Note that the *Fermi* discovery potential continues to extend linearly with time, being its background negligible.

Neutrinos. Equation (10.57) holds for neutrinos as well, but the branching fractions into neutrinos are expected to be smaller, due to the fact that the radiative production of neutrinos is negligible. In addition, experimental detection is more difficult. However, the backgrounds are smaller with respect to the photon case.

Balancing the pros and the cons, gamma rays are the best investigation tool in case the emission comes from a region transparent to photons. However, neutrinos are the best tool in case DM is concentrated in the center of massive objects, the Sun for example, which are opaque to gamma rays. Once gravitationally captured by such massive objects, DM particles lose energy in the interaction with nuclei and then settle into the core, where their densities and annihilation rates can be greatly enhanced; only neutrinos (and axions) can escape these dense objects. The centers of massive objects are among the places to look for a possible neutrino excess from DM annihilation using neutrino telescopes.

No signal has been detected up to now (as in the case of axions from the Sun). A reliable prediction of the sensitivity is difficult, depending on many uncertain parameters like the annihilation cross section, the decay modes and the capture rate. The first two uncertainties are common to the photon channels.

10.4.2.5 Lorentz Symmetry Violation

Variable gamma-ray sources in the VHE region, and in particular AGN, can provide information about possible violations of the Lorentz invariance in the form of a dispersion relation for light expected, for example, in some quantum gravity (QG) models.

Lorentz invariance violation (LIV) at the n-th order in energy can be heuristically incorporated in a perturbation to the relativistic Hamiltonian:

$$E^2 \simeq m^2c^4 + p^2c^2 \left[1 - \xi_n \left(\frac{pc}{E_{\mathrm{LIV,n}}}\right)^n\right], \qquad (10.58)$$
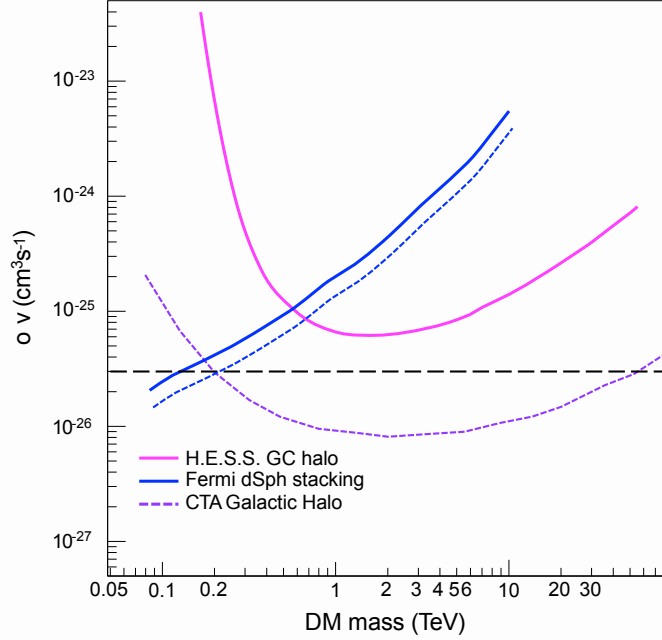
Fig. 10.53 Comparison of the sensitivities in terms of $< \sigma v >$ from the observation of the Milky Way Galactic halo (present results from H.E.S.S., continuous line, and expected results from three years of operation of CTA South, dotted line), and from a stacked sample of dwarf spheroidal galaxies (*Fermi*-LAT). The *Fermi*-LAT lines are relative to 6 years of data analysis (continuous, upper line; this is the present result) and to an extrapolation to 10 years of analyzed data (dotted, lower). The sensitivity curves have been calculated assuming decays into an appropriate mixture $b\bar{b}$ and W^+W^- pairs, and the Einasto dark matter profile. The horizontal dashed line indicates the thermal velocity-averaged cross-section. From "Science with the CTA", September 2018, and from *Fermi*-LAT publications.

which implies that the speed of light ($m = 0$) could have an energy dependence. From the expression $v = \partial E / \partial p$, the modified dispersion relation of photons can be expressed by the leading term of the Taylor series as an energy-dependent light speed

$$v(E) = \frac{\partial E}{\partial p} \simeq c \left[1 - \xi_n \frac{n+1}{2} \left(\frac{E}{E_{\mathrm{LIV,n}}} \right)^n \right], \tag{10.59}$$

where n = 1 or n = 2 corresponds to linear or quadratic energy dependence, and $\xi_n = \pm 1$ is the sign of the LIV correction. If $\xi_n = +1$ ($\xi_n = -1$), high-energy photons travel in vacuum slower (faster) than low-energy photons.

The scale E_{LIV} at which the physics of space–time is expected to break down, requiring modifications or the creation of a new paradigm to avoid singularity problems, is referred to as the "QG energy scale", and is expected to be of the order of the Planck scale—an energy $E_P = M_P c^2 \simeq 1.2 \times 10^{19}$ GeV—or maybe lower, if new particles are discovered at an intermediate scale.

Because of the spectral dispersion, two GRB photons emitted simultaneously by the source would arrive on Earth with a time delay (Δt) if they have different energies. With the magnification of the cosmological distances of the GRBs and the high energies of these photons, the time delay (Δt) caused by the effect of Lorentz invariance violation could be measurable. Taking account of the cosmological expansion and using Eq. 10.59, we write the formula of the time delay as:

$$\Delta t = t_h - t_l = \xi_n \frac{1+n}{2H_0} \frac{E_h^n - E_l^n}{E_{LIV,n}^n} \int_0^z \frac{(1+z')^n dz'}{\sqrt{\Omega_m (1+z')^3 + \Omega_\Lambda}}. \tag{10.60}$$

Here, t_h is the arrival time of the high-energy photon, and t_l is the arrival time of the low-energy photon, with E_h and E_l being the photon energies measured at Earth.

For small z, and at first order,
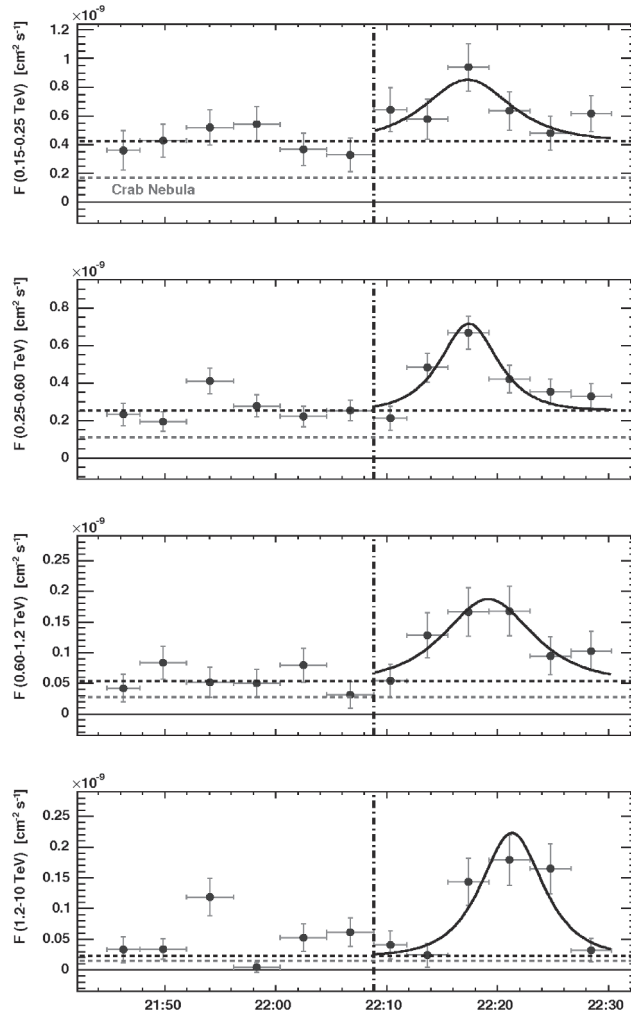
Fig. 10.54 Integral flux of Mkn 501 detected by MAGIC in four different energy ranges. From J. Albert et al., Phys. Lett. B668 (2008) 253.

$$t(E) \simeq d/c(E) \simeq \frac{zc_0}{H_0 c(E)} \simeq zT_H \left(1 - \xi_1 \frac{E}{E_P} \right)$$

where $T_H = 1/H_0 \simeq 5 \times 10^{17}$ s is Hubble's time.

AGN flares (Sect. 10.4.2.2) can be used as experimental tools: they are fast and photons arriving to us travel for long distances.

Mkn 501 (z = 0.034) had a spectacular flare between May and July 2005; it could be analyzed by the MAGIC telescope. The MAGIC data showed a negative correlation between the arrival time of photons and their energy (Fig. 10.54), yielding, if one assumes that the delay is due to linear QG effects, to an evaluation of $E_{\mathrm{LIV}} \sim 0.03\, E_P$. H.E.S.S. observations of the flare in PKS 2155 (Fig. 10.49), however, evidenced no effect, allowing to set a lower limit $E_{\mathrm{LIV}} > 0.04\, E_P$.

Lately, several GRBs observed by the *Fermi* satellite have been used to set more stringent limits. A problem, when setting limits, is that one does not know if photon emission at the source is ordered in energy; thus one has to make hypotheses—for example, that QG effects can only increase the intrinsic dispersion.

The *Fermi* satellite derived strong upper limits at 95 % C.L. from the total degree of dispersion, in the data of four GRBs:

$$E_{\mathrm{LIV},1} > 7.6 E_P .$$

In most QG scenarios violations to the universality of the speed of light happen at order larger than 1: $\Delta t \simeq (E/E_{\mathrm{LIV}})^{\nu}$ with $\nu > 1$. In this case the VHE detectors are even more sensitive with respect to other instruments like *Fermi*; for $\nu = 2$ the data from PKS 2155 give $E_{\mathrm{LIV}} > 10^{-9}\, E_P$.

10.4.2.6 Possible Anomalous Photon Propagation Effects

Some experimental indications exist, that the Universe might be more transparent to gamma rays than computed in Sect. 10.3.4.

As discussed before, the existence of a soft photon background in the Universe leads to a suppression of the observed flux of gamma rays from astrophysical sources through the $\gamma\gamma \to e^+e^-$ pair-production process. Several models have been proposed in the literature to estimate the spectral energy density (SED) of the soft background (EBL); since they are based on suitable experimental evidence (e.g., deep galaxy counts), all models yield consistent results, so that the SED of the EBL is fixed to a very good extent. Basically, the latter reproduces the SED of star-forming galaxies, which is characterized by a visible/ultraviolet hump due to direct emission from stars and by an infrared hump due to the emission from the star-heated warm dust that typically hosts the sites of star formation.

However, the Universe looks more transparent than expected—this is called the "EBL crisis." Basically, two experimental evidences support this conjecture:

- When for each SED of high-z blazars, the data points observed in the optically thin low photon energy regime ($\tau < 1$) are used to fit the VHE spectrum in optically thick regions, points at large attenuation are observed (Fig. 10.55, left). This violates the current EBL models, strongly based on observations, at some 5σ.
- The energy dependence of the gamma opacity τ leads to appreciable modifications of the observed source spectrum with respect to the spectrum at emission, due to the exponential decrease of τ on energy in the VHE gamma region. One would expect naively that the spectral index of blazars at VHE would increase with distance: due to absorption, the SED of blazars should become steeper at increasing distance. This phenomenon has not been observed (Fig. 10.55, right).

Among the possible explanations, a photon mixing with axion-like particles (ALPs), predicted by several extensions of the Standard Model (Sect. 8.4.2), can fix the EBL crisis, and obtain compatibility on the horizon calculation. Since ALPs are characterized by a coupling to two photons, in the presence of an external magnetic field B photon-ALP oscillations can show up. Photons are supposed to be emitted by a blazar in the usual way; some of them can turn into ALPs, either in the emission region, or during their travel. Later, some of the produced ALPs can convert back into photons (for example, in the Milky Way, which has a relatively large magnetic field) and ultimately be detected. In empty space this would obviously produce a flux dimming; remarkably enough, due to the EBL such a double conversion can make the observed flux considerably larger than in the standard situation: in fact, ALPs do not undergo EBL absorption (Fig. 10.56).
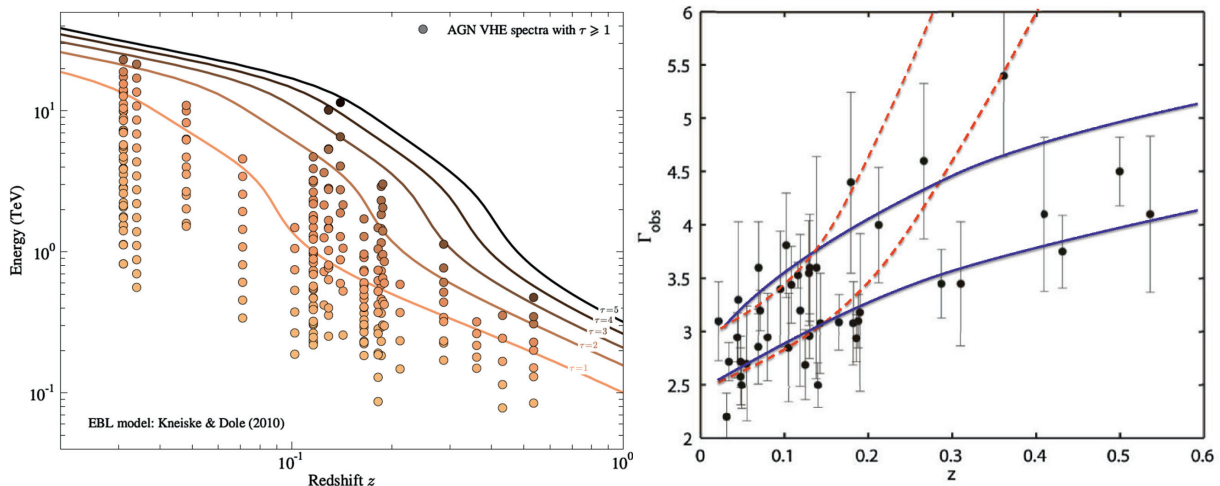
Fig. 10.55 Left: For each individual spectral measurement including points at $\tau > 1$, the corresponding value of z and E are marked in this diagram. The iso-contours for $\tau = 1, 2, 3, 4$ calculated using a minimum EBL model are overlaid. From D. Horns, M. Meyer, JCAP 1202 (2012) 033. Right: Observed values of the spectral index for all blazars detected in VHE; superimposed is the predicted behavior of the observed spectral index from a source at constant intrinsic spectral index within two different scenarios. In the first one (area between the two dotted lines) Γ is computed from EBL absorption; in the second (area between the two solid lines) it is evaluated including also the photon-ALP oscillation. Original from A. de Angelis et al., Mon. Not. R. Astron. Soc. 394 (2009) L21; updated.
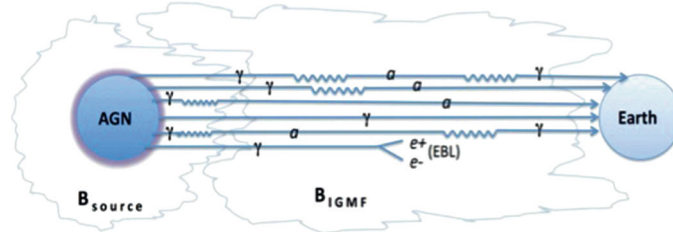
Fig. 10.56 Illustration of gamma ray propagation in the presence of oscillations between gamma rays and axion-like particles. From M.A. Sanchez-Conde et al., Phys. Rev. D79 (2009) 123511.

We concentrate now on the photon transition to ALP in the intergalactic medium. The probability of photon-ALP mixing depends on the value and on the structure of the cosmic magnetic fields, largely unknown (see Sect. 10.3.1).

Both the strength and the correlation length of the cosmic magnetic fields do influence the calculation of the $\gamma \to a$ conversion probability. In the limit of low conversion probability, if s is the size of the typical region, the average probability $P_{\gamma \to a}$ of conversion in a region is

$$P_{\gamma \to a} \simeq 2 \times 10^{-3} \left(\frac{B_T}{1\,\mathrm{nG}} \frac{\lambda_B}{1\,\mathrm{Mpc}} \frac{g_{a\gamma\gamma}}{10^{-10}\,\mathrm{GeV}^{-1}} \right)^2, \tag{10.61}$$

where B_T is the transverse component of the magnetic field.

For a magnetic field of 0.1–1 nG, and a cellular size structure $\lambda_B \sim 1\mathrm{Mpc} - 10$ Mpc, any ALP mass below 10^{-10} eV, with a coupling such that 10^{11} GeV $< M < 10^{13}$ GeV (well within the region experimentally allowed for mass and coupling) can explain the experimental results (Fig. 10.55).

Another possible explanation for the hard spectra of distant blazars, needing a more fine tuning, is that line-of-sight interactions of cosmic rays with CMB radiation and EBL generate secondary gamma rays relatively close to the observer.

LIV and Photon Propagation

A powerful tool to investigate Planck scale departures from Lorentz symmetry could be provided by a possible change in the energy threshold of the pair production process $\gamma_{VHE}\gamma_{EBL} \to e^+e^-$ of gamma rays from cosmological sources. This would affect the optical depth, and thus, photon propagation.

In a collision between a soft photon of energy ϵ and a high-energy photon of energy E, an electron–positron pair could be produced only if E is greater than the threshold energy E_{th}, which depends on ϵ and m_e^2.

Note that also the violation of the Lorentz invariance changes the optical depth. Using a dispersion relation as in Eq. 10.58, one obtains, for $n = 1$ and unmodified law of energy–momentum conservation, that for a given soft-photon energy ϵ, the process $\gamma\gamma \to e^+e^-$ is allowed only if E is greater than a certain threshold energy E_{th} which depends on ϵ and m_e^2. At first order:

$$E_{th}\epsilon + \xi(E_{th}^3/8E_p) \simeq m_e^2. \tag{10.62}$$

The $\xi \to 0$ limit corresponds to the special-relativistic result $E_{th} = m_e^2/\epsilon$. For $|\xi| \sim 1$ and sufficiently small values of ϵ (and correspondingly large values of E_{th}) the Planck scale correction cannot be ignored.

This provides an opportunity for tests based on dynamics. As an example, a 10 TeV photon and a 0.03 eV photon can produce an electron–positron pair according to ordinary special-relativistic kinematics, but they cannot produce a e^+e^- pair according to the dispersion relation in Eq. 10.58, with $n = 1$ and $\xi \sim -1$. The non-observation of EeV gamma rays has already excluded a good part of the parameter range of terms suppressed to first and second order in the Planck scale.

The situation for positive ξ is somewhat different, because a positive ξ decreases the energy requirement for electron–positron pair production.

A Win-Win Situation: Determination of Cosmological Parameters

If no indications of new physics (LIV, anomalous propagation) will be found after all, since the optical depth depends also on the cosmological parameters (Eq. 10.55), its determination constrains the values of the cosmological parameters if the EBL is known, and if only standard processes are at work.

A determination of Ω_M and Ω_Λ independent of the luminosity–distance relation currently used by the Supernovae 1 A observations can be obtained from the spectra of distant AGN.

10.4.3 Astrophysical Neutrinos

Experimental data on astrophysical neutrinos are scarce: their small cross section makes the detection difficult, and a detector with a sensitivity large enough to obtain useful information on astrophysical neutrinos sources should have an active volume larger than 1 km^3. We discussed in Chap. 4 the problems of such detectors.

Up to now we detected astrophysical neutrinos from the Sun, from the center of the Earth, from the supernova SN1987A, one extremely-high-energy neutrino from the blazar TXS 0506 +056, and in addition diffuse very-high-energy astrophysical neutrinos for which we are unable to locate the origin.

The (low-energy) neutrino data from the Sun was discussed in Chap. 9, where we also shortly discussed neutrinos coming from the Earth; hereafter we review briefly the neutrinos produced in the flare of SN1987A and the (very-high-energy) neutrinos detected by IceCube.

10.4.3.1 Neutrinos from SN1987A

On February 23, 1987, a supernova was observed in the Large Magellanic Cloud (LMC), a galaxy satellite of the Milky Way (about 10^{10} solar masses, i.e., 1 % of the Milky Way) at a distance of about 50 kpc from the Earth. As it was the first supernova observed in 1987, it was called SN1987A; it was also the first supernova since 1604 visible with the naked eye. The event was associated with the collapse of the star Sanduleak-69202, a main sequence star of mass about 20 solar masses.

Three hours before the optical detection, a bunch of neutrinos was observed on Earth. SN1987A was the first (and the only up to now) unambiguous detection of neutrinos that can be localized from a source other from the Sun: three water Cherenkov detectors, Kamiokande, the Irvine–Michigan–Brookhaven (IMB) experiment, and the Baksan detector observed 12, 8, and 5 neutrino interaction events, respectively, over a 13 s interval (Fig. 10.57). Within the limited statistics achieved by these first-generation detectors, the number of events and the burst duration were consistent with standard estimates of the energy release and cooling time of a supernova. The energy of neutrinos can be inferred from the energy of the recoil electrons to be in the tens of MeV range, consistent with the origin from a collapse.

The optical counterpart reached an apparent magnitude of about 3. No very high-energy gamma emission was detected (in 1987 gamma detectors were not operating), but gamma rays at the intermediate energies characteristic of gamma transitions could be recorded.

SN1987A allowed also investigations on particle physics properties of neutrinos. The neutrino arrival time distribution sets an upper limit of 10 eV on the neutrino mass; the fact that they did not spread allows setting an upper limit on the magnetic moment $<10^{-12}\mu_B$, where μ_B is the Bohr magneton. A determination of the neutrino velocity can also be derived, being consistent with the speed of light within two parts in 10^{-9}.

10.4.3.2 Very-High-Energy Neutrinos

The IceCube experiment at the South Pole reported for the first time in 2013 the detection of astrophysical neutrinos; after a few years the evidence is much stronger and tens of astrophysical neutrinos are collected every year. IceCube detects the Cherenkov radiation in the Antarctic ice generated by charged particles, mostly muons, produced by neutrino interactions.

The experimental problem is linked to the relatively large background from atmospheric muons, i.e., muons coming from interactions of cosmic rays with the atmosphere, which are recorded, even at a depth of 1450 m, at a rate of about 3000 per second. Two methods are used to identify genuine neutrino events:

1. Use the Earth as a filter to remove the huge background of cosmic-ray muons. i.e., look only to events originated "from the bottom". This limits the neutrino view to a single flavour (the muon flavor, since muons are the only charged particles which have a reasonably long interaction length) and half the sky.
2. Identify neutrinos interacting inside the detector. This method divides the instrumented volume of ice into an outer veto shield and a 500 megaton inner fiducial volume. The advantage of focusing on neutrinos
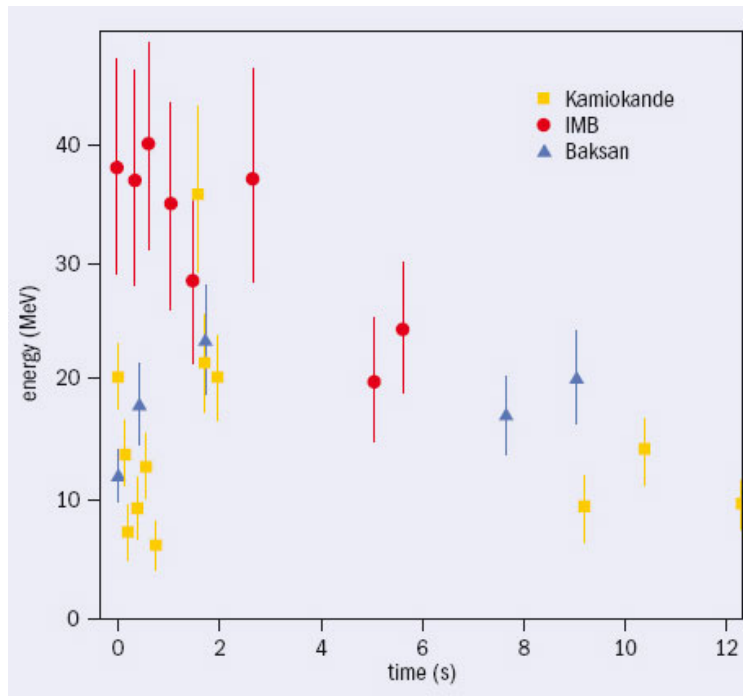
Fig. 10.57 Time-line of the SN1987a neutrino observation. From M. Nakahata, Cern Courier, September 2007.

interacting inside the instrumented volume of ice is that the detector functions as a total absorption calorimeter, and one can have an energy estimate. Also, neutrinos from all directions in the sky can be identified.

Both methods for selecting cosmic neutrinos harvest together about 1 event/month, twice that if one can tolerate a $\sim 25\%$ background. Standard Model physics allows one to infer the energy spectrum of the parent neutrinos – for the highest energy event the most likely energy of the parent neutrino is almost 10 PeV. Data indicate an excess of neutrino events with respect to atmospheric neutrinos above 30 TeV. The cosmic flux above 100 TeV is well described by a power law

$$\Phi_\nu \simeq (0.9 \pm 0.3) \times 10^{-14} \left(\frac{E}{100\,\mathrm{TeV}} \right)^{-2.13 \pm 0.13} \mathrm{GeV}^{-1}\mathrm{m}^{-2}\mathrm{sr}^{-1} \,. \tag{10.63}$$

To give an example, the ratio between the neutrino flux and the charged cosmic ray flux at 100 TeV is

$$\Phi_\nu / \Phi_{CR} \sim 2 \times 10^{-5} \,.$$

The energy and zenith angle dependence observed for completely contained events, shown in Fig. 10.58, is consistent with expectations for a flux of neutrinos produced by cosmic accelerators – a purely atmospheric component is excluded at more than 7σ.

Considerations based on the expected fluxes allow predicting that in a few years we shall reach the statistics required to identify their origin by matching arrival directions with astronomical maps.

Fig. 10.59 shows in Galactic coordinates the arrival directions of cosmic neutrinos for four years of events with interaction vertices inside the detector. The observed neutrino flux is consistent with an isotropic distribution of arrival directions and equal contributions of all neutrino flavours.

A variety of analyses suggest that the cosmic neutrino flux dominates the atmospheric background above an energy that may be as low as 30 TeV, with an energy spectrum that cannot be described as a single power, as was the case for the muon neutrino flux through the Earth for energies exceeding 220 TeV. This is reinforced by the fact that fitting the excess flux in different ranges of energy yields different values for the power-law exponent.

Gamma rays at energies above some 100 TeV are likely to interact with background photons before reaching Earth. The resulting electromagnetic shower subdivides the initial photon energy, resulting in multiple photons in the GeV-TeV energy range by the time the shower reaches Earth. After accounting
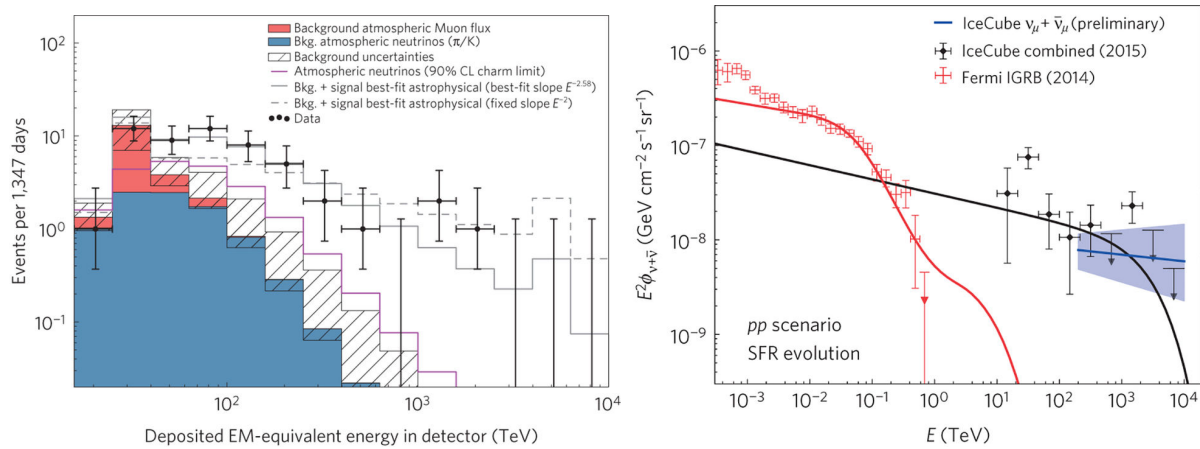
Fig. 10.58 Left: Deposited energies, by neutrinos interacting inside IceCube, observed in four years of data. The hashed region shows uncertainties on the sum of all backgrounds. The atmospheric muon flux (red) and its uncertainty is computed from simulation. The atmospheric neutrino flux is derived from previous measurements. Also shown are two illustrative power-law fits to the spectrum. Data measurements are shown by the black crosses. Right: The astrophysical neutrino flux (black line) observed by IceCube matches the corresponding cascaded gamma-ray flux (red line) observed by *Fermi*, see Fig. 10.47. From F. Halzen, Nature Physics 13 (2017) 232.
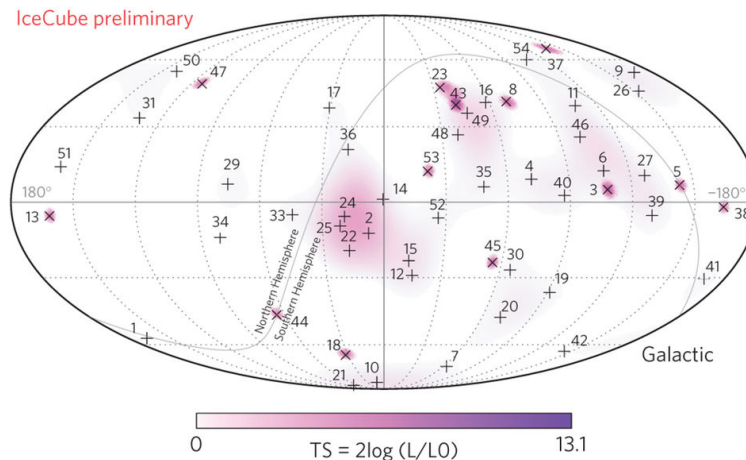
Fig. 10.59 Arrival directions of neutrinos in the four-year starting-event sample in Galactic coordinates. Shower-like events (contained in the detector) are shown with "+" and those containing muon tracks with "x". The colour scale indicates the value of the test statistic (TS) of an unbinned maximum likelihood test searching for anisotropies of the event arrival directions.From F. Halzen, Nature Physics 13 (2017) 232.

for the cascading of the PeV photons in cosmic radiation backgrounds between source and observation, a gamma-ray flux similar to the IceCube neutrino flux matches the extragalactic high-energy gamma-ray flux observed by the *Fermi* satellite as shown in Fig. 10.47, right.

10.4.3.3 The First Multimessenger Neutrino-Gamma Detection: EHE170922

On September 22, 2017, IceCube detected an extremely-high-energy neutrino event, consisting in a muon coming from the bottom of the detector through the Earth with an estimated energy between 100 TeV and 150 TeV, likely produced by a neutrino of energy of $E_\nu \sim 300$ TeV. Promptly alerted, the *Fermi* LAT and MAGIC detected at more than 5σ a flare from the blazar TXS 0506 +056, at a redshift ~ 0.34, within the region of sky consistent with the 50% probability region of the IceCube neutrino (about one degree in size). The MAGIC detection allowed to determine that the electromagnetic emission had a cutoff at ~ 400 GeV.

The simultaneous emission of gamma rays and neutrinos from the same source proves that the "hadronic mechanism" has been seen at work. The estimated energy of a proton producing such a high energy neutrino
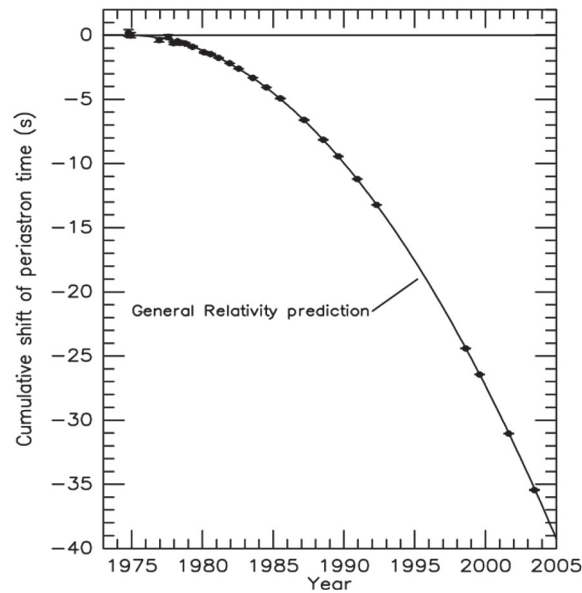
Fig. 10.60 Observed accumulated shifts of the times of periastron in the PSR 1913+16 compared with the general relativity prediction from gravitational radiation. From Joseph H. Taylor Jr.—©The Nobel Foundation 1993.

in a "beam dump" is

$$E_p \gtrsim 20 \, E_\nu \sim 10 - 20 \, \text{PeV} \,, \tag{10.64}$$

an energy above the knee and well appropriate for a blazar; blazar models prefer the target to be a photon gas.

This event opened the era of multimessenger astronomy with neutrinos. The present detection rate of astrophysical neutrinos is $O(1 \text{ event/month})$, and it is thus likely that such events will not be common in the future. It sets however a benchmark for the size of future IceCube-like detectors: a size ten times larger will almost certainly allow detecting clusters of neutrinos from astrophysical hadronic accelerators, as well as larger numbers of neutrinos from a flare like the one detected.

It is important to note that the cutoff energy in the gamma rays detected is much lower than the neutrino energy. This is a consequence of the fact that the energy of the gamma rays is degraded due to the interaction with photons and matter when traveling in the jet and during their cosmic voyage, and agrees qualitatively with the effect shown in Fig. 10.2.

10.4.4 Gravitational Radiation

The graviton, a massless spin 2 particle (this condition is required by the fact that gravity is attractive only), is the proposed mediator of any field theory of gravity. Indeed the coupling of the graviton with matter is predicted to be extremely weak and thus its direct detection is extremely difficult – Einstein had sentenced that it was "impossible to detect" experimentally. However, indirect and direct evidence of gravitational radiation have been clearly demonstrated.

The indirect evidence was firmly established in 1974 by Hulse and Taylor (Nobel Prize in Physics 1993). They observed that the orbital period of the binary pulsar PSR 1913+16, at a distance of about 6400 pc, was decreasing in agreement with the prediction of Einstein general theory of relativity (about 40 s in 30 years, see Fig. 10.60). In such system it was possible to deduce, from the time of arrival of the recorded pulses, the binary orbital parameters. The masses of the two neutron stars were estimated to be about 1.4 solar masses, the period to be 7.75 hours and the maximum and the minimum separation to be 4.8 and 1.1 solar radii respectively. The gravitational waves produced by such a system induce a strain (see Chap. 4), when they now reach Earth, of the order of 10^{-23}; its direct observation is out of the reach of the present ground-based GW detectors but it will be detectable by future space detectors. The two neutron stars will merge in about 300 million years producing then a strain of the order of 10^{-18} at the Earth.
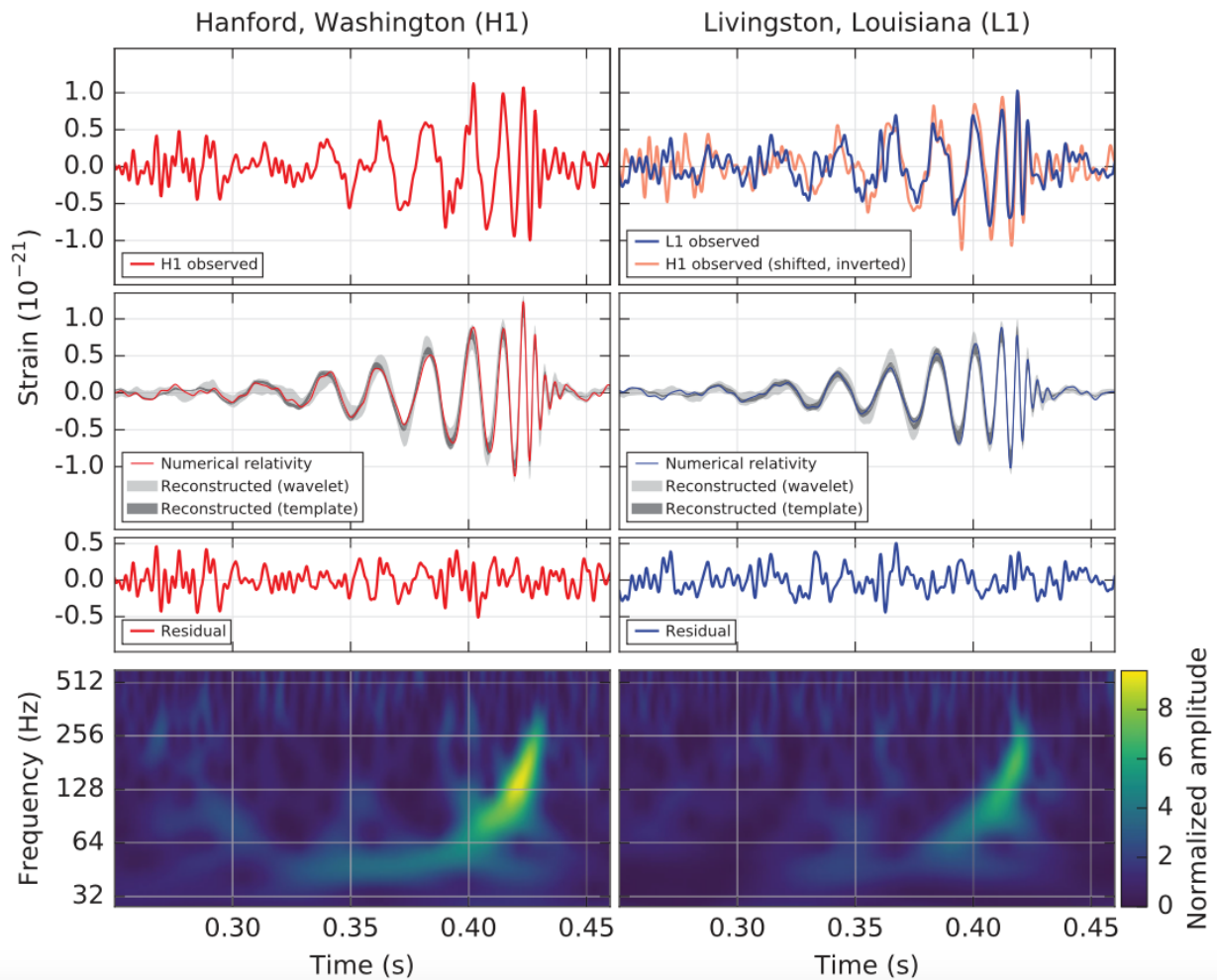
Fig. 10.61 The first gravitational-wave event (GW150914) observed by LIGO: left from the Hanford (H1) site; right from the Livingston (L1) site From Phys. Rev. Lett. 116, 061102 (2016).

The direct evidence was firmly established in 2015 by the LIGO/Virgo collaboration detecting the collapse of pairs of black holes (Nobel Prize in Physics 2017 awarded to Rainer Weiss, Barry C. Barish and Kip S. Thorne). On September 14th, 2015, the two detectors of the LIGO collaboration observed simultaneously a large and clear gravitational wave signal (labelled as GW150914) that matches the prediction of general relativity for the coalescence of a binary black hole system (see Fig. 10.61). The simulation of such merger is shown in Fig. 10.62 where three phases are well identified:

1. *Inspiral*: the approach of the two black holes; in this phase frequency and amplitude increase slowly;
2. *Merger*: the merging of the two black holes; frequency and amplitude increase rapidly;
3. *Ringdown*: the newly formed black hole is distorted and rings down to its final state by emitting characteristic radiation: the ringdown radiation. This radiation has a precise frequency and its amplitude decays exponentially as time goes by. The ringdown phase is similar to that of a church bell or a guitar string when plucked: black holes also have a characteristic sound! After this stage, there is only a single, quiet black hole, and no radiation is emitted.

The observed amplitudes (*strain* - see Chap. 8), are of the order of 10^{-21} and the frequencies are in the range 35 to 250 Hz. The masses of the initial black holes were estimated to be 36^{+5}_{-4} and 29^{+4}_{-4} solar masses while the final black hole mass was estimated to be 62^{+4}_{-4} solar masses. The luminosity distance of such system was estimated to be 410^{+160}_{-180} Mpc.

Four more events were observed by LIGO respectively in December 2015, January 2017 (already during the second observation run), August 2017 (two events, one of which with a positive observation as well by Virgo), again interpreted as the coalescence of binary black hole system:
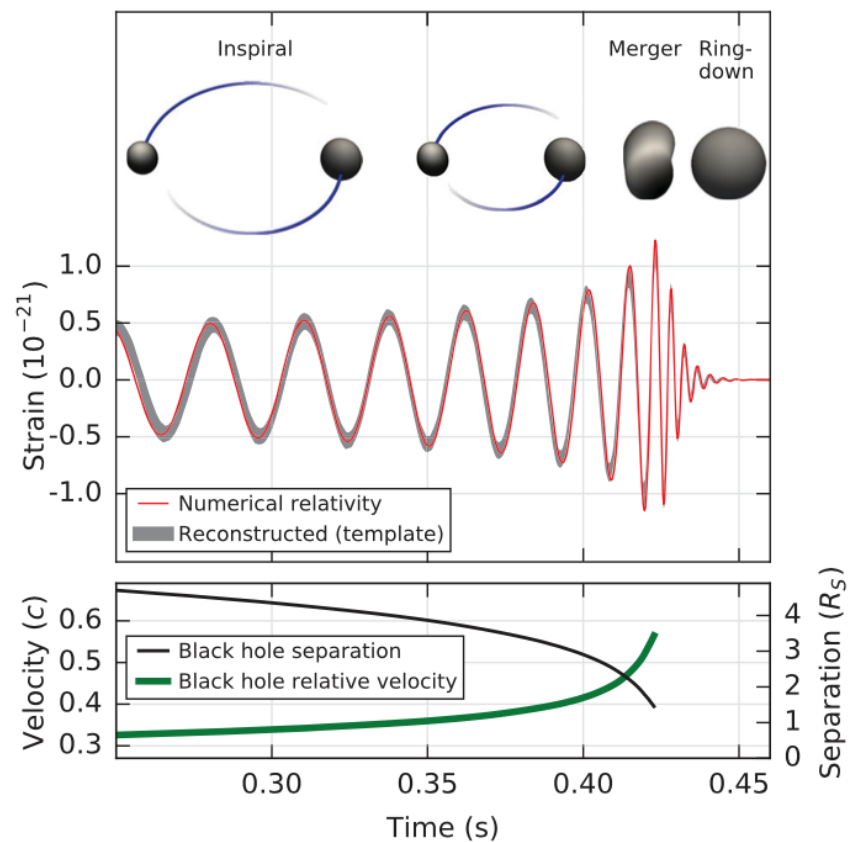
Fig. 10.62 Top: The waveform of the merger of a binary black hole system with the parameters measured from GW150914. Estimated gravitational-wave strain amplitude from GW150914 projected onto H1. Bottom: The BH separation in units of Schwarzschild radii and the relative velocity normalized to the speed of light c. From Phys. Rev. Lett. 116, 061102 (2016).

- In the event GW151226 the masses of the initial black holes were estimated to be $14.2^{+8.3}_{-3.7}$ and $7.5^{+2.3}_{-2.3}$ solar masses while the final BH mass was estimated to be $20.8^{+6.1}_{-1.7}$ solar masses. The luminosity distance of such system was estimated to be 440^{+180}_{-190} Mpc.
- In GW170104 the masses of the initial BHs were estimated to be $31.2^{+8.4}_{-6.0}$ and $19.4^{+5.3}_{-5.9}$ solar masses while the final BH mass was estimated to be $48.7^{+5.7}_{-4.6}$ solar masses. The luminosity distance of such system was estimated to be 340 ± 140 Mpc.
- In GW170608 the masses of the initial BHs were estimated to be 12^{+7}_{-2} and 7 ± 2 solar masses while the final BH mass was estimated to be $18^{+4.8}_{-0.9}$ solar masses. The luminosity distance of such system was estimated to be 880^{+450}_{-390} Mpc.
- GW170814 resulted from the inspiral and merger of a pair of black holes with $30.5^{+5.7}_{-3.0}$ and $25.3^{+2.8}_{-4.2}$ times the mass of the Sun, at a distance of 540^{+130}_{-210} Mpc from Earth. The resulting black hole had a mass of $53.2^{+3.2}_{-2.5}$ solar masses, 2.7 solar masses having been radiated away as gravitational energy. The peak luminosity was about 3.7×10^{49} W.

Contrary to what was previously believed there is thus a significant population of binary BH systems with component masses of tens of solar masses and merger rates that allow their regular detection by the present GW observatories. The study of these events has shown, so far, no evidence of any deviation from the General Relativity predictions. In Fig. 10.63 the masses of the initial and final BH detected mergers are compared to the BHs observed in X rays and to the known neutron star masses.

A special GW event, different in nature from the previous five, has been detected on August 17, 2017.
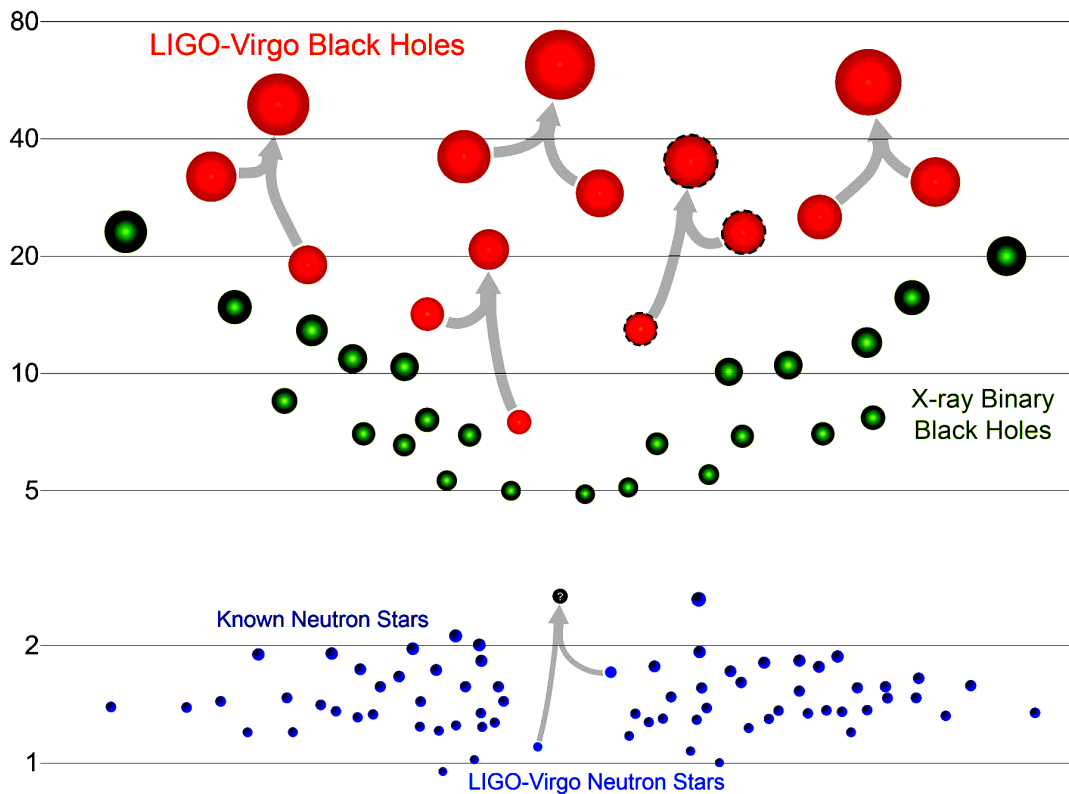
Fig. 10.63 The masses of the black holes and neutron stars measured through GW observations are shown together with those detected through electromagnetic observations. Adapted from LIGO-Virgo/Frank Elavsky/Northwestern University.

10.4.4.1 GW170817, the first multimessenger discovery of a binary neutron star merger

The first observation of a single astrophysical source through both gravitational and electromagnetic waves happened on August 17, 2017. LIGO/Virgo detected a gravitational wave signal possibly associated with the merger of two neutron stars (GW170817), and (1.75 ± 0.05) s later the *Fermi* Gamma-Ray Burst Monitor and the INTEGRAL SPI/ACS detector observed independently in the same sky region (Fig. 10.64) a short, ~ 2 s long, GRB (GRB 170817A) whose time-averaged spectrum is well fit by a power law function with an exponential high-energy cutoff at ~ 80 keV. The masses of the initial neutron stars were estimated to be in the range [1.36, 2.26] solar masses and [0.86, 1.36] solar masses respectively, while the final mass was estimated to be $2.82^{+0.47}_{-0.09} M_\odot$. These observations were followed by an extensive multimessenger campaign covering all the electromagnetic spectrum as well as the neutrino channel: a bright optical transient (SSS17a) was discovered in the NGC 4993 galaxy located at 40 Mpc of the Earth by the Swope Telescope in South America and shortly after by five more teams. The follow-up was then done by ground and space observatories all around the world: X-ray and radio counterparts were discovered respectively ~ 9 days and ~ 16 days after the merger, while no neutrino candidates were seen.

The neutron star merger event is thought to result in a "kilonova", characterized by a short GRB followed by a longer optical afterglow. A total of 16 000 times the mass of the Earth in heavy elements is believed to have formed; for some of them spectroscopical signatures have been observed.

The scientific importance of this event is huge. Just to quote two aspects:

- It provides strong evidence that mergers of binary stars are the cause of short GRBs.
- It provides a limit on the difference between the speed of light and that of gravity. Assuming the first photons were emitted between zero and ten seconds after peak gravitational wave emission, the relative difference between the speeds of gravitational and electromagnetic waves, $|v_{GW} - v_{EM}|/c$, is constrained to be smaller than $\sim 10^{-15}$.

Unlike all previous GW detections, corresponding to BH mergings and not expected to produce a detectable electromagnetic signal, the aftermath of this merger was seen by 70 observatories across the electro-
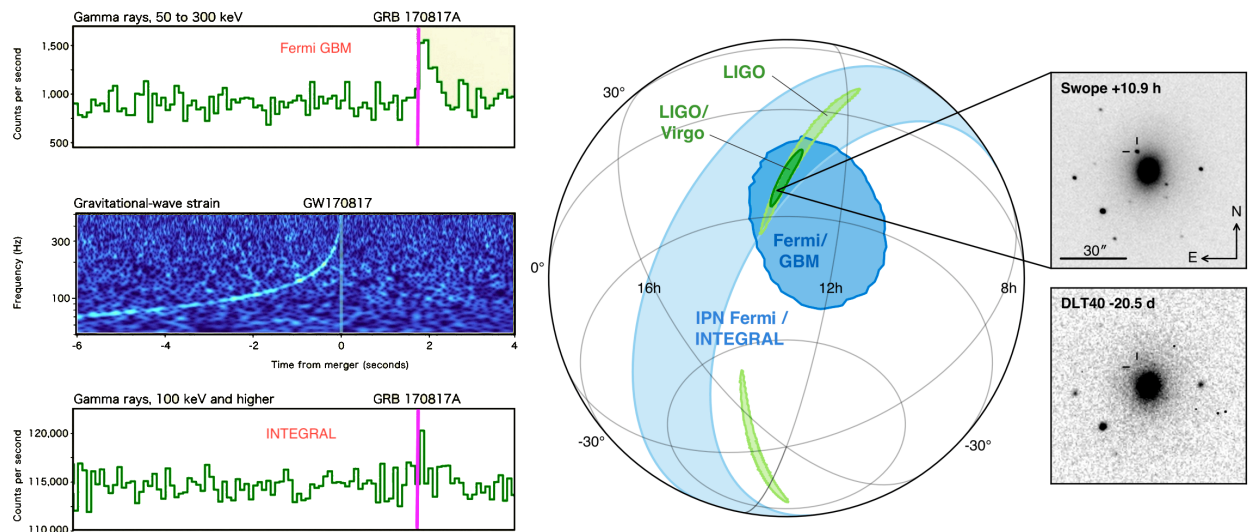
Fig. 10.64 The signals detected by *Fermi* GBM (top left), by LIGO/Virgo (center left), and by INTEGRAL (bottom left); the 90% location contour regions of the GW170817 / GRB 170817A / SSS17a event as determined by LIGO, LIGO-Virgo, INTEGRAL, *Fermi*. The insets show the location of the NGC 4993 galaxy in the images of the Swope (top right) and of the DLT40 (bottom right) optical telescopes respectively 10.9 hr after and 20.5 days before the GW observation. The perpendicular lines indicate the location of the transient in both images.. Courtesy S. Ciprini, ASI.

magnetic spectrum, marking a significant breakthrough for multi-messenger astronomy and opening a new era. Several events of this kind can be expected in the future.

10.5 Future Experiments and Open Questions

The field of astroparticle physics has been extremely successful: five Nobel Prizes (2002, 2006, 2011, 2015 and 2017) have been awarded to astroparticle physics in this millennium.

The next 10-20 years will see a dramatic progress using new detectors to improve the synergy between cosmic messengers: charged cosmic rays, gamma rays, neutrinos and gravitational waves.

10.5.1 Charged Cosmic Rays

More than one hundred years after their discovery, charged cosmic rays are still, and will be, actively studied through many experiments covering many energy decades. Up to the knee region (10^{15} - 10^{16} eV) their origin is basically Galactic and the paradigm that associates their origin with SNRs is in a good shape. Other sources of cosmic rays were found in the Galaxy; however, only one or two Galactic accelerators were found potentially reaching the PeV energies. There is significant evidence that part of the cosmic rays above the EeV come from AGN; however, no individual associations were possible with certainty at these energies. There is evidence that, although GRBs have the energetics for producing CRs above the EeV, their contribution to cosmic rays at extreme energies is negligible.

Measuring with high statistics and precision the different particle (electron, positron, proton, antiprotons, nuclei) spectra, deviations from the Universal power-law behavior expected from the Fermi acceleration mechanism were found with gradual or abrupt changes in energy dependence. Indeed a new era of precision and statistics was recently opened thanks to a new generation of cosmic ray experiments like PAMELA, AMS-02, DAMPE and CALET and, in a different energy-range, ARGO-YBJ and HAWC (see Sect. 10.4); this line will be vigorously pursued in the next years by the present and future (LHAASO, HERD, ...) experiments.

We face thus an enormous challenge to describe cosmic rays, and both the injection (acceleration) and propagation models have to be deeply improved. The increase in computer power allows now multidimensional

particle-in-cell (PIC) kinetic simulations able to cope with the non-linear interplay between energetic particles and electromagnetic fields in strong shock wave environments. These simulations are starting nowadays to reproduce the needed Diffuse Shock Acceleration (DSA) mechanisms with the formation of turbulent structures where magnetic fields can be amplified. A better understanding of the SNR interaction with the interstellar medium as well as of the complex damping, unstable and anisotropic transport mechanisms will lead to a clearer picture of the formation and evolution of stars and galaxies. This will need an interplay with X- and gamma-ray detectors (especially in the MeV region, which marks the interactions of CRs with the environment).

The unexpected bump-like structure observed in the positron spectrum by AMS-02, compatible with the products of the self-annihilation of a Dark Matter particle with a mass around 1 TeV (see Sect. 10.4.1.3), remains to be clarified and probably we will have to wait a few years in order that AMS-02 will have enough statistics to reasonably measure the properties of this structure.

The quest for the origin and nature of UHECRs will remain in the list of highlights for the next decade. So far large-scale anisotropies were found at energies around 10^{19} eV (the dipole structure observed by the Pierre Auger Observatory and the indication of a hotspot by the Telescope Array Experiment–see Sect. 10.4.1.6); on the contrary, just possible weak correlations with individual astrophysical sources locations were reported. Statistics is desperately needed and the increase by a factor four of the initial 700 km^2 area of the TA as well as the upgrade of Auger, with with the introduction of scintillators on the top of the Water Cherenkov Detectors, will for sure help.

Composition at extremely high energies and in particular the physical interpretation of a "GZK-like" cutoff in the observed CRs around 10^{20} eV is a central subject. The scenario of an exhaustion of the sources at these energies is making its way in the community. However our QCD-inspired shower models are not able to describe satisfactorily both the electromagnetic and the hadronic EAS components, and thus no firm conclusion may be achieved: scenarios involving "new Physics" at c.m. energies well above those attained by the LHC accelerator can not be discarded. The upgraded Auger will allow disentangling of the electromagnetic and muonic components of the EAS on an event-by-event basis, and thus may shed some light on this long-standing problem.

The idea, pioneered in the 1990s by John Linsley, Livio Scarsi and Yoshiyuki Takahashi, of a wide field-of-view space observatory able to detect from above the UV light produced in the atmosphere by the very energetic EAS is still under intense discussion. What is called nowadays the "EUSO concept" covers a large range of experimental initiatives and projects and a dedicated space mission may be approved in the next decade. The collection area will be huge and may allow the detection of very high energy tau neutrinos (10^{18} - 10^{19} eV).

10.5.2 Gamma Rays

10.5.2.1 The region till a few MeV

This region has important implications on the science at the TeV and above, since a good knowledge of the spectra in the MeV region can constrain the fit to the emitted spectra at high energies, thus allowing:

- to evidence additional contributions from new physics (dark matter in particular);
- to estimate cosmological absorption, due for example to EBL or to possible interactions with axion-like fields.

On top of this, The 0.3-300 MeV energy range is important per se, since it is the energy region:

- characteristic of nuclear transitions;
- characteristic of the nuclear de-excitation of molecular clouds excited by colliding cosmic rays;
- where one expects the exhaustion of the electromagnetic counterpart of gravitational wave events;
- where one expects gamma rays from the conversion of axions in the core of supernovae.

Unfortunately, it is experimentally difficult to study. It requires an efficient instrument working in the Compton regime with an excellent background subtraction, and possibly with sensitivity to the measurement of polarization. Since COMPTEL, which operated two decades ago, no space instrument obtained extra-solar gamma-ray data in the few MeV range; now we are able to build an instrument one-two orders of magnitudes

more sensitive than COMPTEL based on silicon detector technology, state-of-the-art analog readout, and efficient data acquisition.

Several proposals of satellites have been made, and convergence is likely for an experiment to be launched around 2028.

10.5.2.2 The GeV region

It is difficult to think for this century of an instrument for GeV photons improving substantially the performance of the *Fermi* LAT: the cost of space missions is such that the size of *Fermi* cannot be reasonably overcome with present technologies. New satellites in construction (like the Chinese-Italian mission HERD) will improve some of the aspects of *Fermi*, e.g., calorimetry. For sure a satellite in the GeV region with sensitivity comparable with *Fermi* will be needed in space (*Fermi* could in principle operate till 2028).

10.5.2.3 The sub-TeV and TeV regions

CTA appears to have no rivals for the gamma astrophysics in the sub-TeV and TeV (from a few GeV to a few TeV) energy regions. These are crucial regions for fundamental physics, and for astronomy.

PeVatrons and the nature of the emitters in the Galaxy will be studied in detail. WIMPs will be tested with the "right" sensitivity up to 1 TeV.

CTA will be probably upgraded including state-of-the art photon detection devices of higher efficiencies with respect to the present ones; it can in principle operate till 2050.

10.5.3 The PeV region

Due to the opacity of the Universe to gamma rays, less than a handful of sources could be visible in the Northern sky, and less than a dozen in the Southern sky, all galactic. The experiments in the Northern hemisphere (the extended HAWC, LHAASO, TAIGA/HiSCORE) provide an appropriate coverage of the Northern sky and a detailed study of PeVatrons.

The situation in the Southern hemisphere has room for improvement. An EAS detector in the South might give substantial input with respect to the knowledge of the gamma sky, and of possible PeVatrons in the Galactic center, and outperform in this sense the small-size telescopes of CTA. Several proposals are being formulated now, and they will probably merge. A large detector in Southern America could compete in sensitivity with the SSTs of CTA-South already at 100 TeV, offering in addition a serendipitous approach.

10.5.4 High Energy Neutrinos

The discovery of the very High Energy Astrophysical neutrinos (see Sect. 10.4.3.2) opens the era of the High Energy ($>10^{15}$eV) neutrino astronomy.

Neutrino astronomy will progress along three directions:

- The "large volume" direction. The absorption length of Cherenkov light to which the photomultipliers are sensitive exceeds 100 m in ice. Spacings of 250 m, possibly larger, between photomultipliers, are thus acceptable in IceCube. One can therefore instrument a ten-times-larger volume of ice with the same number of strings used to build IceCube. A next-generation instrument using superior light sensors and this enlarged spacing, provisionally called IceCube-Gen2, could have an affordable cost; construction can take 5 years. IceCube-Gen2 can increase, in the next years, the volume and sensitivity of the present detector by more than an order of magnitude and hopefully will be able to identify the neutrino sources and help to decipher the location of the extremely-high-energy cosmic ray accelerators.
- The "precision" direction. If funded, KM3NeT will consist of 115 strings carrying more than 2 000 optical modules, instrumenting a volume of 3 km^3. The vertical distances between optical modules will be 36 meters, with horizontal distances between detection units of about 90 meters; reconstruction accuracy will

be thus a factor of 2 better than in IceCube. Construction is now ongoing in Sicily. IceCube has discovered a flux of extragalactic cosmic neutrinos with an energy density that matches that of extragalactic high-energy photons and UHE CRs. This may suggest that neutrinos and high-energy CRs share a common origin, and the better resolution of KM3NeT could be the ket to pinpoint sources.

A parallel effort is underway in Lake Baikal with the deep underwater neutrino telescope Baikal-GVD (Gigaton Volume Detector). The first GVD cluster, named DUBNA, was upgraded in spring 2016 to its final size (288 optical modules, 120 meters in diameter, 525 meters high, and instrumented volume of 6 Mton). Each of the eight strings consists of three sections with 12 optical modules. Deployment of a second cluster was completed in spring 2017.

- The "extremely high energy" direction, using new technologies. At extremely high energies, above 100 PeV, a cosmogenic neutrino flux is expected from the interaction of highest energy cosmic-ray protons with the CMB. Predicted fluxes are in a range of approximately 1 event/year/km^3 or lower. The idea to increase the effective volume of detectors to be sensitive to such rates seems unfeasible, unless the EUSO concept (see Chap. 4) is adopted; detection of coherent radio emission up to GHz originated by the neutrino interaction in dense, radio-transparent media, the so-called Askar'yan effect, is preferred. Several prototype detectors are being developed.

Neutrino Astronomy has just started and a rich physics program is ahead of us. A global neutrino network (IceCube-Gen2 in the South Pole, Gigaton Volume Detector (GVD) in the lake Baikal and KM3NeT in the Mediterranean sea) will operate.

10.5.5 Gravitational Waves

The direct determination of gravitational waves (see Sect. 10.4.4) opened the new field of gravitational wave astronomy. In the next years an aggressive experimental program will allow to extend it in sensitivity, precision and frequency range. Indeed LIGO, in the USA, that has started operating in 2015, has been joined by the upgraded Virgo detector, in Italy, in 2017, and soon will be joined by the newcomer KAGRA interferometer, in Japan (for a detector description see Chap. 4). These second generation detectors, possibly including the indian LIGO (INDIGO) gravitational wave detector, will form a large international network allowing the improvement of the angular resolution by more than one order of magnitude, and the present sensitivity by a factor of two. This setup will be probably ready before 2024.

A third generation of detector, the Einstein Telescope, with longer baseline (10 km) and cryogenic mirrors, is under study in Europe and, hopefully, will operate around 2024 with an extended observation range (3 Gpc) and a sensitivity 10 times better then the second generation telescopes. It will be built in underground sites, and it will have three arms, in order to measure by itself the direction of a source and to issue autonomously alerts. A similar detector, four times larger, is under study in the US: the Cosmic Explorer. The number of observed events will increase therefore from a couple per month to a few per day allowing the mapping of the gravitational wave astrophysical sources and their detailed study not excluding the (probable) discovery of unexpected new classes of sources.

The lower frequencies, which are relevant to access gravitational waves emitted in the early Universe and thus to test cosmological models, have to be covered from space based detectors. Two space experiments, LISA (ESA) and DECIGO (JAXA) covering respectively the frequency range from 0.03 mHz to 0.1 Hz and from 0.1 Hz to 10 Hz are planned to operate in 20 years. LISA has been scheduled for launch in 2034.

Gravitational waves observatories will be for sure privileged laboratories for general relativity; namely:

- GWs will allow to perform precision tests of General Relativity. The inspiral phase will allow to test if the inspiral proceeds as predicted by General Relativity. Faster inspirals could signal new fields (for example, charged black holes would radiate more and inspiral faster) or even a nontrivial astrophysical environment (if the inspiral is taking place in a large-density dark matter environment, inspiral would also proceed faster).
- GWs will allow to test the Kerr nature of black holes. In GR, the most general black hole solution belongs to the Kerr family, and is specified by only two parameters: mass and angular momentum. This fact is part of the uniqueness or "no-hair" conjecture[10]. The ringdown phase of black holes allow one to measure precisely the characteristic modes of black holes and to test if they really belong to the Kerr family.

---

[10] The no-hair conjecture, sometimes called "theorem" postulates that all solutions of the equations of gravitation and electromagnetism for a BH can be characterized by only three externally observable parameters: mass, electric charge, and angular

- GWs will allow new probes of quantum gravity.
- GWs will allow us to map the entire compact object content of the universe. Both the inspiral and ringdown phase allow us to measure mass and spin of black holes to an unprecedented precision. If coupled to electromagnetic observations, there is the exciting prospect of determining, in addition, their position. In summary, detailed maps of the black Universe will be possible.

10.5.6 Multi-Messenger Astrophysics

Cosmic ray, neutrino and gravitational waves became, in the last years, full right members of the Astronomy club until then just frequented by the electromagnetic waves in all wavelengths (radio, microwaves, IR, optical, UV, X rays, gamma rays, with a clear need for improvement in the MeV region). In the previous sections each of these channels were individually discussed and their ambitious future experimental programs, involving the upgrade and/or the construction of new observatories at ground or in space, were referred.

The challenge for the next years is also to make a fully efficient combined use of all of these infrastructures, not only making available and analysing a posteriori the collected data, but also performing joint observations whenever a transient phenomenon appeared. Wide field of view observatories should be able to launch "alerts" and trigger the narrow FoV ones.

Networks joining some of these observatories do exist already. Examples are: the GCN (Gamma-ray Coordinates Network) , which reports in real-time (or near real-time) locations of GRBs and other transients detected by spacecrafts (Swift, *Fermi*, INTEGRAL, Athena, etc.) producing also follow-up reports of the observations; the AMON (Astrophysical Multimessenger Observatory Network), which provides correlation analyses (real-time or archival) of astrophysical transients and/or sources – among AMON members are ANTARES, Auger, *Fermi*, HAWC, IceCube, LIGO, the Large Millimeter Telescope, MASTER, the Palomar Transient Factory, Swift, MAGIC, VERITAS.

Multi-messenger astronomy is becoming a powerful tool to monitor and understand the Universe we live in.

Further Reading

[F10.1] M. Spurio, "Particles and Astrophysics (a Multi-Messenger Approach)," Springer 2015. Taking a systematic approach, this book comprehensively presents experimental aspects from the most advanced cosmic ray detectors, in particular detectors of photons at different wavelengths.
[F10.2] T. Stanev, "High-Energy Cosmic Rays," Springer 2010. A classic for experts in the discipline.
[F10.3] D.H. Perkins, "Particle Astrophysics," 2nd edition, Oxford University Press 2008.
[F10.4] K. S. Thorne, unpublished, http://elmer.tapir.caltech.edu/ph237.
[F10.5] T.K. Gaisser, R. Engel, E. Resconi, "Cosmic Rays and Particle Physics", 2nd edition, Cambridge University Press 2016. The classic book written by Gaisser in 1990 recently revisited. A reference for particle acceleration and diffusion.
[F10.6] M. Longair, "High Energy Astrophysics", 3rd edition, Cambridge 2011.

Exercises

1. *Fermi acceleration mechanisms.* In the Fermi acceleration mechanism, charged particles increase considerably their energies crossing back and forth many times the border of a magnetic cloud (second-order Fermi mechanism) or of a shock wave (first-order Fermi mechanism). Compute the number of crossings that a particle must do in each of the mechanisms to gain a factor 10 on its initial energy assuming:

   (a) $\beta = 10^{-4}$ for the magnetic cloud and $\beta = 10^{-2}$ for the shock wave;
   (b) $\beta = 10^{-4}$ for both acceleration mechanisms.

---

momentum. All other information (for which "hair" is a metaphor) disappears behind the BH horizon and is therefore inaccessible to external observers.

2. *Photon spectrum in hadronic cascades.* Demonstrate that in a decay $\pi^0 \to \gamma\gamma$, once boosted for the energy of the emitting π^0, the probability to emit a photon of energy E_γ is constant over the range of kinematically allowed energies.

3. *Top-down production mechanisms for photons: decay of a WIMP.* If a WIMP of mass $M > M_Z$ decays into γZ, estimate the energy of the photon and of the Z.

4. *Acceleration and propagation.* The transparency of the Universe to a given particle depends critically on its nature and energy. In fact, whenever it is possible to open an inelastic channel of the interaction between the *traveling* particle and the CMB, its mean free path diminishes drastically. Assuming that the only relevant phenomena that rules the mean free path of the *traveling* particle is the CMB (CνB), estimate the order of magnitude energies at which the transparency of the Universe changes significantly, for:

   (a) Photons;
   (b) Protons;
   (c) Neutrinos.

   Assume $\langle E_{\gamma_{CMB}} \rangle \simeq 0.24$ meV; $\langle E_{\nu_{C\nu B}} \rangle \simeq 0.17$ meV.

5. *Photon-photon interactions.* Demonstrate that, for an isotropic background of photons, the cross section is maximized for background photons of energy:

$$\epsilon(E) \simeq \left(\frac{900\,\text{GeV}}{E} \right)\,\text{eV} \;.$$

6. *Neutrinos from SN1987A.* Neutrinos from SN1987A, at an energy of about 50 MeV, arrived in a bunch lasting 13 s from a distance of 50 kpc, 3 h before the optical detection of the supernova. What can you say on the neutrino mass? What can you say about the neutrino speed (be careful...)?

7. *Neutrinos from SN1987A, again.* Some (including one of the authors of this book) saw in Fig. 10.57 two lines relating arrival times of neutrinos with energy, and derived the masses of two neutrino species. What can you say about the neutrino masses in relation to the current neutrino mass limits?

8. *Time lag in light propagation.* Suppose that the speed c of light depends on its energy E in such a way that

$$c(E) \simeq c_0 \left(1 + \xi \frac{E^2}{E_P^2} \right) ,$$

   where E_P is the Planck energy (second-order Lorentz Invariance Violation). Compute the time lag between two VHE photons as a function of the energy difference and of the redshift z.

9. *Difference between the speed of light and the speed of gravitational waves.* Derive a limit on the relative difference between the speed of light and the speed of gravitational waves from the fact that the gamma-ray burst GRB170824A at a distance of about 40 Mpc was detected about 1.7 s after the gravitational wave GW170817.

10. *Flux of photons from Crab.* Consider the expression 10.56 in the text and let us assume that the flux of cosmic rays between 0.05 TeV and 2 PeV follows this expression.
    The flux from the most luminous steady (or almost steady) source of gamma rays, the Crab Nebula, follows, according to the measurements from MAGIC, a law

$$N_\gamma(E) \simeq 3.23 \times 10^{-7} \left(\frac{E}{\text{TeV}} \right)^{-2.47 - 0.24 \left(\frac{E}{\text{TeV}} \right)} \text{TeV}^{-1}\text{s}^{-1}\text{m}^{-2} \;. \tag{10.65}$$

    Translate this expression into GeV. Compute the number of photons from Crab hitting every second a surface of $10\,000$ m^2 above a threshold of 50 GeV, 100 GeV, 200 GeV, 1 TeV, up to 500 TeV. Compare this number to the background from the flux of cosmic rays in a cone of 1 degree of radius.

11. *Astronomy with protons?* If the average magnetic field in the Milky Way is 1 μG, what is the minimum energy of a proton coming from Crab Nebula (at a distance of 2 kpc from the Earth) we can detect as "pointing" to the source?

12. *Maximum acceleration energy for electrons.* The synchrotron loss rate is relatively much more important for electrons than for protons. To find the limit placed by synchrotron losses on shock acceleration of electrons, compare the acceleration rate for electrons with the synchrotron loss rate. The latter is negligible at low energy, but increases quadratically with E. Determine the crossover energy, and compare it to supernova ages. Is the acceleration of electrons limited by synchrotron radiation?

13. *Classification of blazars.* Looking to Fig. 10.17, right, how would you classify Markarian 421, BL Lac and 3C279 within the blazar sequence? Why?

14. $\gamma\gamma \to e^+e^-$. Compute the energy threshold for the process as a function of the energy of the target photon, and compare it to the energy for which the absorption of extragalactic gamma-rays is maximal.

15. *Hadronic photoproduction vs. photon-pair production mechanisms.* High-energy protons traveling in the intergalactic space may interact with CMB photons either via a photoproduction mechanism ($p\gamma \to N\pi$) or via a pair production mechanism ($p\gamma \to pe^+e^-$). Assume for the first process a cross section of about 0.5 mb, while for the second process it is some 40 times larger.

   (a) Compute the threshold energies for either production mechanism.
   (b) Calculate the propagation length for protons to lose 90% of their energies in either mechanism.

16. *Mixing photons with paraphotons.* The existence of a neutral particle of tiny mass μ, the paraphoton, coupled to the photon, has been suggested to explain possible anomalies in the CMB spectrum and in photon propagation (the mechanism is similar to the one discussed to the photon-axion mixing, but there are no complications related to spin here). Calling ϕ the mixing angle between the photon and the paraphoton, express the probability of oscillation of a photon to a paraphoton as a function of time (note: the formalism is the same as for neutrino oscillations). Supposing that the paraphoton is sterile, compute a reasonable range of values for ϕ and μ that could explain an enhancement by a factor of 2 for the signal detected at 500 GeV from the AGN 3C279 at $z \simeq 0.54$.

17. *Photon absorption affects the shape of the SED.* TXS 0506 +056 has a redshift of 0.34. What is the fraction of gamma rays absorbed due to interaction with EBL at an energy $E = 400$ GeV? If the measured spectral index if of 2.3, what can you say about the spectral index at emission?

18. *Estimating the energy of a cosmic accelerator from the energy of emitted neutrinos.* How would you estimate the energy of the proton generating a 300 GeV neutrino in the flare of a blazar?

19. *The standard model of particle physics cannot provide dark matter.* Name all particles which are described by the SM and write down through which force(s) they can interact. Why can we rule out that a dark matter particle does interact through the electromagnetic force? Why can we rule out that a dark matter particle does interact through the strong force? Now mark all particles which pass the above requirements and could account for dark matter, and comment.

20. *How well do we know that Dwarf Spheroidals are good targets for hunting Dark Matter?* Draco is a dwarf spheroidal galaxy within the Local Group. Its luminosity is $L = (1.8 \pm 0.8) \times 10^5 L_\odot$ and half of it is contained within a sphere of radius of (120 ± 12) pc. The measured velocity dispersion of the red giant stars in Draco is (10.5 ± 2.2) km/s. What is our best estimate for the mass M of the Draco dSph? What about its M/L ratio? Which are our main uncertainties in such determinations?

21. *Tremaine-Gunn bound.* Assume that neutrinos have a mass, large enough that they are non-relativistic today. This neutrino gas would not be homogeneous, but clustered around galaxies. Assume that they dominate the mass of these galaxies (ignore other matter). We know the mass $M(r)$ within a given radius r in a galaxy from the velocity $v(r)$ of stars rotating around it. The mass could be due to a few species of heavy neutrinos or more species of lighter neutrinos. But the available phase space limits the number of neutrinos with velocities below the escape velocity from the galaxy. This gives a lower limit for the mass of neutrinos. Assume for simplicity that all neutrinos have the same mass. Find a rough estimate for the minimum mass required for neutrinos to dominate the mass of a galaxy. Assume spherical symmetry and that the escape velocity within radius r is the same as at radius r.

A Periodic Table of the Elements

PERIODIC TABLE OF THE ELEMENTS

1 IA	2 IIA	3 IIIB	4 IVB	5 VB	6 VIB	7 VIIB	8	9 VIII	10	11 IB	12 IIB	13 IIIA	14 IVA	15 VA	16 VIA	17 VIIA	18 VIIIA
1 H hydrogen 1.008																	2 He helium 4.002602
3 Li lithium 6.94	4 Be beryllium 9.012182											5 B boron 10.81	6 C carbon 12.0107	7 N nitrogen 14.007	8 O oxygen 15.999	9 F fluorine 18.998403163	10 Ne neon 20.1797
11 Na sodium 22.98976928	12 Mg magnesium 24.305											13 Al aluminum 26.9815385	14 Si silicon 28.085	15 P phosphorus 30.973761998	16 S sulfur 32.06	17 Cl chlorine 35.45	18 Ar argon 39.948
19 K potassium 39.0983	20 Ca calcium 40.078	21 Sc scandium 44.955908	22 Ti titanium 47.867	23 V vanadium 50.9415	24 Cr chromium 51.9961	25 Mn manganese 54.938044	26 Fe iron 55.845	27 Co cobalt 58.933195	28 Ni nickel 58.6934	29 Cu copper 63.546	30 Zn zinc 65.38	31 Ga gallium 69.723	32 Ge germanium 72.630	33 As arsenic 74.921595	34 Se selenium 78.971	35 Br bromine 79.904	36 Kr krypton 83.798
37 Rb rubidium 85.4678	38 Sr strontium 87.62	39 Y yttrium 88.90584	40 Zr zirconium 91.224	41 Nb niobium 92.90637	42 Mo molybdenum 95.95	43 Tc technetium (97.907212)	44 Ru ruthenium 101.07	45 Rh rhodium 102.90550	46 Pd palladium 106.42	47 Ag silver 107.8682	48 Cd cadmium 112.414	49 In indium 114.818	50 Sn tin 118.710	51 Sb antimony 121.760	52 Te tellurium 127.60	53 I iodine 126.90447	54 Xe xenon 131.293
55 Cs caesium 132.90545196	56 Ba barium 137.327	57–71 LANTHANIDES	72 Hf hafnium 178.49	73 Ta tantalum 180.94788	74 W tungsten 183.84	75 Re rhenium 186.207	76 Os osmium 190.23	77 Ir iridium 192.217	78 Pt platinum 195.084	79 Au gold 196.966569	80 Hg mercury 200.592	81 Tl thallium 204.38	82 Pb lead 207.2	83 Bi bismuth 208.98040	84 Po polonium (208.98243)	85 At astatine (209.98715)	86 Rn radon (222.01758)
87 Fr francium (223.01974)	88 Ra radium (226.02541)	89–103 ACTINIDES	104 Rf rutherford. (267.12169)	105 Db dubnium (268.12567)	106 Sg seaborgium (271.13393)	107 Bh bohrium (272.13826)	108 Hs hassium (270.13429)	109 Mt meitnerium (276.15159)	110 Ds darmstadt. (281.16451)	111 Rg roentgen. (280.16514)	112 Cn copernicium (285.17712)	113 Nh nihonium (284.17873)	114 Fl flerovium (289.19042)	115 Mc moscovium (288.19274)	116 Lv livermorium (293.20449)	117 Ts tennessine (292.20746)	118 Og oganesson (294.21392)

Lanthanide series

57 La lanthanum 138.90547	58 Ce cerium 140.116	59 Pr praseodym. 140.90766	60 Nd neodymium 144.242	61 Pm promethium (144.91276)	62 Sm samarium 150.36	63 Eu europium 151.964	64 Gd gadolinium 157.25	65 Tb terbium 158.92535	66 Dy dysprosium 162.500	67 Ho holmium 164.93033	68 Er erbium 167.259	69 Tm thulium 168.93422	70 Yb ytterbium 173.054	71 Lu lutetium 174.9668

Actinide series

89 Ac actinium (227.02775)	90 Th thorium 232.0377	91 Pa protactinium 231.03588	92 U uranium 238.02891	93 Np neptunium (237.04817)	94 Pu plutonium (244.06420)	95 Am americium (243.06138)	96 Cm curium (247.07035)	97 Bk berkelium (247.07031)	98 Cf californium (251.07959)	99 Es einsteinium (252.08298)	100 Fm fermium (257.09511)	101 Md mendelevium (258.09844)	102 No nobelium (259.10103)	103 Lr lawrencium (262.10961)

B Properties of Materials

Material	Z	A	$\langle Z/A \rangle$	Nucl.coll. length λ_T {g cm^{-2}}	Nucl.inter. length λ_I {g cm^{-2}}	Rad.len. X_0 {g cm^{-2}}	$dE/dx\|_{\min}$ { MeV g^{-1}cm^2}	Density {g cm^{-3}} ({g ℓ^{-1}})	Melting point (K)	Boiling point (K)	Refract. index 589.2 nm
H$_2$	1	1.008(7)	0.99212	42.8	52.0	63.05	(4.103)	0.071(0.084)	13.81	20.28	1.11
D$_2$	1	2.014101764(8)	0.49650	51.3	71.8	125.97	(2.053)	0.169(0.168)	18.7	23.65	1.11
He	2	4.002602(2)	0.49967	51.8	71.0	94.32	(1.937)	0.125(0.166)		4.220	1.02
Li	3	6.94(2)	0.43221	52.2	71.3	82.78	1.639	0.534	453.6	1615.	
Be	4	9.0121831(5)	0.44384	55.3	77.8	65.19	1.595	1.848	1560.	2744.	
C diamond	6	12.0107(8)	0.49955	59.2	85.8	42.70	1.725	3.520			2.419
C graphite	6	12.0107(8)	0.49955	59.2	85.8	42.70	1.742	2.210	Sublimes at 4098. K		
N$_2$	7	14.007(2)	0.49976	61.1	89.7	37.99	(1.825)	0.807(1.165)	63.15	77.29	1.20
O$_2$	8	15.999(3)	0.50002	61.3	90.2	34.24	(1.801)	1.141(1.332)	54.36	90.20	1.22
F$_2$	9	18.998403163(6)	0.47372	65.0	97.4	32.93	(1.676)	1.507(1.580)	53.53	85.03	
Ne	10	20.1797(6)	0.49555	65.7	99.0	28.93	(1.724)	1.204(0.839)	24.56	27.07	1.09
N	13	26.9815385(7)	0.48181	69.7	107.2	24.01	1.615	2.699	933.5	2792.	
Al	13	26.9815385(7)	0.48181	69.7	107.2	24.01	1.615	2.699	933.5	2792.	
Si	14	28.0855(3)	0.49848	70.2	108.4	21.82	1.664	2.329	1687.	3538.	3.95
Cl$_2$	17	35.453(2)	0.47951	73.8	115.7	19.28	(1.630)	1.574(2.980)	171.6	239.1	
Ar	18	39.948(1)	0.45059	75.7	119.7	19.55	(1.519)	1.396(1.662)	83.81	87.26	1.23
Ti	22	47.867(1)	0.45961	78.8	126.2	16.16	1.477	4.540	1941.	3560.	
Fe	26	55.845(2)	0.46557	81.7	132.1	13.84	1.451	7.874	1811.	3134.	
Cu	29	63.546(3)	0.45636	84.2	137.3	12.86	1.403	8.960	1358.	2835.	
Ge	32	72.630(1)	0.44053	86.9	143.0	12.25	1.370	5.323	1211.	3106.	
Sn	50	118.710(7)	0.42119	98.2	166.7	8.82	1.263	7.310	505.1	2875.	
Xe	54	131.293(6)	0.41129	100.8	172.1	8.48	(1.255)	2.953(5.483)	161.4	165.1	1.39
W	74	183.84(1)	0.40252	110.4	191.9	6.76	1.145	19.300	3695.	5828.	
Pt	78	195.084(9)	0.39983	112.2	195.7	6.54	1.128	21.450	2042.	4098.	
Au	79	196.966569(5)	0.40108	112.5	196.3	6.46	1.134	19.320	1337.	3129.	
Pb	82	207.2(1)	0.39575	114.1	199.6	6.37	1.122	11.350	600.6	2022.	
U	92	[238.02891(3)]	0.38651	118.6	209.0	6.00	1.081	18.950	1408.	4404.	
Air (dry, 1 atm)			0.49919	61.3	90.1	36.62	(1.815)	(1.205)		78.80	1.0003
Shielding concrete			0.50274	65.1	97.5	26.57	1.711	2.300			
Borosilicate glass (Pyrex)			0.49707	64.6	96.5	28.17	1.696	2.230			
Lead glass			0.42101	95.9	158.0	7.87	1.255	6.220			
Standard rock			0.50000	66.8	101.3	26.54	1.688	2.650			
Methane (CH$_4$)			0.62334	54.0	73.8	46.47	(2.417)	(0.667)	90.68	111.7	
Ethane (C$_2$H$_6$)			0.59861	55.0	75.9	45.66	(2.304)	(1.263)	90.36	184.5	
Propane (C$_3$H$_8$)			0.58962	55.3	76.7	45.37	(2.262)	0.493(1.868)	85.52	231.0	
Butane (C$_4$H$_{10}$)			0.59497	55.5	77.1	45.23	(2.278)	(2.489)	134.9	272.6	
Octane (C$_8$H$_{18}$)			0.57778	55.8	77.8	45.00	2.123	0.703	214.4	398.8	
Paraffin (CH$_3$(CH$_2$)$_{n\approx23}$CH$_3$)			0.57275	56.0	78.3	44.85	2.088	0.930			
Nylon (type 6, 6/6)			0.54790	57.5	81.6	41.92	1.973	1.18			
Polycarbonate (Lexan)			0.52697	58.3	83.6	41.50	1.886	1.20			
Polyethylene ([CH$_2$CH$_2$]$_n$)			0.57034	56.1	78.5	44.77	2.079	0.89			
Polyethylene terephthalate (Mylar)			0.52037	58.9	84.9	39.95	1.848	1.40			
Polyimide film (Kapton)			0.51264	59.2	85.5	40.58	1.820	1.42			
Polymethylmethacrylate (acrylic)			0.53937	58.1	82.8	40.55	1.929	1.19			1.49
Polypropylene			0.55998	56.1	78.5	44.77	2.041	0.90			
Polystyrene ([C$_6$H$_5$CHCH$_2$]$_n$)			0.53768	57.5	81.7	43.79	1.936	1.06			1.59
Polytetrafluoroethylene (Teflon)			0.47992	63.5	94.4	34.84	1.671	2.20			
Polyvinyltoluene			0.54141	57.3	81.3	43.90	1.956	1.03			1.58
Aluminum oxide (sapphire)			0.49038	65.5	98.4	27.94	1.647	3.970	2327.	3273.	1.77
Barium flouride (BaF$_2$)			0.42207	90.8	149.0	9.91	1.303	4.893	1641.	2533.	1.47
Bismuth germanate (BGO)			0.42065	96.2	159.1	7.97	1.251	7.130	1317.		2.15
Carbon dioxide gas (CO$_2$)			0.49989	60.7	88.9	36.20	1.819	(1.842)			
Solid carbon dioxide (dry ice)			0.49989	60.7	88.9	36.20	1.787	1.563	Sublimes at 194.7 K		
Cesium iodide (CsI)			0.41569	100.6	171.5	8.39	1.243	4.510	894.2	1553.	1.79
Lithium fluoride (LiF)			0.46262	61.0	88.7	39.26	1.614	2.635	1121.	1946.	1.39
Lithium hydride (LiH)			0.50321	50.8	68.1	79.62	1.897	0.820	965.		
Lead tungstate (PbWO$_4$)			0.41315	100.6	168.3	7.39	1.229	8.300	1403.		2.20
Silicon dioxide (SiO$_2$, fused quartz)			0.49930	65.2	97.8	27.05	1.699	2.200	1986.	3223.	1.46
Sodium chloride (NaCl)			0.47910	71.2	110.1	21.91	1.847	2.170	1075.	1738.	1.54
Sodium iodide (NaI)			0.42697	93.1	154.6	9.49	1.305	3.667	933.2	1577.	1.77
Water (H$_2$O)			0.55509	58.5	83.3	36.08	1.992	1.000	273.1	373.1	1.33
Silica aerogel			0.50093	65.0	97.3	27.25	1.740	0.200	(0.03 H$_2$O, 0.97 SiO$_2$)		

C Physical and Astrophysical Constants

Quantity	Symbol, Equation	Value
Speed of light in vacuum	c	299 792 458 m s^{-1}
Planck constant	h	6.626 070 040(81)$\times 10^{-34}$ J s
Planck constant, reduced	$\hbar = h/2\pi$	1.054 571 800(13)$\times 10^{-34}$ J s
		$= 6.582\ 119\ 514(40)\ \times 10^{-22}$ MeV s
electron charge magnitude	e	1.602 176 6208(98) $\times 10^{-19}$ C
conversion constant	$\hbar c$	197.326 9788(12) MeV fm
conversion constant	$(\hbar c)^2$	0.389 379 3656(48) GeV^2 mbarn
electron mass	m_e	0.510 998 9461(31) MeV/c^2
		$=9.109\ 383\ 56(11)\times 10^{-31}$ kg
proton mass	m_p	938.272 0813(58) MeV/c^2
		1.672 621 898(21)$\times 10^{-27}$ kg
unified atomic mass unit (u)	$m(^{12}\text{C atom})/12 = (1\text{ g})/(N_A\text{ mol})$	931.494 0954(57) MeV/c^2
		$= 1.660\ 539\ 040(20)\times 10^{-27}$ kg
permittivity of free space	$\epsilon_0 = 1/\mu_0 c^2$	8.854 187 817 $\ldots \times 10^{-12}$ F m^{-1}
permeability of free space	μ_0	$4\pi \times 10^{-7}$ N A^{-2}
fine-structure constant $(Q^2=0)$	$\alpha = e^2/4\pi\epsilon_0\hbar c$	7.297 352 5664(17)$\times 10^{-3} \simeq 1/137$
classical electron radius	$r_e = e^2/4\pi\epsilon_0 m_e c^2$	2.817 940 3227(19)$\times 10^{-15}$ m
(e$^-$ Compton wavelength)/2	$\lambda_e = \hbar/m_e c = r_e \alpha^{-1}$	3.861 592 6764(18)$\times 10^{-13}$ m
Bohr radius (mnucleus $= \infty$)	$a_\infty = 4\pi\epsilon_0\hbar^2/m_e e^2$	0.529 177 210 67(12)$\times 10^{-10}$ m
wavelength of 1 eV/c particle	$hc/(1\text{ eV})$	1.239 841 9739(76)$\times 10^{-6}$ m
Rydberg energy	$hcR_\infty = m_e e^4/2(4\pi\epsilon_0)^2\hbar^2 = m_e c^2\alpha^2/2$	3.605 693 009(84) eV
Thomson cross section	$\sigma_T = 8\pi r_e^2/3$	0.665 245 871 58(91) barn
Bohr magneton	$\mu B = e\hbar/2m_e$	5.788 381 8012(26)$\times 10^{-11}$ MeV T^{-1}
nuclear magneton	$\mu N = e\hbar/2m_p$	3.152 451 2550(15)$\times 10^{-14}$ MeV T^{-1}
gravitational constant	G	6.674 08(31)$\times 10^{-11}$ m^{3}kg^{-1}s^{-2}
		$= 6.708\ 61(31)\times 10^{-39}\ \hbar c$ (GeV/c^2)$^{-2}$
standard gravitational accel.	g_N	9.806 65 m s^{-2}
Avogadro constant	N_A	6.022 140 857(74)$\times 10^{23}$ mol^{-2}
Boltzmann constant	k_B	1.380 648 52(79)$\times 10^{-23}$ J K^{-1}
		$= 8.617\ 3303(50)\times 10^{-5}$ eV K^{-1}
molar volume, ideal gas at STP	$N_A k_B \times 273.15\text{K}/101325$ Pa	22.413 962(13)$\times 10^{-3}$ m^{3}mol^{-1}
Wien displacement law constant	$b = \lambda_{max}T$	2.897 7729(17)$\times 10^{-3}$ m K
Stefan-Boltzmann constant	$\sigma = \pi^2 k_B^4/60\hbar^3 c^2$	5.670 367(13)$\times 10^{-3}$ W m^{-2}K^{-4}
Fermi coupling constant	$G_F/(\hbar c)^3$	1.166 378 7(6)$\times 10^{-5}$ GeV^{-2}
weak-mixing angle	$\sin^2\hat\theta(M_Z)_{(\overline{MS})}$	
$W^\pm$ boson mass	m_W	80.385(15) GeV/c^2
Z boson mass	m_Z	91.1876(21) GeV/c^2
strong coupling constant	$\alpha_s(m_Z)$	0.1182(12)

$\pi \simeq 3.141592653589793$	e $\simeq 2.718\ 281\ 828\ 459\ 045$	$\gamma \simeq 0.577215664901532$

1 in $\equiv 0.0254$ m	1 G $\equiv 10^{-4}$ T	1 eV = 1.602 176 6208(98)$\times 10^{-19}$ J
$k_B T$ at 300 K = $[38.681\ 740(22)]^{-1}$ eV	1 °A $\equiv 0.1$nm	1 dyne $\equiv 10^{-5}$ N
1 eV/c^2 = 1.782 661 907(11) $\times 10^{-36}$ kg	0 °C $\equiv 273.15$ K	1 barn $\equiv 10^{-28}$ m^2
1 erg $\equiv 10^{-7}$ J	2.997 924 58$\times 10^9$ esu = 1C	1 atmosphere $\equiv 760$ Torr $\equiv 101\ 325$ Pa

Quantity	Symbol, Equation	Value
Planck mass	$\sqrt{\hbar c/G}$	$1.220\ 910(29)\times10^{19}$ GeV/c^2=$2.176\ 47(5)\times10^{-8}$kg
Planck length	$\sqrt{\hbar G/c^3}$	$1.616\ 229(38)\ \times10^{-35}$ m
tropical year (equinox to equinox) (2011)	yr	$31\ 556\ 925.2$ s $\approx \pi\times10^7$ s
sidereal year (fixed star to fixed star) (2011)		31558149.8 s $\approx \pi\times10^7$ s
astronomical unit	au	$149\ 597\ 870\ 700$ m
parsec (1 au/1 arc sec)	pc	$3.08567758149\times10^{16}$ m $= 3.262$ ...ly
light year (deprecated unit)	ly	0.3066 pc$=0.946053\ \times10^{16}$ m
Solar mass	$M_\odot$	$1.988\ 48(9)\ \times10^{30}$ kg
Schwarzschild radius of the Sun	$2GM_\odot/c^2$	2.953 km
nominal Solar equatorial radius	$R_\odot$	$6.957\ \times10^8$m
nominal Solar constant	$S_\odot$	1361 W m^{-2}
nominal Solar photosphere temperature	$T_\odot$	5772 K
nominal Solar luminosity	$\mathcal{L}_\odot$	$3.828\ \times10^{26}$ W
Earth mass	$M_\oplus$	$5.972\ 4(3)\ \times10^{24}$ kg
Schwarzschild radius of the Earth	2G M$_\oplus$/2c^2	8.870 mm
nominal Earth equatorial radius	$R_\oplus$	6.3781×10^6m
jansky (flux density)	Jy	10^{-26} W m^{-2} Hz^{-1}
Solar angular velocity around the GC	Θ_0/R_0	$30.3\ \pm0.9$ km s^{-1} kpc^{-1}
Solar distance from GC	R_0	$8.00\ \pm0.25$ kpc
circular velocity at R_0	v_0 or Θ_0	$254(16)$ km s^{-1}
escape velocity from Galaxy	v_{esc}	498 km/s $< v_{esc} < 608$ km/s
local disk density	ρ_{disk}	$312\ \times10^{-24}$ g cm$^{-3} \approx 27$ GeV/c^2 cm^{-3}
local dark matter density	ρ_χ	canonical value 0.4 GeV/c^2 cm^{-3} within factor ~2
present day CMB temperature	T_0	$2.7255(6)$ K
present day CMB dipole amplitude	d	$3.3645(20)$ mK
Solar velocity with respect to CMB	$v_\odot$	$370.09(22)$ km s^{-1}
		towards $(\ell,b) = (263.00(3)^\circ, 48.24(2)^\circ)$
Local Group velocity with respect to CMB	v_{LG}	$627(22)$ km s^{-1} towards $(\ell,b) = (276(3)^\circ, 430(3)^\circ)$
number density of CMB photons	η_γ	$410.7(3)$ (T/2.7255)^3 cm^{-3}
density of CMB photons	ρ_γ	$4.645(4)$(T/2.7255)$^4 \times 10^{-34}$ g/cm$^3 \approx 0.260$ eV/cm^3
entropy density/Boltzmann constant	s/k	$2\ 891.2$ (T/2.7255)^3 cm^{-3}
present day Hubble expansion rate	H_0	$100\ h$ km s^{-1} Mpc$^{-1} = h\times$ (9.777 752 Gyr)$^{-1}$
scale factor for Hubble expansion rate	h	$0.678(9)$
Hubble length	c/H_0	$0.925\ 0629 \times 10^{26}\ h^{-1}$ m$=1.374(18) \times 10^{26}$ m
scale factor for cosmological constant	$c^2/3\ H^2_0$	$2.85247 \times 10^{51}\ h^{-2}$ m$^2 = 6.20(17) \times 10^{51}$ m^2
critical density of the Universe	$\rho_{crit} = 3H_0^2/8\pi G$	$1.878\ 40(9) \times 10^{-29}\ h^2$ g cm^{-3}
		$= 1.053\ 71(5) \times 10^5\ h^2$ (GeV/c^2) cm^{-3}
		$= 2.775\ 37(13) \times 10^{11}\ h^2$ M$_\odot$ Mpc^{-3}
baryon-to-photon ratio (from BBN)	$\eta=\eta_b/\eta_\gamma$	$5.8 \times 10^{-10} \le \eta \le 6.6 \times 10^{-10}$ (95 % CL)
number density of baryons	η_b	$2.503(26) \times 10^{-7}$ cm^{-3}
		$(2.4 \times 10^{-7} <$n$_b <2.7 \times10^{-7})$ cm^{-3}(95% CL)
CMB radiation density of the Universe	$\Omega_\gamma = \rho_\gamma/\rho_{crit}$	2.473×10^{-5} (T/2.7255)$^4\ h^{-2}= 5.38(15) \times10^{-5}$
baryon density of the Universe	$\Omega_b=\rho_b/\rho_{crit}$	$0.02226(23)h^{-2} = 0.0484(10)$
cold dark matter density of the Universe	$\Omega_c = \rho_c/\rho_{crit}$	$0.1186(20)\ h^{-2} = 0.258(11)$
reionization optical depth	τ	$0.066(16)$
scalar spectral index	n_s	$0.968(6)$
dark energy density of the Universe	Ω_Λ	0.692 ± 0.012
fluctuation amplitude at 8 h^{-1} Mpc scale	σ_8	0.815 ± 0.009
redshift of matter-radiation equality	z_{eq}	3365 ± 44
redshift at which optical depth equals unity	z_*	1089.9 ± 0.4
comoving size of sound horizon at z_*	r_*	144.9 ± 0.4 Mpc
age when optical depth equals unity	t_*	373 kyr
redshift at half reionization	z_{reion}	$8.8^{+1.7}_{-1.4}$
redshift when acceleration was zero	z_q	≈ 0.65
age of the Universe	t_0	13.80 ± 0.04 Gyr
effective number of neutrinos	N_{eff}	3.13 ± 0.32
sum of neutrino masses	$\sum m_\nu$	<0.68 eV (Planck CMB); > 0.06 eV (mixing)
curvature	Ω_K	$-0.005^{+0.016}_{-0.017}$(95 %CL)
primordial helium fraction	Y_p	0.245 ± 0.004

D Particle Properties

Gauge Bosons

The gauge bosons all have $J^P = 1^-$.

Particle	Mass	Width	Decay Mode	Fraction (%)
g	0 (assumed)	stable		
γ	0	stable		
$W^\pm$	80.4 GeV/c^2	2.1 GeV/c^2	hadrons	67.41(27)
			$e^+\nu_e$	10.71(16)
			$\mu^+\nu_\mu$	10.63(15)
			$\tau^+\nu_\tau$	11.38(27)
Z	91.2 GeV/c^2	2.5 GeV/c^2	hadrons	69.91(6)
			$\nu_\ell + \bar{\nu}_\ell (all\ \ell)$	20.00(6)
			e^+e^-	3.363(4)
			$\mu^+\mu^-$	3.366(7)
			$\tau^+\tau^-$	3.370(8)

Higgs boson ($J^P = 0^+$)

Particle	Mass	Width
H	125.09(24) GeV/c^2	< 13 MeV/c^2 (~ 4 /MeV/c^2?)

Leptons

All leptons have $J^P = \frac{1}{2}^+$.

Particle	Mass (MeV/c^2)	Lifetime (s)	Decay Mode	Fraction (%)
ν_e	$< 2 \times 10^{-6}$	Stable		
ν_μ	<0.19	Stable		
ν_τ	<18.2	Stable		
$e^\pm$	0.511	Stable		
$\mu^\pm$	105.66	2.197×10^{-6}	$e^+\nu_e\bar{\nu}_v$	≈ 100
$\tau^\pm$	1776.84(12)	$(290.3 \pm 0.5) \times 10^{-15}$	hadrons $+\nu_\tau$	~ 64
			$e^+\nu_e\bar{\nu}_\tau$	17.82(4)
			$\mu^+\nu_\mu\bar{\nu}_\tau$	17.39(4)

Low-Lying Baryons

Particle	I, J^P	Mass (MeV/c^2)	Lifetime or width	Decay Mode	Fraction (%)

Unflavoured states of light quarks ($S = C = B = 0$)
Quark content:
$N = (p, n) : p = uud, n = udd; \Delta^{++} = uuu, \Delta^+ = uud, \Delta^0 = udd, \Delta^- = ddd$

Particle	I, J^P	Mass (MeV/c^2)	Lifetime or width	Decay Mode	Fraction (%)
p	$\frac{1}{2}, \frac{1}{2}^+$	938.272081(6)	$> 2.1 \times 10^{29}$ yr		
n	$\frac{1}{2}, \frac{1}{2}^+$	939.565413(6)	880.2(10) s	$pe^-\bar{\nu}_e$	100
Δ	$\frac{3}{2}, \frac{3}{2}^+$	1232(1)	117(2) MeV	$N\pi$	99.4

Strange baryons (S = -1, C = B = 0)

Quark content: $\Lambda = uds : \Sigma^+ = uus, \Sigma^0 = uds, \Sigma^- = dds$, similarly for Σ^*s.

Particle	I, J^P	Mass (MeV/c^2)	Lifetime or width	Decay Mode	Fraction (%)
Λ	$0, \frac{1}{2}^+$	1115.683(6)	$2.632(20) \times 10^{-10}$ s	$p\pi^-$	63.9(5)
				$n\pi^0$	35.8(5)
Σ^+	$1, \frac{1}{2}^+$	1189.37(7)	$8.018(26) \times 10^{-11}$ s	$p\pi^0$	51.57(30)
				$n\pi^+$	48.31(30)
Σ^0	$1, \frac{1}{2}^+$	1192.642(24)	$7.4(7) \times 10^{-20}$ s	$\Lambda\gamma$	100
Σ^-	$1, \frac{1}{2}^+$	1197.449(30)	$1.479(11) \times 10^{-10}$ s	$n\pi^-$	99.848(5)
Σ^{*+}	$1, \frac{3}{2}^+$	1382.8(4)	37.0(7) MeV	$\Lambda\pi$	87.0(15)
				$\Sigma\pi$	11.7(15)
Σ^{*0}	$1, \frac{3}{2}^+$	1383.7(10)	36(5) MeV	as above	
Σ^+	$1, \frac{3}{2}^+$	1387.2(5)	39.4(21) MeV	as above	

Strange baryons (S = -2, C = B = 0)

Quark content: $\Xi^0 = uss, \Xi^- = dss$, similarly for Ξ^*s.

Particle	I, J^P	Mass (MeV/c^2)	Lifetime or width	Decay Mode	Fraction (%)
Ξ^0	$\frac{1}{2}, \frac{1}{2}^+$	1314.86(20)	$2.90(9) \times 10^{-10}$ s	$\Lambda\pi^0$	99.524(12)
Ξ^-	$\frac{1}{2}, \frac{1}{2}^+$	1321.71(7)	$1.639(15) \times 10^{-10}$ s	$\Lambda\pi^-$	99.887(35)
Ξ^{*0}	$\frac{1}{2}, \frac{3}{2}^+$	1531.80(32)	9.1(5) MeV	$\Xi\pi$	100
Ξ^{*-}	$\frac{1}{2}, \frac{3}{2}^+$	1535.0(6)	9.9(18) MeV	as above	

Low-Lying Baryons

Particle	I, J^P	Mass (MeV/c^2)	Lifetime or width	Decay Mode	Fraction (%)

Strange baryons (S = -3, C = B = 0)

Quark content: $\Omega^- = sss$

Particle	I, J^P	Mass (MeV/c^2)	Lifetime or width	Decay Mode	Fraction (%)
Ω^-	$0, \frac{3}{2}^+$	1672.45(29)	$8.21(11) \times 10^{-11}$ s	ΛK^-	67.8(7)
				$\Xi^0 \pi^-$	23.6(7)
				$\Xi^- \pi^0$	8.6(4)

Charmed baryons (S = 0, C = +1, B = 0)

Quark content: $\Lambda_c^+ = udc : \Sigma^{++} = uuc, \Sigma^+ = udc, \Sigma^- = ddc$, similarly for Σ_c^*s.

Particle	I, J^P	Mass (MeV/c^2)	Lifetime or width	Decay Mode	Fraction (%)
Λ_c^+	$0, \frac{1}{2}^+$	2286.46(14)	$2.00(6) \times 10^{-13}$ s	$n + X$	50(16)
				$p + X$	50(16)
				$\Lambda + X$	35(11)
				$\Sigma^\pm + X$	10(5)
				$e^+ + X$	4.5(17)
Σ_c^{++}	$1, \frac{1}{2}^+$	2453.97(14)	1.89(14) MeV	$\Lambda_c^+ \pi^+$	≈ 100
Σ_c^+	$1, \frac{1}{2}^+$	2452.9(4)	< 4.6 MeV		
Σ_c^0	$1, \frac{1}{2}^+$	2453.75(14)	1.83(15) MeV		
Σ_c^{*++}	$1, \frac{3}{2}^+$	2518.41(20)	14.78(35) MeV	$\Lambda_c^+ \pi^+$	≈ 100
Σ_c^{*+}	$1, \frac{3}{2}^+$	2517.5(23)	< 17 MeV		
Σ_c^{*0}	$1, \frac{3}{2}^+$	2518.48(20)	15.3(4) MeV		

Charmed strange baryons (S = -1, -2, C = +1, B = 0)

Quark content: $\Xi_c^+ = usc, \Xi_c^0 = dsc$, similarly for Ξ_c^* s; $\Omega_c^0 = ssc$

Particle	I, J^P	Mass (MeV/c^2)	Lifetime or width	Decay Mode	Fraction (%)
Ξ_c^+	$\frac{1}{2}, \frac{1}{2}^+$	2467.87(30)	$4.42(26) \times 10^{-13}$ s		
Ξ_c^0	$\frac{1}{2}, \frac{1}{2}^+$	2470.87(29)	$1.12(11) \times 10^{-13}$ s		
Ω_c^0	$\frac{1}{2}, \frac{1}{2}^+$	2695.2(17)	$6.9(1.2) \times 10^{-14}$ s		
Ξ_c^{*+}	$\frac{1}{2}, \frac{3}{2}^+$	2645.53(31)	2.14(19) MeV		
Ξ_c^{*0}	$\frac{1}{2}, \frac{3}{2}^+$	2646.32(31)	2.35(22) MeV		

Bottom baryons ($S = C = 0, B = -1$)

Quark content: $\Lambda_b^0 = udb, \Xi_b^0 = usb, \Xi_b^- = dsb$

Particle	I, J^P	Mass (MeV/c^2)	Lifetime or width	Decay Mode	Fraction (%)
Λ_b^0	$0, \frac{1}{2}^+$	5619.58(17)	1.47(01) ps	$\Lambda_c^+ + X$	$\sim 11.5(2)$
Ξ_b^0	$\frac{1}{2}, \frac{1}{2}^+$	5791.9(5)	1.479(31) ps		
Ξ_b^-	$\frac{1}{2}, \frac{1}{2}^+$	5794.5(14)	1.571(40) ps		

Low-Lying Mesons

Particle	I, J^{PC}	Mass (MeV/c^2)	Lifetime or width	Decay Mode	Fraction (%)

Unflavored states of light quarks ($S = C = B = 0$)
Quark content:
$I = 1$ states, $u\bar{d}$, $\frac{1}{\sqrt{2}}(u\bar{u} - d\bar{d})$, $d\bar{u}$; $I = 0$ states, $c_1(u\bar{u} - d\bar{d}) + c_2 s\bar{s}(c_{1,2}$ are constants)

Particle	I, J^{PC}	Mass (MeV/c^2)	Lifetime or width	Decay Mode	Fraction (%)
$\pi^\pm$	$1, 0^-$	139.57061(24)	$2.6033(5) \times 10^{-8}$ s	$\mu^+\nu_\mu$	99.98770(4)
π^0	$1, 0^{-+}$	134.9770(5)	$8.52(18) \times 10^{-17}$ s	$\gamma\gamma$	98.823(34)
η	$0, 0^{-+}$	547.862(17)	1.31(5) keV	$\gamma\gamma$	39.41(20)
				$\pi^0\pi^0\pi^0$	32.68(23)
				$\pi^+\pi^-\pi^0$	22.92(28)
				$\pi^+\pi^-\gamma$	4.22(8)
ρ	$1, 1^{--}$	775.26(25)	149.1(8) MeV	$\pi\pi$	≈ 100
ω^0	$0, 1^{--}$	782.65(12)	8.49(8) MeV	$\pi^+\pi^-\pi^0$	89.2(7)
				$\pi^0\gamma$	8.40(22)
η'	$0, 0^{-+}$	957.78(6)	0.196(9) MeV	$\pi^+\pi^-\eta$	42.6(7)
				$\rho^0\gamma$	28.9(5)
				$\pi^0\pi^0\eta$	22.8(8)
				$\omega\gamma$	2.62(13)
ϕ	$0, 1^{--}$	1019.460(16)	4.247(16) MeV	K^+K^-	48.9(5)
				$K^0_L + K^0_S$	34.2(4)
				$\rho\pi + \pi^+\pi^-\pi^0$	15.32(32)

Strange mesons ($S = \pm 1, C = B = 0$)
Quark content: $K^+ = u\bar{s}$, $K^0 = d\bar{s}$, $\bar{K}^0 = s\bar{d}$, $K^- = s\bar{u}$, similarly for K^*s

Particle	I, J^{PC}	Mass (MeV/c^2)	Lifetime or width	Decay Mode	Fraction (%)
$K^\pm$	$\frac{1}{2}, 0^-$	493.677(16)	$1.2380(20) \times 10^{-8}$ s	$\mu^+\nu_\mu$	63.56 (11)
				$\pi + \pi^0$	20.67(8)
				$\pi + \pi^+\pi^-$	5.583(24)
				$\pi^0 e^+\nu_e$	5.07(4)
				$\pi^0\mu^+\nu_\mu$	3.352(33)
$K^0, \bar{K}^0$	$\frac{1}{2}, 0^-$	497.611(13)			
K^0_S			$8.954(4) \times 10^{-11}$ s	$\pi^+\pi^-$	69.20(5)
				$\pi^0\pi^0$	30.69(5)
K^0_L			$5.116(21) \times 10^{-8}$ s	$\pi^\pm e^\mp \nu_e(\bar{\nu}_e)$	40.55(11)
				$\pi^\pm \mu^\mp \bar{\nu}_\mu(\bar{\nu}_\mu)$	27.04(7)
				$\pi^0\pi^0\pi^0$	19.52(12)
				$\pi^+\pi^-\pi^0$	12.54(5)
$K^{*\pm}$	$\frac{1}{2}, 1^-$	891.76(25)	50.3(8) MeV	$K\pi$	~ 100
K^{*0}	$\frac{1}{2}, 1^-$	895.55(20)	47.3(5) MeV	$K\pi$	~ 100

Particle	I, J^{PC}	Mass (MeV/c^2)	Lifetime or width	Decay Mode	Fraction (%)

Charmed mesons ($S = 0, C = \pm1, B = 0$)
Quark content: $D^+ = c\bar{d}$, $D^0 = c\bar{u}$, $\bar{D}^0 = u\bar{c}$, $D^- = d\bar{c}$, similarly for D^*s

Particle	I, J^{PC}	Mass (MeV/c^2)	Lifetime or width	Decay Mode	Fraction (%)
$D^\pm$	$\frac{1}{2}, 0^-$	1869.59(9)	1.040(7) ps	$\bar{K}^0 + X$	61(5)
				$K^- + X$	25.7(14)
				$\bar{K}^{*0} + X$	23(5)
				$e^+ + X$	16.07(30)
				$\bar{K}^+ + X$	5.9(8)
$D^0, \bar{D}^0$	$\frac{1}{2}, 0^-$	1864.83(5)	$4.101(15) \times 10^{-13}$ s	$K^- + X$	54.7(28)
				$\bar{K}^0 + X$	47(4)
				$\bar{K}^{*0} + X$	9(4)
				$e^+ + X$	6.49(11)
				$K^+ + X$	3.4(4)
$D^{*\pm}$,	$\frac{1}{2}, 1^-$	2010.26(5)	83.4(18) keV	$D^0\pi^+$	67.7(5)
				$D^+\pi^0$	30.7(5)
$D^{*0}, \bar{D}^{*0}$	$\frac{1}{2}, 1^-$	2006.85(5)	< 2.1 MeV	$D^0\pi^0$	64.7(9)
				$D^0\gamma$	35.3(9)

Charmed strange mesons($S = C = \pm1 B = 0$)
Quark content: $D_s^+ = c\bar{s}$, $D_s^- = s\bar{c}$, similarly for D_s^*s

Particle	I, J^{PC}	Mass (MeV/c^2)	Lifetime or width	Decay Mode	Fraction (%)
$D_s^\pm$,	$0, 0^-$	1968.28(10)	$5.00(7) \times 10^{-13}$ s	$K^+ + X$	28.9(07)
				$K_s^0 + X$	19.0(11)
				$\phi + X$	15.07(10)
				$K^- + X$	18.7(5)
				$e^+ + X$	6.5(4)
				$\tau\nu_\tau$	5.48(23)
$D^{*\pm}$	$0, 1^-$	2112.1(4)	< 1.9 MeV	$D_s^+\gamma$	93.5(7)
				$D_s^+\pi^0$	5.8(7)

Particle	I, J^{PC}	Mass (MeV/c^2)	Lifetime or width	Decay Mode	Fraction (%)

Bottom strange mesons ($S = \pm1, C = 0, B = \pm1$)
Quark content: $B_s^0 = s\bar{b}$, $B_s^0 = b\bar{s}$

Particle	I, J^{PC}	Mass (MeV/c^2)	Lifetime or width	Decay Mode	Fraction (%)
$B_s^0, \bar{B}_s^0$	$0, 0^-$	5366.89(19)	1.505(05) ps	$D_s^- + X$	93(25)
				$D_s^-\ell^+\nu_\ell + X$	8.1(13)

Bottom charmed mesons ($S = 0, B = C = \pm1$)
Quark content: $B_c^+ = c\bar{b}$, $B_c^- = b\bar{c}$

Particle	I, J^{PC}	Mass (MeV/c^2)	Lifetime or width	Decay Mode	Fraction (%)
$B_c^\pm$	$0, 0^-$	6274.9(8)	$5.07(12) \times 10^{-13}$ s		

$c\bar{c}$ mesons

Particle	I, J^{PC}	Mass (MeV/c^2)	Lifetime or width	Decay Mode	Fraction (%)
$J/\psi(1S)$	$0, 1^{--}$	3096.900(6)	92.9(28) keV	hadrons	87.7(5)
				e^+e^-	5.971(32)
				$\mu^+\mu^-$	5.961(33)

$b\bar{b}$ mesons

Particle	I, J^{PC}	Mass (MeV/c^2)	Lifetime or width	Decay Mode	Fraction (%)
$\Upsilon(1S)$	$0, 1^{--}$	9460.30(26)	54.02(125) keV	$\eta' + X$	2.94(24)
				$\tau^+\tau^-$	2.60(10)
				e^+e^-	2.38(11)
				$\mu^+\mu^-$	2.48(5)

Index